



University
of Glasgow

Stortz, Jennifer Ann (2017) *Identification and characterisation of novel Trypanosoma brucei protein kinases involved in repair of cellular damage*. PhD thesis.

<http://theses.gla.ac.uk/8055/>

Copyright and moral rights for this work are retained by the author

A copy can be downloaded for personal non-commercial research or study, without prior permission or charge

This work cannot be reproduced or quoted extensively from without first obtaining permission in writing from the author

The content must not be changed in any way or sold commercially in any format or medium without the formal permission of the author

When referring to this work, full bibliographic details including the author, title, awarding institution and date of the thesis must be given

Enlighten:Theses
<http://theses.gla.ac.uk/>
theses@gla.ac.uk

**Identification and
characterisation of novel
Trypanosoma brucei
protein kinases involved
in repair of cellular damage**

Jennifer Ann Stortz

BSc (Hons)

Submitted in fulfilment of the requirements for the
Degree of Doctor of Philosophy

Wellcome Trust Centre for Molecular Parasitology
Institute of Infection, Immunity and Inflammation
College of Medical Veterinary and Life Sciences
University of Glasgow

April 2017

Abstract

Under genotoxic stress conditions, the genome of any organism may become compromised thus undermining cellular functions and the high fidelity transmission of the genome. Should integrity become compromised, cells have evolved a plethora of pathways to monitor, assess and direct the removal or bypass of genomic lesions. Collectively, this response is known as the DNA damage response (DDR). At the forefront of the DDR are specialised enzymes known as protein kinases (PKs), which act to co-ordinate many aspects of this response.

In the kinetoplastid parasite *Trypanosoma brucei*, the role of PKs in other processes, such as the control of the cell cycle and during differentiation between the mammalian and insect lifecycle stages, have already been investigated using mutant cells lines, RNA interference (RNAi) and genome wide and kinome focused screens. However, virtually no work has examined the role of PKs in the context of genome repair. To this end, two RNAi targeted screens (RITseqs), one to examine the genome as a whole and the other to focus directly on the kinome compliment, were performed by others in the mammalian infection stage of *T. brucei*, searching for genes whose loss sensitises the cells to the presence of the DNA alkylating agent Methyl methanesulfonate (MMS).

To validate both screens here, putative DNA damage associated PKs were examined by RNA interference (RNAi). Across both screens, a total of eleven PKs, whose loss sensitised cells to MMS, were validated in this study by monitoring their proliferation. Amongst these novel PKs were a pseudokinase (Tb6560) and an aurora kinase (TbAUK2), whose functions were investigated using disruption mutants generated in BSF *T. brucei* cells combined with immunolocalisation. Analysis of the Tb6560 mutants revealed the pseudokinase to be non-essential *in vitro* and uncovered a potential role for Tb6560 during endocytosis or internal trafficking. Analysis of the TbAUK2 mutants also revealed this PK to be non-essential *in vitro*. However, when exposed to a variety of genotoxic agents, the growth of the mutants was significantly reduced suggesting TbAUK2 is required for parasite survival under DNA damage conditions. Further phenotypic analysis revealed a potential role for TbAUK2 in the maintenance of the parasite's nuclear genome.

Additionally, the roles of two PKs central to the DDR in other organisms were examined by RNAi. The atypical PKs Ataxia Telangiectasia Mutated (ATM) and the related PK ATM and Rad3 related (ATR) are activated in response to double stranded break (DSB) lesions or replicative lesions, respectively, in other eukaryotes. RNAi of TbATR was associated with perturbation of proliferation, extensive nuclear defects and sensitivity to genotoxic agents. Further analysis also revealed a potential role for this kinase in maintaining transcriptional silencing of bloodstream VSG expression sites (BESs). Conversely, RNAi of TbATM did not disrupt cellular proliferation *in vitro* and nor were TbATM deficient cells sensitised to alkylating or replication blocking agents, suggesting TbATM is not required for *T. brucei* survival or for maintenance of growth in these conditions.

Collectively, these data reveal a diverse array of PKs required for genome maintenance, in BSF parasites, under genotoxic stress conditions. An indepth characterisation of three DNA damage associated PKs uncovered a variety of putative roles ranging from nuclear and chromosomal segregation to cell cycle regulation, proliferation and endocytosis. These data in particular highlight the complexity underpinning a cell's response when threatened with genomic instability. Furthermore, depletion of one kinase, TbATR, was also associated with loss of transcriptional silencing within BESs suggesting that PK activity could operate during antigenic variation, a process vital for the persistence of this parasite within a host.

Table of Contents

Abstract	2
List of Tables	13
List of Figures	14
List of Accompanying Material.....	18
Acknowledgements	19
Author’s Declaration	21
List of Abbreviations and definitions	22
1 Introduction	27
1.1 The Kinetoplastida	28
1.1.1 HAT is a debilitating disease	29
1.1.1.1 Current HAT treatment options.....	31
1.2 The lifecycle of <i>T. brucei</i> ; a dixenous parasite	32
1.3 <i>T. brucei</i> : molecular biology.....	35
1.3.1 The cell body and cell cycle	35
1.4 Avoiding host clearance	39
1.4.1.1 The VSG Coat.....	40
1.4.1.2 <i>T. brucei</i> genome is unusually arranged	41
1.4.1.2.1 BESs.....	43
1.4.1.3 VSG switching.....	44
1.4.1.3.1 Monoallelic expression and transcriptional switching	44
1.4.1.3.2 Recombinational switching.....	46
1.4.1.4 Endocytosis as a method of immune evasion in <i>T. brucei</i>	51
1.5 Kinases and phosphorylation: Co-ordination of cellular communication	52
1.5.1 The human kinome; eukaryotic kinases and atypical kinases	52
1.5.1.1 Eukaryotic Protein Kinases (ePKs).....	52
1.5.1.2 Atypical Protein kinases (aPKs) and Protein Kinase Like (PKL) kinases.....	55
1.5.1.3 Pseudokinases: just a dead kinase?	55
1.5.1.4 Pseudokinases in parasitic organisms.....	56
1.5.2 The <i>T. brucei</i> kinome	56
1.5.2.1 Pseudokinases in <i>T. brucei</i>	58
1.6 DNA Repair and Damage	58
1.6.1.1 Replicative stress.....	60
1.6.2 DNA Repair in <i>T. brucei</i>	61
1.7 Project Objectives	62
2 Materials and Methods	64

2.1	General Bioinformatics	65
2.1.1	Sequence retrieval and examination	65
2.1.2	Homology searching, protein domain analysis and structure prediction	65
2.1.3	General Statistics.....	65
2.2	Molecular Techniques.....	66
2.2.1	Genomic DNA extraction and preparation	66
2.2.2	Agarose Gel.....	66
2.2.3	General Primer design	66
2.2.4	Polymerase Chain Reaction (PCR).....	66
2.2.5	DNA fragment purification	67
2.2.6	Restriction Digest.....	67
2.2.7	Fragment Ligation	68
2.2.8	Transformation of <i>E. coli</i>	68
2.2.9	Construct retrieval and confirmation.....	69
2.2.9.1	Plasmid DNA extraction from bacteria	69
2.2.9.2	Plasmid confirmation by sequencing and restriction digest analysis.....	69
2.3	Gateway® Cloning.....	70
2.4	Construct Design.....	70
2.4.1.1	Endogenous tagging.....	70
2.4.1.1.1	C-terminal	70
2.4.1.1.2	N-terminal tagging.....	71
2.4.1.2	KO constructs	73
2.4.1.3	RxP constructs.....	74
2.5	RNA protocols	75
2.5.1	RNA extraction.....	75
2.5.2	Complementary DNA (cDNA) Preparation	76
2.5.3	qRT-PCR analysis.....	76
2.5.3.1	qRT-PCR Primer design.....	76
2.5.3.2	qRT-PCR.....	77
2.6	RNAseq Analysis.....	77
2.6.1	Sample preparation and sequencing conditions for RNAseq.....	77
2.6.2	Bioinformatics analysis workflow.....	77
2.7	Trypanosome strains and culture	79
2.7.1	Strains	79
2.7.2	Medium and Maintenance of BSF Trypanosome growth <i>in vitro</i>	80
2.7.3	Preparation and stabilates revival	81
2.7.4	Calculating population doubling times	81

2.7.5	Transformation of BSF trypanosomes.....	82
2.7.6	Re-cloning of polyclonal BSF trypanosome populations.....	82
2.7.7	Preparation and retrieval of BSF trypanosomes for molecular biology procedures	82
2.8	BSF trypanosomes cell assays.....	83
2.8.1	Growth analysis of RNAi cell lines.....	83
2.8.2	Growth analysis of other cell lines.....	83
2.8.3	Cell cycle analysis by DAPI	84
2.8.4	Flow cytometry	84
2.9	Antibody and Dye concentrations	85
2.9.1	Immunofluorescence Analysis.....	85
2.9.2	Western blotting.....	85
2.10	Telo-FISH analysis	86
2.11	Microscopy techniques	87
2.11.1	DAPI staining.....	87
2.11.2	Generic IF analysis protocol	87
2.11.3	Mitotracker® staining	88
2.11.4	VSG staining protocol.....	88
2.11.5	Cytoskeletal extraction protocol	88
2.11.6	Tomato Lectin staining.....	89
2.11.7	EM protocols	89
2.11.7.1	SEM	90
2.11.7.2	TEM	90
2.11.7.3	Cryo-immunolabelling.....	90
2.11.8	Image Analysis and preparation.....	91
2.11.8.1	Image Capture.....	91
2.11.8.2	Image preparation	91
2.11.8.3	Quantification of signal intensity.....	92
2.12	Protein Protocols.....	92
2.12.1	Western Blotting	92
2.12.1.1	Sample preparation.....	92
2.12.1.2	Western blot protocol.....	92
2.12.1.3	Transfer protocol	93
2.12.1.4	Antibody detection	93
2.12.2	Immunoprecipitation	94
2.12.2.1	Specific amendments.....	95
2.12.3	Nanoflow HPLC Electrospray Tandem Mass Spectrometry (nLC-ESIMS/MS)	95

2.12.4	Sypro Ruby® staining of SDS-PAGE gels.....	95
2.12.5	Quantification of relative protein levels	96
3	Identifying novel DNA repair-associated protein kinases using RITseq screening	97
3.1	High throughput RNAi screening.....	98
3.1.1	HT-RNAi screening of <i>T. brucei</i>	98
3.1.1.1	<i>T. brucei</i> kinome screening	99
3.1.2	Using RNAi screens to de-convolve DNA damage-associated pathways 100	
3.2	Research Aims.....	100
3.3	Results	101
3.3.1	Screen workflow	101
3.3.1.1	Genome wide RITseq screen.....	101
3.3.1.2	Kinome wide RITseq screen	102
3.3.2	Bioinformatics analysis	103
3.3.2.1	Bioinformatics analysis of the genome wide RITseq screen.....	104
3.3.2.2	Bioinformatics analysis of the kinome wide RITseq screen.....	107
3.3.3	Biological validation of candidates	108
3.3.3.1	RNAi cell lines used for validation.....	109
3.3.3.2	Generation of C-terminal endogenously tagged RNAi lines	110
3.3.3.3	Construct generation and endogenously tagged RNAi cell line generation ...	110
3.3.3.4	Confirmation of endogenously tagged RNAi cell lines by western blot analysis 111	
3.3.4	Growth analysis of RITseq screen candidates	111
3.3.4.1	The genome wide candidates	112
3.3.4.2	The kinome RITseq candidates	114
3.3.5	Cell cycle analysis	115
3.3.5.1	Genome wide RITseq candidates.....	115
3.3.5.2	Kinome wide RITseq candidates	118
3.3.6	Analysis of the expression of γ H2A in the RNAi cell lines <i>in vitro</i> ..	120
3.3.6.1	The genome wide candidates	121
3.3.6.2	The kinome wide candidates	122
3.3.7	Localisation of endogenously myc-tagged kinases.....	123
3.3.7.1	Genome wide RITseq candidate localisation	124
3.3.7.1.1	Localisation of Tb927.10.7780 (TbKFR1)	124
3.4	Discussion	126
3.4.1	RITseq screening for DDR associated PKs in BSF <i>T. brucei</i> parasites 126	

3.4.2	Candidate validation: growth and cell cycle analysis	129
3.4.2.1	Genome wide candidates	129
3.4.2.2	Kinome wide candidates.....	130
3.4.2.3	False positive hits.....	132
3.4.3	Candidate Localisation.....	132
4	Dissecting the function of TbAUK2 in bloodstream form <i>T. brucei</i>	134
4.1	Introduction	135
4.1.1	Aurora Kinases	135
4.1.1.1	AUKA	136
4.1.1.2	AUKB	138
4.1.1.3	AUKC	139
4.2	Aurora Kinases in <i>T. brucei</i> ; what do we know?	139
4.3	Research Aims.....	141
4.4	Results	141
4.4.1	Bioinformatics analysis	141
4.4.1.1	BLAST analysis of TbAUK2.....	141
4.4.1.2	TbAUK2 harbours kinase specific motifs.....	142
4.4.1.3	The <i>T. brucei</i> Aurora Kinases.....	144
4.5	Generation of TbAUK2 null mutant cell lines	145
4.5.1	Gene knockout strategy	146
4.5.2	Integration of knockout constructs and confirmation of knockout clones using PCR analysis	146
4.5.3	Confirmation of knockout clones using qRT-PCR analysis	147
4.5.4	Phenotypic analysis of TbAUK2 ^{-/-} knockout mutant.....	148
4.5.4.1	Growth analysis and cell cycle analysis by DAPI <i>in vitro</i>	148
4.5.4.2	Analysis of the nucleus by DAPI counting and Electron microscopy	151
4.5.4.3	Loss of TbAUK2 is associated with loss of mitotic spindle formation.....	156
4.5.4.4	Morphological analysis of the TbAUK2 ^{-/-} knockout mutants	158
4.6	Analysis of the sensitivity of the TbAUK2 ^{-/-} knockout clones to DNA damaging.....	161
4.6.1	Growth analysis under DNA damage stress	161
4.6.2	Analysis of γH2A expression by IFA and western blot analysis.....	164
4.6.3	Analysis of RAD51 foci formation.....	165
4.7	Localisation of TbAUK2	168
4.7.1	Generation of a TbAUK2 ^{+/-12myc} cell line.....	168
4.7.2	Confirmation of a TbAUK2 ^{+/-12myc} cell line	168
4.7.3	Confirmation of C-terminal tag functionality by assessment of growth <i>in vitro</i>	169

4.7.4	TbAUK2 is a cell cycle regulated nuclear kinase	170
4.7.5	Super resolution analysis of TbAUK2 localisation and 3D reconstruction of localisation	173
4.7.6	Localisation of TbAUK2 following exposure to DNA damaging agents	175
4.8	Identification of potential interaction partners by immunoprecipitation	177
4.9	Re-expression of TbAUK2 in TbAUK2 ^{-/-} knockouts	179
4.9.1	Generation of the re-expresser construct	179
4.9.2	Generation of TbAUK2 ^{-/-/+} cell lines	180
4.9.3	Confirmation of TbAUK2 re-expression by PCR and qRT-PCR analysis	180
4.9.4	Characterisation of TbAUK2 re-expresser cell lines	182
4.9.4.1	Growth analysis in the absence and presence of MMS <i>in vitro</i>	182
4.10	Discussion	183
4.10.1	Insights from the bioinformatics analysis	183
4.10.2	TbAUK2 acts in aspects of mitosis, spindle formation and cellular morphology	185
4.10.2.1	Loss of TbAUK2 affects cell morphology	185
4.10.2.2	Loss of TbAUK2 affects spindle formation and mitosis	186
4.10.3	Loss of TbAUK2 is associated with increased sensitivity to genotoxic stress	188
4.10.4	TbAUK2 shows a punctate nuclear localisation	189
4.10.5	Identification of TbAUK2 interactors may guide functional analysis	190
4.10.6	A preliminary model of TbAUK2 function in BSF cells	191
5	Tb6560 is a pseudokinase that acts in bloodstream form endocytosis ...	194
5.1	Introduction	195
5.1.1	Numb Associated Kinases (NAKs)	195
5.1.1.1	The AP2 Complex and endocytosis	195
5.1.1.2	NAKs in humans	197
5.1.2	Previous reports of Tb6560 in the literature	198
5.2	Research Aims	199
5.3	Results	199
5.3.1	Bioinformatics Analysis	199
5.3.1.1	BLAST analysis of Tb6560	199
5.3.1.2	Tb6560 is a pseudokinase	204
5.3.2	Generation of Tb6560 knockout cell lines	205
5.3.2.1	Gene knockout strategy	206

5.3.2.2	Integration of knockout constructs and confirmation of knockout cell lines by PCR analysis.....	206
5.3.2.3	Verification of knockout clones using qRT PCR analysis	208
5.3.3	Phenotypic analysis of Tb6560 null mutant cell lines	209
5.3.3.1	Growth and DAPI cell cycle analysis <i>in vitro</i>	209
5.3.4	Localisation of Tb6560	211
5.3.4.1	Generation of a Tb6560 ^{+/-12myc} cell line	212
5.3.4.2	Confirmation of a Tb6560 ^{+/-12myc} cell line	212
5.3.4.3	<i>In vitro</i> growth of the Tb6560 ^{+/-12myc} cell lines.....	214
5.3.4.4	Tb927.9.6560 localises to the posterior end of the parasite.....	214
5.3.4.5	Super resolution analysis and 3D reconstruction of Tb6560 localisation.....	216
5.3.4.6	ImmunoGold® labelling of Tb6560	219
5.4	Loss of Tb6560 is associated with increased genotoxic stress sensitivity 220	
5.4.1	Tb6560 knockout mutants are sensitised to genotoxic stress <i>in vitro</i> 220	
5.4.2	Loss of Tb6560 is not associated increased γ H2A expression	222
5.4.3	Localisation of Tb6560 following genotoxic stress exposure	223
5.5	Morphological analysis of Tb6560 null mutants	225
5.5.1.1	Loss of Tb6560 affects cell morphology.....	225
5.5.1.2	High resolution morphological analysis using TEM	227
5.5.1.3	3D Video Reconstruction of the Tb6560 FP	231
5.6	Tb6560 may be involved in BSF endocytosis and trafficking	233
5.7	Identification of potential interacting partners of Tb6560.....	236
5.8	Discussion	238
5.8.1	Tb6560 is likely a NAK pseudokinase	238
5.8.2	Loss of Tb6560 is associated with an enlarged FP and endosomal system defects	240
5.8.3	The localisation and potential interaction partners of Tb6560 supports a role during early endocytosis	242
5.8.4	Tb6560 is unlikely to be directly associated with DNA repair.....	244
5.8.5	Summary	244
6	Analysis of the DNA repair-associated protein kinases TbATR and TbATM in bloodstream form <i>T. brucei</i>	245
6.1	Introduction	246
6.1.1	The PIKK family	246
6.1.2	The roles of ATR and ATM in other eukaryotes.....	249
6.1.2.1	ATR.....	249
6.1.2.2	ATM.....	251

6.2	Chapter Aims	252
6.3	Results	253
6.3.1	Bioinformatics analysis	253
6.3.1.1	BLAST Analysis.....	253
6.3.1.2	Domain predictions.....	255
6.3.1.2.1	TbATR.....	256
6.3.1.2.2	TbATM.....	257
6.3.2	RNAi cell lines used in this chapter	259
6.3.3	Generation of endogenously tagged RNAi cell lines	259
6.3.3.1	Generation of C-terminal endogenously tagged TbATR and TbATM RNAi cell lines 259	
6.3.3.2	Confirmation of endogenously tagged TbATR and TbATM in RNAi cell lines.....	260
6.3.3.3	Localisation of TbATR and TbATM	261
6.3.4	Phenotypic analysis	261
6.3.4.1	<i>In vitro</i> growth analysis.....	261
6.3.5	Nuclear defects arise in TbATR deficient cell lines	265
6.3.5.1	Loss of TbATR is associated with abnormal chromosomal rearrangements.....	268
6.3.6	TbATR is required for cell survival following genotoxic stress.....	271
6.3.7	TbATM is not required for cell survival following MMS or HU exposure 272	
6.3.8	TbATR deficient cells show increased levels of DNA damage- associated markers	273
6.3.9	Loss of TbATR is associated with deregulation of silent VSG expression sites.....	277
6.3.9.1	qRT-PCR analysis reveals de-regulation of silent ESs in the absence of TbATR..	278
6.3.9.2	Loss of TbATR is associated with the de-repression of Pol I associated and surface coat associated genes	280
6.3.9.3	Loss of TbATR is associated with up-regulation of surface antigen-associated transcripts 24 hrs after RNAi.....	282
6.3.9.4	Loss of TbATR at 36hrs post induction was primarily associated with cell cycle and global gene expression.....	286
6.3.9.5	Does loss of TbATR induce VSG switching?	290
6.4	Discussion	292
6.4.1	Both <i>T. brucei</i> ATR and ATM harbour a conserved PIKK KD	292
6.4.1.1	TbATR is essential for BSF cell survival <i>in vitro</i>	294
6.4.1.2	TbATR deficient BSF cells are sensitive to genotoxic stress and show increased expression of γ H2A and RAD51.....	296
6.4.1.3	Loss of TbATM is not associated with proliferation defects or increased sensitivity to genotoxic stress in BSF <i>T. brucei</i>	297

6.4.2	Loss of TbATR is associated with increased VSG expression from silent expression sites	298
7	Future perspectives	303
	References.....	308

List of Tables

Table 1-1: Current HAT treatment options	32
Table 1-2: ePKs have 12 conserved subdomains	54
Table 2-1: Primers required for the sequencing of all construct in this thesis...	69
Table 2-2: Primers required for endogenous tagging	70
Table 2-3: Primers required for KO construct generation	73
Table 2-4: Primers required for RxP construct generation	75
Table 2-5: Primers used for qRT-PCR analysis.....	76
Table 2-6: Antibiotic concentrations for BSF cells	80
Table 2-7: Antisera concentrations used for microscopy procedures	85
Table 2-8: Antibody concentrations used for western blot analysis	86
Table 3-1: Eight PK candidates identified by the genome wide MMS RITseq screen	106
Table 3-2: RNAi cell lines examined	109
Table 4-1: Top five SmartBLAST ‘hits’ for TbAUK2 in the NCBI database	142
Table 4-2: TEM imaging of cells lacking TbAUK2 reveals nuclear defects	151
Table 4-3: Potential interaction partners identified by Mass Spectroscopy analysis.....	178
Table 5-1: Top five SmartBLAST ‘hits’ for Tb6560 in the NCBI database (http://www.ncbi.nlm.nih.gov/). All data was recovered in June 2016.....	200
Table 5-2: Additional SmartBLAST ‘hits’ for Tb6560	201
Table 5-3: Potential Tb6560 interaction partners identified by MS analysis	237
Table 6-1: The members of the PIKK family, their localisation and their regulation.....	247
Table 6-2: Conserved PIKK domains and their potential functions.....	248
Table 6-3: Top 5 ‘hit’s from the SmartBLAST analysis of TbATR	253
Table 6-4: Additional ‘hits’ from the SmartBLAST analysis of TbATR	254
Table 6-5: Top 5 ‘hit’s from the SmartBLAST analysis of TbATM.....	254
Table 6-6: Additional ‘hits’ from the SmartBLAST analysis of TbATM	255
Table 6-7: RNAi cell lines required for this study	259
Table 6-8: DNA damage associated proteins differentially regulated in BSF <i>T. brucei</i> 36 hrs TbATR RNAi induction	290

List of Figures

Figure 1-1: HAT distribution in Africa	30
Figure 1-2: The lifecycle of <i>T. brucei</i>	33
Figure 1-3: Trypanosome cell body structure	36
Figure 1-4: The BSF cell cycle	38
Figure 1-5: The structure of the VSG	41
Figure 1-6: The structure of the <i>T. brucei</i> genome	42
Figure 1-7: Generalised schematic of BES architecture	43
Figure 1-8: Transcriptional switching.....	46
Figure 1-9: Recombination switching.....	47
Figure 1-10: Generalised schematic of HR and HR sub-pathways in eukaryotes .	49
Figure 1-11: Conserved ePK domains	53
Figure 1-12: The <i>T. brucei</i> kinome.....	57
Figure 1-13: The diverse range of DNA lesions and their corresponding DNA repair pathways.....	60
Figure 2-1: C-terminal tagging strategy.....	71
Figure 2-2: N-terminal tagging strategy.....	72
Figure 2-3: KO strategy	74
Figure 2-4: Generic RxP construct	75
Figure 2-5: RNAseq workflow schematic	78
Figure 3-1: Schematic illustration of the genome wide MMS RITseq screen in BSF cells	102
Figure 3-2: Schematic illustration of the kinome wide MMS RITseq screen in BSF cells	103
Figure 3-3: Comparison of the total sequence reads across two independent RITseq screens	104
Figure 3-4: The average MMS+/MMS- ratios of <i>T. brucei</i> genes mapped relative to their position in the genome.....	106
Figure 3-5: A heatmap summary of the MMS+/MMS- ratios for each putative MMS damage response kinase at each time point post induction from two different concentrations of MMS.....	108
Figure 3-6: Confirmation of endogenously tagged RNAi candidate cell lines	111
Figure 3-7: <i>In vitro</i> growth analysis of the genome wide candidates.....	112
Figure 3-8: <i>In vitro</i> growth of the kinome wide PK candidates.....	114
Figure 3-9: <i>In vitro</i> cell cycle analysis of the genome wide PK candidates.....	116
Figure 3-10: Morphology of the genome wide candidates after 48 hrs RNAi induction.....	117
Figure 3-11: <i>In vitro</i> cell cycle analysis of the kinome wide candidate	119
Figure 3-12: Morphology of the kinome wide candidates after 48 hrs RNAi induction.....	120
Figure 3-13: Examination of γ H2A expression in the genome wide PK candidates	122
Figure 3-14: Examination of γ H2A expression in the kinome wide candidates..	123
Figure 3-15: Sub-cellular localisation of Tb927.10.7780.....	125
Figure 4-1 ; AUKs localise dynamically throughout mitosis	136
Figure 4-2: A summary of the interaction partners of AUKA	137
Figure 4-3: A Summary of the interaction partners of AUKB.....	138
Figure 4-4: <i>T. brucei</i> aurora kinases lack sequence motifs typical of eukaryotic AUKs	144
Figure 4-5: A simplified alignment of the three <i>T. brucei</i> aurora kinases	145

Figure 4-6: Schematic illustration of homology regions required for TbAUK2 knockout	145
Figure 4-7: PCR analysis of putative TbAUK2 null mutant and heterozygote clones	147
Figure 4-8: Confirmation of AUK2 knockout clones by qRT-PCR and RT-PCR analysis.....	148
Figure 4-9: Growth and cell cycle analysis of TbAUK2 knockout clones.....	149
Figure 4-10: Representative examples of nuclei imaged by TEM from TbAUK2 ^{-/-} cells	153
Figure 4-11: Loss of TbAUK2 is associated with nuclear ‘blebbing’	155
Figure 4-12: Loss of TbAUK2 is associated with loss of the mitotic spindle	157
Figure 4-13: Loss of TbAUK2 is associated with aberrant cell morphology	160
Figure 4-14: <i>In vitro</i> growth of TbAUK2 ^{-/-} cell lines following treatment with DNA damaging agents	163
Figure 4-15: Loss of TbAUK2 is associated with increased γ H2A expression.....	165
Figure 4-16: Loss of TbAUK2 is associated RAD51 foci formation	167
Figure 4-17: Confirmation of TbAUK2 heterozygote endogenously tagged cell lines	169
Figure 4-18: <i>In vitro</i> growth analysis of TbAUK2 ^{+/-12myc} cell lines	170
Figure 4-19: TbAUK2 localises to the nucleus of BSF cells	171
Figure 4-20: Dynamics of TbAUK2 throughout the cell cycle	172
Figure 4-21: Super resolution and 3D imaging of TbAUK2 localisation	174
Figure 4-22: Localisation of TbAUK2 after MMS exposure	175
Figure 4-23: Super resolution images of TbAUK2 localisation after MMS exposure	176
Figure 4-24: Immunoprecipitation of TbAUK2 ^{+/-12myc} cell line.....	178
Figure 4-25: Schematic of the TbAUK2 re-expression plasmid AUK2::RXP	180
Figure 4-26: Confirmation of TbAUK2 re-expressing cell lines.....	181
Figure 4-27: <i>In vitro</i> growth of TbAUK2 re-expresser clones.....	182
Figure 4-28: Dynamic localisation of TbAUK2 in BSF cells.....	192
Figure 4-29: Loss of TbAUK2 is associated with cell cycle defects.....	193
Figure 5-1: Internalisation of cargo mediated by the AP2 complex.....	197
Figure 5-2: Schematic illustration of conserved motifs and domains in human AAK1 and Tb6560	202
Figure 5-3: Tb6560 shows structural similarity to two human NAK kinases.....	204
Figure 5-4: Tb6560 lacks conserved kinase associated sequence motifs	205
Figure 5-5: Schematic illustration of homology regions required for Tb6560 knockout	206
Figure 5-6: PCR analysis of putative Tb6560 null mutant clones.....	207
Figure 5-7: Confirmation of Tb6560 knockout clones by qRT-PCR	208
Figure 5-8: <i>In vitro</i> growth analysis of Tb6560 null mutant cell lines	211
Figure 5-9: Confirmation of Tb6560 ^{+/-12myc} clones	213
Figure 5-10: <i>In vitro</i> growth analysis of Tb6560 ^{+/-12myc} cell lines	214
Figure 5-11: Tb6560 localises to the posterior end of the parasite	215
Figure 5-12: Super resolution images of Tb6560 localisation	218
Figure 5-13: Localisation of endogenously tagged Tb6560 by ImmunoGold® labelling.....	219
Figure 5-14: <i>In vitro</i> growth analysis of Tb6560 ^{-/-} cells under genotoxic stress.....	221
Figure 5-15: Fluorescence intensity quantification of γ H2A expression in Tb6560 ^{-/-} cell lines.....	223
Figure 5-16: Tb6560 ^{12myc} localisation following DNA damage exposure	224
Figure 5-17: Loss of Tb6560 affects BSF cell morphology	227

Figure 5-18: Internal cellular architecture of wild type Lister 427 BSF <i>T. brucei</i> cells	228
Figure 5-19: Loss of Tb6560 grossly affects structures associated with endocytosis and vesicular trafficking.....	229
Figure 5-20: TEM images of abnormal cellular structures associated with Tb6560 loss.....	230
Figure 5-21: The enlarged FP is unlikely due to disruption at the flagellar entry point.....	231
Figure 5-22: FIB/TEM analysis of Tb6560 knockout cells	232
Figure 5-23: Uptake of tomato lectin into the FP and the early endosome system of wild type BSF <i>T. brucei</i>	234
Figure 5-24: Cells lacking Tb6560 are defective in endocytosis	235
Figure 5-25: Immunoprecipitation from a Tb6560 ^{+/-12myc} cell line using anti-myc antiserum	236
Figure 6-1: The generalised structure of PIKKs	247
Figure 6-2: Canonical activation of ATR in eukaryotes	250
Figure 6-3: Schematic illustration of conserved motifs between the human ATR and the <i>T. brucei</i> ATR	257
Figure 6-4: Schematic illustration of conserved motifs between the human ATM and the <i>T. brucei</i> ATM.....	258
Figure 6-5: Confirmation of endogenously 12myc-tagged TbATR and TbATM by western blot.....	260
Figure 6-6: <i>In vitro</i> growth analysis of TbATR and TbATM RNAi cell lines	262
Figure 6-7: Loss of TbATR results in morphologically aberrant cells	263
Figure 6-8: <i>In vitro</i> cell cycle analysis of TbATR.....	264
Figure 6-9: TbATR is required to maintain the nucleus of BSF cells	266
Figure 6-10: Internal cellular architecture of TbATR-deficient cells	267
Figure 6-11: Telomere positions in the presence of TbATR	269
Figure 6-12: Loss of TbATR is associated with aberrant telomere arrangements	270
Figure 6-13: <i>In vitro</i> loss of TbATR sensitises BSF <i>T. brucei</i> cells to genotoxic stress	271
Figure 6-14: <i>In vitro</i> loss of TbATM is not associated with increased sensitivity to genotoxic stress.....	273
Figure 6-15: Loss of TbATR is associated with increased γ H2A in BSF cells	274
Figure 6-16: Loss of TbATR is associated RAD51 foci formation	276
Figure 6-17: Bloodstream VSG expression sites in the <i>T. brucei</i> Lister 427 strain	278
Figure 6-18: Loss of TbATR is associated with expression of silent VSG RNA transcripts.....	279
Figure 6-19: PCR analysis of RNA samples for RNAseq analysis.....	281
Figure 6-20: Box plot to assess the distribution of the fpkm for each replicate after 24 and 36 hrs growth with and without RNAi.....	282
Figure 6-21: Volcano plot showing transcripts differentially expressed at 24 hrs post TbATR RNAi induction.....	283
Figure 6-22: Pie charts summarising differentially expressed genes at 24 hrs post TbATR RNAi induction.....	285
Figure 6-23: GO terms enriched at 24 hrs post knockdown of TbATR in BSF cells	286
Figure 6-24: Volcano plot showing transcripts differentially expressed at 36 hrs post TbATR RNAi induction.....	287

Figure 6-25: Pie charts summarising the data recovered at 36 hrs post TbATR downregulation	288
Figure 6-26: GO terms enriched at 36hrs post knockdown of TbATR in BSF cells	289
Figure 6-27: Some TbATR depleted cells do not express VSG221 on their surface	291

List of Accompanying Material

Accompanying CD-ROM contains the following files:

- 1) Appendices: Numbered as if Chapter 8
- 2) Chapter3RITseqtables (folder & data within)
- 3) RNAseqDatasetATRBSF2016 (folder & data within)
- 4) MSdataTb6560andTbAUK22016.xlsx
- 5) Tb6560videoreconstruction.mov

Acknowledgements

I would like to thank both my supervisors, Richard McCulloch and Jeremy Mottram, for their support throughout my PhD. Especially to Richard for all his helpful advice and enthusiasm. I would also like thank the BBSRC DTP program for providing the funding for this project and Alex and Vickie (for all the public engagement opportunities).

To all members (past and present) of the McCulloch and Mottram labs- thank you! I have immensely enjoyed getting to know everyone. I wish to specially thank Elaine for her help, guidance and coffee chit-chat, Leandro for all his help with imaging, Nick and Jon for all their bioinformatics wizardry and to Andrea and Catarina not only for being my friends but for agreeing to walk with me down the aisle at my wedding! And finally to Gillian from the GoToAgency; I hope my internship was as valuable to you as it was to me. I also want to thank Tiago for all his help and guidance during my PhD and to Jeziel for just about everything! Thank you both for all the late night gossip, the occasional Brazilian culture class and inspiring me to try a little bit harder each day. Obrigada!

Thank you to my assessors (Markus and Harry) for your helpful suggestions and guidance. In particular I wish to thank Markus (and of course Saskia and the Meissner lab)- their encouragement and support throughout my undergraduate degree drove me to pursue a PhD.

Thank you to my parents Freda and Campbell and my grandparents Ann and Bill (whose middle name is Percy hehe- now everyone knows!) for all their support and acceptance over the years.

Finally, I wish to thank my husband Johannes. For agreeing to marry me (perhaps to silence my endless chatter- who knows!), for staying in Glasgow to do your PhD so you would be beside me and for listening to the endless presentations about trypanosomes (even though I secretly know you love them more than toxo)!

“This is the essence of science. You ask an impertinent question and you’re on your way to a pertinent answer.”

Fox Mulder, FBI

Author's Declaration

I, the author, hereby declare that this thesis and the results presented within are the result of my own work unless otherwise stated. None of the results presented here have been previously used to obtain a degree at any university.

Jennifer Ann Stortz

List of Abbreviations and definitions

aPK	atypical PK
AP	Adaptor protein
ATM	Ataxia-telangiectasia mutated
ATP	Adenosine triphosphate
ATR	ATM and Rad3 related
ATRIP	ATR interacting protein
BB	Basal body
BBB	Blood brain barrier
BES	Blood stream form expression site
BIR	Break-induced replication
BLAST	Basic Local Alignment Search Tool
BLASTp	BLAST(protein)
bp	Base pairs
BRCA	Breast cancer associated
BSD	Blasticidin
BSF	Blood stream form
BVSG	Blood stream form VSG
cDNA	Complementary DNA
CDS	Coding sequence
CFS	Common fragile site
CNS	Central nervous system
CO	Cross over
CSF	Cerebral spinal fluid
CTR	Co-transposed region
C-terminal	Carboxyl terminal
DAPI	4',6-diamidino-2-phenylindole
del	Deletion
DGC	Directional gene cluster
ddH ₂ O	Double distilled water
DDR	DNA damage repair
dHJ	Double Holliday Junction
DIC	Differential interference contrast
DC	Differential interference constrast

D-Loop	Displacement loop
DNA	Deoxyribonucleic acid
DNA-PKcs	DNA dependent protein kinase, catalytic subunit
Dnase	Deoxyribonuclease
dNTP	Deoxynucleotide triphosphate
DSB	Double strand break
DSBR	DSB repair
dsDNA	Double stranded DNA
dsRNA	Double stranded RNA
EDTA	Ethylenediaminetetraacetic acid
EF1 α	Elongation factor 1-alpha
ePK	eukaryotic PK
ERCFS	Early replicating common fragile site
ES	Expression site
ESAG	Expression site associated genes
ESB	Expression site body
ExoI	Exonuclease I
FA	Formaldehyde
FACS	Fluorescence activated cell sorting
FAZ	Flagellar attachment zone
FCS	Foetal calf serum
FITC	Fluorescein isothiocyanate
FP	Flagellar pocket
FPKM	Fragment per million kilobases
G4	Guanine quadruplex
GC	Gene conversion
gDNA	Genomic DNA
GFP	Green fluorescent protein
GPI	Glycophosphatidylinositol
HAT	Human African trypanosomiasis
HDL	High density lipoprotein
HJ	Holliday junction
HMI	Hirumi's modified Isocove's medium
HR	Homologous recombination
HRDC	Helicase and RNaseD C-terminal

Hrs	Hours
HU	Hydroxyurea
HYG	Hygromycin
Ig	Immunoglobulin
IMDM	Isocove's modified Dulbecco's medium
IR	Ionizing radiation
ISG	Invariant surface glycoprotein
kbp	Kilobase pairs
kDa	Kilo-dalton
KD	Kinase domain
kDNA	Kinetoplast DNA
LB	Luria Bertani
LSBSF	Long slender BSF
Mb	Megabase
MBC	Megabase Chromosome
MCF	Metacyclic form
MES	Metacyclic expression site
MMEJ	Microhomology-mediated end joining
MMR	Mismatch repair
MMS	Methyl methansulfonate
MOPS	3-(N-morpholino) propanesulfonic acid
MRN	Mre11-Rad50-Nbs1
mRNA	Messenger RNA
mVSG	Metacyclic VSG
NADH	Nicotinamide adenine dinucleotide (reduced)
NADPH	Nicotinamide-adenine dinucleotide phosphate (reduced)
nDNA	Nuclear DNA
NEO	Neomycin
NER	Nucleotide excision repair
NHEJ	Non-homologous end joining
NTD	Neglected tropical disease
N-terminal	Amino terminal
NTP	Nucleotide triphosphate
ORC1	Origin replication complex 1
ORF	Open reading frame

PAGE	Polyacrylamide gel electrophoresis
PBS	Phosphate buffered saline
PBST	PBS-tween
PCF	Procylic form
PCR	Polymerase chain reaction
PDB	Protein Data Bank
PFA	Paraformaldehyde
PK	Protein kinase
PKL	Protein kinase like
Poll	Polymerase I
PUR	Puromycin
RIF	RNA interference factor
RF	Replication fork
RNA	Ribonucleic acid
RNA pol I	RNA polymerase I
RNAi	RNA interference
ROS	Reactive oxygen species
RPA	Replication protein A
RRNA	Ribosomal RNA
RT	Reverse transcriptase
qRT-PCR	Quantitative reverse transcriptase polymerase chain reaction
RXP	Re-expresser
SCEM	Scanning electron microscopy
SDS	Sodium dodecyl sulphate
SDSA	Synthesis-dependent strand annealing
SEM	Standard error of the mean
SIF	Stumpy induction factor
siRNA	Small interfering RNA
SL	Spliced leader
SMARD	Single molecule analysis of replicated DNA
SOC	Super optimal broth supplemented with glucose
STE	Sterile in yeast
SSA	Single strand annealing
SSB	Single strand break
SSBSF	Short stumpy BSF

ssDNA	Single stranded DNA
S/T	Serine/threonine
SSR	Strand switch region
TAE	Tris acetit acid EDTA buffer
TAC	Tripartite attachment complex
Tb	<i>Trypanosoma brucei</i>
TC	Telomere conversion
TEM	Transmission electron microscopy
Tet	Tetracycline
TetR	Tetracycline repressor
Tet-	Without tetracycline
Tet+	With tetracycline
TLK	Tousled like kinases
TLS	Translesion synthesis
TK	Tyrosine kinase
TPE	Telomere position effect
UTR	Untranslated region
UV	Ultraviolet
VSG	Variant surface glycoprotein
WHO	World health organisation
WT	Wild type

1 Introduction

1.1 The Kinetoplastida

The class Kinetoplastae embodies a highly diverse group of evolutionary ancestral protozoans ranging from free-living Bodonoids to the parasitic African trypanosomes (Lukeš et al. 2014). Kinetoplastids are currently recognised under the phylum Eulgenozoa (supergroup Excavata, group Discoba, subgroup Discicristata, phylum Euglenozoa, class Kinetoplastae). The Kinetoplastae themselves are further divided into the Prokinetoplastina (a subclass currently consisting of two parasitic species; *Ichthyobodo* and *Perskinsela*) and the Metakinetoplastina (a subclass divided into four clades; the Parabodonida, Eubodonida, Neobodonida and the Trypanosomatida; (Lukeš et al. 2014; Adl et al. 2012). Unlike the majority of the Metakinetoplastina, the clade Trypanosomatida consists of only obligate parasites¹, several of which are known aetiological agents of diseases with severe medical and veterinary consequences, in addition to their presence being economically damaging (Steverding 2008; Lukeš et al. 2014). Examples of parasitic trypanosomatids include the African *Trypanosoma brucei* subspecies², ('Salivarian Trypanosomes'; the causative agents of Human African Trypanosomiasis), the *Trypanosoma* species that are causative agents of Nagana (including *T. congolense* and *T. vivax*), *Trypanosoma cruzi* (Chagas Disease or American Trypanosomiasis), and the *Leishmania* species, the causative agents of Leishmaniasis (Leishmaniasis can manifest in two major forms; cutaneous and visceral; leishmaniasis is reviewed in general by Kaye & Scott 2011). Collectively, trypanosomatid parasites cause a range of diseases world-wide, though predominantly the diseases are encountered in the tropics and sub-tropics.

Kinetoplastidae organisms are highly divergent in terms of core biological processes; most notable (and from whence they derive their name) is the presence of the unusual arrangement of their mitochondrial genome referred to as the kinetoplast (or kDNA; Vickerman and Preston, 1976). The kinetoplast is organized as unique arrangement of interlocked DNA circles, known as maxi and

¹ Evidence of parasitism by Trypanosomatids is present in invertebrates, plants and vertebrate organisms across a range of habitats.

² Though numerous trypanosomatid species are present in Africa, *T. brucei brucei*, *T. brucei rhodesiense*, *T. brucei gambiense*, *T. equiperdum*, *T. evansi*, *T. congolense*, *T. simiae*, *T. godfreyi* and *T. vivax* are all known to infect mammals. Only *T. brucei rhodesiense* and *T. brucei gambiense* are considered human infective.

mini circles (the number of each circle type is dependent upon the species; reviewed by Morris et al. 2001; Jensen & Englund 2012). In addition, kinetoplasts are also unusual with respect to the multigenic transcription and replication of the genomes (Marques et al. 2016; Muhich & Boothroyd 1988), their ability to extensively edit their mitochondrial RNA (a process in which minicircle-encoded guide RNAs are involved; reviewed by Stuart et al. 2016), their reliance on post-transcriptional gene expression controls, and the compartmentalisation of glycolysis (Simpson et al. 2006).

1.1.1 HAT is a debilitating disease

The *Trypanosoma brucei* species encompasses three morphologically indistinct sub-species; *T. b. rhodesiense*, *T. b. gambiense* and *T. b. brucei*, all of which cause a form of Trypanosomiasis. Transmission primarily occurs via the bite of an infected Tsetse fly (genus *Glossina*; Kennedy 2013; Steverding 2008), though there are reports of transmission across the placenta and via sexual activity (Olowe 1975; Rocha et al. 2004). *T. b. gambiense* and *T. b. rhodesiense* are the aetiological agents of Human African Trypanosomiasis (HAT), with over 98% of cases being caused by the more common species *T. b. gambiense* over the last 10 years (found in 24 countries across West and Central Africa <http://www.who.int/mediacentre/factsheets/fs259/en/>). *T. b. gambiense* causes a chronic infection, though two sub-groups of *T. b. gambiense* exist (Group 1 and Group 2), which differ in their ability to resist lysis by human serum (Capewell et al. 2011). *T. b. rhodesiense* causes an acute form of the disease and accounts for the remaining reported cases, in an estimated 13 countries across East and Southern Africa (e.g Malawi; Franco et al. 2014). Overlap of the sub-species was reported in Uganda (Picozzi et al. 2005) and a map of HAT distribution is shown in Figure.1-1.

The third subspecies, *T. b. brucei*, is not human infective due to the presence of a high density lipoprotein (HDL) in the serum, which this subspecies cannot resist (reviewed by Stephens et al. 2012). Instead, *T. b. brucei* causes Nagana, which manifests as a severe wasting disease in domestic livestock such as cattle (genus; *Bos taurus*). Nagana represents a huge economic burden, with millions of cattle at risk (Steverding 2008). In indigenous species (including wildebeast,

buffalo and other native bovids such as the genus *Bos indicus*) the disease is often mild.

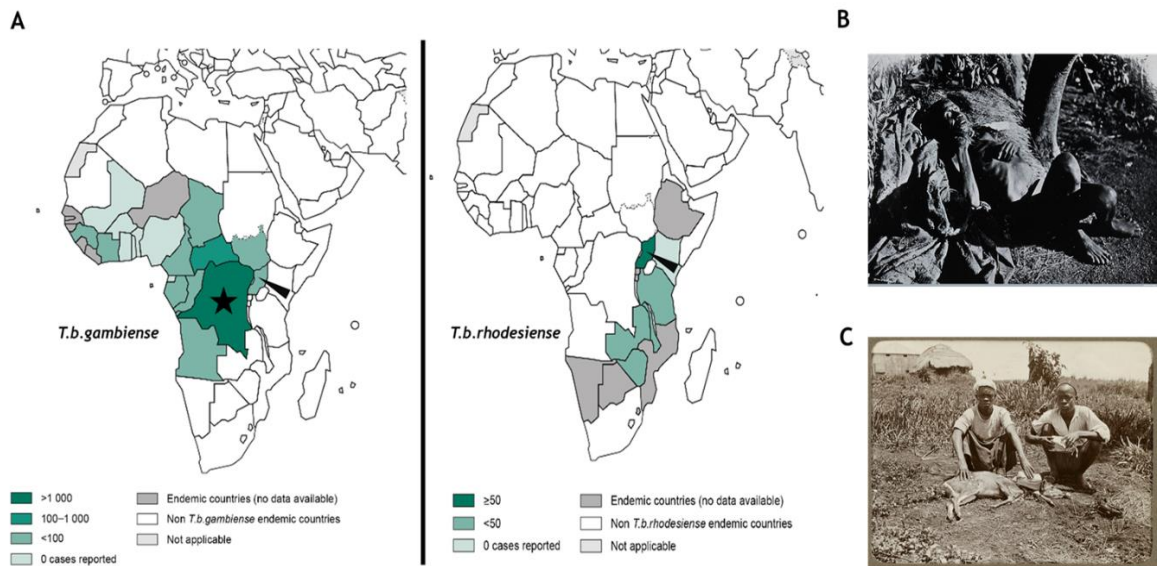


Figure 1-1: HAT distribution in Africa

(A) The distribution of *T. b. gambiense* (left) and *T. b. rhodesiense* (right) in Africa as of 2014. The highest number of cases (3206) reported in 2014 were in the Democratic Republic of Congo (marked by a black star). The black arrow indicates Uganda, the country in which both *T. b. gambiense* and *T. b. rhodesiense* can be found. Map images were accessed in July 2016 and adapted from http://gamapserver.who.int/mapLibrary/Files/Maps/HAT_rh_2014.png and http://gamapserver.who.int/mapLibrary/Files/Maps/HAT_ga_2014.png WHO ©. (B) A sufferer of HAT in Uganda; (C) The effect of Nagana on livestock. Images were provided by the Wellcome trust library. Image reference numbers: V0029100 (B) and L0049104 (C) <http://wellcomeimages.org/>. WHO (all rights reserved). Used with permission.

Chronic HAT can persist with mild symptoms for years, in contrast to the acute form, which can be fatal in under a year from the initial infection (Franco et al. 2014; Kennedy 2013); both are normally lethal if left untreated. Asymptomatic carriers have been reported and may act as a reservoir of the disease (Sudarshi et al. 2014). Two distinct stages of HAT exist. The primary (Haematolympathic) stage has no defining symptoms, making it hard to diagnose; patients often present with periodic fevers and fatigue for up to 7 days. Occasionally, a rash on the body can be observed. Here, the parasites predominantly reside extracellularly in the bloodstream and lymphatic fluids. Non-specific symptoms such as headaches, drowsiness and anorexia have been reported (Kennedy 2013). Parasite migration occurs from the initial site of infection to further areas of the body, including the large organs such as the liver, adipose tissue and the skin (Trindade et al. 2016; Capewell et al. 2016), which may act as a parasite reservoir. The second, late stage (Meningoencephalitic stage) begins with

parasite migration into the Cerebral-Spinal Fluid (CSF) and across the Blood Brain Barrier (BBB; Kennedy 2013). A defining feature of this progression is the appearance of neurological complications, in particular the characteristic disruption of normal sleeping patterns. Patients can develop severe fatigue, seizures, confusion and may become aggressive. Within months to years (Kennedy 2013) the patient can reach a comatose state, resulting in death, though there are reports of survival amongst humans (Sudarshi et al. 2014). What factors govern survival are currently unknown.

Recently, the incidence of HAT has significantly reduced due to increased awareness, surveillance, effective case management and persisting vector control, with < 4000 cases being reported in 2014, though the disease is still endemic in 36 sub-saharan African countries (Franco et al. 2014). Due to the disproportional effect of this disease on poor, rural areas, an estimated 70 million people over 1.55 million km² remain at risk of infection (Steverding 2008). Furthermore, in combination with potentially non-symptomatic human carriers, the disease is also zoonotic. *T. b. rhodesiense* can be found in wild and domestic animals, including antelope, buffalo, cattle and sheep, which persist as a reservoir for human infections and continue to impose a huge economic burden on the country. *T. b. gambiense* has been reported to reside in pigs, though these parasites were shown to be genotypically different from *T. b. gambiense* found in humans (Simo et al. 2006).

Due to the falling number of cases, HAT has been targeted for elimination as a public health concern, alongside diseases such as leprosy, Chagas Disease and lymphatic filariasis by 2020 (NTD RoadMap 2012 [http://www.who.int/neglected_diseases/NTD_RoadMap_2012_Fullversion.pdf]). However, continual monitoring of the parasite may be required to ensure resurgence of the disease does not occur.

1.1.1.1 Current HAT treatment options

Currently, the treatment of HAT relies solely on four single drugs and a combination therapy (summarised in Table 1-1 below; reviewed by Kennedy 2013). Each drug or drug combination has recognised side effects and require prolonged or invasive delivery regimes. Novel drugs with fewer, more acceptable

side-effects may be needed. Ideally, such drugs would be administered orally to help reduce the reliance on medically trained individuals being required for treatment, specifically in rural regions Africa, where there is neither the training nor funding available to provide such a service.

Drug	Delivery Method	Trypanosome species (T.b.g or T.b.r)	Stage of Disease	Drug Side Effects	Reference
Pentamidine	IM or IV	<i>T.b.gambiense</i>	Stage 1	Blood pressure changes With IM inject: pain and irritation to surrounding tissue	G
Suramin	IV	<i>T.b.rhodesiense</i>	Stage 1	Allergic reactions, urinary tract complications	H
Melarsoprol	IV	Both (1 st line <i>T.b.rhodesiense</i> and 2 nd line <i>T.b.gambiense</i>)	Stage 2	Arsenical derived. Burning sensation upon injection and 10% of cases can lead to reactive encephalopathy and death of the patient	A
Eflornithine	IV	<i>T.b.gambiense</i>	Stage 2	Seizures, gastrointestinal complications	B, C
Eflornithine and Nifurtimox	IV	<i>T.b.gambiense</i>	Stage 2	Nifurtimox: neurological complications and gastrointestinal complications	D,E,F

Table 1-1: Current HAT treatment options

Information obtained from the following sources: (A) (Pépin et al. 1995) **(B)** (Burri & Brun 2003) **(C)** (Bacchi et al. 1983). **(D)** (Wegner & Rohwedder 1972). **(E)** (Janssens & De Muynck 1977). **(F)** (Priotto et al. 2007) **(G)** (Doua et al. 1996). **(H)** (Jennings et al. 1983). **General treatment review by** (Kennedy 2013).

1.2 The lifecycle of *T. brucei*; a dixenous parasite

The lifecycle of *T. brucei* is complex, as the parasite cycles between a mammalian host and the Tsetse fly vector (a dixenous lifestyle; see Figure 1-2). Additionally, extensive morphological and metabolic changes occur during development within both hosts (more so within the vector), providing a survival advantages at multiple points.

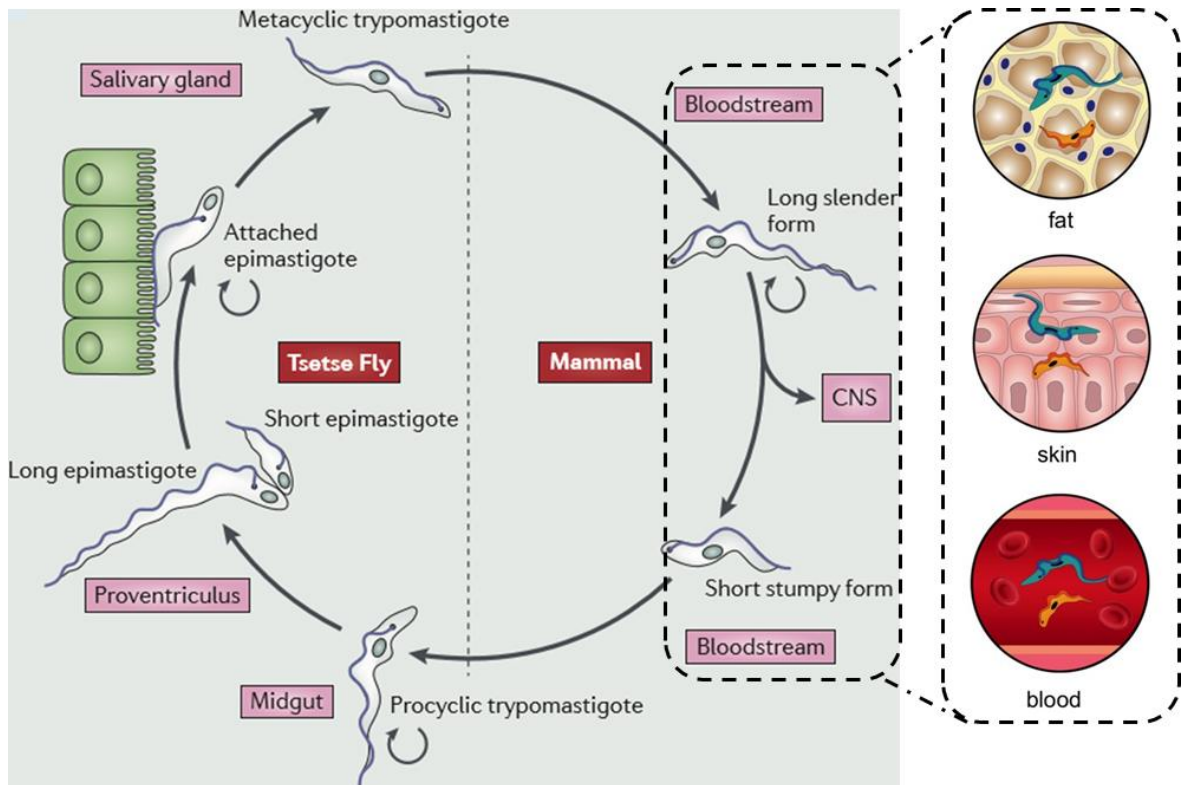


Figure 1-2: The lifecycle of *T. brucei*

A simplified depiction of the *T. brucei* parasite lifecycle. The lifecycle stages are discussed in the text. CNS (Central Nervous System). Figure adapted from (Langousis & Hill 2014)© with permission (Licence number: 3900680426952) and Casas-Sánchez and Acosta-Serrano, 2016 (Casas-Sánchez & Acosta-Serrano 2016).

T. brucei is transmitted when an infected Tsetse fly (~0.1 % of which harbour transmissible *T. b. gambiense*; (Jamonneau et al., 2004) bites a suitable mammalian host. During feeding, non-proliferative metacyclic form (MCF) cells (from the fly's salivary glands) are transmitted into the subcutaneous tissue surrounding the bite. The trypanosomes then migrate to the hosts' bloodstream via the lymphatic fluid. Here, MCF parasites rapidly differentiate into replicative long slender blood stream form (BSF) cells; a highly mobile, free-living form also found in tissues (Langousis & Hill 2014). In addition to inhabiting the bloodstream, recent studies have also demonstrated the presence of parasites persisting in the dermis (and other regions) of the skin (Capewell et al. 2016; Caljon et al. 2016) and within the adipose tissue of mice (Trindade et al. 2016). These 'tissue' forms may represent components of the lifecycle (dashed box, Figure 1-2) which have not been previously described. Furthermore, the presence of trypanosomes in these locations may, in part, explain the presence of asymptomatic carriers; the Macleod group were able to infect Tsetse flies with the skin derived parasites (Capewell et al. 2016).

The BSF lifecycle stage harbours an additional organelle (the glycosome) for the sole purpose of glycolysis. The single BSF mitochondrion is relatively metabolically inactive. BSF cells are covered with a dense coat of proteins known as the Variant Surface Glycoprotein (or VSG), which protect the cells from complement mediated lysis and the humoral immune response, permitting a prolonged, chronic infection in the mammalian host (Horn & McCulloch 2010; Section 1.4). Proliferation of the long slender BSF continues until a critical population density is reached (MacGregor et al. 2012; Mony et al. 2014), resulting in accumulation of a Stumpy Induction Factor (SIF; still to be identified) which triggers differentiation from the long slender to non-replicative short stumpy BSFs. Short stumpy BSFs do not undergo antigenic variation (see below) and are controlled by the host humoral immune response (surviving ~72 hrs in the bloodstream; Langousis & Hill 2014). Short stumpy BSFs are pre-adapted to life inside the vector and when taken up during a blood meal they differentiate into the replicative Procyclic Form cell (PCF). This lifecycle form is distinct from the BSF; the cell is elongated, the kDNA repositions and the mitochondrion becomes metabolically active to circumvent glucose starvation and utilise the abundance of proline in the fly midgut. The most notable change is the surface coat. Early stage PCF cells (within the first week of infection) express a coat of Procyclins comprised of pentapeptide repeats called GPEET. The early stage PCF cells have been shown to undergo a form of Social Motility (Imhof et al. 2014), making them behaviourally distinct from the late stage PCFs, which additionally only express the EP procyclin dipeptide (Acosta-Serrano et al. 2001). Late stage PCFs migrate to the salivary glands of the fly and further differentiate into an intermediate stage, before becoming the Epimastigote form which embeds in the salivary gland wall. Again the surface coat alters and expression of alanine rich proteins, called BARPs, occurs (Urwyler et al. 2007). Sexual exchange can occur, though this may not always be required (Peacock et al. 2011). Parasite differentiation proceeds in the Tsetse salivary gland lumen and the MCF stage primed for the infection of the mammalian host emerges. To survive the initial host infection, the MCF is coated in VSGs specific to this stage (mVSGs; Barry et al. 1998; Ginger et al. 2002) and of a limited repertoire relative to BSF cells. Overall passage through the Tsetse fly takes approximately 30 days (MacGregor et al. 2012), whereas the parasite can live for years in the mammal. To date the longest recorded infection with *T. b. gambiense* in a

human is 29 years (Sudarshi et al. 2014). These above lifecycle stages are specific to the *T. brucei* species; the life cycles of other species, such as *T. vivax* and *T. congolense*, vary (are not discussed further).

1.3 *T. brucei*: molecular biology

1.3.1 The cell body and cell cycle

T. brucei is typically elongated in shape due to an organized arrangement of highly polarised sub-pellicular microtubules running from the anterior to the posterior of the cell (Figure 1-33 A). At the posterior end, a small invagination of the cell membrane occurs to form the flagellar pocket (FP), the only site of endo- and exocytosis on the surface (see section 1.4.1.4). From here, a single flagellum (with a typical 9+2 axonemal arrangement Langousis & Hill 2014) protrudes, initiating from the basal body (BB), which is directly attached to the single kinetoplast by the tripartite attachment complex (TAC). The flagellum is attached laterally along the full length of the cell (reviewed by Field & Carrington 2009) by the flagellar attachment zone (FAZ), and plays a role in both cellular division and motility.

T. brucei cells have a single copy of several organelles: the mitochondrion, the golgi, the kinetoplast, the basal body and the nucleus (Figure 1-3 B). During cell division, these organelles are localised to the posterior and central regions of the parasite, producing a defined and organized assembly of organelles within the cell, though re-positioning of the kinetoplast occurs between lifecycle stages. This makes progression of the cell cycle readily examinable by microscopy, for instance by chromatin staining using DAPI (Woodward & Gull 1990).

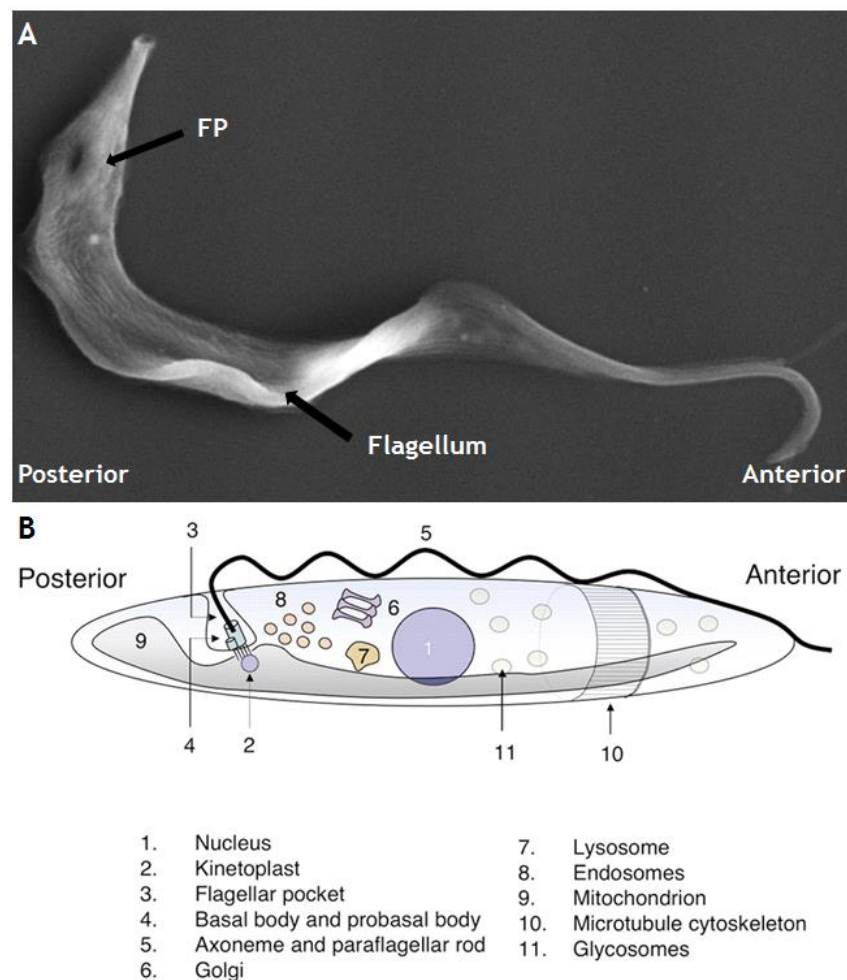


Figure 1-3: Trypanosome cell body structure

(A) SEM image of a BSF trypanosome cell (*T. brucei*). FP = Flagellar pocket. Image captured by L. Lemgruber-Soares for use in this thesis. **(B)** Internal trypanosome cell structure. Refer to image legend for details. Image adapted from (Matthews 2005); The Company of Biologists Limited 2005©. Used with permission (License ID: 3906400295096).

The trypanosome cell cycle, like a typical eukaryotic cell cycle, occurs in four stages, G_0/G_1 , S, G_2 and M (followed by cytokinesis; illustrated in Figure 1-4). Cell cycle progression is co-ordinated by a series of incompletely understood kinase cascades (Hammarton 2007) and, though largely conserved, a number of trypanosomatid-specific processes occur. The cell cycle can be monitored by DAPI staining cells to reveal their n- and kDNA. Uniquely, trypanosomes have evolved two separate S-phases; kDNA replication begins prior to nDNA replication, with the former S-phase being shorter; in addition, kDNA segregation occurs before the beginning of nDNA mitosis. As such, the G_2 -phase for the kinetoplast begins before S-phase is completed for the nDNA, and the kinetoplasts separate during nuclear G_2 -phase (Figure 1-4 B). Observing the relative number of kinetoplasts (K) to nuclei (N) permits an estimate of which cell cycle stage an individual cell is found in (McKean 2003; Hammarton 2007).

During nuclear G_1 (1N1K cells), maturation and duplication of the BB complex occurs, promoting the generation of a new flagellum. The point at which the new flagellum exits the membrane generates a new FP. The golgi complex is then duplicated. The new flagellum is physically attached to the old flagellum, using its structure as a template on which to extend and develop through S-phase (Farr & Gull 2012). When the cells enter later G_1 / S-phase, the kDNA becomes 'elongated' (1N1eK). Separation of the basal body initiates division of the kinetoplast, giving rise to cells possessing a single nucleus and two kinetoplasts (1N2K), which are in nuclear G_2 phase. Following the onset of mitosis, the chromosomes segregate and the nucleus divides, producing a cell with two kinetoplasts and two nuclei (2N2K); cytokinesis has yet to occur. *T. brucei*, like other 'lower' eukaryotes (such as yeast) undergoes a 'closed' mitosis in which the nuclear membrane does not breakdown and re-form. Instead, materials required for replication are trafficked through the nuclear membrane via nuclear pore complexes (NPCs; Daniels et al. 2010). Cytokinesis begins when the new flagellum reaches the anterior end of the old flagellum (a process which occurs throughout the cell cycle). Here, a cleavage furrow forms along the length of the cell, beginning at the anterior end of the cell (though an additional, posterior to anterior form of cytokinesis has been shown to occur Zhou et al. 2016). Now each cell harbours a full set of organelles and can finally separate by abscission into two individual cells by the enzyme spastin (in BSF cells; Benz et al. 2012).

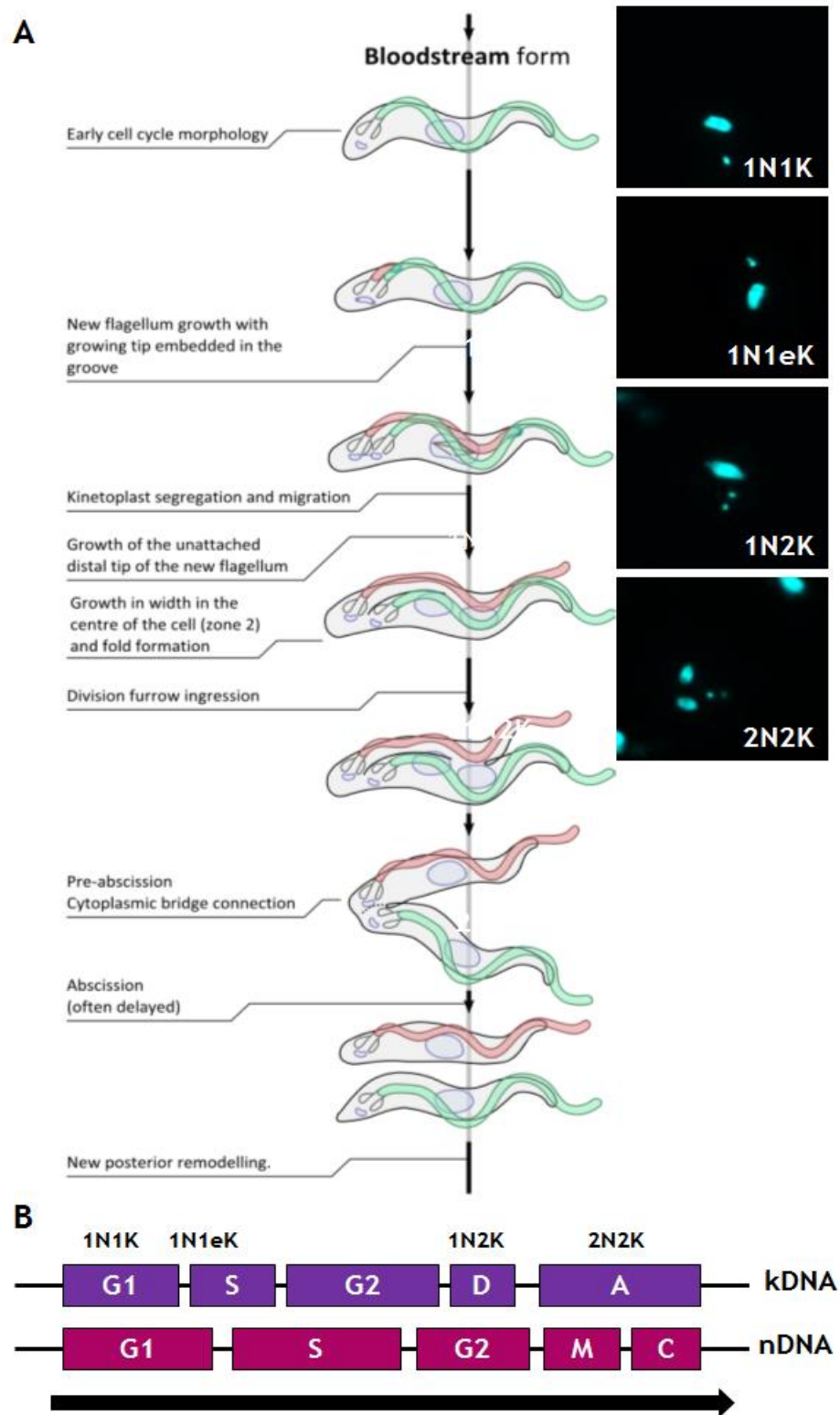


Figure 1-4: The BSF cell cycle

(A) Schematic illustration of the BSF trypanosome cell cycle. Red = new flagellum, Green = old flagellum. Images on the right show DAPI stained nDNA and kDNA configurations of BSF cells. Images were captured on an Axioskop 2. (B) Schematic representation of nDNA and kDNA division timing. D = kDNA division, A- kDNA anaphase, M- nuclear mitosis, C- cytokinesis. Figure kindly provided by C.Marques (University of Dundee) and adapted for this thesis.

1.4 Avoiding host clearance

Colonisation of complex multicellular organisms by other species can be mutually beneficial; on one hand the host organism provides a rich and fertile environment in which the other species can thrive and, on the other, the colonising organism can provide a service for the host in exchange. A commonly cited example of this is the complex (symbiont) relationship between the intestinal microflora and the host; the microflora appears to influence the host immune system (O'Hara & Shanahan 2006). In the case of parasitic organisms, colonisation and nurture is at the expense of the host, often producing nutrient deficits which can result in a disease state. Parasitic organisms range in size from viral particles to bacteria, protozoans and up to larger, multicellular organisms such as helminths and invertebrates. In order for any parasite to survive in (and on) the host without being expelled, they have evolved several strategies to combat clearance. However for the purposes of this thesis, the focus of this section will be specifically on immune evasion by true antigenic variation³.

Once inhabiting a host organism, a parasite faces several challenges, notably the innate and adaptive immune responses. Although the initial innate response must be overcome (to do this, pathogens have evolved multiple strategies; reviewed by Chai et al. 2009; Hornef et al. 2002; Deitsch et al. 2009; Melo et al. 2011; Stijlemans et al. 2016), surviving the ongoing adaptive immune response is critical for the maintenance of a long term infection. Antigenic variation (as defined by Deitsch et al. 2009) is:

“...the capacity of an infecting organism to systematically alter the proteins displayed to the host immune system, such that the host is confronted with a continually changing population that is difficult or impossible to eliminate...”

Antigenic variation relies on the adaptive immune response requiring time to generate a response against a particular antigen. The parasite exploits this time requirement to generate an antigenically distinct variant and express it;

³ “True antigenic variation” refers to the ability of an organism to express multiple variants of a specific protein exposed to the immune system. ‘Phase variation’ (commonly utilised by bacteria) refers to an antigen being turned ‘on’ or ‘off’, or varying between two states.

parasites harbouring the 'old' variant(s) are cleared by the immune response, while those expressing new variants survive. Thus infections by organisms that use antigenic variation frequently manifest as waves of bacteraemia or parasitaemia over a long period of time. The success of this method of survival is highlighted by its presence across numerous different lineages throughout evolution. For example, the aetiological agent of malaria (*Plasmodium falciparum*), is able to switch the erythrocyte membrane protein 1 (EMP1) displayed on the red blood cell surface by transcriptionally switching its repertoire of 60 *var* genes. In the case of the bacteria *Borrelia burgdoferi*, both its Major Surface Protein 2 (MSP2) and a lipoprotein VlsE undergo antigenic variation through a process of gene recombination (Palmer et al. 2009).

For the purpose of this thesis, the focus will be on *T. brucei* antigenic variation, which appears to be a uniquely complex set of mechanisms that rely on a vast 'library' of genes it can access for this sole purpose. *T. brucei* antigenic variation is facilitated by both the parasite's unusual genome architecture and its dense surface coat: the VSG coat.

1.4.1.1 The VSG Coat

Approximately 95% of the BSF parasite's surface is densely coated in a monolayer of VSGs (Figure 1-5; $\sim 2 \times 10^7$ VSG proteins anchored to the cell surface; Mugnier et al. 2016), which 'shield' any invariant surface antigens (for example, invariant surface glycoproteins, or ISG). However, this 'shielding' effect is under debate due to the discovery of an ISG that is predicted to protrude past the VSG on the parasite surface (Ziegelbauer & Overath 1993; Higgins et al. 2013). The VSG protein is homodimeric in structure and approximately 15 nm in size (~ 400 amino acids long). It is affixed to the membrane by a C-terminal Glycosylphosphatidylinositol (GPI) anchor (Schwede et al. 2011). The N-terminus is exposed to the immune system; this is the hyper-variable region. Antigenic variation is mediated by stochastic switching of the VSG coat (at a rate of 10^{-3} switches/cell/division; (Turner & Barry 1989); reviewed by (Morrison et al. 2009; McCulloch et al. 2015; Horn & McCulloch 2010; Glover, Hutchinson, et al. 2013; Günzl et al. 2015)

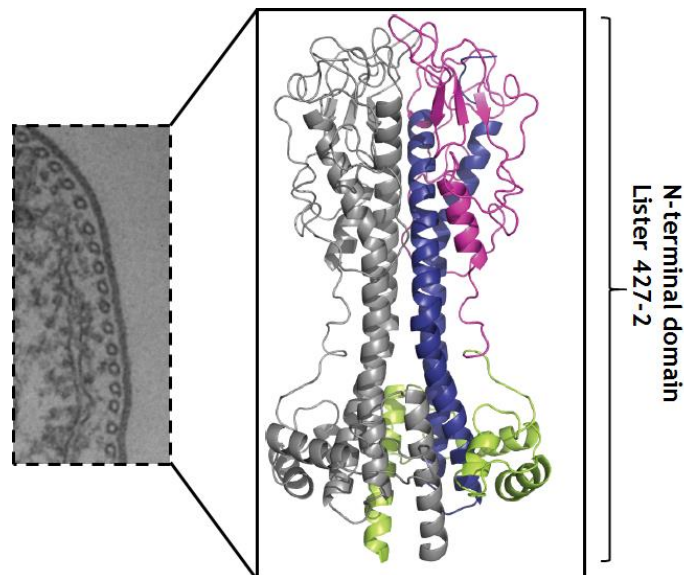


Figure 1-5: The structure of the VSG
 (Dashed box) TEM image of the dense BSF *T.brucei* surface coat; image captured by L.Lemgruber-Soares for use in this thesis. (Solid box) The structure of the N-terminal domain of the VSG antigen Lister 427-2 (vsg1). Image adapted from (Hall 2012).

1.4.1.2 *T. brucei* genome is unusually arranged

The genome of *T. brucei* (927 TREU strain) has 11 diploid Megabase chromosomes (MBC) approximately 0.9 - > 6 Mb in size and annotated from one (the smallest) to eleven (the largest; chromosome size is strain dependent; (El-Sayed et al. 2000)). Interestingly, the chromosomes across the different kinetoplastid organisms show a high level of synteny (El-Sayed et al. 2005). In addition to the MBCs, *T. brucei* has between one to five ‘intermediate’ chromosomes (~150-900 kbp) and 100s of ‘mini-chromosomes’ (50-150 kbp). Over 9000 genes are estimated to be encoded by the *T. brucei* nuclear genome (Berriman et al. 2005); around 20% of the genes (~2500, though estimates are imprecise) are thought to be VSGs, most of which (~80%) are VSG pseudogenes and are primarily found in subtelomeric arrays (Berriman et al. 2005; Marcello & Barry 2007; Callejas et al. 2006). The intermediate and minichromosomes appear only to encode VSG and VSG-associated genes (Wickstead et al. 2004).

The MBCs are organised with ‘house-keeping’ genes clustered towards the chromosomes’ centre. Most of these genes are transcribed by RNA Pol II, though PolI transcribes rRNA and procyclin genes within the interior in a small number of loci, while tRNA genes are transcribed by RNA PolIII from a few loci (Daniels et al. 2010). The subtelomeric regions harbouring extensive VSG arrays and

pseudogenes flank the housekeeping core, appear highly dynamic and are largely untranscribed (Berriman et al. 2005; Wickstead et al. 2004; El-Sayed et al. 2000). Proximal to the telomeres are specialised regions for VSG expression (some are also found on ‘intermediate’ chromosomes). These sites are called Expression Sites (ES) of which ~15 are predicted in the Lister 427 strain and used in BSF cells (BES). More truncated ES (MES) are used to express MCF VSGs (discussed below).

Transcription of the genome is also unusual in all kinetoplastids; most genes are arranged as large polycistronic transcriptional units (or directional gene clusters) containing potentially 100s of open reading frames (Figure 1-6; reviewed by Daniels et al. 2010). The transcription units are separated by strand switch regions (SSRs); which can be divergent, convergent or head-to-tail. Despite the obvious lack of Pol II promoters, transcription is initiated from each SSR, resulting in transcription of a polycistronic RNA from which mRNAs arise by trans-splicing and polyadenylation (reviewed by Michaeli 2011; Preußner et al. 2012). SSRs are marked by chromatin modifications. For example, enrichment of histone H4 acetylated at lysine 10 (H4K10ac), histone H3 trimethylated at lysine 4 (H3K4me3) and histone variants H2Z and H2BZ (Siegel et al. 2009) occurs at transcription initiation sites. Termination appears to occur at sites enriched with H4V and H3V histone variants, and the modified thymidine, Base J (Reynolds et al. 2014).

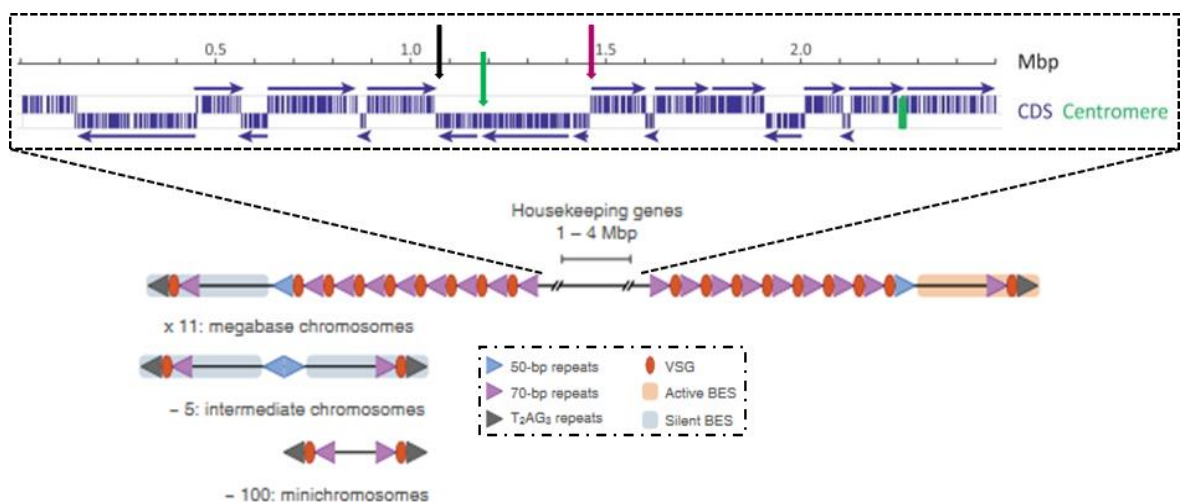


Figure 1-6: The structure of the *T. brucei* genome
The typical structures of *T. brucei* chromosomes; labels are provided in the diagram. The dashed box illustrates the organisation of the ‘housekeeping’ genes (labelled CDS on the diagram) into polycistronic units (blue arrows). The black arrow indicates a convergent

SSR, the green arrow indicates 'head-to-tail' SSR and the pink arrow a divergent SSR. T₂AG₂ repeats are found to cap all *T. brucei* chromosomes. Diagram adapted from (Tiengwe et al. 2014; Glover, Hutchinson, et al. 2013). Not to scale

In addition to intermediate and minichromosomes, *T. brucei* also harbours extra chromosomal elements ('NR-elements', as described by Alford et al. 2003), potentially linked to recombination at the telomeres.

1.4.1.2.1 BESs

The MBCs and some intermediate chromosomes harbour BESs, which show a defined structural organisation (as illustrated in Figure 1-7). In MCFs, metacyclic expression sites (MES) are required for expression of the mVSGs in a manner similar to the BESs, despite differences in the promoter (Ginger et al. 2002). Here, only the single VSG gene is transcribed from the Pol I promoter, making MES the only examples of single gene expression units in the genome (Ginger et al. 2002). In contrast, VSGs in all BES are transcribed in combination with expression site associated genes (ESAGs). Only one BES from the larger repertoire is fully transcribed at one time; this process is known as monoallelic expression (Günzl et al. 2015). BES, like MES and procyclins, are transcribed by RNA Pol I (Günzl et al. 2003). BES are the only sites for expression of the VSG protein and the active BES is associated with an RNA Pol I-containing structure known as the Expression Site Body (ESB), which is required for monoallelic expression and located outwith the nucleolus (Navarro & Gull 2001).

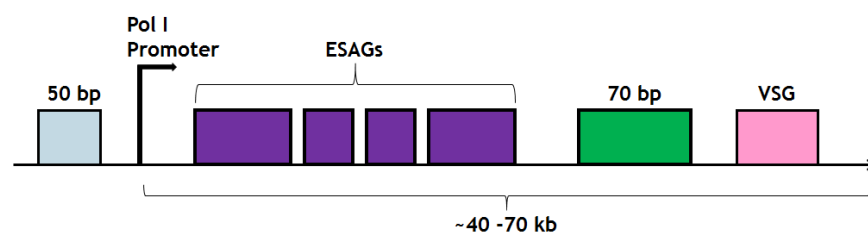


Figure 1-7: Generalised schematic of BES architecture

Upstream of the BES Pol I promoter is a region of 50 bp repeats (grey box), of unknown function. Downstream of the promoter sits multiple ESAG genes (purple boxes) thought to facilitate parasite survival across a number of host environments (Cordon-Obras et al. 2013; Pays et al. 2001). Further downstream is an array of 70 bp repeat sequences (green box), utilised to facilitate homology directed VSG switching (Alford et al. 2009). The same repeats are found proximal to over 90% of VSGs in the subtelomeric arrays (Marcello & Barry 2007). The VSG gene (pink box) is located proximal to the telomere. Not to scale.

1.4.1.3 VSG switching

Broadly, VSG switching can occur transcriptionally (section 1.4.1.3.1) or by gene recombination (section 1.4.1.3.2).

1.4.1.3.1 Monoallelic expression and transcriptional switching

Though VSG expression is monoallelic, meaning a single VSG is transcribed, translated and surface expressed, it is not the case that silent BESs are entirely transcriptionally 'silent'. In fact, it appears transcription is initiated from the promoter, but at a low level and extending for only a small distance into the BES (reviewed by Günzl et al. 2015). Activation of a 'silent' BES and silencing of the 'active' BES appears to be a coordinated process, as simultaneous expression of two or more BES is normally not seen (Chaves et al. 1999). How switching occurs remains not understood fully, though mutation of one chromatin modifier, DOT1B, has been shown to delay the active to silent BES transition (Figueiredo et al. 2008; Batram et al. 2014).

More is understood about the factors that mediate BES silencing. From studies in other eukaryotes, genes in close proximity to the telomeres are often subject to Telomere Position Effect (TPE). Here, the telomere exerts a 'silencing' effect due to spread of protection of the telomere ends mediated by the Shelterin complex (the Shelterin complex is reviewed by Palm & de Lange 2008), which is essential and required to prevent activation of a damage response due to the presence of incompletely replicated DNA ends at the telomere. Loss of *T. brucei* shelterin factors (TbRAP1, TbTRF) causes expression from silent BES (Yang et al. 2009; Pandya et al. 2013; Sanaa E. Jehi et al. 2014). In addition, the core origin recognition complex factor, ORC1/CDC6, has been shown to bind telomeres and RNAi affects VSG transcription and switching (Benmerzouga et al. 2013).

Somewhat paradoxically, loss of two other telomeres factors have different impacts: loss of TbTIF2 (Jehi et al. 2016; Sanaa E Jehi et al. 2014) has been linked to VSG switching, but not silencing of BESs; and mutation of Ku80 (a component of the heterodimeric Ku complex with functions during DNA repair) impairs telomere length but does not detectably affect monoallelic VSG expression (Conway et al. 2002; Janzen et al. 2004). It has also been demonstrated that although a Poll promoter can be silenced by a telomere, this

only occurs when in close proximity (Glover & Horn 2006). Taken together, the significance of TPE for VSG control remains open. Recently, ectopic expression of a second VSG was shown to attenuate the active ES, with silencing appearing to spread from telomere towards the promoter due to DOT1B action (Batram et al. 2014). Most recently, a novel active BES factor, VEX1, has been uncovered whose loss activates silent BES and may act via homology (possibly VSG)-mediated silencing (Glover et al. 2016).

Beyond DOT1B, which generates the H3 methylated lysine 76 histone variant, RNAi of a number of further chromatin modifiers alleviates VSG silencing. These include an FACT subunit (Denninger et al. 2010; Denninger & Rudenko 2014), the linker histone H1 (Povelones et al. 2012), two histone chaperones (Alsford & Horn 2012) and an HMG factor (Narayanan & Rudenko 2013). RNAi of nuclear envelope lamina proteins also appears to play a role, since RNAi of two interacting but functionally and spatially distinct components, TbNUP-1 and TbNUP-2 (DuBois et al. 2012; Maishman et al. 2016), results in de-repression of the silent BES. Intriguingly, while loss of TbNUP1 results in new VSG on the BSF cell surface, suggestive of switching, loss of TbNUP-2 appears not to have the same effect. Nonetheless, these effects may indicate a role for the nuclear envelope in maintaining VSG silencing and thus monoallelic expression; indeed, the nuclear envelope has been implicated in gene silencing in other eukaryotes (reviewed by Towbin et al. 2009).

Maintaining expression of the active VSG BES has also been considered, with a number of factors emerging, including cohesin (Landeira et al. 2009). Beyond this, RNA Pol II BES expression appears, at least in part, to be mediated by the class I transcription factor A (CITFA) complex, which is accumulated at the active BES promoter to a higher level than in the silent BESs (Nguyen et al. 2014). Finally, though the composition of the ESB remains surprisingly unclear, SUMOylation has been found to accumulate in the active, but not inactive, BES and impairment of this modification leads to loss of VSG expression (Lopez-Farfan et al. 2014). A simplified model of transcriptional switching is shown below in Figure 1-8.

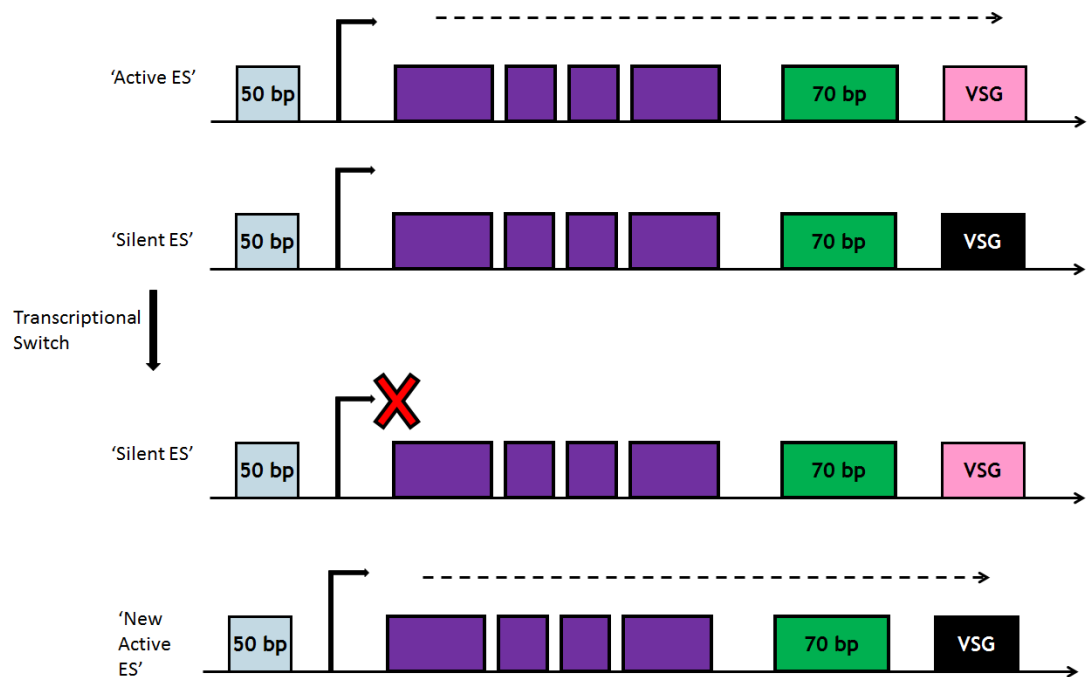


Figure 1-8: Transcriptional switching

Transcription of 'active' BES (with the pink VSG gene) is repressed and transcription of an 'inactive' BES (with the black VSG gene) is turned on; this BES is now the 'active' BES. Dashed arrow indicates transcription occurring. Not to scale.

1.4.1.3.2 Recombinational switching

Switching transcriptionally cannot sustain a long term infection. With ~15 BESs in the Lister 427 strain, only 15 different VSG variants are available. To this end, *T. brucei* more frequently utilises recombinational switching to facilitate antigenic variation. To generate a recombinational switch, a VSG from the silent archive, spread across the silent BES, the subtelomeric arrays, intermediate chromosomes and minichromosomes must be 'moved' into an active BES and is subsequently expressed. Unlike transcriptional switching, recombinational switches occur by several different pathways; gene conversion (GC ;Bernards et al. 1981), telomere crossover (TC; likely a rare event; De Lange et al. 1983) or by generating novel, mosaic VSG genes (as reviewed by McCulloch et al. 2015 and summarised in Figure 1-9).

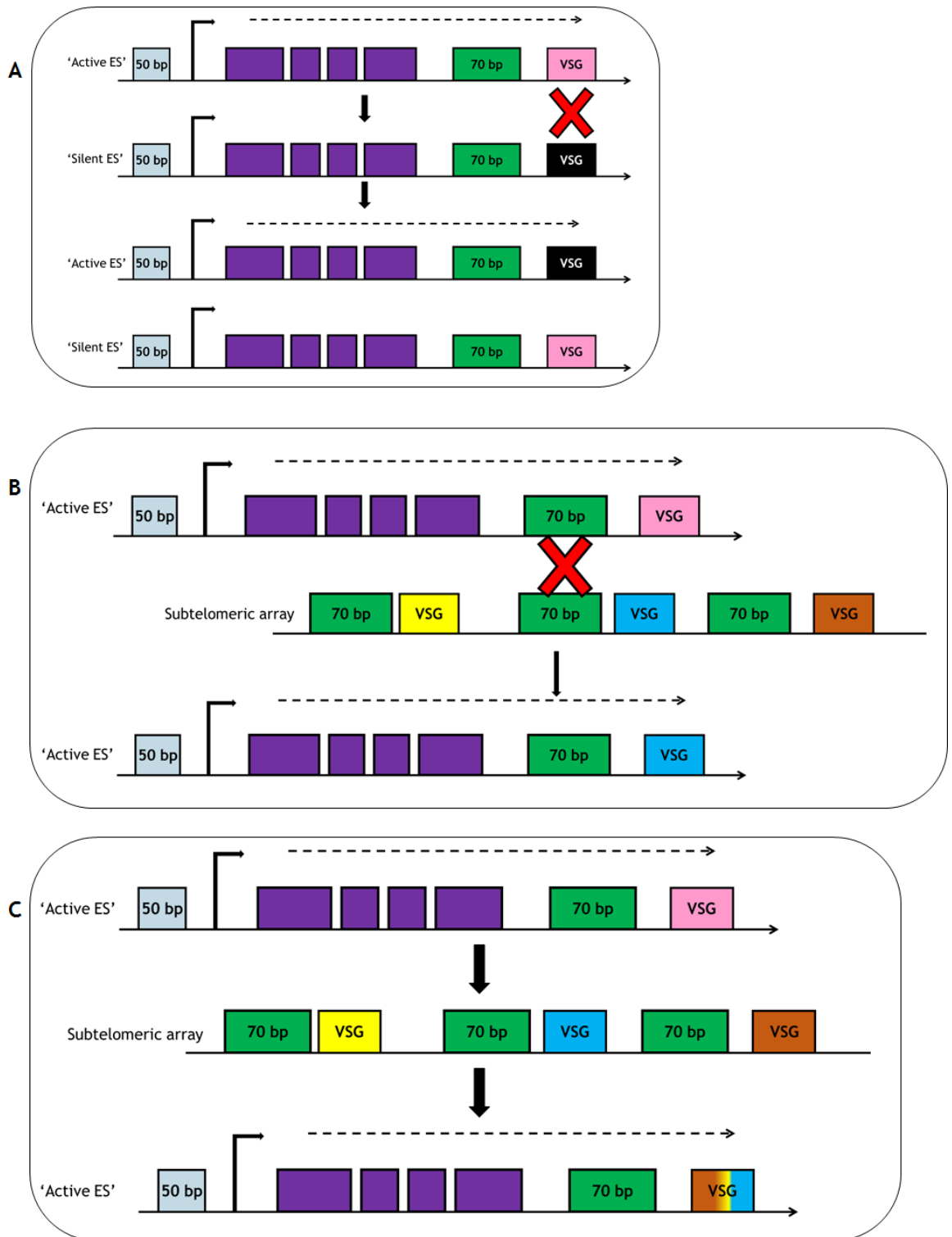


Figure 1-9: Recombination switching

(A) VSG switching by telomere crossover. The telomere of the 'active' BES (pink box) is exchanged for a 'silent' VSG (black box). The 'pink' VSG is still retained in the silent BES as a silent VSG gene. (B) VSG switching by gene conversion. An intact VSG from the silent archive is duplicated into the 'active' BES and replaces the currently expressed VSG gene. Homology can be used from the 70 bp repeats or (if the VSG is telomeric) the telomere can be used as a point of homology (referred to as telomeric conversion), as can the ESAGs (purple boxes). (C) VSG switching using multiple VSG genes or pseudogenes. A novel, intact (mosaic) VSG is generated by segmental gene conversion from fragments of other VSG genes; either intact or from pseudogenes. Unlike the process above, this reaction relies on intra-VSG ORF homology. This process is thought to predominate in late in the

infections (Hall et al. 2013; Marcello & Barry 2007). **Not to scale. Figure generated based on data from** (Devlin 2015).

A common feature associated with over 90% of VSG genes is the presence of a variable 70 bp repeats (array VSG genes typically harbour only small numbers, while in BES-associated VSGs up to 100 repeat sequences have been reported; Alsford et al. 2009). The role of the 70 bp repeats remains a subject of investigation. They may be limited to facilitating homology between archival VSGs and the VSG in the active BES. Alternatively, the repeats may actively promote recombination, perhaps via unusual base pairing properties (Ohshima et al. 1996) due to their sequence content (which comprises of TAA/TAA-like tandem repeats at the 5' region, and conserved TA repeats at the 3' region (Hovel-Miner et al. 2016). However, the available data on such a role is unclear, since though one study suggested DNA breaks localise to the 70 bp repeats in the active BES (Boothroyd et al. 2009), others did not (Glover, Alsford, et al. 2013; Jehi et al. 2014); in addition, two reports have indicated that removal of the 70 bp repeats from the active BES does not impair VSG switching (McCulloch et al. 1997; Boothroyd et al. 2009), while one suggests such a deletion activates the reaction (Hovel-Miner et al. 2016).

What is clear, is that recombinational switching, of at least intact VSGs, exploits the homologous recombination (HR) pathway of DNA repair (and perhaps uses sub-pathways, including synthesis-dependent strand annealing [SDSA] and break induced repair [BIR]) to facilitate these switches (Borst et al. 1996; David Barry & McCulloch 2001). HR is reviewed by Krejci et al. 2012 and summarised in Figure 1-10 below. Other repair pathways, including single strand annealing (SSA) and microhomology mediated end joining (MMEJ), have also been shown to occur in *T. brucei* (Conway et al. 2002; Burton et al. 2007; Glover et al. 2011), but their enzymology is less clear. HR proteins are well documented to be involved in mediating VSG switching. For example, knockouts of TbBRCA2, the TbRAD51-3 paralogue and the core HR catalyst, TbRAD51, severely reduced VSG switching rates (McCulloch & Barry 1999; Dobson et al. 2011; Proudfoot & McCulloch 2006; Hartley & McCulloch 2008). Conversely, other HR factors, such as a topoisomerase TbTOPO 3 α , TbRMI1 and TbRECQ2, (Kim & Cross 2011; Devlin et al. 2016) increase the rate of switching when mutated. Nonetheless, some specialisation of VSG HR switching may occur, since mutation of other TbRAD51

paralogues and a component of the MRN complex (which is recruited to a double stranded break [DSB] lesion in an ataxia telangiectasia mutated (ATM)-dependent manner; ATM and HR are discussed in detail below and in chapter 6 respectively; Shiloh & Ziv 2013; Krejci et al. 2012) do not affect VSG switching.

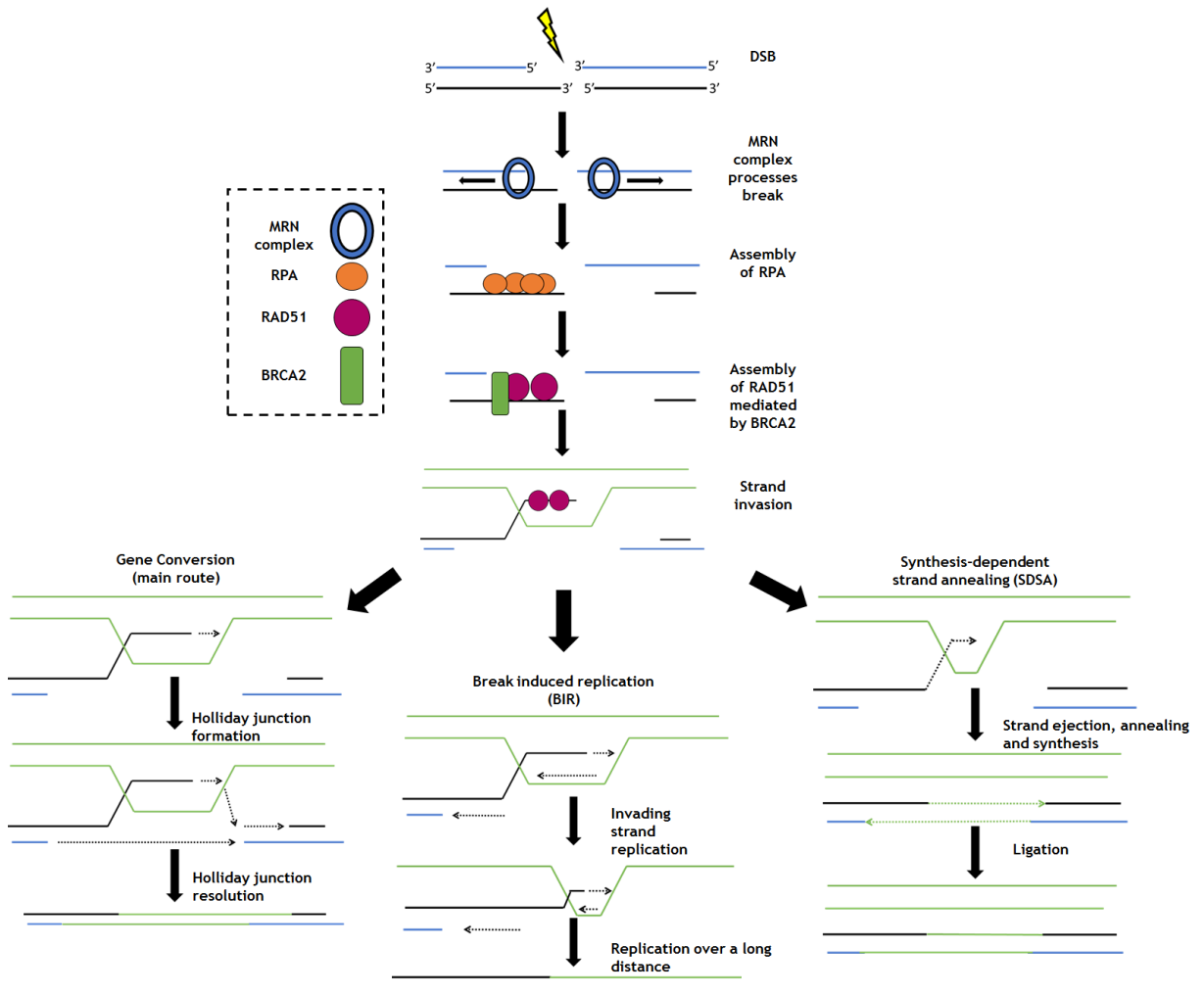


Figure 1-10: Generalised schematic of HR and HR sub-pathways in eukaryotes

Generally, the presence of a double stranded break (DSB) is detected by the Meiotic Recombination Protein 11/Rad50/Nijmegen Breakage Syndrome 1 (MRN) complex. The MRN complex, which harbours exonuclease (5' to 3') activity, resects the break ends to generate 3' overhangs of ssDNA. A second exonuclease (Exo1) further resects these regions. Replication Protein A (RPA) proteins then decorate the ssDNA strand to prevent further damage to this strand. The RPA is replaced by the RAD51 protein, which is loaded onto ssDNA by the breast cancer 2 (BRCA2) protein forming a RAD51-nucleofilament. After, strand invasion (of an undamaged strand) can occur catalysed by RAD51 to form a 'D-loop'. The invading strand is then used as a template for repair of the 3' resected DSB region. Repair proceeds either by gene conversion, BIR or SDSA. Here, Holliday junctions (HJs) form between strands. Strand exchange can occur (resulting in genetic material transfer from the template) and the HJs are resolved. BIR is used when one 3' strand invades to form a D-loop. The D-loop can remodel into a replication fork and replication can continue downstream over a long region of DNA. SDSA involves formation of a D-loop, priming DNA synthesis then removing the invading strand and annealing it to the other complementary DSB strand.

Considering the involvement of HR it was hypothesised that a DNA lesion is responsible for initiating VSG switching. Some work has suggested that DSBs could trigger VSG switching. Boothroyd et al (Boothroyd et al. 2009) demonstrated that directly generating a DSB in The active BES, using an inducible meganuclease, drastically increases the rate of VSG switching. Furthermore, they demonstrated this effect was dependent on the position of the DSB relative to the 70 bp repeats (Boothroyd et al. 2009). Additionally, they detected breaks around the 70 bp repeats. Later, Glover et al (2013) confirmed these findings, showing that a meganuclease -induced break only triggered switching when sited between the 70 bp repeats and VSG in the active BES, not elsewhere in the active BES or in an inactive BES.

Another potential explanation for the trigger of HR- mediated repair has emerged from studying replication timing of the BES. Some studies have speculated that the 70 bp repeats might cause an increased predisposition to stalling replication forks (Kim & Cross 2011). Fork collapse can trigger HR- mediated repair following the formation of single stranded DNA (ssDNA) at the lesion site. Commonly, such ssDNA is detected in an ATM-Rad3 related (ATR)- dependent manner (Zeman & Cimprich 2014; as discussed in chapter 6). Indeed, replicative lesions have been insinuated to facilitate recombination in the both the yeast *S. pombe* (Doe & Whitby 2004) and the bacterium *Neisseria* (here through the formation of DNA-RNA hybrids or 'R-loops'; (Cahoon & Seifert 2009). Now, recent evidence in *T. brucei* supports this theory. Despite *T. brucei* cells lacking the DNA helicase REQ2 (RecQ helicases are involved in genome maintenance; reviewed by Croteau et al. 2014) being defective in DSB repair, they harbour elevated VSG switching rates by recombination at their telomeres. Additionally, DSBs within the active BES were inefficiently repaired in such mutants, arguing against a direct DSB being the VSG switch trigger. Instead, Devlin et al were able to demonstrate that the active BES, alone amongst the 15 BES, replicates early, which could establish conditions that produce stalled replication forks. Though further work is required to scrutinise this model in more depth, the data provides the first indication that replicative lesions may trigger VSG switching by recombination (Devlin et al. 2016).

One area of mechanistic uncertainty in *T. brucei* antigenic variation rests on mosaic VSG formation by segmental gene conversion. It is clear from numerous studies that the huge number of VSG pseudogenes are used as recombination substrates, with considerable reaction flexibility that potentially generates millions of novel VSGs (Mugnier et al. 2015; Hall et al. 2013; McCulloch & Field 2015). However, the machinery which catalyses the reaction, the potential trigger(s) and the location of mosaic assembly remain unknown.

1.4.1.4 Endocytosis as a method of immune evasion in *T. brucei*

The stochastic switching of the VSG antigen permits evasion of the host humoral response. However, during the early infection stages, both complement and less-specific IgM antibodies can become attached to the parasite surface. To overcome these issues, BSF trypanosomes utilise their endocytic pathway to internalise (via hydrodynamic forces; Engstler et al. 2007) and dispense with any attached immune factors during surface coat recycling.

Surface VSGs are first transported in Rab5A-positive vesicles to the early endosome then rapidly recycled to the surface by Rab11-positive vesicles. ISGs, in contrast, are thought to be trafficked by Rab5B vesicles, though can potentially be trafficked to the surface again by Rab11-positive vesicles mediated by the protein RME-8 (Koumandou et al. 2013), or they can enter the endosome system and progress into the late endosome system in a Rab28-mediated manner (endocytosis in *T. brucei* is reviewed by Field & Carrington 2009).

The available evidence suggests BSF *T. brucei* require a highly efficient endocytosis system for VSG recycling and antibody clearance. This process appears to be clathrin-mediated, and does not rely on an AP2 complex, suggesting *T. brucei* has streamlined its endocytosis pathway to maximise clearance and recycling of the VSG (Manna et al. 2013). Most likely this is a further mechanism of immune evasion.

1.5 Kinases and phosphorylation: Co-ordination of cellular communication

Protein kinases (PKs), through their ability to transfer protons via phosphorylation, provide a means of cellular communication. De-regulation of this process can be catastrophic, though severity depends upon the pathway in which an individual PK operates. Nonetheless, a large proportion of human PKs have been directly linked to the onset of disease following de-regulation (for example, in a recent review, ~ 50 PKs were found to contribute to 67 diseases associated with aberrant kinase activity; referred to as 'kinasopathies'; (Lahiry et al. 2010).

Phosphorylation is a post-translational modification, which involves transferring the γ -phosphate of one ATP molecule to the OH- group on a targeted protein at either a serine (S), threonine (T) or tyrosine (Y) residue. The phosphate transfer can then regulate protein activity, for instance through conformational changes or allosterically.

1.5.1 The human kinome; eukaryotic kinases and atypical kinases

The human kinome was published in 2002 (Manning et al. 2002) marking the expansion of the kinase biology field. Over 500 PKs have been identified in the human genome, accounting for ~2% of all human genes. PKs can be further grouped into either eukaryotic protein kinases (ePKs) or atypical protein kinases (aPKs), as discussed below.

1.5.1.1 Eukaryotic Protein Kinases (ePKs)

Over 90% of human kinases are ePKs, all sharing a common protein configuration. ePKs transfer the phosphate to either a serine or a threonine (S/T kinases), a tyrosine (tyrosine kinases) or to a serine, threonine or tyrosine (dual specificity kinases). In addition, PKs able to phosphorylate histidine and other amino acids have been identified, for example histidine (Puttick et al. 2008). The members of the ePK group of kinases are first classified based on 12 highly conserved subdomains throughout the PK structure (Hanks & Hunter 1995), then further classified into eight PK 'families' based on conserved sequence motifs in their catalytic region: Tyrosine Kinases (TKs), Tyrosine Kinase Like kinases (TKLs),

Calcium and Calmodulin-regulated kinases (CAMKs), CDK-like Kinases (CMGCs), Receptor Guanylate Kinases (RGCs), Protein Kinases A, G and C (AGC), Casein Kinase 1 (CK1) and Homologs of yeast Sterile 7, Sterile 11, Sterile 20 (STE) kinases. Despite these groupings, members of the different PK ‘families’ do not strictly adhere to interactions with members of their own group; many often require activation by PKs from other groups or share a common substrate; for instance, the Mitogen Activated Protein Kinases (MAPKs; family CMGC) can be activated by STE kinases (family STE; Ahn et al. 1999).

The highly conserved structure of the ePKs was first observed in the 1990s following the publication of the crystal structure of protein kinase PKA (a cAMP dependent PK; Knighton et al. 1991). A generalised schematic of a typical ePK structure and domain organisation is shown in Figure 1-11 below.

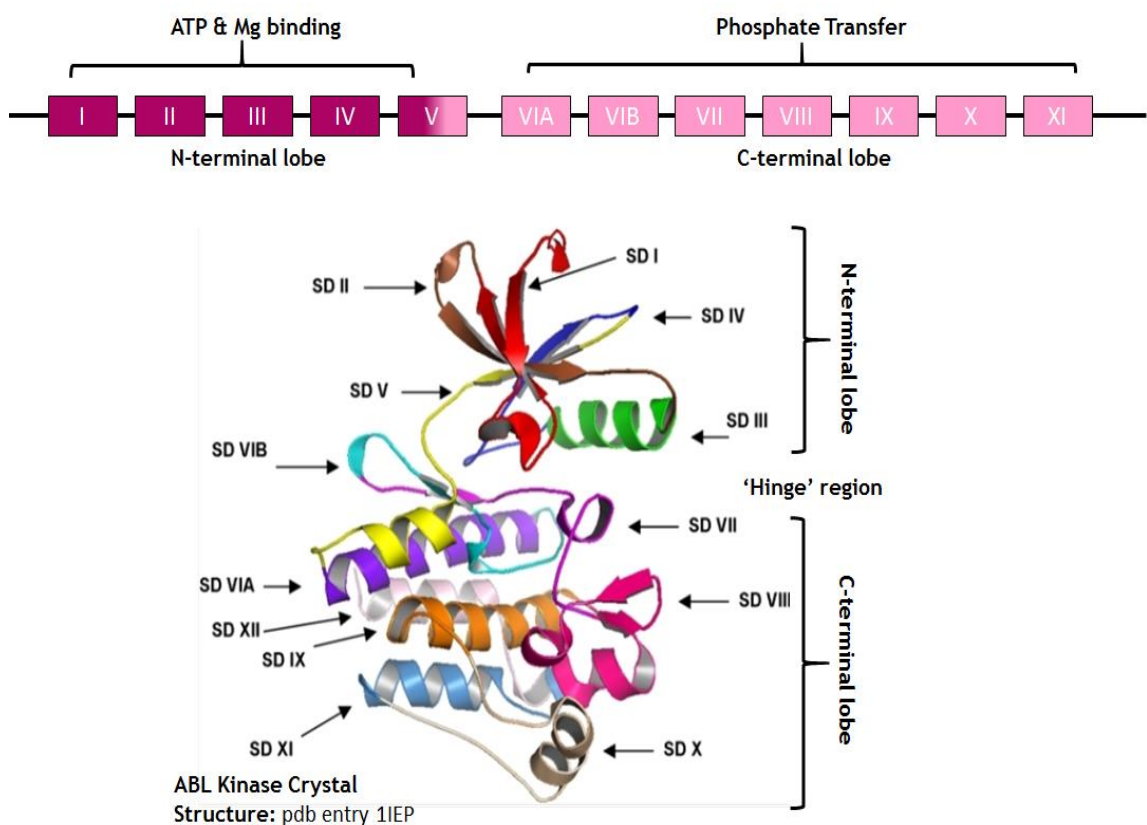


Figure 1-11: Conserved ePK domains

The position of each subdomain within the two lobes is shown schematically (above) and by their approximate position (below) in the structure of the typical ePK, ABL. The role of each subdomain is detailed in Table 1-2 (below) and in the text. Figure adapted from N.Jones and (Dixit & Verkhivker 2009). Not to scale.

ePKs are composed of two ‘lobes’: an N-terminal lobe and a C-terminal lobe. The active site residues required for ATP binding are located in a cleft within

the region linking the two lobes. Subdomains and their functions are shown in Table 2 and discussed below.

Subdomain	Subdomain Name /Feature	Motif (aa)	Function
I	Glycine Rich loop	GxGxxG	ATP Binding
II	Invariant Lysine	AxK	Phosphate transfer
III	α helix domain	E	Forms salt bridge between subdomain II and III; stabilises phosphate transfer
VIB	Catalytic loop	HRDxxxxN	Proton acceptor during phosphorylation Stabilises reaction
VII	DFG motif	DFG	Aspartate required for binding magnesium ions and ATP orientation
VIII	Activation loop/T-Loop & P+1 Loop/Walker A motif	1) APE 2) GxxxxGKT/S	1) Core stability within C-lobe- forms a salt bridge with subdomain XI (E-R) 2) interacts with ATP adenine ring- orientation and docking of ATP
IX	F-helix	DxxxxG	Highly hydrophobic, required for catalytic loop stability
X	GHI		Least conserved region, required for core kinase structure
XI	GHI	R	Core stability within C-lobe

Table 1-2: ePKs have 12 conserved subdomains

The known function(s) of each domain are as detailed in the above table. The information used to generate this table was extracted from (Taylor & Kornev 2011).

The N-terminal ‘lobe’ (or C-helix) is comprised of 5 β -sheets and one α -helix domain. This lobe is both the smaller and more mobile and encompasses subdomains I-IV (reviewed by Taylor & Kornev 2011; see table 1-3). The lobe is primarily required for co-ordinating the orientation of both the phosphate and the magnesium ion relative to the active site. The lobes are connected in a hinge-like fashion by a beta sheet (within the N-terminal lobe) and an alpha helix (within the C-terminal lobe). Additionally, the hinge region can also contribute to peptide binding specificity. Subdomains VI -XI are located in the larger C-terminal lobe, which is composed mostly of α -helices (seven) and four β -strands. Subdomains IV to VIIA primarily contribute to stability of the core kinase structure. Overall, the C-terminal lobe is required for binding the required peptide substrate and facilitating the transfer of the phosphate onto the substrate; for optimal kinase activity, the orientation of the phosphate within the active site is critical.

1.5.1.2 Atypical Protein kinases (aPKs) and Protein Kinase Like (PKL) kinases

aPKs lack the conserved subdomain structure of a typical ePKs but have been reported to harbour kinase activity or show structural homology to other kinases. Currently, four aPK kinase ‘groups’ are recognised (Duong-Ly & Peterson 2013): pyruvate dehydrogenase kinases (PDHKs), nucleoside diphosphate kinases (NDKs), pyruvate kinase (PyK) and structurally atypical putative PKs (SAPPKs; for example, bromodomain containing kinases; Devaiah et al. 2012).

Recently, many aPKs were re-classified into a family of ePKs known as the PKL kinases; these kinases harbour similarities to ePKs in the catalytic domain region and their activation mechanism, yet still lack many of the other conserved features of ePKs. This group encompasses the following kinase groups; ABC1 domain containing kinases, Alpha kinases, phosphatidyl inositol kinases (PIKs), RIO kinases, Phosphatidyl Inositol phosphate kinases (PIPks), AGPHD1 kinases, golgi associated kinases (GASKs) and phosphatidyl inositol 3’ kinase-related kinases (PIKKs). A subset of ‘other’ PKL kinases exist, which are highly diverged in sequence (Kannan et al. 2007).

1.5.1.3 Pseudokinases: just a dead kinase?

In addition to PKs, ~10% of the human kinome are in fact pseudokinases, which are enzymes that appear to lack any catalytic activity based on their protein sequence. Though they lack critical residues required for kinase activity, this does not mean they are incapable of signalling and interactions, even via phosphate transfer, though often their modes of action remain highly elusive (Boudeau et al. 2006; Reiterer et al. 2014; Zeqiraj & van Aalten 2010; Zhang et al. 2012). Instead of acting as kinases, they function as structural elements able to tether incoming substrates (perhaps as part of a kinase signalling pathway), substrate competitors, protein modulators, or act in a manner to allow different signalling pathways access to each other (as suggested by Reiterer et al. 2014).

Pseudokinases typically show loss of three core conserved motifs found in kinases: the HRD motif (His-Arg-Asp), the DFG motif (Asp-Phe-Gly) and the VAIK motif (Val-Ala-Ile-Lys; required for ATP orientation). The origins of these

pseudoenzymes (as discussed by (Zhang et al. 2012; Zeqiraj & van Aalten 2010; Reiterer et al. 2014) are unknown.

Several pseudokinases have now been linked to disease states in vertebrate organisms. For example loss of Kinase suppressor of ras1, KSR1, results in modulation of Ras signalling depending upon the level of KSR1 expression (mutations in Ras proteins themselves are associated with the oncogenic effects in cells; reviewed by Downward 2003).

1.5.1.4 Pseudokinases in parasitic organisms

Pseudokinases in protozoan organisms are increasingly becoming of interest. For example, the causative agent of Giardiasis (*Giardia lamblia*) has ~50% of their predicted kinome as pseudokinases. Interestingly, of the 195 NEK kinases (an expanded family of kinases), an estimated 139 (or 71%) may be pseudokinases (Manning et al. 2011). The expansion of this family and the roles of these pseudokinases are still under investigation. To date, only that action of two active NEK kinases in *G. lamblia* (GlNek1 and GlNek2) have been reported as important regulators of the cell cycle and parasite excystation (Smith et al. 2012).

The obligate intracellular parasite *Toxoplasma gondii* has a predicted 51 pseudokinases from a total kinome of 159 proteins (Peixoto et al. 2010). One pseudokinase (ROP5) is important for the phosphorylation of the rhoptry protein ROP18 (see Dlugonska 2008 for a review on the organelles in *T. gondii*), which is involved in the inactivation of IRG proteins (which are required for resistance of cells to *T. gondii* invasion). Deletion of ROP5 reverted a highly virulent *T. gondii* strain to an avirulent form, highlighting the importance this pseudokinase plays in the establishment of a *T. gondii* infection (Sibley et al. 2009 for a review of rhoptry proteins; Lim et al. 2012; Fleckenstein et al. 2012).

1.5.2 The *T. brucei* kinome

With the publication of the *T. brucei* genome in 2005, the kinome of this parasite could comprehensively be investigated (Parsons et al. 2005). Approximately 2% of the genome of *T. brucei* (a similar complement to that of the human genome) is dedicated to protein kinases, of which there are 158

ePKs, 20 aPKs and an estimated 12 pseudokinases. Figure 1-12 shows a stylised map of the trypanosome kinome detailing only the ePKs. To date, no receptor tyrosine kinases (TKs) or tyrosine kinase like kinases (TKL) have been identified. However, tyrosine phosphorylation occurs in *T. brucei*, though further work is required to identify the PKs responsible (Parsons et al. 1991).

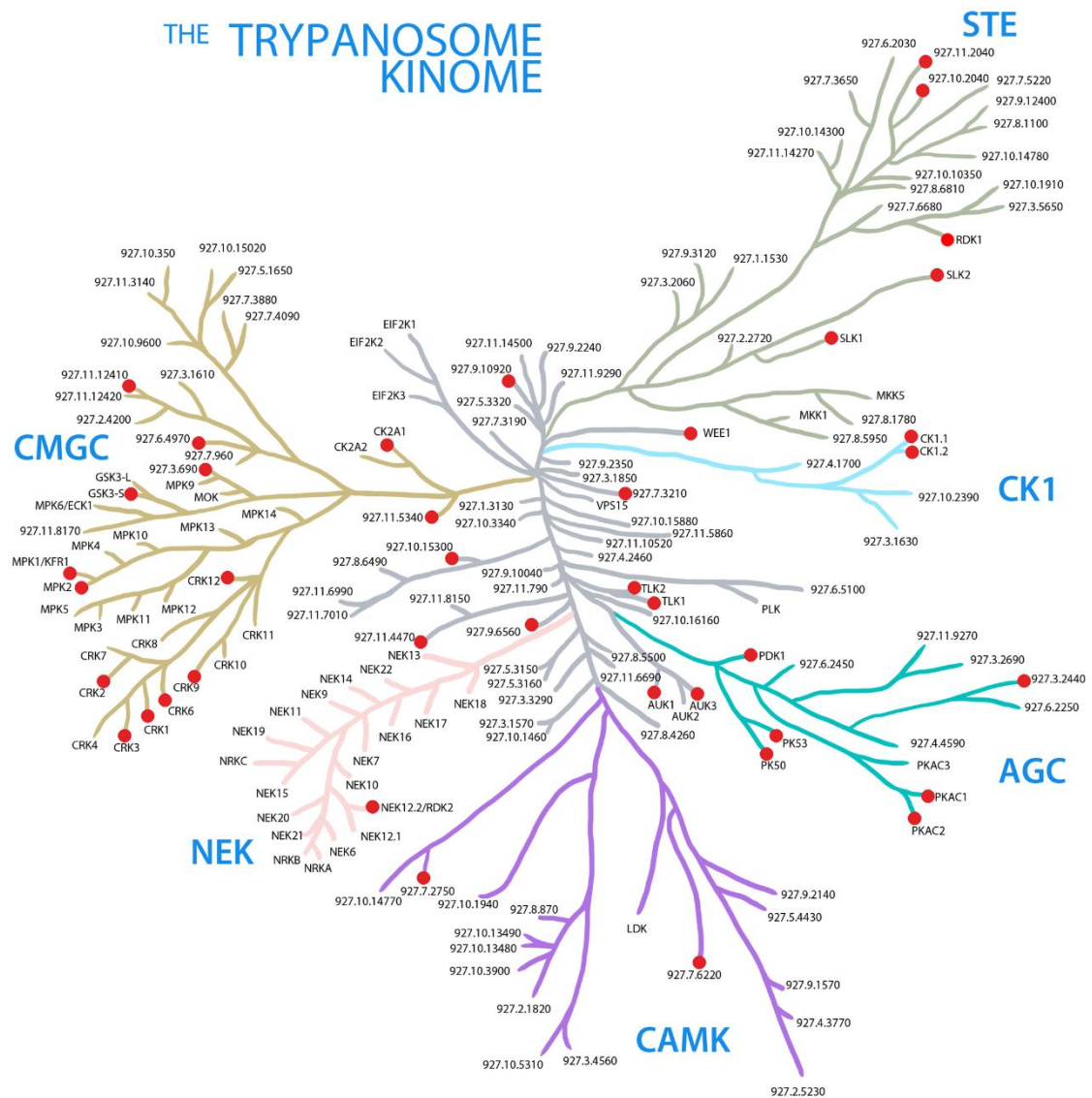


Figure 1-12: The *T. brucei* kinome
Branch lengths are simply representative of family groupings and do not reflect any phylogenetic observations. Red nodes indicate RNAi targeting of the PK affects BSF proliferation *in vitro* from the data presented by (Jones et al. 2014). Families are defined based on protein sequence characteristics. Tree represents 156 ePKs from *T. brucei*. Figure adapted from (Jones et al. 2014).

Contractions and expansions of several PK families have occurred in *T. brucei*. CMGC kinases, STE kinases and NEK kinases show expansion relative to the human kinome, while CAMK kinases and AGC kinases are underrepresented. Expansion of PK families is not a unique feature of trypanosomatid parasites;

over 70% of the *Giardia lamblia* kinome is comprised of NEK kinases (Manning et al. 2011); in humans there are only 11 NEK kinases (Fry et al. 2012) and in *T. brucei* 21 (Parsons et al. 2005; Jones et al. 2014).

Overall, an estimated 22% of the *T. brucei* kinome is required for BSF proliferation, of which ~30% of these kinases produce severe phenotypes when targeted by RNAi (Jones et al. 2014). For example, depletion of the kinase RDK2 (family: NEK Kinase; Tb927.4.5310) results in differentiation from BSF to PCF both *in vitro* and *in vivo* (Jones et al. 2014); the parasite population ceases proliferation ~72 hours post RNAi induction when cultured in HMI-11 BSF medium (data not shown). Studies like the aforementioned and others (Mackey et al. 2011) highlight the importance of protein kinase activity in these parasites.

1.5.2.1 Pseudokinases in *T. brucei*

Of the 190 predicted protein kinases of *T. brucei* an estimated 6% (12) are thought to be pseudokinases; this could be an underestimation due to potential miss-annotation of the reference genomes (Lister 427 or TREU 927; TriTrypDB). Furthermore, of the 12 predicted pseudokinases of *T. brucei*, nine have been shown (by kinome-wide screening with minimal follow up validation) to be required for full parasite viability *in vitro* (Jones et al. 2014). However, to date, there is no known role for any pseudokinase in *T. brucei* or any other kinetoplastid.

1.6 DNA Repair and Damage

Genomic integrity can be challenged at any moment; from endogenous sources of damage such as replicative lesions and metabolic by-products, to exogenous sources including mutagenic chemicals and radiation. To add further complexity, a variety of lesions can form, including double-stranded breaks (DSBs), single stranded breaks (SSBs), replication forks (RF) stalls, cross-linking of DNA strands (intra-or inter), DNA base modifications (such as methylation) or mismatching of DNA bases during replication. Due to the myriad of routes by which genome integrity can be challenged, cells have evolved an extensive array of pathways to repair (or tolerate) any potential lesion which may arise (Figure 1-13). Collectively, these diverse responses are known as the DNA damage response

(DDR). The DDR has been extensively reviewed (Chang & Cimprich 2009; Cimprich & Cortez 2008a; Guleria & Chandna 2015; Kondo et al. 2010; Larsen & Stucki 2015; Nogueira et al. 2011; Podhorecka et al. 2011; Shiloh & Ziv 2013; Zeman & Cimprich 2014) and hence will be briefly discussed below and elaborated on when required in the appropriate chapters.

When a lesion arises, several clear 'signals' can form. For example, the MRN complex or Ku heterodimer localises to DSBs; ssDNA activates members of the poly (ADP ribose) polymerase (PARP) family (as reviewed by Ciccina & Elledge 2010; Cohen-Armon 2007), such as PARP-1, or can be bound by ATRIP (a protein complexed to an atypical PK). Additionally, the phosphorylated histone variant H2A(X) can also arise in response to several lesions (as reviewed by Mah et al. 2010; Kuo & Yang 2008; Dickey et al. 2009), though it does not directly contribute to repair of all damage. Once lesions are then 'sensed' by the above proteins, the signal is further amplified by 'mediator' proteins. For example, MDC1 (Mediator of DNA Damage Checkpoint Protein 1) acts to retain the MRN complex and the Ataxia Telangiectasia Mutated [ATM] PK at DSBs. The signal is then further amplified by 'transducer' proteins. For example, the PIKK kinases ATM and DNA-PKcs (the DNA-dependent kinase catalytic subunit) are activated via MRN and Ku, respectively, on DSBs. A further PIKK kinase, AT-and Rad3 Related (ATR), is activated via ATRIP on some ssDNAs, and MAPK kinase signalling occurs following PARP-1 activation on other ssDNA lesions (Ciccina & Elledge 2010). The specific PK activated predominantly determines which DNA repair pathway is pursued to resolve the lesion. Failure to resolve a DNA lesion, in particular a DSB, is often fatal for the cell (DSB repair is reviewed by (Kakarougkas & Jeggo 2014) and so cell cycle checkpoints can be activated, resulting in stalling of the cell cycle progression to allow time for lesion repair by 'effector' proteins, such as and RAD51 during HR. A description of how each repair pathway operates is beyond the scope of this thesis, but is reviewed in kinetoplastids by (Passos-Silva et al. 2010; Genois et al. 2014). A generalised schematic of known DDR pathways is shown in Figure 1-13.

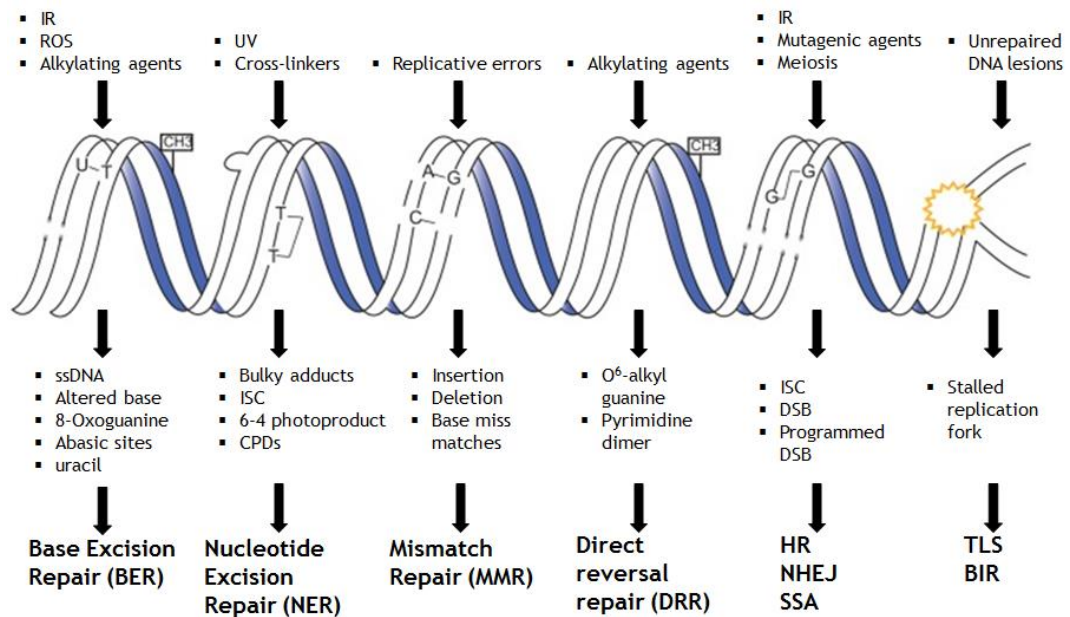


Figure 1-13: The diverse range of DNA lesions and their corresponding DNA repair pathways

The schematic above represents both the diversity of lesions which can form, the source by which they are generated and the myriad of routes required to resolve the lesions. IR (ionizing radiation), ROS (reactive oxygen species), ssDNA (single stranded DNA), UV (ultra violet), ISC (inter/intra strand cross links), DSB (double stranded break), HR (homologous recombination), NHEJ (non-homologous end joining) SSA (single strand annealing), TLS (translesion synthesis) and BIR (break induced repair). Adapted from (Genois et al. 2014) with permission.

1.6.1.1 Replicative stress

As mentioned in section 1.4, recent evidence suggests the involvement of replication-derived lesions to initiate VSG switching. In addition, in any cell lesions that halt replication are the most deleterious to life. As such, replicative stress will be discussed in more detail below.

Replicative stress is a broad term, which encompasses lesions derived from replicative processes predominantly associated with either the slowing, stalling or halting of replication fork progression. A replication fork is a complex structure of many replication proteins (the replisome), which collectively unwind the DNA, synthesis new DNA and remove torsional stress (reviewed by Ciccio & Elledge 2010; Zeman & Cimprich 2014). Replicative stress can arise in many ways. For example, at regions of repetitive sequences, at mismatched base sites, following the activation of oncogenes (like c-myc; as reviewed by Rohban & Campaner 2015), where DNA-RNA hybrid structures (R-loops) form, due to dormant origin firing, at collisions with protein complexes, most notably

transcription, and when the replication machinery encounters ‘fragile’ sites. Little work has examined the replication stresses encountered in the *T. brucei* genome, though mapping replication dynamics revealed slowed replication progression due to head-on encounters with multigenic transcription (Tiengwe et al. 2012). More speculatively, the BESs appear a rich source of such stress: the VSG is immediately adjacent to the shelterin-bound telomere, the BES harbour 70 bp repetitive sequences, and early replication of the active BES site suggests clashes with transcription. In this regard, the recently described ‘early replicating fragile sites’ (which are GC-rich) have been postulated to activate the ATR kinase following lesion formation (Mortusewicz et al. 2013).

Predominantly, DNA lesions such as DSBs and ssDNA arise from stalled replication and subsequently activate pathways which mediate their resolution. Routinely, two outcomes are possible following the stalling of a replication fork; replication fork resolution or replication fork collapse. Though these processes still require further investigation, forks that are able to restart are predominantly assisted by ATR, whereas forks that fail to resolve may produce a DSB causing activation of ATM (Trenz et al. 2006 as reviewed by Allen et al. 2011). More detail on the roles of TbATR and TbATM in these processes is provided in chapter 6.

1.6.2 DNA Repair in *T. brucei*

Extensive work has detailed the action of a wide range of DNA repair pathways in kinetoplastids, including *T. brucei*, revealing that most pathways are generally conserved and active. However, some clear divergences are apparent. Accumulating evidence, based initially on homology searches and later on experimental analyses (Glover et al. 2008; Glover et al. 2011; Burton et al. 2007; Zhang & Matlashewski 2015; Peng et al. 2015), suggests that kinetoplastids do not utilise NHEJ repair, but instead repair of DSBs is dominated by the HR pathway and MMEJ (or SSA; Glover et al. 2008; Glover et al. 2011). NER also appears highly diverged, with a focus on repair of transcription-blocking lesions by an altered NER machinery, perhaps due to the presence of multigenic transcription (Machado et al. 2014). Mismatch repair appears to be required for dealing with oxidative derived lesions in both *T. brucei* and *T. cruzi* (Grazielle-Silva et al. 2015). Even HR has been adapted to the needs of the parasites: the core HR mediator, BRCA2, has undergone structural reorganisation in *T. brucei*

(Hartley & McCulloch 2008; Trenaman et al. 2013), perhaps due to the demands of VSG switching; *T. cruzi* is highly radiation resistant, a process that requires HR (Grynberg et al. 2012; Vieira et al. 2014; Passos-Silva et al. 2010; Regis-da-Silva et al. 2006); and the huge genome plasticity of *Leishmania* is, at least in part, catalysed by HR activities (Laffitte et al. 2016; Genois et al. 2014). Finally, recent work has shown that function of at least one damage sensing complex, the 9-1-1 complex, acts divergently in *Leishmania* (Damasceno et al. 2013; Damasceno et al. 2016). Indeed, another divergence of the *T. brucei* DDR from other eukaryotes is seen in phosphorylation of H2A after damage, generating the γ H2A signal. In all other eukaryotes, phosphorylation of H2A(X) occurs on a Serine, but in *T. brucei* phosphorylation is on a Threonine (130; γ H2A^{Thr130}) within poorly conserved surrounding residues (Glover&Horn 2012).

How the above described differences in repair pathways and proteins affect, and influence, the interconnected DDR of these kinetoplastids parasites remains largely unknown. A striking deficit in our knowledge is in the role of PKs associated with DNA repair. Many components of the DDR undergo PK-mediated phosphorylation during repair in other eukaryotes, including, for example, the HR factors RAD51 (Flott et al. 2011), BRCA2 (Kim et al. 2008) and RAD51 paralogs (Suwaki et al. 2011; Niu et al. 2009). In addition, PK-mediated phosphorylation is a central component of the cascade of protein recruitment and activation during replication. Despite this, little work has examined such modifications in the kinetoplastids. In *Leishmania* KU70 appears to be a target for CRK3 -mediated phosphorylation (Maity et al. 2011), though the purpose of this phosphorylation is currently unknown. In *Plasmodium*, the origin replication complex is regulated by PfPK5 phosphorylation (Deshmukh et al. 2015), though this has not been described in kinetoplastids. Considering the vital roles PKs play in the eukaryotic DDR, and in genome maintenance generally, this is an area in need of investigation. Any insight may reveal novel functions in the regulation and execution of crucial processes, such as *T. brucei* antigenic variation.

1.7 Project Objectives

The aim of this project was to biologically validate two independently performed RITseq screens that were designed to identify PKs with DNA repair-associated roles in BSF *T. brucei* parasites. Specifically, the screens searched for those

factors, including PKs, required for survival in the presence of MMS. One chapter reveals validation and deeper exploration of the MMS sensitivity of several candidate PKs recovered in the screens. The following three chapters examine the functions of an aurora kinase, a pseudokinase and the atypical PIKKs TbATR and TbATM.

2 Materials and Methods

2.1 General Bioinformatics

2.1.1 Sequence retrieval and examination

Kinetoplastid protein and DNA sequences were retrieved from TriTrypDB (current version. 28; <http://tritrypdb.org/tritrypdb/>; Aslett et al. 2010). For RNAseq analysis, the whole genome sequence of *T. brucei brucei* Lister 427 was retrieved from TriTryp DB (v.28; May 2016). Protein sequences from other organisms were retrieved from the NCBI database (<http://www.ncbi.nlm.nih.gov/>). All sequences were input into CLC genomics Workbench 7 (Qiagen) for further examination. This software was also used for the plasmid map construction, primer design, restriction digest design, sequence analyses, plasmid sequencing analysis and sequence alignments.

2.1.2 Homology searching, protein domain analysis and structure prediction

Homology searches were performed using the NCBI database Basic Local Alignment Tool (BLAST; Altschul et al. 1990; <http://blast.ncbi.nlm.nih.gov/Blast.cgi>). The standard (BLOSUM 62) blastp settings were used to BLAST against all non-redundant (nr) protein sequences available in the database. The SmartBLAST feature (standard settings; http://blast.ncbi.nlm.nih.gov/smartblast/?LINK_LOC=BlastHomeLink) was used for a more concise and optimised analysis. Features of this software are available here: http://blast.ncbi.nlm.nih.gov/smartblast/smartBlast.cgi?CMD=Web&PAGE_TYPE=BlastDocs). For protein domain analysis, several web bases programs were used: NCBI BLAST (as above) and InterPro (<https://www.ebi.ac.uk/interpro/>). For generation of structural homology models and protein structure predictions, the RaptorX platform was used (<http://raptorx.uchicago.edu/>).

2.1.3 General Statistics

All statistical analysis was performed using GraphPad Prism 5 (<http://www.graphpad.com/scientific-software/prism/>). The appropriate tests were conducted following advice from J.Wilkes and are as detailed in the corresponding figure legends.

2.2 Molecular Techniques

2.2.1 Genomic DNA extraction and preparation

Cells were harvested as per section 2.7.6 and genomic DNA (gDNA) extracted using the Qiagen Blood and Tissue extraction kit (Qiagen) as per manufacturer's instruction. gDNA was eluted in 50 μ l ddH₂O and stored at 4 °C.

2.2.2 Agarose Gel

Routinely 0.8-1 % (w/v) agarose (UltraPure™ Agarose; Invitrogen) was melted in 1 x TAE buffer (40 mM Tris Base, 19 mM acetic acid, 1 mM EDTA). For DNA visualisation, 3 μ l- 6 μ l of a DNA stain (SYBR® Safe DNA Stain; Life Technologies) was added. For gel loading, 1 x type III DNA Gel-loading buffer was added to the DNA. For fragment size estimation, 1 Kb Plus ladder (Invitrogen) was also loaded. Gels were run between 60-120V (size dependant) 1 x TAE buffer. Gels were visualised using a GelDoc™ XR+ system (BioRad) or myECL™ imager (ThermoFisher Scientific). The software provided was used for gel image capture.

2.2.3 General Primer design

Primers were designed based on the TREU927 sequence using the in-built primer design feature of CLC Genomics Workbench 7. and synthesised as 'unmodified DNA oligos' by Eurofins Genomics (<http://www.eurofins.com/>). The lyophilised primer was reconstituted in ddH₂O upon arrival to give a final primer concentration of 100 pM/ μ l and stored at -20 °C. Primers were used at a working concentration of 10 pM/ μ l in a 50 μ l PCR reaction.

2.2.4 Polymerase Chain Reaction (PCR)

For diagnostic PCR analysis, NEB Taq DNA polymerase (NEB) was used as per manufacturer's instructions. Typically, for a 50 μ l reaction, the following reaction was set up: 1 μ l 1 mM dNTP mix (Promega), 10 μ l 10 x ThermoPol® Buffer, 2.5 μ l Primer 1 (10 pmol stock), 2.5 μ l Primer 2, 4 μ l gDNA, 0.5 μ l Phusion® and 29.5 μ l ddH₂O. For PCR products required for plasmid construction, Phusion® High-Fidelity DNA polymerase (NEB) was used as per manufacturer's

instructions. Phusion® harbours proof-reading activity for amplification of a high fidelity product. Typically, for a 50 µl PCR reaction for cloning, the following reaction was set up: 1 µl 1 mM dNTP mix (Promega), 5 µl 5 x HF Buffer, 2.5 µl Primer 1 (10 pmol stock), 2.5 µl Primer 2, 4 µl gDNA, 0.5 µl Phusion® and 29.5 µl ddH₂O. The following basic program was used for amplification (a variety of thermocycler machines were used throughout this project):

- 98 °C 3 mins (1 cycle ; Phusion®) or 95 °C 5 mins (1 cycle ; NEB Taq DNA polymerase)
- 98 °C 15 sec (1 cycle ; Phusion®) or 95 °C 30 sec (1 cycle ; NEB Taq DNA polymerase)
- 54-60 °C 30 sec (30 cycles; both polymerases; temperature was primer dependent)
- 72 °C 30 sec to 1 min (1 cycle; Phusion®; time was fragment size specific) or 68 °C (1 cycle; time was fragment size specific; NEB Taq DNA polymerase)
- 72 °C 10 mins (1 cycle Phusion®) or 68 °C 10 mins (1 cycle; NEB Taq DNA polymerase)

Resultant fragments were analysed on an agarose gel (section 2.2.2).

2.2.5 DNA fragment purification

For purification of DNA fragments from agarose gels, the appropriate bands were excised using a sterile scalpel blade and purified using the QIAquick Gel purification kit (Qiagen) as per manufacturer's instructions. Purified fragments were eluted in 15-22 µl ddH₂O and stored at 4 °C.

2.2.6 Restriction Digest

Generally, the required PCR fragment was digested with the appropriate restriction enzyme (detailed alongside the primers in the appropriate tables below). The vector backbone was also prepared in this manner. For PCR

fragment digests, 30 μ l reactions were set up as follows: 22 μ l gel extracted PCR fragment, 3 μ l 10 x digest buffer (enzyme dependent), 1 μ l enzyme 1, 1 μ l enzyme 2 and 3 μ l ddH₂O. For vector backbone digests, 30 μ l reactions were set up as follows: 3 μ l of the appropriate vector, 3 μ l 10 x digest buffer (enzyme dependent), 1 μ l enzyme 1, 1 μ l enzyme 2 and 22 μ l ddH₂O. Reactions were incubated at 37 °C for 1 hour. Digested products were resolved on an agarose gel (section 2.2.2) and extracted (section 2.2.5). Digested products were stored at 4°C.

2.2.7 Fragment Ligation

Digested PCR products were ligated into the appropriate vector backbone using T4 DNA ligase (NEB) as per manufacturer's instructions. 10 μ l reactions were set up as follows: 1 μ l 1 x ligation buffer, 0.5 μ l T4 DNA ligase, 2 μ l digested vector, 6.5 μ l digested PCR product (1:2 ratios; vector: PCR product). Reactions were left overnight at 16 °C.

2.2.8 Transformation of *E. coli*

Chemically competent DH5 α *E. coli* bacteria (in house) were thawed on ice (5 mins) then 50 μ l of bacteria were transformed with 3 μ l ligation mix (1 μ l for plasmid re-transformation). The cells incubated on ice for 30 mins then 'heat-shocked' at 42 °C for 45 secs then immediately on ice for 5 mins. 1 ml of SOC media (5 g yeast extract, 20 g tryptone, 0.5 g NaCl, 10 ml 1M MgCl₂, 10 ml 2M glucose, 10 ml 1M MgSO₄ /L) was added to the cells which were subsequently incubated (with agitation) at 37 °C for 1 hour after which the cells were pelleted by gentle centrifugation (10,000 rpm for 1 min) and the pellet re-suspended in ~50 μ l of the remaining supernatant. The cells spread onto Luria-Bertani (LB) broth agar plates ([5 g yeast extract, 10 g tryptone, 10 g NaCl /1L ddH₂O; pH 7.0] and 20 g agar) which were supplemented with 100 μ g ml ampicillin (suitable for all plasmids generated for this study). Plates were incubated at 37 °C for ~18 hours.

2.2.9 Construct retrieval and confirmation

2.2.9.1 Plasmid DNA extraction from bacteria

A 5 ml overnight culture of LB broth (supplemented with 100 µg ml ampicillin; Sigma-Aldrich) was inoculated with a colony containing the required plasmid DNA and left to grow for ~18-24 hrs. 800 µl of the liquid culture was stored in a 50:50 'peptone-glycerol' mix for long term storage at -80 °C. Bacteria were harvested by centrifugation at 2000x g for 10 mins and the plasmid DNA extracted using a QIAprep Spin Miniprep Kit (Qiagen) as per the enclosed instruction manual. A Nanodrop 1000 (Thermo Scientific) was used to determine the concentration of plasmid DNA after extraction (routinely 200-300 ng/µl).

2.2.9.2 Plasmid confirmation by sequencing and restriction digest analysis

The extracted plasmids were subject to restriction digest analysis (section 2.2.6) using appropriate restriction enzymes and resolved on an agarose gel (section 2.2.2). If the correct fragment sizes were observed, the plasmid was then sent for sequencing (service provided by Eurofins Genomics) using the primers detailed in Table 2-1. The sequence results were examined in CLC Genomic Workbench 7 by comparing the plasmid map with the returned sequence.

Primer Number	Name	Sense	Sequence 5'-3'	Use
MP 15	HA/myc	FW	CGT TGG CCG ATT CATT AAT GC	C-terminal myc tag sequence
MP16	HA/myc	RV	TAA TGA CGA ACG GGA AAT GC	C-terminal myc tag sequence
M13 (-43)	M13 uni (-43)	FW	AGG GTT TTC CCA GTC ACG ACG TT	KO plasmid sequence
M13 (-49)	M13 rev (-49)	RV	GAG CGG ATA ACA ATT TCA CAC AGG	KO plasmid sequence
134	Ntermseq FW	FW	GTA TAC CAA CAA GCC CGA AAA C	N-terminal tag sequencing
135	Ntermseq RV	RV	CCT TTC CAC GGA AAA GAC AC	N-terminal tag sequencing
OL4038	Actin IR	FW	TAA GGT CTC GTT GCT GCC	RxP plasmid sequencing (Mottram OL4038)
M13 (-21)	M13 uni (-21)	FW	TGT AAA ACG ACG GCC AGT	RxP plasmid sequencing
RD 134	HYG 1	FW	CGG AAG TGC TTG ACA TTG	RxP plasmid sequencing
RD 135	HYG 2	FW	TTG GCT TGT ATG GAG CAG	RxP plasmid sequencing
191	AUKRXPSEQ 1	FW	TGT GCT GGA ACT ATG TAG	AUK2 RxP plasmid sequencing
192	AUKRXPSEQ 2	FW	GAC GTT ACA GGC TAT TCA	AUK2 RxP plasmid sequencing
24	OL4212	Both	TAATGCCAACTTTGTACAAG	From Mottram primer OL4212 RNAi cassette PCR
OL4161	OL4161	Both	TAATGCCAACTTTGTACAAA	Mottram primer OL4161 RNAi cassette PCR

Table 2-1: Primers required for the sequencing of all construct in this thesis

2.3 Gateway® Cloning

For Gateway© cloning, the following protocol was utilised (as designed and implemented by Jones et al. 2014). An RNAi target fragment and corresponding primers were identified using the TrypanoFAN RNAit software

(<http://trypanofan.bioc.cam.ac.uk/software/RNAit.html>). A detailed protocol and the primers used for Gateway® cloning are shown in chapter 8 (section 8.1.1).

2.4 Construct Design

2.4.1.1 Endogenous tagging

The following primers were used for the endogenous tagging of genes of interest (Table 2-2).

Primer Number	Gene Name	Gene ID	Sense	Sequence	Restriction sites	Use
70	CAMK/KL	Tb927.2.1820	FW	GTAT aagctt AGGAATGAAGAGTTGGGG	HindIII	C-terminal tag
71	CAMK/KL	Tb927.2.1820	RV	GCTA tctaga CATCAGTTCGGTTTCCC	XbaI	C-terminal tag
76	KFR1	Tb927.10.7780	FW	GTAT aagctt TGAAGCCTGCCAATGTTT	HindIII	C-terminal tag
77	KFR1	Tb927.10.7780	RV	GCTA tctaga CAAGGCTAACTTTTGCTTTCCG	XbaI	C-terminal tag
102	AUK2	Tb927.3.3920	FW	GTAT aagctt ACTATGTAGGGGTGGGTC	HindIII	C-terminal tag
103	AUK2	Tb927.3.3920	RV	GCTA tctaga CACGCGAGGACGTTTTCC	XbaI	C-terminal tag
104	Tb927.9.6560	Tb927.9.6560	FW	GTAT aagctt CACTGCGAGCAACCAAAA	HindIII	C-terminal tag
105	Tb927.9.6560	Tb927.9.6560	RV	GCTAtctaga CTTGAAGAGACTGGCGGA	XbaI	C-terminal tag
172	Tb927.7.960	Tb927.7.960	FW	GATC gagctc AAG GCT ATG TGG CAG GGG GAC CC	SacI	C-terminal tag
173	Tb927.7.960	Tb927.7.960	RV	GATC tctaga GTT GTT GGT GGC ATC ATA CAG C	XbaI	C-terminal tag
202	CRK6	Tb927.11.1180	FW	GGTC actagt TCT GAT ACA TTA AGT AGC AAA CT	SpeI	N-terminal tag ORF
203	CRK6	Tb927.11.1180	RV	GGTC ggtacc CGA TAC CAC AAC GTC ATT	KpnI	N-terminal tag ORF
204	CRK6	Tb927.11.1180	FW	GGTC ggtacc GCA GAG CGAACA CGC ATA	KpnI	N-terminal tag 5UTR
205	CRK6	Tb927.11.1180	RV	GGTC ggtacc GAT ATC CAA CCC GTT TCA GT	BamHI	N-terminal tag 5UTR
206	CRK11	Tb927.6.3110	FW	GCACG aagctt GCG ATC CGT TTC CTC ACA	HindIII	C-terminal tag
207	CRK11	Tb927.6.3110	RV	GCACG tctaga AAG TGT GGC CAT GTT CAT GT	XbaI	C-terminal tag
208	MPK2	Tb927.10.5140	FW	GCACG aagctt CCA GTT TGC CGAAGC TAT	HindIII	C-terminal tag
209	MPK2	Tb927.10.5140	RV	GCACG tctaga TTT GTG CAA CAC ACG AGA G	XbaI	C-terminal tag
N/A	ATM	Tb927.2.2260	FW	GTAT aagctt ACC GTT GGG TTG ATT GAG TGG	HindIII	C-terminal tag
N/A	ATM	Tb927.2.2260	RV	GCT tctaga CAG CCA AGG TGA CCA GCC GTG	XbaI	C-terminal tag
N/A	ATR	Tb927.11.14680	FW	GTAT aagctt TTC TGT GTA AAT CGA GGG ACG	HindIII	C-terminal tag
N/A	ATR	Tb927.11.14680	RV	GCT tctaga CAA CCA CGC CAT CCA CCAAT GTA	XbaI	C-terminal tag

Table 2-2: Primers required for endogenous tagging

Primer sequence reads 5'-3'. ORF (open reading frame) and UTR (untranslated region).

2.4.1.1.1 C-terminal

For C-terminal endogenous tagging, the vector pNAT^{x12myc} (as described in Alsford & Horn 2008; kind gift R.Devlin) was used. This construct permits C-terminal tagging with 12 copies of the myc epitope (12myc) and contains a Blastidicin (BSD) resistance cassette for positive selection following transformation. A generic plasmid map is shown in Figure 2-1 alongside the

tagging strategy. Primers which specifically amplify a region of the 3' region of the ORF excluding the stop were designed (Table 2-2). Cloning was performed as described in section 2.2.

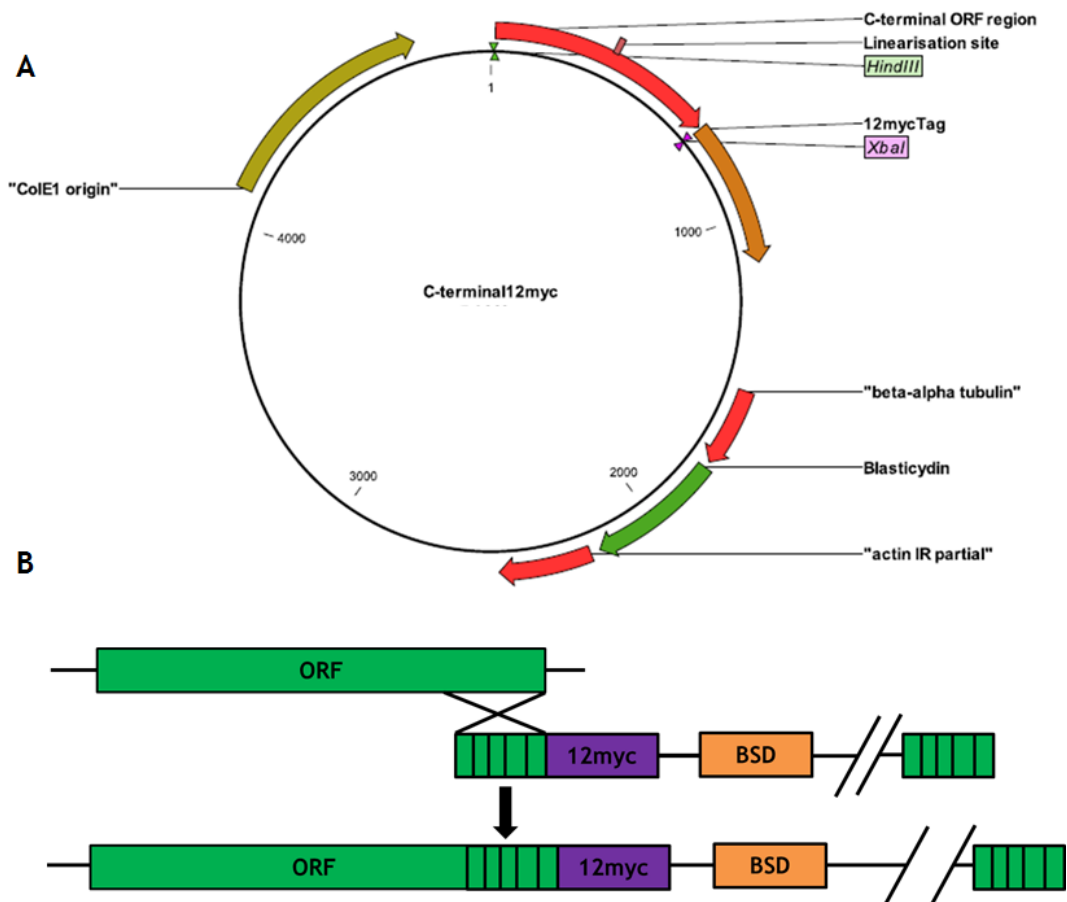


Figure 2-1: C-terminal tagging strategy

(A) Generic plasmid vector map of the construct harbouring an insert (labelled C-terminal ORF region). Routinely, fragments were cloned in between *HindIII* and *XbaI* sites (unless otherwise indicated in Table 2-2). To ensure expression of RNA transcripts tubulin (for transplicing) and actin (for polyadenylation) intergenic regions (IR) were present flanking the blasticidin (BSD) gene (green) in the plasmid. (B) Endogenous tagging strategy. The linearised plasmid was transformed into cells and integrated into the genome by HR (black cross) using the region homologous (black line hashed green box) to the endogenous ORF (green) to permit fusion of the myc tag to the 3' region of the endogenous locus. Not to scale.

2.4.1.1.2 N-terminal tagging

For N-terminal endogenous tagging, the vector pEnT6B (modified from Kelly et al. 2007; kind gift R.Devlin) was used. This construct permits N-terminal tagging with 12 copies of the myc epitope (12myc) and contains a Blasticidin (BSD) resistance cassette for positive selection following transformation. The BSD resistance cassette is flanked by aldolase and actin processing sequences (at the 5' and 3' respectively). A generic plasmid map is shown in Figure 2-2, below

which is the tagging strategy employed. Primers were designed to amplify the 5' region of the ORF (excluding the start codon) and the 3' region of the 5' UTR upstream of the ORF (primer sequences are detailed in Table 2-2) thus the fragment resides downstream of the 12 myc tag. Both fragments are required for HR directed integration following linearization of the construct using KpnI. The 5'UTR fragment does not integrate endogenously into the locus due to trans-splicing of the RNA upstream of the BSD resistance cassette.

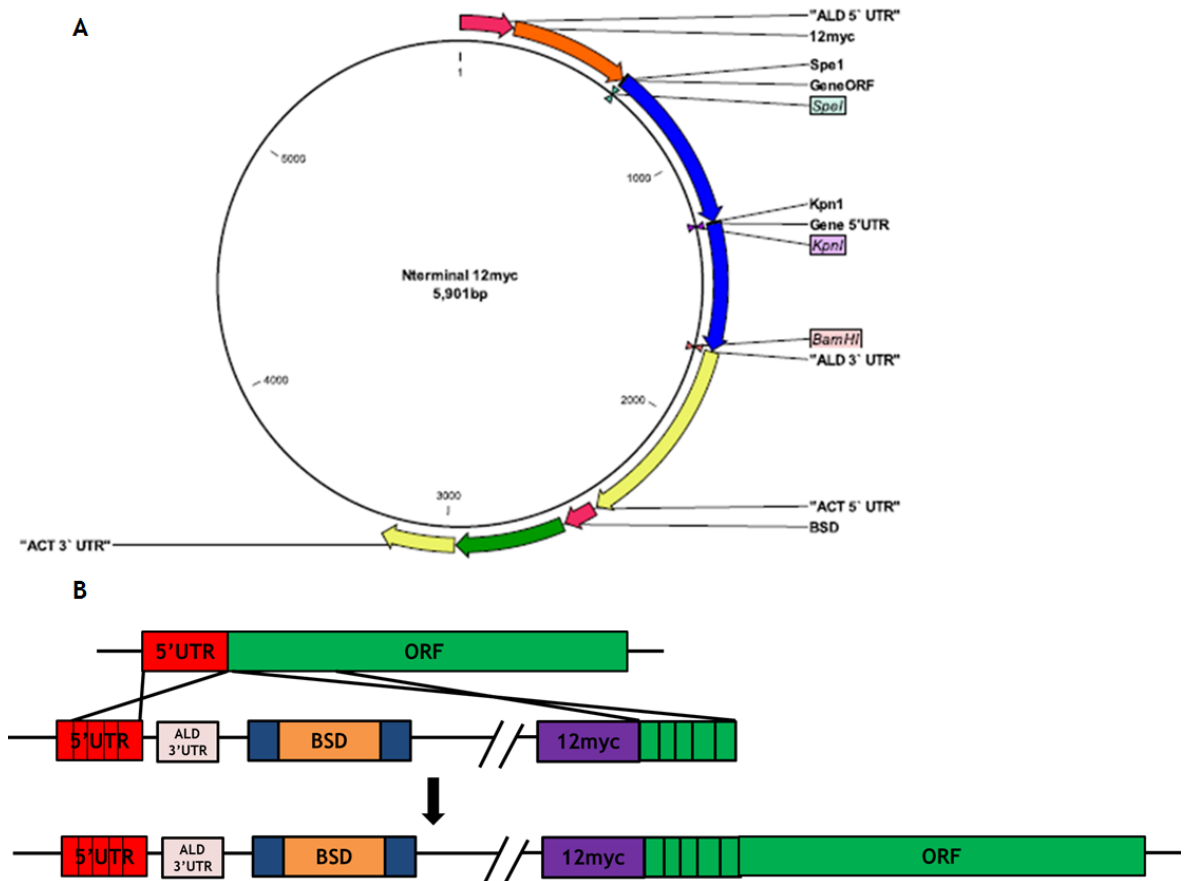


Figure 2-2: N-terminal tagging strategy

(A) Generic plasmid vector map of the construct harbouring inserts (labelled geneORF and gene 5'UTR). The ORF fragment (lacking the ATG start codon) was inserted into the vector using SpeI and KpnI sites. The 5'UTR fragment up to but not including the start codon was cloned between BamHI and KpnI sites. To ensure expression of RNA transcripts, aldolase (ALD; for transplicing) and actin (ACT; for polyadenylation) UTRs were included in the plasmid. These transcripts also flanked the blasticidin gene (BSD; green) in the plasmid. (B) Endogenous tagging strategy. The linearised plasmid (using KpnI) was transformed into cells and integrated into the genome by HR (black cross) using the region homologous (black line hashed green or red boxes) to the endogenous ORF (green) and the endogenous 5'UTR (red) to permit fusion of the myc tag to the 5' region of the endogenous locus. Dark blue boxes = actin 5' and 3' flanking regions respectively. Not to scale.

2.4.1.2 KO constructs

Two constructs were required to generate a KO mutant cell line by replacing each endogenous locus with an antibiotic selection marker for positive selection following transformation. Both vectors were modified from the pmtl23 vector (Devlin et al. 2016; kind gift R.Devlin). These constructs are termed Δ ORF::NEO and Δ ORF::BSD. A generic plasmid map is shown in Figure 2-3, below which is the KO strategy employed. Primers were designed to amplify the 3' region of the 5' UTR upstream and the 5' region of the 3' UTR downstream of the desired gene to facilitate HR directed insertion. In some cases, a proportion of the ORF was used. In addition to harbouring the antibiotic resistance cassette, the parental vector also contained two intergenic sequences derived from *T. brucei* Actin and *T. brucei* B/ α Tubulin (upstream and downstream of the BSD or NEO respectively) to facilitate trans-splicing and polyadenylation required for mRNA transcription (a generalised schematic of the knockout plasmids is shown in Figure 2-3).

The primer sequences are detailed in Table 2-3. Cloning was performed as described in section. The 5'UTR fragment was inserted first followed by the 3'UTR. The final resulting plasmids were confirmed by sequencing and analysis by restriction digest (section 2.2.6). Approximately 10 μ g of the appropriate plasmid DNA was linearised by NotI and concentrated (as per 2.2.6 and 2.2.9). Transformation of the *T. brucei* cells was performed as per section 2.7.4.

Primer Number	Gene Name	Gene ID	Sense	Sequence	Restriction sites	Use
129	Tb927.9.6560	Tb927.9.6560	FW	GCACG aagctt gcggccgc TGA AAA GGA GGG ACA GGA A	HindIII + NotI	Amplifies 5'UTR region
130	Tb927.9.6560	Tb927.9.6560	RV	GCACG tctaga AGC ACC TTC TCA CTT AAC C	XbaI	
131	Tb927.9.6560	Tb927.9.6560	FW	GCACG gagctc ACC AAT GCA AAC TCC ACA	SacI	Amplifies 3'UTR region
132	Tb927.9.6560	Tb927.9.6560	RV	GCACG atcgat gcggccgc GGA TGT GAT TGA GAA TGG G	Clal + NotI	
141	AUK2	Tb927.3.3920	FW	GCACG aagctt gcggccgc GGT TCC TTG TGT TGT TAT CT	HindIII + NotI	Amplifies 5'UTR region
142	AUK2	Tb927.3.3920	RV	GCACG tctaga CTG GAT CAC AAC CCT CGG	XbaI	
143	AUK2	Tb927.3.3920	FW	GCACG gagctc CTG CAG AAA GAC CCC AAC	SacI	Amplifies 3'UTR region
144	AUK2	Tb927.3.3920	RV	GCACG atcgat gcggccgc AGG CCC CGA TAG ATT TTG	Clal + NotI	

Table 2-3: Primers required for KO construct generation
Primer sequence reads 5' to 3'.

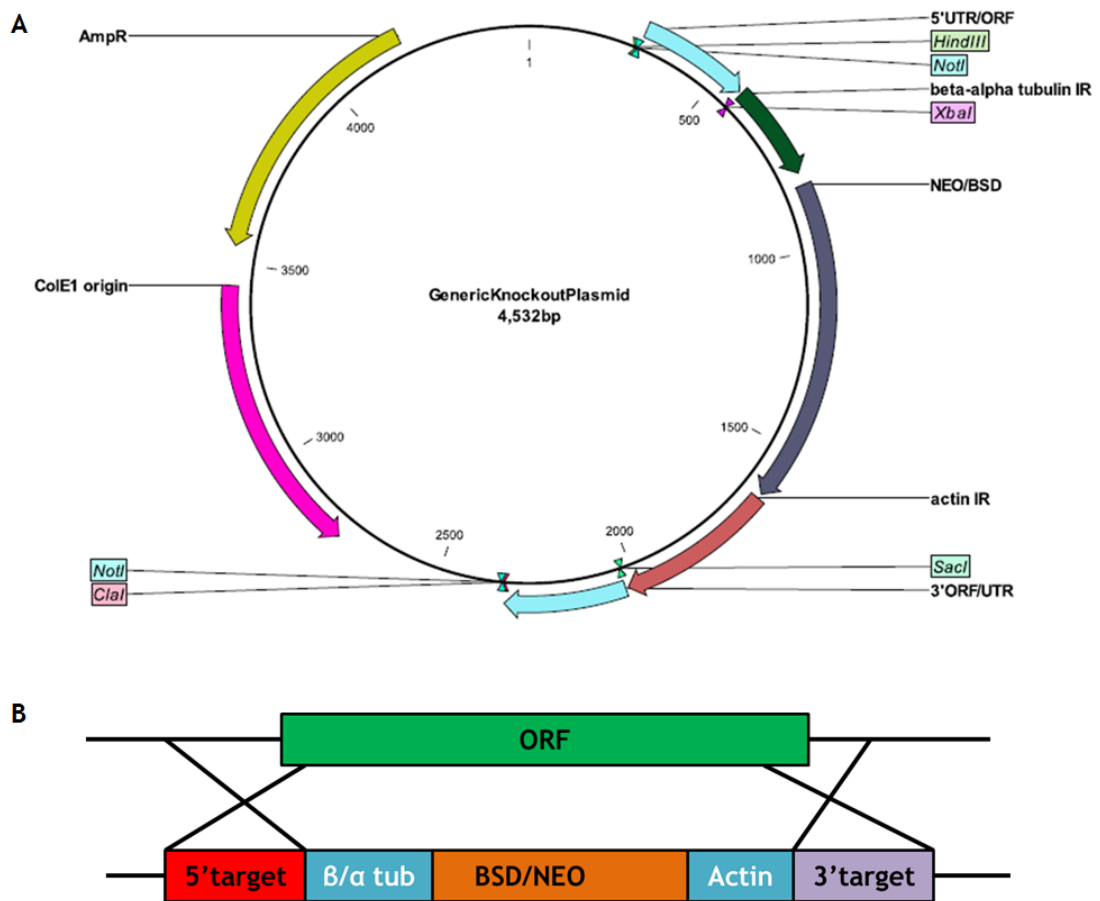


Figure 2-3: KO strategy

(A) Generic plasmid vector map of the construct harbouring inserts (labelled 5'UTR/ORF and 3'UTR/ORF). The 5'UTR/ORF fragment was inserted in using HindIII and XbaI restriction sites. The 3'UTR/ORF fragment was inserted in using Clal and SacI restriction sites. To ensure expression of RNA transcripts, tubulin (for transplicing) and actin (for polyadenylation) intergenic regions were included in the plasmid. These transcripts flanked the blasticidin gene (BSD.NEO; orange) in the plasmid to ensure the correct processing of the selection antibiotic transcript. (B) KO strategy. The linearised plasmid (using NotI) was transformed into cells and integrated into the genome by HR (black cross) using the region homologous (black line purple or red boxes) to the endogenous ORF (green) to facilitate deletion of the endogenous locus. Tub = tubulin, BSD = blasticidin, NEO = neomycin, 'target' refers to the regions of homology used for HR. Not to scale.

2.4.1.3 RxP constructs

For gene re-expression, a modified version of the pGL2070 vector (kind gift, R.Devlin) was used. R.Devlin made the following modifications: the blasticidin resistance gene was replaced with a hygromycin resistance gene and the 6HA tag removed and replaced with a multiple cloning site composed of NheI and XbaI to facilitate insertion of the desired ORF for re-expression. The final construct is integrated into the *T. brucei* Ba tubulin locus by replacing an endogenous α tubulin ORF. A generic RxP plasmid is shown in Figure 2-4. The primers used for cloning are shown in Table 2-4 below.

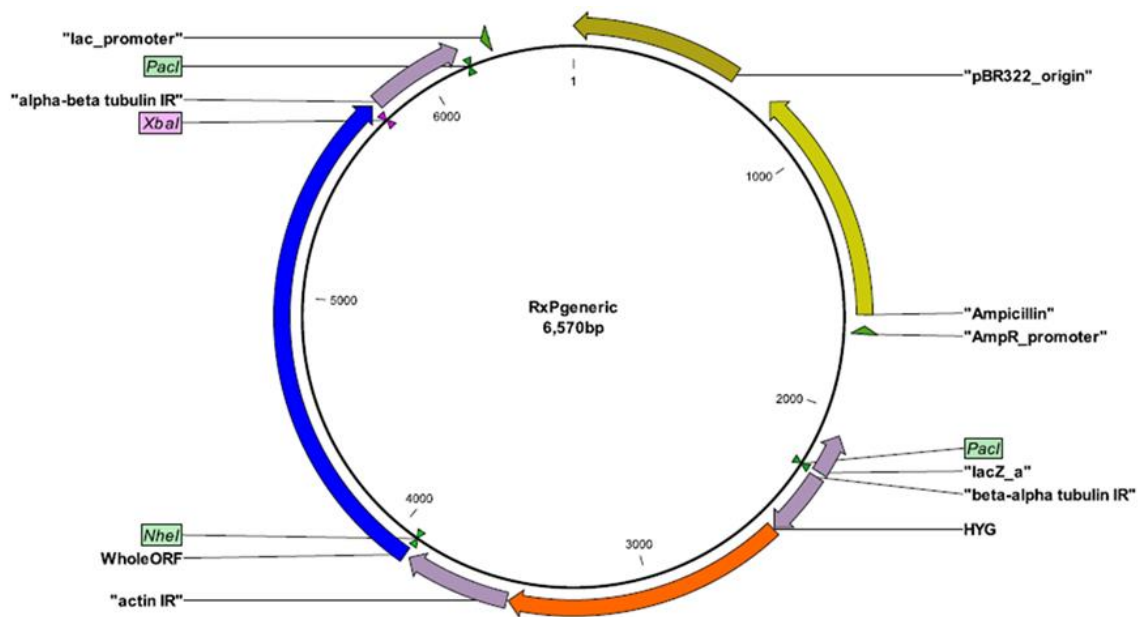


Figure 2-4: Generic RxP construct

The entire ORF of the required gene is cloned into the vector using the *NheI* and *XbaI* restriction sites. The whole ORF is flanked at the 5'UTR by an actin IR and at the 3'UTR by a β tubulin IR region. The resistance cassette gene (HYG) is also flanked in this manner. The β tubulin regions flanking the ORF permit HR mediated integration of the construct into the β tubulin array from which the whole ORF can then be expressed. *NheI* and *XbaI* produce compatible ends when digested. RxP (re-expression), UTR (untranslated region), IR (intergenic region), HYG (hygromycin), ORF (open reading frame).

Primer Number	Gene Name	Gene ID	Sense	Sequence	Restriction sites	Use
178	AUK2	Tb927.3.3920	FW	GGTC gctagc ATG GTT ATT TGG TTT TCC GC	<i>NheI</i>	Amp ORF Tb927.3.3920 for RxP
179	AUK2	Tb927.3.3920	RV	GGTC tctaga TCA CAC GCG AGG ACG TTT TC	<i>XbaI</i>	Amp ORF Tb927.3.3920 for RxP

Table 2-4: Primers required for RxP construct generation
Primer sequence reads 5' to 3'.

2.5 RNA protocols

2.5.1 RNA extraction

For general use, total RNA was extracted from 3×10^7 BSF cells using the RNeasy Mini kit (Qiagen) using the manufacturer's protocol entitled "Purification of Total RNA from Animal Cells using Spin Technology". Off-column DNase I (RNase Free DNase set, Qiagen) was performed after RNA extraction (30 min incubation). The RNA was 'cleaned-up' after DNase digestion as per manufacturer's protocol. The concentration of total RNA was assessed using a NanoDrop 1000TM Spectrophotometer (Thermo Scientific).

For RNA required for RNAseq analysis, 5×10^7 cells were harvested and RNA extracted as described above. For accurate concentration analysis, total RNA samples were analysed using a Qubit® 3.0 Fluorometer (ThermoFisher) as per the manufacturer's guidelines. Total RNA was stored at -80°C until required.

2.5.2 Complementary DNA (cDNA) Preparation

1 μg of total RNA from each sample was converted to cDNA using the SuperScript™ III Reverse Transcriptase Kit (Invitrogen) as per manufacturer's instructions ("First Strand cDNA Synthesis" protocol). Random primers were used for amplification. In all cases, duplicate reactions were set up lacking the reverse transcriptase enzyme to control for gDNA contamination. cDNA was stored at -80°C until required.

2.5.3 qRT-PCR analysis

2.5.3.1 qRT-PCR Primer design

Primers (shown in Table 2-5 below) required for qRT-PCR were designed using the Primer Express® 3.0 software supplied (Applied Biosystems).

Primer Number	Name	Sense	Sequence 5'-3'	Use
N/A	AUK2RTFW2	FW	GGG AGG GTT CGT ACT CTG TTG T	AUK2 (Tb927.3.3920) qRT-PCR
N/A	AUK2RTRV1	RV	TTT CAG CGC AAC GAC TTG AC	
N/A	NAKRTFW2	FW	AAGTGTGGTACACGGGCTCACT	Tb6560 (Tb927.9.6560) qRT-PCR
N/A	NAKRTV1	RV	CCACCTCTTCTCCGGATCTG	
N/A	ATR RT FW	FW	TCTAGTATCGCCGGCAGCTT	ATR qRT-PCR
N/A	ATR RT RV	RV	TTGGCTGTATGGCCTGATCTC	
CT_OL29	Actin q-PCR	FW	CGGACGAGGAACAACTGC	Endogenous control for RT-PCR
CT_OL30	Actin q-PCR	RV	TTTCCATGTCATCCAATTGG	
CT_OL33	VSG221 q-PCR	FW	AGCAGCCAAGAGGTAACAGC	VSG221 qRT-PCR
CT_OL34	VSG221 q-PCR	RV	CAACTGCAGCTTGAAGGAA	
CT_OL35	VSG13 q-PCR	FW	ATAACGCATGGCCATCTTGAC	VSG13 qRT-PCR
CT_OL36	VSG13 q-PCR	RV	GTCGTTGCTGTGGATTGCTC	
CT_OL37	VSGV02 q-PCR	FW	CAGCGCAAGTACAGGACG	VSGT3 qRT-PCR
CT_OL38	VSGV02 q-PCR	RV	TGCTTCGTCGTCGTTAC	
CT_OL39	VSG224 q-PCR	FW	GACGCAGCAGAATCAACAC	VSG224 qRT-PCR
CT_OL40	VSG224 q-PCR	RV	GCTTATTTTGTGTCTGTGCGC	
CT_OL41	VSG800 q-PCR	FW	ACAGACCGCCGACAGTATC	VSG800 qRT-PCR
CT_OL42	VSG800 q-PCR	RV	GTATCTTTGTAGCCGCTGC	
CT_OL7	TbORC1/CDC6 q-PCR	FW	TTCACCCTGTATGCAGGTTT	ORC1/CDC6 qRT-PCR
CT_OL8	TbORC1/CDC6 q-PCR	RV	GGTTCACTGACGCTGTCTTTCC	

Table 2-5: Primers used for qRT-PCR analysis
Primer sequence reads 5' to 3'. CT_OL primers were designed by C.Tiengwe. N/A = no number assigned to this primer.

2.5.3.2 qRT-PCR

To assess RNA levels, the following experiment was set up using the required primers as detailed in Table 2-5. Each sample set was performed as a technical triplicate. The master mix was prepared as follows at 4 °C (but not in direct contact with ice): 12.5 µl SYBR® Green PCR Master Mix (Applied Biosystems), 5 µl RNase free ddH₂O (Qiagen), 2.5 µl of each primer (300 nM stock) and 2.5 µl of the appropriate cDNA (section). The master mix was pipette into a MicroAmp® Optical 96-well reaction plate (Thermo Fisher). Actin (primers x) were used as an endogenous control and ddH₂O (RNase free) was used as a negative control.

The AB 7500 RT PCR system thermocycler conditions for all reactions were 50°C for 2 min (x 1), 95°C for 10 min (x 1), 95°C for 15 sec followed by 60°C for 1 min (x 40) then a dissociation step was added as follows, 95 °C for 15 secs, 60°C for 1 min, 95°C for 15 secs and finally 60°C for 15 secs (x 1). The data was processed as detailed in the AB manual.

2.6 RNAseq Analysis

2.6.1 Sample preparation and sequencing conditions for RNAseq

Total RNA samples were transported on dry ice to the Glasgow Polyomics facility (University of Glasgow). The sample quality was confirmed on an Agilent 2100 Bioanalyzer (Agilent Technologies) prior to the preparation of a stranded RNAseq library using the TruSeq Stranded mRNA Sample Prep kit (Illumina). Samples were sequenced on an Illumina NextSeq 500 (Illumina). All quality control steps prior to and post RNAseq library preparation and the subsequent sequencing of the library was performed at Glasgow Polyomics by J.Gilbraith.

2.6.2 Bioinformatics analysis workflow

Analysis of the RNAseq reads was performed on a console server using the PUTTY client (<http://www.putty.org/>) and the data analysed and assembled in R-Studio (<https://www.rstudio.com/>). All script used in the analysis was kindly written by N.Dickens. Analysis of the data was overseen and contributed to by N.Dickens. Figure 2-5 below details the workflow for this analysis.

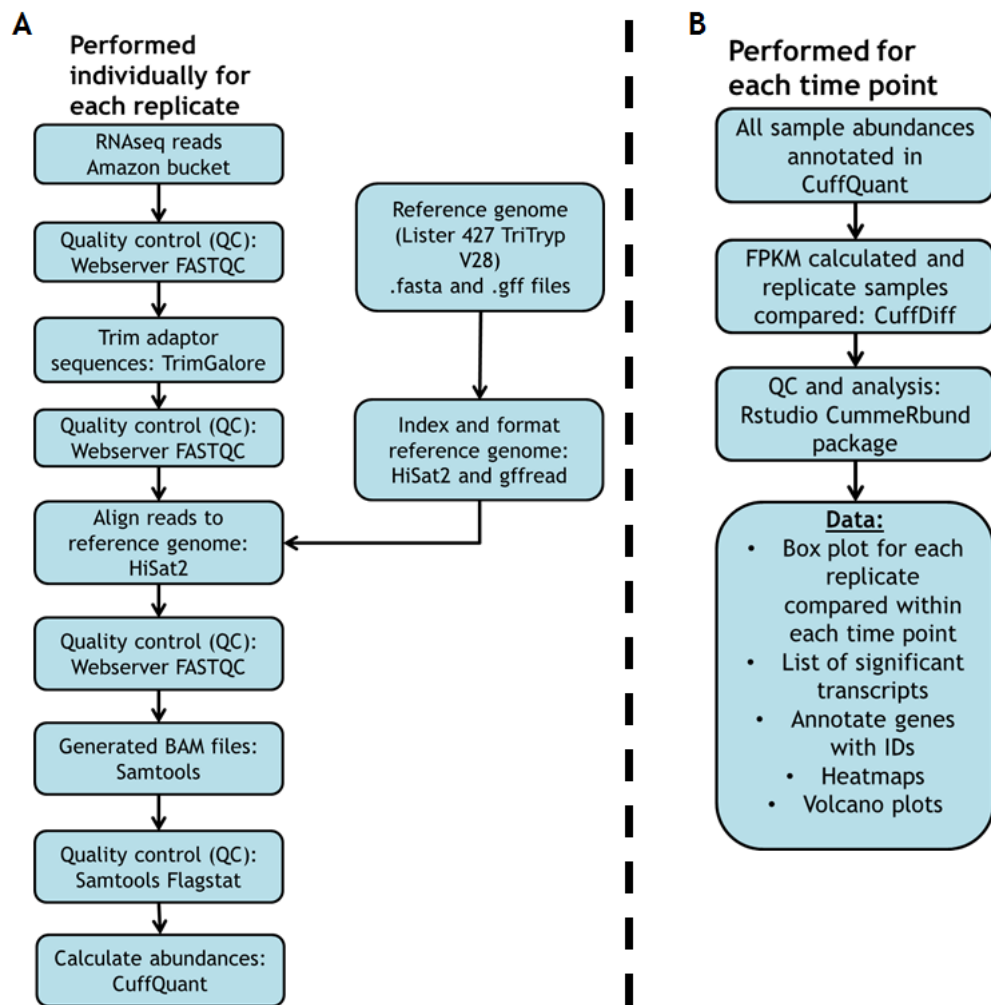


Figure 2-5: RNAseq workflow schematic

A complete explanation of the above schematic is provided in the accompanying text.

The raw sequence reads were provided by Glasgow Polyomics as ‘.fasta’ files. The quality of the reads was subsequently assessed using FASTQC (<http://www.bioinformatics.babraham.ac.uk/projects/fastqc/>). The illumina sequence adaptors were trimmed off the sequence reads using the program TrimGalore (http://www.bioinformatics.babraham.ac.uk/projects/trim_galore/; settings: Q 20 and L 20; rest of the settings were as default). The quality of the reads was then assessed in FASTQC as before. Prior to read alignment to the reference genome, the required reference genome was retrieved from TriTrypDB (V28). For this analysis the Lister 427 genome (Tb427 version 4; v4 and the Tb427_telo version 2; v2) were used. The ‘.gff’ file (which encompasses the gene annotations) was formatted to produce a ‘.gtf’ file using the program gffread (<http://ccb.jhu.edu/software/stringtie/gff.shtml>) using standard settings. The genome was indexed using HiSat2 ‘-build’ command (standard settings; <https://ccb.jhu.edu/software/hisat2/index.shtml>). The sample

sequence reads were then aligned to the indexed reference genome using HiSat2 (standard settings), the alignment quality examined (in FASTQC and using the program IGV) and the subsequently generated files indexed in samtools (<http://samtools.sourceforge.net/>) to generate '.bam' files. The quality of each replicate was assessed in samtools using the 'Flagstat' command. The abundance of each read was then calculated using the CuffQuant program (<http://cole-trapnell-lab.github.io/cufflinks/>); a component of the CuffLinks program set; settings as standard with library type set to 'fr-firststrand'). The process was repeated for each individual replicate within each time point (Figure 2-5A). The FPKM for each read and the subsequent comparison of the reads between each replicate (of which there are three) was performed using the CuffDiff program (standard settings). For obtaining genes differentially expressed across all replicates, the files were imported into and analysed in R studio using the CummerBund R package (<http://compbio.mit.edu/cummeRbund/>; Bioanalyzer). Here the quality of the data was also examined for both time points and for each replicate and various plots generated using the included graphical software (Figure 2-5B).

2.7 Trypanosome strains and culture

2.7.1 Strains

T. brucei brucei Lister 427 cells (Rudenko et al. 1996; McCulloch et al. 1997) were used⁴. This strain is monomorphic remaining as LSBSF cells *in vitro* with a doubling time of ~8 hrs (Proudfoot & McCulloch 2006). For studies requiring RNAi cell lines, a genetically modified strain, termed the 2T1 strain⁵, was utilised (Alsford et al. 2005). The doubling time of this line is approximately 6 hours.

⁴ The Lister 427 strain is derived from a strain known as MITat (Molteno Institute *T. brucei* antigenic type 1.2 clone 221a).

⁵ This strain is ultimately derived from the Lister 427 strain.

2.7.2 Medium and Maintenance of BSF Trypanosome growth *in vitro*

For BSF culturing (Lister 427 and genetically altered Lister 427 cell lines) *in vitro*, 'complete' HMI -9 medium was used (Hirumi & Hirumi 1989). 'Incomplete' HMI-9 was generated using the following recipe (for 4 Litres of culture media):

- Pre-formulated HMI-9 powder (Gibco)
- 200 μM β -mercaptoethanol
- 3 % w/v NaHCO_3

'Incomplete' HMI-9 was filter sterilised with a 0.22 μm bottle top filter unit (Millipore) and stored until required at 4 °C. To 'complete' HMI-9 for culture use, 20 % v/v heat inactivated foetal calf serum (FCS) and 1% penicillin-streptomycin solution (10 U.ml⁻¹ stock solution) and the 'completed' HMI-9 medium was filter sterilised again. Cell lines derived from 2T1 were cultured in HMI-11. To make 'complete' HMI-11, 'incomplete' HMI-9 was supplemented with 10 % (v/v) heat inactivated tetracycline free FCS and 1% penicillin-streptomycin solution (stock as previously described) and again re-filtered as previously described. 'Complete' HMI-9 and HMI-11 were stored at 37°C. Selective drugs were added to cultures containing genetically modified parasites. Table 2-6 details the drugs and concentrations used in this study⁶.

Name	Concentration ($\mu\text{g.ml}^{-1}$)
Blasticidin	10
Neomycin (G418)	2.5
Hygromycin	5
Phleomycin	5
Puromycin	0.2

Table 2-6: Antibiotic concentrations for BSF cells
Selective drugs purchased from InvivoGen.

⁶ All knockout cell lines were maintained in the absence of selective drugs as it was found that in the presence of NEO, cell lines carrying the resistance gene still appeared to be susceptible to the effects of the drug as seen by a slowing in growth in the presence of the drug (data not shown).

In vitro, BSF trypanosomes were cultured in vented flasks or tissue culture plates at 37°C in 5 % CO₂ humidified incubator. To maintain cultures, cells were sub-cultured below a maximum of 1.5 x 10⁶ cells.ml⁻¹. For experimental use, cells were seeded at either 1 x 10⁴ or 1x10⁵ cells.ml⁻¹ and were collected between 6 x10⁵ and 1 x 10⁶ cells.ml⁻¹. Population density was measured using a Neubauer improved haemocytometer (Marienfeld-Superior, Germany) as follows; 10 µl of the culture was loaded onto the haemocytometer and parasites in a 1 mm square region were counted. To determine the number of parasites in the culture (cells.ml⁻¹), the number obtain was multiplied by 10⁴.

2.7.3 Preparation and stabilates revival

Cultures were grown to a maximum density of 1 x 10⁶ cell.ml⁻¹. In a 1.8 ml cryovial, 800 µl of the trypanosome culture and 200 µl of a 50:50 solution of glycerol and the appropriate media for maintaining the cell line were added. The stabilate tube was then labelled with an identification number in the following format (TRY_X; X referring to a sequential number), wrapped in cotton wool and stored at -80°C for ~24 hrs. For long term storage, the stabilate was transferred to a liquid N₂ storage tank (information available in the Freezerworks database [<http://www.freezerworks.com/>]) as requested by the WTCMP). For revival, cryovials were thawed at room temperature before the entire contents added to 9 mls of the appropriate BSF medium (lacking drugs). If required, selective drugs were added 24 hrs later and the cells were maintained as described in the section above.

2.7.4 Calculating population doubling times

Population doubling times were calculated as described in the equation below:

Cell doubling per hour (K) =

$$\frac{(\log_{10} \text{ of the cell concentration at 48hrs}) - (\log_{10} \text{ of the cell concentration at 0 hr})}{(0.301 \times 48 \text{ hrs})}$$

$$\text{Doubling time (g)} = \frac{1}{K}$$

2.7.5 Transformation of BSF trypanosomes

For stable transfection of *T. brucei* BSF cells, 3×10^7 cells ($\sim 1 \times 10^6$ cells.ml⁻¹) were collected by centrifugation (1620 x g for 10 mins; RT). The pellet was re-suspended in remaining media, transferred to a 1.5 ml Eppendorf tube and re-spun at 665 x g for 3 mins. Immediately after, the pellet was re-suspended in 100 µl of Amaxa Human T Cell Nucleofactor Solution (Lonza) and transferred to an electroporation cuvette containing 5 µg of the linearized plasmid (as per section 2.2.6). For electroporation, the programme X-001 pre-programmed onto an Amaxa Nucleofactor II transfection machine (Lonza). Following electroporation, cells were immediately transferred into 30 mls of either HMI-9 or HMI-11 medium (drug free). To achieve clonal populations, two further serial dilutions (1:10) were performed resulting in 3 tubes at 3 concentrations; 1×10^6 cells.ml⁻¹ (A), 1×10^5 cells.ml⁻¹ (B) and finally 1×10^4 cells.ml⁻¹ (C). Tubes were inverted to mix contents evenly. Each tube was plate out separately onto 24 well plates (1 ml/well) and the cells were left to recover for 24 hrs before the addition of antibiotics for selection. The concentration required for each drug is detailed in Table 2-6. Transformants were selected after 7 days following selection antibiotic addition. Plates were examined by light microscopy and the number of well containing live trypanosomes were counted and scored. Routinely, between 6 and 10 wells were selected for further analysis if fewer than 80 % of the wells contained live parasites.

2.7.6 Re-cloning of polyclonal BSF trypanosome populations

To re-clone out cells cultures recovered from transfection, cultures were set up at 0.5×10^1 cells.ml⁻¹ (5 cells.ml⁻¹) in an appropriate volume of appropriate media containing the required selection drugs. At this concentration, one cell should be present in each well. Cultures were mixed well and 200 µl of cells from these cultures were plate out onto a 96 well plate using a multichannel pipette. After ~5-7 days, 6 positive wells were expanded for further analysis.

2.7.7 Preparation and retrieval of BSF trypanosomes for molecular biology procedures

For gDNA and RNA extraction and preparing cells for western blot analysis, an appropriate number of cells were harvested by centrifugation (405 x g for 10

mins). The supernatant was removed and the pellet either immediately frozen (at -20°C for gDNA and -80°C for RNA) or re-suspended in protein loading buffer (section 2.1.2.1.1). Samples were stored until required.

2.8 BSF trypanosomes cell assays

2.8.1 Growth analysis of RNAi cell lines

For growth analysis, RNAi cell lines were set up at a concentration of 6.25×10^2 cells. ml^{-1} in an appropriate volume of HMI-11 medium (tet free) containing the required selective antibiotics (Table 2-6). Cells were left to grow overnight to a density of 1×10^4 cells. ml^{-1} . The following day, the culture was divided into two flasks. Tetracycline (at a concentration of $1 \mu\text{g ml}$) was added to one flask (tet+) and 1.2 mls of each flask was pipette into a 24 well plate and left to grow at 37°C (5 % CO_2) for 72-96hr (unless otherwise stated). Growth was monitored by counting as described in section 2.7.2.

For assessment of growth under genotoxic stress conditions, cells were set up as described however the culture was split into four flasks. Two were induced and to one of these a source of damage was added. Of the remaining two (both non-induced) a source of damage was added to one. In the case of UV exposure, the cells were set up as described above. After 24 hrs induction, 1.2 ml of each flask was pipette into a separate 12 well dish; one for each UV exposure required harbouring both the induced and non-induced cells. The cells were UV irradiated using a Stratagene Stratalinker UV Crosslinker 2400. After exposure, each well was transferred onto a new 24 well plate and left to grow as above.

The following damaging agent concentrations or exposures were used unless stated otherwise: MMS (0.0003 %), UV (1500 J/m^3), HU (0.06 mM) and PHL ($0.1 \mu\text{g}.\text{ml}^{-1}$). Damaging agent stocks were prepared as follows: MMS in medium, HU in ddH_2O and PHL in medium.

2.8.2 Growth analysis of other cell lines

For growth analysis of all other cell lines, cells were set up at a concentration of 1.25×10^3 cells. ml^{-1} in an appropriate volume of HMI-9 medium containing the appropriate selective antibiotics (if required; Table 2-6). Cells were left to grow

overnight to a density of 1×10^4 cells.ml⁻¹. The following day, 1.2 ml of the flask was pipette into a 24 well plate, left to grow and assessed as described in the section above. If a source of damage was required, the culture was split in two and to one flask, damage was added. As no induction was required, UV exposure was performed immediately. The concentrations of damage used are as detailed in the section above.

2.8.3 Cell cycle analysis by DAPI

For cell analysis of all cell lines, cells were set up at a concentration of either 6.25×10^2 cells.ml⁻¹ (RNAi cell lines) or 1.25×10^3 cells.ml⁻¹ (WT cell lines) in an appropriate volume of HMI-9 medium containing the appropriate selective antibiotics (if required; Table 2-6). Cells were left to grow overnight to a density of 1×10^4 cells.ml⁻¹. The culture was split in two (or four if MMS damage was required; MMS was used at a concentration of 0.0003 % [v/v] for this analysis) and 1 µg.ml⁻¹ tetracycline added to one (or two) of the cultures. Cultures were left and the cells harvested by centrifugation (405 x g for 10 mins) at the required time points post induction. If RNAi induction was not required, the cells were set up at 1×10^5 cells.ml⁻¹ and left for 24 hours before harvesting as described. The pellet was then washed in 1x PBS by centrifugation. Cells were then prepared and stain with DAPI as described in section 2.11.1.

2.8.4 Flow cytometry

For flow cytometry, $\sim 2.5 \times 10^6$ cells were collected by centrifugation (405 xg for 10 mins) and washed once in 1x PBS by centrifugation (405 xg for 3 mins). The supernatant was removed and the pellet re-suspended in 1ml 1 % FA in 1x PBS for 10 mins at room temperature. The cells were then washed in 1 ml 1x PBS at 405 xg for 3 mins. The supernatant was removed and if required, the pellet was re-suspended and stored in 1 x PBS at 4 °C for up to 1 month. The PBS was removed and the pellet re-suspended in 2.5 M glycine. The cells were then incubated on ice for 15 mins. The cells were then pelleted (405 xg for 10 mins), the supernatant removed and the pellet re-suspended in 1x PBS 0.01 % Triton-x 100. The samples were then incubated on ice for 30 mins. The cells were pelleted (405 x g for 10 mins) and washed in 1x PBS by centrifugation as described. The supernatant was removed, the pellet re-suspended in 1x PBS

containing 100 $\mu\text{g}.\text{ml}^{-1}$ RNaseA (Qiagen) and the samples incubated at 37 °C for 30 mins. To stain the DNA, propidium iodide (Sigma) to a final concentration of 10 $\mu\text{g}.\text{ml}^{-1}$ was added to each sample and the samples filtered through a fine mesh gauze prior to flow cytometry analysis.

2.9 Antibody and Dye concentrations

2.9.1 Immunofluorescence Analysis

The following antisera concentrations were used for all indirect IF and other microscopy protocols (Table 2-7).

Name	Serotype	Detection	Clone	Concentration	Manufacturer/ provided by
α RAD51	Rabbit (IgG)	RAD51 protein	N/A	1 in 1000	R. McCulloch
α γ H2A	Rabbit (IgG)	Phosphorylated H2A	N/A	1 in 1000	T. Donatelli Serafim
α myc Alexa Fluor® 488 conjugated	Mouse (IgG)	myc epitope	4A6	1 in 500	Millipore
α BILBO-1 (5F2B3 - C8)	Mouse (IgM)	BILBO1 (detection of epitope within coil-coiled domain)	N/A	1 in 100	D. Robinson
α VSG 221	Rabbit (IgG)	VSG variant 221	N/A	1 in 8000	R. McCulloch
α KMX-1	Mouse (IgG2b)	β tubulin	N/A	1 in 10 (in PBS)	T. Hammarton (from K. Gull)
10 nm gold labelled α -mouse	Goat (for IgG H+L)	mouse	N/A	1 in 20	Aurion
Alexa Fluor® 594 α -mouse	Goat (for IgG H+L)	mouse	N/A	1 in 1000	ThermoFisher Scientific
Alexa Fluor® 594 α -rabbit	Goat (for IgG H+L)	rabbit	N/A	1 in 1000	ThermoFisher Scientific
Alexa Fluor® 488 α -mouse	Goat (for IgG H+L)	mouse	N/A	1 in 1000	ThermoFisher Scientific
MitoTracker® Red CMXRos	N/A	mitochondrial membrane potential	N/A	100 nM working	ThermoFisher Scientific
α myc	Mouse (IgG)	myc epitope	4A6	1 in 10	Millipore

Table 2-7: Antisera concentrations used for microscopy procedures

2.9.2 Western blotting

The following antisera concentrations were used for all western blotting protocols (Table 2-8).

Name	Serotype	Detection	Clone	Concentration	Manufacturer/provided by
α myc	Mouse (IgG)	myc epitope	4A6	1 in 7000	Millipore
α -EF-1 α	Mouse (IgG)	EF-1 α	CBP-KK1	1 in 20,000	Millipore
α γ H2A	Rabbit (IgG)	Phosphorylated H2A	N/A	1 in 1000	T.Donatelli Serafim
α VSG 221	Rabbit (IgG)	VSG variant 221	N/A	1 in 8000	R.McCulloch
α VSG 121	Rabbit (IgG)	VSG variant 121	N/A	1 in 8000	D.Horn
α -mouse HRP conjugate	Goat (for IgG H+L)	mouse	N/A	1 in 3000	ThermoFisher Scientific
α -rabbit HRP conjugate	Goat (for IgG H+L)	rabbit	N/A	1 in 5000	ThermoFisher Scientific

Table 2-8: Antibody concentrations used for western blot analysis

Abbreviations: EF1- α (Elongation factor 1- alpha), H2A (Histone 2 A), VSG (Variant surface glycoprotein) and HRP (Horseradish peroxidase).

2.10 Telo-FISH analysis

Approximately 5×10^6 cells were harvested and washed by centrifugation (3000 rpm for 3 mins). The supernatant was removed and the pellet re-suspended in 4%FA in 1x PBS. The cells were then spread onto a poly-L-lysine treated slide and left to settle and fix for 20 mins (room temperature). The cells were then pelleted and washed by centrifugation (x 3). The supernatant was removed and the cells permeabilised with 0.1 % TritonX-100 in 1x PBS for 5 mins then washed as before. The cells were then dehydrated with pre-chilled ethanol in ascending concentrations (70-90-100 %) for 5 mins each concentration. The slide was then left to dry. The telomere-specific probe (as purchased from DAKO.com [Telomere PNA FISH Kit/FITC]) was then heated at 85 °C (in water bath) in hybridisation solution (50 % Formamida, 10 % Dextran, 2x SSPE buffer [1x SSPE: 0.18 M NaCl, 10 mM NaH₂PO₄, 1 mM EDTA, pH 7.7: use buffer at pH 7.9]). Ten microliters of the probe were dilute in 60 μ l hybridisation solution (per sample). After heating the probe, the solution was added to the slide, the slide sealed and heated at 95 °C for 5 mins in a water bath (the slide was placed in a falcon filled with ddH₂O). After, the slide was then placed at 37°C for 16hrs. The slide was then washed for 30 mins with 2 x SSC (Thermo Fisher)/50 % Formamide at 37°C, then for 60 mins at 50 °C in 0.2 x SSC and finally for 10 mins at room temperature in 4 x SSC. The supernatant was then removed and the slide stained with DAPI as per section 2.11.1.

2.11 Microscopy techniques

2.11.1 DAPI staining

All solutions required were filtered prior to use. Approximately 2×10^6 cells were harvested by centrifugation (405x g for 10 mins). The pellet was washed in 1x PBS by centrifugation (405x g for 3 mins), the supernatant removed and the pellet re-suspended in ~50 μ l 1xPBS. The cells were settled for 5 mins on a 12 well glass (Menzel-Gläser) slide treated with Poly-L-Lysine (Sigma). A wax barrier was drawn around the wells using a PAP pen (Life Technologies). The supernatant was removed and 25 μ l 4 % formaldehyde (FA) was added for 4 mins. The FA was removed and the cells washed 3 x in 50 μ l 1x PBS for 5 mins. To each well, 5 μ l of DAPI (SouthernBiotech) was added and incubated at room temperature for 4 mins. A coverslip was then added and sealed with nail varnish. Slides were stored in the dark at 4 °C.

2.11.2 Generic IF analysis protocol

For IF analysis, cells were collected, washed and fixed as described above (section 2.11.1). For staining requiring permeabilisation, cells were permeabilised with 25 μ l 1x PBS/Triton X-100 (Thermo Scientific) for 10 mins. To neutralise free -aldehyde groups, 100 mM glycine was added for 20 mins. The wells were then washed three times in 1x PBS for 5 mins. The wells were blocked for 1hr with 25 μ l blocking solution (1 % BSA [Sigma], 0.2 % Tween-20 in 1 x PBS) in a wet chamber. After, 25 μ l of the required primary antiserum diluted in blocking solution was then added and incubated for 1hr in wet chamber. The wells were then washed 2 x with 1 x PBS for 5 mins. Twenty-five microliters of the appropriate secondary antisera were added to each well and then incubated for 1hr in a wet chamber. After which the cells were washed three times with 1x PBS for 5 mins. The cells were then DAPI stained and the slides stored as described above.

For staining requiring KMX-1 antiserum, cells were harvested and fixed as per section 2.11.1. The cells were then washed three times in 1x PBS for 5 mins after which they were stained as described above with the following

modification; cells were blocked and the antibody diluted in 1 % BSA only. DAPI was added as above and slides stored as above.

2.11.3 Mitotracker® staining

For Mitotracker® staining, $\sim 1 \times 10^6$ cells were collected in a 1.5 ml Eppendorf tube, pelleted by centrifugation at 405 xg for 10 mins. The pellet was re-suspended in 1 ml of the appropriate medium in an Eppendorf. Mitotracker® to a final concentration of 100 mM was added to the culture and the cells left for 15 mins at 37 °C in the dark. After, the cells were harvested by centrifugation (405 xg for 10 mins), the supernatant removed and the cells washed by centrifugation in 1 x PBS. The cells were then processed for indirect IF analysis (section 2.11.2).

2.11.4 VSG staining protocol

For VSG staining, 500 μ l cells were added to 500 μ l 2 % FA in an Eppendorf and fixed for 1 hr at 4 °C. The cells were centrifuged at 6000 rpm for 1 min, washed in 1 ml 1 x PBS (2x; cold) by centrifugation as before. The supernatant was removed and the pellet re-suspended in 1 % BSA (1 x PBS; cold) then centrifuged as before. Most of the supernatant was removed and the cells re-suspended in $\sim 10 \mu$ l of the remaining supernatant and spread onto wells of a poly-L-lysine treated slide. The slides were left overnight to dry after which the wells were re-hydrated in 1x PBS (50 μ l/well for 5 mins [3 x]). The cells were then blocked in 50 % FCS:PBS (50 μ l) for 15 mins. The primary antibody (Table 2-7) diluted in 3 % FCS:PBS was then added to the cells (25 μ l/well) and incubated in a wet chamber for 1 hr. After which the antibody was removed and the wells were washed in 1x PBS as before. The secondary antibody (Table 2-7) diluted in 3 % FCS:PBS and added to the cells (25 μ l/well) then incubated for 1 hr in a wet chamber. The wells were washed as before and the slide DAPI stained and mounted as per section 2.11.1.

2.11.5 Cytoskeletal extraction protocol

For cytoskeletal extracts, $\sim 2 \times 10^6$ cells were harvested by centrifugation (1000 xg for 10 mins) then washed in 1xPBS. The supernatant was removed and the cells re-suspended in 25 μ l 0.25 % NP40 in 100 mM PIPES (Sigma) with 1 mM $MgCl_2$

(Sigma) pH 6.8. The cells were settled onto a poly-L-lysine treated slide for 10 mins. The supernatant was removed and the cells washed 2 x 5 mins in 100 mM PIPES with 1 mM $MgCl_2$ (pH 6.8). After the final wash, the supernatant was removed and the cells fixed in 3% FA (in 1x PBS) for 10 mins followed by neutralisation using 100 mM glycine for 5 mins (2x). The glycine was then removed and the cells washed in 1x PBS. The slides were then placed in a wet chamber and incubated with 25 μ l/well of α BILBO1 antiserum in 1x PBS for 1 hr. After which the wells were washed 2 x for 5 mins in 1x PBS. The wells were then incubated with 25 μ l/well of secondary α mouse 594 antiserum (Table 2-7) for 1 hr in a wet chamber. The slides were processed for DAPI staining and storage as per section 2.11.1. Protocol kindly provided by D.Robinson (University of Bordeaux).

2.11.6 Tomato Lectin staining

For endocytosis assays requiring tomato lectin (TL), $\sim 1.5 \times 10^6$ cells were collected by centrifugation at 500 xg for 5mins at 4°C. The pellet was re-suspended in 1ml cold 1x PBS. The cells were washed once by centrifugation as above and re-suspended in 100 μ l 1 x PBS. A poly-L-lysine slide was prepared as per section 2.11.1 on which the cells were settled for 10mins at 4°C. The supernatant was removed and 25 μ l (per well) of TL:FITC conjugate (Sigma; in 1 x PBS) was added. TL:FITC was prepared by diluting 17 μ l of the stock solution in 200 μ l 1 x PBS for usage). The slides were incubated in the dark at 4°C for 45 mins. After, the supernatant was removed and the wells washed 2 x with 1 x PBS (cold; performed at 4 °C). The cells were fixed at 4 °C for 30 mins in 3 % FA in 1x PBS. After, the wells were neutralised with 100 mM glycine (Sigma) then stained with DAPI as per section 2.11.1. Protocol kindly provided by A.Albisetti (University of Bordeaux).

2.11.7 EM protocols

All EM sample preparation following fixation and EM imaging was performed by L.Lemgruber-Soares.

2.11.7.1 SEM

Approximately 5×10^6 cells were fixed in 2.5 % glutaraldehyde and 4 % PFA in 0.1 M phosphate buffer. Samples were stored in fixation solution at 4 °C until required. The cells were then settled on a poly-L-lysine cover slip then washed with 0.1 M phosphate buffer. The cells were then dehydrated in ascending ethanol solutions (from 30 % to 100 %) and critical point dried. After, the coverslips were metal coated (gold/palladium) and visualised on a Jeol 6400 scanning electron microscope (Jeol, Japan).

2.11.7.2 TEM

Approximately 5×10^6 cells were fixed in 2.5 % glutaraldehyde and 4 % PFA in 0.1 M sodium cacodylate buffer (pH 7.2) then post-fixed for 45 mins in 1 % osmium tetroxide and 2.5 % potassium ferrocyanide (pH 7.3) in 0.1 M sodium cacodylate buffer in the dark. The cells were washed several times with 0.1 M cacodylate buffer and the samples stained (*en bloc*) with 2 % aqueous uranyl acetate then dehydrated in acetone solutions (30, 50, 70, 90 and 100 %). The samples were then embedded in Epon resin and sectioned (ultrathin sectioning). The samples were visualised on a Tecnai T20 transmission electron microscope (FEI, Netherlands).

2.11.7.3 Cryo-immunolabelling

Approximately 5×10^6 cells were fixed in 4 % PFA and 0.2 % glutaraldehyde in 0.1 M phosphate buffer (pH 7.2). The samples were then infiltrated in 2.1 M sucrose overnight then rapidly frozen (by immersion) in liquid nitrogen. Cryosections were prepared at -100 °C using an Ultracut cryo-ultramicrotome (Leica). Cryosections were then blocked in 3 % BSA in phosphate buffer then incubated with the primary antibody (Table 2-7; diluted in blocking buffer) for 1 hr. The cryosections were then washed several times in blocking buffer then incubated for 1 hr with 10 nM gold-labelled antiserum (Table 2-7) diluted in blocking buffer.

2.11.8 Image Analysis and preparation

2.11.8.1 Image Capture

For images captured on an Axioskop 2 (Zeiss) fluorescence microscope, the 63 x DC magnification lens was used to acquire images using the provided ZEN software package (Zeiss; http://www.zeiss.com/corporate/en_de/home.html). All EM images were captured as stated above. DeltaVision images were captured on an Olympus IX71 DeltaVision Core System (Applied Precision, GW) using a 1.40/100 x lens were acquired using the SoftWoRx suite 2.0 software (Applied Precision, GE). Z-stacks were acquired of varying thickness (no more than 10 μm) and the images de-convolved (conservative ratio; 1024x1024 resolution) by the SoftWoRx software. High resolution images were captured on an Elyra PS.1 super resolution microscope (Zeiss) using the structure illuminated microscopy technique. For all images, the 1.4/63 x lens was used. Z-stacks were captured using ZEN software.

Differential interference contrast (DC) imaging was used to visualise the whole cell (Axioskop2) and a UV filter was used to visualise DAPI. Alexa Fluor 488 conjugate antibodies were visualised using a fluorescein isothiocyanate (FITC) filter (520 nm). Alexa Fluor 594 conjugate antibodies were visualised using a rhodamine filter (673 nm).

2.11.8.2 Image preparation

All images captured on an Elyra microscope as described above were processed initially by L.Lemgruber-Soares. The raw images were acquired using the provided ZEN Black Edition Imaging Software tool (Zeiss). The images were then aligned to the channel alignment files generated on the day of imaging using the aforementioned software. All images were processed in ImageJ/Fiji (<http://fiji.sc/Fiji>; Schindelin et al. 2012). For most images, excluding the ones used for quantification of the DAPI signal, both the contrast and brightness of the DAPI signal was enhanced to improve visualisation. For all images, the background was subtracted and suitable false colours were assigned to the fluorescence channels. All EM images were processed by L.Lemgruber-Soares. The 3D video shown in chapter 5 was generated using a combination of EM images (processed by L.Lemgruber-Soares) captured in chronological order.

FIB/TEM (focused ion beam/transmission electron microscopy; Medeiros et al. 2012) was performed on a single Tb6560 -/- cell (see chapter 5). The alignment of the images was performed in Jmod (Kremer et al. 1996) and the 3D images were generated using the IMARIS software (<http://www.bitplane.com/imaris/imaris>; V.8.2). All images are at the same scale. Scale bar =100 nm.

2.11.8.3 Quantification of signal intensity

For fluorescence intensity measurements (of DAPI, γ H2A and myc) a region of interest (ROI; 21x21 pixels) was drawn around individual cell nuclei. The background was then subtracted with a radius of 50 pixels. The mean pixel intensity and the fold change calculated in MS Excel (Microsoft®).

2.12 Protein Protocols

2.12.1 Western Blotting

2.12.1.1 Sample preparation

Routinely 1×10^6 - 2.5×10^6 cells were harvested by centrifugation 1620 xg for 10 mins at room temperature. The supernatant was removed and the pellets re-suspended in 10 μ l 1x protein loading buffer (PLB: 250 μ l 4x NuPAGE® LDS sample buffer [Invitrogen], 750 μ l 1x PBS and 25 μ l β -mercaptoethanol) and denatured at 100 °C for 10 mins. Samples were stored at -20 °C until required. For high molecular weight proteins, 20 μ l 2x Roche cOmplete Mini protease inhibitor cocktail tablets was added to the loading buffer.

2.12.1.2 Western blot protocol

Whole cell lysates were separated by SDS-PAGE using the following NuPAGE® Novex® pre-cast gels: 4-12 % Bis-Tris, 10 % Bis-Tris, 12 % Bis-Tris and 3-8 % Tris-acetate gels. The appropriate gel was selected based on protein size and is detailed in the accompanying figure legend where appropriate. The gels were run as per the manufacturer's instructions.

2.12.1.3 Transfer protocol

For blotting on to the PVDF membrane, the proteins from the SDS-PAGE gel were transferred using a Mini Trans-Blot® Cell (Bio-Rad). The PVDF (Amersham Bio) membrane was immersed completely in 100 % methanol for 1 min prior to submersion in transfer buffer (25 mM Tris pH 8.3, 192 mM Glycine and 20 % [v/v] methanol). The filter paper, foam and the gel(s) were also equilibrated in transfer buffer for 10 mins before assembling the components into the tank. The components were assembled as follows: black side of the plastic cassette-2x foam-1x filter paper-gel-PDVF membrane-1x filter paper-1x foam. The plastic cassette was closed and placed in the tank alongside an ice block. The transfer was performed by electrophoresis at 100 V for 2hrs (most proteins) or for high molecular weight proteins at 400 mM for one hour followed by 90 mM overnight (performed at 4°C). The membrane after transfer was incubated for 10 mins in the dark with Ponceau-S solution (Sigma) to confirm transfer of proteins has occurred.

2.12.1.4 Antibody detection

After transfer, membranes were washed once in 1x PBST (PBS, 0.01 % Tween-20 [Sigma]) for 10 mins on a rocker then the membrane was incubated for 1hr in blocking solution (1x PBST, 5 % Milk powder [Marvel]) or if required, overnight at 4 °C. After, the membrane was rinsed once for 10 mins in 1x PBST then placed in blocking buffer containing the required primary antisera (Table 2-8) for one hour. The membrane was then rinsed once in 1x PBST for 20 mins then placed in blocking solution containing the appropriate secondary antisera (Table 2-8) for one hour. After, the membrane was washed in 1x PBST for 30 mins then the SuperSignal West Pico Chemiluminescent Substrate (Thermo-Fisher) or ECL Prime Western Blotting Detection Reagent (Amersham) were pipette evenly onto the membrane which was subsequently incubated in the dark for 5 mins. The membrane was then exposed to an X-ray film (Kodak) or an ECL Hyperfilm (Amersham) for ~one second to overnight and the film developed using a Kodak M-25-M X-omat processor. For westerns requiring quantification, see section 2.12.5 for image capture.

PVDF membranes were stripped if required using the Restore Western Blot Stripping Buffer (Thermo-Fisher). The membrane was placed in the buffer on a shaker for 8 mins then washed with 1x PBST re-staining.

2.12.2 Immunoprecipitation

Approximately 50 μl of Dyna-beads® (M-280 Sheep α -mouse IgG, Novex®) were collected in a 2 ml Eppendorf then washed in 1 ml blocking solution (0.5 % BSA in 1x PBS, pH 7.2). The beads were collected using a DnyaMag™-2 magnet (Life Technology) and the supernatant removed. The previous step was repeated twice then the beads finally re-suspended in 125 μl blocking solution and 5 μg α -myc antiserum (α -mouse clone 4A6; Millipore). The beads were left rotating overnight at 4 °C. After 24 hrs and prior to addition of the cells, the bead were washed with blocking solution 3 x and re-suspended in 50 μl blocking solution.

For IP analysis, between 2-3x 10⁸ cells were harvested from a culture of BSF cells at a concentration of ~ 8x 10⁵ cells ml by centrifugation at 1620x g for 10 mins. The cell pellet was washed in 1x PBS by centrifugation. Approximately 2.5 x 10⁶ cells were re-suspended in PLB (section 2.12.1) as a pre-lysis (PL) sample and stored at -20 °C. The pellet was re-suspended in 1 ml whole cell extract buffer (WCE: 50 mM Hepes pH 7.55, 100 mM NaCl, 1 mM EDTA pH 8.0, 1 mM EGTA pH 8.0, 10 % glycerol, 1 % Triton X-100, 1 mM DTT and 2x complete protease and phosphatase inhibitor cocktail; Roche) and lysed at 4 °C for 30 mins. The lysate was centrifuged for 30 mins at 4 °C (15 000 xg). Approximately 30 μl of the supernatant was re-suspended in 10 μl 4x PLB and stored at -20 °C (Input sample). The remaining supernatant (~ 900 μl) was added to the 50 μl magnetic beads and incubated at 4 °C for 2hrs. After which the beads were collected using the magnet as previously described and 30 μl of the supernatant was collected, added to 10 μl 4 x PLB and stored at - 20 °C (Flowthrough sample). The remaining supernatant was discarded and the beads washed 3x using cold wash buffer (WB: 50 mM Hepes pH 7.55, 100 mM NaCl, 1 mM EDTA pH 8.0, 1 mM EGTA pH 8.0, 10 % glycerol, 0.1 % Triton X-100, and 2x complete protease and phosphatase inhibitor cocktail; Roche) by placing the Eppendorf on the magnet, removing the WB and gently re-suspending the beads by swirling the tube. After the final wash step, the samples were centrifuged at 1000 x g for 3 mins at 4 °C, placed again on the magnet and the supernatant discarded. The beads were re-

suspended in 15 μl 1x PLB, incubated at 70 °C for 10 mins and then centrifuged (room temperature) at 15 000 xg for 1 min. The beads were then placed on the magnet and the supernatant collected and re-suspended in 15 μl 1 x PLB (Eluate sample). 1 μl was added to 9 μl 1 x PLB for running on an SDS-PAGE gel (as described in section 2.12.1.2).

2.12.2.1 Specific amendments

The WCE buffer for the IP performed in chapter 5, section 5.7, did not contain Phosphatase inhibitors.

2.12.3 Nanoflow HPLC Electrospray Tandem Mass Spectrometry (nLC-ESIMS/MS)

nLC-ESIMS/MS analysis was performed at Glasgow Polyomics (University of Glasgow). The following protocol was used (kindly provided by R.Burchmore).

Peptides were solubilised in 2% acetonitrile and 0.1 % trifluoroacetic acid then fractionated on a nanoflow uHPLC system (Thermo RSLC nano). The results were analysed by electrospray ionisation (ESI) mass spectrometry using an Amazon Speed ion trap MS/MS (Bruker Daltonics). A Pepmap C18 reversed phase column (LC Packings) was used to separate the peptides which were subsequently desalted and concentrated (4 mins) then exposed to an acetonitrile gradient (0.1% [v/v] formic acid, 3.2-32% [v/v] 4-27 mins, 32- 80% [v/v] 27-36 mins, held at 80 % [v/v] 36 - 41 mins then re-equilibrated at 3.2 %). This was performed for a total of 45 mins. For the analytical column, a solvent flow rate of 0.3 $\mu\text{l}.\text{min}^{-1}$ was used, for the trap column solvent a flow rate of 25 $\mu\text{l}.\text{min}^{-1}$ was used. Solvent flow used: 2% acetonitrile with 0.1 % (v/v) trifluoroacetic acid. For analysis, the most abundant peptides were examined. The data was assessed using the Data Analysis software (Bruker) and the Matrix Science Mascot Daemon server (v2.4.1). The annotated protein database from TriTrypDB was used to identify proteins from which the peptides were produced.

2.12.4 Sypro Ruby® staining of SDS-PAGE gels

For protein gel staining, the gel was fixed in a polypropylene container on a shaker in 100 ml 7 % (v/v) Acetic Acid and 50 % (v/v) Methanol diluted in MilliQ

water for 2 x 30 mins. The fixation solution was discarded and 60 ml SYPRO® Ruby gel stain (Molecular Probes™, Life Technologies) was added and left overnight on a shaker at room temperature. The following day, the gel was transferred to a new polypropylene container and washed on a shaker for 30 mins in 7 % (v/v) Acetic Acid and 10% (v/v) Methanol diluted in MilliQ water. The wash solution discarded and the gel washed twice on a shaker for 5 mins with MilliQ water. The gel was imaged using a Typhoon 8600 Variable Mode Imager (Amersham Biosciences) using the 457 nm Blue I and Blue II emission filters.

2.12.5 Quantification of relative protein levels

Protein levels were quantified from western blots performed as detailed in section 2.12.1. The image was captured on a myECL™ Imager (ThermoFisher Scientific) system using the 'Interactive Chemi-luminescence' feature of the installed software. Using this software prevented over exposure of the signal. The digital file was input into ImageJ and the intensity of each band was measured by first highlighting the loading control lane (using >analyse>gels>select first lane). The lanes were then plotted, a line drawn across the base of each peak and the peaks labelled. This was repeated for the sample lanes. The intensity was calculated by normalising each sample to the loading control and calculating the relative fold change to the control sample. The data analysis was performed in MS Excel (Microsoft®).

3 Identifying novel DNA repair-associated protein kinases using RITseq screening

3.1 High throughput RNAi screening

High-throughput (HT) screens combine a forward genetic approach, to examine a large number of genes at once, with assays for phenotypic effects of gene loss. Reverse genetic techniques, such as RNAi mediated gene knockdown (sometimes exploiting an inducible RNAi system; such as Zuber et al. 2011 RNAi is reviewed by Wilson & Doudna 2013, provide a rapid, potentially genome-wide approach to tackle such screens (Carpenter & Sabatini 2004; Echeverri & Perrimon 2006; Zuber et al. 2011). Furthermore, when combined with next generation DNA sequencing (NGS; a review of NGS technology is presented by Liu et al. 2012), the loss of each gene can be assessed relative to another, providing quantifiable categories of phenotype severity with greater sensitivity and coverage than, for example, a microarray-based screen (Sims et al. 2011; Bassik et al. 2009).

3.1.1 HT-RNAi screening of *T. brucei*

HT-screens provide a wealth of data and, since the discovery of RNAi in *T. brucei* in 1998 (Ngô et al. 1998), screens exploiting this system have been developed (as reviewed by (Kolev et al. 2011). Indeed, given that other members of the kinetoplastid family either lack a functional RNAi pathway (including *L. major*) or are less amenable to genetic manipulation (including other members of the *Leishmania* spp. and *T. cruzi*⁷), exploitation of RNAi could be argued to make *T. brucei* a model for biological discovery in the kinetoplastids. Considerable effort was undertaken to develop tetracycline inducible systems for RNAi (such as described in (Alsford et al. 2005)), but it was the generation of a genome-wide RNAi fragment library (Morris et al. 2002) that allowed HT screening in *T. brucei* to become feasible.

The first genome wide RNAi screen performed in trypanosomes was conducted by generating a large ‘pooled’ culture of PCF parasites, in which each parasite carried a random RNAi target sequence (Morris et al. 2002). This approach was used to link the EP procyclin surface coat and the process of glycolysis in mediating changes to the surface coat. Later, harnessing of IScel-mediated DNA

⁷ *T. cruzi*, *T. congolense* and *L. braziliensis* are all known to contain functional RNAi systems however the ability of these systems to be exploited to the same extent to that of *T. brucei* is difficult (Inoue et al. 2002; DaRocha et al. 2004; Lye et al. 2010).

cleavage to enormously increase transformation efficiency allowed two parallel screens to be performed, which additionally used NGS to map gene-specific effects; this has been termed RNAi targeted sequencing or 'RITseq'. Alsford and colleagues (2011) successfully used RITseq to examine the genome as a whole, by looking for genes required for growth *in vitro* and for BSF to PCF differentiation (Alsford et al. 2011). In another early RITseq screen (Baker et al. 2011), growth in the presence of Nifurtimox or Eflornithine revealed that RNAi loss of nitroreductase (NTR) and an amino acid transporter (AAT6) were required for resistance to Nifurtimox or Eflornithine respectively (in BSF cells). Other studies have since used such positive selection during RITseq to examine resistance to a wider range of anti-trypanosome compounds (Gould et al. 2013; Alsford et al. 2012), as well to examine quorum sensing during differentiation (Mony et al. 2014) and innate immune response-associated proteins (Alsford et al. 2014).

3.1.1.1 *T. brucei* kinome screening

Screening a whole genome using siRNA methods allows comprehensive coverage, but may be limited by depth of sequencing and the need for a clear phenotypic screen. Another approach has been to examine a smaller number of genes in a pathway, or to focus on a specific group of proteins. Numerous studies have been undertaken to examine the kinase complement (the 'kinome') of an organism using siRNA libraries (e.g. Morgan-Lappe et al. 2006; Arora et al. 2010; Prudêncio et al. 2008). One motivation is the availability of inhibitor libraries, as well as innate interest in these proteins stemming from their ability to coordinate many cellular reactions. In 2014, Jones and colleagues examined the kinome of *T. brucei* BSF cells to identify protein kinases (PKs) involved in coordinating the cell cycle. Briefly, a library of cell lines was generated, each conditionally expressing an RNAi target fragment recognising one of the 190 PKs of *T. brucei*. Each RNAi effect was examined individually, screening for loss of growth and then performing more detailed examination of cell cycle defects for a selection of PKs. When compared with the RITseq screen performed by Alsford et al (2011), ~70% of PKs produced similar growth impairments in the kinome screen.

3.1.2 Using RNAi screens to de-convolve DNA damage-associated pathways

HT- RNAi screening approaches to identify proteins involved in the DNA damage response (DDR) have provided unprecedented insight into both the DDR and the oncogenic transformation of cell lines (reviewed by Diehl et al. 2014). Using whole genome RNAi libraries, genes required for cell survival to methyl methanesulfonate (MMS; Chang et al. 2002; Ravi et al. 2009; Rooney et al. 2009), hydroxyurea (HU; Kavanaugh et al. 2015), oxidative stress (Nagaoka-Yasuda et al. 2007), replicative stress (Kotov et al. 2014; Kavanaugh et al. 2015) and other therapeutic agents, such as Gemcitabine (Smith et al. 2014), have been identified and characterised. However, the predominant methodology has not included NGS to identify the target genes, with most approaches examining growth or factor localisation in individual RNAi clones. To date, few examples are available of kinome-focused RNAi screens to identify kinase which act in DDR pathways. Arora and colleagues (Arora et al. 2010) used an siRNA library transformed into ovarian cancer cells and tested for PKs involved in modulating the response to cisplatin using a CellTitre-Glo luminescence assay; 55 PKs were identified, amongst which were MAPKs, PLKs, CHK1 and ATR. A second kinome screen identified PKs involved in phosphorylation of the histone variant H2AX following exposure to radiation; 46 PKs with indirect or direct roles were recovered (Benzina et al. 2015).

In *T. brucei* no HT-RNAi screen has been performed to identify any gene, including PKs, with potential roles during the DDR. The closest any study has come to date has involved examining the transcriptional and proteomic changes in response to gamma radiation in *T. cruzi*, which have suggested protein phosphorylation is a central component of irradiation tolerance (Vieira et al. 2014; Grynberg et al. 2012).

3.2 Research Aims

The aim of this chapter was to biologically validate two independently performed RITseq screens, one genome-wide and one kinome-wide, which sought to identify PKs and wider factors with roles in the response of BSF *T. brucei* to MMS exposure. Considering the central role of PKs in cell cycle control,

including after DNA damage, the work described here is focused on PKs and only a brief explanation of the (unpublished) screens is provided. For both screens, the Sn2 alkylating agent MMS was chosen as a source of genotoxic stress because of its wide-ranging effects. MMS is a chemical with both electrophilic and methylating properties and can interact with nucleophilic DNA bases (particularly guanine and adenine) to produce bulky methylated base adducts. These adducts can result in base mismatches, replication fork stalling, strand breaks and, ultimately, affect protein synthesis. Resolution of DNA lesions can occur through a variety of pathways such as direct adduct reversal, BER, NER, MMR, TLS and HR (reviewed by (Wyatt & Pittman 2006)). Furthermore, genes required for cellular survival following MMS stress have been examined by HT screens in *E. coli* (Rooney et al. 2009), yeast (Chang et al. 2002) and *Drosophila melanogaster* (Ravi et al. 2009), thus allowing comparison between organisms.

3.3 Results

3.3.1 Screen workflow

3.3.1.1 Genome wide RITseq screen

The genome wide RITseq screen was performed as a single experiment (with technical duplicates) by S. Alford (LSHTM), as outlined in Figure 3-1. Sequencing of RNAi targets PCR-amplified from RNAi induced and MMS treated or untreated cells was performed at Glasgow Polyomics using IonTorrent semiconductor technology (ThermoFisher) and the sequence analysed by J. Wilkes (University of Glasgow). Biological validation was performed by the author, unless stated otherwise.

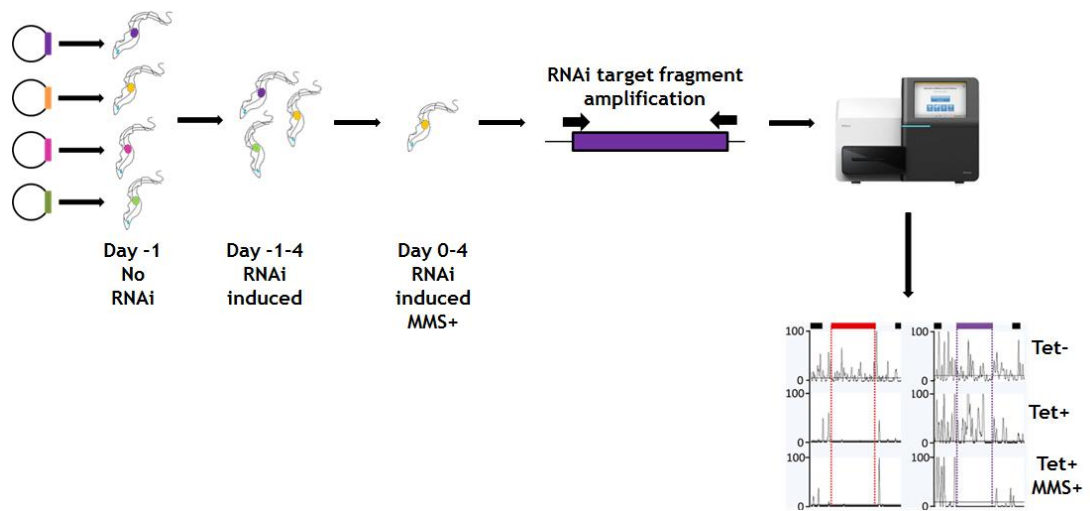


Figure 3-1: Schematic illustration of the genome wide MMS RITseq screen in BSF cells
 The constructs and cell lines were generated as described (Glover et al. 2015). RNAi was induced (with tetracycline, Tet) in the transformed parasites for 24hrs and gDNA was prepared. The culture were then each split in four and MMS (0.0003% v/v) was added to two induced cultures, but omitted from the two others. All cells were grown for four days (5 days total RNAi induction), gDNA was prepared, a limited-cycle PCR performed (by G. Hamilton), the products fragmented, a library prepared and sequenced using IonTorrent semi-conductor technology. Sequence reads were mapped to the TREU927 reference genome and genes with greater loss of reads following RNAi induction (Tet+) in the presence of MMS (Tet+MMS+) than in RNAi uninduced, untreated cells were identified.

3.3.1.2 Kinome wide RITseq screen

The kinome wide RITseq screen was performed by T. Donatelli-Serafim (now NIH, Washington) using a pooled culture (generated by F. Fernandes-Cortez) containing all BSF cell lines that individually target all *T. brucei* PKs (Jones et al. 2014), and thus accounting for the kinome. In this RITseq approach (Figure 3-2), cells were grown in two concentrations of MMS, with (Tet+) and without (Tet-) RNAi, and samples were prepared every 24 hr for 4 days. After PCR amplification of the RNAi inserts, the products were sequenced by Eurofins Genomics (Germany) on an Illumina NextSeq 500 platform (Illumina) and relative abundance determined by mapping to the genome.

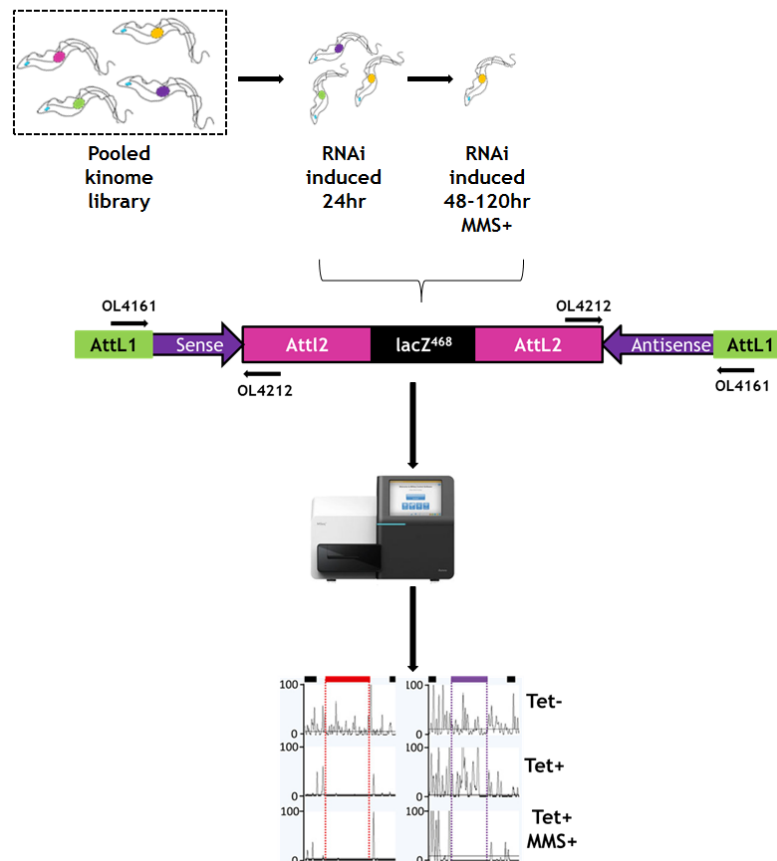


Figure 3-2: Schematic illustration of the kinome wide MMS RITseq screen in BSF cells 181 individual RNAi cell lines representing 190 PKs were pooled into one culture, passaged once and split in two; tetracycline was added to one culture to induce RNAi knockdown. After 24 hrs, gDNA was collected and each culture split in three; 0.0002 % MMS (v/v) or 0.0003 % MMS (v/v) was added to two cultures, and one was grown without damage. gDNA was harvested at 24, 48, 72 and 96 hrs subsequently and the RNAi fragments amplified by limited cycle PCR using an RNAi target cassette specific primer (sequence 5'-TAATGCCAACTTTGTACAAA-3'; F.Fernandes-Cortez, T.Donatelli Serafim and N.Jones). An Illumina adapted library was prepared from each PCR and sequenced using Illumina technology. Sequence reads were mapped to a reference genome comprising the PK genes and genes with a loss of reads following RNAi induction (Tet+) in the presence of MMS (Tet+MMS+) were identified relative to the undamaged controls.

3.3.2 Bioinformatics analysis

Processing of the raw sequence read data and the subsequent mapping analyses of both RITseq screens was performed by J. Wilkes, R. McCulloch and T. Donatelli-Serafim. Normalised sequence reads, including the read mapping ratios and gene identifications are available in the accompanying CD; these data are being archived on TriTrypDB.org. As the aim of this thesis was to examine PKs with potential DNA repair associated roles, the discussion of the bioinformatics analysis presented here is limited to this. A wider range of pathways identified using the genome-wide RITseq approach is being prepared for publication.

3.3.2.1 Bioinformatics analysis of the genome wide RITseq screen

In contrast to the RNAi target amplification by semi-specific PCR described by Alford et al (2011), the approach here performed limited cycle PCR amplification using primers common to all inserts described by Baker et al (2011). In addition, sequence reads were mapped to a ‘minimal’ genome artificially generated from the *T. brucei* TREU 927 reference genome. Included within this ‘minimal genome’ was 9849 protein and RNA coding sequences (CDS) and the surrounding CDS regions including a random 30 bp sequence between each transcript to minimise inaccurate mapping to the ‘minimal’ genome. Non-coding sequences were excluded from the analysis. Despite these differences, when read depth for every gene was compared in the fifth and six day RNAi induced samples from this RITseq screen and that of Alford et al. (2012) respectively, the profiles were comparable (Figure 3-3).

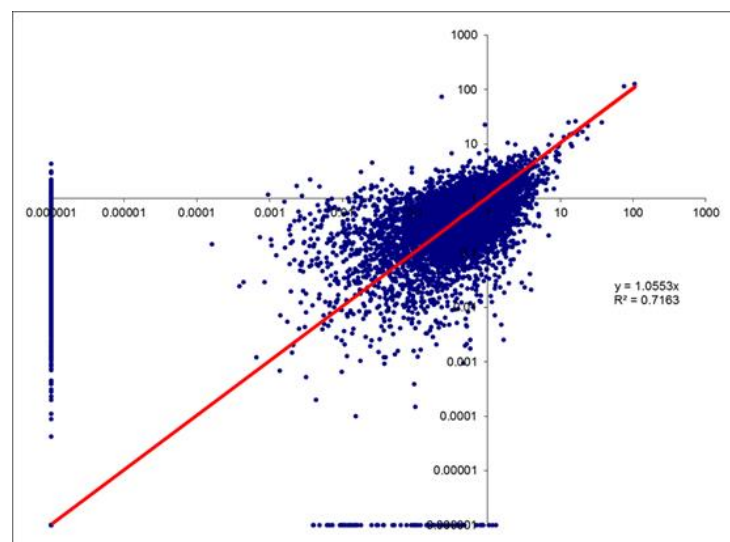


Figure 3-3: Comparison of the total sequence reads across two independent RITseq screens The total number of sequence reads which mapped to the minimal *T. brucei* genome were compared at day six (Alford et al. 2012) and day five (this study) post-RNAi induction. The coefficient of determination is shown. The axes are shown as a log scale on which the total number of sequence reads for both screens are plotted. The plot was generated by J.Wilkes.

To identify genes important for BSF *T. brucei* survival in the presence of MMS following RNAi the reads for each gene, normalised relative to total reads and the CDS length and averaged from the repeats, was determined. The resulting value was then compared in the MMS-treated and untreated data and expressed as an MMS+/MMS- ratio (all values are shown in the accompanying CD; see folder labelled Chapter3RITseqtables and the subsequently enclosed tables labelled

TableS1-S4; the raw genome wide RITseq reads are encompassed in the folder within entitled RawRITseqreads). MMS⁺/MMS⁻ ratios were calculated as follows; the sequence reads which mapped to all annotated genes were obtained. These reads were then normalised both relative to the length of the coding sequence of each gene and to the total number of reads in the library. The resulting values were averaged for both the duplicate induced (Tet⁺), MMS⁻ samples and the induced (Tet⁺) MMS⁺ samples. The MMS⁺/MMS⁻ ratios were then calculated by determining the ratio of reads from the Tet⁺MMS⁺ samples relative to the Tet⁺MMS⁻ samples. In principle, all genes of <1 MMS⁺/MMS⁻ are genes whose RNAi results in impaired growth in the presence of damage, and thus are potential 'hits' for further validation. All MMS⁺/MMS⁻ ratios were plotted on a scatter plot relative to the chromosomal location of the gene within the *T. brucei* genome (Figure 3-4). Applying an MMS⁺/MMS⁻ cutoff of 0.5 revealed 274 genes (including 44 VSGs, which are likely artefacts), amongst which nine PKs were recovered (Table 3-1 and Figure 3-4; chapter 8, section 8.3, Figure 8-1 A&B). When the predicted GO terms were analysed for these 230 genes an enrichment of protein kinase activity was observed (~2-fold increase; see chapter 8, section 8.2, Figure 8-1 C for GOterms), potentially highlighting the importance of kinases following exposure to MMS stress. The 8 PKs represent ~ 4 % of the kinome, but other PKs with known roles in the DDR in other organisms were not recovered. Notably, neither the predicted *T. brucei* homologs of ATR (TbATR; Tb927.11.14680; ratio: 1.875) and ATM (TbATM; Tb927.2.2260; ratio: 1.17), the commonly cited 'master-regulators' of the DDR were identified as candidates, and nor was TbWEE1 (*T. brucei* homolog: Tb927.4.3420; ratio: 1.64), which is phosphorylated in response to genotoxic stress in an ATR-dependent manner (WEE1 activity and function is reviewed by Matheson et al. 2016).

Four different kinase families were represented in the eight PKs with MMS⁺/MMS⁻ ratios <0.5: CAMK (Tb927.2.1820 [TbCAMK/KL] not shown in Figure 3.4; see legend] and Tb927.2.5230), CMGC (Tb927.10.7780 [TbKFR1], Tb927.6.4220 and Tb927.8.5390), Other (Tb927.3.3920 [TbAUK2] and Tb927.9.6560) and STE (Tb927.8.5950). Identification of the eight PKs provided a means to validate the MMS RITseq screen. As only one gene in this cohort (TbAUK2 [Tb927.3.3920]; chapter 4) had been implicated in genome maintenance previously, two other repair candidate PKs, the tousled kinases

[TbTLK1 and 2], were also examined further, despite both not having a ratio of <0.5 (Tb927.8.7220 [TbTLK2], 0.68; Tb927.4.5180 [TbTLK1], 1.15). These PKs were chosen due to their important roles in metazoans and yeasts in DNA repair and genome maintenance (Benedetti 2012). In addition, TLKs are known interaction partners of ATR, ATM, RAD9 (a component of the 9-1-1 complex) and aurora kinases (as reviewed by Benedetti 2012). TbTLK1 in *T. brucei* is required for the maintenance of genome integrity in BSF cells (Li et al. 2007), but evidence of a role in the *T. brucei* DDR has been yet to be examined. The roles of TbATR and TbATM are examined in chapter 6.

Gene ID (<i>T. brucei</i>)	Kinase Family	Annotation (TriTrypDB)	MMS+/MMS- Ratio
Tb927.2.1820	CAMK/CAMKL		<0.1
Tb927.8.5950	STE		0.308
Tb927.2.5230	CAMK		0.352
Tb927.10.7780	CMGC/MAPK	KFR1	0.369
Tb927.3.3920	ACG/AUK	AUK2	0.373
Tb927.6.4220	CMGC/MAPK	MAPK5	0.426
Tb927.9.6560	Other/NAK		0.495
Tb927.8.5390	CMGC/CDK	CRK4	0.497

Table 3-1: Eight PK candidates identified by the genome wide MMS RITseq screen
The table details the 8 PKs identified along with their Gene ID (TriTrypDB v28), the corresponding annotation (if present) and the averaged MMS+/MMS- ratio.

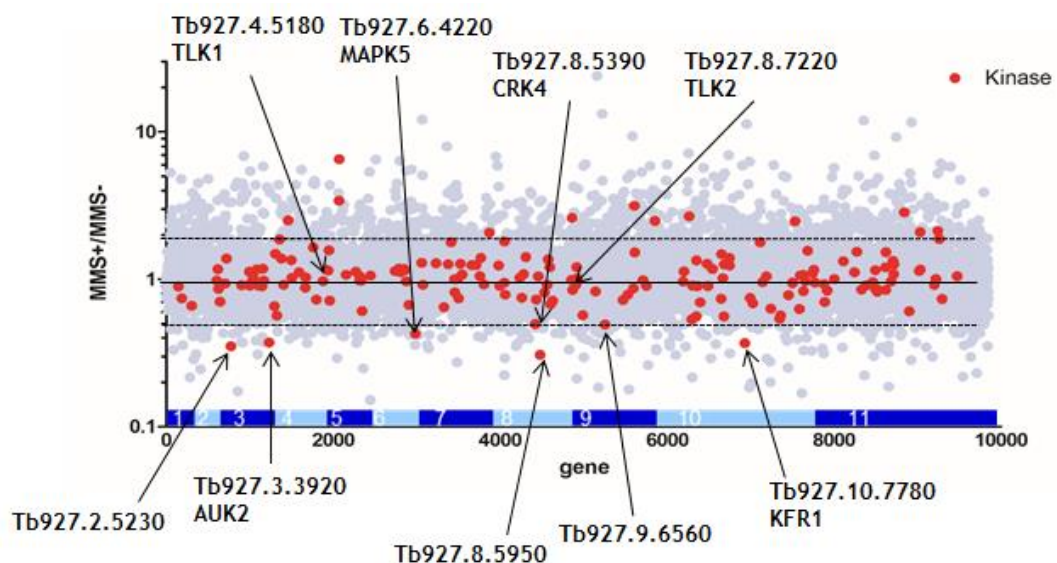


Figure 3-4: The average MMS+/MMS- ratios of *T. brucei* genes mapped relative to their position in the genome.

The MMS+/MMS- ratio of each gene (grey dot) was plotted on a scatter plot relative to the genomic location of the gene across the 11 megabase chromosomes (lower bar) of *T. brucei*. A ratio of 1 = no change (solid black line), >0.5 suggests increased resistance to MMS (higher dashed line), <0.5 suggests increased sensitivity to MMS (lower dashed line). All protein kinases (PKs) are highlighted in red and the candidate PKs examined further are indicated by a black arrow. CAMK (Tb927.2.1820) could not be mapped due an MMS+/MMS – ratio of <0.1.

3.3.2.2 Bioinformatics analysis of the kinome wide RITseq screen

The bioinformatics analysis of the kinome-focused RITseq screen was performed using a similar pipeline to the genome-wide RITseq, but reads were mapped only to the PK genes. This approach permitted quantitative monitoring of loss of individual PKs with time and in the presence of both a low (0.0002 %) and high (0.0003 %) concentration of MMS. In addition, the loss of PKs in the presence of MMS could be compared against loss without damage, allowing identification of essential PKs whose loss is accelerated by MMS. In this approach, reads were normalised between the barcoded groups and the 10 lowest read counts were excluded from each repeat, reducing variability. All read depth data and MMS+/MMS- ratios for each PK are displayed in the accompanying CD (see folder labelled Chapter3RITseqtables and the subsequently enclosed table TableS4). Approximately 98 % of the kinome was identified across the experimental replicates; the remaining 2 % could not be mapped in any sample, suggesting they were lost during growth.

In total, over the course of the experiment (from 48 to 120 hrs growth), 23 PKs were revealed as being important for survival in the presence of MMS. Eight of these genes had MMS+/MMS- ratios which gradually reduced at both MMS concentrations but showed no change in abundance in the RNAi-induced, undamaged samples relative to the uninduced, undamaged cells. These PKs were considered non-essential. 15 PK genes showed loss of reads in the RNAi-induced, undamaged samples relative to the uninduced, undamaged cells, indicating they are important for growth (essential), but showed increased loss of reads in the presence of MMS damage after RNAi. These data are summarised in Table 3-2 below.

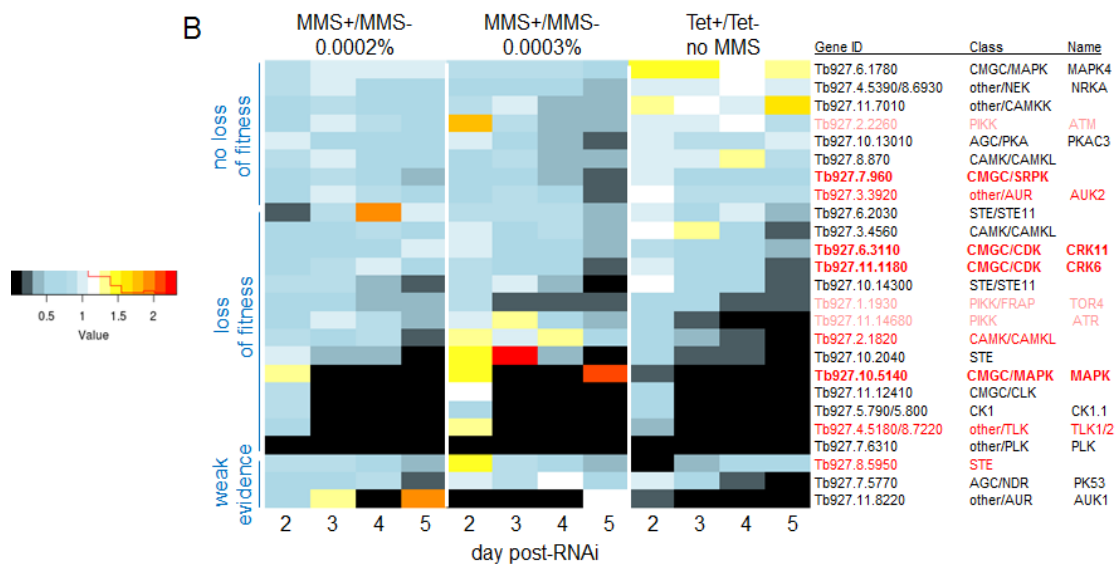


Figure 3-5: A heatmap summary of the MMS+/MMS- ratios for each putative MMS damage response kinase at each time point post induction from two different concentrations of MMS The heatmap shows data from two independent experiments for each concentration of MMS at each timepoint. To illustrate which genes are important for cell survival in the absence of MMS, the reads from the Tet+ samples were set relative to the corresponding Tet- samples for each timepoint. The colours range from black (an MMS+/MMS- ratio of 0) to red (an MMS+/MMS- ratio of > 2). The kinases represented by the heatmap are arranged into three categories; no loss of fitness, loss of fitness and weak evidence for a role during the MMS damage response. The kinases are referred to on the left of the heatmap by their gene ID, the kinase class to which they belong and their name (if annotated in the reference genome). Genes highlighted in **bold red** were absent from the genome wide RITseq screen but were validated (see section 3.3.4.2). Those highlighted in **red** were common to both the genome wide screen and the kinome wide screen and those highlighted in **pink** are thought to act in other eukaryotes during the repair of MMS induced damage. Heatmap generated by J.Wilkes and assembled by R.McCulloch for use in this thesis.

Three of these PKs (Tb927.2.1820 [TbCAMK/KL], Tb927.3.3920 [TbAUK2] and Tb927.8.5950) were common to both screens. In addition, both TbATR and TbATM had MMS+/MMS- ratios < 0.5 (0.382 and 0.430 respectively) at 120 hrs post induction in the kinome RITseq screen. Furthermore, TbTLK1/2 (as a double knockdown RNAi lined was used) appeared amongst the essential candidates, with a particularly severe loss of reads after RNAi. Finally, TbTOR4 was highlighted, consistent with a role for TOR signalling in response to MMS treatment in other eukaryotes (Ravi et al. 2009).

3.3.3 Biological validation of candidates

Validation and characterisation of the PK candidates identified from both RITseq screens was achieved by examining: 1) growth in the presence or absence of genotoxic stress after RNAi; 2) cell cycle progression after RNAi and damage; 3) expression of γ H2A (a marker of genotoxic stress) and 4) localisation of each

protein. The sections below provide these data for nine PK genes that showed evidence of a role in damage repair. However, in total, nine genome-wide candidates and seven kinome-wide candidates were examined for growth, and RNAi against seven of these genes (four from the whole-genome screen and three from the kinome screen) showed no preliminary evidence for increased sensitivity to MMS (data provided in chapter 8, section 8.2, Table 8-2 and Figure 8-3); as these were considered to be false positives, no further phenotypes were examined.

3.3.3.1 RNAi cell lines used for validation

RNAi lines (generated as described in chapter 2, section 2.3 and chapter 8, section 8.1.1) were kindly provided by E.Brown (University of York), N.Jones (University of York) and A.Hamilton (University of Glasgow). The table (Table 3-3) below describes the RNAi cell lines examined in depth. The RNAi cell line termed TbTLK1/2 targets both Tb927.8.7220 (TbTLK2) and Tb927.4.5180 (TbTLK1). The parental RNAi cell line (2T1; kind gift S.Alsford) was examined to ensure no phenotypes could be attributed simply to addition of tetracycline (data shown in chapter 8, section 8.2, Figure 8-2).

Gene ID	Annotation (TriTrypDB v.28)	Stabilate number	Plasmid number	Puromycin sensitivity
Tb927.9.6560	Other/NAK	STL 423	pTL 161	Sensitive
Tb927.10.7780	KFR1	STL 605	pTL 106	Sensitive
Tb927.3.3920	AUK2	STL 243	pTL 154	Sensitive
Tb927.2.1820	CAMK	STL 235	pTL 186	Sensitive
Tb927.8.7220/ Tb927.4.5180	TLK1/2	STL 587	pTL 167	Sensitive
Tb927.11.1180	CRK6	STL 888	pTL 175	Sensitive
Tb927.7.960		STL 689	pTL 105	Sensitive
Tb927.6.3110	CRK11	STL 603	pTL 71	Resistant
Tb927.10.5140	MPK2	STL 613	pTL 101	Sensitive

Table 3-2: RNAi cell lines examined

Details of the cell lines used for all PK candidates. The STL number refers to the stabilate number, according to the Mottram laboratory system for labelling. The plasmid number (pTL) numbered as according to the Mottram plasmid repository. Puromycin sensitivity was

examined prior to freezing as recommended by S.Alsford. Orange (genome wide candidates), blue (kinome wide candidates).

3.3.3.2 Generation of C-terminal endogenously tagged RNAi lines

To assess the efficiency of gene silencing in the RNAi cell lines and to explore the sub cellular localisation of each PK, endogenous tagging in the corresponding RNAi cell line was undertaken for each candidate. Tagging with 12 copies of the myc epitope was chosen due to the wide availability of commercial antibodies for detection. C-terminal tagging constructs were generated as per section 2.4.1.1.1; only Tb927.11.1180 was N-terminally tagged, using the strategy detailed in section 2.4.1.1.2. For the TbTLK1/2 RNAi cell line, no attempt was made to tag either gene; localisation of both has been described nuclear (Li et al. 2007) and the growth effects of RNAi are documented.

3.3.3.3 Construct generation and endogenously tagged RNAi cell line generation

The constructs were named as follows: Tb927.9.6560^{12myc}, Tb927.10.7780^{12myc}, Tb927.2.1820^{12myc}, Tb927.3.3920^{12myc}, Tb927.10.5140^{12myc}, Tb927.7.960^{12myc}, Tb927.6.3110^{12myc} and ^{12myc}Tb927.11.1180. Primers used for cloning are detailed (section 2.4.1.1) and all, with the exception of one (Tb927.9.6560^{12myc}), were confirmed by Sanger sequencing (section 2.2.9.2). One non-synonymous mutation (T1720S) was observed in the Tb927.9.6560^{12myc} construct, but multiple PCR amplifications yielded the same mutation, suggesting the amino acid may be miss-annotated in the reference genome sequence or the parasite strain used here harbours this mutation. As serine and threonine are similar with regards to the structure of their sidechain extensions and, furthermore, can both be phosphorylated on their hydroxyl group the function of the endogenous protein is not expected to be compromised by integration of the tagging construct.

Each endogenous tagging construct was transformed into the appropriate RNAi cell line and transformants selected as described in section 2.7.4. Routinely, six to ten clones were expanded for further analysis and confirmed as described below.

3.3.3.4 Confirmation of endogenously tagged RNAi cell lines by western blot analysis

Though multiple transformants were readily recovered from each transfection, surprisingly few showed expression of the 12myc tag in some cases by western blot analysis (performed as per section 2.12.1; Figure 3-5), for reasons unknown. Nonetheless, in all cases clones expressing proteins of the approximate size for each tagged PK were recovered, with one exception: endogenously tagged Tb927.11.1180 (TbCRK6) resolved at a lower than expected size (~25 kDa rather than the predicted ~51.1 kDa). This is discussed further in section 3.4.3. One myc-tagged clone was taken forward in each case.

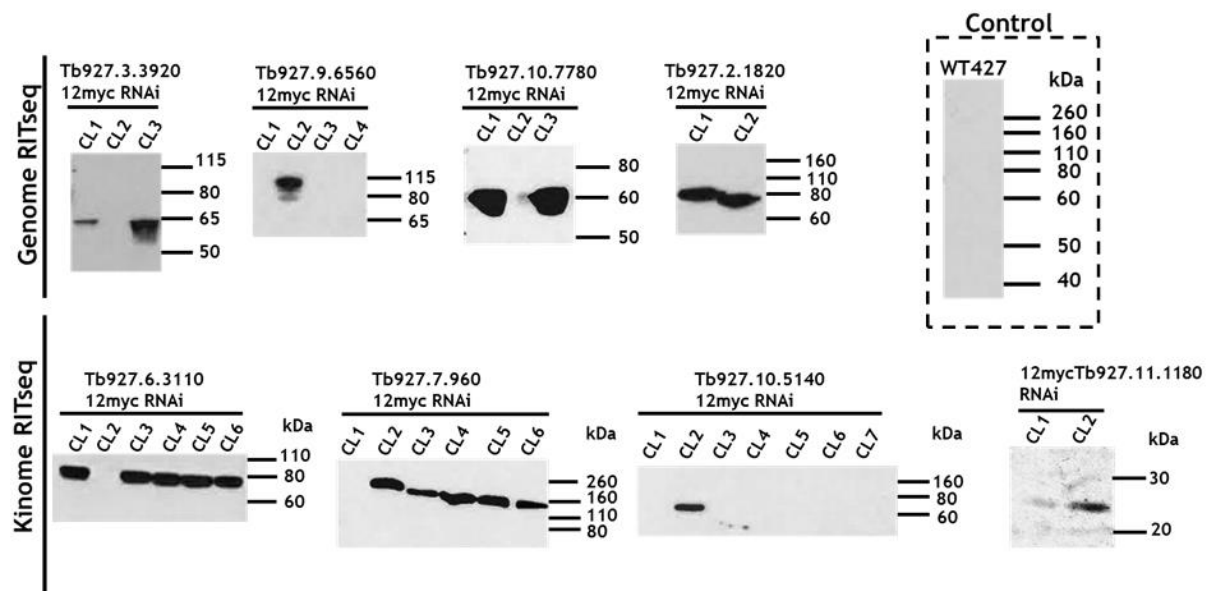


Figure 3-6: Confirmation of endogenously tagged RNAi candidate cell lines
Western blot analysis of whole cell extracts from myc-tagging transformants, as indicated by gene IDs. The ladder shows the size in kDa. Wild type (WT427) cells were used as a negative control. Protein was resolved on a 10% BT gel (in the case of Tb927.11.1180 [TbCRK6], a 12 % gel was used). The following sizes refer to the predicted molecular weight (MW) of the protein (from TriTrypDB) + the MW of the 12myc tag (14.4 kDa): Tb927.3.3920 TbAUK2; 56.5 kDa), Tb927.9.6560 (94.6 kDa), Tb927.10.7780 (TbKFR1; 53.8 kDa), Tb927.2.1820 (TbCAMK'KL; 84.9 kDa), Tb927.6.3110 (TbCRK11; 63.3 kDa), Tb927.7.960 (107.6 kDa), Tb927.10.5140 (TbMPK2; 64.1 kDa) and Tb927.11.1180 (TbCRK6; 51.1 kDa). Ladder used: Novex® Sharp Pre-Stained Protein Standard (ThermoFisher) or Spectra™ multicolor broad range protein ladder (Thermofisher).

3.3.4 Growth analysis of RITseq screen candidates

Growth of each PK candidate was monitored by examining cellular proliferation in the presence or absence of 0.0003 % MMS, with or without RNAi induction.

This assay was performed as described in section 2.8.1.

3.3.4.1 The genome wide candidates

Of the five RNAi cell lines examined, double knockdown of TbTLK1/2 was the only RNAi that showed a severe impairment of cell proliferation in the absence of MMS from 24 hrs post induction (Figure 3-6). At 96 hrs post induction, very few cells remained in culture and all harboured aberrant morphology (below). This growth reduction is in keeping with the phenotypes observed by (Li et al. 2007). The other four genes did not appear to be required for proliferation as proliferation continued following RNAi knockdown.

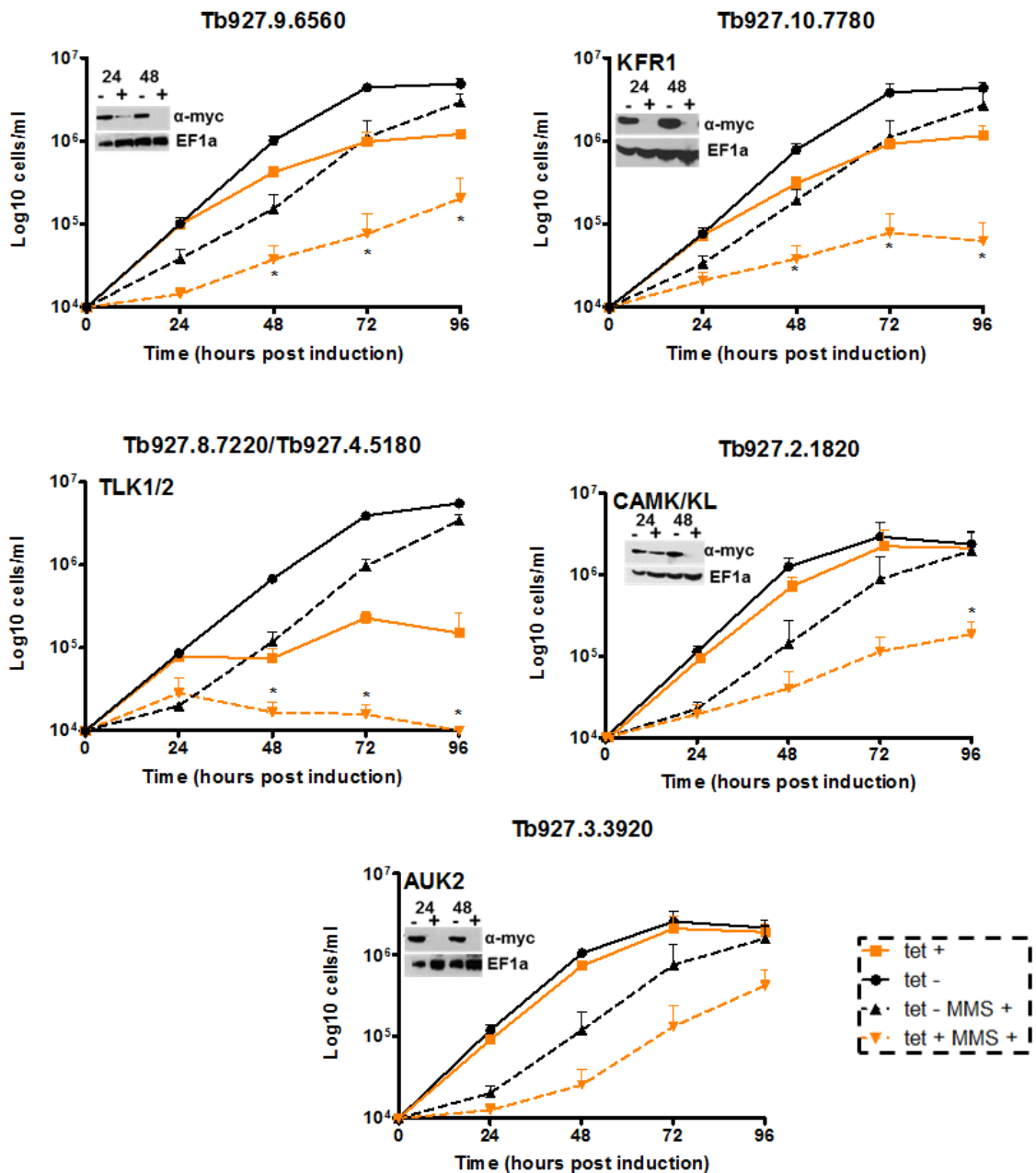


Figure 3-7: *In vitro* growth analysis of the genome wide candidates

Growth analysis of each genome wide PK candidate with (Tet+) or without (Tet-) RNAi induction and with (MMS+) or without (MMS-) exposure to MMS (0.0003%). Error bars represent \pm SEM, n=3. For statistical analysis, tet - cells in the presence of MMS (dashed black line) were compared with the tet + cells in the presence of MMS (dashed orange line) at each time point. (*) = $p < 0.05$ as determined by a Mann Whitney U test. The western blots show whole cell extracts after 24 or 48 hrs growth with (+) or without (-) RNA induction, probed with α myc or α EF1 α (as a loading control) antiserum. White space indicates images aligned from the same or different images.

Two cell lines Tb927.10.7780 [TbKFR1] and Tb927.9.6560; Figure 3-6) showed a slight impediment in growth after RNAi (between 48-96 hrs post induction. Indeed, this reduced proliferation for both cell lines is consistent with data reported by Jones and colleagues (Jones et al. 2014). From 48 hr post induction, loss of TbKFR1 and Tb927.9.6560 was associated with the appearance of morphologically aberrant cells, which were predominantly 'rounded' in appearance in the latter case. RNAi against the two remaining PKs (Tb927.2.1820, [TbCAMK/KL]; and Tb927.3.3920, TbAUK2) had no clear growth perturbation. Consistent with this, RNAi knockdown of TbAUK2 has been previously investigated in both BSF and PCF cells and no growth effect has been reported (Tu et al. 2006). Western blots showed that RNAi induced loss of the cognate myc-tagged protein in all cases.

Following RNAi induction in the presence of MMS, the growth of each cell line was significantly reduced relative to the induced population in the absence of MMS and was reduced relative the uninduced, MMS-treated cells, suggesting each gene is required for survival under MMS stress conditions. These data, combined with the RITseq data (an MMS+/MMS- ratio of < 0.5), provide the first demonstration of any *T. brucei* kinase with a role in BSF trypanosomes' response to MMS exposure.

3.3.4.2 The kinome RITseq candidates

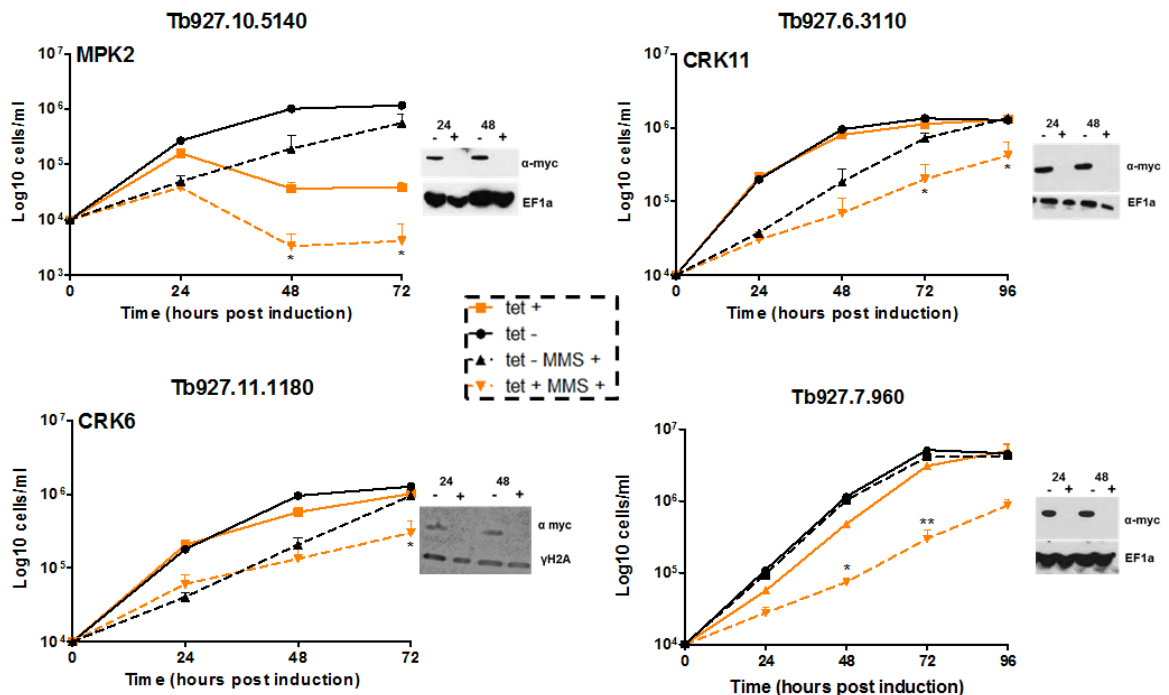


Figure 3-8: *In vitro* growth of the kinome wide PK candidates

Growth analysis of each kinome wide candidate following RNAi knockdown and following exposure to MMS (0.0003%). The error bars represent \pm SEM, $n=3$. For statistical analysis, tet - cells in the presence of MMS (dashed black line) were compared with the tet + cells in the presence of MMS (dashed orange line) at each time point. (*) = $p < 0.05$ and (**) = $p < 0.005$ as determined by a Mann Whitney U test. The western blots shown confirm protein knockdown using the endogenously tagged RNAi cell lines (generated in section 3.3.3.2). The endogenously tagged protein (~ sizes of each are annotated in Figure 3-5) was detected using α myc antiserum and EF1 α was used as a loading control (due to the size of Tb927.11.1180, γ H2A was used as a loading control [14.2 kDa in size; (Glover & Horn 2012)]. In each, by 48 hrs the protein signal was lost in the induced cells. Western blots were exposed between 1 min to 30 mins (for Tb927.11.1180). The growth curve for Tb927.7.960 was performed by T.Donatelli-Serafim (in duplicate). White space indicates images aligned from the same blot.

Following RNAi knockdown of Tb927.10.5140 (TbMPK2; Figure 3-7), a severe reduction of growth from 24 hrs was observed, suggesting this gene is essential for *in vitro* BSF survival, a phenotype closely resembling that reported by Jones and colleagues (Jones et al. 2014). Additionally, gross morphological changes could be observed after RNAi, with the cells notably larger than a non-induced BSF cell. RNAi against two PKs (Tb927.6.3110 [TbCRK11] and Tb927.11.1180 [TbCRK6]) showed little to no effect on cell growth following RNAi induction, in contrast with the report of a slight slowing of the growth after TbCRK6 RNAi by Jones et al. 2014. Though TbCRK11 show no loss of fitness after RNAi, from 24 hrs post induction, some cells in the population harboured aberrant, rounded morphology. RNAi against Tb927.7.960 produced a very mild growth effect at 24

and 48 hrs post induction, but the cells reached the same final density as uninduced.

When the RNAi was induced in the presence of MMS, a significant reduction in the growth was again observed (relative to all controls) for each PK, confirming that loss of each gene sensitised the cells to MMS.

3.3.5 Cell cycle analysis

To examine whether the nine PKs play a role during cell cycle progression, an analysis of the DNA content was undertaken after RNAi with and without MMS exposure. Cells were prepared for analysis and DAPI stained (to visualise the nDNA and kDNA) as detailed in section 2.8.3 and section 2.11.1. The cells were categorised according to their ratio of kDNA to nDNA to give an estimation of the cell cycle stage of each individual cell (as described by Benmerzouga et al. 2013) with '1N1K' corresponding to G1/S phase (~ 80 % of cells), '1N2K' to S/G2 phase (~ 10% of cells) and '2N2K' to M phase (~ 5 % of cells). Any cell unable to be identified under these categories was considered as 'other'. These data are shown in Figures 3-9 (genome wide candidates) and 3-11 (kinome candidates).

3.3.5.1 Genome wide RITseq candidates

Of the five RNAi lines analysed, only the double knockdown of TbTLK1/2 had a clear effect on cell cycle progression (Figure 3-8). From as early as 24 hrs post induction >10% of the population lacked any detectable nucleus (1K0N; 'zoids') and at 48 hrs the number of zoids increased to ~ 25 % of the population. Additionally, over 25% of the population were classified as 'other'; these cells possessed enlarged, aberrant nuclei, suggesting a block during nuclear division. However, no significant increase in 1N2K cells were detected following induction, suggesting nuclear S-phase was not significantly affected or was a G2/M arrest affected. Overall, the lack of an S-phase stall and the production of 'zoid' cells suggest a defect in the checkpoint(s) monitoring nuclear S-M phase transition.

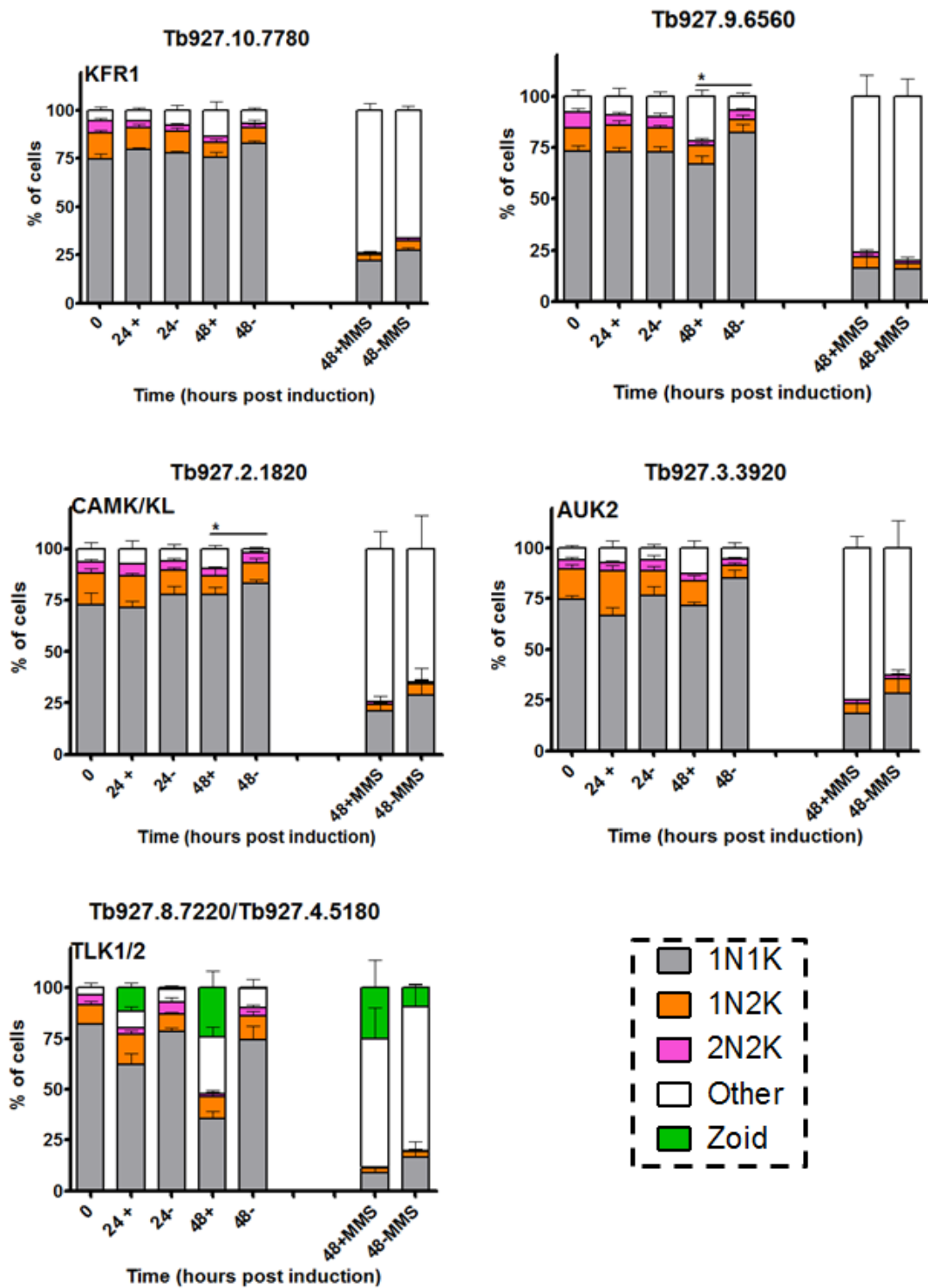


Figure 3-9: *In vitro* cell cycle analysis of the genome wide PK candidates. Cells were collected from tetracycline induced ($1 \mu\text{g/ml}^{-1}$) or uninduced cultures at 24 and 48 hrs. Cells were also harvested from cultures induced or uninduced in the presence of 0.0003 % MMS (v/v). Cells were fixed as per section 2.11.1 and stained with DAPI. The number of 1N1K, 1N2K, 2N2K and 'other' (including 0N1K, zoid) cells were counted and expressed as a percentage of the total population. The error bars represent \pm SEM ($n = 3, > 200$ cells counted per experiment). Significance was calculated by comparing 'other' cells from the non-induced individually with 'other' cells from the induced cells using a Mann Whitney U test (one tailed). (*) = $p < 0.05$. Cells were counted on an Axioskop 2.

For the other four RNAi lines examined, very little disruption of the cell cycle was observed (Figure 3-8), though in all cases, at ~48 hrs post induction, a small increase in ‘other’ cells were noted (TbKFR1 [~13 % on average], Tb927.9.6560 [~21 % on average], TbAUK2 [~12 % on average] and TbCAMK/KL [~9 % on average]). Examples of aberrant cells from each induced RNAi cell line at this time point is shown in Figure 3-9. For Tb927.9.6560, the nDNA appeared smaller in size after RNAi and, in a few cells the kDNA appeared undetectable or indistinguishable from the nuclear signal. In addition, for Tb927.9.6560 the typical morphology of a trypomastigote cells was lost and a ‘rounded’ or ‘clumped’ cell morphologies began to appear (investigated in chapter 5). In contrast for TbKFR1 and TbAUK2, aberrant cells appeared to have increased DNA content, though this was not significant in the case of TbKFR1.

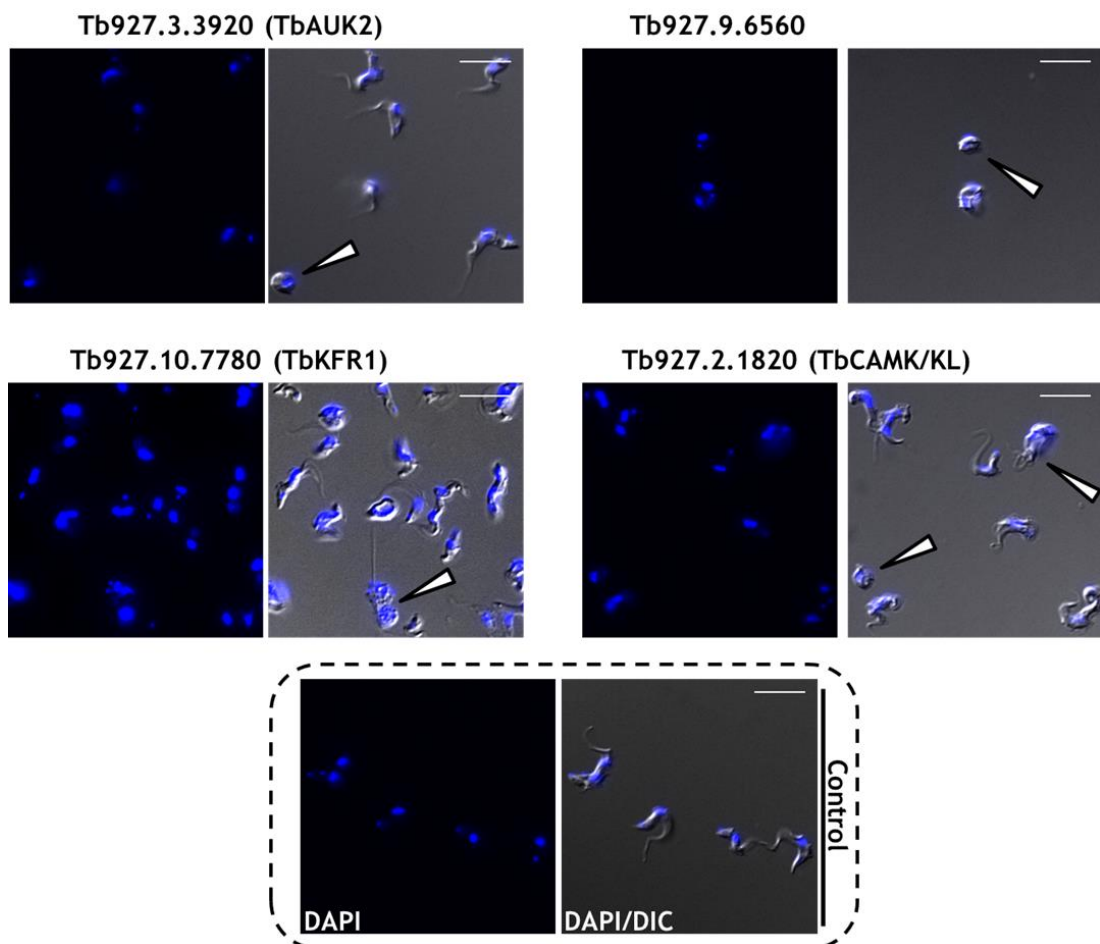


Figure 3-10: Morphology of the genome wide candidates after 48 hrs RNAi induction
 Images of cells post induction for each candidate. DAPI was used to visualise nDNA and kDNA (blue) and DIC imaging was used to view the cell body. In the black dashed box are representative images of cells in the absence of tetracycline induction (images taken from the Tb927.2.1820 cell line). White arrow indicated cells with ‘other’ phenotypes. Images were captured on an Axioskop2 (Zeiss) and processed in ImageJ (as per section 2.11.8). Scale bar = 10 μ m. No images of TbTLK1/2 are shown.

When TbAUK2 was knocked down, a transient increase in 1N2K cells was observed at 24 hrs (on average 21 % of the cells were 1N2K post induction compared to the 12 % observed in the uninduced culture), indicating a potential stall during nuclear S-or G2 phase that was not maintained until at 48 hrs, when aberrant cells appeared (which are further characterised in chapter 4). Overall, the main observable effects are linked to the nucleus (lesser so to kDNA changes) suggesting that these PKs may be involved in maintaining some aspect of the BSF nucleus; perhaps with RNAi disrupting nuclear mitosis.

The cell cycle was also examined post RNAi induction under MMS stress to test if exposure to MMS revealed an increased, specific defect during cell cycle progression. Cells were exposed to 0.0003 % MMS (v/v) and collected as described in section 2.8.3 and section 2.11.1. In all cases, no significant difference was seen after RNAi induction when compared with the pronounced cell cycle defects MMS caused to uninduced cells. Consistently, after 12 hrs (data available in chapter 8, section 8.2, Figure 8-4) exposure to MMS (regardless of induction status), a large increase (~ 30 % of the population) in 1N2K cells became apparent, suggesting MMS induces a stall during nuclear S/G2 phase. At later time points the number of 1N2K cells reduced dramatically and instead a large increase (~50 % of the population at 24 hrs, and ~70 % at 48 hrs) in aberrant 'other' cells were detected. These data suggest that BSF cells exposed to MMS simply continue replication (after a transient stall during S-phase) and, unlike human cells (for example as shown by Cliby et al. 1998), may fail to monitor nuclear damage as stringently resulting in the appearance of aberrant cells.

3.3.5.2 Kinome wide RITseq candidates

For the kinome wide RITseq candidates, a similar analysis was undertaken (conducted as described in the sections above), though the effect of RNAi knockdown on the cell cycle was not examined in the presence of MMS (Figure 3-10). Knockdown of TbCRK11 (Tb927.6.3110) produced no changes in the cell cycle relative to the control, consistent with the lack of any measurable disruption in growth (Figure 3-10). RNAi of both TbCRK6 (Tb927.11.1180) and Tb927.7.960, after 48 hrs, caused a small increase in aberrant cells (though only for Tb927.7.960 was this significant). For TbCRK6, the RNAi induced cells

adopted a clear rounded morphology (Figure 3-10), though further characterisation was not undertaken.

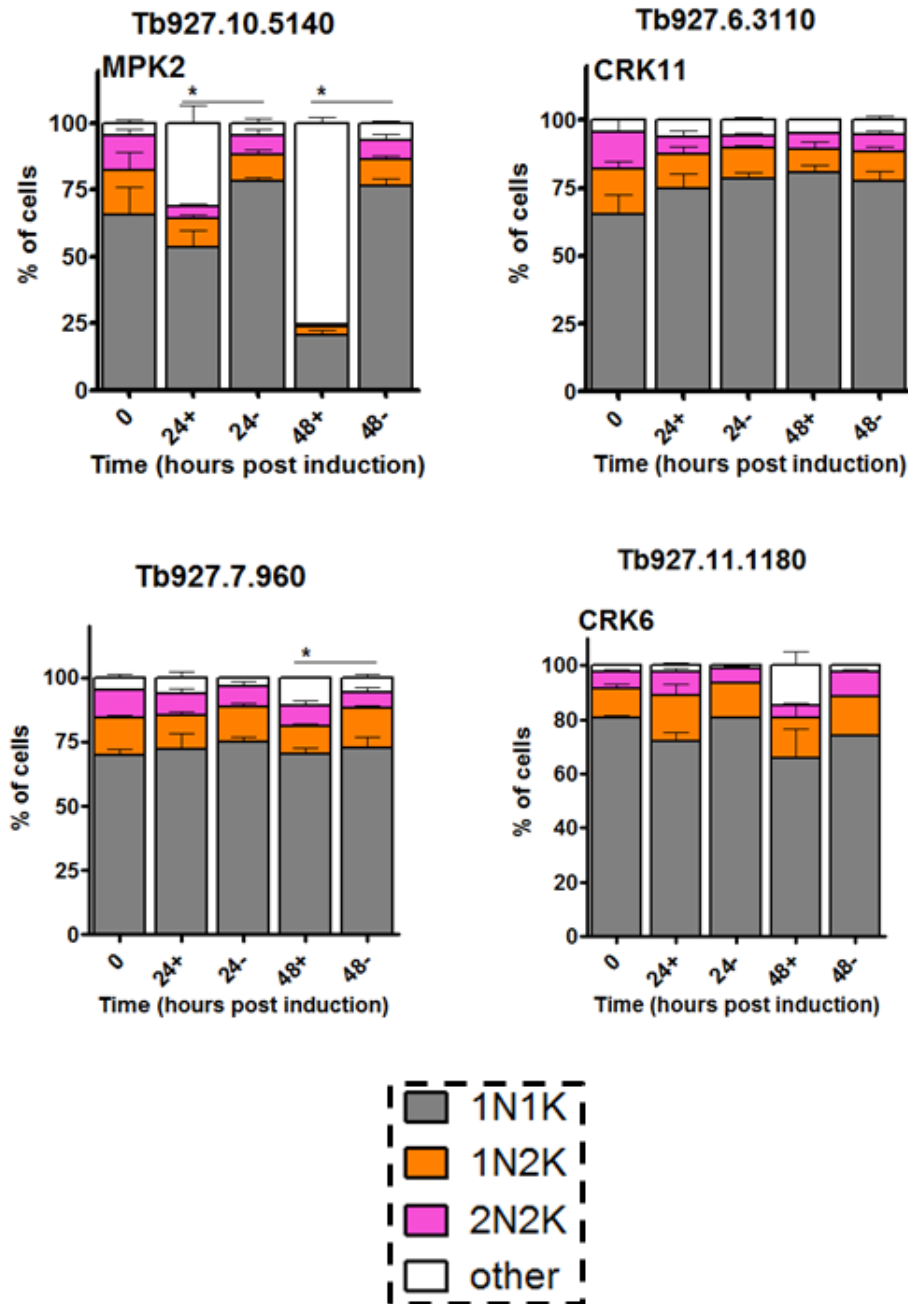


Figure 3-11: *In vitro* cell cycle analysis of the kinome wide candidate

Cells were collected from tetracycline induced (1 $\mu\text{g/ml}$) or uninduced cultures at 24 and 48 hrs. Cells were also harvested from cultures induced or uninduced in the presence of 0.0003% MMS (v/v). Cells were fixed as per section 2.11.1 and or stained with DAPI. The number of 1N1K, 1N2K, 2N2K and 'other' (including 0N1K, zoid) cells were counted and expressed as a percentage of the total population. The error bars represent \pm SEM (n=3, >200 cells counted per experiment). Significance was calculated by comparing 'other' cells from the non-induced individually with 'other' cells from the induced cells using a Mann Whitney U test (one tailed). (*) = p<0.05. Cells were counted on an Axioskop 2.

In the case of TbMPK2 (Tb927.10.5140), from 24 hrs post induction (Figure 3-10), a significant increase in aberrant ('other') cells was observed (~20 % of the

population, which increased to over ~70 % at 48 hrs). Morphologically (Figure 3-10), the cells produced a variety of phenotypes ranging from rounded, abnormally shaped (but unable to categorise) or clumped. It is unclear as to the origin of these defects.

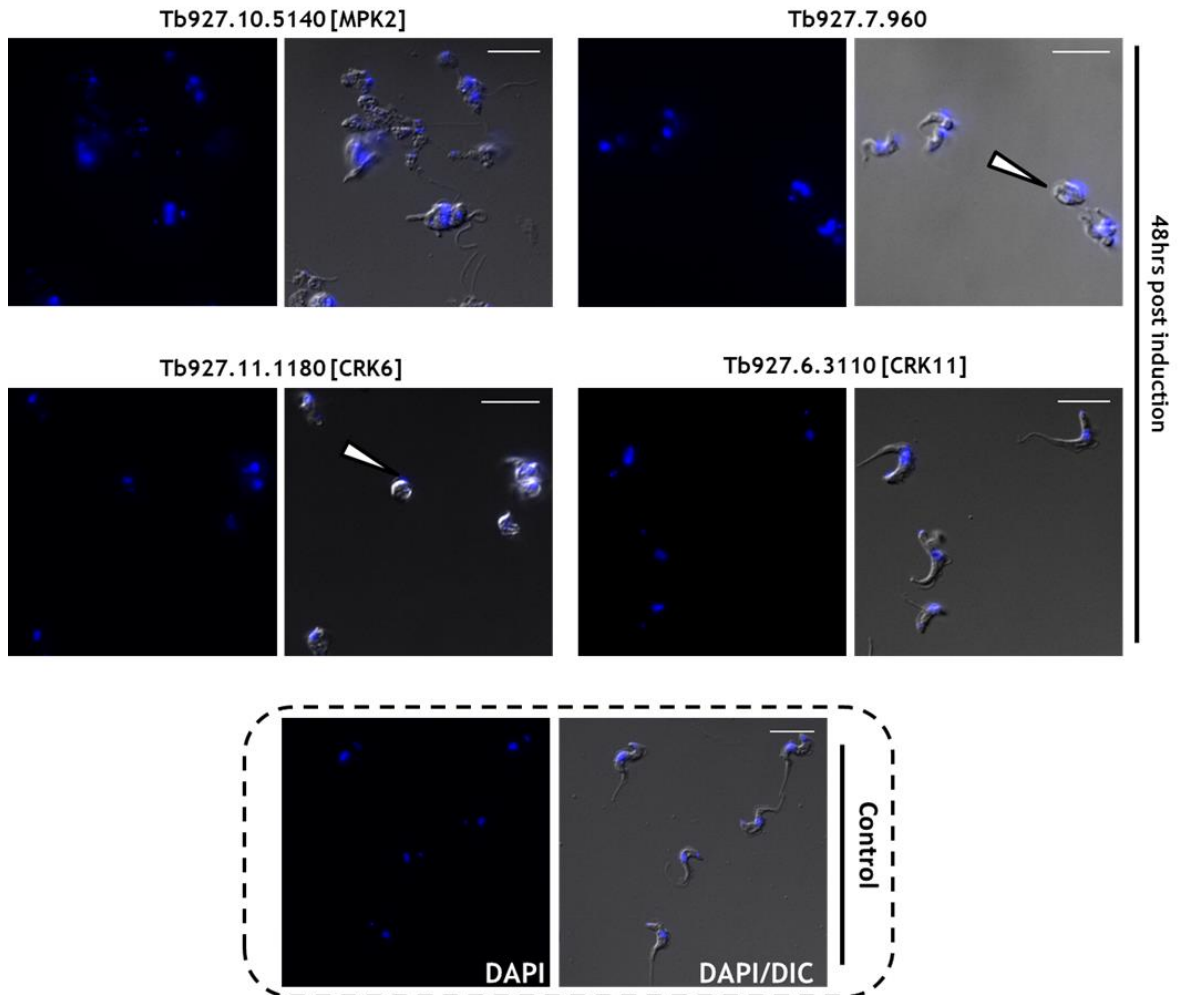


Figure 3-12: Morphology of the kinome wide candidates after 48 hrs RNAi induction
 Images of cells post induction for each candidate. DAPI was used to visualise nDNA and kDNA (blue) and DC imaging was used to view the cell body. In the black dashed box are representative images of cells in the absence of tetracycline induction (images taken from the Tb927.10.5140 cell line). White arrows indicate cells with ‘other’ phenotypes. Images were captured on an Axioskop2 (Zeiss) and processed in ImageJ (as per section 2.11.8). Scale bar = 10 μ m.

3.3.6 Analysis of the expression of γ H2A in the RNAi cell lines *in vitro*

As discussed in chapter 1 (section 1.6), one of the earliest signals of DNA damage (such as DSBs), is the phosphorylation of the core histone H2A or the histone variant H2AX, generating γ H2A(X). In *T. brucei* this variant histone is referred to as H2A (γ H2A^{Thr130} or γ H2A when phosphorylated) and is expressed after a range

of damage (Glover & Horn 2012), In mammals ~ 46 PKs have been implicated in this phosphorylation, the ATM and ATR kinases are best understood (Benzina et al. 2015). In *T. brucei* the PK(s) that phosphorylate H2A, using a non-canonical threonine, has yet to be determined. Here, we tested whether loss of the PKs induced γ H2A, or abolished the response after MMS treatment.

As shown in Figure 3-12, the 2T1 parental cell line produces little expression of γ H2A under standard culture conditions, with the low level of expression perhaps explained by the antiserum cross reacting with the unphosphorylated H2A. When the 2T1 cells were exposed to genotoxic stress (by the addition of 0.0003 % MMS for 24 hrs), expression levels of γ H2A radically increased (Figure 3-12), consistent with previous findings.

3.3.6.1 The genome wide candidates

Of the five candidates recovered from the genome wide screen, only one showed clear changes in the expression of γ H2A (Figure 3-12). All cell lysates were collected at 48 hrs post RNAi induction. MMS was added after 24 hrs RNAi induction at a concentration of 0.0003 %. Knockdown of Tb927.9.6560 or Tb927.2.1820 did not result in an observable increase in the expression of γ H2A, while RNAi of Tb927.10.7780 (TbKFR1) or Tb927.3.3920 (TbAUK2) caused, at most, only a slight increase (this expression was not quantified). Furthermore, in all cases following MMS induction, increased expression of γ H2A could be seen to the same extent in the induced and uninduced cells. Overall, from this analysis, none of the PKs play a major role in H2A phosphorylation. In fact, Tb927.9.6560 appears to be a pseudokinase, and so may not have the capacity to phosphorylate any substrate (see chapter 4). As RNAi of Tb927.10.7780 (TbKFR1) and Tb927.9.6560 both produced an observable defect growth defect, the level of γ H2A generated may not always directly correlate with a slow growth phenotype, meaning this pattern of growth may not always be due to nuclear defects that cause DNA damage.

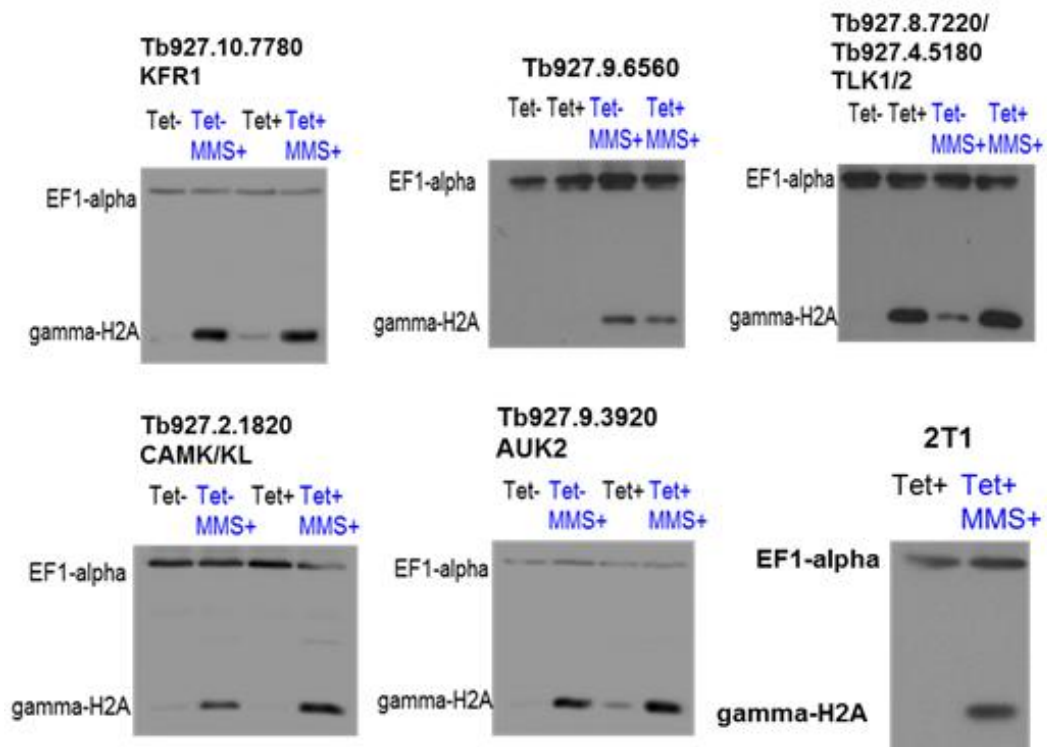


Figure 3-13: Examination of γ H2A expression in the genome wide PK candidates
Cells were induced (with 1 μ g/ml-1 tetracycline) or left uninduced for 24 hrs. At 24 hrs, MMS (to a concentration of 0.0003% [v/v]) was added to an induced and an uninduced culture. Whole cell lysates were collected as described in section 2.12.1. Whole cell extracts were separated on 15 % BT gels, blotted and γ H2A was detected using α γ H2A antiserum and α EF1 α was used as a loading control. Westerns were performed by T.Donatelli-Serafim.

In the case of the double knockdown of TbTLK1/2, an increased level of γ H2A expression was observed even in the absence of MMS, suggesting loss of TbTLK1/2 results in the accumulation of DNA lesions, which is perhaps in keeping with the severe nuclear abnormalities observed after RNAi. However, the level of γ H2A did not alter after MMS exposure and RNAi.

3.3.6.2 The kinome wide candidates

The kinome wide PK candidates were next analysed as above. Only TbCRK11 (Tb927.6.3110) showed an increased expression of γ H2A in the absence of MMS damage and after RNAi (Figure 3-13). This was unexpected, as neither an effect on cell growth or cell cycle could be detected and reinforces the suggestion that accumulation of the histone variant is not merely a reflection of growth impairment. Consistent with this, knockdown of TbMPK2 (Tb927.10.5140), which profoundly impairs growth from as early as 24 hrs post induction; Figure 3-7), did not result in an increased expression of γ H2A. Equally, RNAi of Tb927.7.690 or

TbCRK6 (Tb927.11.1180), which moderately affect growth, caused no observable increase in γ H2A expression.

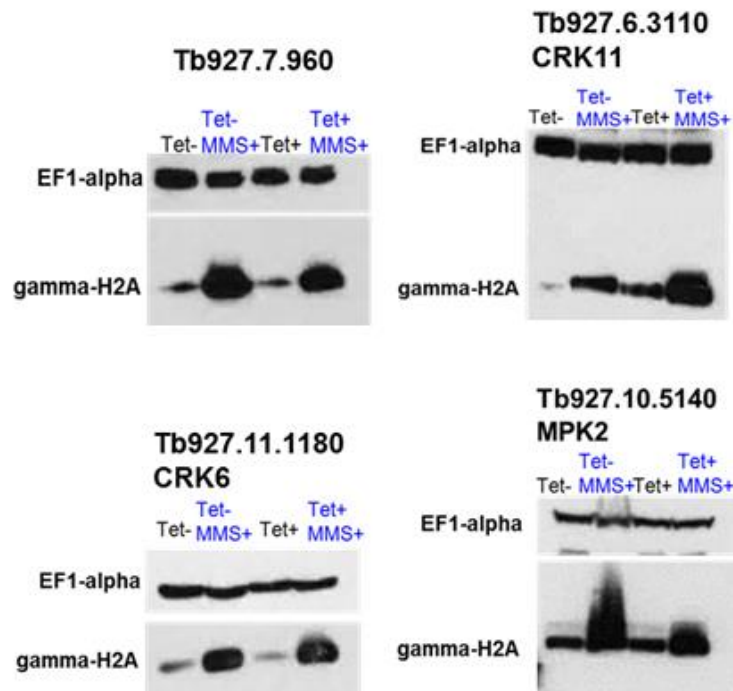


Figure 3-14: Examination of γ H2A expression in the kinome wide candidates
Cells were induced (with 1 μ g/ml-1 tetracycline) or left uninduced for 24 hrs. At 24 hrs, MMS (to a concentration of 0.0003% [v/v]) was added to an induced and an uninduced culture. Whole cell lysates were collected as described in section 2.12.2. Whole cell extracts were separated on 15 % BT gels, blotted and γ H2A was detected using α γ H2A antiserum (T. Donatelli-Serafim) and α EF1 α was used as a loading control. Exposure: 1-30 seconds.

As for the genome-wide PKs, loss of none of the kinome PK candidates resulted in altered levels of γ H2A in the presence of MMS relative to the uninduced cells therefore it is unlikely any of these kinases is the major enzyme contributing to the phosphorylation of H2A.

3.3.7 Localisation of endogenously myc-tagged kinases

Determining the sub-cellular localisation of each PK may provide further insight into their role in *T. brucei*. To this end, cells expressing the myc-tagged PK variants were prepared for indirect IFA as described in section 2.11.1 and section 2.11.2 and stained with α -mouse α -myc FITC-conjugated antibody; additionally, nDNA and kDNA were stained with DAPI. 2T1 cells were used as a control to account for background fluorescence. Routinely, two tagged clones were selected for analysis though data is only shown for one as no observable differences were noted between any clones. As only one allele was endogenously

tagged, it is unclear whether the endogenous tagged allele is functional, with the exception of Tb927.10.7780 (TbKFR1; chapter 8, section 8.2, Figure 8-5, Tb927.9.6560 (chapter 5) and Tb927.3.3920 (TbAUK2; chapter 4).

3.3.7.1 Genome wide RITseq candidate localisation

No attempt was made to examine the localisation of either TbTLK1 or TbTLK2, as this has been previously assessed (Li et al. 2007; both are nuclear). Amongst the genome-wide PK candidates, Tb927.9.6560 localised in close proximity to the kDNA, and Tb927.3.3920 localised to the nucleus, as detailed in chapter 5 and chapter 4, respectively. Localisation of Tb927.10.7780 will be discussed further below. No distinct signal could be seen for Tb927.2.1820 (data not shown). WT cells were also endogenously tagged using the same construct, with the same results, though a faint cytoplasmic signal could be observed. It is possible that this kinase localises diffusely throughout the cytoplasm. As loss of this PK resulted in sensitisation of the cells to MMS, an attempt to localise the protein after growth of the tagged cells for 18 hrs in MMS (0.0003 %); however, as before, no distinct signal could be identified; instead a faint cytoplasmic signal was observed.

Unfortunately, unlike the genome-wide candidates, no discrete localisation could be clearly ascertained for any of the kinome-wide candidates by indirect IF analysis. All the PKs appeared to stain diffusely throughout the cytoplasm of the cell (chapter 8, section 8.2, Figure 8-7). As for Tb927.2.1820, localisation of each PK was also tested after exposure to MMS, but no MMS-induced localisation was revealed (chapter 8, section 8.2, Figure 8-7).

3.3.7.1.1 Localisation of Tb927.10.7780 (TbKFR1)

The subcellular localisation of Tb927.10.7780 (TbKFR1) has not been reported in *T. brucei*. However, the *L. mexicana* ortholog (56 % sequence identity to TbKFR1), when expressed from an episome as a C-terminal GFP fusion, was shown to localise diffusely throughout the cytoplasm of promastigote cells (M. Wiese, personal communication).

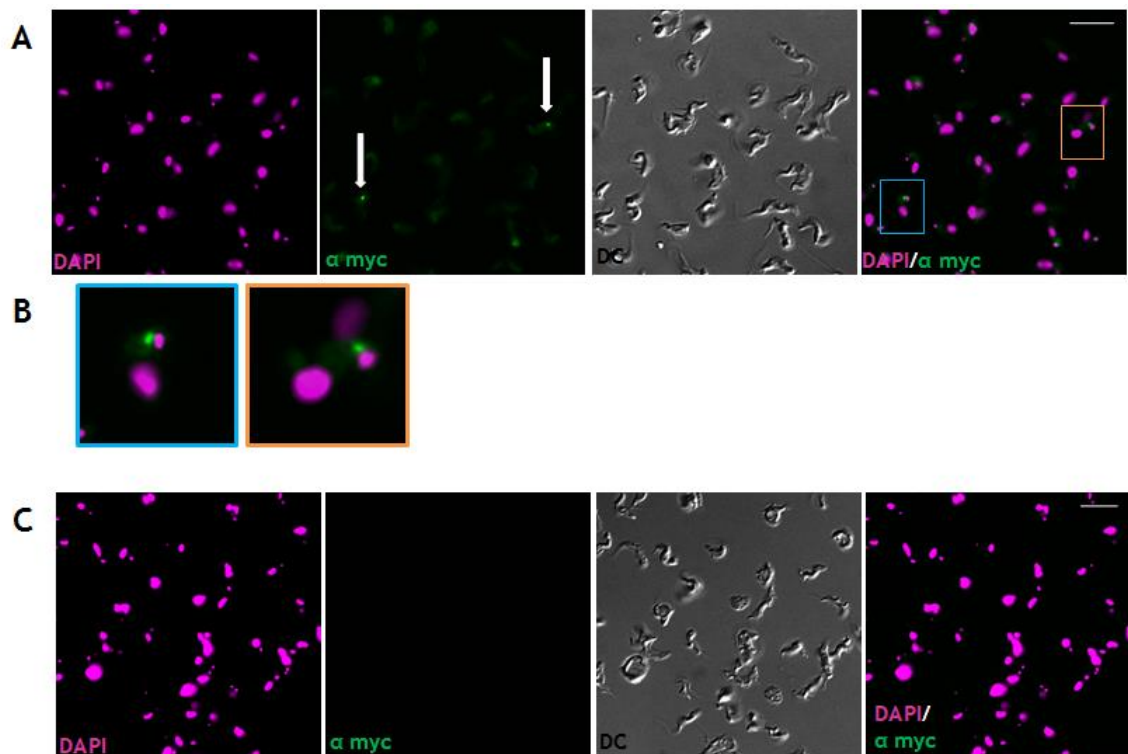


Figure 3-15: Sub-cellular localisation of Tb927.10.7780

(A) Representative field of view image of Tb927.10.7780-myc localisation in BSF cells. Cells were harvested, fixed and stained with DAPI (to visualise nDNA and kDNA; magenta) and α -myc antiserum (to visualise the endogenous myc tag; green). DC imaging was used to visualise the cell body. White arrows indicate cells harbouring Tb927.10.7780 localisation. (B) Close up images corresponding to the blue and orange boxes shown in (A). (C) Representative field of view image of Tb927.10.7780 localisation in BSF cell following 48 hrs RNAi induction. Cells were prepared as above. Scale bar = 10 μ m. Images of Tb927.10.7780^{12myc} RNAi CL1 were captured on an Axioskop2 and processed in ImageJ as per section 2.11.8.

Unexpectedly, the localisation of the endogenously myc- tagged Tb927.10.7780 (TbKFR1) did not match the pattern described in *Leishmania*. Instead, no distinct signal could be observed in ~90 % of BSF *T. brucei* cells, regardless of their cell cycle stage status (Figure 3-15). Instead a faint cytoplasmic signal was observed in these cells. However, in ~10 % of cells a small, and in addition to a faint cytoplasmic signal, a single focus could be seen in at the posterior end of the cell in close proximity to the kDNA (though it did not appear to co-localise with the kDNA; Figure 3-15 B). This localisation pattern could only be observed in 1N1K cells (G1 phase). To confirm this localisation was not simply an artefact, RNAi knockdown was induced in the endogenously tagged RNAi cell line for 48 hrs and indirect IF performed again. Here, the faint cytoplasmic signal could not be detected and no foci could be observed in any cell (Figure 3-15 C), suggesting the discrete signal localisation and the faint cytoplasmic signal are indeed due to the presence of the PK. Localisation of TbKFR1-myc did not differ following MMS

exposure (for 18 hrs; 0.0003 %; chapter 8, section 8.2, Figure 8-6). As ~80 % of cells are in G1 (1N1K; Benmerzouga et al. 2013), it is unclear why small percentage of 1N1K cells show this discrete localisation. Potentially, these cells could be within a specific stage of G1. Why such localisation is not seen in *Leishmania* is unclear.

3.4 Discussion

3.4.1 RITseq screening for DDR associated PKs in BSF *T. brucei* parasites

Kinase signalling is vital for the co-ordination of the DDR in most eukaryotes and acts from the initial detection of a DNA lesion by atypical PKs like ATR and ATM, to signal amplification via PKs like CHK1 and CHK2 (as reviewed by Marechal & Zou 2013), and subsequent downstream control of the cell cycle by PKs like WEE1 (as reviewed by Matheson et al. 2016), CDKs (as reviewed by Duursma & Cimprich 2010) and AUKB (Mackay & Ullman 2015). The range of PKs that contribute to DDR signalling has only to date been explored in mammals, where screening suggests a wide network acts. At least 55 PKs (~10 % of the human kinome), acting across a number of pathways, modulate sensitivity of ovarian cancer cells to the therapeutic agent cisplatin (Arora et al. 2010). In addition, a range of mammalian PKs have been identified that contribute to γ H2AX phosphorylation (Benzina et al. 2015).

To date, there has been no description of a PK with a role in the DDR of *T. brucei*, or any related parasite. In the case of *T. brucei*, PKs involved in the regulation of the DDR may be of specific interest considering a recent report which links DSBs and the likely presence of replicative lesions during the process of VSG switching (Devlin et al. 2016). In fact, the only kinase implicated in the VSG switching process, phosphatidylinositol 5-kinase (TbPIP5K), is not implicated in the phosphorylation of proteins, as it is a component of the inositol phosphate pathway and is predicted to phosphorylate phosphatidylinositols. Therefore TbPIP5K is unlikely to act directly on the genome (Cestari & Stuart 2015).

Searching for genes with DNA repair associated roles has been performed in a variety of organisms (for example as detailed in Ravi et al. 2009; Rooney et al.

2009; Pan et al. 2012), revealing the network of pathways required to respond to the large variety of lesions encountered. The work detailed in this chapter represents the first attempt to perform such a screen in a protozoan parasite to look for genes whose loss sensitises *T. brucei* BSF cells to MMS. From a genome-wide RNAi screen, a total of eight PK candidates were initially identified and nine PKs tested further. Five of the PKs were validated *in vitro* as being involved in cellular survival following MMS treatment; homologs of two of these PKs (TbTLK1/2 and TbAUK2) have been previously implicated in the DDR in other organisms (Benedetti 2012; Vader & Lens 2008; Carmena et al. 2009), but not in *T. brucei*; the four other PKs are novel in all organisms. Additionally, a kinome focused screen was performed (using a previously established library of RNAi cell lines; Jones et al. 2014). This approach revealed 23 PK candidates, including three seen in the whole genome screen, and TbTLK1/2. From the 19 new candidates, eight were examined further, and four were validated; after RNAi induction, their loss sensitised BSF cells to MMS *in vitro*. In addition to the nine PKs now validated, TbATR and TbATM were detected in the kinome MMS screen. Considering their well-characterised roles (in other eukaryotes) as ‘master-regulators’ of the DDR (Marechal & Zou 2013), both should be considered as putative damage response PKs in *T. brucei*. In total, across both screens, there are at least 11 PKs in BSF *T. brucei* parasites whose loss is associated with increased sensitivity to MMS; these PKs may act during the DDR. In addition to these validated candidates, preliminary data suggested eight PKs (of the 28 PKs predicted across both screens), may in fact be false positive ‘hits’. However, it is still possible more DNA repair associated PKs are present within the remaining untested genes. Further work would be required to analyse these remaining candidates. If *T. brucei* does indeed require a similar proportion of its kinome to DNA damage signalling compared with the complement of PKs revealed by limited studies in mammals, it is possible PKs additional to those discussed here are present.

More PKs were identified using the kinome wide screening approach as opposed to the genome wide screen, perhaps for several reasons. Foremost, the data from the genome-wide screen was collected from a single time point (5 days) following RNAi induction, and only after 4 days growth in one concentration of MMS. In contrast, the data from the kinome wide screen was collected as a time

course ranging from 24 hrs to 120 hrs post induction in the presence of two MMS concentrations, hence allowing the effect of PK depletion to be assessed progressively and with greater sensitivity. An added complication is the potential for RNAi cell lines, particularly those targeting essential genes, to revert following induction over a period of time, for instance becoming insensitive to tetracycline. This effect may explain why TbATR failed to be identified as a candidate in the genome wide screen. At 72-96 hrs post RNAi induction, TbATR appears to revert and recover proliferation (chapter 6). Indeed, it is notable that none of the essential PK candidates in the kinome screen were detected in the whole genome screen. Finally, the much greater read depth provided by the kinome screen is likely to allow detection of genes with minor roles, where small changes in MMS/MMS ratio could be detected.

From the kinome wide screen, a range of sensitivities to MMS could be detected after RNAi of the PKs identified. For some (for example, Tb927.7.960), a prolonged exposure to MMS resulted in a reduced MMS⁺/MMS⁻ ratio. Others (for example Tb927.1.1930) showed a rapid reduction. It is possible these differences may be explained by differing levels of RNAi knockdown. However, it is equally possible that these differences perhaps reveal PKs which act either at early or late stages in the response to MMS. Whether they act within a single pathway or within multiple is unclear at this stage. Another interesting consideration is as to why some of the PKs examined by RNAi are essential for survival following MMS stress and others are perhaps dispensable. This may support a role for the requirement of multiple pathways to facilitate BSF survival following MMS exposure (see below). Though only TbATR and TbATM were investigated further in chapter 6, other PKs with known roles in the DDR of other eukaryotes were also identified, including a polo-like kinase (TbPLK; Tb927.7.6310; MMS⁺/MMS⁻: 1.397), the aurora kinase 1 (TbAUK1; Tb927.11.8220; MMS⁺/MMS⁻: 1.528), the Nima related kinases (NEK) TbNRKA/B (a dual targeting RNAi line was used; Tb927.4.5390/Tb927.8.6930; MMS⁺/MMS⁻: 0.717) and the target of rapamycin-4 (TOR4) kinase (Tb927.1.1930; MMS⁺/MMS⁻: 0.744). Though none of these were examined further, investigation of these PKs may shed further light on the parasites response to MMS exposure.

When comparing the genome-wide screens for DNA damage response factors in yeast (Chang et al. 2002), *Drosophila* (Ravi et al. 2009) and *E. coli* (Rooney et al. 2009), it is clear that a reasonably conserved network for MMS survival operates; DDR pathways associated with the repair of base adducts were enriched (generally). Such pathways include NER, BER and MMR. Additionally, genes associated with DNA replication and HR were also enriched in these screens. As previously eluded to, the PKs identified in these screens may operate within several pathways activated in response to MMS. Of course a key remaining question is if and how these PKs interact with common or specific elements of these pathways, many of which have been characterised (Genois et al. 2014).

3.4.2 Candidate validation: growth and cell cycle analysis

Chapters 4 and 5 provide in depth analysis of the functions of two of the PK candidates: Tb927.9.6560 and Tb927.3.3920 (TbAUK2). Below I discuss what is known about the other validated PKs.

3.4.2.1 Genome wide candidates

Loss of TbTLK1/2 resulted in a drastic reduction in cell growth and the formation of 'zoid' cells, though as this cell line targets both PKs, the phenotype could result from lack of either or both. However, data produced by Li and colleagues, using RNAi cell lines targeting each PK independently, suggest the drastic reduction in growth is due to the loss of TbTLK1. TbTLK1 RNAi results in an accumulation of cells in S-phase of the cell cycle and abnormal segregation of chromosomes and spindle machinery (Li et al. 2007) in both the PCF (2007) and BSF (Z. Li, Umeyama, et al. 2008) of the cell. In our hands, the phenotype of the double RNAi closely resembles these findings. BSF cells forming 'zoids' after RNAi have been described, including following loss of ORC1/CDC6 (Marques et al. 2016). This may be in keeping with a role for TbTLK1/2 during DNA replication, which may explain the increased MMS sensitivity. Nonetheless, further work will be needed to determine whether TbTLK1/2 directly interact with replication factors, in addition to described interaction of TbTLK1 with TbAUK1 and histone modifiers (Li et al. 2007). Aside from this, previous research has linked TLKs to genome maintenance (as reviewed by Benedetti 2012), which is in keeping with

the role of TbTLK1/2 in response to MMS, though to date such activities have been thought to largely be metazoan-specific.

Tb927.10.7780 (TbKFR1) is regarded as an essential gene (Hua & Wang 1997), since attempts to delete the ORF (in PCF cells) were unsuccessful. Indeed, a knockout of this gene was attempted in WT BSF cells, and despite transformants being recovered, there was evidence of gene duplication resulting in retention of a gene copy (data not shown). Despite this, the recovered transformants appeared to be sensitive to MMS stress (data not shown). In contrast, though LmMPK1 has been shown to be required to form skin lesions *in vivo* (Wiese 1998) the gene can be knocked out *in vitro*, suggesting a less critical role in *L. mexicana*. Though the function of this PK (TbKFR1/Tb927.10.7780) in the *T. brucei* cell is unclear, further investigation of the localisation may provide a greater insight into its role.

No growth effect after RNAi induction, nor disruption of the cell cycle, was seen when Tb927.2.1820 (CAMK/KL) was targeted. There are no reports in the literature on the function of this kinase. When analysed by BLASTp (data not shown) the protein did not appear to show homology to any human PK; instead the PK was most homologous to calcineurin B-like (CBL)-interacting S/T kinases in plants (*Arabidopsis* and *Glycine*). Interestingly, these calcium activated kinases are thought to be important for sensing environmental stress signals. Furthermore, the plant PKs interact with a multigene family (the CBL proteins) to transduce an extracellular ionic salt signals into an intracellular phosphorylation signal (reviewed by Luan 2009). Such functions in sensing extracellular stress could be in keeping with a role for Tb927.2.1820 in the detection of MMS stress.

3.4.2.2 Kinome wide candidates

From the kinome wide candidates, only one PK (Tb927.10.5140; TbMPK2) was essential for BSF proliferation, though its loss did not appear to affect progression of the cell cycle; instead, aberrant cells began to accumulate shortly after RNAi induction. This PK (under the name TbMAPK6) has been functionally examined in PCF and BSF cells (Wei & Li 2014). In BSF cells, Wei and Li report similar defects to those described in this thesis, and suggest a role during BSF

cytokinesis. The process of cytokinesis is intimately linked to DDR processes in other organisms, and many damage-associated PKs, like the aurora kinases, have both repair and cell division functions (Pan et al. 2012; Fry et al. 2012; Carmena et al. 2012; Fu et al. 2007; Goldenson & Crispino 2015). As MAPK kinases are components of signal transduction pathways in *T. brucei* (Wei & Li 2014), it is possible that this acts in such a pathway to signal damage. In fact, activation of MAPKs has been shown to occur following PARP-1 activation, an early DDR signal (Cohen-Armon 2007).

For the other candidates, growth did not appear to be affected nor were any defects in cell cycle progression observed. In contrast, when TbCRK6 (Tb927.11.1180) was knocked down by Jones et al (2014), growth was slowed; furthermore, growth defects in PCF cells are seen following TbCRK6 knockdown (Tu & Wang 2004). Interestingly, when TbCRK6 was knocked down, cells with a 'rounded; appearance (akin to those observed following the knockdown of Tb927.9.6560; see chapter 5) were seen, perhaps suggesting a common role in endocytosis and/or trafficking. It is interesting that, in addition to TbCRK6, a second cdc2-related kinases (TbCRK11) were identified and validated as having a role in the response to MMS exposure. CRKs (or cdc2-related kinases) in *T. brucei*, when paired with a cyclin (CYC), have been shown to regulate the transitions between cell cycles stages (for example, CYC2-CRK3 may be required for the G1-S phase transition; Hammarton et al. 2003). Indeed, control and regulation of the cell cycle is a key process following DDR activation. It is possible that these PKs mediate DNA damage associated cell cycle checkpoints.

The final candidate (Tb927.7.960) shows sequence homology to a serine rich PK (SRPK; family: CMGC). Interestingly, in *P. falciparum*, the kinase PfSRPK1 (also an SRPK) was shown to be involved in mRNA trans-splicing regulation. Furthermore, in other eukaryotes, the functions of SRPKs range from mRNA processing to the mediation of import into the nucleus (Dixit et al. 2010). This may be of interest due to *T. brucei*'s need to regulate gene expression post-transcriptionally and may suggested the PK controls gene expression in response to MMS stress. Intriguingly, this PK was identified in a RITseq screen designed to identify PKs required for survival *in vivo* (Fernandes-Cortez et al. in preparation).

3.4.2.3 False positive hits

As expected, several ‘false-positive’ candidates were identified from both screens (chapter 8, section 8.2, Figure 8-3). Despite showing MMS+/MMS- ratios of <0.5, when examined *in vitro*, no sensitivity to MMS could be detected relative to the controls. Surprisingly, several NEK kinases were detected and examined (including TbNEK19 and TbNRKA/B) though none, when targeted by RNAi, showed increased sensitivity to MMS. NEK kinases are an expanded family of PKs in *T. brucei* with known roles in the DDR in other eukaryotes (Moniz et al. 2011). It is therefore perhaps surprising that no NEK kinase examined showed increased sensitivity to MMS stress. TbNRKA and TbNRKB are instead hypothesised to have a potential role in differentiation from BSF to PCF (Gale & Parsons 1993; Gale et al. 1994; Jones et al. 2014). As the level of knockdown for each false positive hit was not assessed, it is possible that some of the cell lines failed to produce adequate gene knockdown.

3.4.3 Candidate Localisation

Of the eight candidates endogenously tagged, localisation could only be clearly determined for three: Tb927.10.77880 (TbKFR1), Tb927.3.3920 (TbAUK2; see chapter 4) and Tb927.9.6560 (Tb6560, see chapter 5). Interestingly, only one (TbAUK2) was nuclear; the other two localised in close proximity to the kDNA.

For Tb927.10.7780, the endogenous tagging construct was transformed into WT cells and the other allele deleted in order to confirm functionality of the tag (as describe in section 2.4.1.2). This was undertaken due to the unusual localisation exhibited by this PK; indeed, the tag appeared to be functional and the population appeared to be clonal. Additionally, super resolution images were captured, clearly demonstrating the PK forms a particular structure within the cell near the kDNA. It is possible this PK may be associated with the FP, since the signal did not co-localise with the kDNA. However, the detailed spatial position of this kinase and the very limited cell cycle stage during which it localises is unclear. However, TbKFR1 is also a MAPK family member, and therefore putatively part of a signalling cascade. Perhaps TbKFR1 is recruited to its discrete region in response to an incoming stimulus, perhaps via the FP. TbKFR1 shows strong sequence homology to kinases within a MAPK signalling

cascade controlling a mating pathway in *S. cerevisiae*: the KSS1, FUS3 and ERK1 kinases (KSS1FUS3 Related Kinase 1 or KFR1). In addition, TbKFR1 appears to be lifecycle regulated, with more protein activity being observed in the BSF relative to the PCF (Hua & Wang 1994; Hua & Wang 1997). Perhaps within this circumstantial evidence are clues to understand the function of TbKFR1.

No distinct localisation could be determined for any of the kinome-wide candidates however it is possible that these kinases may localise diffusely throughout the cytoplasm of the cell; further analysis is required to confirm this statement. Conversely, it is possible that epitope tagging the PKs interrupts function and the kinases are unable to correctly localise within the cell ; due to time constraints, functionality of each tagged variant could not be confirmed. However, TbMAPK6 (Tb927.10.5140/TbMPK2) has been previously been shown to localise diffusely throughout the cell across all cell cycle stages in *T. brucei* BSF and PCF cells (Wei & Li 2014). In addition, an SRPK kinase in *P. falciparum* has been reported to be cytosolic (Dixit et al. 2010).

Neither CRK could be localised, despite other members of this family being visualised by endogenous tagging. For example, TbCRK9 (a CRK involved in pre-mRNA transplicing; Badjatia et al. 2016) localises diffusely throughout the nucleus (Gourguechon & Wang 2009). Endogenously tagging Tb927.11.1180 (TbCRK6) proved challenging and was finally achieved by N-terminally tagging the gene. However, when examined by western blot, the size at which the protein resolved and the predicted MW were different; the endogenously tagged gene was ~50% smaller than the expected size. The reason for this is unknown; potentially the ORF could be miss-annotated, or perhaps the kinase is post-transcriptionally processed (i.e cleaved upon, for example, following a phosphorylation event) which may explain the reduced size. Nonetheless, when knockdown of the gene was induced in the tagged RNAi cell line, the signal was lost, suggesting the correct gene was endogenously tagged. Further work would be required to determine the reason behind this size difference.

4 Dissecting the function of TbAUK2 in bloodstream form *T. brucei*

4.1 Introduction

4.1.1 Aurora Kinases

Aurora kinases (AUKs) maintain normal cellular proliferation, with functions ranging from chromosomal duplication, DNA checkpoint signalling, chromosome segregation, and overseeing and co-ordinating the processes of mitosis and meiosis. Defects or deregulation of AUKs in mammals commonly manifest as cancer; e.g. over expression of AUKs is observed in breast cancer, ovarian cancer and leukaemia (as reviewed by D'Assoro, Haddad, & Galanis, 2015; Mountzios, Terpos, & Dimopoulos, 2008). With such crucial roles AUKs provide vast potential as anticancer targets, and are at the forefront of drug discovery programmes.

The AUK family of serine/threonine kinases (family ACG) is conserved across the eukaryotic kingdom and the first AUK was identified in the budding yeast *S. cerevisiae* (Chan & Botstein 1993). All yeasts only have one AUK, which is a homolog of AUKB (below) and is termed IPI1p in *S. cerevisiae* and Ark1 in *S. pombe*. Most multicellular eukaryotes have two AUKs, termed AUKA and AUKB in vertebrates; (Carmena & Earnshaw 2003)⁸. A third aurora kinase (AUKC) is found in mammals only (Sasai et al. 2004; Kimmins et al. 2007).

The three human AUKs are similar at their C-termini, which host the catalytic domain. AUKA, B and C share ~70% sequence homology in this region. The N-terminal regions are notably varied, perhaps due to the functional divergence shown by each kinase; in addition, the N-terminus contains several important regulatory domains (discussed below). Though characterisation of the roles of the AUKs in a typical multicellular eukaryotic cell is ongoing, it appears that each AUK plays vitally different roles and act distinctly during nuclear division, though functional overlap can be observed (Sasai et al. 2004; Fu et al. 2007). Numerous interaction partners for AUKs have also been described (Samudio & Vélez 2015). A summary of the dynamic localisation of each human AUK is

⁸ *C. elegans*, *D. melanogaster* and *X. laevis* each only have two (AUKA and AUKB). *A. thaliana* has three, which are classified into two distinct groups and appear to have diverged functions from AUKs of other eukaryotes (reviewed by Weimer, Demidov, Lermontova, Beeckman, & Van Damme, 2016).

illustrated in Figure 4-1, and a summary of function for each is presented below.

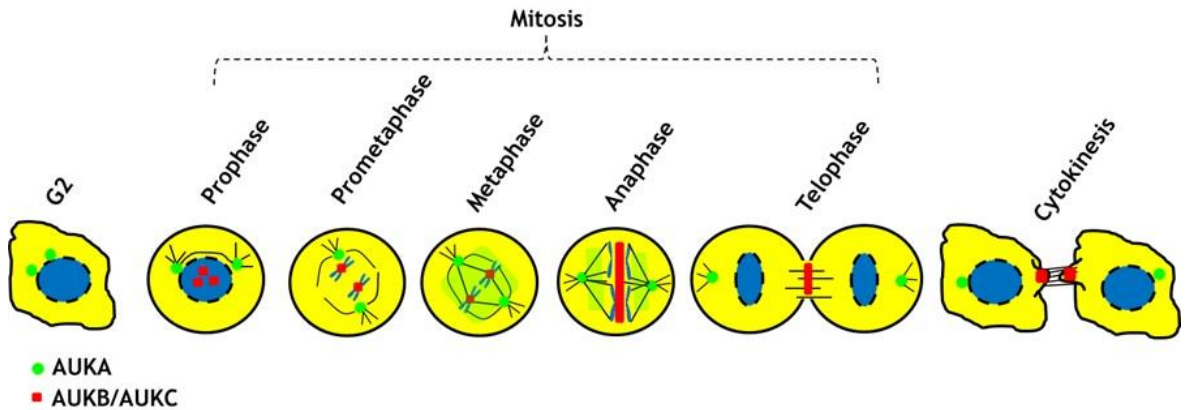


Figure 4-1 ; AUKs localise dynamically throughout mitosis

AUKA (green circles) localises to the centromere throughout mitosis. During metaphase and anaphase, AUKA moves to the spindle poles. Both AUKA and AUKB protein levels are highly reduced during G1 phase of the cell cycle due to degradation (for AUKC this is unknown; (Stewart & Fang 2005). AUKB and AUKC (red circles) are both associated with the chromosomal passenger complex CPC at kinetochores. During anaphase the kinases move to the centre spindle (red rectangle), after which they it progress to the contractile ring during cytokinesis. Figure adapted from (Giet et al. 2005).

4.1.1.1 AUKA

Overexpression of AUKA is a common hallmark of cancers (reviewed by D'Assoro et al., 2015; Vader & Lens, 2008). Furthermore, cells with high levels of AUKA continue cellular proliferation in the presence of DNA damage (such as Cisplatin or X-rays), due to de-regulation of the DDR, since excess AUKA over-rides the spindle assembly checkpoint (Krystyniak et al. 2006; Katayama et al. 2012; Sun et al. 2014). Conversely, the loss of AUKA is required for normal cellular proliferation and ablation of only a single allele is associated with tumour development in mice⁹. The precise regulation of AUKA is therefore critical to maintaining normal cell proliferation.

AUKA has numerous interaction partners (Figure 4-2). Mainly, AUKA (in human cells) aids centrosome maturation, the initiation of mitosis (through phosphorylation of the polo-like kinase PLK1¹⁰; reviewed by(Asteriti, De Mattia, & Guarguaglini, 2015; Carmena, Ruchaud, & Earnshaw, 2009; Lindqvist,

⁹ Embryos of mice lacking AUKA do not progress past the 16 cell stage. Mice which are heterozygote at the locus encoding for the AUKA gene have an increased rate of tumour development (up to 3 fold increase; Lu et al., 2008).

¹⁰ PLK1 is phosphorylated (in human cells) on a threonine at position 210 (T210) by AUKA (Asteriti et al. 2015).

Rodríguez-Bravo, & Medema, 2009 and Samudio & Vélez, 2015), re-entry to mitosis following cell cycle arrest, and formation of the spindle poles (when associated with a microtubule binding protein known as TPX2). AUKA is also required for cytokinesis (during abscission).

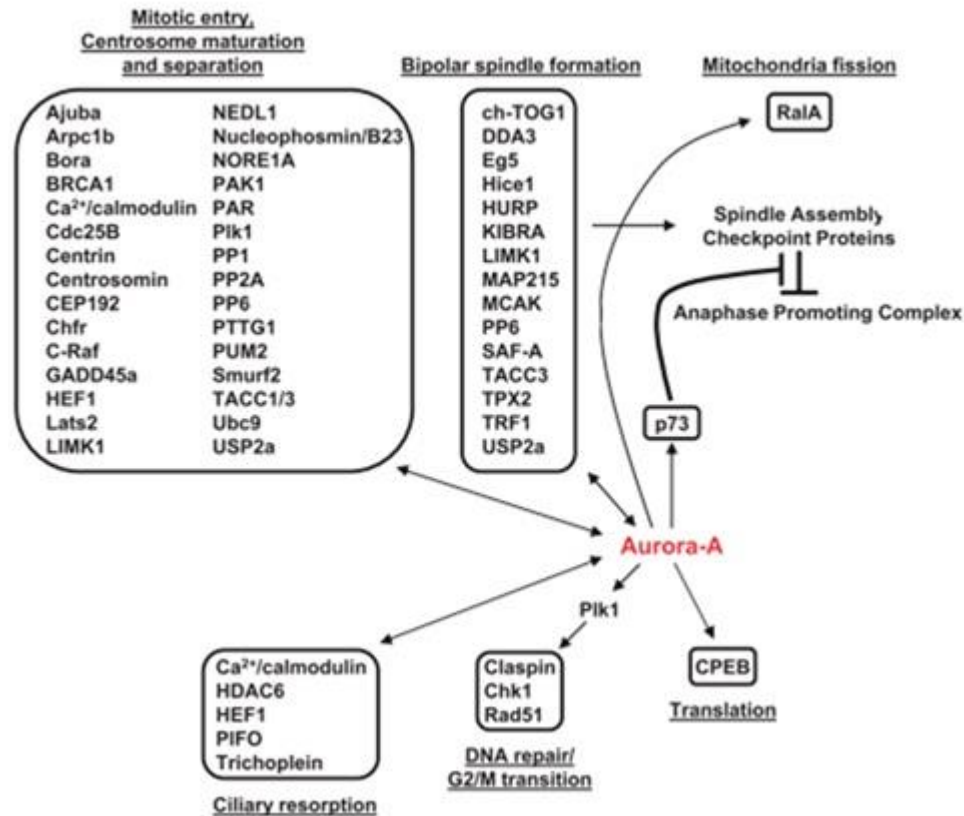


Figure 4-2: A summary of the interaction partners of AUKA

AUKA has numerous interaction partners depending on the role the kinase is required to perform. For example, when AUKA is overexpressed, it represses RAD51 function, which in turn represses homologous recombination (Sourisseau et al. 2010). Figure adapted from (Samudio & Vélez 2015).

Following the observation that AUKA can interact with spindle microtubules during mitosis, Ritchey and Chakrabarti (Ritchey & Chakrabarti 2014) showed AUKA is also important for modulation of the actin cytoskeleton, via Cofilin (an actin depolymerising protein; Ritchey & Chakrabarti, 2014) and other cytoskeleton-associated proteins. This is consistent with separation of centrosomes requiring the cell's actin cytoskeleton. The diverse roles of AUKA throughout mitosis are reflected in its dynamic localisation (Figure 4-1). Regulation of AUKA activity is mediated by its interaction partners (Figure 4-2) and by irreversible ubiquitin-directed degradation (Crane, Kloepfer, & Ruderman, 2004 and reviewed by Lindon, Grant, & Min, 2016).

4.1.1.2 AUKB

Overexpression of AUKB, like AUKA, has been implicated in cancer (Smith et al. 2005; Falchook et al. 2015). However, a direct role of AUKB in oncogenesis is unclear. Instead, the interaction partners (such as the tumour suppressor protein p53; Gully et al., 2012) of AUKB may influence the development of carcinomas. AUKB activation, unlike AUKA, is associated with the Chromosomal Passenger Complex (CPC; other members of this complex include INCENP, Survivin and Borealin; the functions of the CPC are reviewed by Carmena, Wheelock, Funabiki, & Earnshaw, 2012). Additional interaction partners of AUKB are summarised in Figure 4-3.

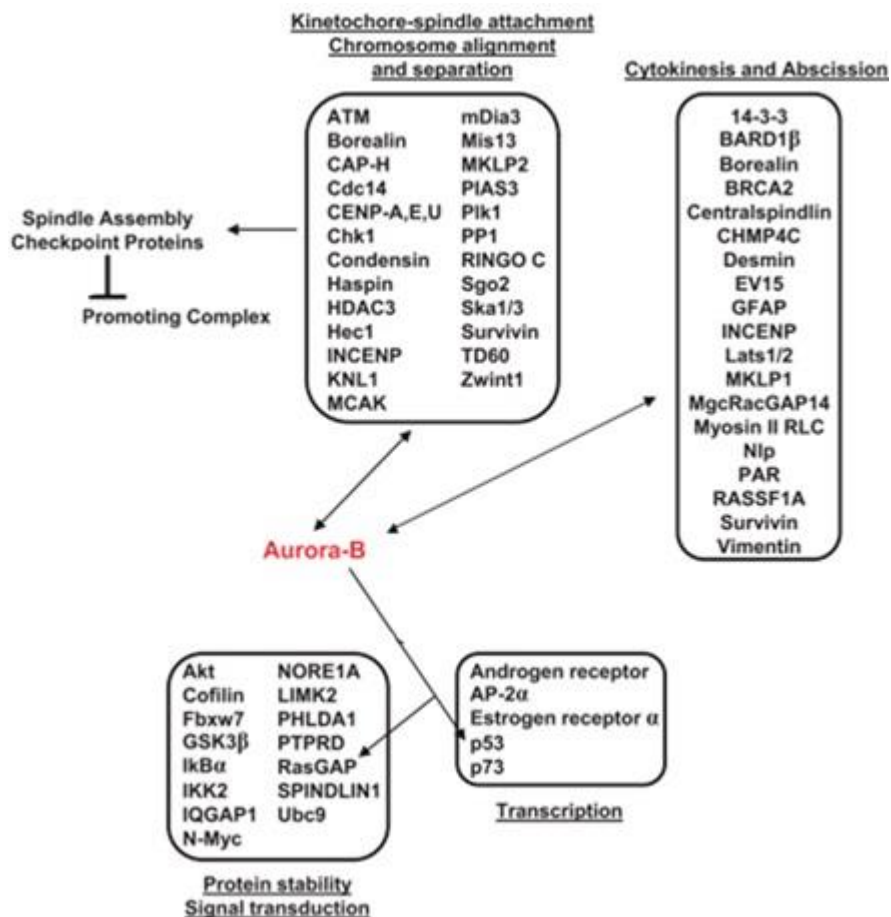


Figure 4-3: A Summary of the interaction partners of AUKB

AUKB also had a wide range of interaction partners. For example, AUKB forms a complex with Borealin (Dasra), INCENP and survivin known as the chromosomal passenger complex. This complex is required to co-ordinate functions such as the alignment of chromosomes and cytokinesis. In addition, this complex modulates the kinase activity of AUKB (reviewed by (Vader et al. 2006; Carmena et al. 2012). **Figure adapted from (Samudio & Vélez 2015).**

As part of the CPC, AUKB monitors and co-ordinates spindle formation, chromosome segregation and cytokinesis (reviewed by Afonso, Figueiredo, &

Maiato, 2016; Carmena et al., 2009; Samudio & Vélez, 2015). AUKB is required during sister chromatid bi-orientation and cohesion at the spindle mid-zone. AUKB can phosphorylate (and regulate) several protein components of the kinetochore to correct mis-orientation of sister chromatids. AUKB is physically moved from its substrates, thereby reducing its activity (Maresca & Salmon 2009; Carmena et al. 2012; Lampson & Cheeseman 2011) and stabilising the kinetochores with the correct sister chromatid orientation at the spindle mid-zone. The dynamic localisation of AUKB throughout mitosis is mostly distinct from AUKA, highlighting the functional divergence of these kinases (Figure 4-1). Several proteins influence AUKB activation, notably INCENP, TLK-1 (Riefler et al. 2008) and CHK1 (Petsalaki & Zachos 2013), the latter of which; acts in response to stimulation from the atypical kinase ATR (Liu et al. 2000), providing a direct link to the DDR. As for AUKA, regulation of AUKB activity can be mediated by irreversible ubiquitin-directed degradation (Crane et al., 2004 and reviewed by Lindon et al., 2016).

4.1.1.3 AUKC

AUKC defects are associated with infertility and AUKC expression, unlike A and B, is limited to germ cells (Sasai et al. 2004; Kimmins et al. 2007). Like AUKB, AUKC comprises part of the CPC, localising at the centromeres during early meiosis and subsequently re-localising as meiosis progresses to the spindle mid-zone. AUKC, primarily, is important for chromosome segregation and cytokinesis (much like AUKB). In oocytes and spermatocytes deficiencies and deletions in the AUKC gene results in polyploid cells (Dieterich et al. 2007; Balboula & Schindler 2014) highlighting the role this kinase plays in the co-ordination of meiosis.

4.2 Aurora Kinases in *T. brucei*; what do we know?

Remarkably for a protozoan, *T. brucei* has three aurora kinases (TbAUK1 [Tb927.11.8220], TbAUK2 [Tb927.3.3920] and TbAUK3 [Tb927.9.1670]) and AUKs are of interest as drug targets in *T. brucei*, given the range of inhibitors available. Indeed, TbAUK1 is at the forefront of a drive towards 'drug repurposing' for the treatment of neglected tropical diseases (Ochiana et al.

2013). The *L. donovani* AUK LdAIRK has also been suggested to be a potential drug target (Chhajjer et al. 2016).

Functional characterisation for each AUK has been undertaken, though with a primary focus on TbAUK1 (a potential homology of AUKB), across both lifecycle stages. TbAUK1 is essential (as shown by RNAi; Tu et al. 2006) for cell proliferation in both PCF and BSF *T. brucei* cells (Li & Wang, 2006), though it exhibits some life cycle stage specific functions. In PCF cells knockdown of TbAUK1 prevents entry into both nuclear and kinetoplast S phase; the converse effect is observed in BSF cells, where the nucleus and kinetoplast continued to replicate generating cells with large, polyploid nuclei and multikinetoplasts. In addition, the morphology of the BSF becomes grossly affected, with the cells adopting a 'rounded' appearance, possibly linking TbAUK1 to the control of microtubules; again, this effect is not observed in PCF cells (Li, Umeyama, & Wang, 2009).

TbAUK1, like AUKB, localises to the centromeres and, as mitosis progresses, the kinase re-localises to the spindle mid-zone, both observations consistent with TbAUK1 being required for the movement of the CPC¹¹ during mitosis and cytokinesis, and for the transition from metaphase to anaphase (Li et al. 2009). Recently TbAUK1 has been shown to regulate Polo-like Kinase (TbPLK1) during cytokinesis via a trypanosomatid specific protein known as TbCIF1; TbCIF1 permits the recruitment of TbAUK1 to the new FAZ, allowing TbAUK1 to drive the initiation of cytokinesis (similar to the roles both AUKA and AUKB play in human cells; see sections 4.1.1.1 and 4.1.1.2 above). In the absence of TbCIF1, cytokinesis proceeds in the opposite direction ('reverse cytokinesis'). Identification of a specific trypanosomatid AUK binding factor highlights the potential functional divergence of the *T. brucei* AUKs from those of vertebrate eukaryotes (Zhou et al. 2016).

Strikingly, no phenotypes were initially observed for either TbAUK2 or TbAUK3 in the PCF stage after RNAi induction (Tu et al. 2006). Later, one report (Jones et

¹¹ Interestingly, divergence of the CPC appears to have occurred with *T. brucei*, which has two proteins termed TbCPC1 and TbCPC2 that are distinct from the three originally described CPC proteins (Li et al., 2008).

al. 2014) suggested BSF knockdown of TbAUK3 results in a slow growth phenotype with arrest during mitosis and cytokinesis (an effect reproduced as part of a kinome RITseq screen; D.Paape and J.Stortz, unpublished).

TbAUK2 was identified in the screen detailed in chapter 3 to have a potential role in cellular survival to MMS stress and in an kinome wide RITseq screen as a kinase potentially required for survival in mice *in vivo* (Fernandes-Cortez et al. 2016, *in preparation*). These observations represent the first description of any roles for TbAUK2 in BSF *T. brucei*.

4.3 Research Aims

RNAi Knockdown of TbAUK2 did not significantly alter cell proliferation except following exposure to MMS. The aim of this chapter was to further probe the function of TbAUK2 by generating knockout mutants in BSF cells and localising the protein.

4.4 Results

4.4.1 Bioinformatics analysis

TbAUK2 is encoded for by the gene Tb927.9.3920 (TriTrypDB v.28), predicting a protein of ~42.1 kDa (380 amino acids). TbAUK2 orthologs can be found across the kinetoplastid phylum, as ascertained from the genomes available in TriTrypDB (v.28).

4.4.1.1 BLAST analysis of TbAUK2

TbAUK1 is considered the homolog of the human aurora kinase AUKB (Tu et al. 2006). To identify genes with potential homology to TbAUK2, the protein sequence of TbAUK2 was used as a query sequence and analysed using the BLASTp algorithm (BLOSUM62; version; BLASTp 2.3.1; <http://blast.ncbi.nlm.nih.gov/Blast.cgi>). The sequence was compared against all non-redundant (nr) protein sequences available in the NCBI database (Li et al. 2013) and analysed using the 'SmartBLAST' feature (NCBI; currently under development) as described in section 2.1.2.

The top five ‘hits’ (in addition to the original reference sequence) identified are indicated in Table 4-1 (a list of additional hits from the SmartBLAST analysis are summarised in chapter 8, section 8.3, Table 8-4). TbAUK2 is conserved across the kinetoplastid phylum. One of the top hits beyond the kinetoplastids was *H. sapiens* AUKA (NP_003591.2; E-value = $6e^{-53}$), suggesting TbAUK2 may be homologous to this AUK. In support of this, TbAUK2 also showed highest levels of sequence homology to aurora A kinases in other eukaryotes, for example to AUKA (36%) in the *Mus musculus* ($5e^{-52}$; NP_001278114.1) and Aurora A (36%) in the *D. melanogaster* ($1e^{-51}$; NP476749.1). In contrast, homology to AUKB and AUKC homologues was slightly lower.

Name of protein	Species	Query Cover (%)	E Value	Identity (%)	Accession Number
Serine/threonine-protein kinase	<i>Trypanosoma brucei brucei</i> TREU 927	100	0.0	100	XP_843984.1
Protein kinase, putative	<i>Trypanosoma brucei gambiense</i> DAL972	100	0.0	99	XP_011772377.1
Putative serine/threonine-protein kinase	<i>Trypanosoma congolense</i> IL3000	99	$1e^{-154}$	62	CCC89821.1
Putative serine/threonine-protein kinase	<i>Trypanosoma vivax</i> Y486	95	$2e^{-135}$	58	CCC47144.1
Serine/threonine-protein kinase, putative	<i>Leishmania donovani</i>	80	$2e^{-89}$	49	XP_003862559.1
Aurora kinase A	<i>Homo sapiens</i>	76	$6e^{-53}$	37	NP_003591.2

Table 4-1: Top five SmartBLAST ‘hits’ for TbAUK2 in the NCBI database (<http://www.ncbi.nlm.nih.gov/>). All data was recovered in June 2016.

4.4.1.2 TbAUK2 harbours kinase specific motifs

Protein kinases have several sequence motifs required to facilitate their kinase activity (as discussed in section 1.5). To ask if TbAUK2 harbours these conserved motifs, the TbAUK2 protein sequence was aligned against a human kinase (c-Src) using the Kinase Sequence Database (<http://sequoia.ucsf.edu/ksd/>) and against human AUKA (as an example of a typical aurora kinase). The resulting alignment was viewed using CLC genomic Workbench 7 (chapter 8, section 8.3, Figure 8-8). TbAUK2 contains most typical features of a protein kinase, though the GxGxxG motif lacks the final ‘G’ (G170; replaced with an S). Such non-canonical GxGxxG motifs have been reported in several other kinases, such as human TLK1 and TLK2 (Silljé et al. 1999) and in the MAP Kinase (LF4) in *Chlamydomonas reinhardtii* (Berman, Wilson, Haas 2003). Since all such proteins have kinase activity, the motif divergence does not necessarily infer compromised kinase

function in TbAUK2. The activation loop of all three *T. brucei* AUKs was predominantly conserved (chapter 8, section 8.3, Figure 8-8 and Figure 4-4), though in the case of TbAUK2, a conserved motif associated with aurora kinases is lacking.

AUKs in other eukaryotes harbour specific conserved sequence motifs required for regulation of their activity (Fu et al. 2007; Lindon et al. 2016). To look for these conserved motifs in all *T. brucei* AUKs, their protein sequences were retrieved from TriTrypDB (v.28; TbAUK1 [Tb927.11.8220], TbAUK2 [Tb927.3.3920] and TbAUK3 [Tb927.9.1670]) and compared with the protein sequences for each human AUK (retrieved from the NCBI database; AUKA [NP_003591.2], AUKB [NP_001300879.1] and AUKC [NP_003151.2]). The aligned sequences were examined in CLC genomics Workbench 7 and a summary of the motifs that were sought and their conservation is provided in Figure 4-4.

The 'DAD-box' is a type of 'A-box' motif required to control AUKA degradation during late M-G1 (Castro et al. 2002). Degradation of AUKA additionally requires a C-terminally located 'D-box', without an associated 'KEN' motif (Crane et al. 2004). In contrast, AUKB requires both a KEN motif and an A-box in order to be degraded during M-G1 (though the timing of this differs from AUKA; (Stewart & Fang 2005; Lindon et al. 2016). The requirements and pathways to degrade AUKC are as yet unpublished. All AUKs of *T. brucei* were missing several of these motifs. No KEN motif could be detected, and nor could a DAD-box or A box be identified, in any TbAUK. Only a D-box motif could be identified, and in each TbAUK. However, the mode of action of this motif for regulating AUK expression usually requires an additional N-terminal motif (the A-box or DAD box motif; Lindon et al., 2016), which is a feature the *T. brucei* aurora kinases lack (discussed below).

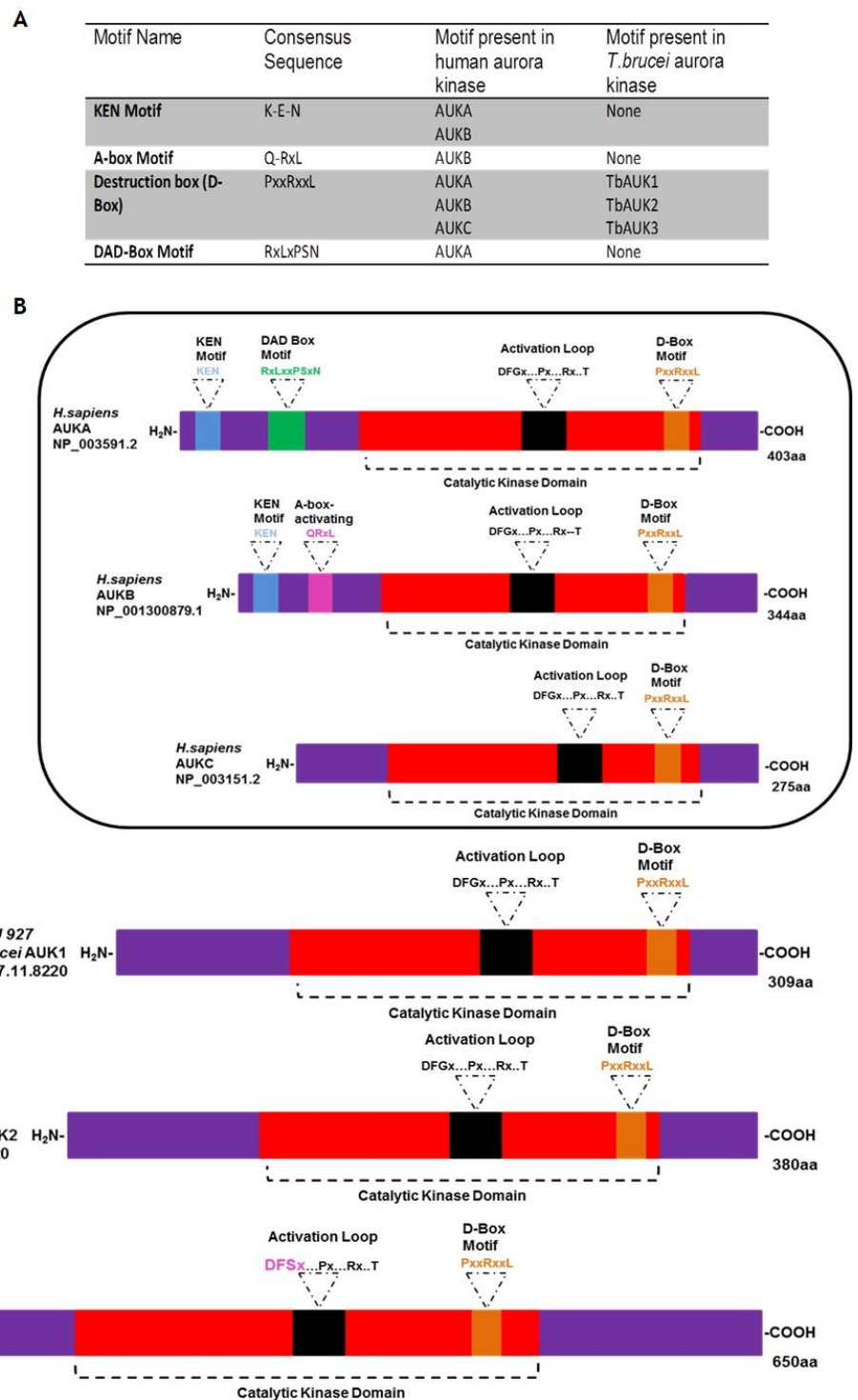


Figure 4-4: *T. brucei* aurora kinases lack sequence motifs typical of eukaryotic AUKs
(A) The conserved regulatory motifs of aurora kinases in *H. sapiens*, their consensus sequence and in which aurora kinase the motif is present, and their likely conservation in *T. brucei* AUKs. **(B)** An illustration of the approximate location of sequence motifs identified in human (Black box) and trypanosomatid AUKs (below), and their position relative to the conserved kinase domain (red box). Not to scale.

4.4.1.3 The *T. brucei* Aurora Kinases

TbAUK2 has ~31% sequence identity to TbAUK1 (E-value = $4e^{-38}$) and ~32% to TbAUK3 (E-value = $2e^{-33}$). From the simplified alignment in Figure 4-5 (a detailed

alignment is available in chapter 8, section 8.3, Figure 8-9), the three *T. brucei* AUKs show a similar pattern of conservation to the human AUKs, with notable homology across most of the length. However, TbAUK3 appears to have an extended C-terminal region with little to no homology to the other *T. brucei* AUKs, consistent with this protein being the largest (with a predicted size of ~72.3 kDa; TbAUK1 is ~35.5 kDa). The potential function of the C-terminal extension in TbAUK3, which is not seen in any of human AUKs, is unknown.

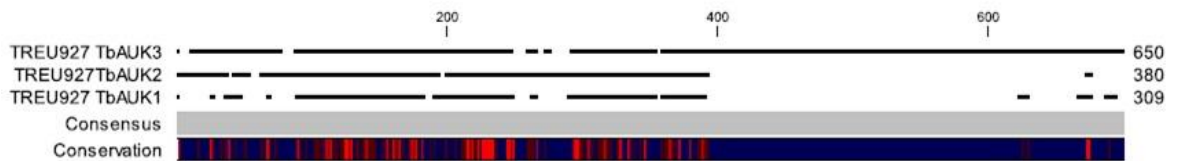


Figure 4-5: A simplified alignment of the three *T. brucei* aurora kinases
The amino acid sequences for each kinase (retrieved from TriTrypDB.org, V 28) were aligned in CLC Genomics Workbench 7. The solid black lines represent regions of alignment. The lower bar shows the level of sequence conservation in that particular region. Conservation is illustrated as a gradient; the brightest red colour reflects 100% conservation and the blue colour represents 0% conservation.

4.5 Generation of TbAUK2 null mutant cell lines

Aurora kinases in other organisms are required for cell viability (Vader & Lens 2008). In contrast, RNAi of TbAUK2 suggests this gene is not required for survival under *in vitro* conditions. To test this, mutants lacking the TbAUK2 gene were generated. The constructs and strategy applied to generate knockout cell lines is detailed in chapter 2 section 2.4.1.2. Briefly, the majority of the ORF was replaced with antibiotic resistance cassettes by integration of knockout constructs by homologous recombination following transformation. Figure 4-6 illustrates the regions used for homology driven recombination of TbAUK2 knockout constructs after transformation.



Figure 4-6: Schematic illustration of homology regions required for TbAUK2 knockout
A region of the 5'UTR (including part of the Open Reading Frame (ORF) and a region of the 3'UTR (Untranslated Region, and including part of the ORF) were amplified by PCR (black arrows show primer positions in the genome). The primer numbers are highlighted in brackets beside the expected fragment sizes for the two PCR products; bp (base pairs). The

amplified regions were cloned into knockout vectors (as per section 2.2). Primer sequences are available in section 2.4.1.2. Not to scale.

4.5.1 Gene knockout strategy

Disruption of the TbAUK2 ORF (deleting 834 bp, from amino acids 75 to 353) was achieved sequentially through two rounds of transformation into wild type (WT) BSF *T. brucei* Lister 427 cells. WT cells were first transformed with the construct Δ AUK2::BSD to produce putative heterozygote cell lines (+/-). One validated clone (TbAUK2^{+/-}) was chosen for a second round of transformation with the construct Δ AUK2::NEO and neomycin clonal transformants selected (using G418). At this stage, the selective antibiotics were removed from the media due to the slowing of growth observed in the presence of G418 (data now shown).

4.5.2 Integration of knockout constructs and confirmation of knockout clones using PCR analysis

To confirm the generation of TbAUK2^{+/-} and TbAUK2^{-/-} cell lines, putative +/- and -/- clones were harvested and their gDNA extracted. PCR analysis was performed to confirm absence of the ORF and the correct integration of both knockout constructs. Figure 4-7 shows the PCR strategy and agarose gels of PCR on the clones examined. As the +/- cell line was generated by integration of the Δ AUK2::BSD construct, diagnostic PCR amplification was seen for this construct but not for the Δ AUK2::NEO construct, and PCR amplification of the TbAUK2 ORF was seen. No PCR amplification of the TbAUK2 ORF was detected in the putative -/- clones, whereas diagnostic PCR amplification of both integrated constructs was observed, suggesting the expected deletion of the TbAUK2 ORF had occurred. The white arrows indicate the two -/- clones chosen for further analysis (referred to as TbAUK2^{-/-} CL1 and TbAUK2^{-/-} CL2).

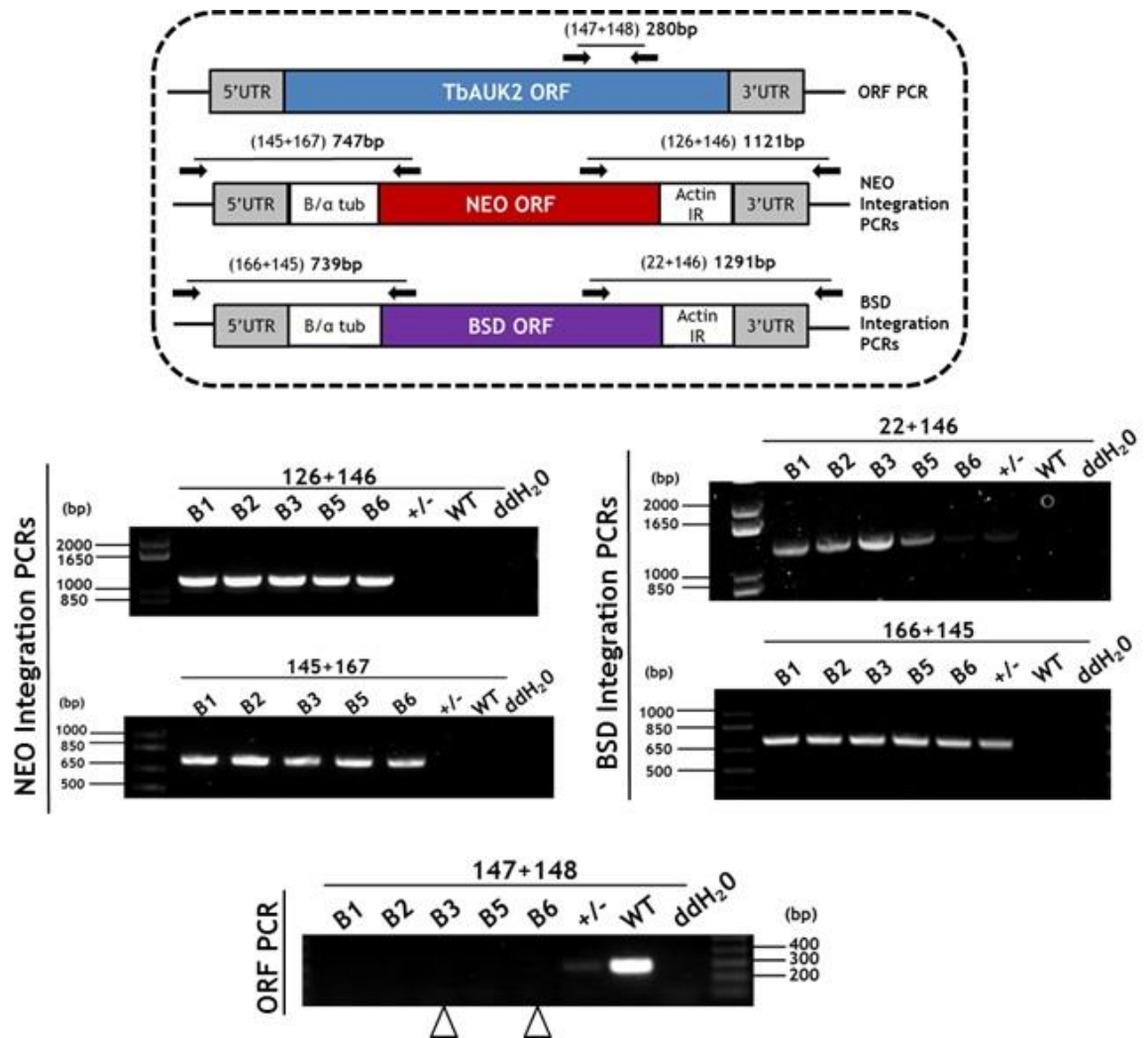


Figure 4-7: PCR analysis of putative TbAUK2 null mutant and heterozygote clones
 (Top) Schematic illustration of expected fragment sizes amplified by PCR (bp), diagnostic primers used (black arrows) and their position in the genome. Primer sequences are available in Table 2-3 section. Not to scale. (Below) Agarose gels of diagnostic integration PCRs, which were performed using the primer pairs detailed in A (testing for integration of NEO or BSD, or testing for the presence of intact ORF) using gDNA from five $-/-$ clones (B1-B3, B5 and B6), wild type (WT) cells, heterozygote $+/-$ cells, or using double distilled water (ddH₂O) as a negative control. All PCRs were performed on the same gDNA samples. NEO (Neomycin), BSD (Blasticidin), B/ α tub (Beta/Alpha Tubulin), Actin IR (Actin intergenic region), gDNA (genomic DNA). For each gel, size markers are shown (bp). White arrows indicated clones used for further analysis (B3 referred to as CL1 and B6 referred to as CL2 in the remainder of this chapter).

4.5.3 Confirmation of knockout clones using qRT-PCR analysis

To test for loss of TbAUK2 expression in both knockout clones, qRT-PCR and PCR analyses were performed on cDNA prepared as described in chapter 2 section 2.5. Relative to the WT cells (where the level of RNA was arbitrarily set to 100 %; Figure 4-8), the TbAUK2 $^{+/-}$ cell line had ~50 % less RNA transcript, whereas in both knockout clones, no RNA transcript could be detected. To test this further, end-point RT-PCR was used to attempt to PCR amplify a region of the ORF (~280

bp) (Figure 4-8, right panel). This region of the ORF failed to PCR amplify from cDNA from either knockout clone, but PCR amplified from both WT and TbAUK2^{+/-} cells. To confirm the presence of cDNA, a control PCR (which amplified a region of the Tb927.9.6560 gene) was performed and PCR amplification occurred in the knockout cDNAs. PCR from samples treated in the same way but lacking RT enzyme showed the PCR products were derived from cDNA and not gDNA.

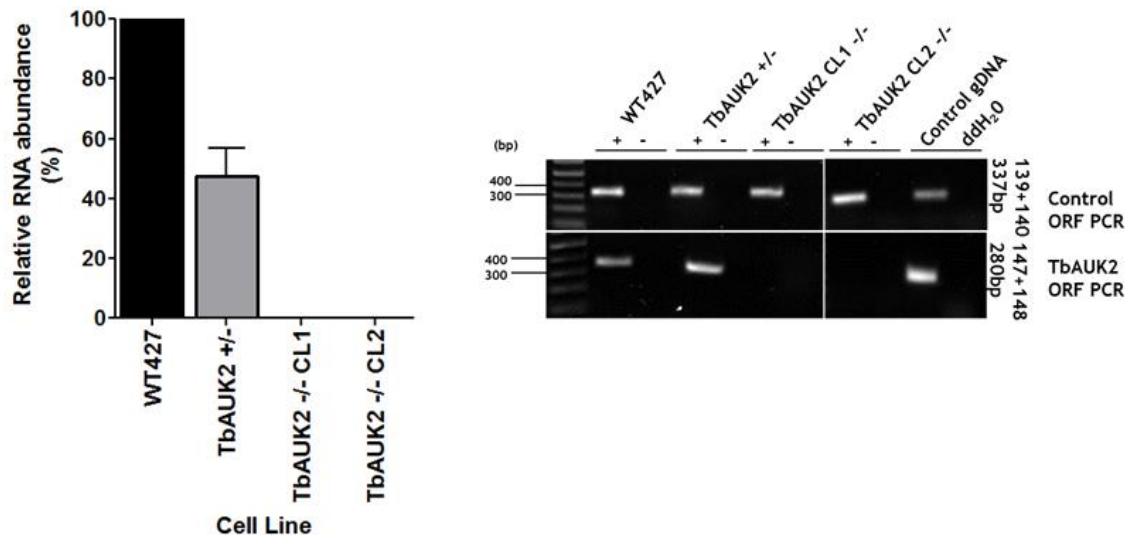


Figure 4-8: Confirmation of AUK2 knockout clones by qRT-PCR and RT-PCR analysis
RNA from each cell line was prepared from which cDNA was generated. qRT-PCR (results shown on the left graph) was performed to examine expression level of TbAUK2 in WT, heterozygote (+/-) and knockout (-/-) cell lines using primers AUK2RTFW2 and AUK2RTRV1 (Table 2-5 detailed in section 2.5.3.1. Expression of TbAUK2 in the WT was arbitrarily set to 100% expression. The agarose gel image on the right shows end-point RT-PCR performed on the same cDNA. An RT- (-) control was included to control for gDNA contamination. A control PCR was performed to confirm validity of the cDNA (top image). The primers used are detailed beside the gel image, including the expected fragment size. White space between images represents images from different sections of the gel aligned. Sizes shown (kb plus ladder, bp). cDNA (complementary DNA), qRT-PCR (quantitative real time PCR), rt - (reverse transcriptase negative), n=2 (except for TbAUK2^{-/-} CL1, n = 1).

4.5.4 Phenotypic analysis of TbAUK2^{-/-} knockout mutant

4.5.4.1 Growth analysis and cell cycle analysis by DAPI *in vitro*

To ask whether loss of TbAUK2 was detrimental to cell survival, growth of both TbAUK2^{-/-} clones (CL1 and CL2) was assessed relative to WT and TbAUK2^{+/-} cells. Growth curves were performed as per section 2.8.1 and are shown in Figure 4-9 A. No antibiotics were added to the media to ensure any effect on growth could not simply be attributed to the presence of a selective drug.

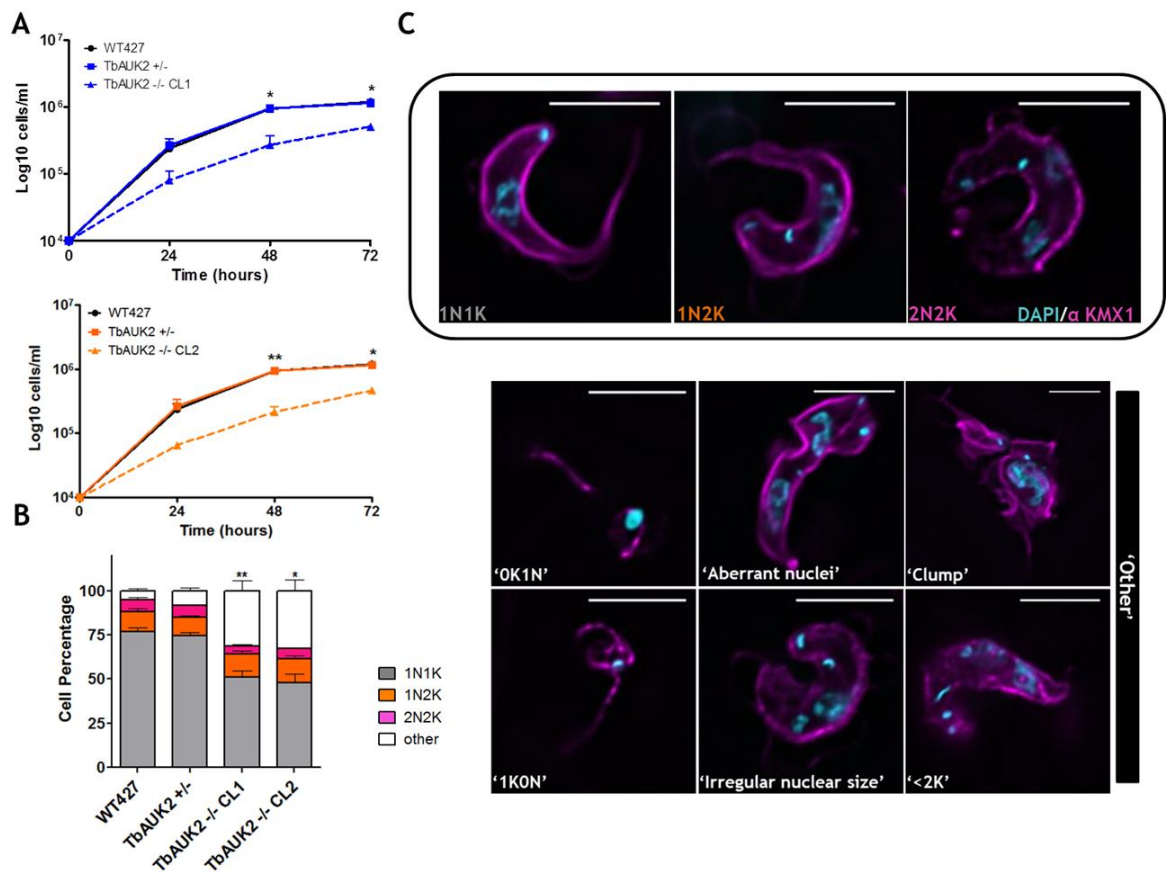


Figure 4-9: Growth and cell cycle analysis of TbAUK2 knockout clones

(A) Growth of TbAUK2 knockout clones (CL1 shown by a dashed blue line [top graph]; CL2 shown by a dashed orange line [bottom graph]) was assessed by counting every 24 hours for 72 hours and plotted on a logarithmic scale alongside the growth of WT (solid black line) and TbAUK2 +/- cells (solid blue line [top graph] or solid orange line [bottom graph]). Error bars indicate \pm SEM (n=3). (*) = $p < 0.05$, (**) = $p < 0.005$. Significance was assessed using a Mann Whitney U test (B) Cell cycle analysis. Cells were fixed and stained with DAPI, each cell type counted and plotted as a percentage of the total number of cells (n = >200 cells/experiment; n=3). Error bars represent \pm SEM. Aberrant cells were classified as 'other' based on DAPI content alone. (*) = $p < 0.05$, (**) = $p < 0.005$, WT cells at each time point compared with the TbAUK2 -/- clone; Mann Whitney U test. (C) Representative images of cells from the TbAUK2 -/- CL1 cell line. Cells were fixed and stained with DAPI (see section 2.11.1 and 2.11.2; cyan) and α -KMX1 antiserum (to detect tubulin; magenta). Highlighted in the box are cells conforming to the normal 1N1K, 1N2K or 2N2K categories. Below are cells representative of the range of 'others' observed. Images captured on a DeltaVision microscope, de-convolved and processed as per section 2.11.8. Scale bar = 5 μ m.

The TbAUK2^{+/-} cell line showed no significant effect on growth when compared with WT cells. However, in contrast to the results of the TbAUK2 RNAi knockdown (chapter 3), both TbAUK2^{-/-} clones showed a significant reduction ($p < 0.05$) in growth relative to WT. In the time frame of these experiments the -/- cells did not reach the same maximal density seen for WT cells, and the slope of the growth curves indicated increased population doubling times (with an approximate doubling time of 10 - 11 hrs for both clones compared to 7 - 8 hrs

for the parental WT427 cell line; see section 2.7.4 for the mathematical formula).

Loss of aurora kinases is also associated with cell cycle arrest in other organisms (Vader & Lens 2008). To ask whether the above growth impairment may be explained by an altered cell cycle in the $-/-$ mutants, cells were prepared for indirect IF (as described in section 2.11.1 and 2.11.2) and stained with DAPI (to visualise the nDNA and the kDNA) and α -KMX1 antiserum (to visualise tubulin and thus the cell body). The cell cycle stage of individual cells in the population was assessed as described in chapter 3 section 3.3.5, and the data is represented in Figure 4-9 B. Any cell that did not conform to normal cell cycle stages with 1n1k, 1N2K or 2N2K DNA content, as detected by DAPI, (section 2.11.1) were classified as 'other'. No significant change in the proportion of the population that were either 1N2K or 2N2K cells was observed, suggesting progression into S phase and through mitosis was unchanged. However, a pronounced loss of 1N1K cells was observed that correlated with a significant increase in the number of cells with aberrant DNA content. Approximately 30 % of the cells (consistent in both clones) had aberrant nDNA and kDNA ratios, such as 0N1K or 1N0K. In addition, cells with observably aberrant nDNA staining were seen, perhaps suggesting abnormal division of the nucleus. Several nDNA aberrancies manifested: nuclear 'blebs' (see below), one nuclei appearing smaller than the other (in 2N2K cells), cells with enlarged, misshapen nuclei, or cells with faintly stained, small nuclei. In addition, cell 'clumps' could be observed (discussed in section 4.10.2; see Figure 4-C for examples of aberrant cell types), where it was difficult to discern nDNA and kDNA content. Taken together, the diverse, predominantly nuclear-focused phenotypes of the aberrant cells appear to indicate important, potentially widespread nuclear functions for TbAUK1. As the mutants appear unperturbed during progress from G1-S-G2 (based on the DAPI cell cycle data), the phenotypes indicate mitotic deficiency. Furthermore, the presence of cells with aberrant DNA suggests cytokinesis can occur even with inaccurate genome segregation, suggesting the absence of a G2/M or M/cytokinesis checkpoint. However, the identification of cell clumps may suggest activation of a checkpoint at cytokinesis in some circumstances.

Based on the above analysis, the role of TbAUK2 appears to overlap (at least in part) with the functions of TbAUK1. For example, RNAi of TbAUK1 in BSF cells predominantly results in multinucleated and multi kinetoplast cells (Li & Wang 2006); these cells can be observed in the absence of TbAUK2, though multi-kinetoplast cells were not predominant. However, as TbAUK2^{-/-} mutants are viable, TbAUK2 may be subservient to TbAUK1 or required for different purposes during the cell cycle. In this regard, why a small population of ^{-/-} cells display abnormalities is unclear.

4.5.4.2 Analysis of the nucleus by DAPI counting and Electron microscopy

Loss of TbAUK2 results in ~30 % of the total cell population having aberrant nuclear content. Two different methods of imaging were performed to investigate this observation further. First, transmission electron microscopy (TEM) was performed to examine the nuclear ultrastructure of WT, TbAUK2^{+/-} and TbAUK2^{-/-} cells (CL2 was used for this analysis). The samples were harvested and fixed as described in section 2.11.7.2. Figure 4-10 depicts representative images from this analysis (additional images are available in chapter 8, section 8.3, Figure 8-10, including cells whose structure was difficult to interpret: 'unclear phenotype') and the results of this comparison are summarised in Table 4-2.

Phenotypic Feature	Cell Line (No. cells examined)		
	WT 427 (18)	TbAUK2 ^{+/-} (11)	TbAUK2 ^{-/-} (31)
No observable nuclear defect	16	8	15
Phenotype Unclear	0	2	2
Cells with aberrant nuclei	2	0	6
Cells with nuclear 'blebs'	0	1	8

Table 4-2: TEM imaging of cells lacking TbAUK2 reveals nuclear defects
Nuclei of cells imaged by TEM were examined and categorised depending upon the extent of the nuclear defect, n=1.

The majority of the WT cells (~89 %) had no observable nuclear defect except in the case of two cells; one cell had large electron dense vesicles in its nucleus and the other presented an unusual arrangement of membranes within the nucleus. In the TbAUK2^{-/-} cell line, ~48 % of the cells had no observable nuclear defect, meaning 52 % were aberrant. ~6 % of these cells (2) could not be classified, due to extensive morphological divergence from the WT cells; indeed,

no clear nucleus could be observed in one of these cells. Approximately 19% of the cells had observable nuclear defects, including intra-nuclear membranes, the presence of electron dense vesicles in the nucleus and, potentially, cells with nuclei of differing sizes. In ~27 % of cells nuclear 'blebbing' could be seen (see below for further analysis).

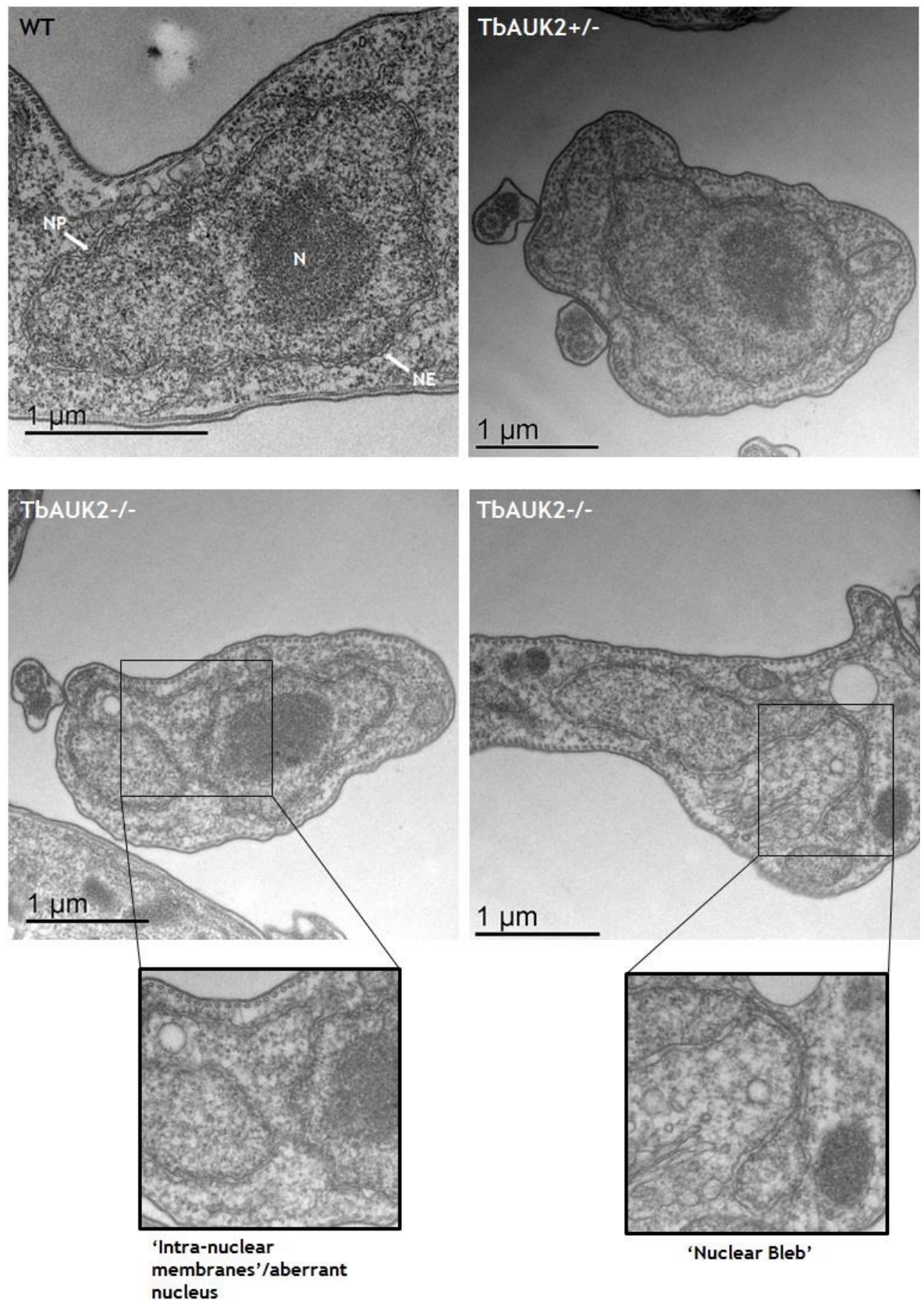


Figure 4-10: Representative examples of nuclei imaged by TEM from TbAUK2 ^{-/-} cells
 Representative example of nuclei from WT (top left), TbAUK2^{+/-} (top right) and TbAUK2 ^{-/-} CL2 cells (lower two images). Highlighted in the black boxes are close up images of a nucleus with an unusual arrangement of nuclear membranes (lower left), or with a nuclear 'bleb' (lower right). Scale bar sizes are indicated on each image. Further processing and imaging of the samples was kindly conducted by L.Lemgruber Soares.

A higher percentage of aberrant nuclei were imaged by TEM in the knockout cells than were detected in the cell cycle analysis. This could potentially be attributed to two factors. Firstly, a smaller data set was available for the EM analysis; over 200 cells were imaged for the cell cycle analysis, in contrast to 31 imaged by TEM. Secondly, DAPI staining might not reveal the presence of all defects within the nucleus, such as nuclear membrane defects

To examine further the proposed nuclear blebbing in the $-/-$ mutants, since this was potentially a predominant phenotype, high resolution images of the nuclei from WT, TbAUK2 $^{+/-}$ and both TbAUK2 $^{-/-}$ clones were captured on a DeltaVision microscope. To quantify the extent to which blebs form in the cells, over 200 images were examined in each case. Here, only cells with discernible nuclear blebs were considered: cells with aberrant nuclei but no apparent nuclear blebs were placed in the 'no-bleb' category, which also included cells with apparently normal nuclei. These data are graphed in Figure 4-11, which also provides a representative image of a nuclear bleb (Figure 4-11 below the graph).

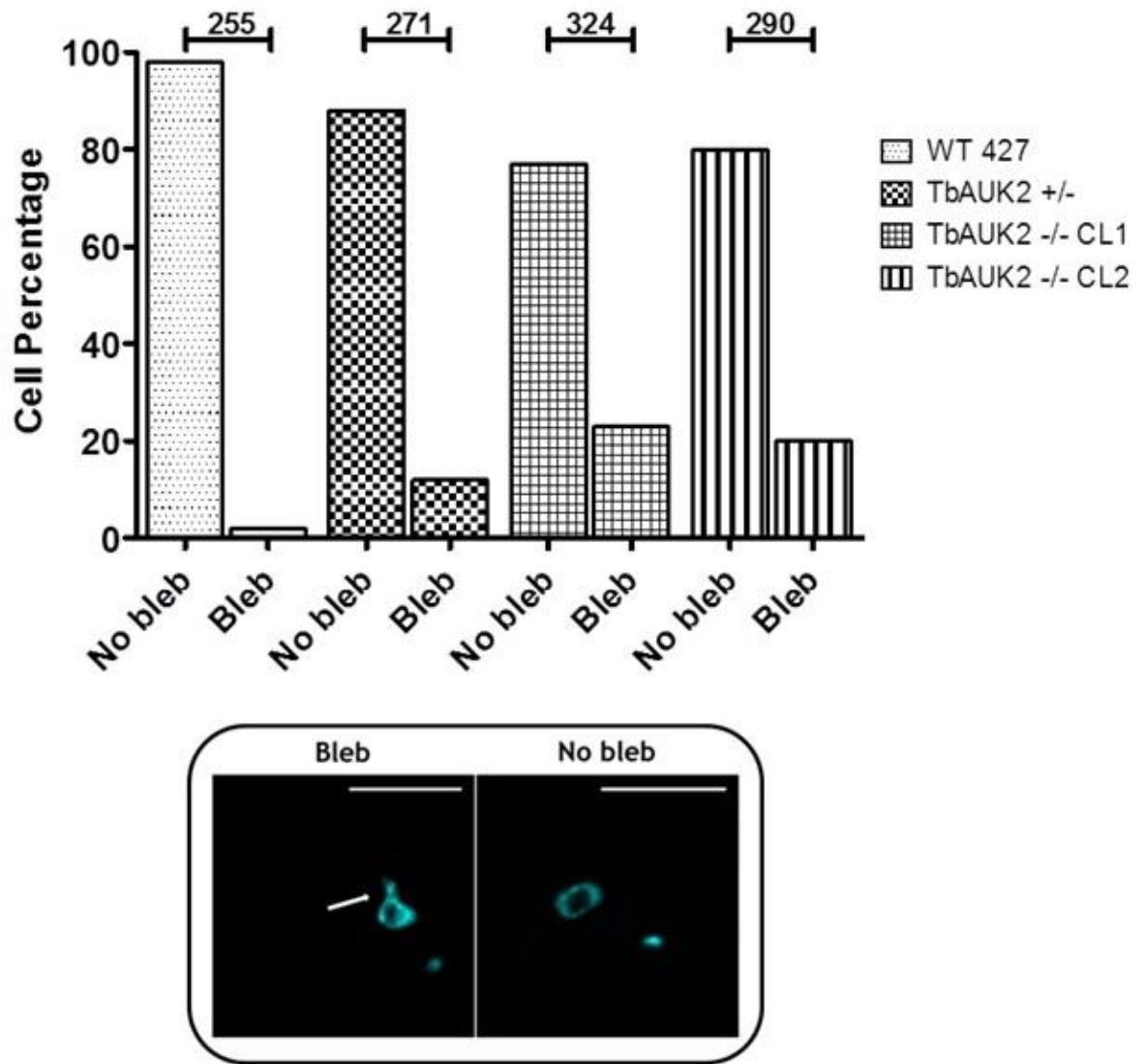


Figure 4-11: Loss of TbAUK2 is associated with nuclear ‘blebbing’
 Over 250 cells were imaged and examined for the presence of nuclear ‘blebs’. Cells were scored either as ‘bleb’ or as having ‘no bleb’. Each category is expressed as a percentage of the total cell count (n=1). Outlined in the black box are representative examples of the two cell categories (DAPI; cyan). Images were captured on a DeltaVision microscope, deconvolved and processed as per section 2.11.8. Scale bar = 5 μ m.

Cells with nuclear blebs were rare in the WT cells, amounting to only ~2 % of those examined. Cells with nuclear blebs were around 10-fold more common in the TbAUK2 ^{-/-} cells, accounting for 20-23 % of the population. Intriguingly, ~12 % of TbAUK2 ^{+/-} cells appeared to have nuclear blebs, indicating loss of one allele may be detrimental. These data appear consistent with the TEM data, though whether the blebs indicate simply loss of nuclear membrane integrity or reflect underlying changes in chromosome content is unclear.

4.5.4.3 Loss of TbAUK2 is associated with loss of mitotic spindle formation

Mammalian AUKA and AUKB are implicated in formation of the mitotic spindle (Asteriti et al. 2015; Mountzios et al. 2008). To ask if the phenotypes above may derive from altered mitotic spindles in TbAUK2^{-/-} cell lines, indirect IF analysis was performed as per section 2.11.2. WT, TbAUK2^{+/-} and both TbAUK2^{-/-} clones were stained with DAPI (to visualise the nDNA and kDNA) and α KMX-1 (to visualise the spindle). Images were captured on a DeltaVision microscope and the number of 1N2K cells with/without a spindle were counted and expressed as a percentage of the total population. This data is represented in the graph below (Figure 4-12 A). Representative images of a mitotic spindle (in WT cells) and of a TbAUK2^{-/-} CL1 cell lacking a detectable mitotic spindle (despite elongation of the nucleus) are shown in the black box (Figure 4-12 B).

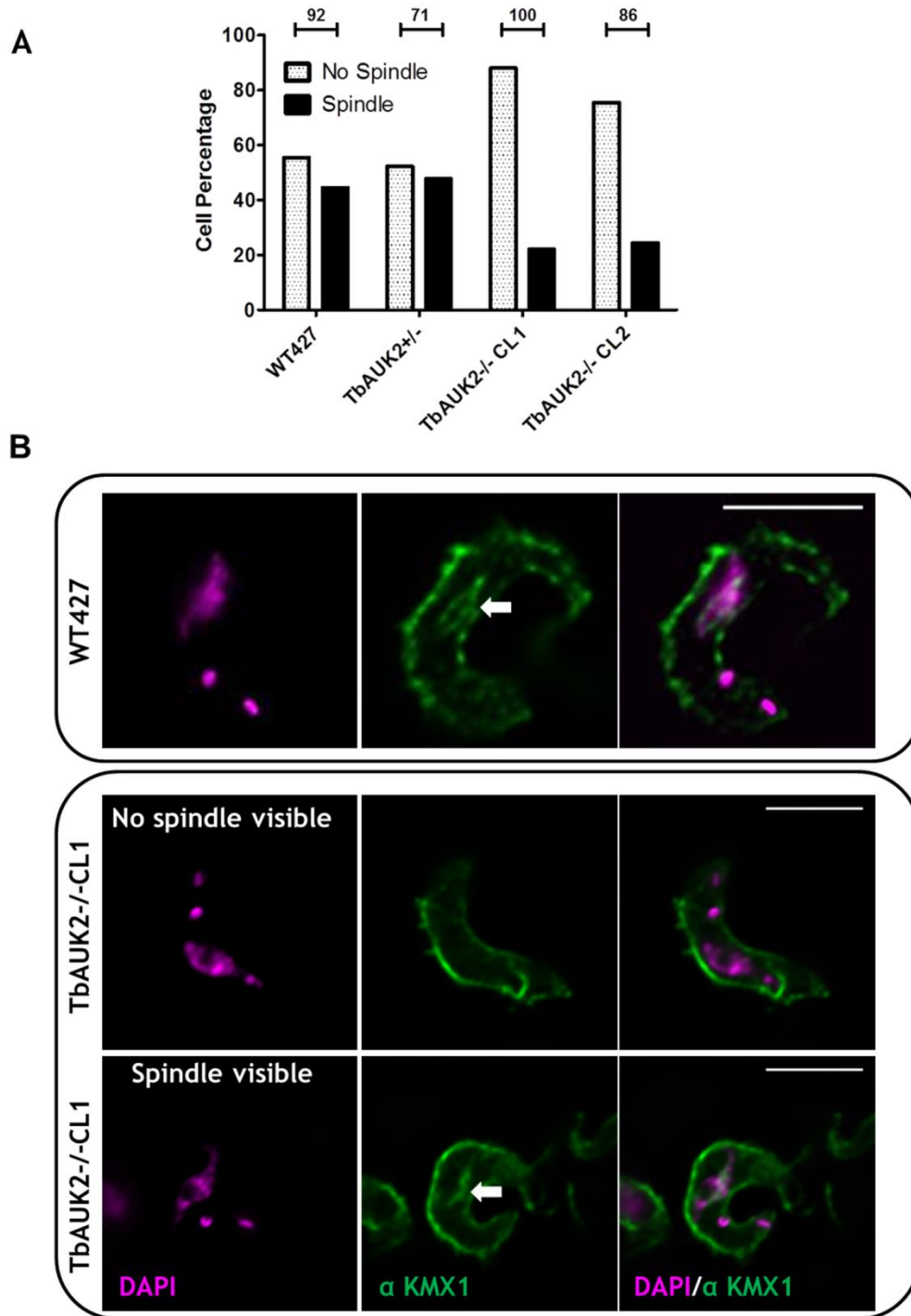


Figure 4-12: Loss of TbAUK2 is associated with loss of the mitotic spindle
(A) Analysis of the mitotic spindle of 1N2K cells in WT, TbAUK2^{+/-} and TbAUK2^{-/-} cells. Images of 1N2K cells were captured as per section 2.11.2 and 2.11.8 and categorised depending upon the presence (spindle) or absence of (no spindle) of a mitotic spindle by staining with α KMX-1 antiserum. The counts were represented as a percentage of the total cells examined (n=1). The number of cells counted per cell line is indicated above the corresponding bars. **(B)** Representative images of a WT cell with an intact mitotic spindle (indicated by the white arrow) and a TbAUK2^{-/-} cells without a detectable spindle (upper panel) and with a detectable spindle (lower panel; indicated by a white arrow). The nDNA and kDNA were visualised by DAPI (magenta) and the mitotic spindle using α KMX-1 antibody (green). Scale bar = 5 μ m. Images captured on a DeltaVision microscope, deconvolved and processed as per section 2.11.8.

In previous work, approximately 50% of 1N2K WT cells have a clear oval-shaped nuclear spindle (Tu et al. 2006), which is comparable with ~44% of WT 1N2K cells in this experiment. The relative number of cells with and without detectable spindles appeared unchanged in the TbAUK2^{+/-} cell line. However, in both TbAUK2^{-/-} clones only ~20-25% of 1N2K cells had an observable mitotic spindle, with the majority of cells not staining for this structure. The ~50% reduction in -/- cells with a spindle relative to WT and TbAUK2^{+/-} cells is in keeping with a potential role for TbAUK2 during nDNA mitosis, and may account for the appearance of aberrant nuclei; lack of a mitotic spindle may result in miss-division of the chromosomes during mitosis.

4.5.4.4 Morphological analysis of the TbAUK2^{-/-} knockout mutants

In cell lines lacking aurora kinases, cell morphology routinely becomes distorted (Huck et al. 2010; Tao et al. 2008; King 2008; Ritchey & Chakrabarti 2014). Here, a proportion of the TbAUK2^{-/-} cells appeared to have lost typical trypanomastigote morphology, manifesting as either rounded cells (akin to those described for TbAUK1 (Li & Wang, 2006), multinucleated clumps, or cells which did not present with a specific classifiable morphology ('aberrant'). To examine this further, morphology of the knockout cells was compared with WT and TbAUK2^{+/-} cells, evaluating cells shape by DIC imaging. These data are graphed in Figures 4-13 A and B (original cell numbers available in the accompanying CD in the excel file labelled [Cellcountmasterspreadsheet.xls](#); this spreadsheet encompasses all the raw counts from each chapter).

Only approximately 4 % of WT cells could be classified as morphologically defective, a proportion that appeared to increase to ~8 % of the TbAUK2^{+/-} cells. Strikingly, in both knockout clones ~33-39 % of the population was morphologically defective, a similar proportion to those observed with aberrant DNA content (see above; Figure 4-13 A). To further understand these morphological defects, the aberrant cells in each cell line were further classified into three categories ('rounded', 'multinucleated clumps' and 'aberrant'), depending on their visual appearance (Figure 4-13 B). Figure 4-13 C depicts a representative field of view image from TbAUK2^{-/-} CL2 and, below, a representative image for each category. The predominant morphological defect present in WT cells were those with an unclassifiable morphology ('aberrant',

~85 %). These cells also predominated the morphologically defective TbAUK2^{+/-} cells. In the knockout cell lines again a further significant increase in cells with a 'rounded' morphology were observed (~35-36 %), though the predominant morphological defect remained aberrant cells.

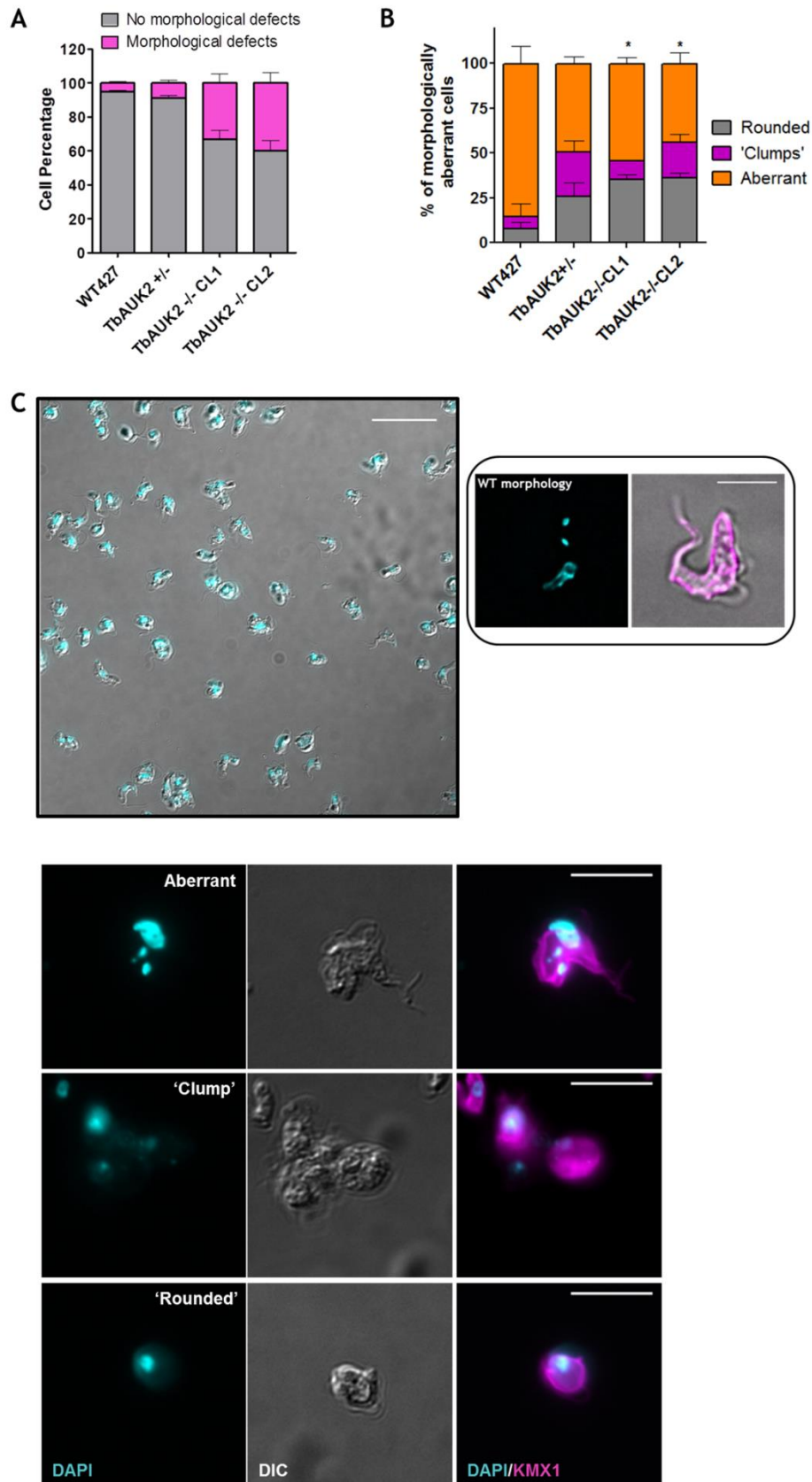


Figure 4-13: Loss of TbAUK2 is associated with aberrant cell morphology
(A) Cells were examined and any with morphology which did not conform to the trypomastigote shape were considered as having morphological defects (expressed as a percentage of the total cell counts; $n=3$). Over 200 cells/experiment were counted for this analysis. Error bars represent \pm SEM. Significance was assessed by a Mann Whitney U test
(B) Cells with morphological defects were further classified into three categories depending

upon their appearance; rounded, clumps or aberrant. Each category is shown as percentage of the total number of cells with morphological defects, as shown in (A). Over 200 cells/experiment were counted for this analysis (n=3). (** = $p < 0.005$; rounded cells from WT and the appropriate TbAUK2 $-/-$ clone were examined by a Mann Whitney U test. Error bars represent \pm SEM. (C) Representative field of view of DAPI (to visualise nDNA and kDNA; cyan) and α KMX-1 (to visualise β tubulin; magenta) stained cells from the TbAUK2 $-/-$ CL2 cell line. In the black box is a representative example of the typical trypanomastigote shape. Below are representative images from each aberrant morphology categories. Scale bar = 5 μ m. Images were captured on an Axioskop2 microscope (Zeiss) and processed in ImageJ (as per section 2.11.8).

From this analysis, loss of TbAUK2 affects cellular morphology at a level consistent with the percentage of DNA defects observed, perhaps suggesting that cells with aberrant nuclear DNA account for the cells with aberrant morphology. Why loss of TbAUK2 results in increased levels of notably rounded cells is unclear, but, in addition to loss of the mitotic spindle, TbAUK2 deficient cells might potentially lose other structural filaments, since aurora kinases have been linked to maintenance of cell structure via interactions with microtubules (Ritchey & Chakrabarti 2014).

4.6 Analysis of the sensitivity of the TbAUK2 $-/-$ knockout clones to DNA damaging

Loss of aurora kinases is associated with increased sensitivity to genotoxic agents (Wang, Liu, Jin, Fan, & Zhan, 2006). In human cells, downregulation of AUKA (by RNAi) sensitises the cells to genotoxic agents such as UV, cisplatin (Wang et al., 2006) and IR (Tao et al. 2007). RNAi knockdown of TbAUK2 sensitised BSF *T. brucei* cells to MMS (chapter 3). Here, we asked whether sensitivity to MMS, and wider DNA damage, is also seen in the knockout cell lines. Furthermore, the presence of known markers of DNA damage (γ H2A and RAD51) was examined.

4.6.1 Growth analysis under DNA damage stress

To determine whether loss of TbAUK2 sensitised the cells to a variety of DNA damage sources, the knockout cell lines were exposed to MMS, PHL, UV and HU in turn. Growth of the cells was measured and compared with WT and TbAUK2 $+/-$ cells. Growth curves were performed as described in section 2.8.2 and cultures were set up as described in section 2.8.2. The data for WT and $-/-$ mutants at single doses of damage are represented in Figure 14.4; data for the TbAUK2 $+/-$ cells is available in chapter 8, section 8.3, Figure 8-11.

Both knockout clones showed an increased sensitivity, relative to the WT, to all of the genotoxic agents, suggesting a wide range of damage impairs growth in the absence of TbAUK2; in contrast, no significant reduction in growth following exposure to any damage source was observed in the TbAUK2^{+/-} cells (chapter 8, section 8.3, Figure 8-11).

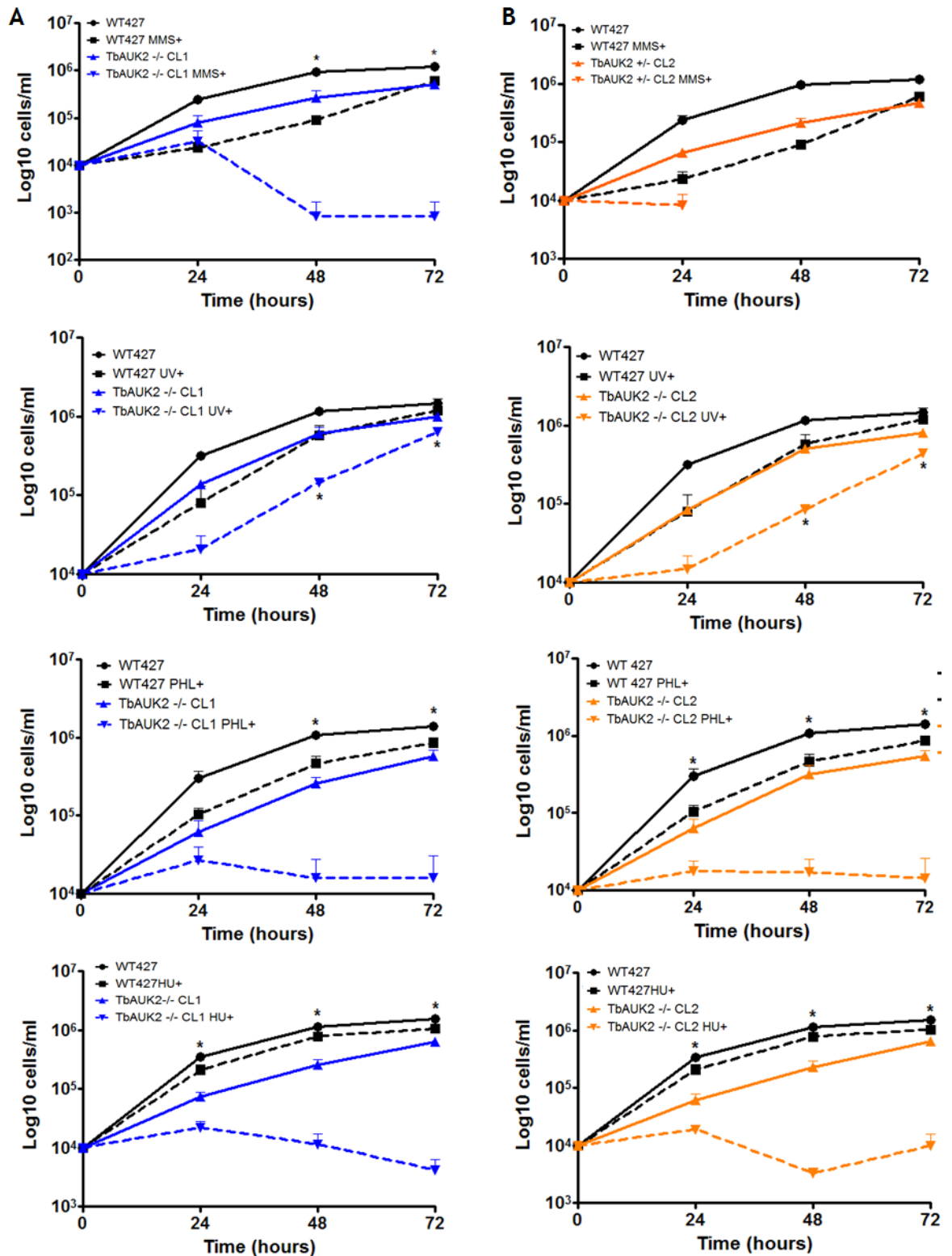


Figure 4-14: *In vitro* growth of TbAUK2 *-/-* cell lines following treatment with DNA damaging agents

(A) Growth analysis of TbAUK2 *-/-* CL1 under a variety of genotoxic stress sources. MMS (0.0003%), UV (1500 J/m²), PHL (0.1 ug/ml) and HU (0.06mM). The data is plotted on a logarithmic scale. The error bars represent \pm SEM. For statistical analysis, WT cells under genotoxic stress at the appropriate time point were compared with TbAUK2 *-/-* cells. (*) = $p < 0.05$, (**) = $p < 0.005$; Mann Whitney U test. (B) Growth analysis of TbAUK2 *-/-* CL2 under a variety of genotoxic stress sources. MMS (0.0003%), UV (1500 J/m²), PHL (0.1 ug/ml) and HU (0.06mM). The data is plotted on a logarithmic scale. The error bars represent \pm SEM. For

statistical analysis, WT cells under genotoxic stress at the appropriate time point were compared with TbAUK2 *-/-* cells. (*)= $p < 0.05$, (**) = $p < 0.005$; Mann Whitney U test.

4.6.2 Analysis of γ H2A expression by IFA and western blot analysis

Overexpression of AUKA in human cells may de-regulate the DDR by reducing the formation of γ H2AX foci in cells exposed to genotoxic agents (Sun et al. 2014). Conversely, blocking AUKA activity resulted in an increase in γ H2AX fluorescence (Moretti et al., 2011) whereas overexpressing AUKA under non-genotoxic conditions did not appear to alter γ H2AX foci formation (Sourisseau et al. 2010). Overall, AUKA appears to regulate γ H2AX expression in human cells. To ask whether the loss of TbAUK2 was associated with the accumulation, or conversely the loss of γ H2A, expression of this chromatin modification was examined by indirect IF (as described in section 2.11.2) and western blot analysis (as described in section 2.12.1). In all cases WT, TbAUK2 *+/-* and TbAUK2 *-/-* CL1 and CL2 whole cell extracts or slides were probed with α - γ H2A antiserum (kind gift; T.Donatelli Serafim) in the absence of exposure to DNA damage. From Figure 4-15 A and B an increase in the number of cells with detectable anti- γ H2A signal was seen in both knockout clones, and the cells with such signal were frequently morphologically aberrant. The α - γ H2A signal appeared mainly as diffuse signal throughout the nucleus, without clear nuclear foci, such as seen after induced damage (Glover and Horn, 2012). Indeed, occasionally such a signal was seen in WT cells. Western blot analysis confirmed the increased signal in the IF, with a notably more abundant putative γ H2A band of ~14.2 kDa in the *-/-* mutants. The fold change was calculated relative to the level in WT cells, revealing that expression of γ H2A was ~3 fold higher in CL1 and ~7 fold higher in CL2, with little evidence for accumulation of γ H2A in the *+/-* cells (Figure 4-15 C). Loss of TbAUK2 therefore appears to result increased nuclear DNA damage, or extended accumulation of unrepaired damage.

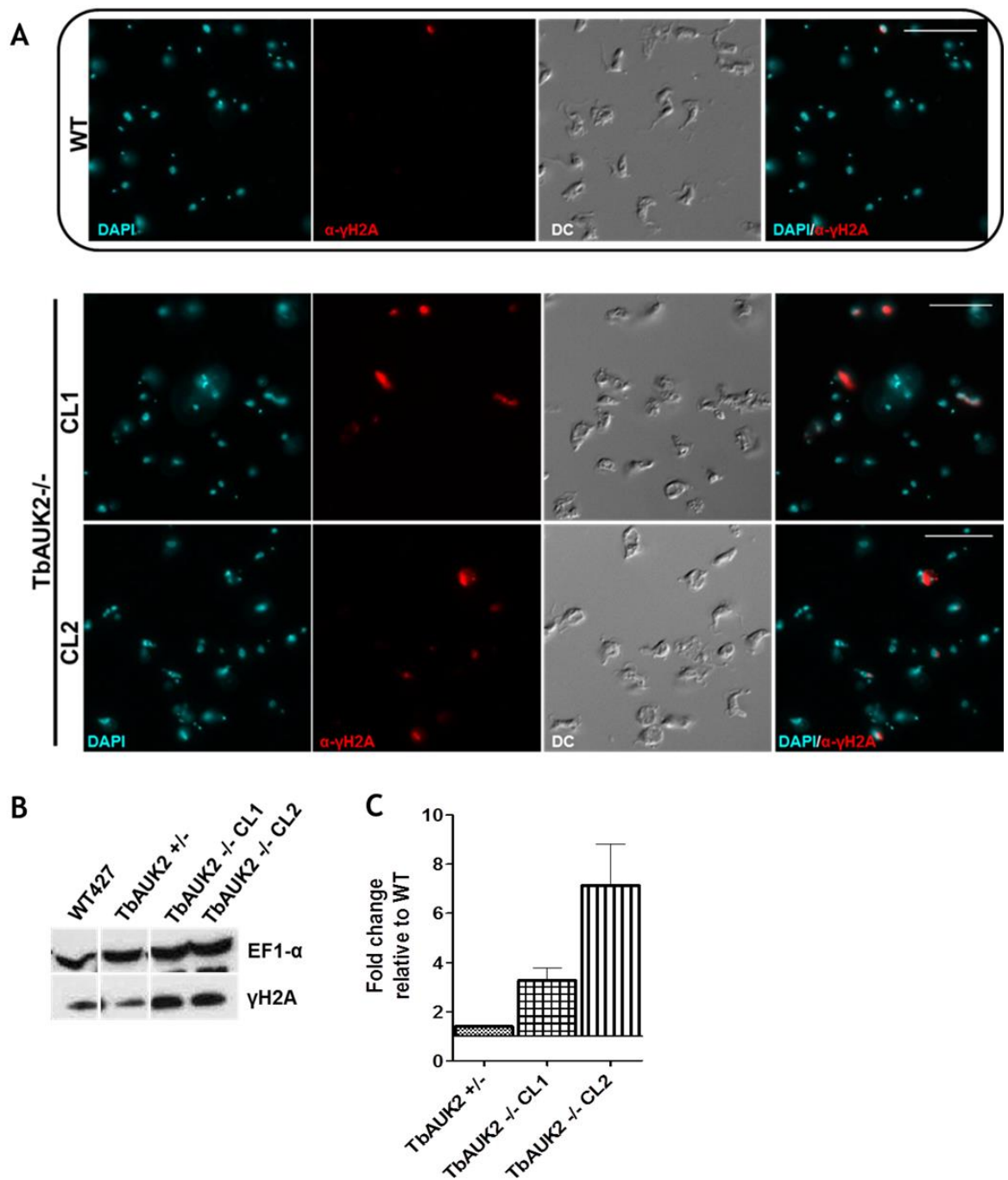


Figure 4-15: Loss of TbAUK2 is associated with increased γ H2A expression
(A) Representative field of view images from WT (black box) and TbAUK2^{-/-} (below) cells stained with DAPI (to visualise the nDNA and kDNA; cyan) and γ H2A (to visualise phosphorylated H2A; red). Scale bars = 10 μ m. Images captured on an Axioskop2 and processed in Image J as per section 2.12.5. **(B)** Representative western blot of whole cell extracts from WT, TbAUK2^{+/-} and TbAUK2^{-/-} cell lines. The membrane was probed with γ H2A antibody to detect phosphorylated H2A. EF1 α was used as a loading control. White space denotes images from different areas of the same blot re-aligned. **(C)** Quantification of western blot signal using ImageJ (as per section 2.11.8.3) and expressed as the fold change relative to WT cells. Error bars represent \pm SEM, n=2.

4.6.3 Analysis of RAD51 foci formation

To evaluate further the nature of the increased nuclear DNA damage in the TbAUK2^{-/-} cells, localisation of RAD51 was next examined. Overexpression of

AUKA in human cells blocks RAD51 recruitment in the presence of a DSB; a function that AUKA performs in addition to its role during the cell cycle (Sourisseau et al. 2010; Y. Wang et al. 2014; Katsha et al. 2015). To investigate RAD51 localisation in the absence of TbAUK2, indirect IF analysis was performed on WT cells, TbAUK2 +/- cells and both TbAUK2 -/- clones. In addition, WT cells were treated for 18 hrs with PHL to induce DNA damage, as a positive control for the formation of RAD51 subnuclear foci, as has been described previously (Devlin et al. 2016). The cells were probed with an anti-RAD51 antiserum, which predominantly produces a diffuse signal throughout the cell in the absence of induced damage (Figure 4-16 B). In only ~1% of WT cells could subnuclear RAD51 foci be observed, as scored by counting the number of cells in the population with one or more discrete, punctate spots in their nucleus (Figure 4-16 A). Treatment with PHL increased the number of WT cells with RAD51 foci to ~23% of the population, consistent with previous work (Dobson et al. 2011; Hartley & McCulloch 2008).

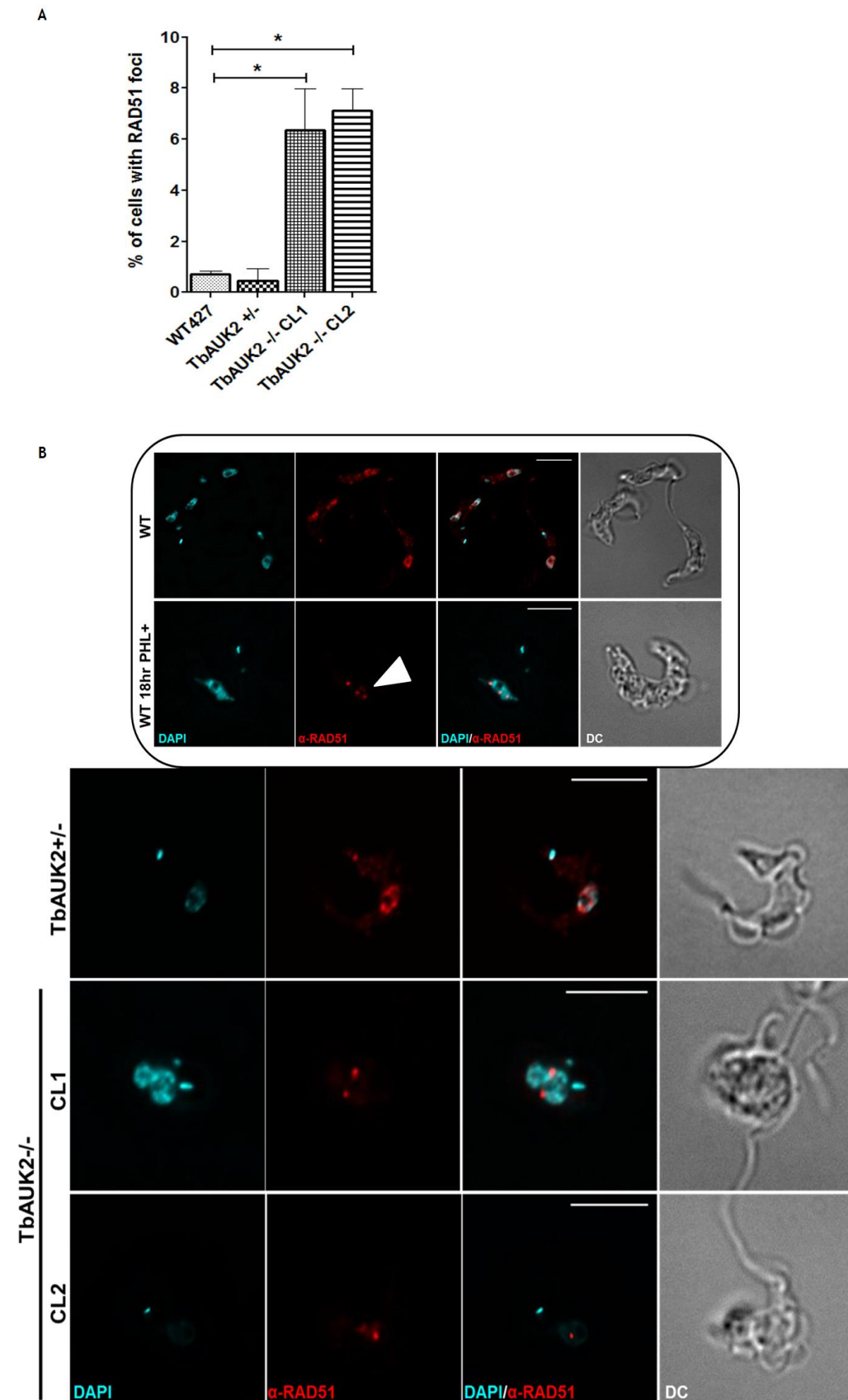


Figure 4-16: Loss of TbAUK2 is associated RAD51 foci formation

(A) RAD51 foci formation. Over 200 cells were counted for each cell line. The numbers of cells with RAD51 foci in their nuclei are shown expressed as a percentage of the total cell population. Error bars represent \pm SEM (n=3). (*) = $p < 0.05$, (**) = $p < 0.005$ (Mann Whitney U test). (B) Representative images of cells with RAD51 foci. Cells were fixed and probed with α RAD51 antiserum (red). nDNA and kDNA were visualised by DAPI (cyan). Images were

captured on a DeltaVision confocal microscope, de-convolved and processed in ImageJ as per section 2.11.8. Representative *-/-* cells lacking TbAUK2 are shown in the panel below the black box. In the black box are WT cells grown in the absence of PHL (top images) or the presence of PHL (lower set; control). Scale bar = 5 μ m. White arrow indicated RAD51 foci formation.

No change in the proportion of TbAUK2 *+/-* cells with RAD51 foci was observed. However, in the knockout cells, up to ~9% of the population had RAD51 foci, suggesting the absence of TbAUK2 results in pronounced accumulation of nuclear damage to which RAD51 localises. Notably, in some cases RAD51 foci were seen where clear nuclear DAPI staining was absent, suggesting these cells may harbour aberrant nuclei.

4.7 Localisation of TbAUK2

Aurora kinases in other organisms show dynamic patterns of localisation in the nucleus (section 4.1.1). To examine this in *T. brucei*, TbAUK2 was endogenously epitope tagged and the functionality of the tagged protein evaluated.

4.7.1 Generation of a TbAUK2^{+/-12myc} cell line

The construct Tb927.3.3920^{12myc} (generated as per section 2.4.1.1.1) was first transformed into WT cells. The knockout construct (Δ AUK2::NEO; section 2.4.1.2) was subsequently transformed into putative endogenously tagged cells. Both constructs were prepared for transformation as described (section 2.2.9). Putative heterozygote tagged clones were selected for described in section 2.7.4.

4.7.2 Confirmation of a TbAUK2^{+/-12myc} cell line

To confirm deletion of one allele and retention of the endogenously tagged allele, the putative TbAUK2^{+/-12myc} clones were analysed by, first, western blot analysis (as per section 2.12.1). As shown in Figure 4-17 B all clones still expressed a protein of ~56 kDa that is recognised by anti-myc antiserum. This size is consistent with myc-tagged TbAUK2 (14.4 kDa myc epitope + 42.1 kDa Tb927.3.3920). Secondly, integration of the Δ AUK2::NEO construct was undertaken by PCR analysis (as detailed in Figure 14-17 A). Five of the six transformants examined expressed putative myc-tagged TbAUK2 and had

correctly integrated the knockout construct (Figure 4-17 C). Two clones were chosen further analysis (TbAUK2^{+/-12myc} CL1 and TbAUK2^{+/-12myc} CL2).

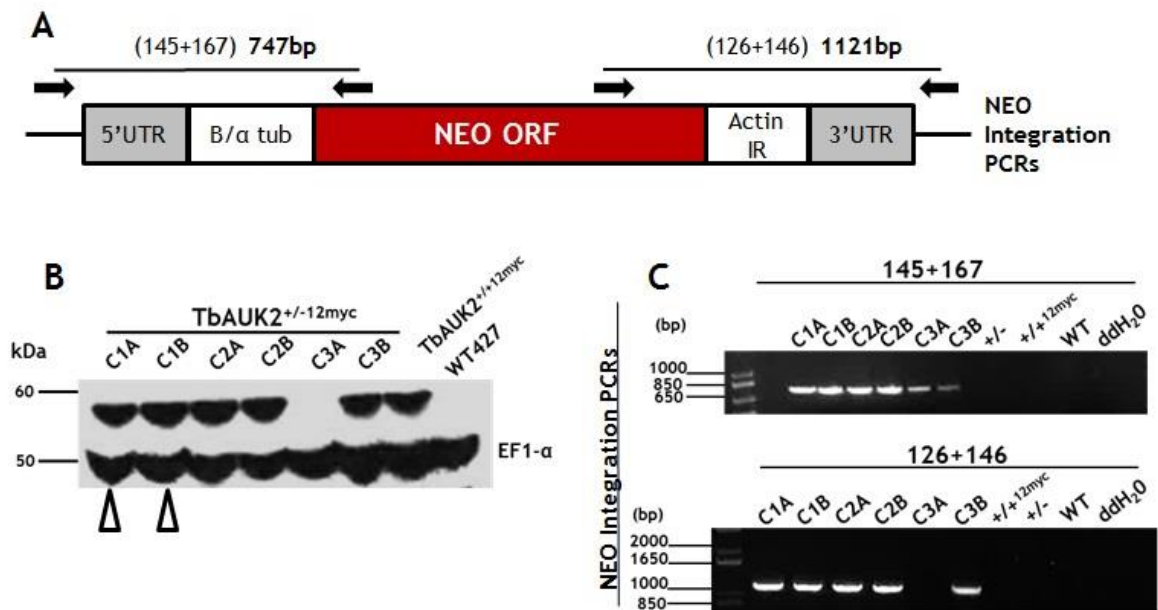


Figure 4-17: Confirmation of TbAUK2 heterozygote endogenously tagged cell lines
(A) Schematic illustration of the PCR analysis performed on putative heterozygote tagged clones. Primer position in the genome is indicated by a black arrow, primer number is shown in brackets beside the expected fragment size. Not to scale. **(B)** Western blot analysis of putative heterozygote tagged clones. Western blot analysis was performed on whole cell lysates. Lysates from WT cells and the original endogenously tagged cell line were run as – and + controls, respectively. The membrane was probed with α myc antibody. EF1 α was used as a loading control. Two clones were chosen for further analysis (indicated by the white arrows). **(C)** Agarose gel showing the PCR analysis testing for integration of the ΔAUK2::NEO construct into the genome of putative heterozygote tagged cell lines. Double distilled water was used as a negative control. All PCRs were performed on the same gDNA sample. NEO (Neomycin), B/α tub (Beta/Alpha Tubulin), Actin IR (Actin intergenic region), WT (Wild type), gDNA (genomic DNA), ddH₂O (double distilled water). (+/-) TbAUK2^{+/-} cell line, (+/+12myc) original endogenous tag cell line. Sizes shown (kb plus ladder; bp).

4.7.3 Confirmation of C-terminal tag functionality by assessment of growth *in vitro*

To ask whether C-terminal tagging of TbAUK2 disrupted function, growth of both the TbAUK2^{+/-12myc} clones was examined and compared to WT and TbAUK2^{+/-} cells. In addition, growth was assessed under MMS stress conditions. If gene function was interrupted, it was hypothesised that the TbAUK2^{+/-12myc} cell line would show a similar growth phenotype to the knockout cell lines, assuming that only the tagged allele is present. This analysis was performed as detailed in section 2.8.2. As depicted in Figure 4-18, growth of the TbAUK2^{+/-12myc} clones in

the absence or presence of MMS was not significantly affected in comparison to the WT cells, suggesting the epitope tag does not interrupt function.

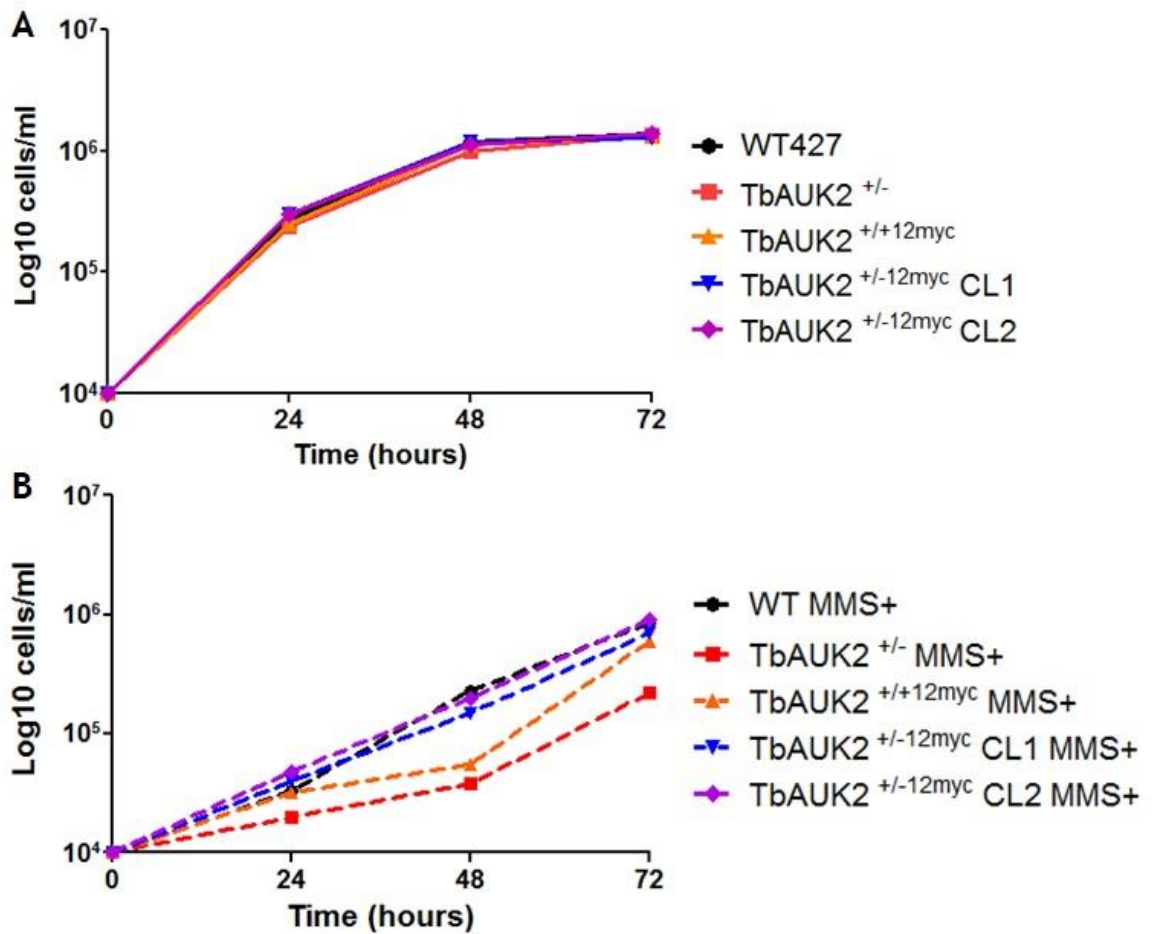


Figure 4-18: *In vitro* growth analysis of TbAUK2^{+/-12myc} cell lines
(A) Growth analysis of TbAUK2^{+/-12myc} cell lines. Growth was compared to WT, TbAUK2^{+/-} and TbAUK2^{+/+12myc} cells. **(B)** Growth analysis of TbAUK2^{+/-12myc} cell lines in the presence of MMS. Growth was compared to WT, TbAUK2^{+/-} and TbAUK2^{+/+12myc} cells in the presence of MMS (0.0003 %). Cell density was plotted on a log scale and represents data from one experiment.

4.7.4 TbAUK2 is a cell cycle regulated nuclear kinase

To evaluate the pattern of TbAUK2 localisation, indirect IF analysis was performed on both TbAUK2^{+/-12myc} clones (as per section 2.11.2). WT cells were fixed and used as a control to account for any non-specific antibody binding or background fluorescence (chapter 8, section 8.3, Figure 8-12). The cells were stained with DAPI (to visualise the nDNA and the kDNA) and with an α -myc::FITC conjugated antibody (to visualise the myc epitope). DC imaging was used to visualise the cell body. The IF images shown in Figure 4-19 are representative

images from one clone ($TbAUK2^{+/-12myc}$ CL1; no observable differences were noted between clones).

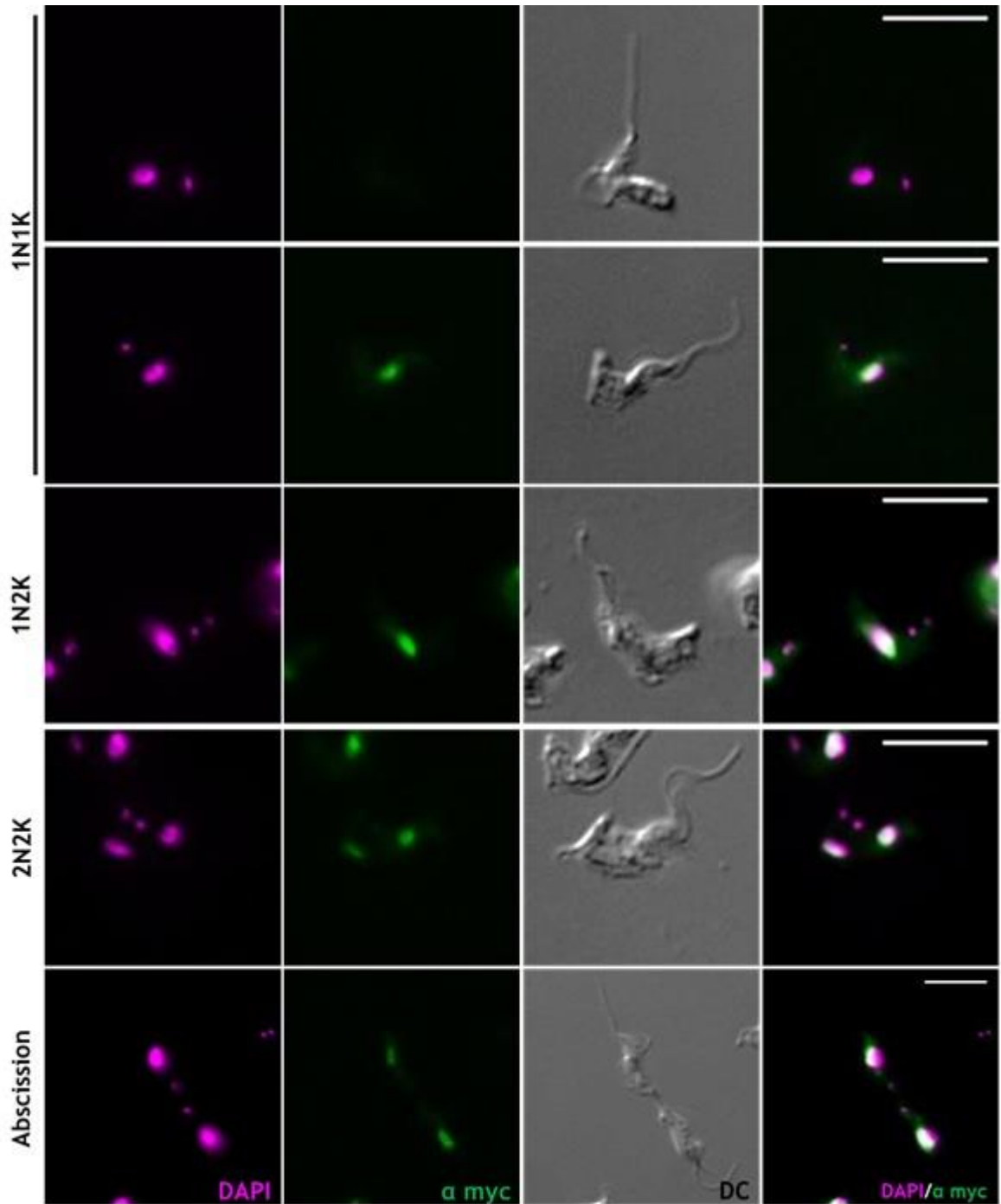


Figure 4-19: TbAUK2 localises to the nucleus of BSF cells

Representative images of cells from each cell cycle stage fixed and stained with α myc to visualise the myc tagged TbAUK2 (green). The nDNA and kDNA were stained with DAPI (magenta). The cell body was visualised by DC imaging. Images were captured on an Axioskop 2 and processed in ImageJ as per section 2.11.8. Scale bars = 5 μ m. Images captured of $TbAUK2^{+/-12myc}$ CL2.

Anti-myc signal was observed diffusely within the nucleus of all cell cycle stages (Figure 4-20). However, in ~10% of 1N1K cells no signal was detected (as shown

by the graph in chapter 8, section 8.3, Figure 8-13). This pattern of localisation was also observed in the PCF cells when TbAUK2 was C-terminally tagged with YFP (unpublished data, personal correspondence B.Akiyoshi, University of Oxford). Furthermore, as the cell cycle progressed, the intensity of the staining appeared to increase, with a greater intensity in 1N2K cells relative to 1N1K. To quantify this, the signal intensity for DAPI (nuclear staining) and FITC (the endogenous tag) was measured in Image J as per section 2.11.8.3. TbAUK2^{+/-}12myc CL1 was chosen for this analysis. Based on the DAPI intensity plot, the tagged cells progress through the cell cycle as expected, since a significant increase in the DAPI signal was observed in 1N2K cells (S-phase; Figure 4-20 A) and this reduced in each nucleus of 2N2K cells (M) to the levels seen in 1N1K cells (G1). Consistent with the intensity increase of the DAPI signal during S-phase, the signal intensity of TbAUK2 also peaked in 1N2K cells ($p < 0.005$; $n = 253$; Figure 4-20 B). Due to the weak signal of TbAUK2, several cells fell below background levels (this was an average of 179.6 pixels in WT cells). These cells were not excluded from this analysis and are thus represented in the group of cells showing signal lower than that of the WT background.

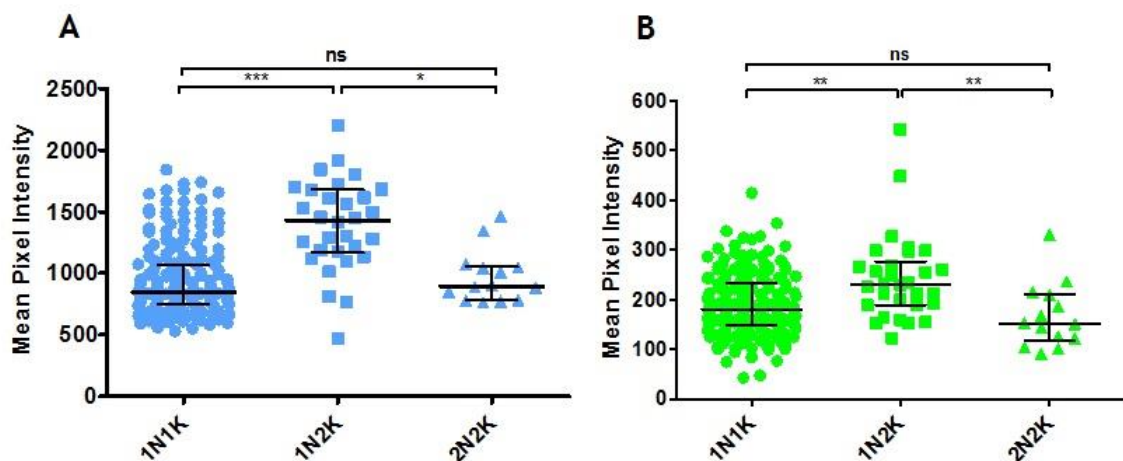


Figure 4-20: Dynamics of TbAUK2 throughout the cell cycle

(A) Intensity of DAPI (nDNA) was measured using ImageJ. A region of interest (21x21 pixels) was drawn around each nucleus and the mean pixel intensity recorded (represented by a 'dot' on the graph). The error bars represent the median value and the interquartile range. Significance was assessed using the Kruskal-Wallis non parametric test. (*) $p < 0.05$, (**) $p < 0.005$ and (***) $p < 0.0005$. $n = 253$ cells, $n = 1$. Results are shown from one experiment. (B) Intensity of myc was measured as described for (A). The data was plotted as per (A) and the statistical analysis performed as per (A). Clone used: TbAUK2^{+/-}12myc CL1. Background intensity in the FITC channel was found to be an average of 179.6 pixels in WT427 cells.

The above data provide evidence for cell cycle changes in TbAUK2 expression or localisation, perhaps indicating regulation. The identity of the small number of

1N1K cells without detectable TbAUK2 staining are unknown, but they could be in an early stage of G1, given that none appeared to have elongated kinetoplasts (the cell stage which marks the entry into nuclear S-phase). Increased signal for TbAUK2 in 1N2K cells appears to mirror the increased quantity of nuclear DNA during replication. Human aurora kinases also show a cell cycle regulated pattern of localisation and, indeed, the localisation pattern of TbAUK2 is potentially most like that of AUKA in human cells, since the centralised localisation of AUKB and AUKC during anaphase was not detected (Figure 4-1). However, from the immunolocalisation to date, no discrete subnuclear TbAUK2 localisation could be revealed.

4.7.5 Super resolution analysis of TbAUK2 localisation and 3D reconstruction of localisation

To ask if TbAUK2 adopts discrete subnuclear localisation, structure-illuminated super-resolution imaging (SIM) was performed. Indirect IF staining was performed as detailed in the section above. Images were captured on a Zeiss Elyra Super Resolution Microscope. WT cells were used as a control (chapter 8, section 8.3, Figure 8-14).

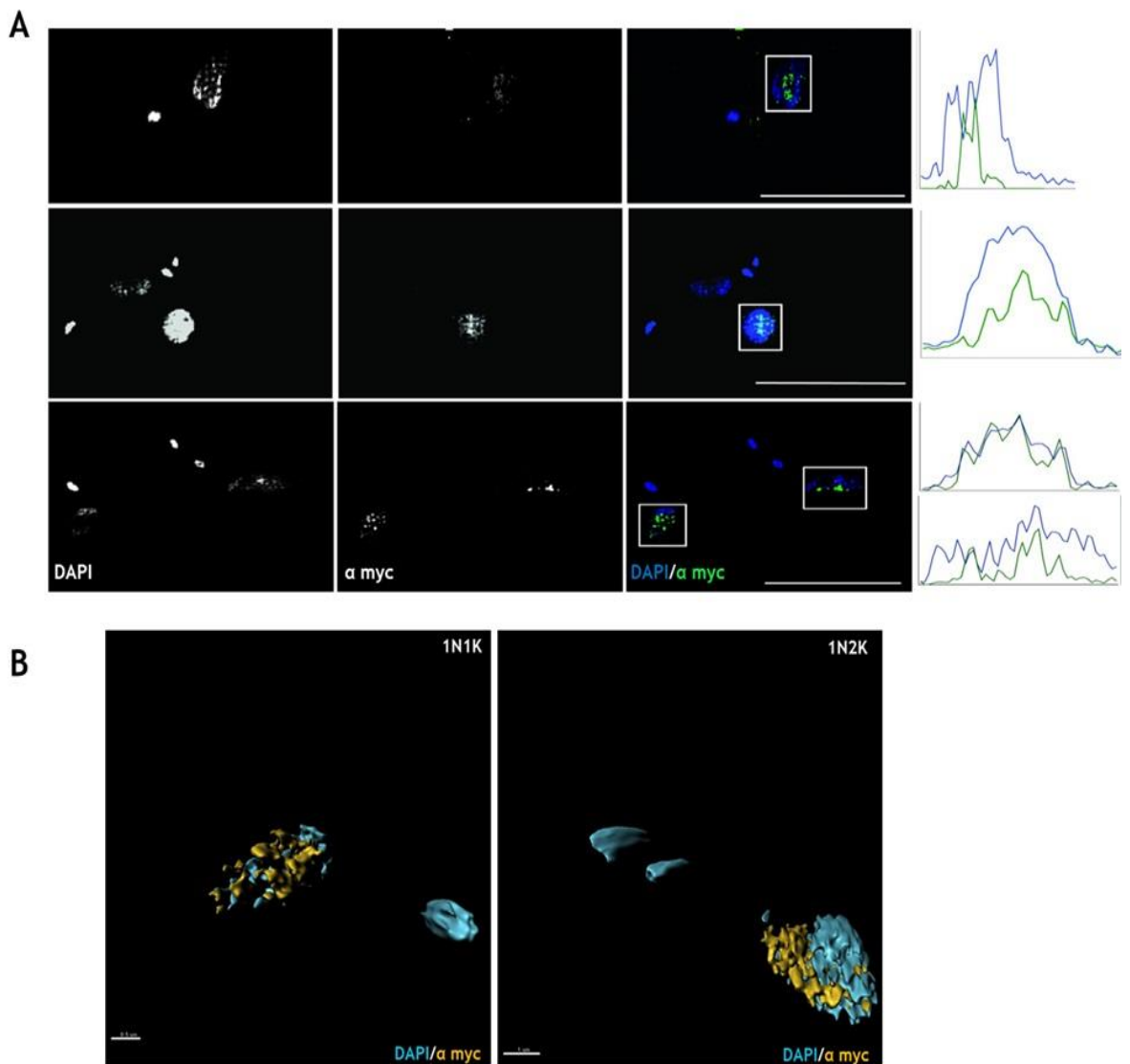


Figure 4-21: Super resolution and 3D imaging of TbAUK2 localisation
(A) Super resolution images of TbAUK2 localisation in BSF cells. The graphs show fluorescence intensity (arbitrary units; AU) plotted for both the DAPI (blue) and anti-myc (green) signal. The white box represents the area from which the fluorescence intensity was measured (using ImageJ) to generate the graph. Fluorescence intensity (as AU) is plotted (X-axis) over distance (μm ; Y-axis). Scale bar = 5 μm . **(B)** 3D reconstructions of TbAUK2 localisation. The images were generated from super resolution stack images captured on an Elyra (Zeiss) super resolution microscope. 3D images were generated using the IMARIS software (<http://www.bitplane.com/imiris/imiris>; V.8.2). Image on the left (scale bar = 0.1 μm). Image on the right (scale bar = 1 μm). Images are of TbAUK2^{+/-12myc} CL2 cells. The images captured and the 3D reconstructions shown in Figure 4-21 B were prepared under the supervision of L. Lemgruber Soares.

Localisation of TbAUK2 in 2N2K cells could not be imaged successfully using SIM; as signal was detected by confocal microscopy in this population of cells, it is possible TbAUK2 localises diffusely in this cell cycle stage. In contrast, in 1N1K and 1N2K cells, a punctate pattern was observed in all cells with localisation. In 1N1K cells, the anti-myc signal appeared as spots throughout the nucleus, while in 1N2K cells the localisation appeared to shift towards the centre of the

nucleus. These data suggest TbAUK2 is not stationary in the nucleus, but instead moves to different regions during the cell cycle. Despite this, TbAUK2 appears not re-localise as dynamically as TbAUK1, which shows a similar pattern of localisation to human AUKB (Carmena et al. 2009). TbAUK1 localises diffusely in the nucleus during interphase before progressing to the mitotic spindle during anaphase. TbAUK1 finally re-localises to the flagellar attachment zone prior to cytokinesis (Tu et al. 2006; Zhou et al. 2016).

4.7.6 Localisation of TbAUK2 following exposure to DNA damaging agents

Given the sensitivity of TbAUK2 mutants to several DNA damage sources, super resolution images of the localisation of TbAUK2 were next captured under MMS stress. Before indirect IF was performed (as per section 2.11.2), the cells were first exposed to PHL, MMS and UV as detailed in section 2.8.1. As no difference in the localisation could be detected following the generation of DNA damage by any of the three sources, IF images of representative localisation are only shown following MMS treatment in Figures 4-22 and 4-23 (using TbAUK2^{+/-12myc} CL2; localisation after other sources of damage are available in chapter 8, section 8.3, Figure 8-15). Cells were fixed and stained as per section 2.11.2. Images were first captured on an Axioskop 2 and processed in ImageJ as per section 2.11.8. WT cells were used to as a control for background levels of fluorescence or to account for any non-specific binding of the α myc antibody.

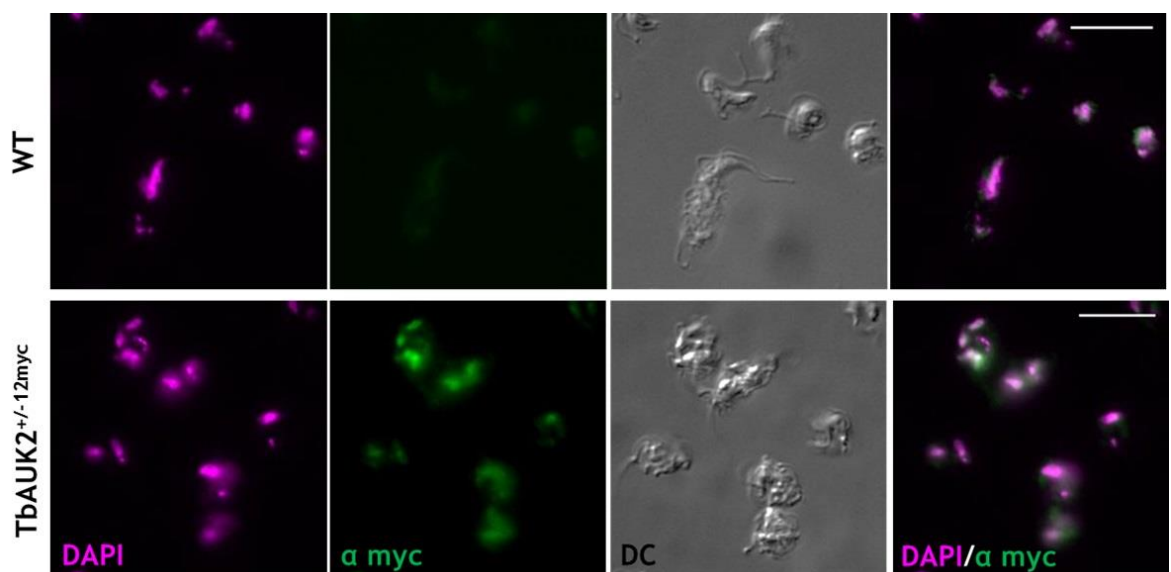


Figure 4-22: Localisation of TbAUK2 after MMS exposure

The cells were exposed to 0.0003 % (v/v) MMS for 18 hours before fixation and IF analysis. WT cells (top panel) were used as a control. The myc tag (green) was visualised using α myc:FITC conjugate antibody. The nDNA and kDNA were stained with DAPI (magenta). Scale bar = 10 μ m.

No clearly observable changes in localisation were observed following MMS exposure (Figure 4-22), and regions of more intense anti-myc signal appeared to correspond with higher DAPI staining, perhaps due to chromatin changes after damage. However, preliminary SIM images (Figure 4-23) appeared to suggest TbAUK2 forms a greater number of puncta throughout the nucleus after MMS treatment. Further analysis would be required to explore this observation in more detail.

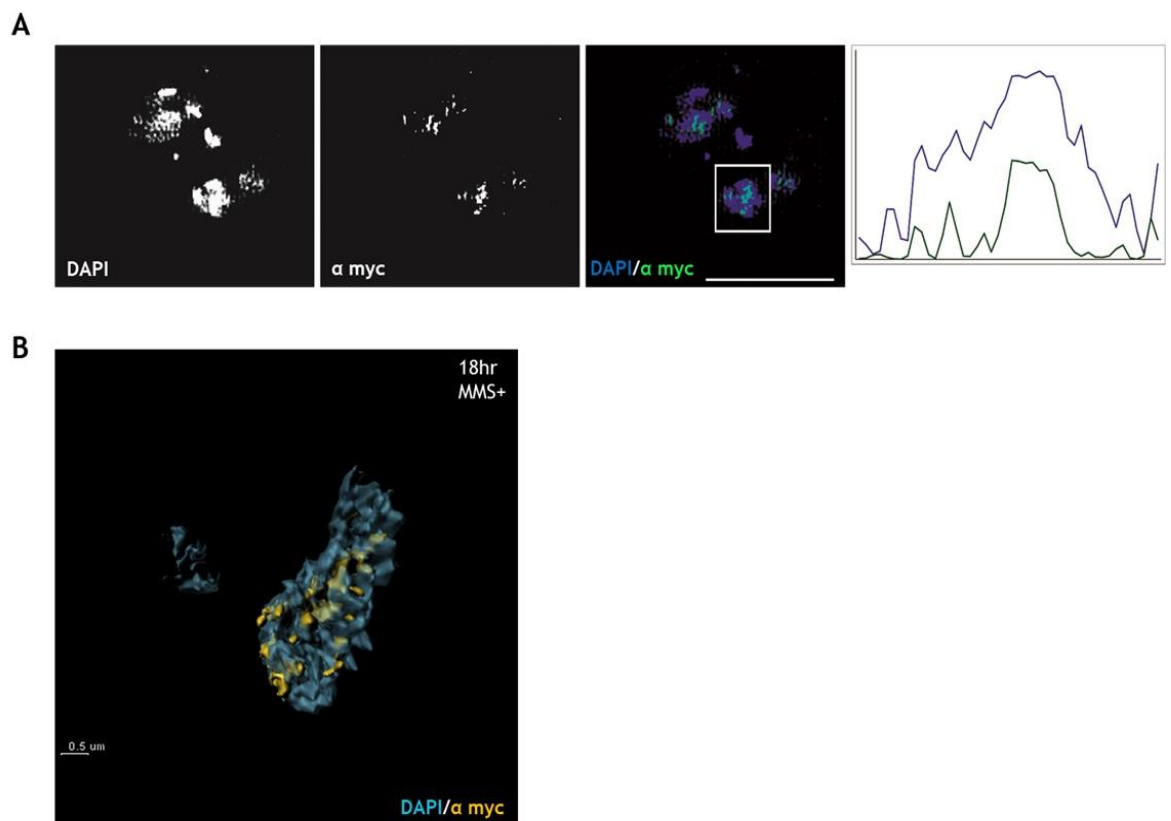


Figure 4-23: Super resolution images of TbAUK2 localisation after MMS exposure
(A) Cells were fixed and stained as per section 2.11.2 following 18 hrs exposure to MMS (0.0003 % [v/v]). Cells were imaged on an Elyra (Zeiss) microscope by structure illuminated microscopy. The nDNA and kDNA were visualised by DAPI (blue) and the endogenous tag detected by α myc antibody (green). Scale bar = 5 μ m. **(B)** 3D reconstruction of TbAUK2 localisation following 18 hrs MMS exposure. 3D reconstruction was generated using IMARIS software (V8.2) as described in the figure legend above. Scale bar = 0.5 μ m. Images in **(A)** and **(B)** are of TbAUK2^{+/-12myc} CL2.

4.8 Identification of potential interaction partners by immunoprecipitation

Aurora kinases in other eukaryotes have a wealth of interaction partners to facilitate their functions within a proliferating cell (see section 4.1.1). To attempt to identify potential interaction partners of TbAUK2 an immunoprecipitation (IP) was performed as described in section 2.12.2 with anti-myc antiserum using the myc tagged TbAUK2^{+/-12myc} cell line. The protocol is as detailed in section 2.12.2; all modifications are as detailed in section 2.12.2. To control for non-specific binding of proteins to the Dyna beads (as prepared in section 2.12.2), WT cells were used as a negative control. No attempt was made to perform this IP after DNA damage due to the difficulty in harvesting the required cell number for this analysis. To allow for identification of interaction partners visually and by mass spectroscopy, an IP was performed. The final eluate of one IP (S1) was separated on a 10% BT gel by SDS-PAGE and stained with SYPRO® Ruby before imaging on a Typhoon (section 2.12.4). No clear differences were observed between the eluate of TbAUK2^{+/-12myc} cells and WT cells. Nor could a band corresponding to TbAUK2^{+/-12myc} was seen (Figure 4-24 A).

A second eluate sample (S2) from both cells was sent for mass spectroscopy analysis (section 2.12.3; Glasgow Proteomics Facility; the WT sample was run first) and a western blot was performed (section 2.12.1 and 2.12.2), verifying that TbAUK2^{12myc} could only be detected (as indicated by the black arrow; Figure 4-24 B) in the eluate of the TbAUK2^{+/-12myc} sample. Described below are the proteins identified (summarised in Table 4-3) from MS analysis, which are proteins only detected in the experimental and not control (WT) IPs (see the file supplied on the accompanying CD entitled [MSdataTb6560andTbAUK22016.xls](#) for all proteins identified in both samples). TbAUK2 could not be identified in either the IP from the TbAUK2^{+/-12myc} cells or from the WT cells. The reason for this is unknown; however, as the whole eluate was sent for MS, it is possible the weak expression of the tagged protein was masked by more abundant peptides from other proteins.

It is important to note that none of the putative interaction partners have been verified by further analysis (such as performing a repeat IP, directed co-IP or

reciprocal IP) and therefore all hits presented here must be treated as preliminary.

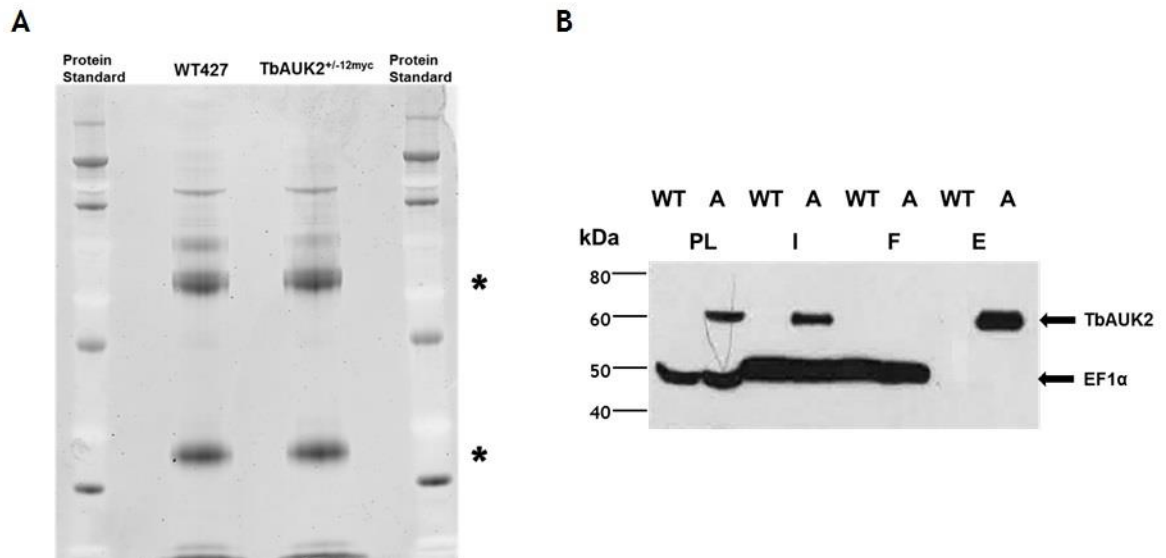


Figure 4-24: Immunoprecipitation of TbAUK2+/-12myc cell line
(A) Sypro Ruby stained SDS-PAGE gel showing the eluate fractions from WT and TbAUK2+/-12myc (S1) cell lines. The dark bands in line with the (*) indicate the heavy and light chains of the myc antibody. Protein Standard (Novex® Sharp Pre-Stained protein ladder; ThermoFisher). **(B)** Western blot analysis on all fractions of the IP from TbAUK2 +/- 12myc S2. The antibody chains were not detected by this western. WT (Wild Type), A (TbAUK2+/-12myc CL1), PL (Pre-lysis), I (Input/Lysate), F (Flowthrough), E (Eluate). The black arrows show the position of the endogenously tagged protein and to the loading control EF1 α . S2 eluate was sent for Mass Spectroscopy (MS) analysis. Gel image captured on a Typhoon 9400.

Table 4-3 details the proteins identified from the IP that were absent in the WT sample and, in addition, were not detected in an anti-myc IP performed independently by another researcher in the lab (unpublished data, A.C. Zurita-Leal) using BSF cells expressing a putatively unrelated myc-tagged protein.

TbAUK2+/-12myc					
Gene ID	Annotation	MW (kDa)	Annotation (Based on <i>H.sapiens</i>)	Predicted Domains	Protein Score
Tb927.9.1980	Hypothetical	78.488	No hits; Kinetoplastid specific	No hits	35
Tb927.4.2000	RuvB -like DNA helicase	52.611	RuvB like helicase	ATP binding, Walker A motif, TIP49, P loop NTPase	17
Tb927.7.3670	TrkAN domain	71.465	NADP-dependent oxidoreductase domain containing protein 1	NADP Predicted domain	16
Tb927.3.5020	FLAM6	155.861	cAMP dependant Protein Kinase beta-subunit	Crp domains and CAP_ED domains	15
Tb927.10.4160	predicted Zn finger protein	42.498	E3 Ubiquitin protein ligase	RING domain	15

Table 4-3: Potential interaction partners identified by Mass Spectroscopy analysis
 'Hits' shown were only present in the endogenously tagged cell line. Any protein identified in the WT sample was excluded from this analysis. Samples were analysed using MASCOT software. Protein sequence for each 'hit' was analysed by BLASTp using the SmartBLAST feature. Displayed in the table are the potential corresponding human homologs. Pale red (kinetoplastid specific), pale orange (potential DNA repair related function).

Two factors may be of interest, but would require validation as true interactors of TbAUK2. The first was a RuvB- like helicase; members of the RuvB family, first identified in prokaryotes, are important for Holliday junction formation and in overcoming replication fork stalling (Baharoglu et al. 2006). In addition, a hypothetical protein with a Zn finger containing ubiquitin ligase like domain was identified. Aurora kinases have been shown to be negatively regulated by ubiquitination (as reviewed by Lindon et al., 2016) and, additionally, Zn finger domains can bind DNA (Krishna et al. 2003).

4.9 Re-expression of TbAUK2 in TbAUK2^{-/-} knockouts

To determine whether the phenotypic effects observed in the TbAUK2^{-/-} cells are attributed simply to loss of TbAUK2 gene or if they result from secondary effects, mutant cells re-expressing TbAUK2 gene were generated.

4.9.1 Generation of the re-expresser construct

To strategy for gene re-expression and the methodology used to generate the re-expresser constructs is as described in section 2.4.1.3. Figure 4-25 illustrates the position of the primers used for PCR amplification of the complete TbAUK2 ORF, which was inserted into a plasmid (TbAUK2::RXP) that allow integration of the gene into the tubulin locus, with mRNA processing provided by non-endogenous sequences.

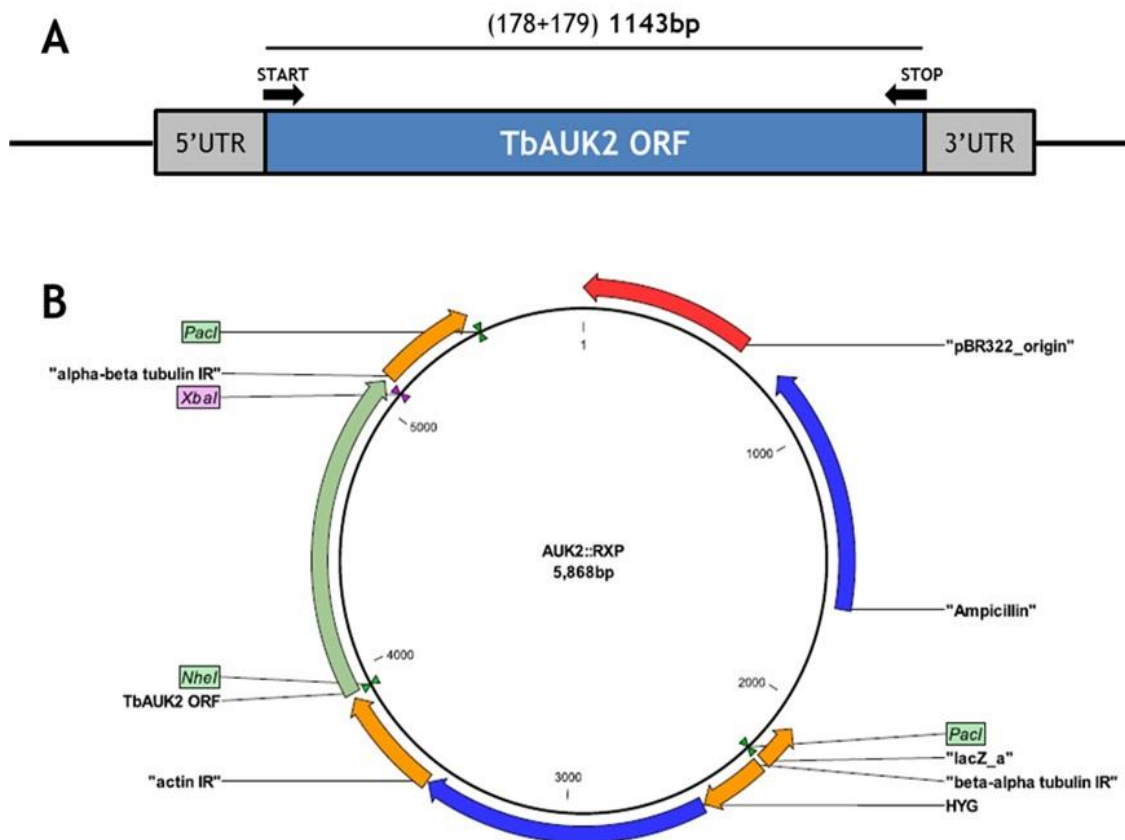


Figure 4-25: Schematic of the TbAUK2 re-expression plasmid AUK2::RXP
(A) Schematic representation of the region PCR amplified for re-expression. The whole ORF (including the start and stop codons) was required for re-expression. The primers required are indicated in brackets beside the expected PCR fragment size. The primer positions in the genome are indicated by black arrows. **(B)** A representative illustration of the AUK2::RXP construct. The PCR fragment was cloned in using *NheI* and *XbaI* restriction sites. AUK2::RXP was linearised with *PacI* prior to transformation into BSF cells. Schematic generated by CLC Genomics Workbench 7. Not to scale.

4.9.2 Generation of TbAUK2^{-/-} cell lines

To re-express the TbAUK2 gene, the TbAUK2^{-/-} CL2 cell line was transformed with the *PacI* digested TbAUK2::RXP construct. Transformants were selected for as per section 2.7.4. Only a few transformants were recovered, potentially due to poor growth of the TbAUK2^{-/-} cell lines or perhaps indicative of a role in for TbAUK2 in recombination. Two clones were chosen and expanded for further analysis.

4.9.3 Confirmation of TbAUK2 re-expression by PCR and qRT-PCR analysis

To confirm re-expression of TbAUK2 in the putative re-expresser clones two analyses were undertaken. First, correct integration of the TbAUK2::RXP

construct into the genome was examined by PCR, as depicted in Figure 4-26 A&B.

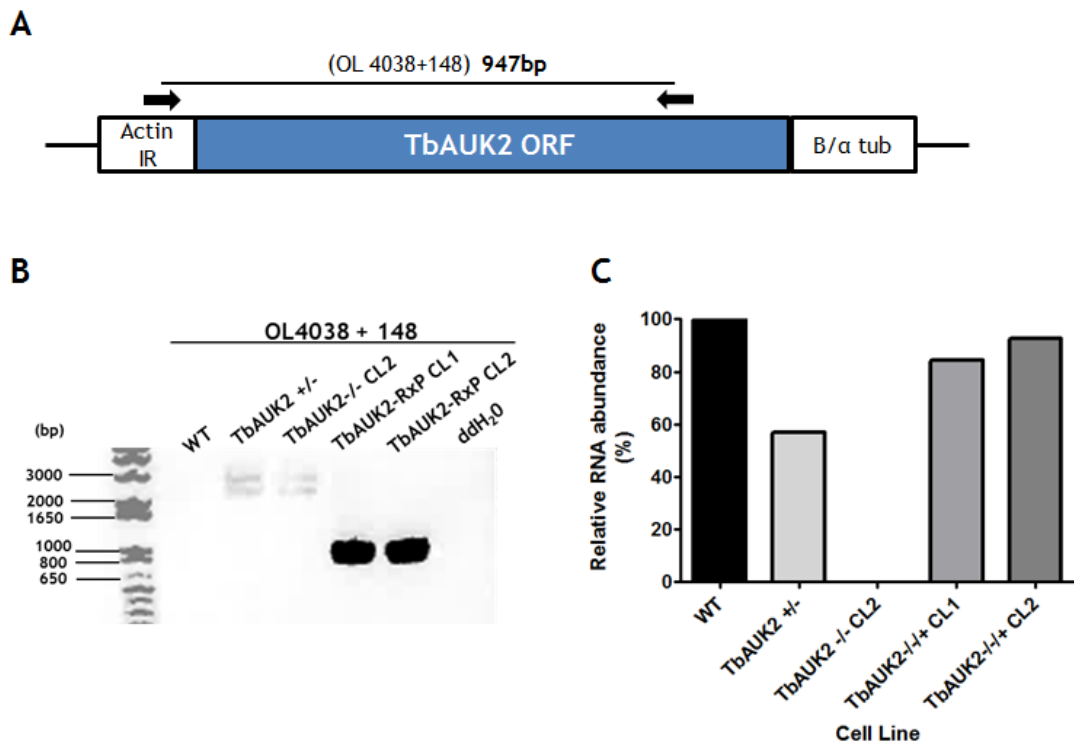


Figure 4-26: Confirmation of TbAUK2 re-expressing cell lines

(A) Schematic illustration of expected fragment size amplified by PCR (bp), diagnostic primers used (black arrows) and their position in the genome. Primer sequences are available in Table 2-3 and Table 2-1. Not to scale. (B) Agarose gels of diagnostic integration PCR, performed using the primer pairs detailed in A (testing for integration of the RxP construct using gDNA from two $-/-/+$ clones (RxP CL1 and RxP CL2), wild type (WT) cells, heterozygote $+/-$ cells, TbAUK2 $-/-$ cells (CL2) or using double distilled water (ddH₂O) as a negative control. All PCRs were performed on the same gDNA samples. B/α tub (Beta/Alpha Tubulin), Actin IR (Actin intergenic region), gDNA (genomic DNA), ORF (open reading frame). For each gel, size markers are shown (bp). (C) RNA from each cell line was prepared from which cDNA was generated. qRT-PCR was performed to examine expression level of TbAUK2 in WT, heterozygote ($+/-$), knockout ($-/-$) and both re-expressor ($-/-/+$) cell lines using primers AUK2RTFW2 and AUK2RTRV1 (Table 2-5 detailed in section 2.5.3.1). Expression of TbAUK2 in the WT was arbitrarily set to 100% expression. A low level of gDNA contamination could be detected in the WT and heterozygote samples (data not shown).

From the PCR, the construct appeared to have correctly integrated in both clones. Secondly, expression of TbAUK2 RNA was examined by qRT-PCR. RNA was extracted from the re-expressor clones and cDNA was generated as per section 2.5. qRT-PCR was performed to determine the level of expression relative to the WT cells (as a control), the TbAUK2 $+/-$ cells and the knockout clone used for the original transformation (TbAUK2 $-/-$ CL2). The confirmed re-expressor clones are referred to as TbAUK2 $-/-/+$ CL1 and TbAUK2 $-/-/+$ CL2 in this thesis.

4.9.4 Characterisation of TbAUK2 re-expresser cell lines

4.9.4.1 Growth analysis in the absence and presence of MMS *in vitro*

Loss of TbAUK2 significantly reduced proliferation *in vitro*. To determine if re-expression of the TbAUK2 gene restored growth to a WT level, the growth of two re-expresser cells was compared to WT and TbAUK2^{-/-} CL2 cells in the absence of any antibiotic selection. The growth assay was set up and monitored as described in section 2.8.2. The growth *in vitro* of both TbAUK2^{-/-/+} clones appeared more comparable to WT cells than the -/- mutants (Figure 4-26 A).

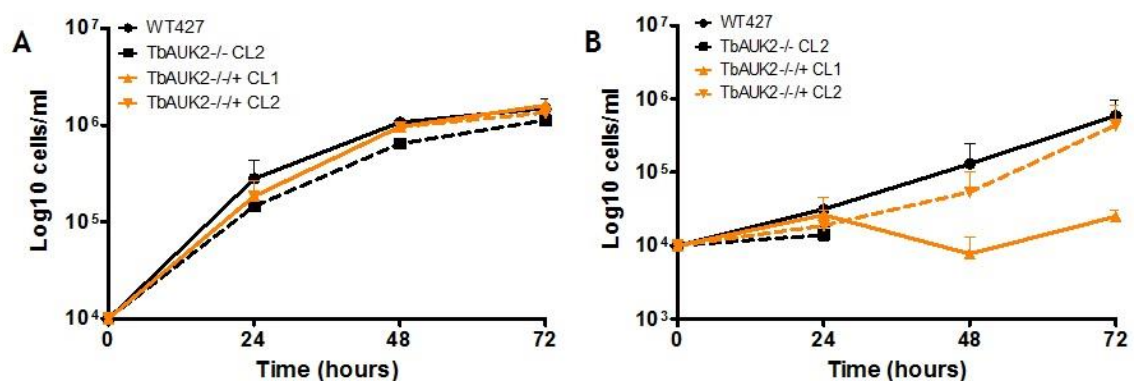


Figure 4-27: *In vitro* growth of TbAUK2 re-expresser clones

(A) Growth of re-expresser clones was examined *in vitro* and compared to WT and the parental TbAUK2 knockout clone. The data is plotted on a logarithmic scale. The error bars represent \pm SEM (n=2). (B) Growth of re-expresser clones *in vitro* following exposure to MMS. Cells were exposed to 0.0003% MMS and growth assessed as per section 2.8.2. The data is plotted on a logarithmic scale. The error bars represent \pm SEM, n=2.

To test the effect of TbAUK2 re-expression further, growth (Figure 4-26 B) of the TbAUK2^{-/-/+} cells were monitored and compared to TbAUK2^{-/-} CL2 and WT cells in the presence of MMS (0.0003 %). The cells were set up and growth monitored as per section 2.8.2. Beyond 24 hrs post exposure to MMS, no cells could be recorded for the TbAUK2^{-/-} CL2 cell line, reflecting its sensitivity to genotoxic stress conditions (Figure 4-26 B). Conversely, the growth of both re-expresser clones was more comparable to growth of the WT cells in the presence of MMS, though one clone appeared to be more sensitive than the other, for reasons that are unclear. Taken together, these data suggest re-expression of TbAUK2 in -/- mutants is able to complement at least two phenotypic impairments.

4.10 Discussion

The purpose of this chapter was to examine the role of TbAUK2 in BSF *T. brucei* cells, in particular pertaining to a potential role in DNA repair. As little characterisation of TbAUK2 has been undertaken, the data detailed in this chapter represent the first insights into TbAUK2 function in the BSF lifecycle stage of *T. brucei*. Discussed below is how the data presented here relates to the biology of other aurora kinases and to the parasite.

4.10.1 Insights from the bioinformatics analysis

Aurora kinases (universally found in the Eukarya) are required to co-ordinate numerous aspects of cell proliferation (Goldenson & Crispino 2015) and though these kinases are well studied across this kingdom, their evolutionary origin has yet to be deciphered. As such, insights from early branching eukaryotes like the trypanosome may further our understanding of these critical enzymes. The AUK family is conventionally considered to have expanded in line with increasing eukaryote complexity. For example, in yeasts and the amoeboid *Dictyostelium discoideum* (both single celled organism), only one AUK has been described. In 'lower' metazoans, such as *D. melanogaster*, typically two AUKs (AUKA and AUKB) are found, while in mammals, three are present (AUKA, AUKB and AUKC). In keeping with this proposed progression, the single AUK in yeast and *D. discoideum* appears able to perform the functions of both AUKA and AUKB (Li et al. 2008), which display differing localisation and possess distinct interaction partners in humans. Indeed, human AUKC appears to have evolved specifically for aspects of gametocyte function. If correct, this evolutionary scenario raises an obvious question; why do the kinetoplastids require three AUKs? The data provided here on *T. brucei* AUK2 suggests distinct functions from AUK1, the best characterised kinetoplastid AUK to date (discussed below; Li & Wang, 2006; Tu et al., 2006). Such diversification raises the question of what aspects of kinetoplastid biology requires these extra layers of complexity.

In the context of the above discussion, it is worth mentioning the divergence of aurora kinases is also seen within plants. In some plants, three AUKs have arisen and are found in two subgroups: the α -group (comprising AUK1 and AUK2) and β -group (comprising AUK3). In contrast, some other plants only possess two α -

group AUKs (Weimer et al. 2016). These data may indicate further specialisation of roles, but AUK characterisation in plants is still in its early stages.

Nonetheless, the aurora kinases appear very 'adaptable' to the needs of an individual organism. In addition, aurora kinase redundancy has yet to be reported, perhaps suggesting organisms evolve as many AUKs as they require.

TbAUK1 appears to be the kinetoplastid homolog of AUKB, based on functional studies. Assigning potential orthology of TbAUK2 and TbAUK3 based on sequence homology is not simple. While TbAUK3 has a C-terminal extension that distinguishes it from the two other kinetoplastid AUKs, TbAUK1 and TbAUK2 are of similar size and share similar levels of homology to all three of the human AUKs. In addition, one of the defining features of AUKA (the DAD/A box) is not present in any *T. brucei* AUK, suggesting each may be more closely related to AUKB in terms of regulation. However, the top 'hits' from a BLAST analysis using the sequence of TbAUK2 are predominantly annotated as the AUKA kinases, despite the absence of conserved DAD/A box or KEN motifs. As these motifs are required for degradation by ubiquitination, it is possible all the *T. brucei* AUKs are subjected to distinct regulation from their human homologs, and hence sequence identity may be a poor predictor of AUKA homology. Interestingly, though yeast Ark1 has a KEN box motif, it does not appear to play a role in Ark1 degradation (Levenson et al. 2002). Indeed, Ark1 levels do not appear to be regulated throughout the cell cycle, as AUKs are observed to do in human cells. As *T. brucei* AUKs appear to have diverged earlier than most eukaryotic aurora kinases (as indicated by phylogenetic analysis performed by Li et al. 2008), it is possible that the KEN, A and/or DAD box motifs arose later and have come to act in expression regulation only in some circumstances. In this regard, it is notable that AUKC also does not possess either a KEN motif or an A-box/DAD-box, but localises dynamically throughout the cell cycle. All the *T. brucei* AUKs do, however, contain a D-box domain (section 4.4.1.2) in their C-termini, suggesting their activity is regulated in some manner.

Overall, the evolutionary history of AUK kinases remains unclear and assigning a human homolog of TbAUK2 (and indeed TbAUK3) based on sequence comparisons may be premature. Instead, functional analysis may be the clearest route to assign functional homology. Indeed, understanding why trypanosomatids require

three AUKs will require functional analysis of TbAUK3. It is worth noting that further protein kinase family expansions are seen in trypanosomatids (Parsons et al. 2005). For example, the NEK (NimA related kinase) kinases are an expanded family (22 members in *T. brucei* compared with 11 members in *H. sapiens*), though not all appear to have a functional role or their roles are trypanosome-specific (Jones et al. 2014).

4.10.2 TbAUK2 acts in aspects of mitosis, spindle formation and cellular morphology

4.10.2.1 Loss of TbAUK2 affects cell morphology

Phenotypic analysis of TbAUK2 null mutants reveals that this AUK plays a role in co-ordinating nuclear division in BSF parasites. Loss of TbAUK2 significantly reduces cell proliferation, which is associated with nuclear and morphological aberrancies. In terms of morphology, ~30% of the total population lost the typical trypanomastigote shape, either manifesting as ‘rounded’ cells (~35%), ‘clumps’ (~10%) or simply that appeared large and distorted in shape (‘aberrant’; ~55%). Following RNAi of TbAUK1 in BSF cells, such morphological defects can also be observed, but appeared to be less pronounced, perhaps related to the fact that RNAi of TbAUK2 in the absence of genotoxic stress had little effect on in vitro growth. A clear explanation for the ‘rounded’ appearance of the TbAUK2^{-/-} cells remains elusive, though chemical inhibition of the *L. donovani* putative AUKB homologue (LdAIRK) was shown to produce cells with a rounded and distorted shape (Chhajer et al. 2016). Potentially, therefore, aurora kinases in kinetoplastids may play a role in cell morphology. In human cells, loss of morphology (as the result of defective cytokinesis) has been commonly reported following knockdown of AUKs. siRNA targeting AUKA results in large and distorted HCT116 cell, and the same is true following addition of an AUKA inhibitor MLN8054 (Huck et al. 2010). This affect was also observed following siRNA targeting AUKB in HeLa cells (Delaval et al. 2004). To date, several groups have now shown that aurora kinases are directly involved in regulating microtubules, cytokinesis and, recently, the actin cytoskeleton (Delaval et al. 2004; Giet et al. 2002; Marumoto et al. 2003; Ritchey & Chakrabarti 2014).

RNAi of TbAUK1 in BSF cells is lethal and leads to the generation of potentially the same rounded cells seen in the TbAUK2^{-/-} mutants. Whether this commonality indicates overlapping roles of TbAUK1 and TbAUK2, or even the proteins acting together, is unclear. However, loss of TbAUK2 is not lethal, meaning it may be subservient to TbAUK1 or that TbAUK1 may compensate for TbAUK2 loss. In addition to spindle microtubules, the subpellicular microtubule corset of the parasite is responsible for maintaining the highly polarised shape of the trypomastigote and is required for cytokinesis to occur. Some of the first steps of cytokinesis utilise newly synthesised microtubules as a ‘guide’ on which to direct cell separation. Furthermore, rather than all subpellicular microtubules being synthesised anew for the daughter cell, a series of (semi-) inheritance events occur in which some subpellicular microtubules from the mother cell are incorporated into the daughter cell (as shown by Wheeler, Scheumann, Wickstead, Gull, & Vaughan, 2013). Hence, microtubules and their co-ordination are not only required for mitosis but also to facilitate cytokinesis, meaning aberrant morphology, mitosis and cytokinesis may be linked through microtubule TbAUK functions. Indeed, the importance of TbAUK1 during cytokinesis was shown recently by Zhou and colleagues (Zhou et al. 2016). *T. brucei*'s mechanism of cytokinesis occurs in the absence of an actomyosin contractile ring (Zhou et al. 2016) and shows considerable divergence from the last common ancestor of eukaryotes, implying *T. brucei* may utilise an ancient method of cytokinesis. If both TbAUK1 and TbAUK2 activity is required to facilitate cytokinesis, an ancient evolutionary link between cytokinesis and aurora kinases is revealed (Zhou et al. 2016), raising the question of why some eukaryotes evolved to conduct this central process with only one AUK.

4.10.2.2 Loss of TbAUK2 affects spindle formation and mitosis

When nDNA and kDNA content were examined in TbAUK2^{-/-} cells, ~30 % of the population had an aberrant nuclear content; a similar percentage to cells with morphological defects. Furthermore, a corresponding loss of 1N1K cells was associated with an increase in aberrant cells. In particular, the presence of ‘intra-nuclear’ membranes and nuclear ‘blebs’ (~20-27 % of a population) was noted, suggesting miss-segregation of nDNA occurs in these cells. In support of this, when the cells were stained for KMX-1 to visualise the mitotic spindle, it was found that the number of 1N2K cells (cells in S-phase) with a mitotic spindle

was reduced by ~50 %. Failing to effectively form a mitotic spindle may account for this miss-division of nuclei during mitosis. RNAi-mediated loss of TbAUK1 also abolished nuclear spindle formation in BSF cells (Li & Wang, 2006), reinforcing the overlap between the two AUKs. The accumulation of cells with aberrant nDNA and kDNA ratios, including absence of both genomes, suggests cytokinesis may continue in the TbAUK2^{-/-} mutants, despite impaired mitosis. As large, multinucleated cells also formed in the mutants, it is possible that loss of TbAUK2 impairs signalling a cytokinesis checkpoint, but that other factors can perform some such signalling in its absence. No apparent effect on kDNA was observed (as was the case following the loss of TbAUK1; Li & Wang, 2006), indicating both TbAUKs provide nuclear functions.

Loss of AUKs in other eukaryotes also results in mitotic spindle defects and miss-segregation of sister chromatids (Mountzios et al. 2008; Vader & Lens 2008; Tao et al. 2008), amongst other mitosis wide defects. In germline cells, loss of AUKA or AUKB is lethal as the mitotic spindle is defective (Lu et al. 2008; Balboula & Schindler 2014; Hoar et al. 2007). Furthermore, loss of AUKA results in chromosome miss-alignment, which is sensed and the cells are halted in mitosis; however, such cells can bypass the stall and continue through the cell cycle, resulting in aberrant nuclear segregation (Fu et al. 2007; Goldenson & Crispino 2015). In these circumstances the tumour suppressor protein p53 can arrest cells in G1, but since p53 has not been identified in trypanosomatids, this additional control measure cannot be implemented and cells with potential nuclear aberrancies enter a new cell cycle. In the case of AUKB (and AUKC) mutants, the primary phenotype manifests as a failure to segregate chromosomes (as reviewed by Goldenson & Crispino, 2015).

AUKA and AUKB have been shown to co-ordinate aspects of the nuclear envelope with chromosome condensation and mitotic spindle formation (Mora-Bermúdez et al. 2007). In HeLa cells, inhibiting AUKB during anaphase has little effect on nuclear structure (the envelope), but inhibition during early mitosis results in slower dissociation of the nuclear envelope from chromosomes, suggesting AUKB is required for the breakdown of the nuclear envelope during mitosis. Such an 'open' mitosis in which the nuclear envelope is disassembled before separation of sister chromatids is not seen in the trypanosomatids. *T. brucei*, like yeast,

undergoes a 'closed' mitosis in which the nuclear pores permit entry and exit of materials required for mitosis (as reviewed by Daniels, Gull, & Wickstead, 2010; DuBois et al., 2012). In the TbAUK2^{-/-} mutants a link between miss-segregation of nuclear DNA and the nuclear envelope is seen in that the blebs appear to contain genetic material (as shown by DAPI staining). As mentioned above, TbAUK1 is required for the formation of the mitotic spindle and movements of the spindle during mitosis (Tu et al. 2006). However, TbAUK1 does not appear to regulate spindle assembly through the centrosome. Potentially, therefore, TbAUK2 may play a role in how the spindle of *T. brucei* is arranged to permit an 'even' division of genetic material between the two developing daughter cells. As little is known about how *T. brucei* actively co-ordinates this aspect of division, these data may provide the first indication that nuclear envelope maintenance, growth or division during mitosis is, in part, regulated by an aurora kinase. Moreover, this is the first indication of distinct functions for TbAUK1 and TbAUK2.

4.10.3 Loss of TbAUK2 is associated with increased sensitivity to genotoxic stress

Aurora kinases in humans are intimately linked to the development of cancer (Vader & Lens 2008; Fu et al. 2007; Goldenson & Crispino 2015). For example, activity of AUKA must be finely tuned to prevent over- or under expression of AUKA, since both scenarios are detrimental to cells. AUKA is considered as a DNA repair-associated kinase, whereas AUKB's role in cancer appears to be mediated through its interaction partners rather than directly by its activity (Y. Wang et al. 2014; Gully et al. 2012; Vader & Lens 2008).

As seen in the RNAi cell line (which is sensitive to MMS on tetracycline induction), TbAUK2^{-/-} cell are sensitive to several sources of genotoxic stress, consistent with a potential role in monitoring the nucleus for DNA damage. In human cell lines, loss or de-regulation of AUKA sensitises cells to DNA damage¹² caused by UV, cisplatin (Wang et al., 2006), etoposide (a DSB agent; Krystyniak et al., 2006) and HU (Leontovich et al. 2013). Furthermore, it has been reported that knockdown of AUKA is associated with increased γ H2AX (Moretti, et al. 2011;

¹² This effect may be cell line specific (Wang et al., 2014).

in some cell lines) and RAD51 foci (Yang et al. 2010), phenotypes that closely mirror the effects on these DNA damage associated markers in *T. brucei* BSF cells lacking TbAUK2. Thus, TbAUK2's functions may be analogous to those of human AUKA, though it should be noted these effects have not been examined in TbAUK1 depleted *T. brucei* cells.

Numerous studies in other organisms have highlighted the role of the aurora kinases in the development of cancer, which arises predominantly as the result of defects during centrosome formation, chromosomal segregation or the inability to trigger a cell cycle check point. AUKA has been shown to phosphorylate and interact with proteins with well-established roles in the DDR. Notably, BRCA1 and BRCA2 have both been shown to interact with AUKA: AUKA binding to BRCA1 results in the loss of the G2/M checkpoint, while blocking AUKA activity results in increased BRCA2 repair foci following genotoxic stress. CHK1 (a central kinase, which can be activated upon phosphorylation from the ATR kinase) activity is also affected when AUKA becomes de-regulated and, as a consequence, the HR response becomes defective (Sourisseau et al. 2010). To date, such roles for TbAUK1 or TbAUK2 have not been tested, but would be valuable, particularly as HR is the primary method used by *T. brucei* to deal with DSBs breaks (Glover et al. 2008). Indeed, HR is a critical mechanism for VSG switching (Glover, Alford, et al. 2013), meaning testing TbAUK roles in this process would be valuable; to date, only silent VSG expression has been examined in the TbAUK2 -/- cells, with inconclusive results (chapter 8, section 8.3, Figure 8-16).

An attempt was made to overexpress TbAUK2 in BSF cells (chapter 8, section 8.3, Figure 8-17), but did not result in increased tolerance to MMS stress (unlike overexpression of AUKA in human cells when exposed to cisplatin or UV; Wang et al., 2006) and no nuclear or morphological defects were observed. Though further tests are required, these data may suggest regulation of TbAUK2 levels.

4.10.4 TbAUK2 shows a punctate nuclear localisation

A hallmark of aurora kinases is their dynamic localisation throughout the cell cycle from late G2 to mitosis (Carmena et al., 2009; see section 4.1.1). In addition, the levels of AUKA and AUKB are much reduced in G1 cells (Lindon et

al. 2016). Dynamic localisation is also observed for TbAUK1, which begins as a diffuse signal in 1N1K and 1N2K cells and translocates to the midzone of in 2N2K cells, mimicking the localisation of AUKB in human cells (Li & Wang 2006; Carmena et al. 2009). Though dynamism of TbAUK2 may not be as pronounced, super resolution images show TbAUK2 localises in a punctate fashion throughout the nuclei of 1N1K cells and 1N2K cells. In 1N1K cells, localisation appeared throughout the nucleus, whereas in 1N2K cells the kinase appeared to localise towards the centre; potentially in the region of spindle mid-zone. This localisation is reminiscent of AUKA in human cells (see section 4.1.1). Localisation of TbAUK2 could not be observed by SIM in 2N2K cells, which could be due to the localisation becoming more diffuse, perhaps as it is no longer required to perform functions during this cell cycle stage. These data may be consistent with the observation that TbAUK2 appears absent in ~9-10% of the G1 population. Potentially these cells could be in early G1, suggesting a more limited absence of AUKs from human G1 cells. Furthermore, in PCF cells, when TbAUK2 was endogenously tagged (C-terminally with YFP), the same absence of localisation was observed in a small percentage of cells (personal communication, B. Akiyoshi, University of Oxford). As cells progress through the cell cycle, the signal of TbAUK2 appears to peak significantly in 1N2K cells (cells which are entering into G2 and mitosis). Taken together, these data indicate TbAUK2 re-localises during the cell cycle in ways distinct from TbAUK1, providing further evidence for discrete functions.

Under genotoxic stress, no obvious re-localisation of TbAUK2 occurred, though the pattern appeared to be more dispersed, suggesting TbAUK2 does not re-localise to form specific foci in response to damage like RAD51, BRCA2 or γ H2AX (Trenaman et al. 2013; Glover & Horn 2012; Dobson et al. 2011). However co-localisation studies with these markers are required to test this inference.

4.10.5 Identification of TbAUK2 interactors may guide functional analysis

Aurora kinases have a plethora of distinct interaction partners (section 4.1.1; as reviewed by Samudio & Vélez, 2015). To date, many common interaction partners of Aurora kinases have yet to be identified as interaction partners of TbAUK2, including TbATM, TbATR and TbBRCA2. Indeed, it is notable that

TbAUK1 interacts with two potentially novel factors in the CPC (Li et al., 2008). Here, we made a preliminary attempt to ask if common or novel factors interact with TbAUK2, using anti-myc IP from the TbAUK2^{+/-12myc} cell line. No canonical interaction partners of aurora kinases were identified in a small sample of five of the proteins identified by mass spectroscopy. As no validation of interactions was performed, these must be treated with caution. Nevertheless, two proteins appeared to be connected with cellular metabolism and may be worthy of follow up analyses.

RuvB helicases are members of the AAA+ family of ATPases. Humans have two: RuvBL1 (also known as Pontin; TIP49a) and RuvBL2 (also known as Reptin; TIP49b); *T. brucei* also appears to express two (Tb927.4.1270 and Tb927.4.2000), the latter of which is a candidate TbAUK2 interactor. No work has examined RuvB function in kinetoplastids. In human cells, RuvBL1 and 2 form a complex. Loss of RuvBL1 is fatal, with cells displaying chromosomal segregation abnormalities (Gentili et al. 2015), and loss of RuvBL2 is associated with decondensation of chromosomes after mitosis (Magalska et al. 2016). Recently, RuvBL1 was shown to co-localise with and be phosphorylated by the kinase PLK1 (Gentili et al. 2015), a prominent substrate of AUKA. Additionally, RuvBL1/2 shows a dynamic localisation: RuvBL1 translocates to the mitotic spindle and to intracellular bridges that form during cytokinesis, while RuvBL2 localises at the midbody between cells and in the nucleus (Gentili et al. 2015). To date, no interaction of AUKs and RuvBL helicases has been shown, but our observation may suggest this occurs and could be conserved. The second protein shows homology to ubiquitin ligases (E3s) and possesses a Zinc finger domain. Regulation of aurora kinase activity through degradation by ubiquitination is extensively cited as the mechanism by which their cell cycle expression is controlled (as reviewed by Lindon et al., 2016).

4.10.6 A preliminary model of TbAUK2 function in BSF cells

Figures 4-27 and 4-28 provide a summary of the findings in this chapter, modelling the localisation and potential roles of TbAUK2 in BSF *T. brucei*. Firstly, TbAUK2 in a dividing cell appears to localise at S-G2 phases as potential foci distributed throughout the nucleus. When the cells enter into G2-M, the localisation appears to focus at the centre of the nucleus, though still as a

punctate pattern. When the cell enters mitosis, and proceeds to cytokinesis, the localisation becomes weaker, suggesting a reduced level of the kinase. Finally, just following cytokinesis, in the new 'daughter' cells (1N1K) localisation of TbAUK2 cannot be detected.

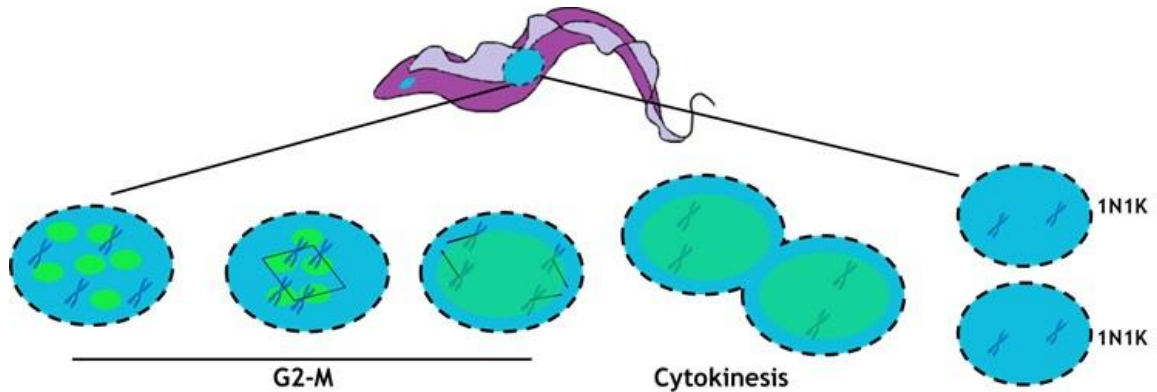


Figure 4-28: Dynamic localisation of TbAUK2 in BSF cells

A description of the figure is given in the accompanying text. Localisation of TbAUK2 is represented by green dots. Not to scale.

Secondly, when TbAUK2 is absent, gross morphological defects arise in a subpopulation of cells. Why some cells appear normal remains unclear, but if loss of TbAUK2 can be compensated by another kinase some cells might form a spindle normally, segregate the genetic material and proceed to cytokinesis, generating two daughter cells that maintain the population. However, when a mutant BSF cell enters S-phase, potentially several defects can occur. If cells fail to form a spindle (or have spindle defects), the cells miss-segregate their chromosomes; this effect may be exacerbated if a mitotic spindle checkpoint fails to signal and nuclear aberrancies are not detected. When the aberrant cells enter G2/M, further abnormalities may develop, as suggested by the appearance of nuclear 'blebs', intra-nuclear membranes, incorrectly sized nuclei and large, swollen multinucleated cells. Again, if there is mitosis checkpoint failure, aberrant nuclei and aberrant chromosome segregation may not be detected, with cells arising from mitosis with abnormal nuclear DNA content and abnormal or absent nuclei. The fates of these defective cells are unknown, but it is likely most will die, though some may enter a new nuclear S-phase, accounting for multinucleated cells.

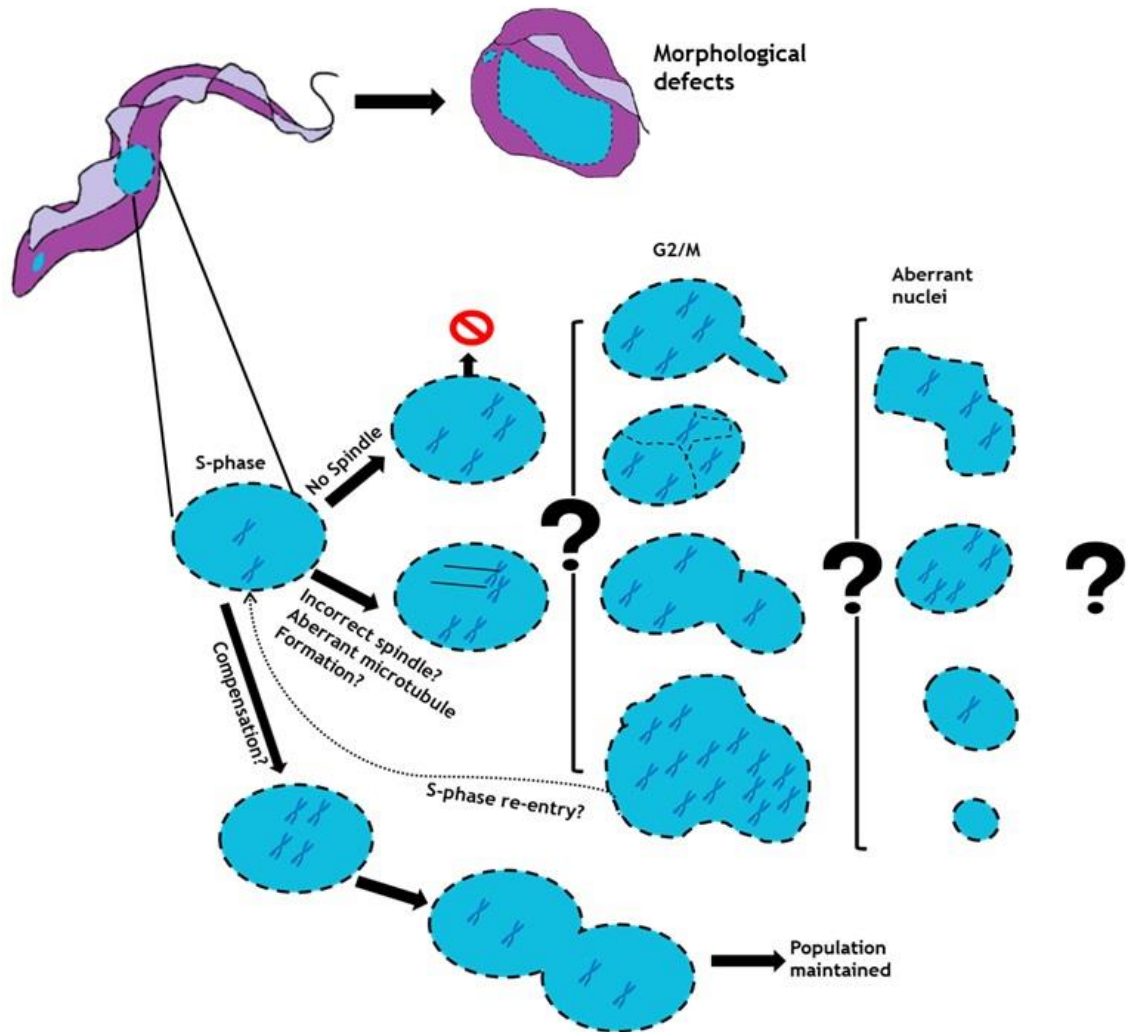


Figure 4-29: Loss of TbAUK2 is associated with cell cycle defects
 An explanation of this figure is discussed in the text above. Question marks highlight areas of biology still to be uncovered. Not to scale.

5 Tb6560 is a pseudokinase that acts in bloodstream form endocytosis

5.1 Introduction

This chapter describes functional analysis of Tb927.9.6560, one of the protein kinases validated as displaying sensitivity to MMS in chapter 3. To provide context to the findings, an introduction to trypanosomatid endocytosis is provided below (see section 1.4.1.1), as is a discussion of pseudokinases (refer to section 1.5.2.1). Tb927.9.6560 is currently annotated as a NAK pseudokinase (Jones et al. 2014; Parsons et al. 2005) though additional sequence analysis will be described (section 5.3.1) that explored this annotation further. From herein, the protein was referred to as Tb6560 and all putative cell lines required for the analysis of this protein are named accordingly.

5.1.1 Numb Associated Kinases (NAKs)

The *D. melanogaster* NAK (the first described Numb Associated Kinase), is an S/T protein kinase (PK), which interacts with the protein Numb (Chien et al. 1998) via the Numb phosphotyrosine binding domain (PTB), ultimately mediating asymmetric division of *Drosophila* sensory cells (Frise et al. 1996). NAK also interacts with the α -adaptin subunit of the AP2 complex (Santolini et al. 2000; Peng et al. 2009) in human cells, permitting Numb to regulate Notch signalling (an evolutionary conserved method of cellular communication; reviewed by Bray, 2006; Guruharsha, Kankel, & Artavanis-Tsakonas, 2012). Thus, Notch signalling in one *D. melanogaster* daughter cell (Frise et al. 1996) is repressed and subsequently promotes asymmetric division. To date, Notch signalling has only been described in metazoans.

5.1.1.1 The AP2 Complex and endocytosis

The AP2 complex is a stable heterotetrameric adaptor complex found in most metazoans (Faini et al. 2013), which functions during clathrin mediated endocytosis (CME) internalisation of cargo via clathrin coated pits (CCPs) and clathrin coated vesicles (CCVs). The complex is comprised of four subunits, or 'adaptins', linked by flexible polypeptide linkers known as 'ear' domains. Targeting of the complex is thought to occur first by an interaction between the α subunit and phosphoinositides from the membrane bilayer. Subsequently, the complex undergoes a significant conformational change (Collins et al. 2002; Jackson et al. 2010) and phosphorylation by a NAK kinase (section 5.1.1.2) to

permit the binding of specific peptide motifs (such as Yxx ϕ and [DE]xxxL[LIM]; Kelly et al. 2008,), which are expressed on incoming cargo (for example, the transmembrane transferrin receptor protein or the major histocompatibility complex class II). The AP2 complex performs a variety of functions to aid cargo internalisation via CCVs. The β 2 subunit can directly bind the clathrin heavy chain, thus contributing to the assembly of CCVs and their internalisation. Clathrin and the AP2 complex also aid the development of CCP curvature and invagination (Figure 5-1). Once the cargo is secured in the CCP, the pit internalises and is separated (by scission) from the plasma membrane, a reaction often mediated by Dynamin (a large GTPase; Cocucci, Gaudin, & Kirchhausen, 2014; Praefcke & McMahon, 2004). Next, the clathrin coat of the internalised vesicle is disassembled via the AP2 complex, which interacts with proteins including another NAK kinase known as GAK/Auxillin which in turn interacts with the heatshock protein 70 (Hsp70) required for CCV disassembly ((Umeda et al. 2000). The complex is then removed by a dephosphorylation (by the aforementioned NAK kinase) reaction mediated by Rab5 (a small GTPase; Semerdjieva et al. 2008) to permit progression of the CCV into the endocytic pathway. Now, the vesicle can enter the endosomal pathway, for example in the case of phosphoinositides (PI; important cellular signalling molecules (Shin et al. 2005).

Sorting of cargo by the endosome pathway is a multifaceted process relying on sorting signals in the form of pH gradients, geometry of endosomal vesicles, signals from the cargo itself and other post-translational modifications (reviewed by (Gruenberg 2001; Elkin et al. 2016). For example, early endosomes have a pH range of ~6.5-5.5 and are composed of either tubular-like structures (for recycling, ~pH 6.5) or larger, spherical vesicles (for degradation, ~ pH 5.5). Receptors from the cell surface often harbour ligands that are degraded at a higher pH and accumulate due to the large surface area of the tubular endosomes. Here, these proteins are then rapidly trafficked back to the cell surface for export. Ligands dissociating at lower pH are predominantly targeted for degradation in the lysosomes or targeted for further sorting and modification in the *trans*-golgi network (TGN). Other sorting signals, such as ubiquitinated cargo, can be recognised and sorted via the endosomal sorting complexes

required for transport (ESCRT) machinery (reviewed by Henne, Buchkovich, & Emr, 2011).

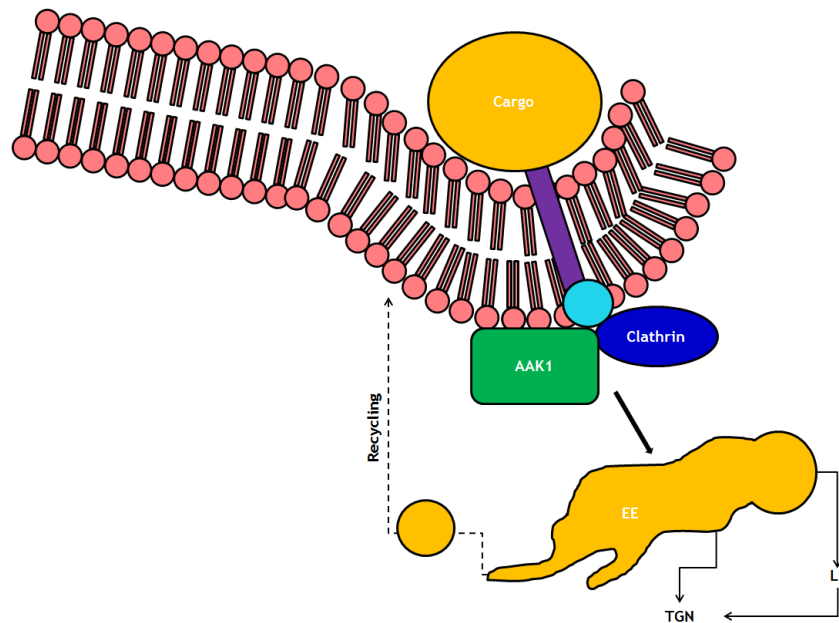


Figure 5-1: Internalisation of cargo mediated by the AP2 complex.

Cargo (orange circle) is internalised by invagination of the lipid bilayer through the action of AAK1 (green rectangle) in conjunction with the AP2 complex (pale blue circle and a peptide signal (purple rectangle). A fuller description of this process is presented in the text, but internalisation leads to the cargo to the EE (Early Endosome), LE (Late Endosome) and TGN (*trans*-golgi Network). Diagram constructed based on data from (Gruenberg 2001; Elkin et al. 2016).

5.1.1.2 NAKs in humans

Humans have four NAK kinases: adaptor associated kinase 1 (AAK1), BMP-2-inducible kinase (BIKE/BMP2K), myristoylated and palmitoylated serine/threonine kinase 1 (MPSK1; also known as STK16, PKL12 and Krct) and cyclin G associated kinase (GAK, also auxillin 2; Smythe & Ayscough, 2003; Sorrell, Szklarz, Abdul Azeez, Elkins, & Knapp, 2016). These S/T kinases act primarily to control components of the endocytosis pathway. Generally, these kinases show little structural conservation outwith their kinase domain region; for example, AAK1 (accession number: NP_055726.3) shows ~ 76% identity within the N-terminal region harbouring the kinase domain to BMP-2 (accession number: NP_942595.1) though overall harbours only ~50% identity across the whole protein sequence.

The roles of the NAKs in humans overlap. For example, BMP-2 was shown to both associate with CCVs (as determined by SILAC analysis) and co-localised with the

AP2 complex (Borner et al. 2012). GAK harbours a J-domain, which can interact and regulate 70 kDa heat shock proteins (Umeda et al. 2000; Walsh et al. 2004; Zhang et al. 2005), whose activity is linked to functions such as disassembly of the clathrin coat (reviewed by Eisenberg & Greene, 2007; Xing et al., 2010). Additionally, the GAK harbours a clathrin binding domain (Park et al. 2015) and may be required to facilitate assembly of both AP2 and accumulation at the plasma membrane and the Golgi (Korolchuk & Banting 2002; Zhang et al. 2005; Lee et al. 2005). MSPK1 is the least understood, only showing a distant relationship to the other NAK kinases. MSPK1 localises to the Golgi and may both regulate the activity of a GTPase (Eswaran et al. 2008) and aid during cargo sorting within the secretory network (Striz, Bernad, & Tuma, 2014).

The final human NAK (AAK1) is a well-established co-ordinator of endocytosis (Smythe & Ayscough 2003) and regulator of Numb protein activity (Sorensen & Conner 2008). AAK1, which localises to CCPs, binds the AP2 complex and phosphorylates (in a clathrin modulated manner; Conner & Schmid, 2003) the $\mu 2$ subunit to enhance AP2 affinity for membrane bound sorting signals and to promote signal tethering to CCPs (Jackson et al. 2003); without AAK1 phosphorylation, uptake of molecules such as transferrin (Conner & Schmid 2003) is blocked. In addition, uptake of the Flavivirus Hepatitis C (HCV) is also mediated by phosphorylation of the $\mu 2$ subunit by AAK1 (Neveu et al. 2015), further supporting the important role this kinase plays during endocytosis.

5.1.2 Previous reports of Tb6560 in the literature

In 2005, Tb6560 was identified as encoding a potential pseudokinase (Parsons et al. 2005) due to the presence of conserved pseudokinase-like motifs in the sequence (see section 1.5.1.3 and section 1.5.2.1). In 2014, a kinome-wide RNAi screen demonstrated that downregulation of Tb6560 slowed cell proliferation of *in vitro* BSF parasites (Jones et al. 2014); no further characterisation was undertaken. In 2015, Tb6560 was identified as part of a screen aiming to identify protein components of stress granules (Fritz et al., 2015). Tb6560 was not found in stress granules but, upon serum starvation of in PCF cells, the protein (visualised by a C-terminal YFP tag) localised towards the posterior end of the parasite close to the flagellar pocket (FP); the functionality of the tagged variant was not confirmed nor was any further characterisation undertaken.

5.2 Research Aims

Knockdown of Tb6560 in BSF cells affected cell proliferation and sensitivity to MMS (chapter 3). The aim of this chapter was to determine the role of Tb6560 by generating knockout mutants and by localising the protein in BSF parasites.

5.3 Results

5.3.1 Bioinformatics Analysis

Differences in sequence were observed when the predicted protein sequences of Tb6560 from the sequenced strains of *T. brucei* (Lister 427 and TREU 927) were compared (as shown in chapter 8, section 8.4, Figure 8-18). The work in this chapter utilised the gene information from TREU 927 (accession number Tb6560; TriTrypDB.org, v28). This gene is predicted to encode a protein 80.2 kDa in size (726 amino acids).

5.3.1.1 BLAST analysis of Tb6560

To attempt to identify a potential homolog of the protein outwith the kinetoplastid phylum, the predicted protein sequence of Tb6560 was retrieved from TriTrypDB.org (V.28) and analysed using the BLASTp algorithm (BLOSUM62; version; BLASTp2.3.1; <http://blast.ncbi.nlm.nih.gov/Blast.cgi>). The sequence was 'BLASTed' against all non-redundant (nr) protein sequences available in the NCBI database (Li et al. 2013) and analysed using the 'SmartBLAST' feature (NCBI; currently under development) as described in section 2.1.2.

The top 'five' hits (including the original reference sequence) are shown in Table 5-1. The top hits are specific to the kinetoplastid phylum, of which all were hypothetical proteins. A further protein of unknown function, but with much lower sequence similarity, was also identified in the amoeboid organism *Dictyostelium discoideum*.

Name of Protein	Species	Query cover (%)	E-value	Identity (%)	Accession Number
Protein kinase	<i>T. b. brucei</i> TREU 927	95	0.0	100	XP_827022.1
Protein kinase, putative	<i>T. b. gambiense</i> DAL972	95	0.0	92	XP_011776542.1
Putative protein kinase	<i>T. congolense</i> IL3000	99	0.0	59	CCC92831.1
Protein kinase, putative	<i>L. donovani</i>	84	4e-139	40	XP_003859605.1
Hypothetical protein DDB G0280111	<i>D. discoideum</i> AX4	35	2e-28	28	XP_641248.1

Table 5-1: Top five SmartBLAST ‘hits’ for Tb6560 in the NCBI database (<http://www.ncbi.nlm.nih.gov/>). All data was recovered in June 2016.

When a wider range of BLASTp ‘hits’ were examined (Table 5-3), the Tb6560 protein showed sequence similarity to AP2 associated proteins: *H. sapiens* AP2 associated protein kinase 1 or AAK1 (30% identity; [E-value = $2e^{-24}$]), the Ppk29 kinase in *S. pombe* (33% identity; [E-value = $1e^{-22}$]), a Numb associated kinase in *D. melanogaster* (28% identity; [E-value = $1e^{-20}$]) and to a group of protein kinases known as ‘NAKs’ in plants and yeasts (for example, the putative NAK protein kinase in *Rhizopus microsporus*; 30% identity; [E-value = $1e^{-22}$]). In all cases, the sequence homology revealed by SmartBLAST did not cover all the polypeptide and appeared instead to be predominantly within the N-terminal kinase domain region.

Name of Protein	Species	Query cover (%)	E-value	Identity (%)	Accession Number
AP2-associated protein kinase 1 isoform X1	<i>D. rerio</i>	35	2e-24	29	XP_005167369.1
AP2-associated protein kinase 1	<i>H. sapiens</i>	33	2e-24	30	NP_055726.3
AP2 associated protein kinase 1 isoform X2	<i>M. musculus</i>	32	4e-24	30	XP_006506255.1
Ark1/Prk1 family protein kinase Ppk29	<i>S. pombe 972h-</i>	28	1e-22	33	NP_596027.1
Numb-associated kinase isoform A	<i>D. melanogaster</i>	32	1e-20	28	NP_477165.1
AP2-associated protein kinase 1 isoform X2	<i>D. rerio</i>	35	2e-24	29	XP_005167370.1
AP2-associated protein kinase 1 isoform X3`	<i>D. rerio</i>	35	4e-24	29	XP_697452.5
AP2-associated protein kinase 1 isoform X4	<i>D. rerio</i>	35	4e-24	29	XP_005167372.1
AP2 associated protein kinase 1 isoform 1	<i>M. musculus</i>	32	4e-24	30	NP_001035195.1
AP2 associated protein kinase 1 isoform X1	<i>M. musculus</i>	33	4e-24	30	XP_006506254.1
AP2 associated protein kinase 1 isoform X5	<i>D. rerio</i>	35	4e-24	29	XP_005167373.1
AP2 associated protein kinase 1 isoform 2	<i>M. musculus</i>	33	6e-24	30	NP_808430.2
BMP-2-inducible protein kinase	<i>M. musculus</i>	36	4e-21	27	NP_542439.1

Table 5-2: Additional SmartBLAST ‘hits’ for Tb6560. Several duplicate ‘hits’ were removed from this analysis. Accession numbers and the data above were correct as of June 2016 when this data was collected.

The predominance of predicted mouse AAK1 and BMP-2 proteins amongst the ‘hits’ suggests Tb6560 does indeed encode a NAK-related kinase. Indeed, when the protein sequence of *H. sapiens* AAK1 (NP_055726.3) was analysed by the SmartBLAST function (following a BLASTp analysis), the hypothetical *L. donovani* protein (XP_003859605.1; table 5-1) was revealed (31% identity; E value = $8e^{-30}$), which is a likely kinetoplastid ortholog of Tb6560 (Table 5-1; see below).

To examine the NAK homology further, the predicted protein sequence of Tb6560 was aligned to the protein sequences of *H. sapiens* AAK1 (NP_055726.3), *M. musculus* AP2 associated protein kinase isoform 1 (NP_j001035195.1) and *S. pombe* Ppk29 (NP_596027.1) in CLC genomics Workbench 7 (for a detailed alignment see chapter 8, section 8.4, Figure 8-19). Primarily, a higher degree of conservation was observed within the N-termini of each protein, where the

predicted kinase domain is located. The greatest conservation of the kinase domain is consistent with sequence comparisons of the human NAK kinases, where the C-termini are variable (Sorrell et al. 2016).

Beyond the kinase domain, several important motifs can be identified in AP2 associated protein kinases: a DPF motif (for α adaptin interactions; Owen et al., 1999), a DLL motif (for clathrin binding; Morgan, Prasad, Hao, Augustine, & Lafer, 2000) and an NPF motif (for EH domain interactions; de Beer et al., 2000). All of these motifs potentially co-ordinate interactions required during clathrin-mediated endocytosis. The protein sequence of Tb6560 was compared with AAK1 (NP_055726.3) to test for the presence of each motif, though none were convincingly identified with the exception of a 'DPF' motif at position 719-721 in the C-terminus (Figure 5-2). Retention of the DPF motif may indicate Tb6560 interacts with an adaptin-like protein (Owen et al. 1999), but whether the absence of the other motifs indicates divergence in wider interactions is unclear. AAK1 has a characteristic N-terminal G-rich region (of unknown function); this was also absent in the Tb6560 sequence. However, a C-terminal Q-rich region could be observed in the *T. brucei* sequence, in addition to a poly-alanine motif. Both of these features can be seen in the human AAK1 protein sequence, though their biological significance is unknown. No additional domains could be identified using Interpro protein domain analysis, but the generalised schematic of motif and domain conservation between AAK1 and Tb6560 (Figure 5-2) suggests broadly related functions.

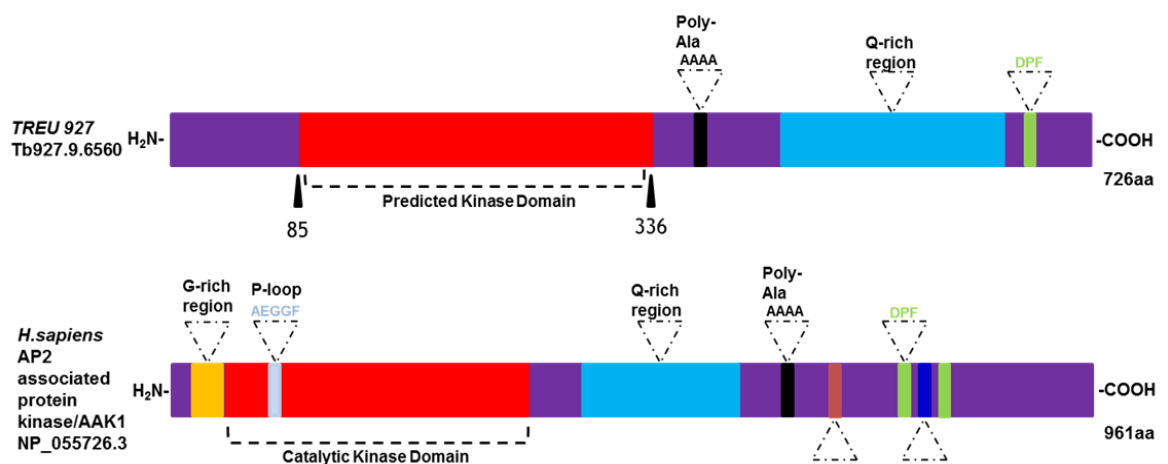


Figure 5-2: Schematic illustration of conserved motifs and domains in human AAK1 and Tb6560

The polypeptide sequences of *H. sapiens* AAK1 and Tb6560 are shown in purple, and predicted numbers of amino acids (aa) indicated. Not to scale. Conserved sequence motifs of AAK1 are annotated as dotted triangles and coloured blocks, while the larger kinase domain is shown as a red block. Positions of the domain and motifs, and their potential conservation in Tb6560, were determined using Interpro (<http://www.ebi.ac.uk/interpro/>).

The structure of Tb6560 was also predicted using the RaptorX protein structure and function predictor portal (Källberg et al. 2012). The results of this analysis are shown in Figure 5-3. The recently solved crystal structures of human AAK1 and BMP-2 (Sorrell et al. 2016) were used to model the predicted protein structure of Tb6560 with high confidence ($p = 5.54e^{-10}$ and $p = 3.9 e^{-9}$), further supporting the hypothesis that Tb6560 may harbour similarities to these two NAK kinases. The mouse PK38 structure ($p = 3.7e^{-9}$) was also used as a high confidence model in conjunction with the two NAK kinase models to predict the structure of this protein. The N-terminal region of Tb6560, including the predicted kinase domain, appears to be comprised predominantly of α helices with a small arrangement of β sheets towards the C-terminus. In contrast, the modelling suggests considerable disorder at the C-terminus, though whether this might adopt a more ordered structure when bound to interacting factors is unclear.

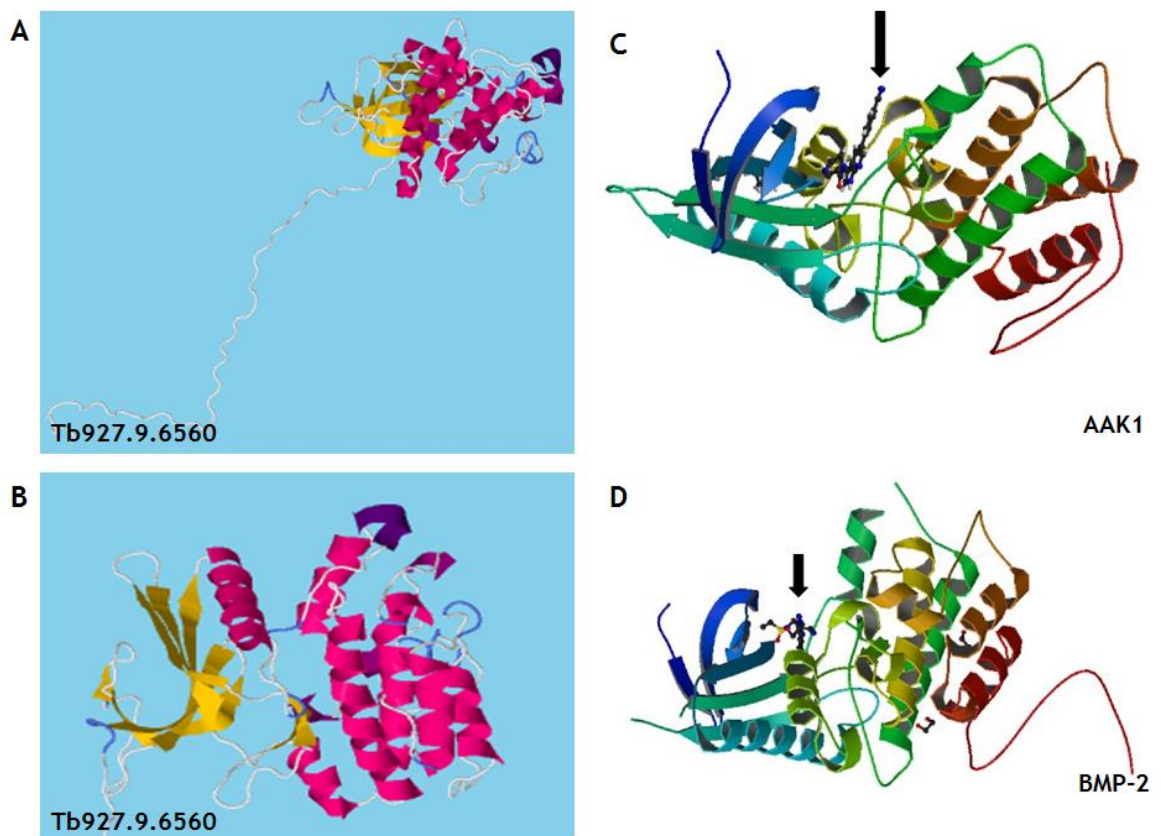


Figure 5-3: Tb6560 shows structural similarity to two human NAK kinases
 (A+B) Predicted 3D structural model of the Tb6560 protein using the RaptorX web portal (<http://raptorx.uchicago.edu/>), as performed on the 28-6-2016, showing the complete protein (A) and the more ordered N-terminus (B). Structural prediction was modelled on the crystal structures of AAK1 (PDB ID: 514qA), BMP-2 (PDB ID: 4w9xA), and PK38 (*M. musculus*; PDB ID: 4bfmA) all of which are available in the PDB. The better template was 514qA, which was modelled with high confidence ($5.54e-10$). ~46% of the residues were modelled; the other 54 % were predicted as regions of disorder (long tail in A). Yellow (β sheet), Pink+ Purple (α helix). (C) Schematic illustration of the 3D crystal structure of the human kinase AAK1 complexed with an AAK1 dual inhibitor (LKB1; indicated by the black arrow; PDB ID: 5L4Q). (D) Schematic illustration of the 3D crystal structure of the human kinase BMP2K complexed with baricitinib (indicated by the black arrow; PDB ID: 4W9xA). (C+D) 3D structure images retrieved from the PDB. Crystal structure determined by (Sorrell et al. 2016) (C and D). Coloured according PDB colouring. Structures orientated from N-terminus to C-terminus (left to right) where possible.

5.3.1.2 Tb6560 is a pseudokinase

When the sequence of Tb6560 was examined, several key kinase-associated motifs were absent. To illustrate this, the predicted sequence of Tb6560 was aligned against a canonical (and known active) protein human kinase (c-Src) using the Kinase Sequence Database (KSD). The alignment is shown in Figure 5-4 (for a complete alignment refer to chapter 8, section 8.4, Figure 8-19). No GxGxxG motif, which is required for ATP binding, could be detected, and nor could an 'HRD' motif that is required to stabilise the orientation of ATP in the pocket; instead, the protein had an 'HRN' motif, suggesting a non-synonymous

mutation found in several pseudokinases (reviewed by Reiterer, Eysers, & Farhan, 2014). Finally, the ‘DFG’ motif required for magnesium binding was also absent, and replaced with an ‘NFR’ motif. Only an APE motif (found at the end of kinase activation loops in eukaryotes) was identified. Taken together, and despite the generalised homology of Tb6560 with NAKs in the kinase domain, this analysis suggests it is unlikely Tb6560 could function as an active kinase, given the absence of so many core kinase functional motifs.

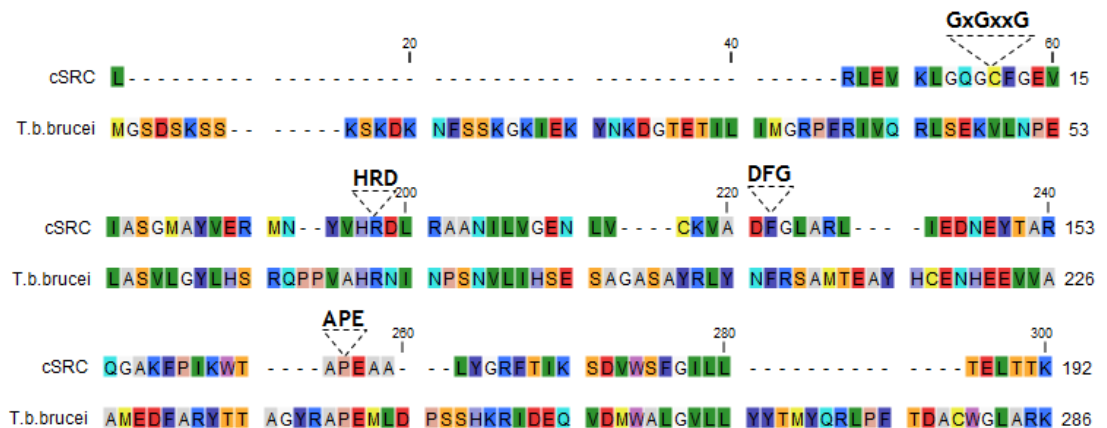


Figure 5-4: Tb6560 lacks conserved kinase associated sequence motifs

The protein sequences of Tb6560 (retrieved from TriTrypDB, v28; referred to as *T.b.brucei* on the diagram) and c-Src (GenBank ID 125711) were aligned in CLC Genomics Workbench 7. The dashed triangles mark sequence motifs GxGxxG, HRD, DFG in c-SRC.

The sequence of Tb6560 was next compared with related kinetoplastid proteins using the protein BLAST function available on TriTrypDB.org to examine whether its orthologues are also predicted pseudokinases, and indeed this was the case (a sequence alignment of the orthologues of Tb6560 in *T. cruzi*, *L. mexicana*, *L. major* and *T. evansi* is shown in chapter 8, section 8.4, Figure 8-20). All kinetoplastid proteins presented high sequence conservation in their N-terminal ends and highly divergent C-terminal regions. However, all kinetoplastid orthologues appeared to lack kinase specific motifs noted to be absent in Tb6560, suggesting the evolution of this protein as a pseudokinase arose in the ancestor of these parasites.

5.3.2 Generation of Tb6560 knockout cell lines

From 48 hours after RNAi, cells with reduced Tb6560 levels showed a small reduction in growth *in vitro* (chapter 3 in which this protein is referred to as Tb927.9.6560) and aberrant cells could also be observed in the population

(chapter 3 section 3.3.5.1). As RNAi-mediated loss of this gene product did not appear lethal, knockout cell lines (lacking both alleles of the gene) were generated to probe the role of this protein further.

Figure 5-5 details the regions of Tb6560 used for homology-driven recombination required to generate disruption cell lines.



Figure 5-5: Schematic illustration of homology regions required for Tb6560 knockout
 A region of the 5'UTR (including part of the Open Reading Frame (ORF) and a region of the 3'UTR (Untranslated Region, and including part of the ORF) were amplified by PCR (black arrows show primer positions in the genome). The primer numbers are highlighted in brackets beside the expected fragment sizes for the two PCR products; bp (base pairs). The amplified regions were cloned into knockout vectors (as per section 2.4.1.2). Primer sequences are available in section 2.4.1.3. Not to scale.

5.3.2.1 Gene knockout strategy

Disruption of the Tb6560 ORF (deleting 1832 bp, from amino acids 50 to 610) was achieved sequentially through two rounds of transformation into wild type (WT) BSF *T. brucei* Lister 427 cells. Cells were first transformed with the construct $\Delta 927.9.6560::\text{NEO}$ and G418 resistant clones selected (section 2.7.4) to produce putative heterozygote (+/-) cell lines. One validated clone (Tb6560^{+/-}) was chosen for a second round of transformation with the construct $\Delta 927.9.6560::\text{BSD}$ and blasticidin clonal transformants selected. At this stage, the selective antibiotics were removed from the media due to the slowing of growth observed in the presence of G418 (data not shown).

5.3.2.2 Integration of knockout constructs and confirmation of knockout cell lines by PCR analysis

Putative Tb6560^{+/-} cell lines were confirmed by diagnostic PCR analysis using gDNA extracted from the transformants (section 2.2.1). The strategy employed and the agarose gels confirming integration are shown in Figure 5-6 (Putative +/- cell lines are shown in chapter 8, section 8.4, Figure 8-21). The analysis confirmed integration of both constructs into the knockout cell lines, since PCR products of the expected size were generated linking both antibiotic ORFs and flanking gene sequence. In addition, absence of the intact gene in the -/- clones

was demonstrated by the lack of amplification of a 337 bp fragment within the deleted portion of the Tb6560 ORF. Two $-/-$ clones were analysed in all further analysis (referred to as Tb6560 $^{-/-}$ CL1, and Tb6560 $^{-/-}$ CL2).

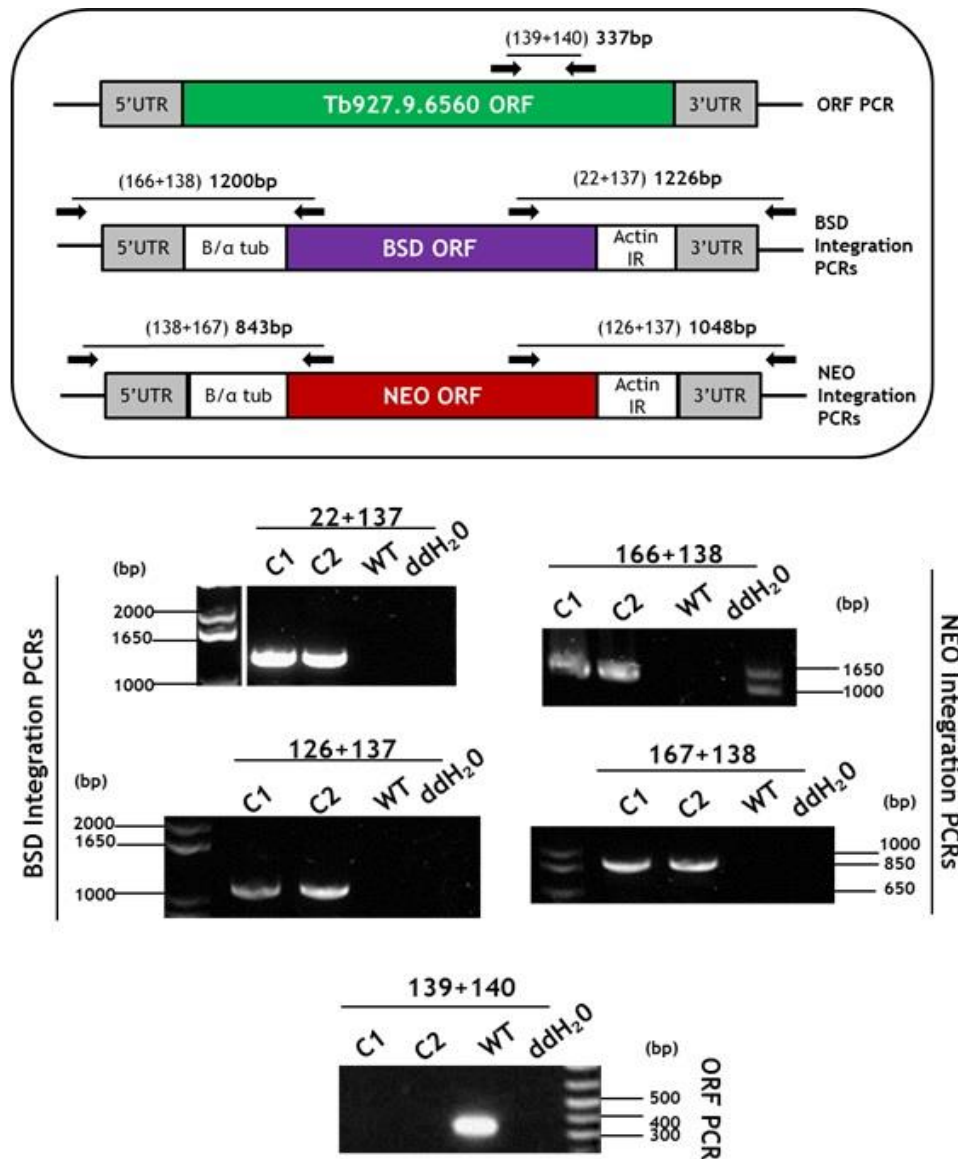


Figure 5-6: PCR analysis of putative Tb6560 null mutant clones

(Top) Schematic illustration of expected fragment sizes amplified by PCR (bp), diagnostic primers used (black arrows) and their position in the genome. Primer sequences are available in section 2.4.1.2. Not to scale. (Below) Agarose gels of diagnostic integration PCRs, which were performed using the primer pairs detailed in A (testing for integration of NEO or BSD, or testing for the presence of intact ORF) using gDNA from two $-/-$ clones (CL1, CL2), wild type (WT) cells, or using double distilled water (ddH₂O) as a negative control. All PCRs were performed on the same gDNA samples. NEO (Neomycin), BSD (Blasticidin), B/ α tub (Beta/Alpha Tubulin), Actin IR (Actin intergenic region), gDNA (genomic DNA). For each gel, size markers are shown (bp).

5.3.2.3 Verification of knockout clones using qRT PCR analysis

In addition to PCR analysis, qRT-PCR analysis was performed on cDNA to test for expression of Tb6560 RNA transcripts. Total RNA was extracted from WT, +/- and -/- cell lines as described in section 2.5.1 and cDNA generated as per section 2.5.2. To control for the presence of undigested gDNA, a second reaction lacking the reverse transcriptase (-RT) enzyme was set up for each sample; gDNA contamination could not be detected in any of the samples by qRT-PCR analysis (data not shown). Primers suitable for qRT-PCR were designed and optimised as described in section 2.5.3.1 (primer sequences are available aforementioned section). The graph below (Figure 5-7) shows the RNA levels of the Tb6560 gene in each sample relative to the WT RNA levels (normalised to actin), expressed as a percentage. As partial recovery of some phenotypes was observed after prolonged passage of the knockout cell lines (see below), RNA was harvested at passage 2 (P2; ~1 week in culture after transformation) and passage 13 (P13; ~3 weeks in culture) to ensure the recovery could not be attributed to outgrowth of non-mutants cells from a non-clonal population. Relative to WT cells, the Tb6560^{+/-} cell line showed ~55% expression Tb6560 transcript, whereas in both knockout clones (and at both the early and late passage), no RNA transcript could be detected.

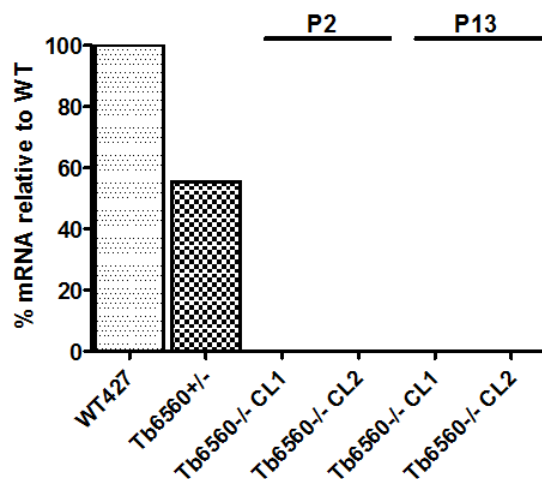


Figure 5-7: Confirmation of Tb6560 knockout clones by qRT-PCR
qRT-PCR analysis was performed as described in section 2.5.3.2. RNA transcript levels in both knockout clones (-/- CL1 and -/- CL2) and the Tb6560^{+/-} cell line are shown as a percentage of RNA relative to the levels observed in wild type (WT) cells. The graph represents average data from one experiment, which was performed as a technical triplicate.

5.3.3 Phenotypic analysis of Tb6560 null mutant cell lines

5.3.3.1 Growth and DAPI cell cycle analysis *in vitro*

Since viable knockout mutants were generated, Tb6560 is not essential for the survival of BSF *T.brucei* cells *in vitro*. Nonetheless, following knockdown of Tb6560, the cells grew more slowly and a small population appeared morphologically aberrant (see chapter 3). To understand if these phenotypes are also seen in null mutants that lack all Tb6560 protein, the growth of both knockout clones was assessed relative to WT and Tb6560^{+/-} cells (as described in section 2.8.2). This data is shown in Figure 5-8. No selective drugs were added to the medium to ensure any growth effects could not be attributed to the presence of antibiotic.

Growth of the heterozygote cell line was not significantly affected when compared to WT cells. In contrast, a significant reduction in growth rate was observed in both knockout clones (Figure 5-8 A and B). Though both knockout clones reached approximately the same maximum cell density as WT and +/- cells, this was delayed (~72 hrs for the knockout clones, compared with ~48 hrs for WT cells), indicating increased population doubling times (with approximate doubling times of 9 - 10 hrs for Tb9650 CL1 and 8 - 9 hrs for Tb6560 CL2 compared with 7 - 8 hrs for the WT427 parental cell line; calculated as described in section 2.7.4). When continually passaged in culture for over 3 weeks, the growth impediment appeared to recover, at least in part (data not shown). Given this, all subsequent assays were performed using cells within the 3 weeks from stabilate retrieval.

To ask whether the reduced proliferation of the -/- cells could be attributed to disruption of the cell cycle, cells were prepared for indirect immunofluorescence (IF, as described in section 2.11.2) with α -KMX1 antiserum (to visualise tubulin) and stained with DAPI (to visualise nDNA and kDNA). DAPI staining allowed the cell cycle stage of individual cells within the cell populations to be assessed (as per section 2.8.3) and these data represented in Figure 5-8 C and representative images shown in Figure 5-8 D. Any cell that did not conform to the normal cell cycle categories (1N1K, 1N2K, 2N2K) was simply classified as 'other' for this analysis. In comparison to WT cells, no significant

difference in cell cycle distribution was observed in the +/- cell line; in both cases, only a very small percentage of aberrant cells were seen. For both knockout clones, a significant increase in 'other' cells was observed (~20 % of the population), which was associated with a decrease in the proportion of 1N1K and 1N2K cells; no obvious change in numbers of 2N2K cells was apparent. These 'other' cells were classified as such based on their nuclear number alone. Generally, the nDNA stained by DAPI appeared smaller and less rounded than was observed in WT cells, and was also potentially fainter (as observed by eye), perhaps suggesting a lower content of nDNA or altered chromatin packing. Additionally, clearly defined kDNA signal appeared to be undetectable in some cells, either indicating that kDNA was absent or that the nDNA signal masked the kDNA signal as a result of shape distortion. Though these data may be interpreted as an altered cell cycle, the morphology of the -/- cells was also affected (this is further investigated in section 5.5 below) and in some rounded cells clear nDNA and kDNA signals could be discerned (Figure 5-8 D). Though the cells were simply stained with tubulin to determine the gross structure of the cell, it is clear that the typical trypomastigote shape has become lost in the absence of this protein; however, no clear loss of tubulin could be observed suggesting Tb6560 is unlikely to play a role in the formation of the parasite's tubulin network. Based on the data presented below, it seems likely that the apparent changes in cell cycle suggested by the increased levels of 'other' cells may be most simply explained by wider changes in cell morphology, rather than by changes in nDNA or kDNA replication, meaning that loss of Tb6560 does not primarily affect the cell cycle.

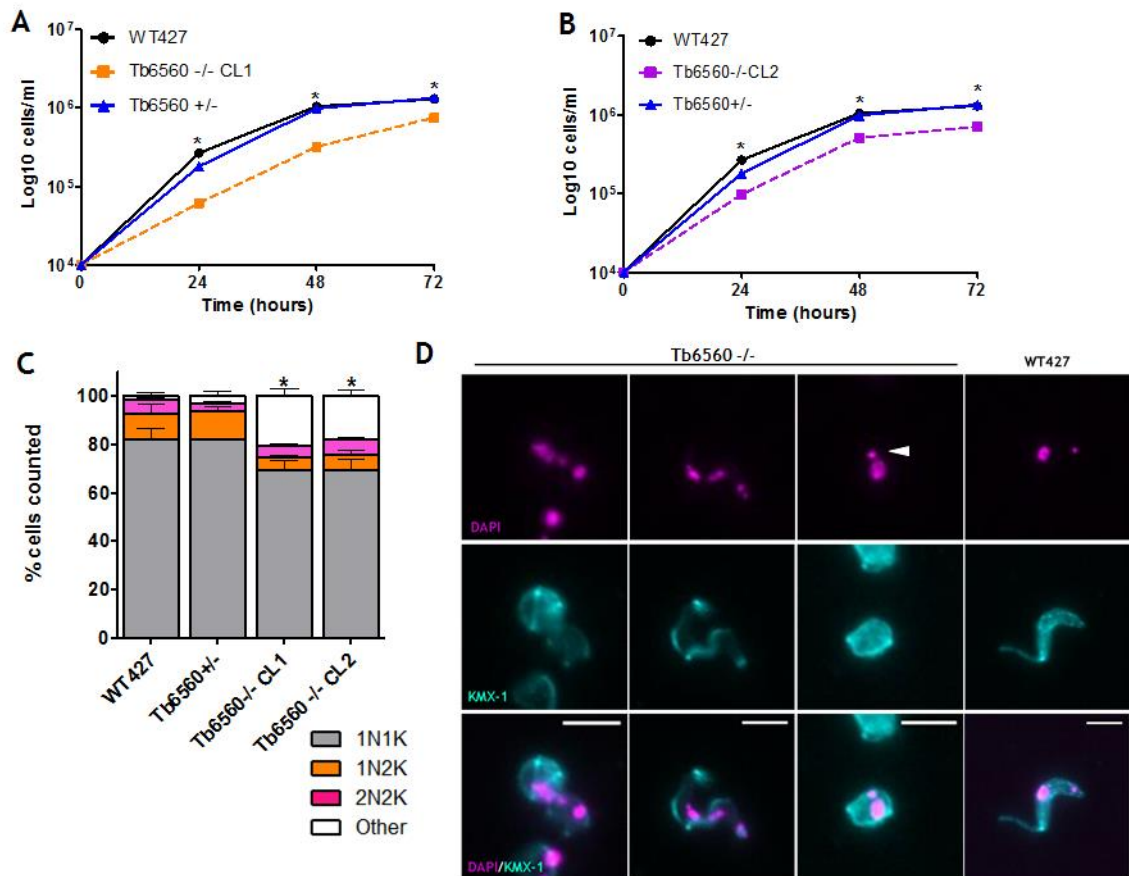


Figure 5-8: *In vitro* growth analysis of Tb6560 null mutant cell lines

(A) *In vitro* growth curves. Error bars show \pm SEM (n=3). Statistical significance was calculated to compare the density of WT cells at each individual time point to the corresponding null mutant clone (CL1 or CL2; A and B) using a Mann Whitney U test (one tailed); (*) = $p < 0.05$. (B) Cell cycle analysis *in vitro*. Cells were stained with DAPI and the number of 1N1K, 1N2K, 2N2K and 'other' cells were counted and expressed as a percentage of the total population (for each cell line over 200 cells were counted per experiment). Error bars represent \pm SEM (n=3). Significance was calculated by comparing 'other' cells from WT individually with 'other' cells from each knockout clone using a Mann Whitney U test (one tailed); (*) = $p < 0.05$. (D) Representative IF images of -/- 'other' cells, as well as a cell with rounded morphology but discrete single nDNA and kDNA staining (arrowed). The cells were stained with DAPI (to visualise the nDNA and kDNA; magenta) and KMX-1 antiserum (to visualise β tubulin; cyan). A 1N1K WT cell is show as an example of the most frequent nDNA and kDNA configuration. Images were captured on an Axioskop2 (Zeiss) and processed as per section 2.11.8 in ImageJ. Scale bar = 5 μ m.

5.3.4 Localisation of Tb6560

In previous work, Fritz et al., 2015) have shown that YFP-tagged Tb6560 localises to the posterior of PCF *T. brucei* cells. To ask if this is true also in BSF cells, and to investigate this localisation further, we set out to endogenously tag the protein in heterozygote cells, allowing the functionality of the tagged variant to be assessed.

5.3.4.1 Generation of a $Tb6560^{+/-12myc}$ cell line

The endogenous tagging strategy employed is as described in section 2.4.1.1.1. The construct generated ($Tb6560^{12myc}$) permits C-terminal tagging of the endogenous gene with 12 copies of the myc epitope when transformed into WT cells (section 2.4.1.1.1). To evaluate functionality the knockout construct $\Delta 927.9.6560::NEO$ was then transformed into putatively endogenously tagged cell lines, meaning the only expressed copy of the protein should be 12myc tagged.

5.3.4.2 Confirmation of a $Tb6560^{+/-12myc}$ cell line

To confirm the generation of a $Tb6560^{+/-12myc}$ cell line, gDNA was harvested from putative clones (section 2.2.1) and three independent PCRs performed to confirm integration of the $\Delta 927.9.6560::NEO$ knockout construct into the genome; gDNA from WT cells and ddH₂O were used as a controls to account for any contamination. Figure 5-9 A shows location of the primers in the genome, and the expected sizes of the PCRs. The integration PCRs are shown in Figure 5-9 B below. Both constructs appeared to be correctly integrated into the parasite genome as evident from the presence of fragments of the expected size amplifying from each clone.

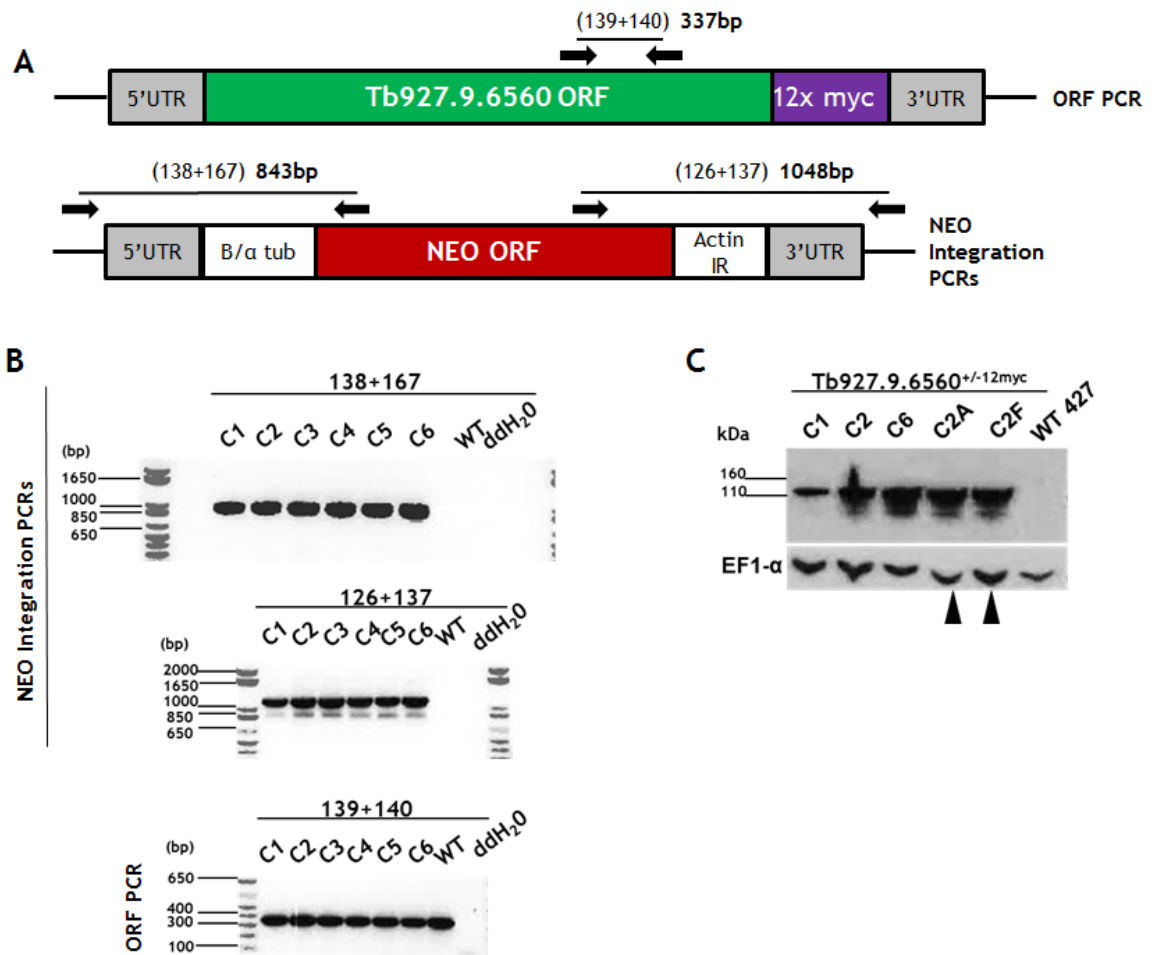


Figure 5-9: Confirmation of Tb6560^{+/-12myc} clones

(A) Schematic illustration of expected PCR fragment sizes in bold beside which the primers (for sequences refer to Table 2-3 used are detailed in brackets. Black arrows = primer localisation in the genome. Not to scale. (B) Integration PCRs. Images show integration of the Δ927.9.6560::NEO construct into endogenously tagged clones. PCRs were all performed on the same gDNA with ddH₂O was used as a negative control. NEO (Neomycin), BSD (Blasticidin), B/α tub (Beta/Alpha Tubulin), Actin IR (Actin intergenic region), WT (Wild type), gDNA (genomic DNA), ddH₂O (double distilled water). Sizes shown (kb plus ladder; bp). (C) Confirmation of endogenously tagged Tb6560^{+/-12myc} cell lines by western blot analysis. Whole cell extracts were separated by electrophoresis, blotted and the membranes probed with α myc antiserum (to detect the myc epitope) and α EF1α antiserum (as a loading control). The black arrows represent the two clones chosen for further analysis.

All clones correctly integrated the knockout construct into the genomic locus. Furthermore, the Tb6560 ORF could still be detected in all clones. To test for expression of the 12myc tagged protein, whole cell extracts were prepared from each clone and a western blot analysis performed (section 2.12.1; Figure 5-9 C). A band of ~110 kDa was observed in each clone, which is a higher molecular weight than expected (the predicted size is 94.6 kDa; 80.2 kDa endogenous polypeptide + 14.4 kDa myc tag). However, the same size protein was seen in the Tb6560^{12mycRNAi} cells and when the RNAi against Tb6560 was induced, the signal on the western was ablated, arguing the protein detected is in fact

endogenously 12myc tagged Tb6560 (see section 3.3.3.4). Two clones were chosen and expanded for further experiments; Tb927.9.6560^{+/-12myc} CL1 (C2A) and Tb927.9.6560^{+/-12myc} CL2 (C2F). Both clones were derived from the original clone Tb6560^{+/-12myc} C2.

5.3.4.3 *In vitro* growth of the Tb6560^{+/-12myc} cell lines

To confirm functionality of the tagged variant, the growth of both Tb6560^{+/-12myc} clones was examined and compared with WT, Tb6560^{+/-} and Tb6560^{-/-} CL2 cells (section 2.8.2). As depicted in Figure 5-10, no significant proliferation defects, comparable with that seen for the -/- cells were observed in either clone relative to WT or Tb6560^{+/-} cells, suggesting the endogenous tag does not hinder gene function.

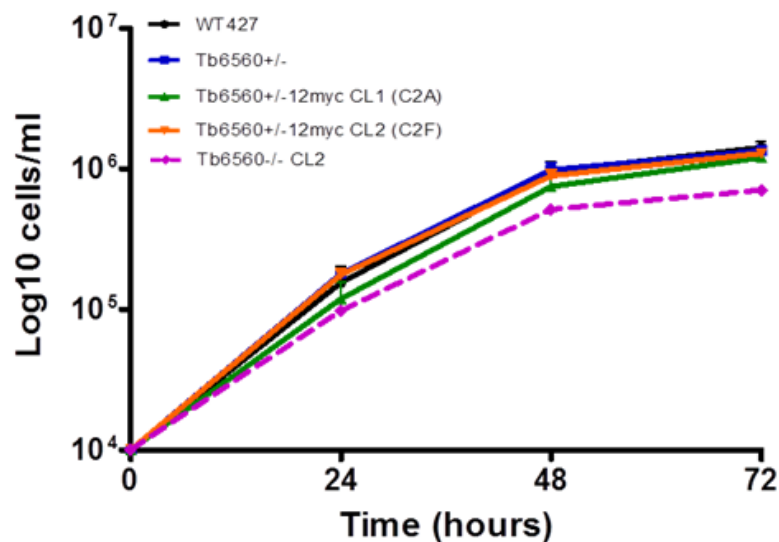


Figure 5-10: *In vitro* growth analysis of Tb6560^{+/-12myc} cell lines
Growth of Tb6560^{+/-12myc} cell lines (CL1 and CL2) was assessed as described in section relative to WT, Tb6560^{+/-} and the Tb6560^{-/-} C2. No significant differences were observed relative to the WT cells. At 48 hours, the growth of the Tb6560^{-/-} cell line was significantly reduced when compared to both Tb6560^{+/-12myc} CL1 and CL2 clones ($p < 0.05$, Mann-Whitney U test). Error bars represent \pm SEM, $n=3$.

5.3.4.4 Tb927.9.6560 localises to the posterior end of the parasite

From the study performed by Fritz and colleagues, Tb6560-YFP was found to localise at the posterior end of PCF cells (Fritz et al. 2015) only under stress conditions. In contrast, the results presented here suggest constitutive localisation in BSF cells under routine *in vitro* culture conditions.

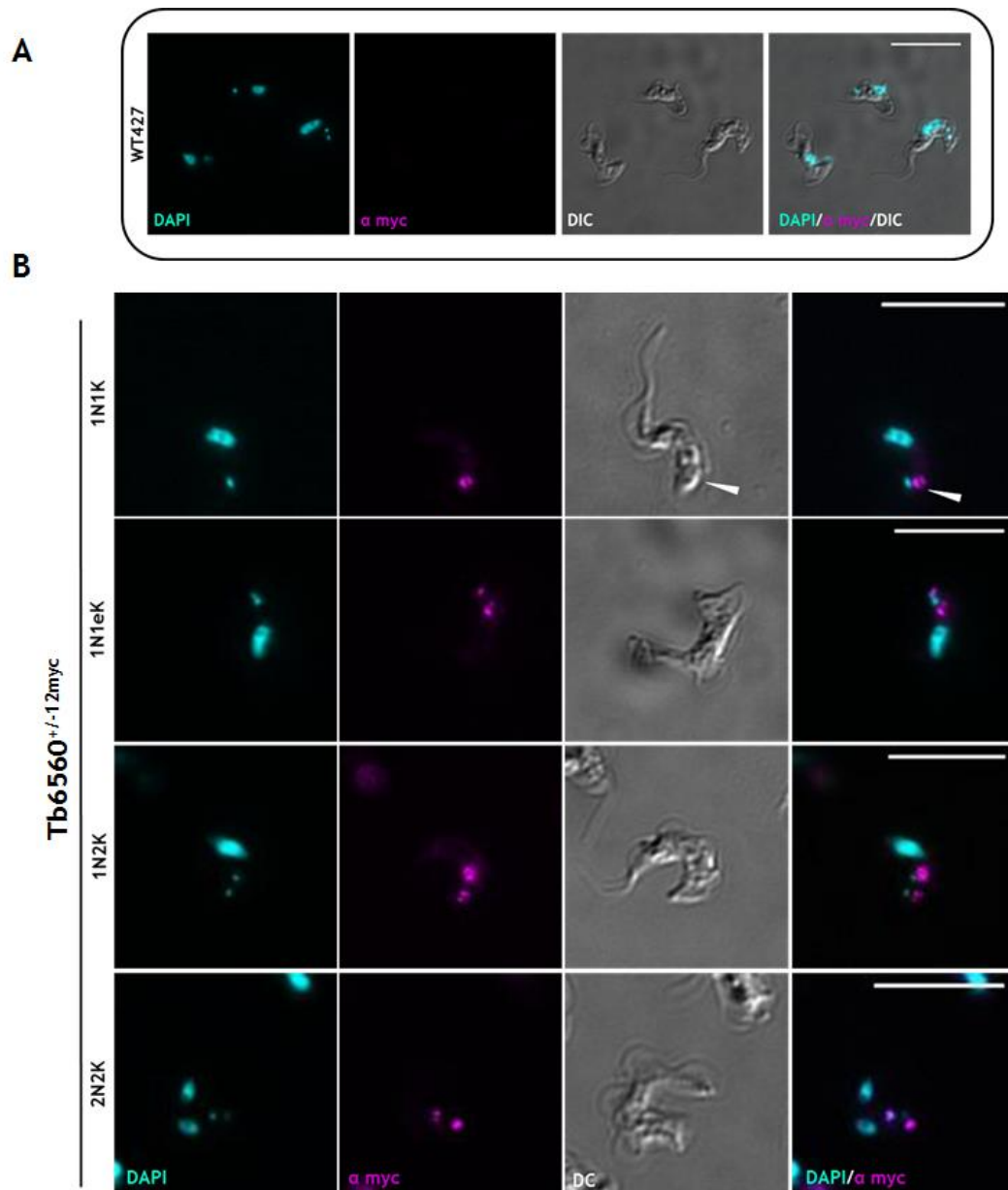


Figure 5-11: Tb6560 localises to the posterior end of the parasite

Cells were fixed as per section 2.11.2 and probed with α myc antiserum (to visualise the myc epitope; magenta) and DAPI (to visualise the nDNA and kDNA; cyan). The cell body was visualised by Differential interference contrast (DIC) microscopy. Representative images of WT control cells (A) and of the localisation of Tb6560 in 1N1K, 1N1eK, 1N2K and 2N2K cells (B). Images were captured on an Axioskop2 (Zeiss) and images processed as per section 2.11.8 using ImageJ. Scale bar represents 10 μ m. Images are from Tb6560^{+/-12myc} CL1.

To determine the localisation of 12myc-tagged Tb6560 indirect IF was performed as per section 2.11.2 using α -myc antiserum. To evaluate subcellular localisation through the cell cycle, nDNA and kDNA were visualised by DAPI and the cell body was visualised by DC imaging. Both tagged clones were examined in this manner with equivalent results, and so images are shown for just one clone (Figure 5-11). In addition, WT cells were examined to control for any non-specific antibody binding and background fluorescence. Discrete anti-myc signal could be

localised in 100 % of cells and across all cell cycle stages (Figure 5-11). In all cases the signal was at the posterior end of the cell and was close to, but did not overlap with, the kDNA. Strikingly, the 'focal' signal followed the process of kDNA division. In cells in which the kDNA was replicated and dividing, but had not yet undergone segregation (1N1eK cells), two anti-myc foci could be detected around the kDNA. In 1N2K cells (where the kDNA has segregated but nuclear mitosis has not occurred), anti-myc signal was seen adjacent to each kDNA. Intriguingly, in both cases the anti-myc foci appeared to be unequal in size. Finally, in 2N2K cells that have undergone mitosis but not cytokinesis, two clear and perhaps more equally sized anti-myc foci were seen beside each kDNA. These data indicate a pronounced and discrete localisation of Tb6560 near the kDNA and, furthermore, suggest the protein associates with a structure (or structures) whose division precedes division of the kDNA and may develop unequally. As a result, the data may suggest the pseudokinase could be a component of the basal body, the flagellar pocket collar and/ or the flagellar pocket, each of which are found in this part of the cell.

Attempts to co-localise Tb6560 with TbBIBLO-1 were undertaken, in order to begin to address the potential association of the pseudokinase with one of these structures (data not shown). However, this proved unsuccessful. TbBIBLO-1 is embedded in the cytoskeleton as a core component of the FPC (Florimond et al. 2015) and, as such, requires removal of the cell membrane for visualisation. In these conditions, Tb6560 localisation was lost (chapter 8, section 8.4, Figure 8-22). Though the reasons for this finding were not tested further, it may suggest the protein membrane associated and may not be part of the FPC.

5.3.4.5 Super resolution analysis and 3D reconstruction of Tb6560 localisation

To further analyse the localisation pattern of Tb6560, super resolution structural illuminated microscopy (SR-SIM) was undertaken and 3D images were generated.

As most markers available for the FP and FPC required cytoskeletal extracts to be prepared, a dual staining was performed to detect the C-terminally 12myc tagged Tb6560 protein and the single mitochondrion of the cell in order to establish a more accurate localisation in the absence of such markers. Cells were

first labelled for 15 mins (at 37°C) with Mitotracker® (as per section 2.11.3) prior to fixation, and an IF with α -myc antiserum and staining with DAPI performed (as per section 2.11.2). Mitotracker® (in its reduced form) is taken up by actively respiring cells, in which the dye becomes oxidised and sequesters into the mitochondrion. Representative images are shown in Figure 5-12.

SR-SIM revealed that the anti-myc foci observed previously adopted a more defined localisation in the cell, with the signal in 1N1K arranged in a 'horse-shoe' like shape around the kDNA. In some cases, the signal appeared almost to be a ring with greater intensity at one side, whereas in other images it appeared to be an arrangement of foci at the anterior end of the kDNA. These data suggest localisation of Tb6560 may be more dynamic than static. Indeed, dynamic localisation was confirmed depending on the cell cycle stage and reflecting the earlier IF (Figure 5-11). Cells undergoing kinetoplast S-phase (1N1eK) had two spatially distinct arrangements of the protein at either end of the dividing kinetoplast. In all cases, the anterior end of the kinetoplast appeared to harbour a larger concentration of the protein, where the 'horse-shoe' shaped appearance could be seen. The other, posterior end appeared to harbour a lower (but still punctate) concentration of the protein. In cells that had divided the kinetoplast (1N2K cell), the signal reflected the protein localisation in 1N1eK cells, with a greater intensity and more pronounced horseshoe shape near one kDNA compared with the other. Once the nDNA and kDNA had both divided (2N2K cell), the protein localisation became a more defined 'horse-shoe' shape adjacent to each kDNA, with a more similar signal intensity at each (Figure 5-12 B), suggesting equalisation of the concentration of the protein in close proximity to the daughter kinetoplasts.

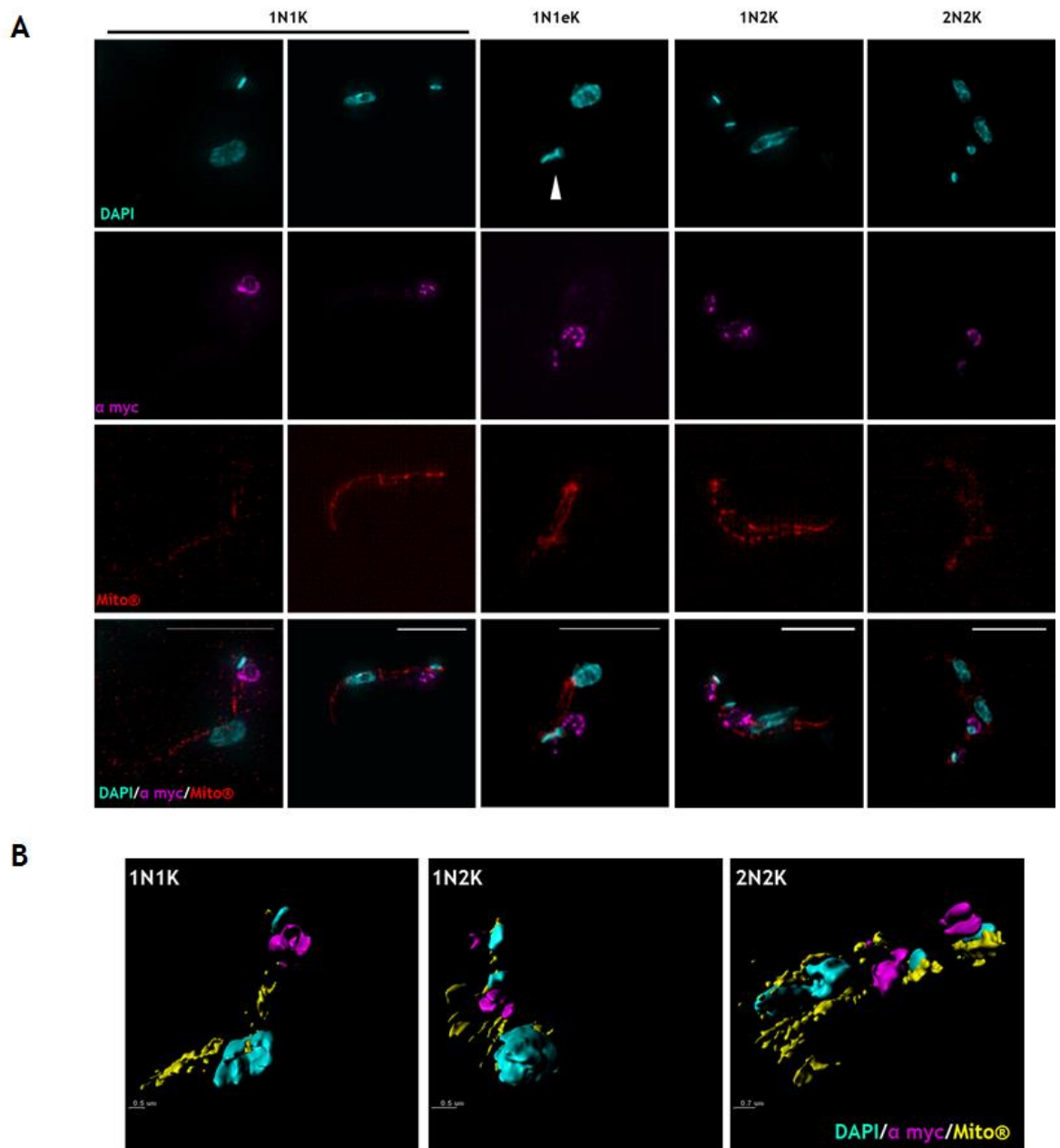


Figure 5-12: Super resolution images of Tb6560 localisation

(A) $Tb6560^{+/-12myc}$ cells were stained with Mitotracker® prior to fixation. Top panel: nDNA and kDNA stained with DAPI (cyan). Second panel: $Tb6560^{+/-12myc}$ stained with anti-myc (magenta). Third panel: mitochondrion stained with Mitotracker® (red). Bottom panel: Merged image of DAPI, myc and Mitotracker®. Scale bar represents 5 μ m. (B) 3D reconstructions of Tb6560 localisation. The images were generated from super resolution stack images captured on an Elyra (Zeiss) super resolution microscope. 3D images were generated using IMARIS software (<http://www.bitplane.com/imaris/imaris>; V.8.2). Scale bars (from left to right) = 0.5 μ m, 0.5 μ m and 0.7 μ m. Image on the right (scale bar = 1 μ m). Images are of $Tb6560^{+/-12myc}$. The images above were captured under the supervision of L. Lemgruber Soares.

Taken together, these data verify that Tb6560 has a dynamic, cell cycle-dependent localisation. This dynamism appears distinct from that of TbBILBO-1 (Florimond et al. 2015), suggesting the pseudokinase may not be a component of the FPC, but may instead be associated with the FP, the endosomal system or an

unanticipated structure. However, whether the protein accumulates in such regions in response to a particular signal, such as stress (Fritz et al. 2015), is not tested by this approach.

5.3.4.6 ImmunoGold® labelling of Tb6560

ImmunoGold® labelling was next performed on the Tb6560^{+/-12myc} cell line to further probe the localisation pattern of the pseudokinase. Cells were fixed, stained with α myc antiserum and detected using serotype specific ImmunoGold® particles (10 nm), and processed for TEM imaging (as per sections 2.11.72 and 2.11.73). Representative images are shown in Figure 5-13 A and B.

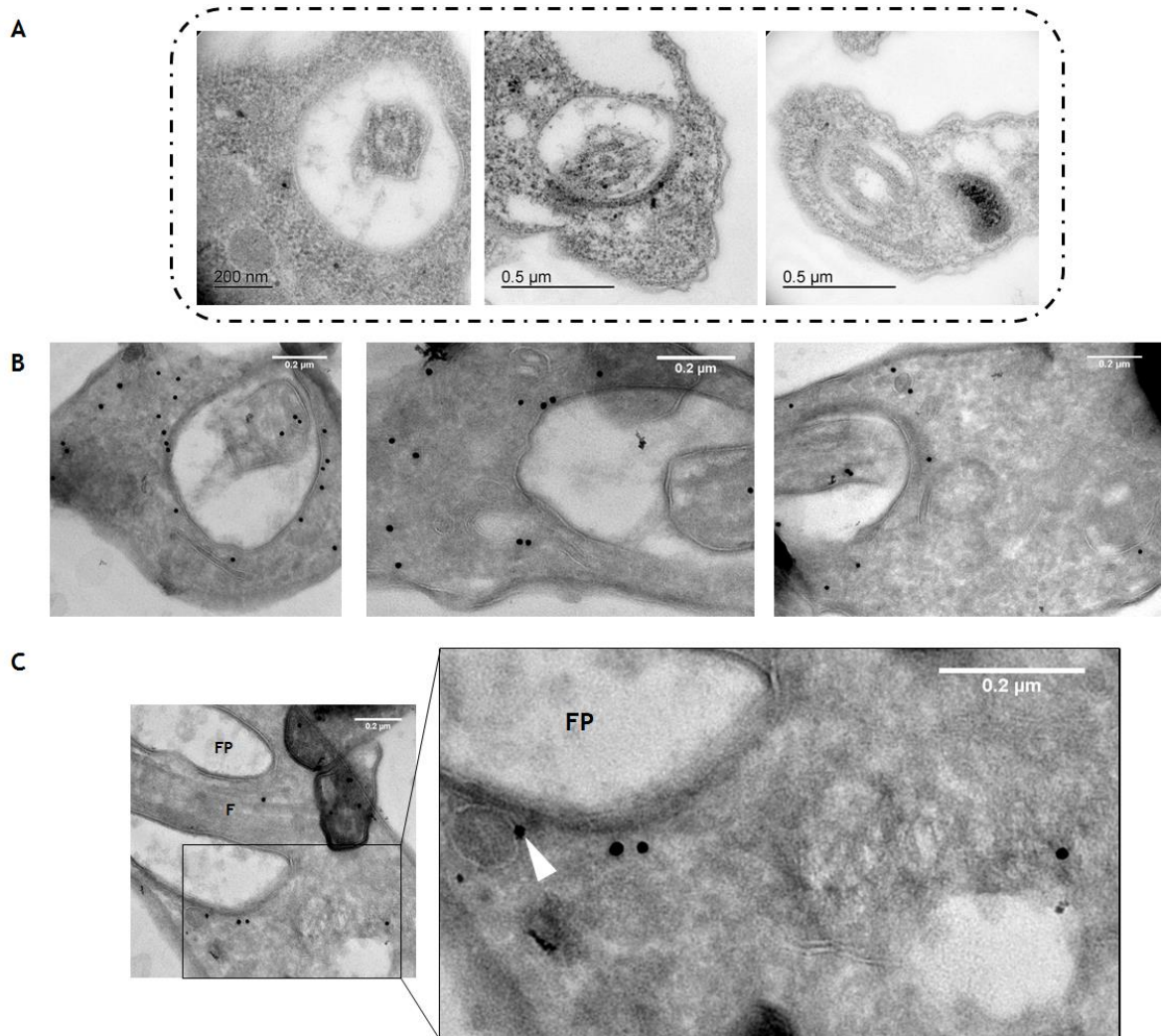


Figure 5-13: Localisation of endogenously tagged Tb6560 by ImmunoGold® labelling
(A) Representative images of WT cells used as a control for non-specific localisation. Scale bars = 200 nm (left image) and 0.5 μ m (middle and right image). **(B)** Representative images of Tb6560 localisation. 12myc-tagged protein was detected using ImmunoGold® particles in three Tb6560^{+/-12myc} CL1 cells **(C)** A representative image of Tb6560^{+/-12myc} localisation with an enlarged section highlighted by the black box. A vesicle associated ImmunoGold® particle is indicated by the white arrow. FP (Flagellar Pocket), F (Flagellum). Images were captured

on an Tecnai T20 EM microscope by TEM by L. Lemgruber-Soares. The scale bar was added in ImageJ = 0.2 μm for all images.

Again, in these experiments most of the anti-myc signal localised to the posterior region of the cell, with a noted proximity to the FP. No clear 'horse-shoe' shaped structure was observed. Instead, the signal appeared more dispersed, with many foci around the FP and with others more distal in the cytoplasm. In several cases where the signal was not at the FP membrane, co-localisation could be detected with membrane-bound structures, some of which appeared to be vesicle-like (Figure 5-13 B). Additionally, localisation could occasionally be observed within the FP and on the flagellum itself. Further images are required for a more in depth analysis of Tb6560 localisation by immunolocalisation.

To summarise, these EM data appear compatible with the indirect IF imaging of Tb6560, suggesting a dynamic localisation in the cell posterior and adjacent to the kDNA, which is often associated with both vesicle structures and the FP membrane.

5.4 Loss of Tb6560 is associated with increased genotoxic stress sensitivity

Knockdown of Tb6560 significantly increased cell sensitivity to MMS (see chapter 3). To examine whether this sensitivity to MMS is also seen in the knockout mutants, and reflects wider sensitivity to other sources of genotoxic stress, the following section describes a series of experiments testing the predicted role of Tb6560 in the response to agents that cause DNA damage.

5.4.1 Tb6560 knockout mutants are sensitised to genotoxic stress *in vitro*

To ask if loss of Tb6560 sensitises *T. brucei* BSF cells to various sources of genotoxic stress, growth was analysed as per section 2.8.2. Cultures were set up (as per section 2.8.2) in media containing a single concentration of MMS, PHL or HU, as well as after exposure to a single dose of UV. Cell growth of the $-/-$ mutants was measured with time and compared with WT and Tb6560^{+/-} cells, and with cells grown in the absence of damage. For simplicity only the WT and -

Δ growth curves are shown in Figure 5-14 A and B, but data for the Tb6560^{+/+} cell line is available in chapter 8, section 8.4, Figure 8-23.

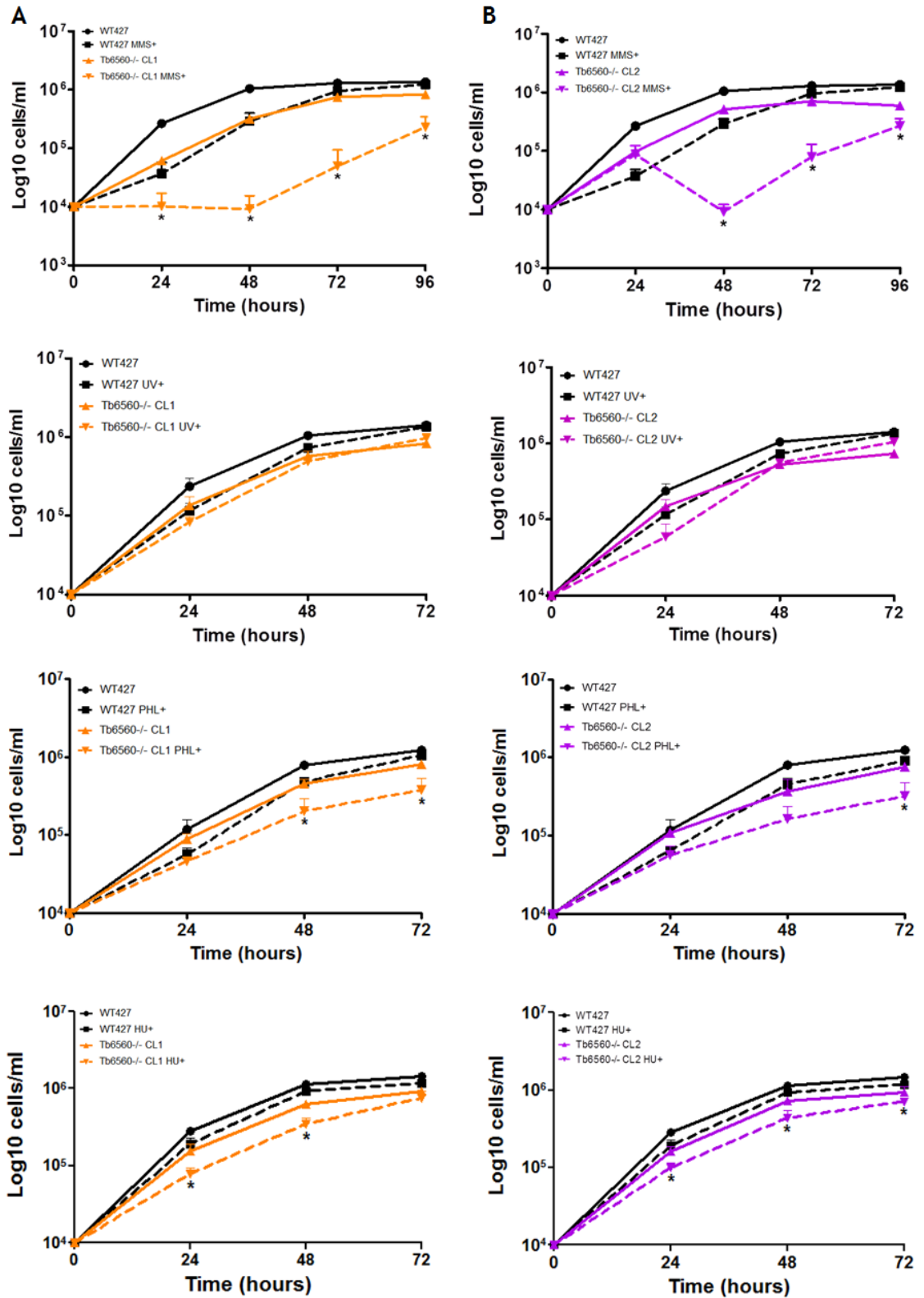


Figure 5-14: *In vitro* growth analysis of Tb6560^{-/-} cells under genotoxic stress
Growth analysis of Tb6560^{-/-} CL1 (A, orange lines) and CL2 (B, pink lines) in the presence (dashed lines) or absence (solid lines) of a variety of genotoxic stress conditions: MMS (0.0003 %), UV (1500 J/m²), PHL (0.1 µg/ml) and HU (0.06 mM). Black lines depict growth of

the WT cells. Error bars represent \pm SEM; n=3. For statistical analysis, WT cells under genotoxic stress at each time point were compared with the corresponding Tb6560^{-/-} cells; (*) = p<0.05 as determined by a Mann Whitney U test.

When exposed each of the aforementioned sources of genotoxic stress, with the exception of UV, growth of the Tb6560^{-/-} clones was significantly reduced. Moreover, and again with the exception of UV, the extent of the growth impairment in the presence of the genotoxic agents was more pronounced in the -/- cells than in WT, arguing that loss of Tb6560 results in increased sensitivity. Exposure to HU and PHL only exaggerated the growth phenotype already exhibited by the null mutant clones and proliferation continued. In contrast, when exposed to MMS growth notably stopped in the mutants for around 48 hrs before resuming, perhaps suggesting greater sensitivity to this treatment. The lack of increased sensitivity of the -/- mutants to UV, which has been shown to cause nuclear damage requiring DNA repair (Machado et al. 2014), indicates Tb6560 does not act in response to all genotoxic agents. In addition, cells exposed to these concentrations of UV, PHL and HU tend to retain recognisable trypan blue morphology (Figure 5-16 and below). In the case of exposure to MMS treatment, though DNA lesions also form the architecture of the cell is more compromised (Figure 5-16). Given the non-nuclear localisation of the pseudokinase, which may be associated with the FP or the endosomal system, the greater sensitivity of the -/- mutants to MMS may be explained by a compromised ability to respond to damage outwith the nucleus.

5.4.2 Loss of Tb6560 is not associated increased γ H2A expression

To test for the presence of genotoxic stress signalling, and to look for evidence of nuclear damage in the mutants, expression of γ H2A was examined by indirect IF analysis. Tb6560^{-/-} and WT cells were harvested at a density of $\sim 5 \times 10^5$ cells/ml, fixed and stained with DAPI (to visualise the nDNA and kDNA) and anti γ H2A antiserum (as per section 2.11.2). Expression of γ H2A was examined by measuring the fluorescence intensity of anti- γ H2A signal in the nuclei of cells (as per section 2.11.8.3). However, when the fluorescence intensity was measured from each Tb6560^{-/-} clone and calculated relative to the WT background level (Figure 5-15), no significant increase in γ H2A levels could be determined (representative images are shown in chapter 8, section 8.4, Figure 8-24). Though

γ H2A can be considered as a general marker of genotoxic stress, primarily expression of γ H2A is triggered in response to direct DNA lesions, such as double strand breaks (DSBs; Kuo & Yang, 2008). Thus, despite the demonstration that $-/-$ mutants display increased sensitivity to genotoxic stress (previous section), the negligible change in nuclear γ H2A levels indicate it is unlikely Tb6560 plays a direct role in the nuclear response to DNA damage.

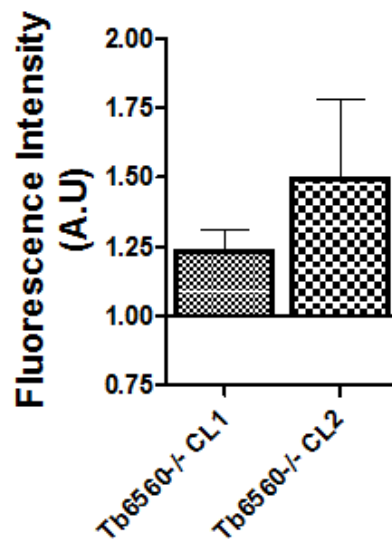


Figure 5-15: Fluorescence intensity quantification of γ H2A expression in Tb6560^{-/-} cell lines
Fluorescence intensity from > 400 nuclei from WT, Tb6560^{-/-}CL1 and Tb6560^{-/-}CL2 cells was measured as per section 2.11.8.3 in ImageJ. The WT fluorescence was arbitrarily assigned a value of 1 and the fold change calculated for each knockout clone relative to the WT level. These values are expressed as arbitrary units (AU). Error bars represent \pm SEM of 4 independent experiments. No significance could be detected using a Wilcoxon matched pairs-signed rank test.

5.4.3 Localisation of Tb6560 following genotoxic stress exposure

To test further if Tb6560 does not play a role in the response to nuclear damage, localisation was examined following exposure to PHL, HU, UV or MMS, asking if the discrete localisation seen in undamaged cells changes, for instance by translocation of the protein to the nucleus.

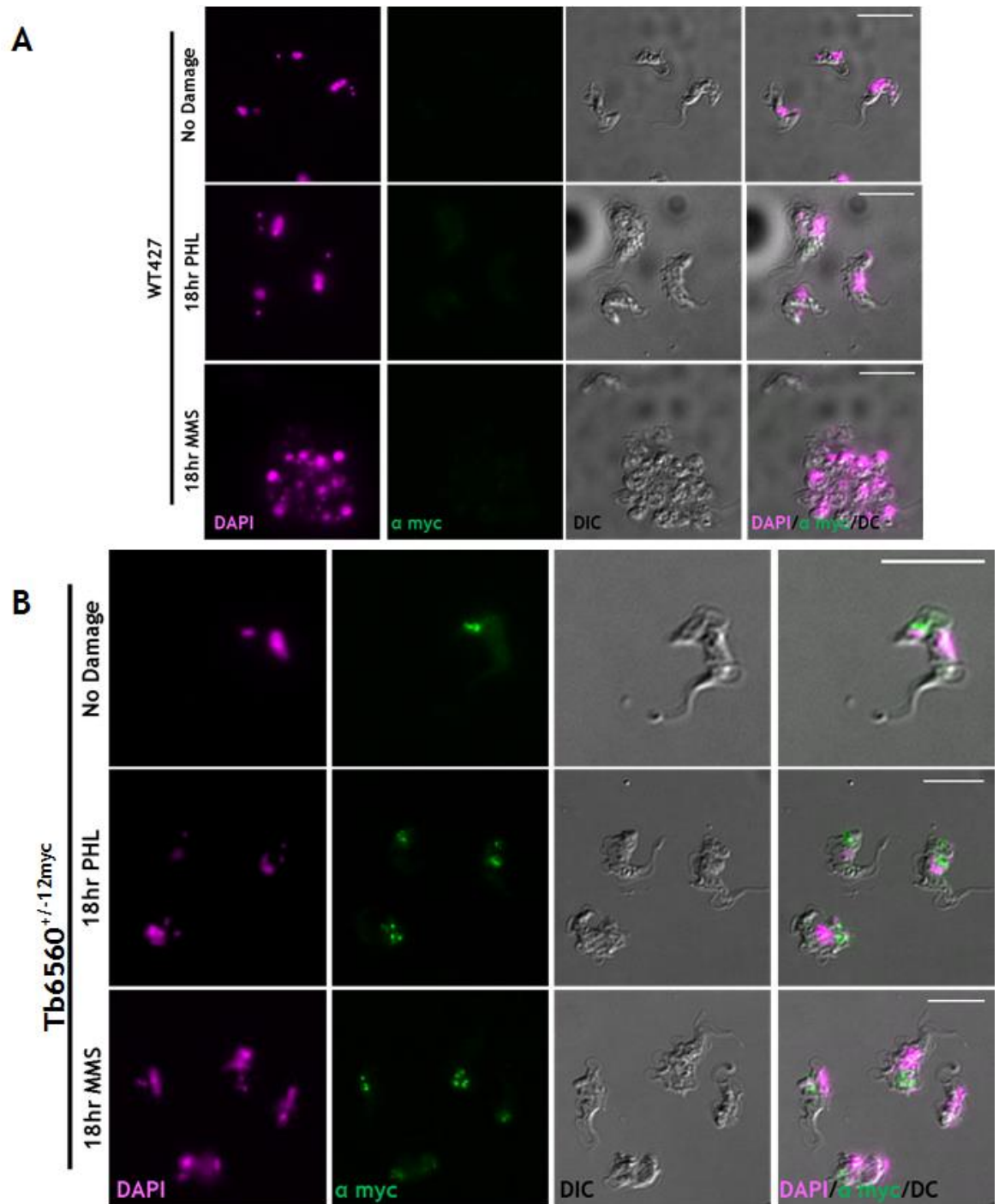


Figure 5-16: Tb6560^{12myc} localisation following DNA damage exposure
 WT427 cells (A) and Tb6560^{+/-12myc} cells (B) were exposed to MMS (0.0003 %) or PHL (1 $\mu\text{g}\cdot\text{ml}^{-1}$) for 18 hrs, fixed and stained as per section 2.11.2. Representative images are shown and were captured on an Axioskop2 (Zeiss) and processed as per section 2.11.8 using ImageJ. Untreated WT and -/- cells are shown for comparison. Scale bar represents 10 μm . Images shown are from Tb6560^{+/-12myc} CL1.

Tb6560^{+/-12myc} cells were exposed to 18 hours of a damaging agent, fixed and an indirect IF analysis was performed (section 2.11.2). The nDNA and kDNA were visualised by DAPI staining, the cell body visualise by DC imaging and the myc tag visualised by α myc antiserum.

Localisation of Tb6560-12myc did not appear to be affected following UV exposure or growth in the presence of HU (images shown in chapter 8, section 8.4, Figure 8-25). Following PHL and MMS exposure, localisation of the anti-myc signal around the kDNA was also comparable to that of the untreated control cells, though after PHL exposure often a larger region of the posterior end of the parasite harboured the myc signal, sometimes appearing as a large focus particularly in 1N1K cells. In the later cell cycle stage, the localisation appeared more dispersed and punctate, though still within the posterior end of the parasite (Figure 5-16 B; middle panel) and not in the nucleus. After MMS exposure (Figure 5-16 B; lower panel), the anti-myc signal appeared more dispersed and disordered than the untreated cells. In some cells, the localisation was very punctate, in contrast to others in which localisation either could not be observed or an increased signal could be seen. Nonetheless, where signal was seen it remained around the kDNA and was not nuclear. Indeed, in cells harbouring multiple kinetoplasts, a focus of localisation could often be observed in close proximity to each kinetoplast.

In summary, the anterior localisation of Tb6560 was normally still observed following exposure to genotoxic agents and appeared to remain associated with the FP/kDNA region of the cell. Thus, any pathway mediating recruitment to site of localisation was largely unaltered by such treatment and any putative function in mediating nuclear DNA repair is not reflected in detectable nuclear localisation.

5.5 Morphological analysis of Tb6560 null mutants

As indicated previously, loss of Tb6560 was associated with the appearance of cells with aberrant morphology (see chapter 3, section 3.3.5). This section describes experiments that explore this change in morphology in greater depth.

5.5.1.1 Loss of Tb6560 affects cell morphology

To examine cellular morphology, cells from the two knockout clones, and from the Tb6560^{+/-} and WT lines, were harvested and indirect IF analysis was performed with α -KMX1 antiserum. The nDNA and kDNA were stained with DAPI and the cell body visualised by DC imaging. The population was visually

examined and cells that did not conform to a trypomastigote shape were counted and expressed as a percentage of the total population (as shown in Figure 5-17 A and B). Approximately 7 % of WT cells and 3 % of Tb6560^{+/-} cells appeared visually aberrant, in contrast to ~44-46 % of cells from the Tb927.9.6560^{-/-} lines.

For further investigation, visually aberrant cells were further categorised depending upon the morphology observed. These categories were as follows: aberrant (cells which had no clearly definable defect), rounded (cells which appeared rounded in shape) and 'BigEye' (cells with what appeared to be enlarged FPs but were not rounded in shape; Allen, Goulding, & Field, 2003). Representative images of each category are shown in Figure 15-17 C. This categorisation revealed the increase in aberrant cells was primarily accounted for by a significant increase in 'rounded' cells (~20 % of all cells) in both Tb6560^{-/-} clones when compared to WT cells. In many cases, the flagellum could not be clearly observed, or appeared short in length. The next most common category was aberrant, but not clearly rounded, cells (> 20% of cells). Finally, a small increase in cells with the 'BigEye' phenotype was observed in both mutants (~ 5% of cells) relative to WT. When the 'rounded' cells were examined in more detail, two sub-categories could be detected. In around 30 % an enlarged vesicle-like structure was clearly discernible; for the remaining 70 % of 'rounded' cells, this was not the case (Figure 15-17 B). If the enlarged vesicle is the cause of cell rounding, why this should be absent in ~70 % of 'rounded' is unclear. However, as mentioned by Allen et al. 2003, cells with enlarged FPs are often fragile and fail to retain the structure following centrifugation. Thus, it is possible that many cells with these enlarged structures were lost during the indirect IF analysis here. 'Rounded' *T. brucei* cells have also been observed following clathrin knockdown (particularly PCF cells; Allen et al. 2003), and this effect has been attributed to the presence of a swollen FP (BSF) and internal vesicle pressure (PCF). Thus, some of the swollen cells in the Tb6560^{-/-} mutants may not be attributed to an enlarged flagellar pocket; instead an increase in internal vesicles may account for this phenotype. Furthermore, the variation regarding the degree of 'rounding' could be attributed to differences in the level of vesicles present in each cell.

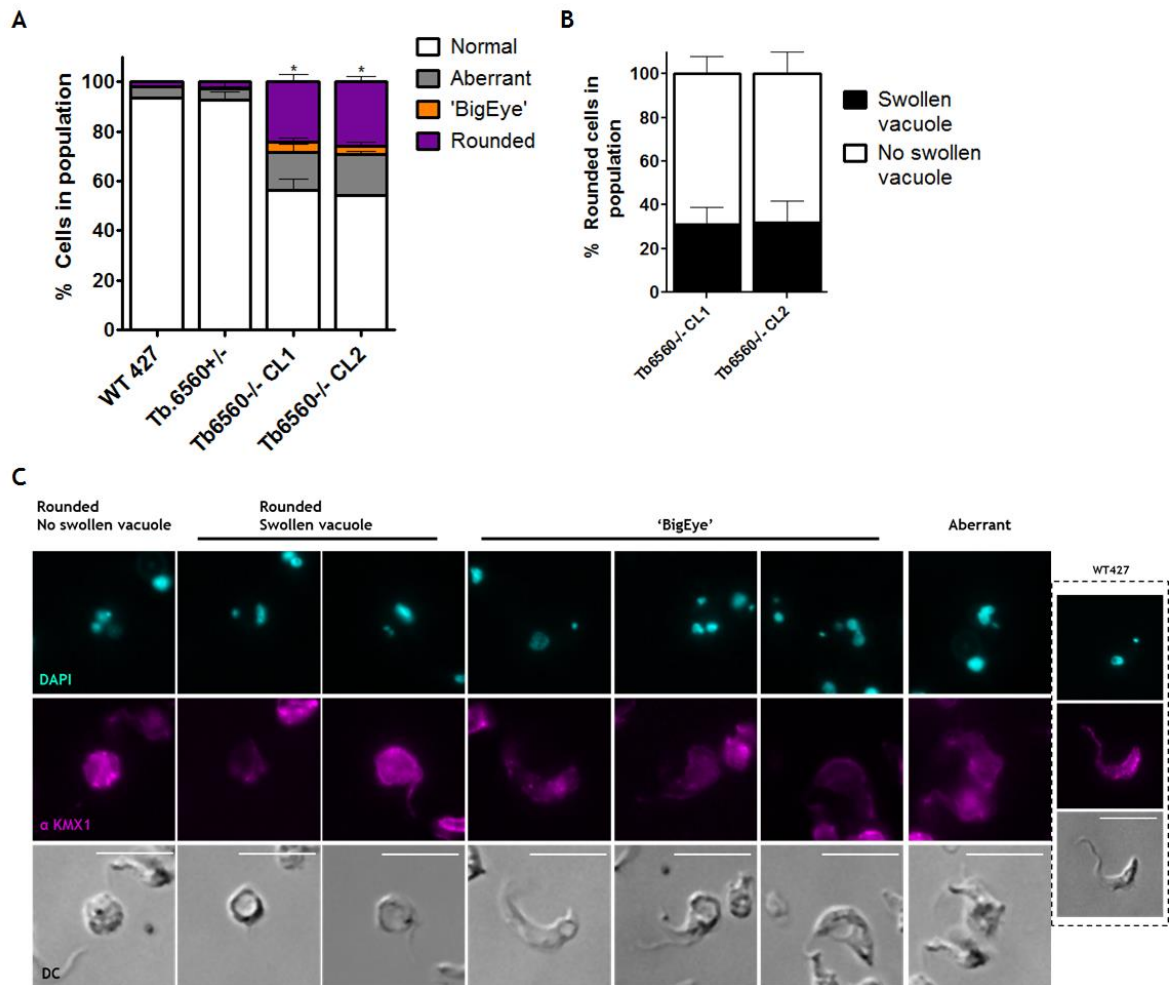


Figure 5-17: Loss of Tb6560 affects BSF cell morphology

(A) Cells were examined and the morphology categorised as detailed in the figure. The number of cells in each category is expressed as a percentage of the total cell counts. Over 200 cells per experiment were counted. Error bars represent \pm SEM; $n=3$. Significance was assessed by a Mann Whitney U test: (*) = $p<0.05$. (B) Cells with a 'rounded' morphology were further classified depending upon the presence or absence of a large swollen vacuole structure. Each category is shown as percentage of the total number of 'rounded' cells counted in (A). Over 200 cells per experiment were counted ($n=3$). Error bars represent \pm SEM. (C) Representative images of DAPI (to visualise nDNA and kDNA; cyan) and α KMX-1 (to visualise β tubulin; magenta) stained Tb6560^{-/-} CL1 cells from each category. The cell body is visualised by DC. In the black dashed box is a representative WT cell. Scale bar = 10 μ m. Images were captured on an Axioskop2 (Zeiss) and processed in ImageJ (as per section 2.11.8).

5.5.1.2 High resolution morphological analysis using TEM

To examine the swollen vesicle-like structure further and to potentially determine why this structure was absent in some morphologically aberrant cells, the internal structures of the cell were examined by TEM. The cells were fixed and imaged as per section 2.11.7.2. Representative images of WT cells are shown in Figure 5-18 and annotated for reference, while images of Tb6560^{-/-}

mutants are shown in Figures 19 and 20. Images of Tb6560^{+/-} cells are shown in chapter 8, section 8.4, Figure 8-26.

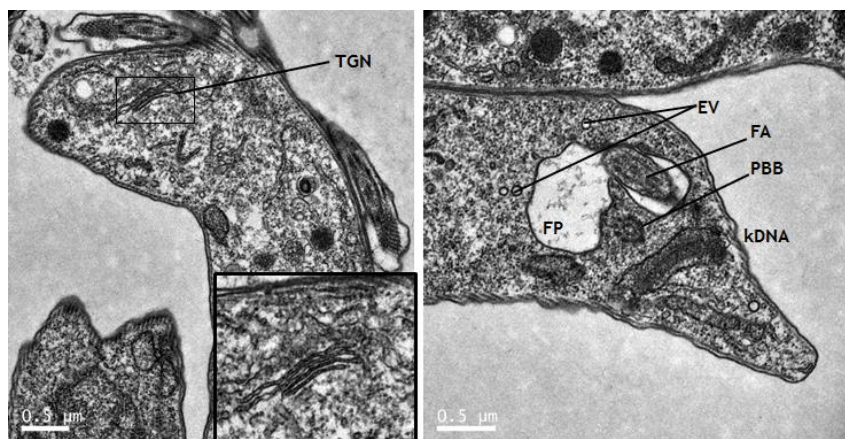


Figure 5-18: Internal cellular architecture of wild type Lister 427 BSF *T. brucei* cells
BSF *T. brucei* cells were fixed (section 2.11.7.2) and imaged by TEM. Important features of the cell posterior are annotated. The insert black box (left image) is an enlarged region of this image as highlighted. TGN (*trans*-golgi network), EV (endocytic vesicle), FA (flagellar axoneme), PBB (pro-basal body), FP (flagellar pocket) and kDNA (kinetoplast DNA). Images were captured on a Tecnai T20 transmission electron microscope and processed in section 2.11.7. Scale bars = 0.5 μm.

Upon loss of Tb6560, significant and complex alterations, ranging in severity, were observed in the internal morphology. Representative images are shown in Figure 5-19. No clear kDNA-or nDNA defects could be observed. In one cell, the nuclear membrane appeared disrupted, but the phenotype of this cell was particularly severe and it is possible the general cell structure was breaking down (Figure 5-19 G).

Of the 34 images captured from the Tb6560^{-/-} CL1 cell line (Figure 5-19 A-I), 29 cells examined had an enlarged FP. That the enlarged structure was the FP was based on several observed features: the presence of an electron dense coating on the inner surface of the membrane (most likely the VSG coat), a flagellum entry point (and the presence of a FAZ), and the presence of a glycan rich matrix within the enlarged FP. Routinely, the FP encompassed almost the entire cell volume (Figure 5-19 A-F). Interestingly, the FP did not retain a spherical shape, and instead the membrane was folded and misshapen, suggesting that membrane transport may be defective. Occasionally, densely coated objects could be observed within the FP (Figure 5-19 I). The remaining five cells examined did not harbour an enlarged FP; for two of the cells (Figure 5-19, G&H), no clear defects could be observed, whereas the remaining three

harboured multiple electron dense and electron light vesicles. In addition, defects in the endosomal and the *trans*-golgi network (TGN Figure 5-20) were observed (Figure 5-20 A&B), appearing as swollen ‘vesicle-like’ structures, some with internal cargo (occasionally very electron dense; Figure 5-20 C&D) and others lacking any clear contents (see Figure 5-19 A-F below).

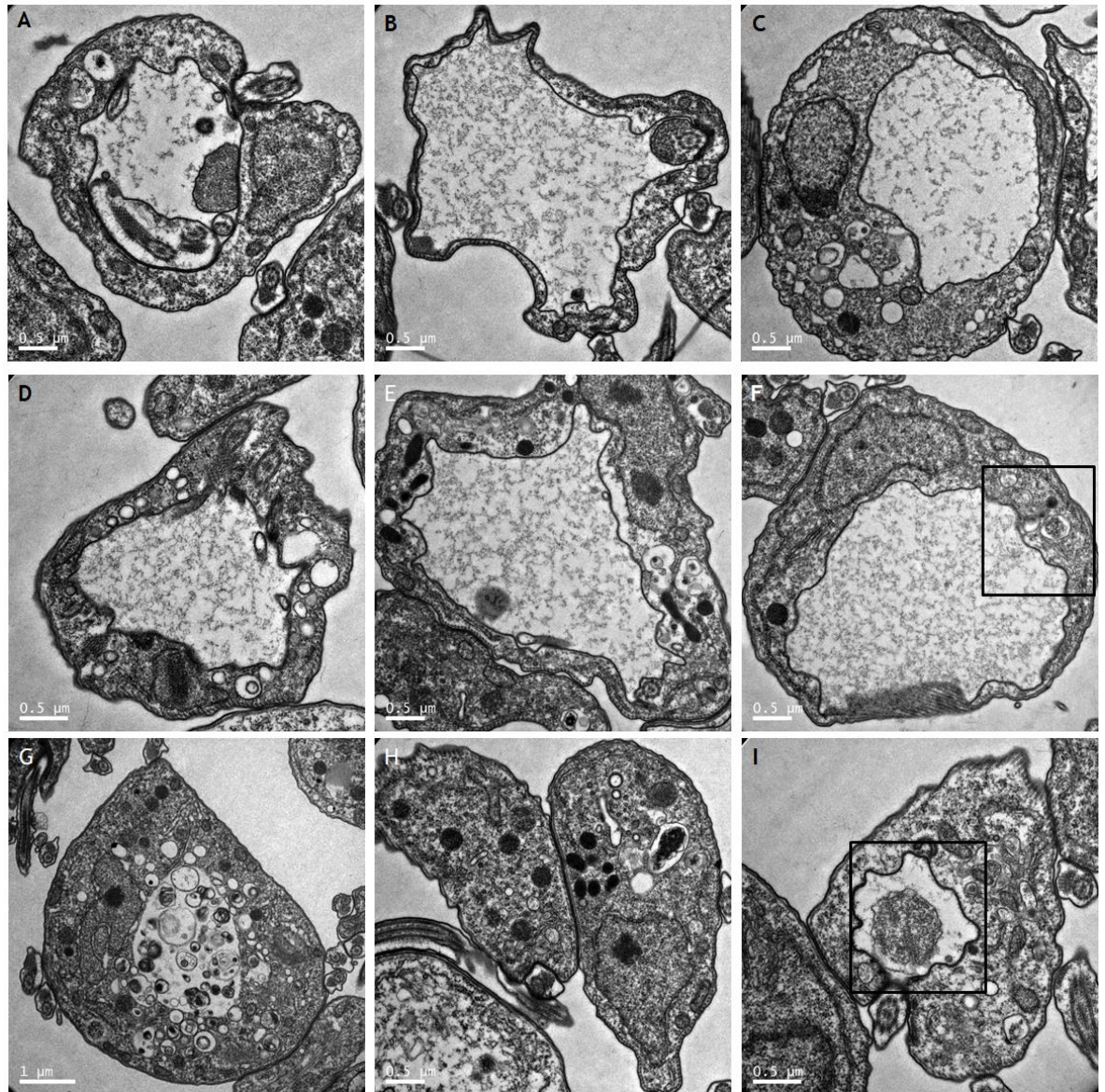


Figure 5-19: Loss of Tb6560 grossly affects structures associated with endocytosis and vesicular trafficking

Representative images of the Tb6560^{-/-} CL1 cell line. Cells were fixed as per x and imaged on a Tecnai T20 transmission electron microscope using TEM. The black boxes indicate areas enlarged in Figure 5-20 for clearer viewing. Images were processed in ImageJ and Adobe Photoshop. The top left image shows disruption of the nuclear membrane. Scale bars are as annotated on the images (between 1-0.5 μm).

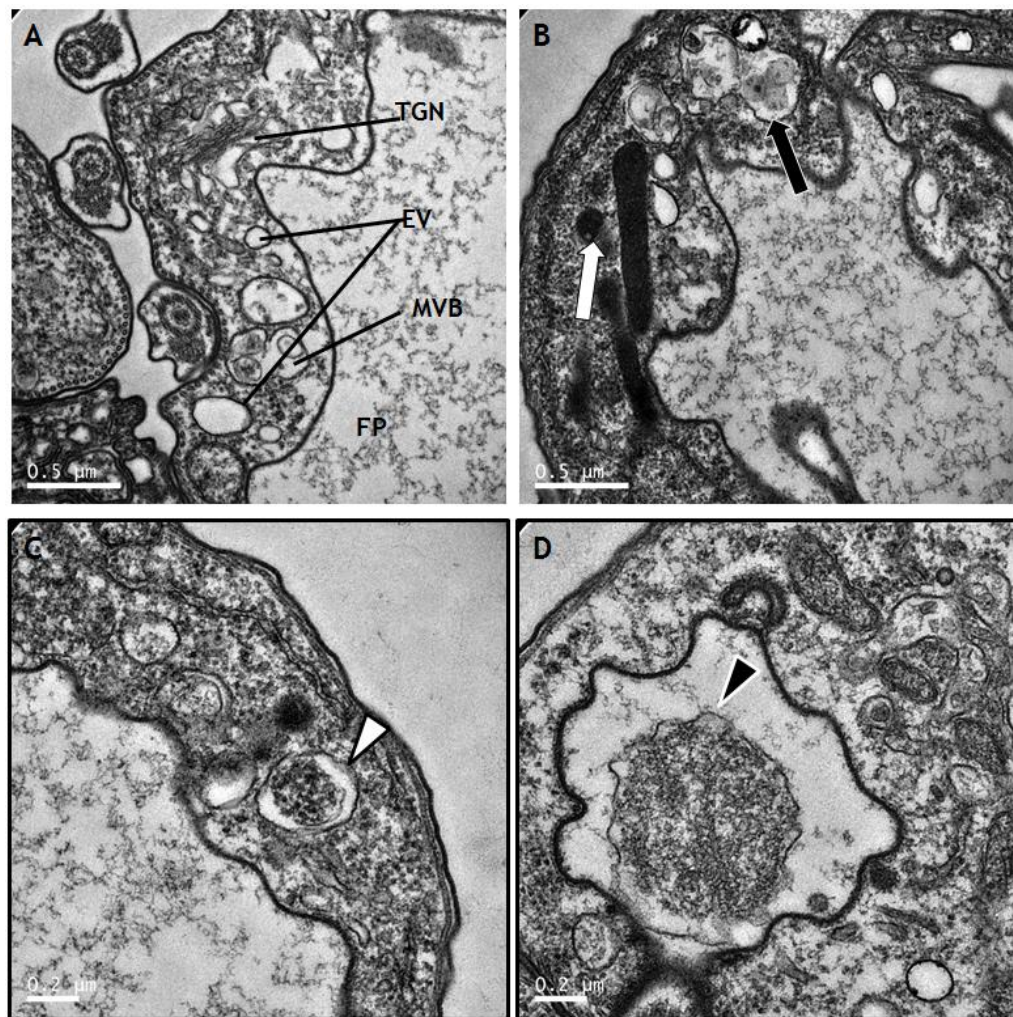


Figure 5-20: TEM images of abnormal cellular structures associated with Tb6560 loss
Enlarged images of abnormal endosomal and golgi networks observed in Tb6560 knockout mutants. A. The image is annotated as follows: EV (endocytic vesicle), TGN (*trans*-golgi network), MVB (multi-vesicular body) and FP (flagellar pocket). B. An electron dense granule is shown by a solid white arrow (top right) and an abnormal vesicle-like structure highlighted by a solid black arrow (top right). C. A vesicle harbouring cargo is indicated by a solid white triangle. D. A large mass in the FP is indicated by a solid black arrow (bottom right). Scale bars = 0.5 μm (top panel) and 0.2 μm (bottom panel). Images of Tb6560^{-/-} CL1 were captured on a Tecnai T20 transmission electron microscope and processed in x.

To determine whether FP swelling could be explained by a FPC defect, the point at which the flagellum entered the FP was examined in more detail in the mutants (Figure 5-21 shows representative images). However, no noticeable defects were observed, suggesting swelling is not due to a ‘loosening’ of the connection between the flagellum entry site and the FP membrane and thus an influx of extracellular material. Indeed, when the localisation of TbBILBO-1 was examined in the KO cell line (data shown in chapter 8, section 8.4, Figure 8-27), the protein did not appear to miss-localise, suggesting the absence of Tb6560 does not affect TbBILBO-1 in its role providing structural support to the FPC,

consistent with the EM data showing the entry point of the flagellum does not appear to be compromised.

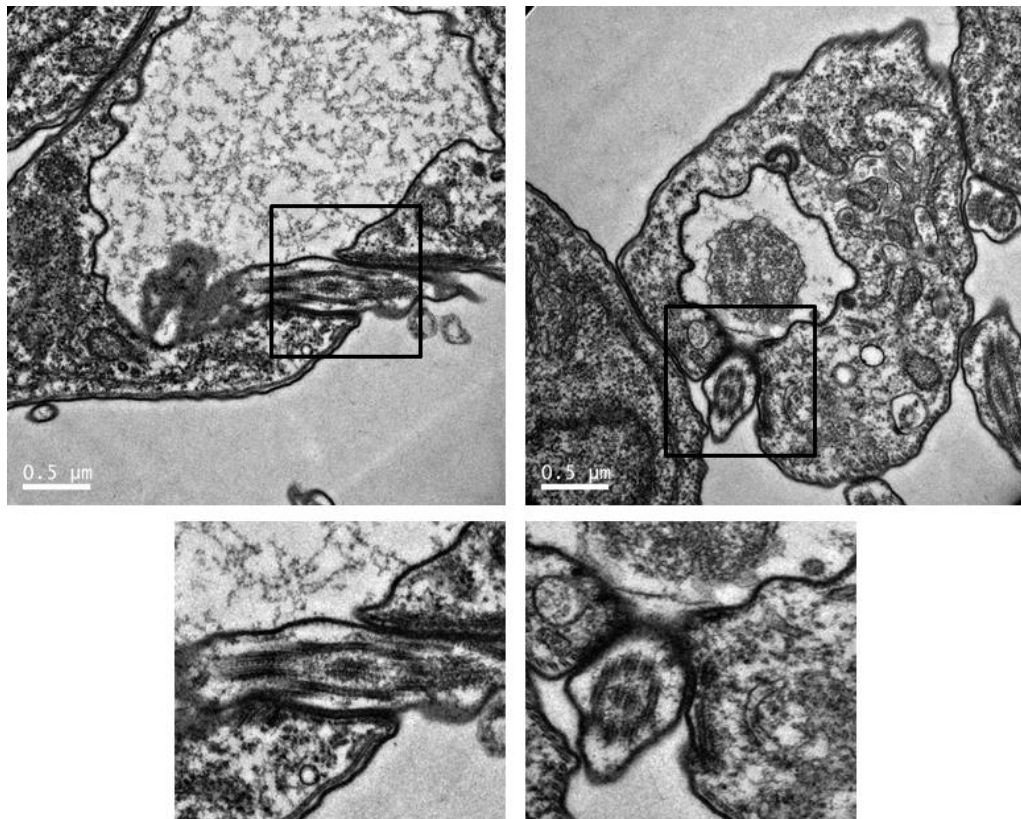


Figure 5-21: The enlarged FP is unlikely due to disruption at the flagellar entry point. The entry point of the flagellum into the FP (via the FPC) was imaged by TEM as per section 2.11.7.2. Enlarged images of the image indicated by the black box are shown below the corresponding picture. The images were captured on a Tecnai 20 transmission electron microscope and processed in ImageJ by L.Lemgruber-Soares. Images from Tb6560^{-/-} CL1 were shown. Scale bars = 0.5 μm.

5.5.1.3 3D Video Reconstruction of the Tb6560 FP

To visualise the 3D architecture of a BSF cell following the loss of Tb6560, focused ion beam/scanning electron microscopy (FIB/SEM) imaging was performed to generate a morphometric 3D reconstruction of a cell based on a robust statistical analysis. This technique has been used effectively to assess, for example, *Plasmodium* parasites within erythrocytes (Medeiros et al. 2012). The 3D reconstruction was performed by L.Lemgruber-Soares (as detailed in the figure legend below). A video is provided as supplementary material (Accompanying CD; file entitled [Tb6560videoreconstruction.mov](#)). Still frame images from the video are presented in Figure 5-22 A-H.

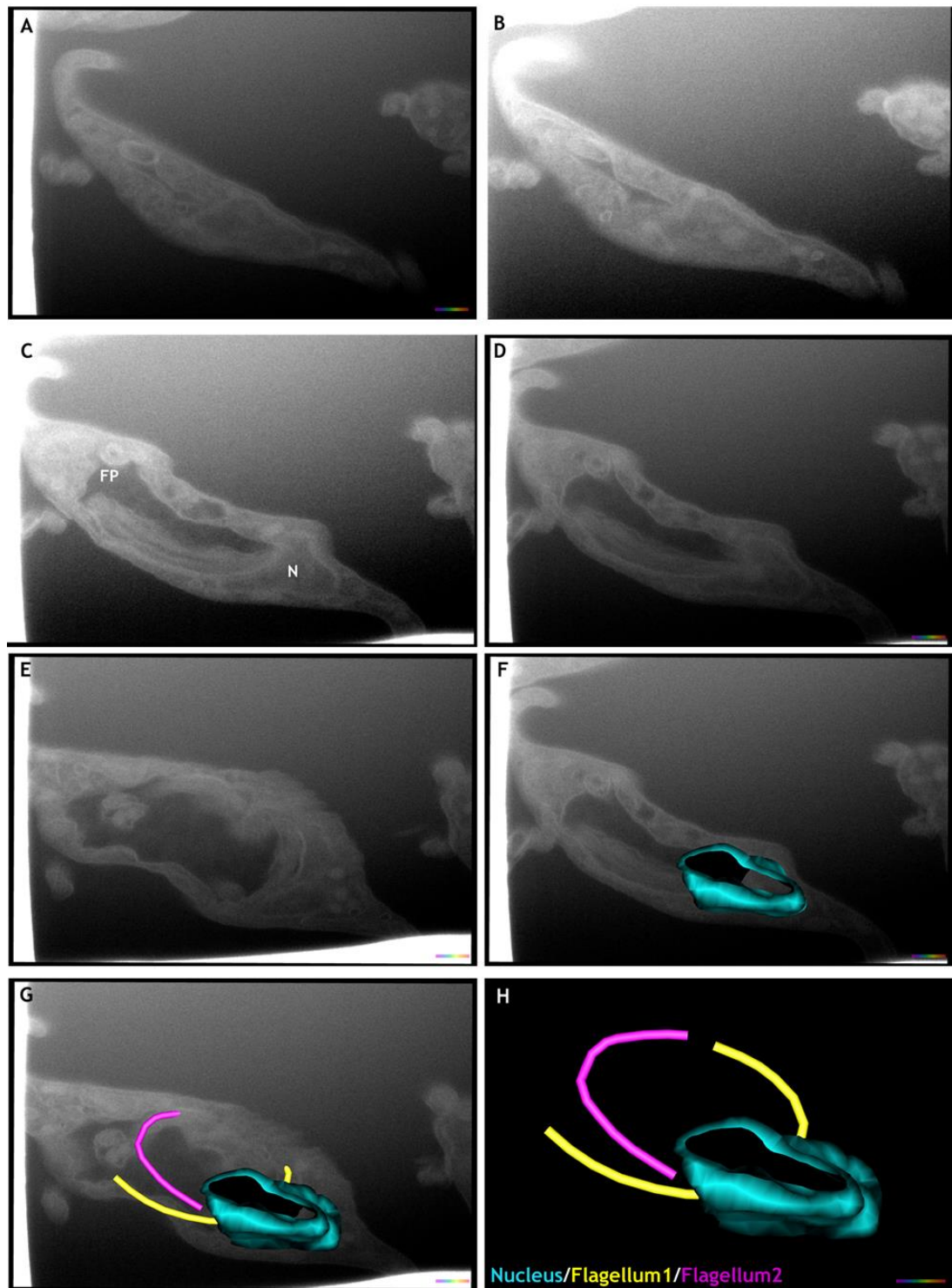


Figure 5-22: FIB/TEM analysis of Tb6560 knockout cells

(A-H) Images from different stages of the video in chronological order captured for FIB/TEM analysis of a Tb927.9.6560^{-/-} CL1 cell. The alignment of the images was performed in Jmod (Midas; Boulder, Colorado; (Kremer et al. 1996) and the 3D images were generated using the IMARIS software (<http://www.bitplane.com/imaris/imaris>; V.8.2). All images are at the same scale. Scale bar =100 nm. Image capture and preparation was performed by L.Lemgruber-Soares.

From this analysis, it is clear that the FP occupies a vast proportion of the cell body. In addition, flagellum development does not appear impaired. Interestingly, enlargement of the FP predated cellular division in this cell as no

other nucleus could be detected in this cell, though no clear 'daughter' FP can be observed. Considering the flagellar pocket forms upon flagellum exit from the original 'parental' cell, it is possible that the process of FP formation is also disrupted in a dividing cell. In keeping with this hypothesis, no knockout cells with a 'LittleEye' phenotype (a 'LittleEye' phenotype indicates swelling of the developing flagellar pocket of the daughter cell) could be clearly observed, which would arise due to a swelling of the 'daughter' FP (Allen et al. 2003).

In all, the EM images in section 5.5.1.2 and from the FIB/TEM analysis, confirm the swollen vacuole observed is the FP of the cell; perhaps explaining the morphology distortion. FP swelling may increase the internal pressure and eventually distort the subpellicular 'corset' of the parasites resulting in a 'rounded' shape. In addition, some cells also harboured endosomal system and TGN defects suggesting that loss of Tb6560 not only affects bulk endocytosis but also the transport of internal cytoplasmic vesicles through the endosomal system and to the TGN.

5.6 Tb6560 may be involved in BSF endocytosis and trafficking

Loss of Tb6560 results in cells with enlarged FP, multiple internal vesicle-like structures and defects in both the endosomal system and the TGN (section 5.5). An explanation for this range of cellular changes is impaired endocytosis, perhaps including subsequent trafficking of internal vesicles. To test this hypothesis, an endocytosis assay was performed to assess the ability of the knockout cell lines to uptake tomato lectin (TL; Nolan, Geuskens, & Pays, 1999). The assay was performed as described in section 2.11.6 at 4 °C to examine TL uptake into primarily the FP and the early endosomal trafficking system.

In WT and Tb6560^{+/-} cells (representative images are shown in Figure 5-23 and 5-24), TL was readily up taken into the FP and the early endosome system, as expected (Figure 5-23). A larger number of cells are shown in the images in chapter 8, section 8.4, Figure 8-28.

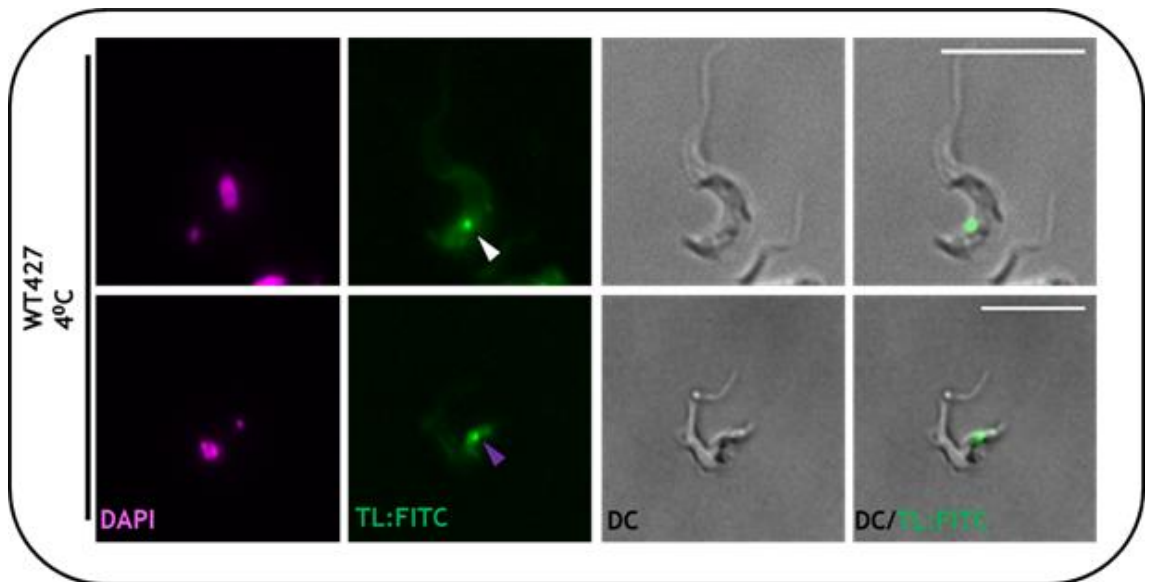


Figure 5-23: Uptake of tomato lectin into the FP and the early endosome system of wild type BSF *T. brucei*

Images are representative examples of wild type BSF *T. brucei* (WT427) cells showing uptake of FITC-conjugated tomato lectin (TL). The white arrow indicates TL in the early endosome system. The purple arrow indicates TL in the FP. Images were captured on an Axioskop2 and processed in ImageJ as per section 2.11.8. Scale bar = 10 μ m.

In contrast, the results from the knockout cells proved a challenge to interpret. Several different localisations of the lectin could be detected, representative images of which are shown in Figure 5-24. In most rounded cells lectin staining appeared diffusely throughout the cell but within this, more localised, intense accumulation of TL, potentially in the FP, was observed in many cells. In some other cells, including unrounded cells, small distinct foci of TL localisation could additionally be detected outwith the predicted region of the FP, and most likely within cytoplasmic vesicles. Finally, normal uptake of TL was also seen in a small population of cells, many of which were unrounded.

The range of TL accumulation in the mutants, seemingly in both the FP and cytoplasmic vesicles of some cells, appears to mirror the abnormal morphology of the cells revealed by EM. Taken together, these data suggest that though endocytosis and internalisation of cargo is not blocked entirely, it is clearly impaired in the knockout cells. With such a diversity of TL distribution, it was difficult to decipher if a single stage of the endocytosis and trafficking pathway is lost in the mutants, perhaps suggesting Tb6560 operates at multiple points during this process. Additional assays are required to assess this phenotype.

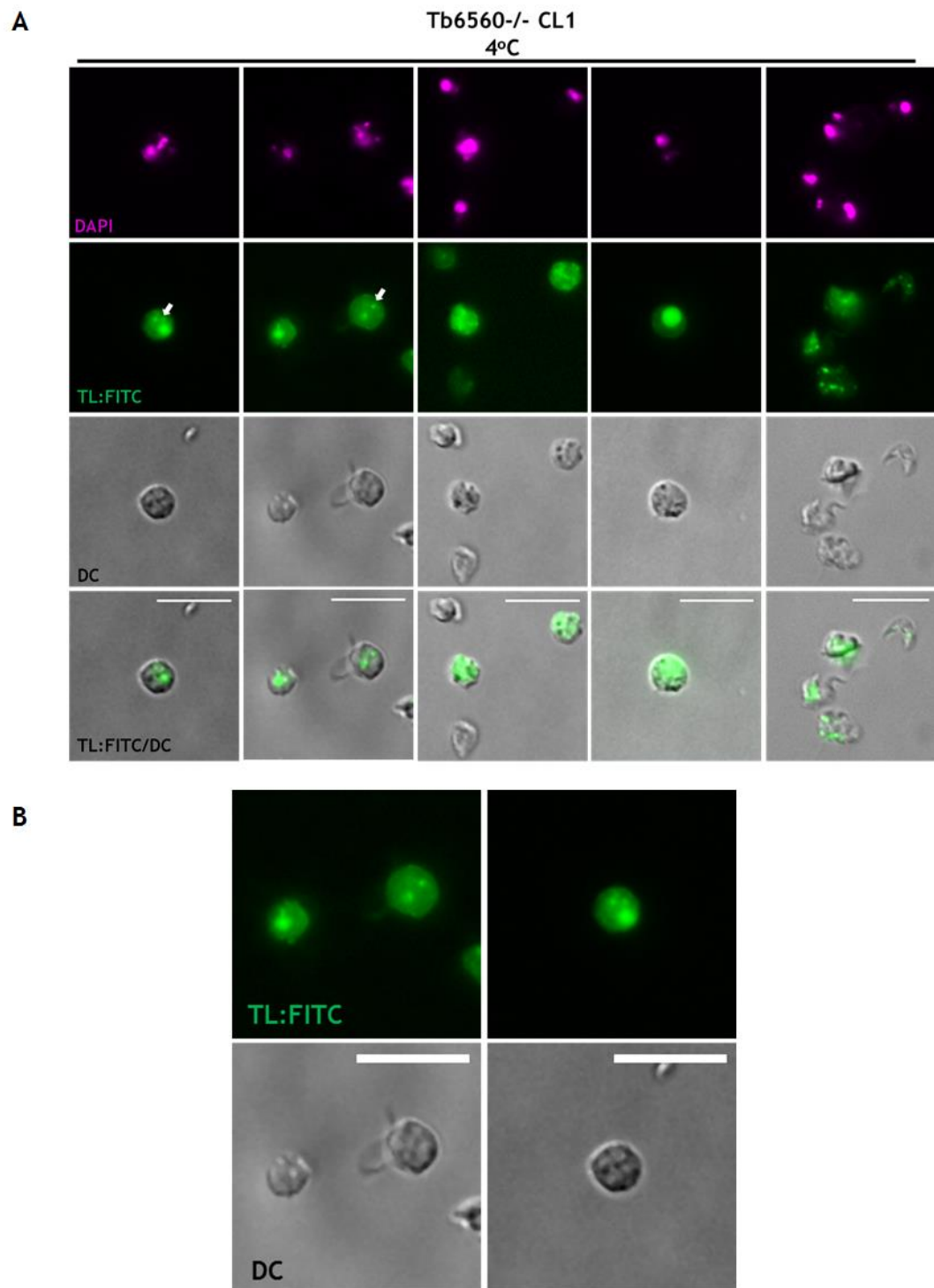


Figure 5-24: Cells lacking Tb6560 are defective in endocytosis
(A) Representative images of FITC-conjugated tomato lectin (TL) uptake in Tb6560^{-/-} knockout cells. The white arrows highlight internal vesicles also harbouring TL. **(B)** Enlarged examples of Tb6560 knockout cells showing uptake of TL into both the FP and internal vesicles. DC = differential interference contrast microscopy. Images captured on an Axioskop2 and processed in ImageJ as per section 2.11.8. Scale bar = 10 μ m.

5.7 Identification of potential interacting partners of Tb6560

If Tb927.9.6560 is involved in endocytosis, interaction partners could aid in deciphering a potential role for this protein in BSF *T. brucei* parasites. To this end, an immunoprecipitation (IP) was performed (as per section 2.12.2), using anti-myc antiserum to recover Tb6560-12myc from the Tb6560^{+/-12myc} cell line. WT cells were used to control for any non-specific binding of proteins to the Dyna beads. To allow for identification of interaction partners visually and by mass spectroscopy, an IP was performed. The final eluate of one IP (S1) was separated on 4-12 % BT gel by SDS-PAGE and stained with SYPRO® Ruby before imaging on a Typhoon (section 2.12.4). One band was clearly unique to the Tb6560^{+/-12myc} eluate, and was judged to be Tb6560^{+/-12myc} based on size and clear identification of the protein by mass spectroscopy (Figure 5-25 A; section 2.12.3). No other clear differences could be observed between the eluate of Tb6560^{+/-12myc} cells and WT cells.

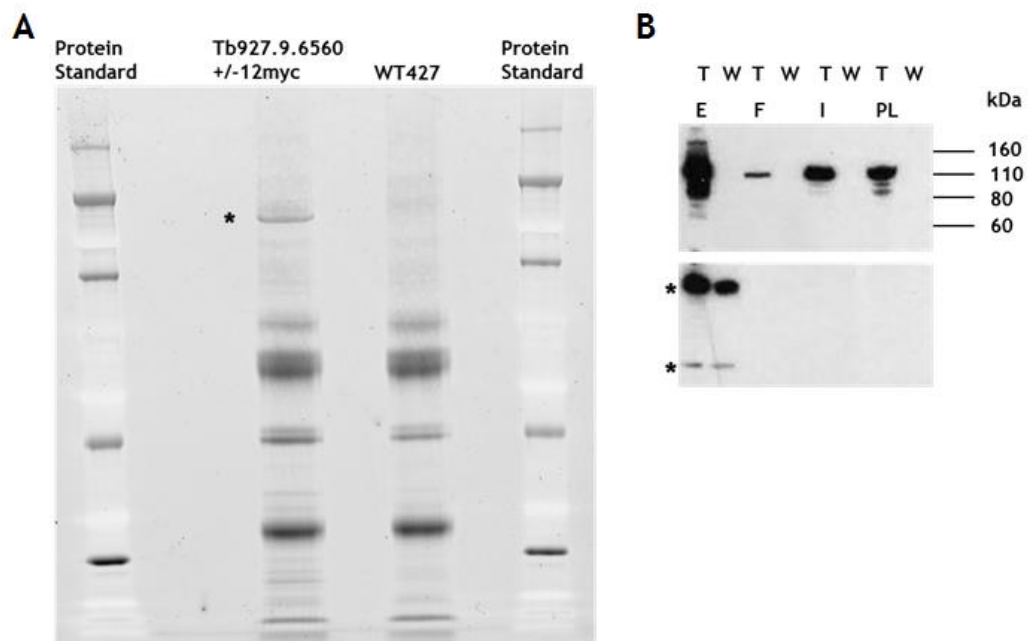


Figure 5-25: Immunoprecipitation from a Tb6560^{+/-12myc} cell line using anti-myc antiserum (A) Image of a SyproRuby®-stained gel of eluate from an anti-myc immunoprecipitation (IP) from Tb6560^{+/-12myc} and wild type (WT427) cells (eluate S1). The (*) indicates C-terminally tagged Tb6560 (~94.6 kDa). Protein standard markers are shown (Novex® pre-stained protein standard ladder). (B) Western blot analysis confirming IP of Tb6560^{+/-12myc}. The (*) marks both the heavy and light chain of the α myc antibody. E = eluate (S2), F = flow through, I = input, PL = pre lysis, W = WT427 and T = Tb6560^{+/-12myc}.

A second eluate sample (S2) from both cells was sent for mass spectroscopy analysis (section 2.12.3; Glasgow Polyomics Facility; the WT sample was run first) and a western blot was performed (section 2.12.1), verifying that Tb6560^{12myc} could only be detected (Figure 5-25 B) in the eluate of the Tb6560^{+/-12myc} sample. Described below are the proteins identified (summarised in Table 5-3) from MS analysis, which are proteins only detected in the experimental and not control (WT) IPs (Accompanying CD; see file entitled [MSdataTb6560andTbAUK22016.xls](#) for all proteins identified in both samples). Tb6560 was identified in the IP from the Tb6560^{+/-12myc} cells and not WT, as expected.

Gene ID	MW (kDa)	Annotation (TriTrypDB)	Annotation (NCBI database)	Predicted domains (Interpro)	Protein Score (MS analysis)
Tb927.9.6560	80.2	Hyp. Cons.	AP2 associated protein kinase (<i>H.sapiens</i>)	PK-like	130
Tb927.6.4520	52.59	Tumour Supp. Mitostatin, putative	Trichohyalin predicted homology domain protein (<i>H.sapiens</i>)	Trichohyalin predicted homology domain	31
Tb927.10.5870	49.468	Hyp. Cons.	Trypanosomatids only	None	30
Tb927.8.3000	57.311	Hyp. Cons.	Predominantly Kinetoplastid specific	None	26
Tb927.10.520	46.782	ATPase Tb1 (putative)	Predominantly Kinetoplastid specific	TM helix	23
Tb927.11.5330	87.025	Hyp. Cons.	Predominantly Kinetoplastid specific	None	19
Tb927.8.5310	37.609	Polyketide cyclase/dehydrase and lipid transport, putative	Coenzyme Q-binding protein COQ10 homolog A, mitochondrial isoform (<i>H.sapiens</i>)	Coenzyme Q-binding protein, START-like domain	16
Tb927.11.2430	48.497	Cytoplasmic dynein 2 heavy chain, putative	Cytoplasmic dynein 2 heavy chain 2 isoform 1 (<i>H.sapiens</i>)	Dynein heavy chain, P-loop domain, ATPase AAA domain	15
Tb927.8.1210	77.788	Hyp. Cons.	GluZincin domain Kin K39 (<i>M.antarcticus</i> ; E-value: 1.6) Cap-gly domain linker protein 1 (<i>A.suum</i> ; E-value: 2e-04)	Coiled coil regions	14

Table 5-3: Potential Tb6560 interaction partners identified by MS analysis
Proteins shown were those proteins only present in an anti-myc IP from Tb6560^{+/-12myc} cells; all proteins also identified in IP from wild type cells were excluded. Samples were analysed using MASCOT software. Protein sequence for each 'hit' was analysed by BLASTp using the SmartBLAST feature and domains examined by Interpro analysis. Displayed above are also any potential corresponding human homologs. Hyp. Cons. = hypothetical conserved, MW = molecular weight.

It should be noted that these data have not been verified by further analysis (e.g. repeat IP, directed co-IP or reciprocal IP), so must be treated as preliminary. Nonetheless, two proteins were revealed that may be consistent with the predicted endocytotic function of Tb6560. Most proteins were annotated as hypothetical and kinetoplastid specific. When analysed by BLASTp (section 2.1.2) and Interpro (section 2.1.2), no specific domains could be identified in most. However, one hypothetical protein (Tb927.8.1210) showed sequence homology to a cap-gly domain linker protein (54 % coverage, E-value $2e^{-04}$, 27 % identity) in the helminth *Ascaris suum*, and very weak homology to a kinesin (Kin K39 from *Moesziomyces antarcticus*). Cap-gly domain containing

proteins may facilitate microtubule interactions (Wang et al. 2014). The protein was also predicted to possess a potential zinc binding site (a Gluzincin domain; this was not identified using the Interpro search and therefore may be a false identification). The second notable protein was the predicted heavy chain of dynein (Tb927.11.2430). To date, this protein has only been shown to be required for retrograde trafficking within the flagellum (Blisnick et al. 2014), so whether it is compatible with the function predicted here remains unclear. Three other proteins appear to be associated with the mitochondrion. Tb927.10.520 is a subunit of the F₀F₁-ATP synthase complex required for the production of energy for the mitochondrion (by generating ATP) in the PCF stage; loss of this gene reduces *in vitro* PCF cell growth and is required for the structural integrity of the ATP synthase complex (Zíková et al. 2009). A role for this protein is still under investigation; though considering the increased activity of the PCF mitochondrion, it is a surprise as to why this would have been identified in this study due to the compartmentalisation of glycolysis in the BSF (the glycosome; Opperdoes & Borst, 1977) and the downstream respiratory chain not being required (reviewed by Coley, Dodson, Morris, & Morris, 2011). In addition, the second protein (Tb927.6.4520) was identified as harbouring a Trichohyalin-plectin-homology domain, potentially required for the tethering of the mitochondrion to the ER and to maintain its morphology (Cerqua et al. 2010). The final protein (Tb927.8.5310) showed sequence homology to a Coenzyme Q binding protein, which in humans is involved in the respiratory chain of the mitochondrion (the importance of coenzyme Q is reviewed by (Hargreaves 2014). None of these proteins obviously fit with the data presented in this chapter, though the close proximity of Tb6560 localisation to the parasite's mitochondrion may cause them to be pronounced contaminants. Indeed, no clear mitochondrial defects were observed by TEM (section 5.5.1.2). Further work is required to test any of these potential interactions.

5.8 Discussion

5.8.1 Tb6560 is likely a NAK pseudokinase

Several interesting and surprising outcomes resulted from a fresh examination of the Tb6560 sequence. Though not specific to *T. brucei* or the kinetoplastids, several unusual features were observed when compared to the potential

homolog of this gene in *H. sapiens*. Firstly, the N-terminal region of Tb6560 is revealed to show clear sequence homology to the N-terminal region to *H. sapiens* AAK1 and to *M. musculus* BMP-2, both of which are part of the NAK kinase family, whose members predominantly function during endocytosis. The N-terminal region harbours the kinase domain of the NAKs and is highly conserved between members. Indeed, using protein structure prediction software (section), both the recently crystallised structures of AAK1 and BMP-2 were used to produce a high confidence predicted model of Tb6560's N-terminal region. In contrast, the C-terminal region (accounting for ~ 50 % of the protein sequence) of Tb6560 was predicted to be highly disordered. A common feature of NAK kinases is considerable variation between the C-terminal domains of family members, which may reflect divergence in the diverse roles of these kinases (Sorrell et al. 2016). Thus, the predicted disorder in the C-terminal region of Tb6560 may be consistent with lineage-specific roles of this part of NAKs. Though many AAK1-specific motifs were absent in Tb6560 and its kinetoplastid orthologues, a motif for α adaptin interaction could be identified within the C-terminal region of all of them. This motif is required for AAK1 to interact with the AP2 complex. The AP2 complex is found in both *Leishmania* and *T. cruzi*, but remains largely uncharacterised (Manna et al. 2013). As discussed in section 1.4.1.4, components of the AP2 complex are absent in *T. brucei* (Manna et al. 2013). Clearly, it would be interesting to investigate whether Tb6560 orthologs bind components of the kinetoplastid AP2 complex.

A second notable observation from the sequence analysis of Tb6560 and its orthologues was the lack of conserved kinase residues; in all the kinetoplastids examined, the protein appeared to be a pseudokinase. A key function of AAK1 in *H. sapiens* is phosphorylation of the μ 2 subunit of the AP2 complex to enhance the complex's affinity for incoming cargo (Jackson et al. 2003) during CME. If Tb6560 does not have kinase activity, an adaptation of function is suggested, for reasons that remain unclear if it acts, like AAK1, in endocytosis. One possibility is that kinetoplastids possess a diverged AP2 system (or at least regulation mechanism). Indeed, it is striking that a potential lack of all AP2 complex subunits appears limited to *T. brucei* amongst the kinetoplastids, a loss that has been associated with the acquisition of the VSG coat in these parasites (Manna et al. 2013). It is however unclear whether Tb6560 ever harboured kinase

activity and could function in a similar role to AAK1 or if Tb6560 homologs were all initially pseudokinases and, perhaps driven by the need for a more complex endocytosis system, other eukaryotes required their homologs of Tb6560 to function as a kinase.

In BSF *T. brucei* parasites the rate of endocytosis is very high to facilitate both recycling of the VSG and clearance of antibody-VSG complexes (Engstler et al. 2007). The lack of AP2-mediated cargo sorting in *T. brucei* is thought to have ‘streamlined’ this process to maximise VSG recycling to the cell surface (Manna et al. 2013). Indeed, endocytosis across synaptic vesicles also does not require an AP2 complex (Gu et al. 2008). However, the data here reveal a key kinase component of AP2-mediated endocytosis, which has evolved to be a pseudokinase in all kinetoplastids. This raises the obvious questions about the purpose of this protein in *T. brucei* and, more broadly, the regulation of the AP2 complex in other kinetoplastids. As discussed below, Tb6560 is not essential, but its loss impairs BSF growth *in vitro*; why does *T. brucei* harbour a component of the eukaryotic AP2 complex if other components of the complex are absent?

The involvement of a pseudokinase in an endocytosis pathway is not without precedent. In human cells, the Janus kinase, JAK2 (via its pseudokinase domain), can perform endocytic functions independent from its kinase activity (Putters et al. 2011).

5.8.2 Loss of Tb6560 is associated with an enlarged FP and endosomal system defects

This work suggests Tb6560 is a pseudokinase homolog of AAK1, or perhaps of the other related NAK kinases. Unlike endocytic components such as clathrin (Allen et al. 2003) and Rab5 GTPases (Hall et al. 2004), Tb6560 is not essential for BSF cell survival and does not appear to induce a cell cycle block, though cell proliferation is reduced and a variety of morphological defects arose associated with its loss. Over 40 % of the cells in the knockout cell lines were morphologically aberrant; ~30 % of these aberrancies could be attributed to a potential endocytosis defect and, indeed, by TEM (section 5.5.1.2) it was confirmed that some of these cells harboured enlarged FPs similar to that reported following clathrin, RAB5A and Rab5B knockdown (Allen et al. 2003; Hall

et al. 2004). This phenotype could be in fact be more severe as it is known that cells presenting with a 'BigEye' phenotype are fragile and can become destroyed following centrifugation; potentially the remaining rounded cells also harboured enlarged FPs (Allen et al. 2003). In all knockout cells examined with an enlarged FP, the spherical shape of the pocket was lost (it instead appeared folded or irregularly shaped), suggesting a potential defect in membrane trafficking or recycling (similar to that observed following Rab5A and B knockdown in BSF parasites; Hall et al., 2004) Cells with enlarged FPs were also shown to accumulate TL in the pocket. Taken together, these data suggest a role for Tb6560 during endocytosis.

Loss of Tb6560 also produced cells with defective endosomal systems (multiple vesicles and unusual arrangements of endosomal structures) and, occasionally, TGN defects were also observed. These phenotypes are similar to that observed in PCF cells following clathrin knockdown, which has been attributed to a defect during endosomal trafficking: vesicles perhaps failing to fuse to their target. Tb6560 may therefore also support vesicular trafficking following endocytosis, possibly early in the process during, for example, surface coat recycling. In support of this, accumulation of TL could be observed in cytoplasmic vesicles in cells devoid of Tb6560. Again, however, the viability of Tb6560 mutants suggests any endocytic block is only partial.

TL is up taken in a similar manner to type I transmembrane proteins like VSG, ISG and the transferrin receptor (Nolan et al. 1999). Lila Koumandou and colleagues have further demonstrated that in *T. brucei*, ISGs and transferrin appear to be differentially 'sorted' from the surface VSGs in a receptor-mediated manner (directed by RME-8; Lila Koumandou, Boehm, Horder, & Field, 2013). To date, it has yet to be confirmed whether other proteins can use the RME-8 signal to facilitate the initial uptake into the cell; loss of RME-8 does not produce an enlarged FP, suggesting it functions after cargo internalisation (Lila Koumandou et al. 2013). It has been assumed that the lack of an AP2 complex means this process of sorting is not required and, indeed, to manage the high turnover rate of the VSG coat this may in part be the case. However it is still possible that other proteins may require sorting before entry, though perhaps not as stringently as in higher eukaryotes. There is no doubt that that Rab5A/B

and 11 are required for trafficking of these proteins but, upon knockdown, the predominant phenotype is not an enlargement of the FP, suggesting again these proteins function after internalisation of cargo. Loss of Tb6560 appears to primarily produce an enlarged FP, suggesting it may act earlier in endocytosis than these GTPases, though the presence of internal vesicles may suggest it also functions to aid early endosomes too. Overall, the accumulation of TL into cytoplasmic vesicles and into the FP in Tb6560 mutants suggests two things: 1) some cargo becomes trapped within the FP; and 2) some cargo can enter the cell, perhaps reflecting the presence of two separate entry pathways.

Two further observations of the Tb6560 mutants are worth noting, but have not been further investigated. First is the partial recovery observed following serial passaging in culture for over 3 weeks; the number of cells with visually observable aberrancies appear too reduced and growth improved. This may suggest the cells are able to compensate in part for the loss of this protein, or perhaps recycling of the surface coat proteome is somewhat reduced following serial passaging. The second, connected observation is that even though the *-/-* mutants should be devoid of Tb6560 protein, the phenotypes described are seen only in around half the population. Whether this indicates a response to growth conditions, or may be due to compensation during selection for the mutants, is unclear.

5.8.3 The localisation and potential interaction partners of Tb6560 supports a role during early endocytosis

Localisation of Tb6560 in BSF cells is both complex and dynamic. Tb6560 is located at the posterior region of the cell between the kDNA and the nDNA, where other components of the polarised endosome system localise in *T. brucei* (Field & Carrington 2009). Occasionally, the protein appeared to localise to the flagellum itself, though this observation was limited to EM analysis. Though the protein adopts localisation within this region constitutively, it appears to move dynamically throughout the cell cycle, perhaps due to its close association with the FP and early endocytic vesicles (section 5.3.4.6). TbRab5A and B appear to localise closer to the nucleus than Tb6560, consistent with their role as part of the endosome system. Localisation of Tb6560 appears remarkably close to the FP, on occasion almost associating with the FP membrane, perhaps

strengthening the suggestion that Tb6560 may act during an early endocytosis event. By localising within this region, the protein has access to the FP membrane, potentially incoming vesicles and the flagellum.

In keeping with a potential role in endocytosis and vesicular trafficking, two putative interaction partners were recovered by IP that have potential roles in these pathways. Recovery of the heavy chain of dynein and a potential cap-gly domain containing protein may suggest Tb6560 mediates the physical movement of intracellular vesicles. These potential interaction partners require validation by endogenously tagging each one and performing a co-immunoprecipitation experiment in the endogenously tagged Tb6560^{+/-} cell line. Nonetheless, vesicles decorated with Rab5 are moved in a dynein mediated manner (Sato et al. 2008) and, in *Drosophila* dendrites, this is thought to be co-ordinated by NAK (the *D. melanogaster* homolog of AAK1 (Yang et al. 2011)). *T. brucei* utilises Rab5 positive vesicles to traffic proteins like the transferrin receptor to the tubulated endosomes, though little is known about what is co-ordinating the movement of these vesicles. Indeed, AAK1 in humans is required for uptake and recycling of the transferrin receptor, though this activity utilises AAK1's kinase activity, suggesting a difference from Tb6560 (Conner & Schmid, 2003; Ricotta, Conner, Schmid, Von Figura, & Höning, 2002). In *T. brucei*, TbCH2.2 mediates retrograde intraflagellar transport (Blisnick et al. 2014) and localises in a similar pattern to that of Tb6560. However, loss of TbCH2.2 does not result in an enlarged FP, nor were endosomal defects observed (Blisnick et al. 2014). It is possible flagellar defects were overlooked in the Tb6560 mutants, as no direct examination of this structure was undertaken. However, when a preliminary examination of the FAZ by indirect IF (data not shown) was undertaken, no clear defects were observed. Mutants with highly distorted morphology still harboured the FAZ and the flagellum appeared to run along the full length of the cell body. Furthermore, from the FIB/TEM analysis, the -/- cells examined appeared to generate two flagella of approximately similar lengths, suggesting that generation of the flagella is not impaired. In contrast, loss of TbDHC2.2 results in reduced flagellar lengths (Blisnick et al. 2014). Tentatively, therefore, it appears Tb6560 and TbCH2.2 provide distinct functions, though further investigation may be required.

5.8.4 Tb6560 is unlikely to be directly associated with DNA repair

Despite significant growth reductions following exposure to different genotoxic agents, and a slightly elevated level of γ H2A expression, it is unlikely that the primary role of Tb6560 is during the DNA damage response. The increased γ H2A signal could be attributed to the morphological distortion observed in over 40 % of the cells, perhaps due to the nucleus becoming physically compressed due to the FP pocket expansion. Furthermore, the localisation of the protein suggests it is unlikely to influence repair of the nuclear or mitochondrial genomes. Indeed, the localisation was little changed by DNA damage exposure, suggesting re-localisation of the protein (to for example the nucleus) does not occur. Furthermore, the sensitivity to chemical agents such as MMS could potentially be linked to defective endocytosis. During MMS stress, in addition to DNA lesions, cellular structures become compromised and require repair (plasma membrane repair is reviewed by Andrews, Almeida, & Corrotte, 2014). The repair following exposure to, for example, a chemical agent, is not solely limited to the repair of nuclear DNA lesions, damage also occurs to the cellular architecture and organelles; this must also be resolved for normal cellular proliferation to continue (Andrews et al. 2014). Furthermore, if the genotoxic chemical is still present in the environment, the cell may need to assume measures to limit further uptake (Shen et al. 2012). For example, reduced uptake of the drug Cisplatin (CP; a commonly used chemotherapeutic drug) is associated with reduced efficacy (Chauhan et al. 2003). The localisation of Tb6560 suggests a potential association with the FP and possibly the endosomal network and thus potentially involved in the trafficking of material into (and around) the cell. This process of renewal following cellular damage has yet to be examined in *T. brucei*.

5.8.5 Summary

Overall, the work in this chapter represents both the characterisation of a novel pseudokinase with a function during BSF endocytosis and, potentially, the identification of a new, minor 'AP2-like' trafficking pathway in these parasites. Potentially Tb6560 may function in the physical movement of vesicles within the cytoplasm to the endosome system, and perhaps also to the flagellum.

6 Analysis of the DNA repair-associated protein kinases TbATR and TbATM in bloodstream form *T. brucei*

6.1 Introduction

As discussed in chapter 1, control of a cell's fate following the detection of a DNA lesion is mediated by the DNA damage response (DDR). At the centre of this response are atypical PKs (aPKs), notably ATR, ATM and DNA-PKcs.

6.1.1 The PIKK family

The members of the phosphatidyl inositol 3' kinase-related kinase (PIKK) family (mTOR, ATR, ATM, DNA-PK, TTRAP and SMG-1; unabbreviated names are shown in Table 6-1) do not possess a typical eukaryotic PK (ePK) structure (section 1.5), though members of this family share several conserved domains (discussed below). The PIKK kinases are named after their apparent sequence similarity (within their kinase domain; KD) to a family of lipid kinases (phosphatidyl inositol-3 kinases; PI3Ks), though the PIKKs do not phosphorylate lipids, only proteins. Typically, these PKs are known for their ability to interact with nucleotides, their large molecular sizes (ranging from ~300 kDa to ~500 kDa; Baretic & Williams 2014), their S/T kinase activity (for example, ATR and ATM are thought to preferentially phosphorylate S/T residues in immediate proximity to a Q residue; for mTOR, this can be a Proline or another hydrophobic amino acid; (Hsu et al. 2011; Abraham 2001) and, finally, their requirement for an interacting protein to aid their activation and/or mediate their activity (see Table 6-1 below). One member, the transcription/transformation associated protein (TTRAP), does not appear to harbour phosphotransferase capabilities and thus is likely to lack kinase activity. TTRAP's roles appear to be linked to regulation of histones (Cai et al. 2003), to the oncogenes c-MYC and E1A/E2F (both transcription factors; McMahon et al. 1998) and to the cell cycle-regulating kinase Wee1 (Calonge et al. 2010).

PIKK	Ataxia telangiectasia mutated (ATM/Tel1p)	ATM and Rad3 related (ATR/Mec1p)	DNA protein kinase catalytic subunit (DNA-PKcs)	Suppressor of morphogenesis in genitalia-1 (SMG-1)	Mechanistic target of rapamycin (mTOR/Tro1p+Tor2p)
Localisation	dsDNA	ssDNA	dsDNA	mRNA	Endomembranes
Regulatory Protein	NBS1 (Xrs2p)	ATRIP (Dcd2p)	Ku70/80	UPF1/SMG-8/SMG-9	RAPTOR/RICTOR/mLS T8/DEPTOR (Kog1p/Tco89p/Avo3p/Lst8p)
Activating protein	Mre11/RAD50 (Mre11p/Rad50p)	TopBP1 (Dpb11p)	Ku/DNA	UPF2	RHEB/TSC1/2/AMPK (Rhbpl/Snf1p)

Table 6-1: The members of the PIKK family, their localisation and their regulation Mammalian protein names are shown, with the *S. cerevisiae* homolog name in brackets. Table and information adapted from (Baretić & Williams 2014).

Structurally, the PIKKs show a high level of conservation and, with the publication of the crystal structures of most members (Wang et al. 2016 [ATM/Tel1], Baretić et al. 2016 [TOR/mTOR], Melero et al. 2014 [SMG-1] and Sibanda et al. 2010 [DNA-PK]), it is clear there are several interesting features of this kinase family. A generalised schematic of the structure of each kinase is shown in Figure 6-1 alongside the crystal structure of Tel1, the *S. cerevisiae* homolog of ATM (Wang et al. 2016).

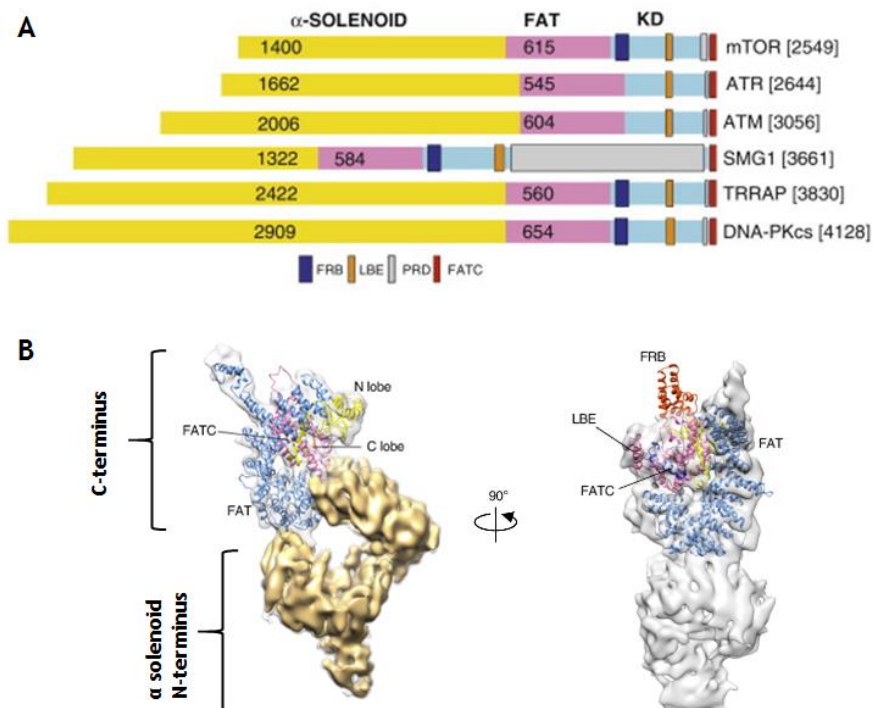


Figure 6-1: The generalised structure of PIKKs

(A) A generalised schematic of the structure of PIKKs from *H. sapiens*. Not to scale; size (in amino acids) is shown in brackets. (B) Architecture of a Tel1 monomer (the *S. cerevisiae* homolog of ATM). Model was fitted, colour coded and generated as described in (Wang et al.

2016). **(A)** Adapted from (Baretić & Williams 2014). **(B)** Adapted from (Wang et al. 2016). **All abbreviations in the diagram are explained in the text.**

Several domains and features are conserved between members; proposed functions are shown in Table 6-2. Typically, each PK has an extensive ‘superhelix’, or α solenoid, which comprises HEAT repeat arrays (Perry & Kleckner 2003) and provides stability to the structure (Takai et al. 2007). Located at the C-terminal end of the N-terminal region is the FAT domain, which also harbours HEAT repeat domains and is associated with the C-terminal Kinase domain (KD). The KD (also known as the ‘head’ region) is highly conserved between PIKKs and harbours other conserved sub-domains, such as the LST8-binding element (LBE), the FRB domain (absent from ATR and ATM) and, at the immediate C-terminal region, a PRD and a FATC domain.

Domain/Feature	Location	Function	Examples/References
α solenoid	N-terminus ‘Superhelix’ α helix repeats Present in all PIKKs	Structural support and potentially regulation of kinase activity Extension of the FAT domain	In ATM the solenoid is tightly packed to the FAT and KD (A)
FAT (FRAP, ATM and TTRAP)	N-terminus (close proximity to KD) Harbours subdomains within HRD TRD (TPR repeat containing) HRN (Heat repeat containing)	Encircles ~50% of the KD Retains structural integrity of KD Regulates Kinase activity	(A&B)
KD	C-terminus ~400 amino acids	Kinase activity, low sequence conservation to ePK KDs	SMG-1 has a more centrally located KD (B)
FRB (FKBP12 rapamycin binding domain)	C-terminus N-terminal to the KD (part of the FAT domain) Absent in ATR and ATM	Regulation of kinase activity	FKBP12:rapamycin complex inhibits mTOR activity when bound to the FRB domain (C)
LBE (LST8 binding element)	C-terminus	Interact with co-regulatory subunits Regulates kinase activity	mTOR can bind mammalian lethal with sec thirteen protein 8 (mLST8) to regulate its activity (D)
PRD (PIKK regulatory domain)	C-terminus (between KD and FATC domains)	~ 16-82 aa Regulates PK activity Required for posttranslational modifications and protein-protein interactions	<ul style="list-style-type: none"> • Deletion of PRD stops kinase activity (E) • PRD domain of ATR interacts with TopBP1 (E) • PRD domain of ATM interacts with Tip60, an acetyltransferase linked to DNA damage signalling (E)
FATC (FAT C-terminal)	C-terminus (most C-terminal region of the protein)	~ 30 aa Highly conserved between members Regulates kinase activity and protein-protein interactions	<ul style="list-style-type: none"> • Mutation of SMG-1 FATC domain can reduce kinase activity by >90% (E) • Tip60 can bind to the FATC domain of ATM and DNA-PKcs (E) • Rfa1 (a component of RPA complex in yeast) can bind FATC of ATR (Mec1p) and TopBP1 (Dcd2; E)

Table 6-2: Conserved PIKK domains and their potential functions

Table generated based on data from **(A)** (Wang et al. 2016), **(B)** (Baretić & Williams 2014), **(C)** (Schmelzle & Hall 2000), **2000**, **(D)** (Yang et al. 2013), **(E)** (Lempiäinen & Halazonetis 2009).

6.1.2 The roles of ATR and ATM in other eukaryotes

ATR was identified ~20 years ago (Bentley et al. 1996; Cimprich et al. 1996; Gatti et al. 1988) and, to date, remains at the forefront of research into the DDR. Another PIKK family member, ATM, is also heavily involved in the regulation of the DDR and the functions of ATR and ATM are not exclusive (Shiotani et al. 2013; Chanoux et al. 2009). To this end, the role of ATM was also briefly investigated in this chapter and is thus briefly introduced below.

6.1.2.1 ATR

ATR is often termed the ‘master regulator’ of the DDR and its importance in organism fecundity is complex. Whereas ATR null mutants are viable in plants (Culligan et al. 2004), the gene is essential in yeast (Cha & Kleckner 2002) and mammals (Brown & Baltimore 2000). ATR disruption is lethal during mouse embryogenesis (Brown & Baltimore 2000) and downregulating the gene in adult mice produces the onset of age-related symptoms such as osteoporosis (weakening of the bones; Ruzankina et al. 2007). In humans, mutations in the ATR gene result in Seckel Syndrome (or microcephalic primordial dwarfism; O’Driscoll et al. 2003) due to the vital role ATR plays in responding to a variety of DNA lesions, many of which are derived from replication. Interestingly, Seckel Syndrome does not result in a predisposition to cancers (O’Driscoll & Jeggo 2003; O’Driscoll et al. 2004), despite loss of ATR being associated with genome instabilities.

ATR is thought to be activated in response to the presence of ssDNA, often associated with stalled replication forks, since this kinase exerts its function during S-phase of the cell cycle. Canonically, ATR is activated in the following manner (as detailed in Figure 6-2; for reviews see Fokas et al. 2014; Kidiyoor et al. 2016). When ssDNA is formed, ssDNA is coated by RPA. RPA in turn recruits the ATR interacting partner (ATRIP), which is stably complexed to ATR and thus recruits ATR to the lesion site. Independently, RPA recruits the clamp loader protein RAD17, which loads the 9-1-1 complex (a heterotrimeric complex comprising Rad9-Hus1-Rad1). The 9-1-1 complex (via Rad9) recruits the ATR activating protein TopBP1, which is required for the activation of ATR; preventing this interaction ablates ATR signalling (Mordes et al. 2008) and

downstream phosphorylation pathways. TopBP1 interacts with the PRD domain of ATR and activates the kinase via its ATR activation domain (AAD; reviewed by Mordes et al. 2008). Once activated, ATR can activate (by phosphorylation) the kinase check point kinase 1 (CHK1/CHEK1). TopBP1 also aids in bringing CHK1 into contact with ATR. CHK1 has numerous interaction partners and, once activated, it can phosphorylate proteins like Cdc25a to prevent cell cycle progression (a G2 arrest) and block or slow late origin firing (Shechter et al. 2004). CHK1 phosphorylation can also prevent entry to S-phase (Capasso et al. 2002 and reviewed by Yu 2007).

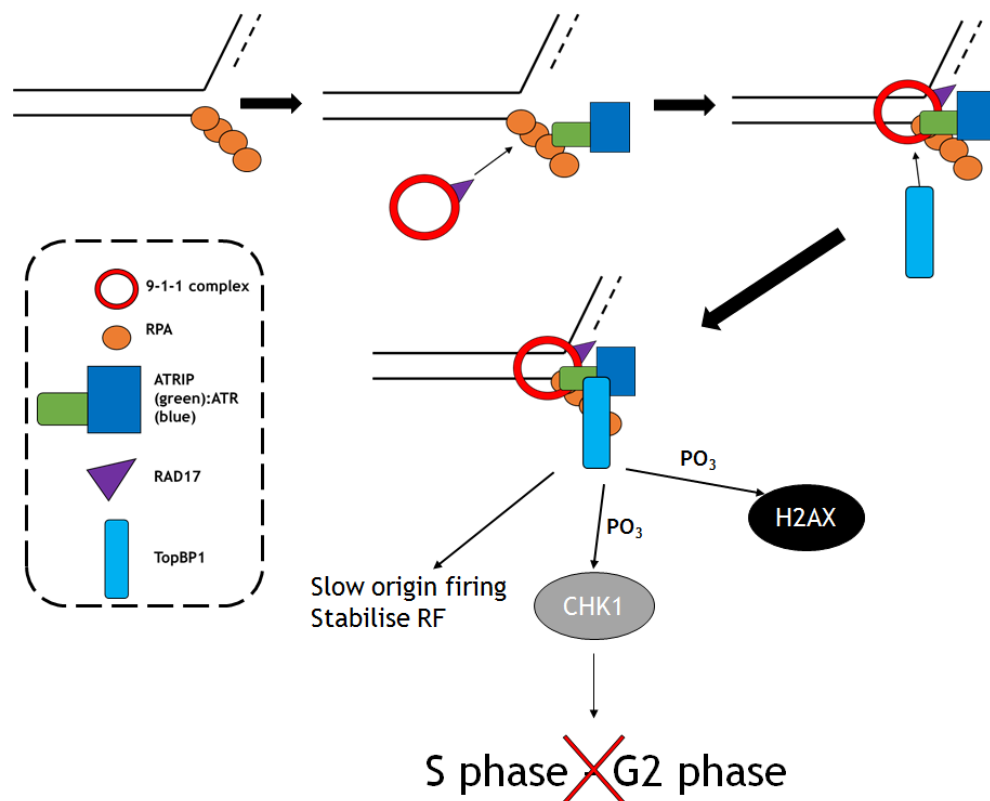


Figure 6-2: Canonical activation of ATR in eukaryotes

A full description of the process illustrated in the figure is available in the text. A key of shapes used to represent proteins is shown in the dashed box. Figure constructed based on information from (Cimprich & Cortez 2008a), (Bartek et al. 2004), (Hammarton et al. 2004) and (Lobrich & Jeggo 2007).

Activation of ATR can also occur from several other sources, such as mechanical stress to or deformation of the nuclear envelope (though the mechanism behind this is not understood; Kumar et al. 2014), stress from the nucleolus (ATR can localise here under mechanical stress), cytoplasmic stress, and even an association between ATR and the centrosomes. These mechanisms of ATR activation are still being investigated and highlight the diverse range of

regulatory functions this kinase can perform in a cell (as reviewed by Kidiyoor et al. 2016).

The function of TbATR has been preliminarily examined in both the PCF and BSF of *T. brucei*, but with conflicting results. In PCF and BSF cells it was initially reported that TbATR is a non-essential PK when targeted by RNAi (Forsythe 2012). However, Jones et al. (2014) reported that loss of TbATR was detrimental to BSF proliferation. As many pathways of the DDR (and many of their component proteins) are conserved within the kinetoplastids, it is plausible, given the role ATR performs in other eukaryotes, that this kinase may also play an important role in mediating the DDR. However, limited information is available regarding TbATR and its downstream interaction partners in these parasites. Several proteins key in the mediation of TbATR activity have yet to be identified by sequence homology, such as the *T. brucei* homolog of ATRIP and the CHK1. In contrast, TopBP1 has been identified (Genois et al. 2014) and the 9-1-1 complex, of which the RAD9 component can directly interact with TopBP1 to activate ATR in other eukaryotes (ATR activation by TopBP1 is reviewed by Burrows & Elledge 2008), has been characterised in detail in *L. major* (Damasceno et al. 2016; Damasceno et al. 2013), perhaps suggesting this arm of the ATR pathway may operate. However, the *Leishmania* 9-1-1 complex harbours functional divergence from its known roles in higher eukaryotes: whereas loss of RAD9 increases sensitivity to genotoxic stress, Hus1 loss increases survival. Thus, exactly how TbATR might act in the kinetoplastid DDR is unclear.

6.1.2.2 ATM

Mutations of the ATM gene in humans are hallmarks of the autosomal recessive condition known as Ataxia-Telgancietasia (A-T/ 'Louis-Bar Syndrome'), a neurodegenerative and generally debilitating syndrome (Savitsky et al. 1995). Unlike ATR, ATM is not essential in yeast (Lustig & Petes 1986) or mammals (Xu et al. 1996), where disruption of the gene is associated with genomic fragility and infertility (Xu et al. 1996). Despite this, recent evidence suggests ATM may be a critical PK; mice harbouring a kinase dead (or catalytically inactive ATM) were shown to die during embryogenesis (Yamamoto et al. 2012; Daniel et al. 2012). Human ATM mutant cells show an increased sensitivity to IR sources, indicating ATM is required to detect DSBs. ATM is important for guiding the

repair of DSBs by either NHEJ (G1 phase) or HR (S-phase), though more recently roles for ATM have been described following replicative stress-induced lesions (Schmidt et al. 2014) and in the regulation of ROSs (Ito et al. 2007; Formichi et al. 2000; Xie et al. 2001), suggesting we are still far from understanding all roles of this PIKK. ATM is recruited to DSBs as an inactive dimer by the MRN complex, which the kinase autophosphorylates, leading to release of one ATM monomer and activation of the other. ATM can phosphorylate critical downstream proteins, such as the variant histone H2AX (generating the histone variant γ H2AX), the tumour suppressor protein p53 (St. Clair & Manfredi 2006; Zilfou & Lowe 2009; Marechal & Zou 2013) and PKs such as checkpoint kinase 2 (CHK2/CHEK2), resulting in cell cycle stall at G1-S. ATM has also been shown to mediate G2-M stalling, though this checkpoint activation may be due to ATM acting in conjunction with ATR to repair stalled replication forks (Cimprich & Cortez 2008b; Ammazalorso et al. 2010). For a comprehensive review on the role of ATM in other eukaryotes, the reader is referred to Shiloh & Ziv 2013.

Like ATR, the role of ATM is unclear in *T. brucei*. Previous data suggested TbATM to be essential for PCF and BSF proliferation (Forsythe 2012). Furthermore, *T. brucei* does not appear to undergo NHEJ, and nor does it appear to harbour a p53 protein, though a potential homolog of the PK CHK2 is present. Hence, regulation of the DSB repair may be diverged from other eukaryotes.

Components of the MRN complex (TbMRE11 and TbRAD50) have been examined in *T. brucei* (Tan et al. 2002; for TbRAD50 this data is unpublished, J. Stortz and M. Prorocic) and *Leishmania* (Laffitte et al. 2016) and, when knocked out, cells become sensitised to genotoxic stress, suggesting the MRN complex may act through ATM, but no direct evaluation of this route has been conducted.

However, it should be noted that ATR has also been shown to interact with the MRN complex in other eukaryotes, facilitating activation via TopBP1 (Duursma et al. 2013).

6.2 Chapter Aims

The aim of this chapter is to explore the role of TbATR in BSF cells in more depth and, briefly, to examine the role of TbATM.

6.3 Results

6.3.1 Bioinformatics analysis

TbATR (a predicted protein ~320.6 kDa in size; 2860 amino acids) is encoded for by the gene Tb927.11.14680. TbATM (~468.5 kDa in size; 4277 amino acids) is encoded for by the gene Tb927.2.2260 (TriTrypDB v.28).

6.3.1.1 BLAST Analysis

Using BLASTp within TriTrypDB with the protein sequence of the predicted ATR homolog of *T. brucei* retrieved highly conserved orthologues from related kinetoplastid organisms, suggesting the PK is present across this grouping (data not shown). To identify homologs in other organisms, the same analysis was performed using the NCBI database and BLASTp hits were identified using the ‘SmartBLAST’ feature as described in chapter 4. The top five best ‘hits’ for ATR are shown in Table 6-3.

Name of protein	Species	Query Cover (%)	E Value	Identity (%)	Accession Number
PIKK, putative	<i>T. b. gambiense</i> DAL972	100	0.0	99	XP_011780791.1
Putative PIKK	<i>T. vivax</i> Y486	99	0.0	49	CCC54057.1
PIKK	<i>T. grayi</i>	99	0.0	50	XP_009306375.1
PIKK, putative	<i>L. donovani</i>	58	0.0	39	XP_003863568.1
S/T PK ATR	<i>A. thaliana</i>	45	2e-126	26	NP_198898.2

Table 6-3: Top 5 ‘hit’s from the SmartBLAST analysis of TbATR
The top ‘hits’ retrieved from the SmartBLAST analysis using the protein sequence of TbATR (as retrieved from TriTrypDB v28). The analysis was performed in August 2016.

As expected, the most conserved homologs were from kinetoplastid family members. More distantly related, but still well conserved, were characterised ATRs from other eukaryotes (Table 6-3 and Table 6-4). ATR from *A. thaliana* showed the greatest identity (45% identity, E value = $2e^{-126}$), followed by hits to ATR from *M. musculus*, *D. rerio*, *H. sapiens*, and to Rad3 from *S. pombe* and Mec1 (*S. cerevisiae*); E values between $E = e^{-119}$ to $E = e^{-98}$. More distant homology

was seen to further PIKK family members: ATM from *C. elegans* and *M. musculus*, and mTOR from *M. musculus* and *C. elegans* (Table 6-4).

Name of protein	Species	Query Cover (%)	E Value	Identity (%)	Accession Number
ATR isoform X3	<i>M. musculus</i>	45	9e-119	26	XP_006511251.1
ATR	<i>D. rerio</i>	49	2e-115	25	XP_696163.5
ATR isoform X3	<i>H. sapiens</i>	45	6e-114	25	XP_016862132.1
Rad3	<i>S. pombe</i>	45	5e-105	24	NP_595357.1
MEC1	<i>S. cerevisiae</i>	26	9e-98	26	NP_009694.3
ATM	<i>C. elegans</i>	19	6e-45	26	NP_001256128.1
ATM isoform X1	<i>M. musculus</i>	13	6e-43	28	XP_011240687.1
Target of rapamycin homology	<i>C. elegans</i>	12	3e-40	28	NP_491552.2
mTOR	<i>M. musculus</i>	10	3e-40	30	NP_064393.2

Table 6-4: Additional 'hits' from the SmartBLAST analysis of TbATR
Additional 'hits' retrieved from the SmartBLAST analysis using the protein sequence of ATR (as retrieved from TriTrypDB v28). The analysis was performed in August 2016.

When the above process was repeated for Tb927.2.2260, encoding the predicted homolog of TbATM, it was found that, as described for TbATR, highly conserved orthologues can be identified across the kinetoplastid phylum (Table 6-5). Again, *T. brucei* ATM appeared to share highest sequence conservation beyond kinetoplastids with ATM from a plant species (*G. max*; Soybean).

Name of protein	Species	Query Cover (%)	E Value	Identity (%)	Accession Number
Phosphatidylinositol kinase domain protein	<i>T. b. gambiense</i> DAL972	100	0.0	99	XP_011771668.1
Phosphatidylinositol kinase domain protein, fragment	<i>T. vivax</i> Y486	99	0.0	48	CCC46616.1
Unnamed protein product	<i>T. congolense</i>	68	0.0	60	CCC89447.1
PIKK, putative	<i>L. donovani</i>	50	3e-153	44	XP_003857906.1
ATM isoform X4	<i>G. max</i>	17	2e-100	34	XP_014630271.1

Table 6-5: Top 5 'hit's from the SmartBLAST analysis of TbATM
The top 'hits' retrieved from the SmartBLAST analysis using the protein sequence of TbATM (as retrieved from TriTrypDB v28). The analysis was performed in August 2016.

Name of protein	Species	Query Cover (%)	E Value	Identity (%)	Accession Number
ATM	<i>A. thaliana</i>	17	2e-97	34	NP_190402.6
ATM	<i>M. musculus</i>	16	9e-97	32	NP_031525.2
ATM isoform X8	<i>H. sapiens</i>	16	2e-95	32	XP_006718908.1
ATM	<i>D. rerio</i>	16	9e-91	31	XP_002664603.3
ATM	<i>S. pombe</i>	16	9e-73	29	NP_588126.1

Table 6-6: Additional 'hits' from the SmartBLAST analysis of TbATM
 Additional 'hits' retrieved from the SmartBLAST analysis using the protein sequence of TbATM (as retrieved from TriTrypDB v28). The analysis was performed in August 2016.

SmartBLAST analysis with *T. brucei* TbATM further revealed ATM orthologs from other organisms with high confidence (E values between $E = e^{-97}$ to $E = e^{-73}$; Table 6-6).

For both of *T. brucei* ATR and ATM, the primary region of homology was within the C-terminus region of the kinases, which harbours the highly conserved KD. For TbATM, a lower level of sequence conservation was observed. For example, ~45 % of the sequence of *T. brucei* ATR could be aligned against *A. thaliana* ATR (Evalue $E = 2e^{-126}$), of which ~26 % of the sequence was identical. In contrast, for TbATM, only 17 % of the *T. brucei* sequence could be aligned against *A. thaliana* ATM (E value $E = 2e^{-97}$) of which 34 % was identical.

6.3.1.2 Domain predictions

PIKKs have a highly conserved structure (as discussed above), with many PIKK-specific domains, including the FAT and HEAT repeat domains located within the N-terminal region, and the FATC located at the C-terminal of the kinase. These domains are required to mediate kinase activity and maintain kinase structure (as reviewed by Baretić & Williams 2014). To examine whether these domains are present in the *T. brucei* homologs of ATR and ATM, conserved domains were searched for using the Interpro and NCBI database webserver. Additionally, the kinases were aligned against the corresponding homolog in *H. sapiens* and *S. cerevisiae* (data shown in chapter 8, section 8.5, Figure 8-29 [TbATR] and Figure 8-30 [TbATM]) using CLC Genomics Workbench 7. The structure of both *T. brucei* kinases was also modelled using the RaptorX webserver program; however, due

to the size of each protein the majority of the N-terminal domain was modelled separately from the remaining protein sequence (the sequence size input into the program is limited to 2500 aa; both kinases are considerably larger). Data from the Raptor analyses are shown in chapter 8, section 8.5, Figure 8-31.

6.3.1.2.1 TbATR

Several PIKK-specific domains could be identified in *T. brucei* ATR (Figure 6-3 A). From the predicted structural model of the protein (chapter 8, section 8.5, Figure 8-31), the N-terminal region appeared primarily composed of helical repeats, in keeping with the presence of the α -solenoid domain (RaptorX analysis suggested ~ 70 % of the first 2477 amino acids form α helices). Such a structure is in keeping with the likely presence of HEAT repeat domains, though when examined at the sequence level very little conservation was observed between the predicted human ATR HEAT repeats and the potential location of the *T. brucei* ATR HEAT repeats. FAT, FATC, KD and a UME domain were all readily identified, with a similar positioning relative to human ATR. The function of the UME domain is still under investigation, but it is associated with nucleolar proteins harbouring FAT and FATC domains (as detailed by the SMART; <http://smart.embl-heidelberg.de/>). Importantly, when both the catalytic and activation loops of the KD were examined, it was found that the sequence was highly conserved between ATRs from *T. brucei*, *H. sapiens* and *S. cerevisiae*, highlighting the conservation of the KD (Figure 6-3 B). The PRD domain of *T. brucei* did not appear highly conserved relative to the human ATR PRD domain, though its potential position is marked in Figure 6-3 A. Within the PRD domain are residues with which the ATR activating protein and TopBP1 can interact. These residues include a lysine (K2589) and a His-Val-Leu (HVL) triad; mutation of these residues reduces ATR activation by TopBP1 (reviewed by Burrows & Elledge 2008). Though a potential homolog of TopBP1 was identified in the *T. brucei* genome, alignment of the human ATR and the *T. brucei* ATR sequences did not reveal conserved residues within the KD region in a similar position (chapter 8, section 8.5, Figure 8-29 [TbATR] and Figure 8-30 [TbATM]). Another domain conserved across members of the PIKK is an LBE domain (Table 6-2), but this could also not be identified in the *T. brucei* ATR sequence.

In humans, ATR is phosphorylated on a threonine (T1989) within the FAT domain, which is critical for its activation; the phosphorylation occurs when ATR:ATRIP complexes associate with RPA bound ssDNA (Liu et al. 2011). The same modified residue is also recognised by TopBP1. However, no clearly positionally conserved T residue could be found in *T. brucei* ATR.

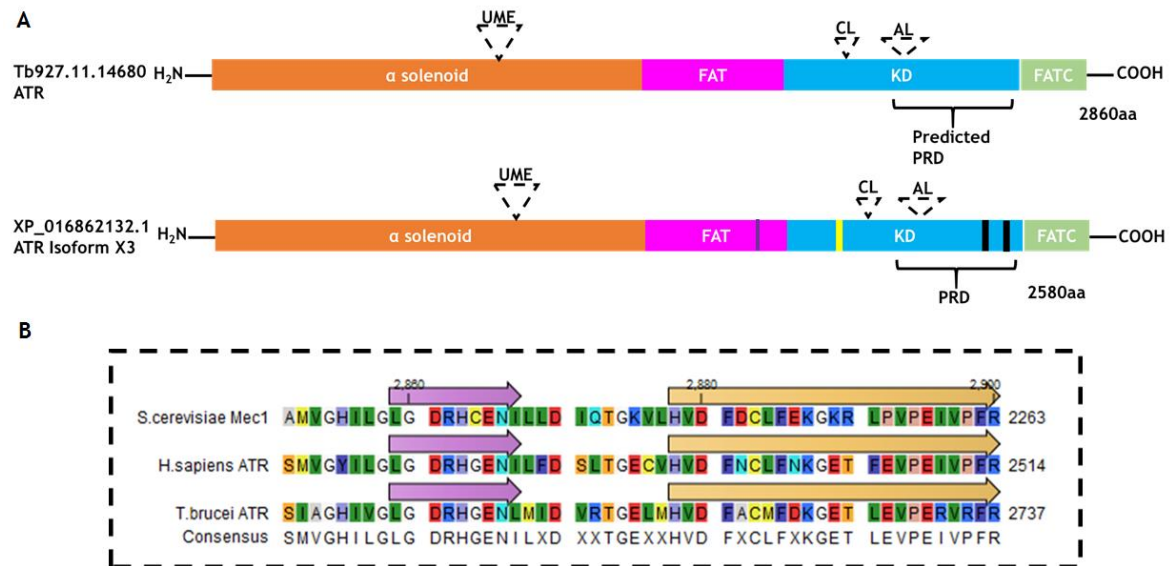


Figure 6-3: Schematic illustration of conserved motifs between the human ATR and the *T. brucei* ATR

(A) The conserved sequence motifs of TbATR found in the protein sequence of *T. brucei* ATR compared with the conserved sequence motifs of ATR in *H. sapiens*. The sequence motif is annotated above its location. Dark blue bar (T1989 modification), Yellow bar (LBE domain), Black bars (K2589 and the HVL motifs respectively required for ATR activation by TopBP1), CL (catalytic loop) and AL (activation loop). Not to scale. The domains in the figure above are based on the position of the domain as determined using Interpro, NCBI searches and from data in the following papers: (Liu et al. 2011; Burrows & Elledge 2008) **(B)** The catalytic (purple arrow) and activation (orange arrow) loops of ATR from *H. sapiens*, *S. cerevisiae* (Mec1) and *T. brucei*. The sequence alignment was performed in CLC genomic workbench 7. Mec1 accession number: NP_009694.3.

6.3.1.2.2 TbATM

As for TbATR, the N-terminal domain of this kinase was predicted to adopt an α -solenoid structure typical of PIKKs; ~ 57 % of the N-terminal domain (spanning the first 2499 amino acids; a schematic of the domain order in TbATM is shown in Figure 6-4 A) was predicted to be arranged as α -helices (chapter 8, section 8.5, Figure 8-31 C&D). Several PIKK-specific domains could also be identified in the sequence of *T. brucei* ATM, with the notable exception of a FAT domain. As this domain is required for stabilisation of the kinase structure and its activation, its potential absence or divergence may suggest that the regulation of TbATM activity is divergent from that of the human ATM kinase. In addition, neither an

LBE or a TAN domain could be identified. The TAN domain of ATM is important for the localisation of ATM to a DSB and to prevent telomere shortening (as shown from studies in *S. cerevisiae*; Seidel et al. 2008).

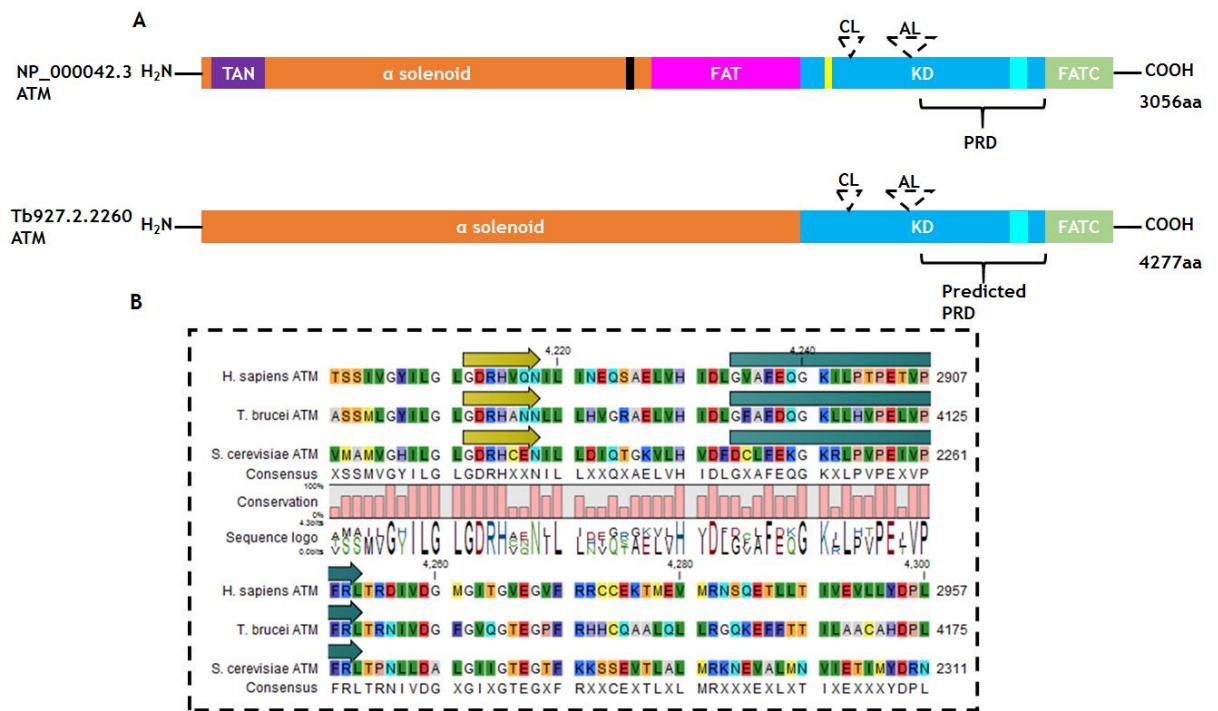


Figure 6-4: Schematic illustration of conserved motifs between the human ATM and the *T. brucei* ATM

(A) The conserved sequence motifs of ATM found in the protein sequence of *T. brucei* ATM compared with the conserved sequence motifs of ATM in *H. sapiens*. The sequence motif is annotated above its location. Black bar (S1981 modification), Yellow bar (LBE domain), Turquoise bar (K3016 [*H. sapiens*], K4237 [*T. brucei*]), CL (catalytic loop) and AL (activation loop). Not to scale. The domains in the figure above are based on the position of the domain as determined using Interpro, NCBI searches and from data in the following papers: (Liu et al. 2011; Burrows & Elledge 2008; Seidel et al. 2008). (B) The catalytic (yellow arrow) and activation (blue arrow) loops of ATR from *H. sapiens*, *S. cerevisiae* Tel1) and *T. brucei*. The sequence alignment was performed in CLC genomic workbench 7. Tel1 accession number: KZV13216.1.

As observed for TbATR, both the catalytic and activation loops (Figure 6-4 B) harboured a high level of sequence conservation between the *H. sapiens*, *S. cerevisiae* and *T. brucei* ATM (a full alignment is shown in chapter 8, section 8.5, Figure 8-30).

Several key phosphorylation sites have also been identified in human ATM, with the most prominent being a serine residue in position 1981 (S1981); ATM is autophosphorylated here in order to become activated (Bakkenist & Kastan 2003). This residue was absent in *T. brucei* and, interestingly, no phosphorylation sites were identified on the *T. brucei* ATM kinase (Urbaniak et

al. 2013), though other post translational modifications may occur. One key conserved residue within the C-terminal domain of the *T. brucei* ATM was found. This residue, a lysine at position 3016, is acetylated by the histone acetyltransferase Tip60, and is required for ATM activation (Sun et al. 2007). Alignment of the human and *T. brucei* ATM sequences predicted the equivalent a lysine to be at position 4237 in *T. brucei* ATM.

6.3.2 RNAi cell lines used in this chapter

Both TbATR BSF RNAi lines used were kindly provided by E. Brown (University of York). The TbATM RNAi targeting construct and the subsequently produced BSF RNAi cell line were generated, transformed and selected for as described in section 2.3 and 2.7.4. One clone was used in this study (cell lines are detailed in the table below; Table 6-7).

Gene ID	Annotation (TriTrypDB v.28)	Stabilate number	Plasmid number/name	Puromycin status
Tb927.11.14680	ATR	STL0081	pTL50	Sensitive
Tb927.11.14680	ATR	STL0082	pTL50	Sensitive
Tb927.2.2260	ATM	TRY18446	ATM RNAi	Resistant

Table 6-7: RNAi cell lines required for this study

The STL/TRY number refers to the stabilate number as numbered according to the Mottram and McCulloch laboratory systems for stabilate labelling. The plasmid number (pTL) is as according to the Mottram laboratory plasmid repository numbering system. Puromycin sensitivity was examined prior to freezing.

6.3.3 Generation of endogenously tagged RNAi cell lines

6.3.3.1 Generation of C-terminal endogenously tagged TbATR and TbATM RNAi cell lines

To assess gene knockdown following RNAi induction, the TbATM and TbATR genes were C-terminally endogenously tagged with the 12 myc epitope in their cognate RNAi cell line using the strategy described in section 2.4.1.1.1. The primers and restriction sites used for cloning are described in Table 2-2. The constructs were assessed by restriction digest analyses (section 2.2.6) and the insert sequences

were confirmed by sequence analysis (as per section 2.2.9). The resulting constructs (TbATR^{12myc} and TbATM^{12myc}) were linearised by restriction digestion (as detailed in section 2.2.6) prior to transformation into the respective RNAi cell line; one TbATR RNAi clone (TbATR RNAi CL2) and the sole TbATM RNAi clone were transformed. Transformants were selected as detailed in section 2.7.4 and several clones were recovered and expanded for further analysis.

6.3.3.2 Confirmation of endogenously tagged TbATR and TbATM in RNAi cell lines

Putatively tagged clones were examined for expression of myc-tagged protein by western blot analysis, which was performed as described in section 2.12.1. The western blots are shown in Figure 6-5.

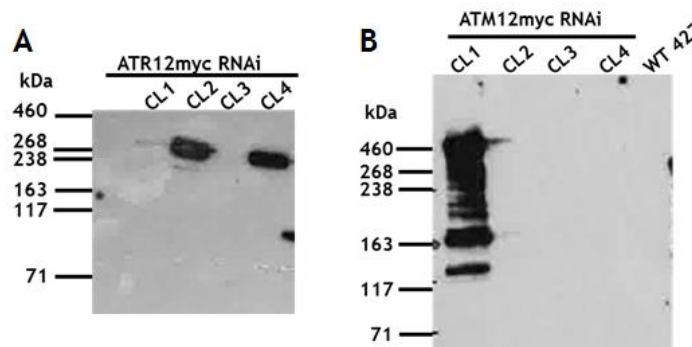


Figure 6-5: Confirmation of endogenously 12myc-tagged TbATR and TbATM by western blot Western blot analysis performed as per section 2.12.1 on putatively tagged ATR RNAi (A) and ATM RNAi transformant clones. The ladder shows size markers in kDa. Wild type (WT) 427 cells were used as a negative control. Whole cell extracts were resolved on a 3-8% BT gel. The following sizes refer to the predicted molecular weight (MW) of the tagged proteins (from TriTrypDB) + the MW of the 12myc tag (14.4 kDa). Tb927.2.2260 (TbATM: 482.8 kDa) and Tb927.11.14680 (TbATR: 335 kDa). Ladder used: HiMark™ Pre-Stained Protein Standard (ThermoFisher).

Two of four TbATR RNAi transformants expressed myc-tagged protein of approximately the expected size. In contrast, only one TbATM RNAi transformant revealed a signal, which was seen as multiple bands. The highest molecular weight appeared compatible with the expected size of TbATM-12myc, and so degradation may explain the smaller species (even though protease and phosphatase inhibitors were added). One clone for each gene was expanded for further analysis.

6.3.3.3 Localisation of TbATR and TbATM

Despite potentially successfully endogenously tagging TbATR and TbATM in their respective RNAi cell lines, no clear detection of the anti-myc signal could be ascertained for either PK by indirect IF using α -myc antiserum to detect the epitope tag (data not shown). Even when the cells were subjected to genotoxic stress, by growing them in $1 \mu\text{g}/\text{ml}^{-1}$ PHL or 0.0003 % MMS for 18 hrs, again no detectable myc signal could be obtained (data not shown). Endogenously tagging TbATR at the N-terminus (in wild type 427 cells) was also attempted, but myc-tagged transformants were not recovered (data not shown).

6.3.4 Phenotypic analysis

6.3.4.1 *In vitro* growth analysis

To examine the effect of TbATR or TbATM loss in BSF parasites *in vitro*, cell proliferation was examined (as detailed in section 2.8.1) following RNAi knockdown using two TbATR RNAi clones (one harbouring an endogenous myc tagged variant) and one endogenously tagged TbATM RNAi clone. The assay was performed as detailed in section 2.8.1.

Approximately 24 hrs after TbATR knockdown, growth of both clones (CL1 and CL2) was reduced relative to the non-induced control (Figure 6-6 A). From ~48 hrs, growth of the RNAi induced cells appeared to recover, but the cell density was markedly lower than the controls throughout the experiment. qRT-PCR of the untagged clone, and western analysis of the endogenously tagged clone, showed growth impairment was accompanied by reduced levels of TbATR RNA and loss of detectable TbATR-12myc protein from 24 hrs onwards (Figure 6-6 B&C). Scanning electron microscope (SEM; as described in section 2.11.7.1; Figure 6-7) of cells 36 hrs and 48 hrs post RNAi induction revealed the ultrastructure of cells that could be readily seen to be morphologically aberrant by light microscopy between 48-72 hrs of growth (data not shown). Commonly, large clumps of cells, or enlarged cells with a 'ruffled' membrane appearance, could be observed. At ~96 hrs post induction, when the loss of proliferation appeared much less pronounced, the number of morphologically aberrant cells in the populations became reduced for both clones (data not shown) perhaps

suggesting selection for RNAi cells that had become insensitive to tetracycline RNAi induction.

In striking contrast, no proliferation defects were observed following RNAi knockdown of TbATM (Figure 6-6 D), even after 7 days of growth. The lack of a growth defect could not be attributed to impaired RNAi induction, since from 24 hrs post-induction loss of myc-tagged protein was observed by western blot analysis (Figure 6-6 E). These data suggest that TbATM, unlike TbATR, is non-essential for *in vitro* BSF proliferation, though generation of a null mutant would be necessary to confirm this prediction.

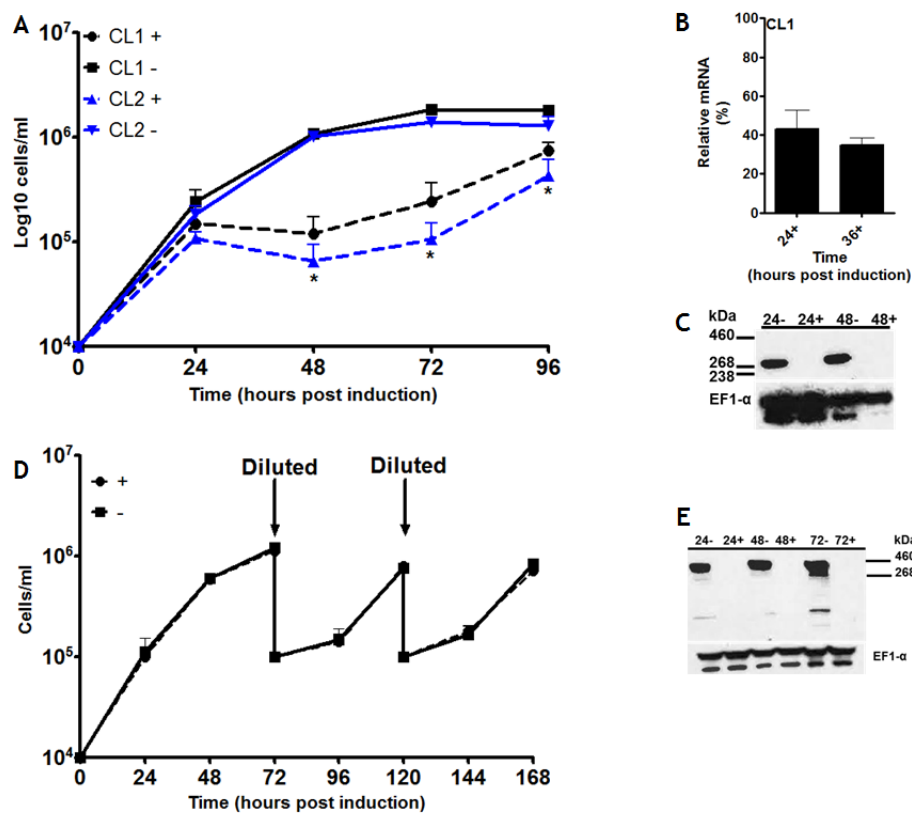


Figure 6-6: *In vitro* growth analysis of TbATR and TbATM RNAi cell lines

Growth analysis of TbATR (A) and TbATM (D) RNAi cell lines after induction of gene knockdown using tetracycline ($1 \mu\text{g}\cdot\text{ml}^{-1}$). The (+) denotes tetracycline induced samples. The (-) denotes the uninduced samples. The error bars represent \pm SEM, $n=3$ (A) and \pm SEM, $n=2$ (D). For statistical analysis for (A), tet - cells (blue [CL2] and black [CL1] dashed lines) were compared with their corresponding tet + cells (blue [CL2] and black [CL1] solid lines) at each time point; (*) = $p < 0.05$ as determined by a Mann Whitney U test. (B) qRT-PCR analysis, comparing TbATR RNA abundance in TbATR CL1 cells 24 and 36 post RNAi induction (+) relative to uninduced (set at 100%). (C) and (E) show western blots to evaluate levels of TbATR-12myc and TbATM-12myc, respectively, after 24, 48 and 72 hrs growth with (+) and without (-) induction of RNAi. The endogenously myc-tagged proteins were detected using α myc antiserum, and EF1 α was used as a loading control. White space indicates images excised and aligned from a larger blot.

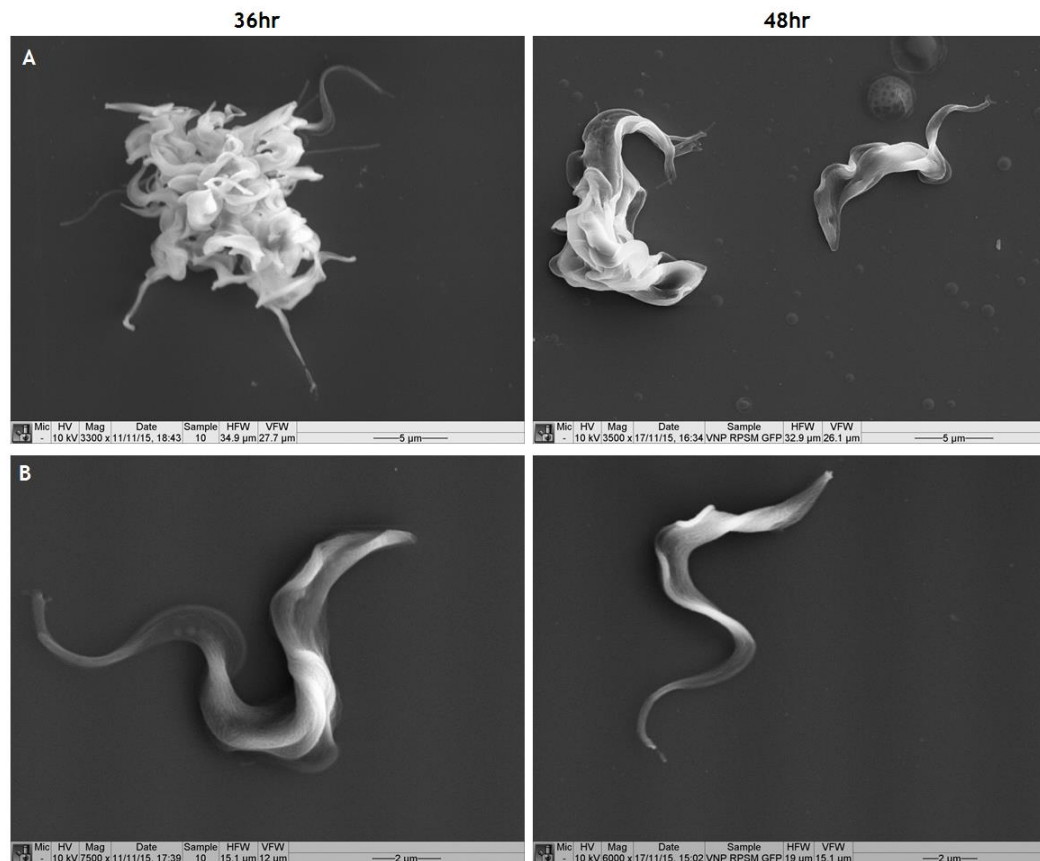


Figure 6-7: Loss of TbATR results in morphologically aberrant cells
 Representative SEM images of morphological abnormalities in induced (A) cells and non-induced (B) cells at 36hrs (left images) and 48hrs (right images) post RNAi induction. Images were captured on a Jeol 6400 scanning electron microscope (section 2.11.7.1) and processed by L.Lemgruber-Soares. Scale bars: top= 5 μm ; below= 2 μm .

In other eukaryotes, loss of ATR prevents S-phase checkpoint activation in the face of replicative stress, resulting in the accumulation of DNA lesions and chromosomal aberrations (Zeman & Cimprich 2014; Pennarun et al. 2010) as the nDNA continues to replicate without ATR signalling for repair. With this in mind, the cell cycle profile following TbATR knockdown was examined *in vitro* by flow cytometry (section 2.8.4) and DAPI staining (section 2.8.3 and 2.11.1), as shown in Figure 6-8. No such analysis was performed following loss of TbATM.

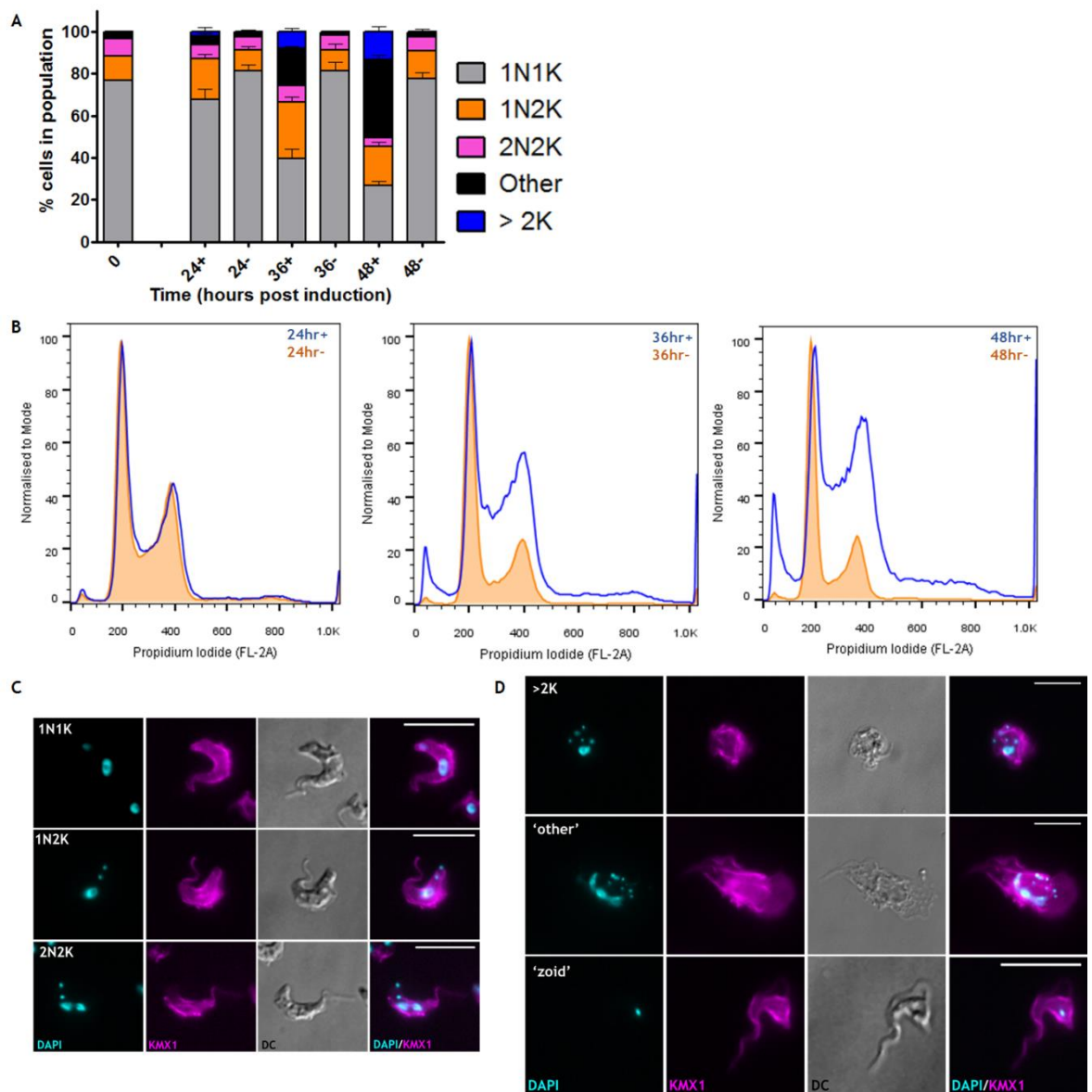


Figure 6-8: *In vitro* cell cycle analysis of TbATR

The cell cycle following loss of TbATR (A) was examined by DAPI staining to visualise the nDNA and the kDNA (section 2.11.1). The number of cells in each category was counted and is expressed as a percentage of the total number of cells counted. The error bars show \pm SEM, $n=3$. Over 200 cells were counted per experiment. The cell cycle was also examined by flow cytometry (C) as per section 2.8.4. The distribution of each population of cells is shown according to their DNA content. 50000 events were captured with the number of cells normalised to the mode. DNA was stained with propidium iodide (FL-2A channel). Tet + (blue line) and Tet - (orange plot) are shown as overlapped histograms. These data are from one experiment, a second experiment is shown in chapter 8, section 8.5, Figure 8-32. The histograms were generated using FlowJo V10 software (<http://www.flowjo.com/>). Representative images of uninduced cells (C) and cells induced for 48 hrs with $1 \mu\text{g/ml}^{-1}$ tetracycline (D). Cells were fixed as per section 2.11.1 and stained with DAPI (to visualise the n- and kDNA; cyan) and α KMX-1 antiserum (to visualise tubulin; magenta; section 2.11.2). The cell body was visualised by differential interference contrast microscopy (labelled as DC). Scale bar = $10 \mu\text{m}$. Images were captured on an Axioskop 2.

Loss of TbATR significantly affected cell cycle progression of BSF *T. brucei*. At 24 hrs post induction, very few effects on DNA content were seen in the flow cytometry analysis, though DAPI staining suggested a small increase in 1N2K

cells. These minor effects are in keeping with slight reduction in growth (Figure 6-8 A) at this time point. However, at 36 hrs post induction, a significant increase in 1N2K cells was observed by DAPI counting, suggesting a stall during S-phase of the cell cycle; this was confirmed by the flow cytometry analysis, where both an increase in an S-phase population and cells with 4N DNA content was observed. Furthermore, at 36 hrs a significant increase in aberrant cells was observed. A notable class of these cells were those with multiple kinetoplasts, perhaps consistent with loss of the checkpoint signalling the completion of nDNA replication and triggering the onset of cytokinesis, meaning the kinetoplast can enter a new round of replication. Often these cells also had enlarged, miss-shapen or fragmented nuclei (discussed in more detail in section 6.3.5, below; 'others'; see Figure 6-8 C&D for representative images). From the flow cytometry data (Figure 6-8 B), two populations of cells began to appear outwith the normal constraints of the cell cycle; those with $< 2N$ DNA content and those with $> 2N$. The former population may correspond with 'zoid' cells, which lack a nucleus. Indeed, some anucleate cells could be seen following DAPI staining (see Figure 6-8 D; lower panel); though, these were a minor population and were classed simply as 'other' cells. Nonetheless, the detection of this subset of cells may provide further evidence that cytokinesis can proceed after TbATR RNAi, despite aberrant nuclear division or replication. Multinucleated cells were also observed by DAPI staining, in keeping with the flow cytometry observations. In some of these cells, the nDNA content was uneven, perhaps suggested the DNA had become fragmented; indeed, in some cases it was difficult to judge whether the perceived extra kinetoplasts were in fact just pieces of fragmented nDNA. At 48 hrs post induction, the above effects increased yet further. An increase in 1N2K cells and further increased numbers of 'others', including $> 2K$ cells, were observed suggesting a persistent S-phase stall and aberrant or perhaps absent cytokinesis; these data were supported by further increases in altered DNA content seen by flow cytometry.

6.3.5 Nuclear defects arise in TbATR deficient cell lines

Gross nuclear defects and chromosomal rearrangements are associated with the loss of ATR in eukaryotic cells (Pennarun et al. 2010) and, indeed, from 36 hrs post RNAi induction, *T. brucei* cells with aberrant nuclear content were observed by DAPI staining and flow cytometry. To investigate this further, the

ultrastructure of the nucleus (section 2.11.7.2) and the position of the telomeres (and thus the arrangement of the chromosomes; section 2.10) were examined following TbATR knockdown.

Cells were collected at 24 hrs, 36 hrs and 48 hrs post RNAi induction and first stained with DAPI (as per section 2.11.1). Several categories of nuclear defects could be clearly assigned to cells and could be seen to increase with time (Figure 6-9 A). Representative images of the different categories are shown in Figure 6-9 B.

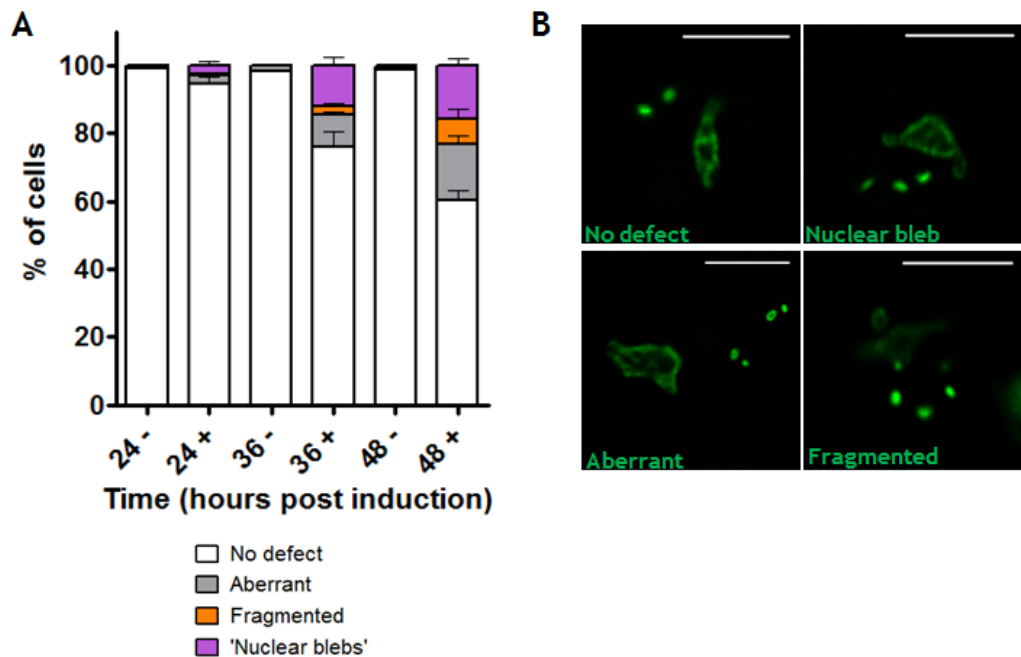


Figure 6-9: TbATR is required to maintain the nucleus of BSF cells

(A) Cells were fixed at 24, 36 and 48 hrs post RNAi induction and DAPI stained. The nuclei of cells were examined on an Axioskop2 and categorised depending upon the perceived defect. Examples of these defects are shown in (B). Each category was expressed as percentage of the total number of cells counted. Error bars = \pm SEM, n=3. (B) Representative images of different nuclear configurations (the nuclei are stained with DAPI; green) observed at 36 hrs post induction. Images are captured from the TbATR RNAi CL1 cell line on a DeltaVision microscope and processed as per section 2.11.8. Scale bar = 5 μ m.

In keeping with the cell cycle analysis, no clear nuclear defects could be observed in the majority of cells following RNAi induction. However, as many cells were beginning to form large cell clumps at 36 and 48 hrs, it is possible that the number of cells with nuclear defects is underestimated. Cells with notably abnormal nuclei (such as enlarged), but which could not be classified as having a specific phenotype, were simply classed as 'aberrant' and increased in the RNAi population with time. Beyond these cells, at both 36 hrs and 48 hrs

post induction cells with fragmented nuclei (7 % at 48hrs) or nuclei with protruding structures (referred to as ‘blebs’; 15 % at 48 hrs), were widespread and again increased with time, suggesting either a breakdown of the nuclear architecture or potentially incorrectly segregating nDNA.

To investigate these observations further, the ultrastructure of the nucleus was examined by TEM of cells 36 hrs post induction. Images representative of cells with aberrant nuclei are shown in Figure 6-10.

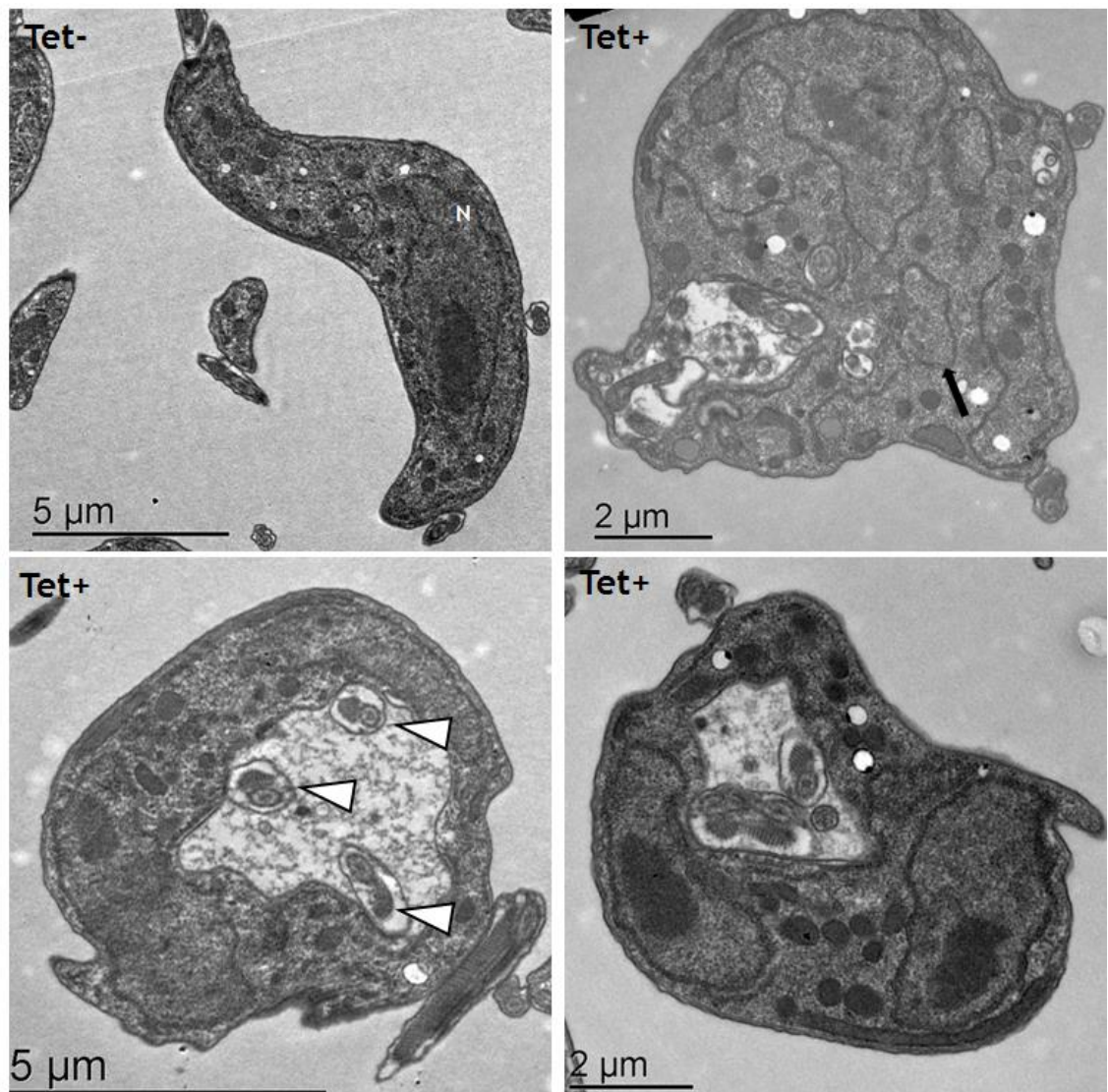


Figure 6-10: Internal cellular architecture of TbATR-deficient cells
Cells were fixed at 36 hrs post RNAi induction (as per section 2.11.7.2) and imaged by TEM by L.Lemgruber-Soares. The top left panel shows an uninduced cell. The black arrow (top right) indicates extra nuclear membrane. The white triangles (bottom left) highlight the presence of three internal flagella. Images were captured on a Tecnai T20 EM microscope and processed in Adobe Photoshop (by L.Lemgruber-Soares). Scale bars are as labelled.

As expected, in the non-induced population, no nuclear defects could be observed. However, at 36 hrs post induction, cells with multiple kinetoplasts could be readily detected; in some cases, this was associated with aberrant nDNA (Figure 6-10; lower panels), while in others, no clear nuclear defects could be detected (Figure 6-10, lower right panel). Additionally, clear changes in nuclear architecture or envelope organisation could be seen, consistent with the DAPI analysis (as indicated with the black arrow in Figure 6-10; upper right panel).

6.3.5.1 Loss of TbATR is associated with abnormal chromosomal rearrangements

Loss of ATR has been shown to result in chromosomal lesions, including the fusion of sister chromatids and telomere destabilisation (Pennarun et al. 2010). To investigate a potential role for TbATR in maintaining chromosome structure in BSF *T. brucei*, telomere-fluorescence *in situ* hybridisation (Telo-FISH) was performed. Telo-FISH was performed using a probe designed to detect the *T. brucei* telomeric repeat sequence, TTAGGG. Given the relative number of mini- and megabase-chromosomes, it is likely that most Telo-FISH signal detects the former. Consistent with previous work (DuBois et al. 2012), in uninduced TbATR RNAi cells, the telomeres localised diffusely around the nucleus during interphase; often resembling small foci. Upon entry to G2 phase, the telomeres were detected as forming a ‘plane’ at the centre of the nucleus. After mitosis occurred, the telomeres re-localised to opposite poles of each nucleus. These localisation patterns are shown in Figure 6-11, with images captured by SR-SIM microscopy (section 2.11.8.1).

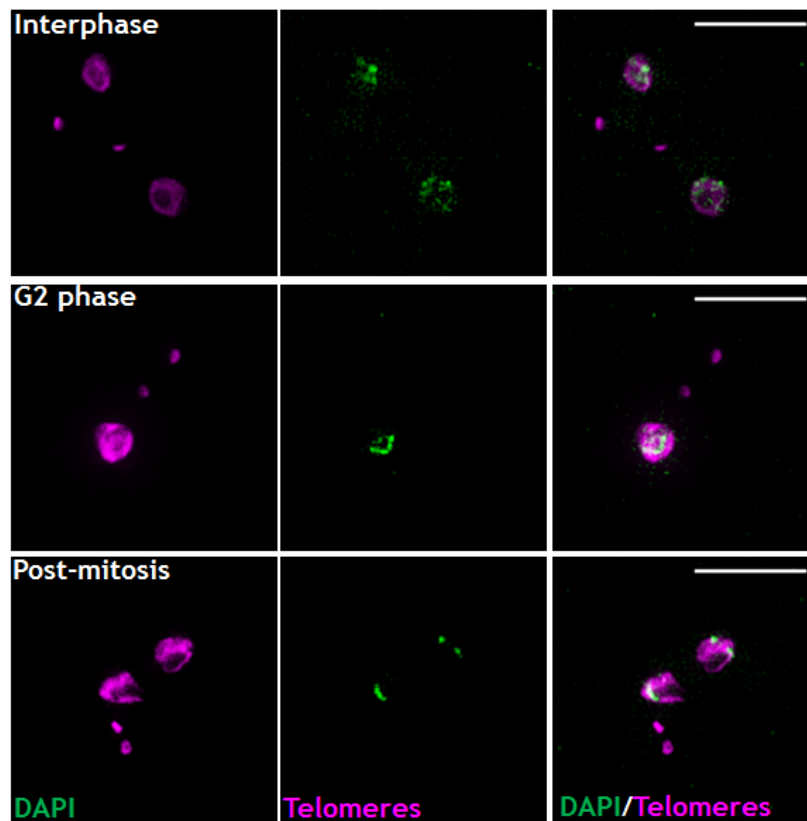


Figure 6-11: Telomere positions in the presence of TbATR
 Telo-FISH was performed on non-induced TbATR CL1 RNAi cells (collected after 36 hrs of growth) as described in section 2.8.1. The nDNA and kDNA were stained with DAPI (magenta), and the telomeres detected with a FITC conjugated probe (green). Images captured on an Elyra super resolution microscope (Zeiss) and processed as per section 2.11.8. Scale bar = 5 μ m.

Upon loss of TbATR, aberrant telomere arrangements could be observed. Altered signals could be seen 36 hrs after RNAi (representative images are shown in Figure 6-12 A-D). In some cells, a reduced spread of signal was detected, which may be the result of many cells not harbouring the small diffuse foci observed in the non-induced cells, but instead, larger, elongated foci could be observed (Figure 6-12 A). These data may suggest accumulation of telomeres in these regions; whether this is due to chromosome movement or fusion cannot be determined in this analysis. In some 1N2K cells (Figure 6-12 A) accumulation of signal along a central plane was seen but did not localise to the centre of the nucleus, perhaps explaining why some chromosomes might be incorrectly segregated during mitosis. Perhaps consistent with this, in some cells in which two nuclei appear to be separating (Figure 6-12 B&C) the telomeric signals appeared not always to localise to the expected poles. Finally, clear evidence for fragmentation of the nucleus was seen, where telomere signal was found in many small DAPI stained elements (as shown in Figure 6-12 D). As stated

previously, it is possible that cells scored with multiple kinetoplasts may instead harbour fragmented pieces of the nucleus.

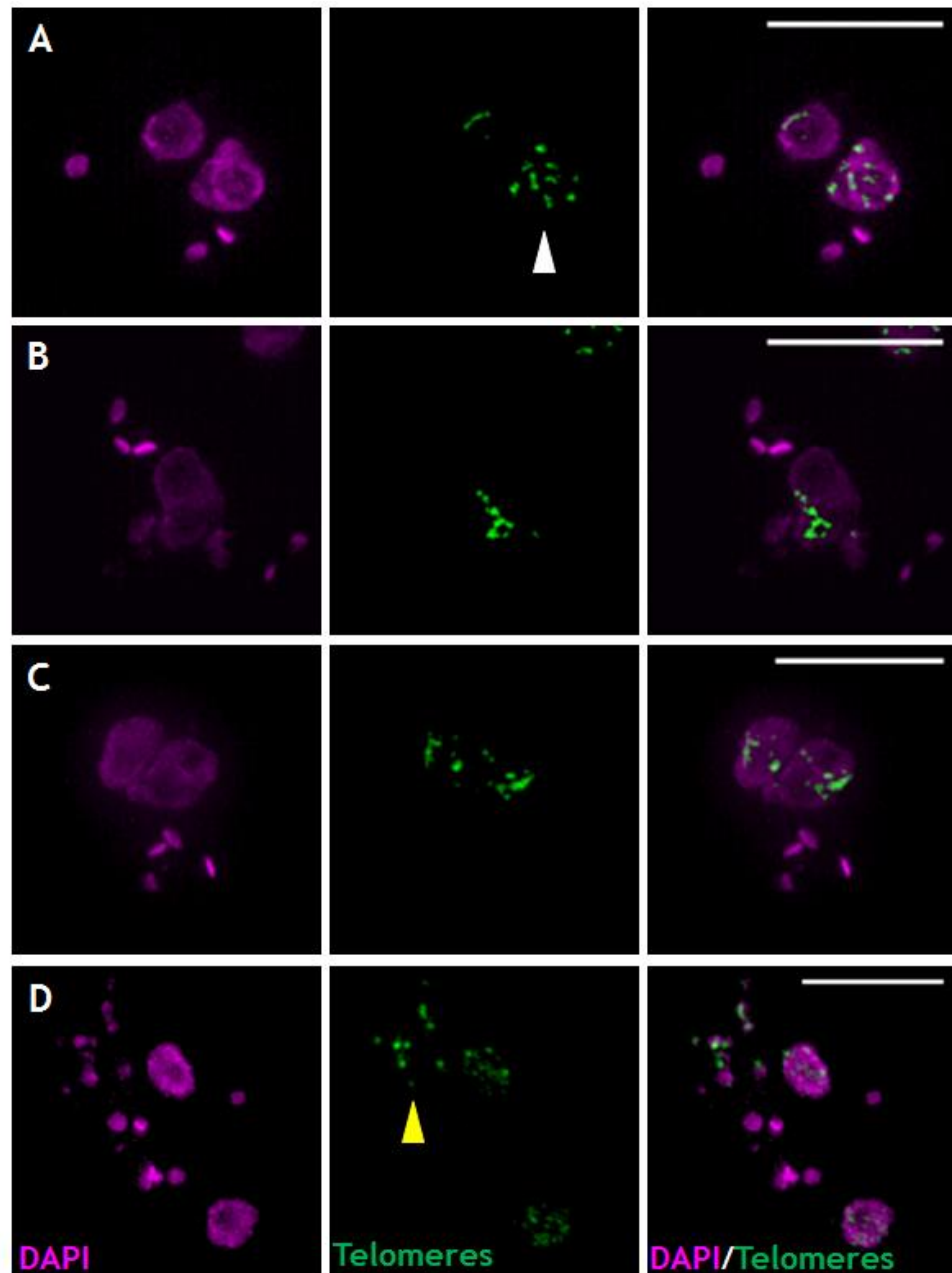


Figure 6-12: Loss of TbATR is associated with aberrant telomere arrangements
Telo-FISH was performed on TbATR CL1 RNAi induced cells (collected at 36 hrs post induction; A-D) as described in section. The nDNA and kDNA were stained with DAPI (magenta) and the telomeres detected with a FITC conjugated probe (green). White arrow indicates elongated foci (A). Yellow arrow indicates telomere signal in fragments of the nucleus (D). Images were captured on an Elyra super resolution microscope (Zeiss) and processed as per section 2.11.8. Scale bar = 5 μ m.

6.3.6 TbATR is required for cell survival following genotoxic stress

In other eukaryotes, loss of ATR is associated with sensitisation of cells to sources of genotoxic stress, including replicative stress (Herr et al. 2015) and following UV exposure (Kawasumi et al. 2011). To examine whether loss of TbATR sensitised BSF *T. brucei* to various sources of genotoxic stress, growth of the cells was monitored following RNAi induction in the presence or absence of MMS, HU or a single UV exposure (performed as per section 2.81). These data are shown in Figure 6-13 A&B.

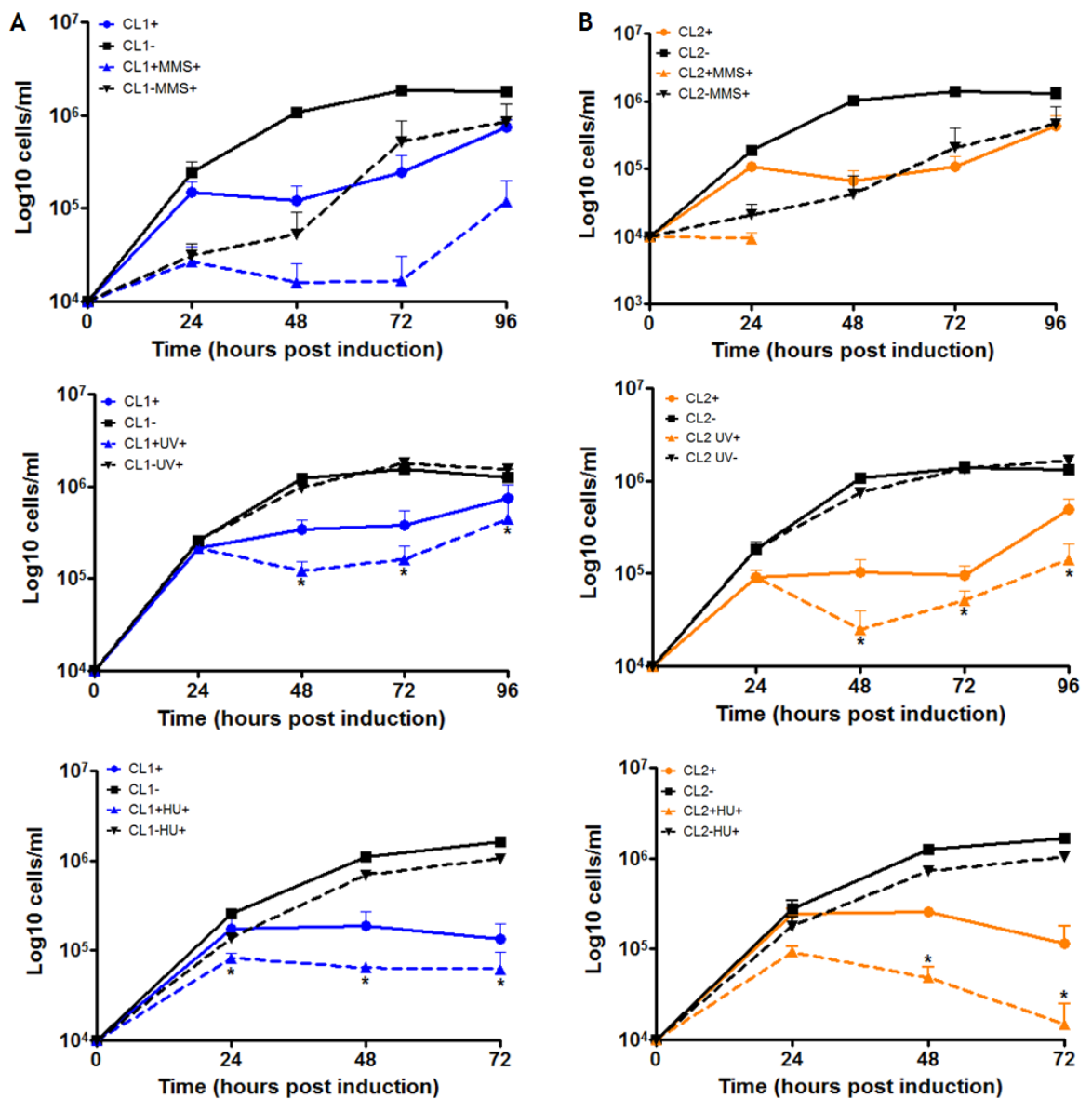


Figure 6-13: *In vitro* loss of TbATR sensitises BSF *T. brucei* cells to genotoxic stress
 Growth curves were conducted as described in section 2.8.1. (A) and (B) show growth analysis of TbATR RNAi CL1 and CL2, respectively, under a variety of genotoxic stress sources: MMS (0.0003 %), UV (1500 J/m²) and HU (0.06 mM). The (+) denotes tetracycline

induced samples. The (-) denotes the uninduced samples. The error bars represent \pm SEM, $n=3$. For statistical analysis, uninduced cells in the presence of damage were compared with the corresponding induced cell line. (*) = $p<0.05$ as determined by a Mann Whitney U test.

In keeping with the results presented in section 6.3.4, loss of TbATR caused a reduced rate of proliferation and the appearance of aberrant cells and, again, 72-96 hrs post induction, proliferation began to recover. When the RNAi induced cells were grown in the presence of MMS (a DNA alkylating agent; at a concentration of 0.0003 %) proliferation was reduced relative to the non-induced cells exposed to MMS from as early as 24 hrs post induction. At 96 hrs post induction, the proliferation of the TbATR CL1 cell line began to recover despite being exposed to MMS (Figure 6-13 A; top graph). However, no such effect was seen with the TbATR CL2 cell line, where addition of MMS resulted in death after RNAi (Figure 6-13 B; top graph), despite the corresponding induced population in the absence of damage beginning to recover.

In addition to becoming sensitive to MMS exposure, loss of TbATR also significantly sensitised the cells to hydroxyurea (HU; which stalls replication; 0.06 mM) and to UV exposure (a crosslinking agent; 1500 J/m²). Taken together, loss of TbATR sensitised BSF cells to a range of genotoxic agents, suggesting TbATR contributes to the response of *T. brucei* to different types of DNA lesions.

6.3.7 TbATM is not required for cell survival following MMS or HU exposure

When the levels of ATM are reduced, human cells become highly sensitised to sources of DSBs such as ionising radiation (IR) and more moderately to alkylating and cross linking agents (Shiloh & Ziv 2013). In the case of HU exposure, though loss of ATM itself does not directly signal HU damage (Kurose et al. 2006; Chaturvedi et al. 1999), sensitivity is seen because ATM is can function to facilitate the restart of stalled replication forks that arise after this treatment (Ewald et al. 2008), though the mechanisms are still being investigated (Trenz et al. 2006; Ewald et al. 2008; Sowd et al. 2013).

The RNAi cell lines used for this study are resistant to the DSB inducing agent phleomycin (PHL) and no source of IR was available. As a result, we were limited to asking if loss of TbATM causes the expected moderate sensitivity to

replicative stress, by measuring growth in the presence of MMS (0.0003 %) or HU (0.06 mM), as described in section 2.8.1. However, loss of TbATM in BSF cells was not associated with any significant loss of proliferation in the presence of either source of genotoxic stress (Figure 6-14), suggesting TbATM is not required for cell survival following MMS or HU damage.

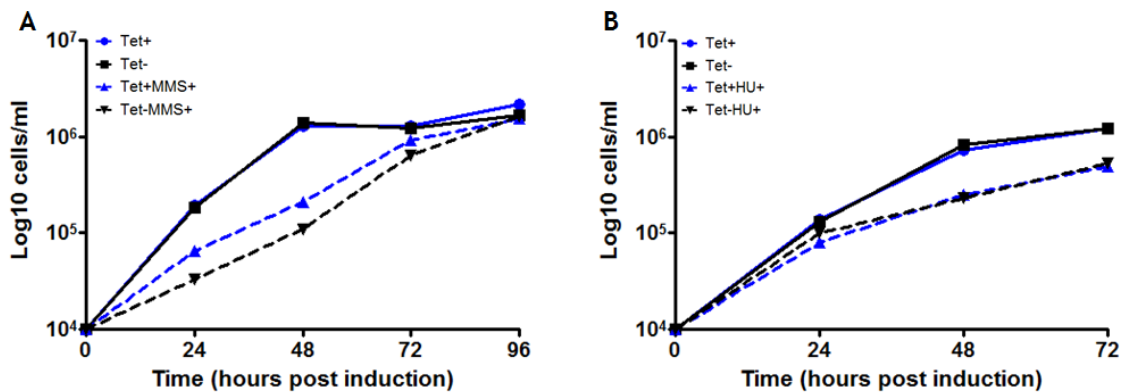


Figure 6-14: *In vitro* loss of TbATM is not associated with increased sensitivity to genotoxic stress

Growth curves were conducted as described in section 2.8.1. Cells were grown in the presence of 1 $\mu\text{g/ml}^{-1}$ tetracycline (solid blue line) to induced RNAi or in the absence of tetracycline (solid black line) as a control. Cells in the presence of a damage source in the induced population are shown by a dashed blue line. The dashed black line represents the uninduced population grown in the presence of a genotoxic agent. (A) and (B) show growth analysis of TbATM RNAi, under a variety of genotoxic stress sources: MMS (A; 0.0003 %) and HU (B; 0.06 mM). Cells were grown continuously in the presence of genotoxic stress. Both curves were performed once.

6.3.8 TbATR deficient cells show increased levels of DNA damage-associated markers

Suppression of ATR by RNAi in other eukaryotes is associated with elevated levels of $\gamma\text{H2A(X)}$ and RAD51 foci formation (Chanoux et al. 2009; Podhorecka et al. 2011). To determine whether loss of TbATR also results in detectable damage in *T. brucei*, indirect IF analysis (section 2.11.2) was performed to examine levels of γH2A (as detected by $\alpha\text{-}\gamma\text{H2A}$ antiserum; section 2.11) after TbATR RNAi. Our $\alpha\text{-}\gamma\text{H2A}$ antiserum stains the nucleus of an undamaged, uninduced RNAi (Figure 6-15 C; chapter 8, section 8.5, Figure 8-33) for reasons that remain unclear. Thus, the pattern of staining was examined after RNAi and the fluorescence intensity of the γH2A signal in the nucleus of multiple cells was measured individually using ImageJ (section 2.11.8.3) for both the induced and non-induced samples. Figure 6-15 A plots the fold change in fluorescence intensity in the RNAi induced nuclei relative to the non-induced samples.

From as early as 24 hrs after TbATR knockdown, ~2.5 fold increased levels of γ H2A were detected, with the fold change increasing at each subsequent time point: ~3.5 fold higher 36 hrs post induction and ~5 fold higher after 48 hrs. To evaluate this observation further, western blot analysis was performed (as per section 2.12.1.2; Figure 6-15 B) at the same time points, confirming increased levels of γ H2A after RNAi. Indeed, quantification of the western signals revealed a similar time-dependent response, with levels of γ H2A increased ~5 fold after 48 hrs (data shown in chapter 8, section 8.5, Figure 8-33 C).

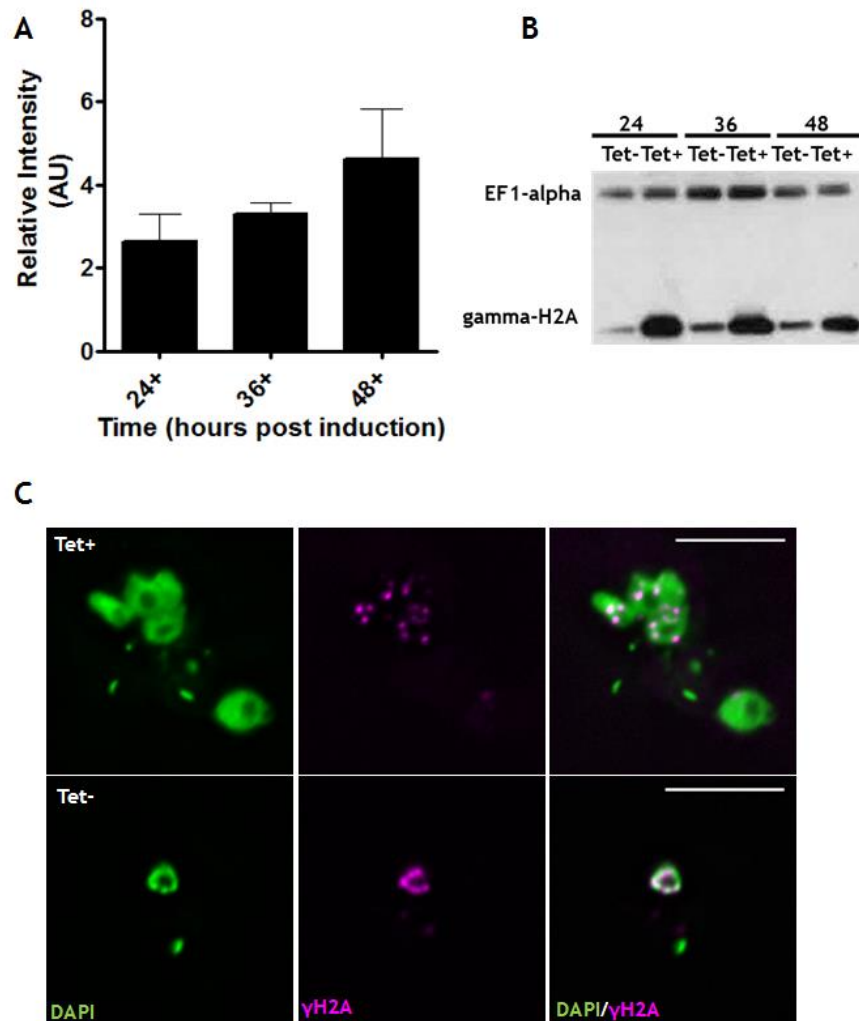


Figure 6-15: Loss of TbATR is associated with increased γ H2A in BSF cells
(A) RNAi induced (+) and non-induced cells were fixed at the time points shown and stained with α γ H2A and DAPI. The fluorescence intensity signal of γ H2A in the nucleus in >200 cells was measured in ImageJ and the intensity measurements at each time point averaged. Fold change in intensity (arbitrary units, AU) is plotted for each induced time point relative to the combined average of all unduced time points (Figure 6-15 A). Error bars represent \pm SEM, n=3. **(B)** Western blot of whole cell extracts from RNAi induced (Tet+) or uninduced (Tet-) cells probed with antisera recognising γ H2A and EF1- α (as a loading control); an intensity plot of the western signals is shown in chapter 8, section 8.5, Figure 8-33 C. **(C)** Representative images of γ H2A localisation in induced (Tet+) and uninduced (Tet-) cells after 36hrs growth. Indirect IF analysis was performed, with α γ H2A (magenta) antiserum

(Table 2-7). DNA was stained with DAPI (green). Images were captured on a DeltaVision microscope from the RNAi cell line TbATR CL1. Scale bar = 5 μ m.

Beyond the changes in levels of γ H2A, imaging the IF on a higher resolution microscope (Olympus IX71 DeltaVision Core System; Applied Precision; Figure 6-15 C) suggested that TbATR RNAi may result in a changed distribution of the modified histone. In many RNAi induced cells generalised nuclear staining was no longer seen, but instead the signal took the form of multiple puncta, perhaps representing nuclear foci of γ H2A. The same pattern has been described in ATR-depleted human cells (Chanoux et al. 2009), as well as after the generation of DSBs in *T. brucei* (Glover&Horn 2012). Though the nature of the DNA damage being recognised by γ H2A after TbATR RNAi cannot be inferred, the pattern of staining may be consistent with genome fragmentation.

To probe the nuclear damage revealed by staining further, we next looked at localisation of RAD51, which is known to relocalise to discrete nuclear foci after DSBs induced by IScel or PHL(Glover et al.,. 2013; Devlin et al. 2016).

Localisation of RAD51 was examined for by indirect IF using α -RAD51 antiserum (section 2.11.2) following TbATR knockdown up 48 hrs post induction. These data are shown in Figure 6-16 A&B below.

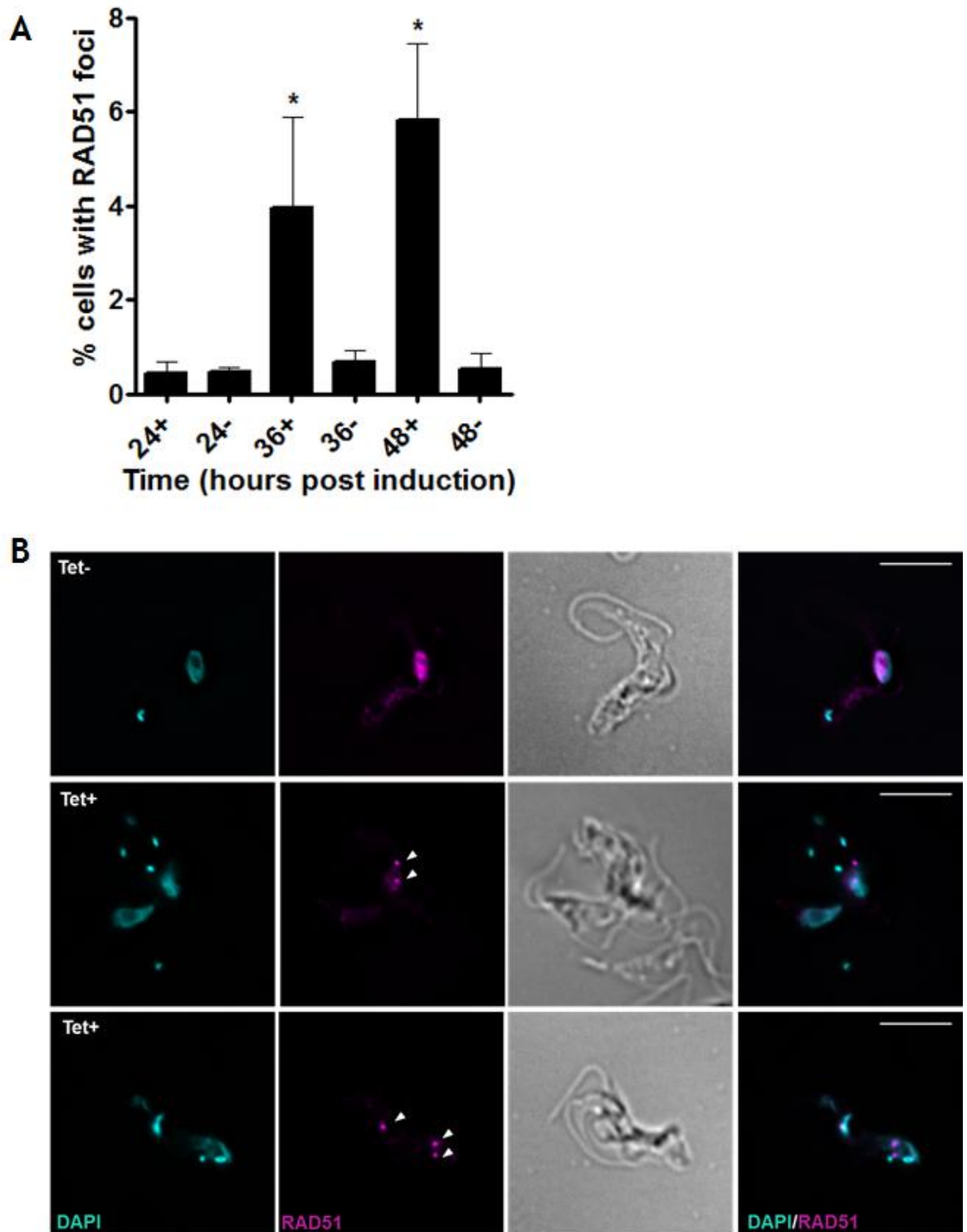


Figure 6-16: Loss of TbATR is associated RAD51 foci formation

(A) The cells were fixed and stained with α RAD51 and DAPI as per section. The number of cells with nuclear RAD51 foci was counted and expressed as a percentage of the total number of cells counted. Over 200 cells were counted per experiment. The error bars represent \pm SEM, $n=3$. Significance was determined by performing a Mann Whitney U test. (*) means $p=0.05$. '+' (induced with $1 \mu\text{g/ml}^{-1}$ tetracycline) '-' (un-induced) (B) Representative images of RAD51 localisation in induced (Tet+) and uninduced (Tet-) cells at 48hrs post induction. Indirect IF analysis was performed as per section 2.11.2 with RAD51 being detected with α RAD51 (magenta) antiserum (Table 2-7). The morphology of the parasites was visualised using DIC imaging. The n- and kDNA were stained with DAPI (green). Representative images were captured on a DeltaVision microscope from the RNAi cell line TbATR CL1. Scale bar = $5 \mu\text{m}$.

In keeping with previous work, in the absence of RNAi only a small (~1 %) part of the population had detectable nuclear foci detected by anti-RAD51 antiserum, with most cells having diffuse staining both in the nucleus and cytoplasm (Devlin et al. 2016; Dobson et al. 2011; Hartley & McCulloch 2008). However, 36 and 48 hrs after TbATR RNAi, in keeping with results in mammalian cells (Chanoux et al. 2009), loss of TbATR in BSF *T. brucei* resulted in a significant increase in the number of cells with RAD51 foci: after 48 hrs up to 7 % of the population harboured foci, though predominantly just a single focus in each cell (Figure 6-16 B shows the representative localisation of TbRAD51 in an induced and uninduced cell; data for the number of foci observed per cell is not shown). The apparent decrease in fluorescence intensity following TbRAD51 re-localisation from the diffuse nuclear staining to the foci following TbATR depletion cannot be explained with this analysis. However it is important to consider that it may be of biological relevance (such as degradation of TbRAD51 occurring following TbATR depletion) though additional experiments are required to examine this effect further. Intriguingly, the timing of RAD51 accumulation into foci was delayed relative to the increased levels of γ H2A after RNAi, suggesting the formation of putative RAD51 repair foci follows the generation of modified histone.

6.3.9 Loss of TbATR is associated with deregulation of silent VSG expression sites

ATR, in other eukaryotes, is required to stabilise stalled replication forks, protect and maintain telomere integrity and stability, and prevent breaks within common fragile sites (CFSs) including at telomeres (McNees et al. 2010). Given the recently revealed link between replication timing and VSG expression site (ES) transcription status (Devlin et al. 2016), and the location of VSG ES at telomeres, we sought to ask if TbATR RNAi might affect VSG expression.

To test this hypothesis further, qRT-PCR and RNAseq analyses were performed on both TbATR RNAi cell line clones. In the Lister 427 WT strain (from which the cell lines in this chapter are derived), 14 unique BESs have been identified (Figure 6-17; Hertz-Fowler et al. 2008). The cell lines used in this thesis predominantly express VSG221, which is located in BES 1 (telo40); this is the active ES. All other ESs are considered transcriptionally silent.

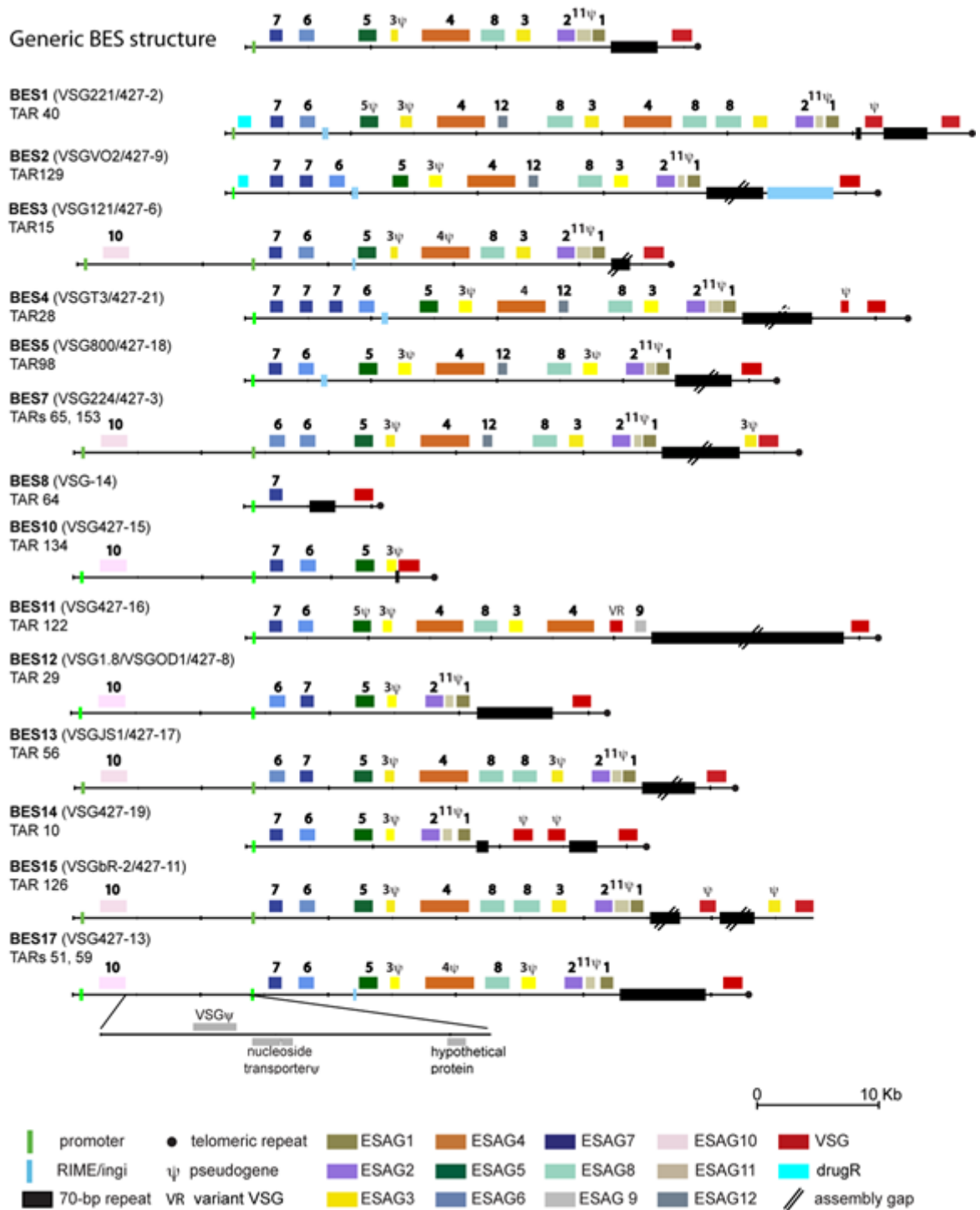


Figure 6-17: Bloodstream VSG expression sites in the *T. brucei* Lister 427 strain
 The schematic above depicts the bloodstream expression sites (BESs) annotated in the *T. brucei* Lister 427 genome following TAR (transformation-associated recombination) cloning. Identification of ESAGs (expression site associated genes), VSGs (variant surface glycoprotein), pseudogenes and other ES features are shown below. Figure reproduced in full from (Hertz-Fowler et al. 2008) (all rights reserved).

6.3.9.1 qRT-PCR analysis reveals de-regulation of silent ESs in the absence of TbATR

To investigate whether loss of TbATR resulted in de-repression of VSG transcription in the silent ESs, qRT-PCR analysis was performed to measure RNA

transcript abundance for four silent VSGs (VSG13, VSG800, VSG224 and T3 in Figure 6-18) 24 and 36 hrs post induction of TbATR RNAi. This analysis was performed on both TbATR RNAi clones. Additionally, the RNA level of the actively expressed VSG (VSG 221) was examined. Finally, knockdown of TbATR for each experiment was tested (Figure 6-18 A&B), and effects on levels of general transcription were assessed by examining transcript levels for the ORC1/CDC6 gene, encoding a factor central to *T. brucei* DNA replication (Marques et al. 2016). RNA was prepared as per section 2.5.1 and 2.5.2 and the qRT-PCR analysis was performed as per section 2.5.3, using the primers detailed in Table 2-5.

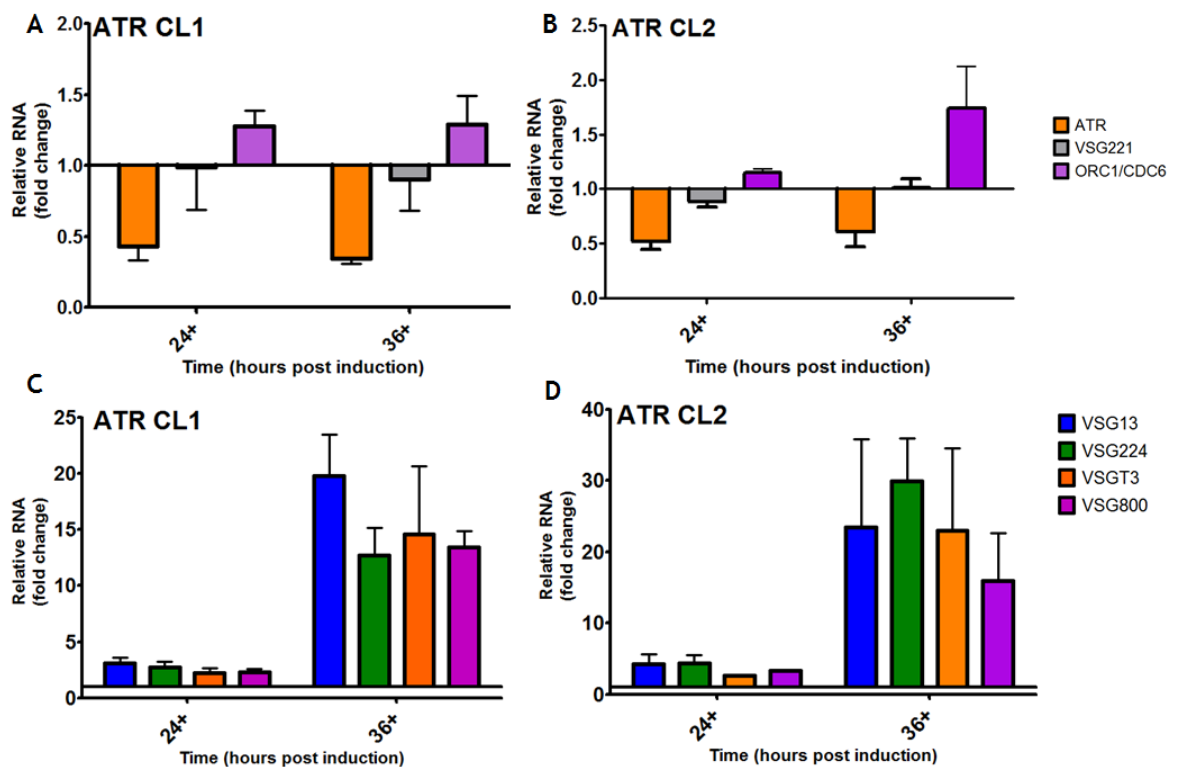


Figure 6-18: Loss of TbATR is associated with expression of silent VSG RNA transcripts
 The levels of gene expression were assessed by qRT-PCR in RNA samples prepared from TbATR RNAi clones CL 1 (A & C) and CL2 (B & D) after growth for 24 or 36 hrs with (+) or without induction of RNAi. Error bars = \pm SEM (n=3 for CL1, and n=2 for CL2). Each biological replicate was performed as a technical triplicate. The CT values for each sample were generated by averaging the CT values across the triplicate technical repeats. The relative fold change for each gene examined was then determined by calculating the $\Delta\Delta CT$ value (equation shown in section) for each gene normalised to an endogenous control (for this experiment, actin was used). The levels of RNA for the uninduced samples were set to 1 (represented by the black line), and the levels in the RNAi induced expressed relative that control. The following VSGs were examined: VSG13 (telo 59 and 51; BES 17), VSG221 (telo 40; BES1), VSG224 (telo65 and 153; BES7), VSGT3 (telo 3 and 28; BES4) and VSG800 (telo 98; BES5). VSG13 and VSGT3 are located on intermediate chromosomes. VSG224, VSG221 and VSG800 are located on megabase chromosomes. Named as detailed in (Hertz-Fowler et al. 2008). Relative changes of RNA from TbATR and a non-VSG gene, ORC1/CDC6, are also shown.

For both clones, the level of the TbATR transcript was reduced (by ~60 % for CL1 and ~50 % for CL2), as expected. For ORC1/CDC6, less than a 2-fold change (and thus not considered significant) in transcript levels was observed at both time points. VSG221 displayed no clear change in RNA levels, though the abundance of this actively expressed VSG may impede detection of changes by CT measures (Figure 6-18 A&B).

In contrast to the limited changes seen for VSG221 and ORC1/CDC6, a modest but clear 3-5-fold increase in VSG transcript levels from the silent ESs could be detected 24 hrs after TbATR RNAi in both clones. Strikingly, 36 hrs after RNAi a much greater increase in silent VSG transcripts was seen, ranging from ~10-25 fold in CL1 and ~15-35 fold in CL2 (Figure 6-18 C&D).

Overall, RNA transcripts from previously silent ESs could be detected after TbATR loss, either because TbATR is required to maintain transcriptional silencing at the sub-telomeres or because loss of ATR leads to elevated VSG switching.

6.3.9.2 Loss of TbATR is associated with the de-repression of Pol I associated and surface coat associated genes

To ask if the effect seen on silent VSGs after loss of TbATR in BSF cells was specific to the VSG BES or reflected more widespread changes in transcription, cells were sampled at 24 and 36 hrs post induction and RNAseq was performed (as per section 2.6) on total RNA. BSF cells were harvested and RNA prepared as described in section 2.6 from two biological replicates of induced and uninduced TbATR CL1 cells and from a single replicate of TbATR CL2, providing triplicate induced and uninduced samples at both time points. PCR analysis was performed on the isolated RNA (as per section 2.2.4; primers used are detailed in Figure 6-19) to test for the presence of gDNA contamination (as shown below); no contamination could be clearly detected. The sample concentration was measured as per section 2.6 (data shown in chapter 8, section 8.5, Table 8-5) and an RNAseq library prepared for each sample as described in section. A stranded library was prepared using a TruSeq Stranded mRNA Library Prep Kit (Illumina), the library was Paired-End sequenced using an Illumina NextSeq 500 using a Mid-Output Flow cell generating read lengths of 75 bp. The

bioinformatics analysis performed as described in section 2.6.2. The total number of reads for each sample, the percentage mapped and the number and percentage properly paired as presented in chapter 8, section 8.5, Table 8-6.

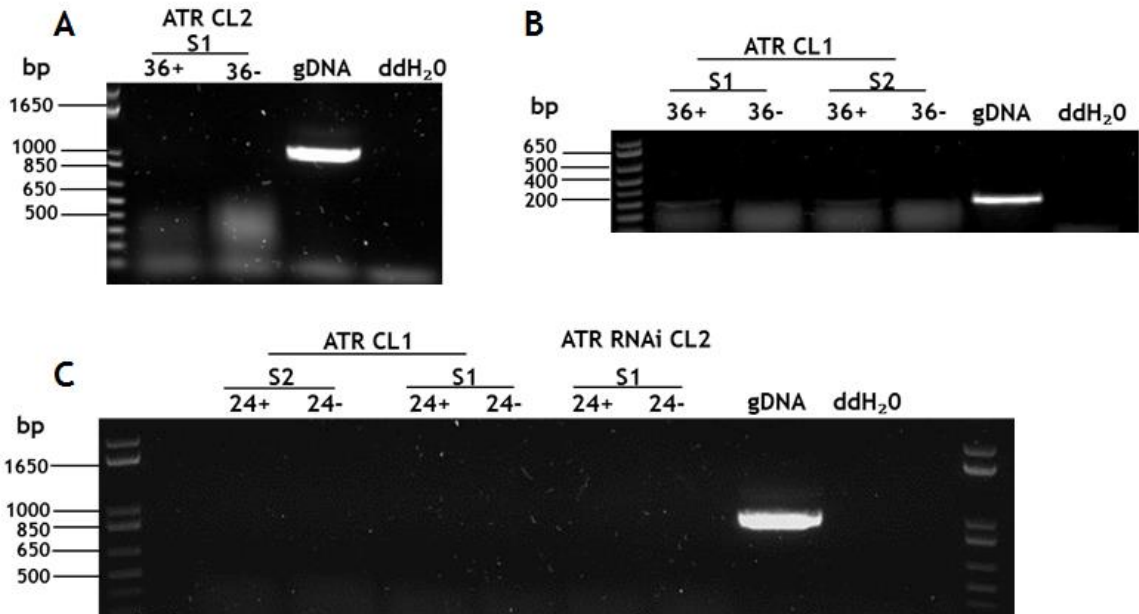


Figure 6-19: PCR analysis of RNA samples for RNAseq analysis

A PCR analysis of RNA extracted for RNAseq analysis was performed using the primers 148 and 147 (A and B) and primers 139 and 140 (C) as detailed in section (refer to Table 2-3 for primer sequences). The figure shows an agarose gel of the PCR reactions. Genome DNA (gDNA) was used as positive control and RNase free double distilled water (ddH₂O) as a negative control. S1 = sample 1, S2 = sample 2; 24 and 36 refer to the time points of the RNAi induced (+) and uninduced (-) cells in each sample, which represents an independent experiment. Size markers are shown in bp.

To assess the distribution of the sequence fragments per kilobase transcript per million bases (fpkm) across each individual replicate, a box plot was generated in RStudio using the 'csboxplot' command (as per section 2.6.2), plotting the log₁₀ transformed fpkm for each read. The box plots for each individual replicate at 24 hrs (Figure 6-20A) and 36 hrs (Figure 6-20 B), with or without RNAi induction, shows the spread of data for all replicates at both time points were comparable, with similar interquartile ranges of ~ 1 (for 24 hrs) and 1.25 (36 hrs) and medians of ~2 (for all replicates).

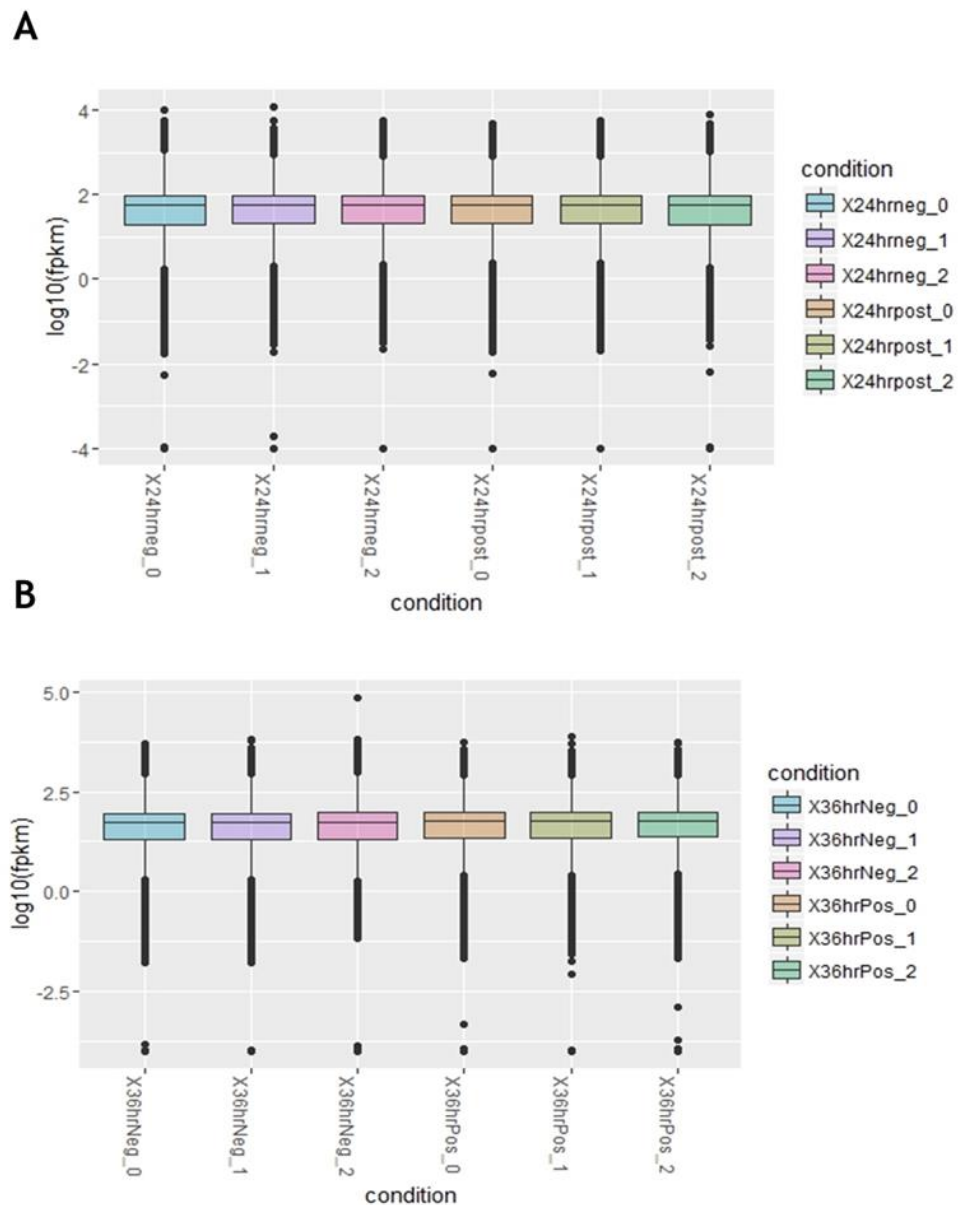


Figure 6-20: Box plot to assess the distribution of the fpkm for each replicate after 24 and 36 hrs growth with and without RNAi

The boxplot was generated in RStudio as per section 2.6.2. The \log_{10} transformed fpkm values for each read were plotted for each individual replicate (0, 1, 2) at 24 hrs (A) and 36 (B) with (Pos) or without (Neg) RNAi induction against TbATR. Outlier values are represented as black dots at either end of the box plot. The box represents the interquartile range of the values within each sample, within which the median value is indicated by the central line.

6.3.9.3 Loss of TbATR is associated with up-regulation of surface antigen-associated transcripts 24 hrs after RNAi

Analysis of the pattern of genes that showed altered RNA levels after TbATR RNAi suggested a difference both in the pattern and number of differentially expressed genes at 24 and 36 hrs. As a result, the data will be separated into the two points. Heatmaps of differentially expressed transcripts after 24 and 36 hrs

RNAi induction are shown in the accompanying CD (see files presented in the folder [RNAseqDatasetATRBSF2016](#)→ Heatmaps→ 24hr.pdf and 36hr.pdf). For a complete list of all gene transcripts differentially expressed at 24 hrs post RNAi induction, see the accompanying CD (file entitled labelled [RNAseqDatasetATRBSF2016](#)).

To ask how many transcripts displayed altered levels after 24 hrs TbATR RNAi, fold change (\log_2 transformed FC) in average FPKM for the three replicates was plotted on a volcano plot relative to the significance for each gene (the \log_{10} transformed p-value), using the CuffDiff software in RStudio (as per section 2.6.2). The plot was generated using the 'csvgolcano' command as per section (Figure 6-21). At 24 hrs, 150 gene transcripts were judged to be significantly differentially expressed in the RNAi induced cells relative to the uninduced (red dots).

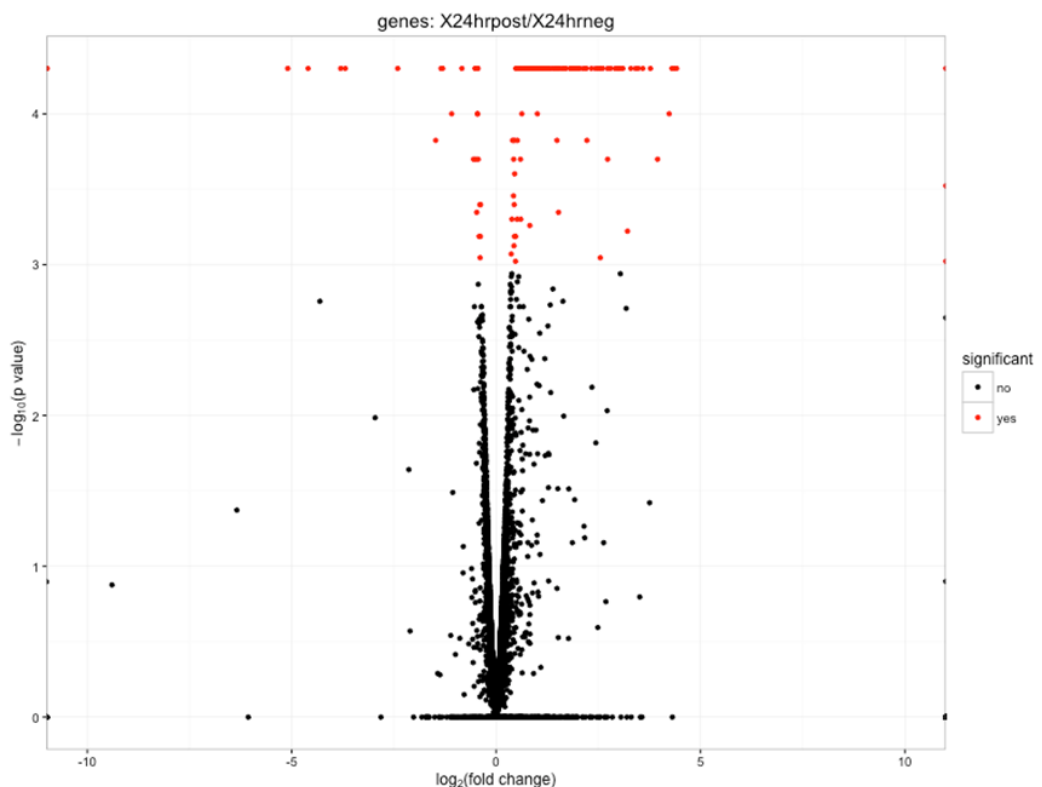


Figure 6-21: Volcano plot showing transcripts differentially expressed at 24 hrs post TbATR RNAi induction

The \log_{10} transformed p-values for each gene identified by RNAseq are plotted against the \log_2 transformed fold change in FPKM (as determined by CuffLinks) in RStudio (<https://www.rstudio.com/>), as described in section 2.6.2. Red dots correspond to significantly differentially expressed transcripts.

Examination of the 150 genes that displayed differential transcript levels revealed surface antigen associated genes to be the most abundant category (52 %; Figure 6-22 A). Included in this category are ESAGs, VSGs, procyclins (EP and GPEET) and procyclin-associated genes (PAGs). Strikingly, virtually all of these transcripts were significantly more abundant after TbATR RNAi: ~ 95 % of the total number of surface antigen associated genes detected, or 60.5 % of all up-regulated transcripts; Figure 6-22 B. Indeed, at 24 hrs ~83 % of all changes were increases in RNA levels.

Increased RNA transcripts corresponding to the VSG from seven silent BES were seen: BES11 (Tb427.BES122.11), BES15 (Tb427.BES126.15), BES2 (Tb427.BES129.14), BES10 (Tb427.BES134.6), BES12 (Tb427.BES29.9), BES13 (Tb427.BES56.13), BES8 (Tb427.BES64.2) and BES5 (Tb427.BES98.12). In addition, one of the VSG RNA transcripts tested by qRT-PCR analysis was seen, with a comparable fold change (~3 fold: BES5 [Tb427.BES98.12 or VSG800]). These data suggest that loss of ATR affects all silent BES. Mapping reads to specific ESAGs is more complicated than VSGs due to greater homology, but increased RNA levels were predicted for multiple ESAGs from multiple BES, suggesting ATR-induced expression changes are not limited to the VSG but potentially cover the whole BES. The same pattern of very predominantly increased RNA levels were seen for procyclin and PAG genes, suggesting that loss of silencing of RNA PolII-transcribed genes may be a common, early response to TbATR RNAi.

The remaining differentially expressed transcripts (Figure 6-22 C; ~ 47 %) were either hypothetical genes of unknown function (~ 15 %), or genes with predicted functions from the genome annotations (~ 31 %). To ask if the latter genes corresponded with any functional categories, GO term enrichment was evaluated for all 150 genes (Figure 6-23). However, all enriched terms corresponded with host-parasite interaction, in keeping with the overwhelming focus of surface gene expression changes at this time point. Manual examination of the annotated genes revealed five predicted peptidases, as well as a gene associated with nuclear transport (FC: -1.39), two genes associated with nucleolar RNA binding (FC: both > -1.3), an RNA binding protein (FC: 1.677) and two ribosomal genes (FC: -1.3, <13.9). These latter genes may indicate nuclear and nucleolar

structure alterations that appeared to be seen more clearly after 36 hrs (below). Given ATR is predicted to act in repair signalling, changes in repair and kinase gene expression levels were sought. No kinases were detected, and only two DNA repair associated genes: an apoptosis-associated gene known as Bax (a target of the p53 tumour suppressor transcription factor; Miyashita & Reed 1995) and, as expected, TbATR (FC: -2.5).

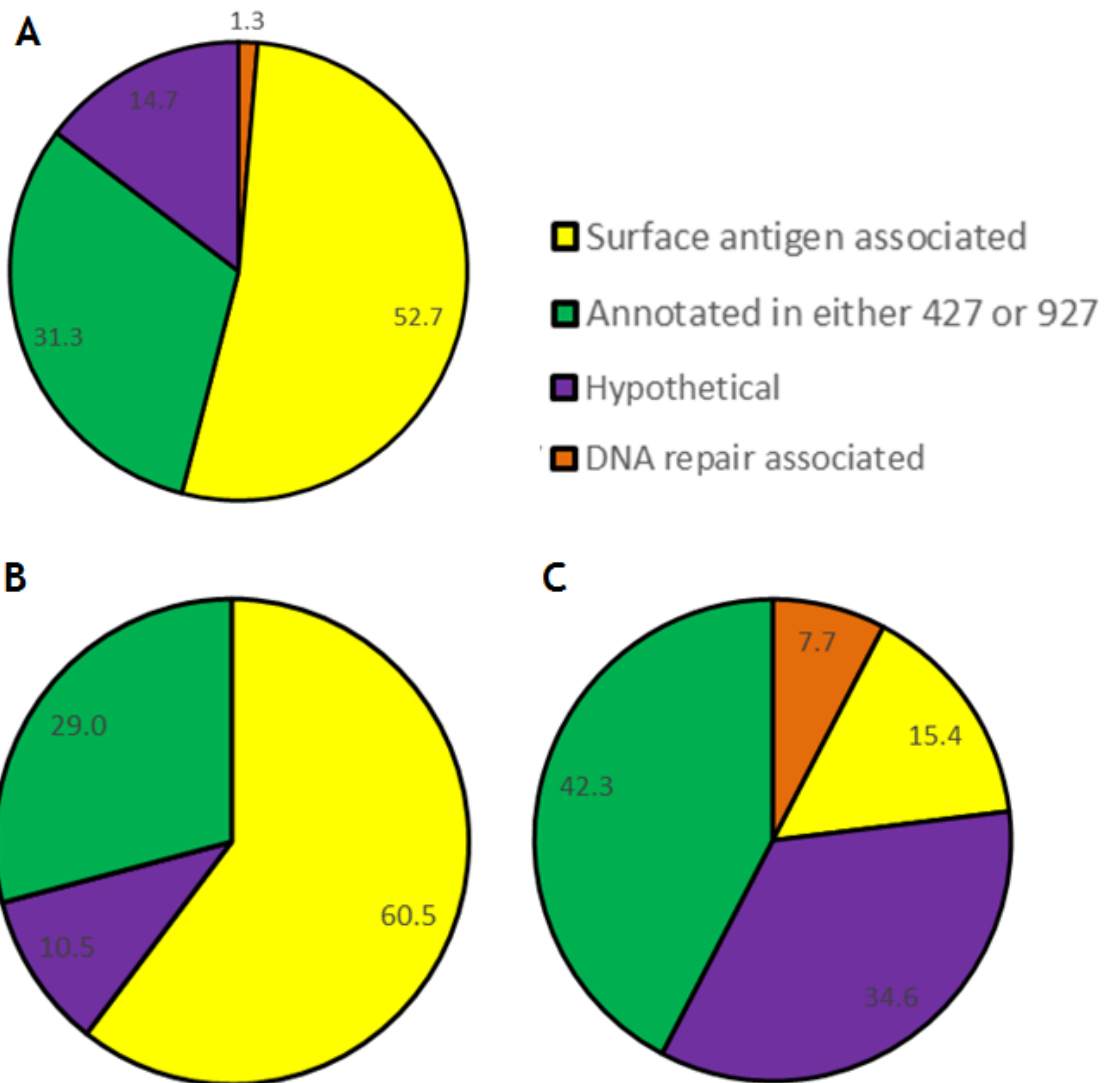


Figure 6-22: Pie charts summarising differentially expressed genes at 24 hrs post TbATR RNAi induction

All differentially expressed genes were classified into four categories: DNA damage associated, surface antigen associated, genes with annotations, and hypothetical genes. The number of genes in these categories are expressed as a percentage of the total number of genes that showed a significant change in transcript level (A; 150 total), as well as those that show a significant increase (B, 124) or decrease (C, 26). Genes with annotations refers to genes with an annotated putative function in either the Lister 427 or the TREU 927 reference genome.

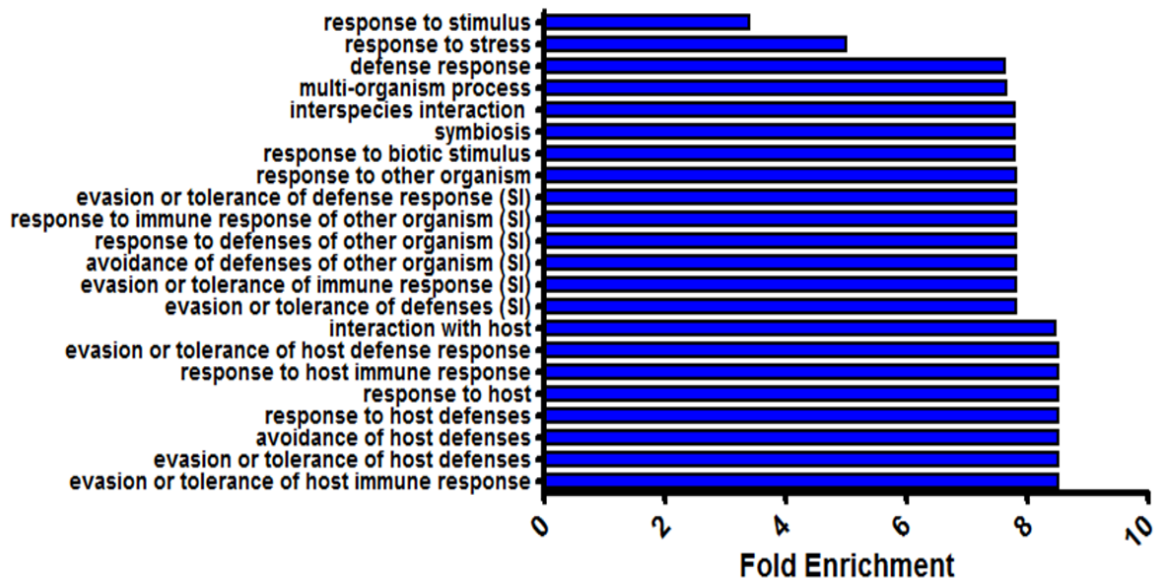


Figure 6-23: GO terms enriched at 24 hrs post knockdown of TbATR in BSF cells
GO terms were retrieved from TriTrypDB based on the gene annotations associated with each gene. SI = symbiont interaction.

6.3.9.4 Loss of TbATR at 36hrs post induction was primarily associated with cell cycle and global gene expression

At 36 hrs post induction, ~10 fold more transcripts were differentially expressed (1431 transcripts in total) as represented by the red dots on the Volcano plot in Figure 6-24 (data was plotted as described for 24 hrs post induction in the section above). The data is summarised in the pie charts shown in Figure 6-25 A-C.

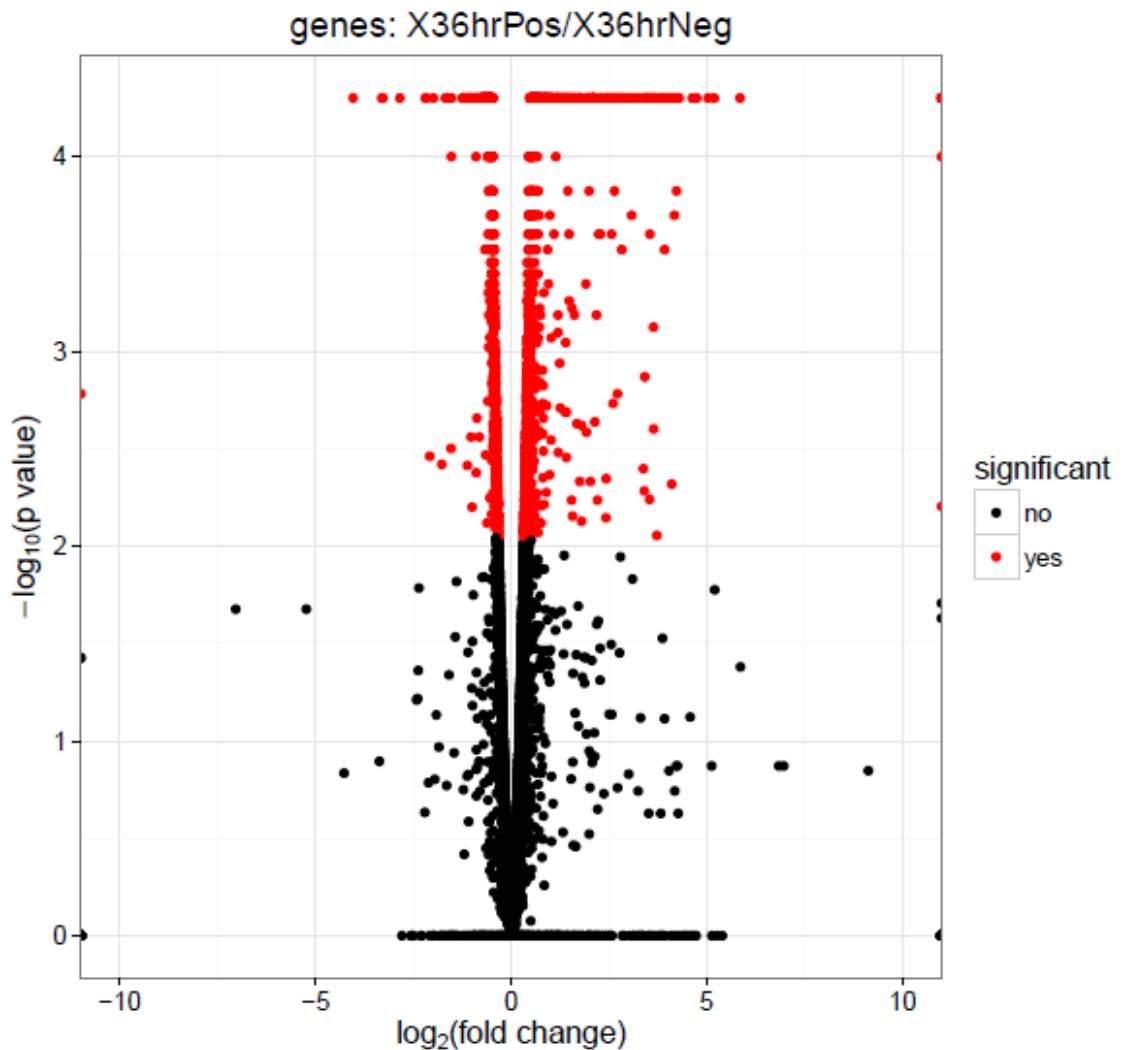


Figure 6-24: Volcano plot showing transcripts differentially expressed at 36 hrs post TbATR RNAi induction

The log₁₀ transformed p-values for each gene identified by RNAseq are plotted against the log₂ transformed fold change in FPKM (as determined by CuffLinks) in RStudio (<https://www.rstudio.com/>), as described in section 2.6.2. Red dots correspond to significantly differentially expressed transcripts.

At this time point after TbATR RNAi, RNA transcripts of VSGs from nine silent BESs were seen, with increased FCs (of ~6-57) relative to 24 hrs. Amongst the VSGs were VSG800 and VSGT3, which showed FCs of ~11 and 6, close to the qRT-PCR analysis (Figure 6-18 C&D). Interestingly, at this time point four genes, corresponding to ESAGs 6, 7, 8 and 1, from the active ES (BES1, but referred to in the annotations as BES40, based on TAR40; accompanying CD; [RNAseqDatasetATRBSF2016](#)) were predicted to have reduced RNA levels (FCs of ~-16.5, -9.9, -1.4, -1.9). VSG221 was not seen in the mapping, but these ESAGs were the only BES-associated genes predicted to be reduced in transcript level after TbATR RNAi, with all others increased. These data are compatible with loss

of expression from the active BES in conjunction with the silent BESs becoming de-repressed.

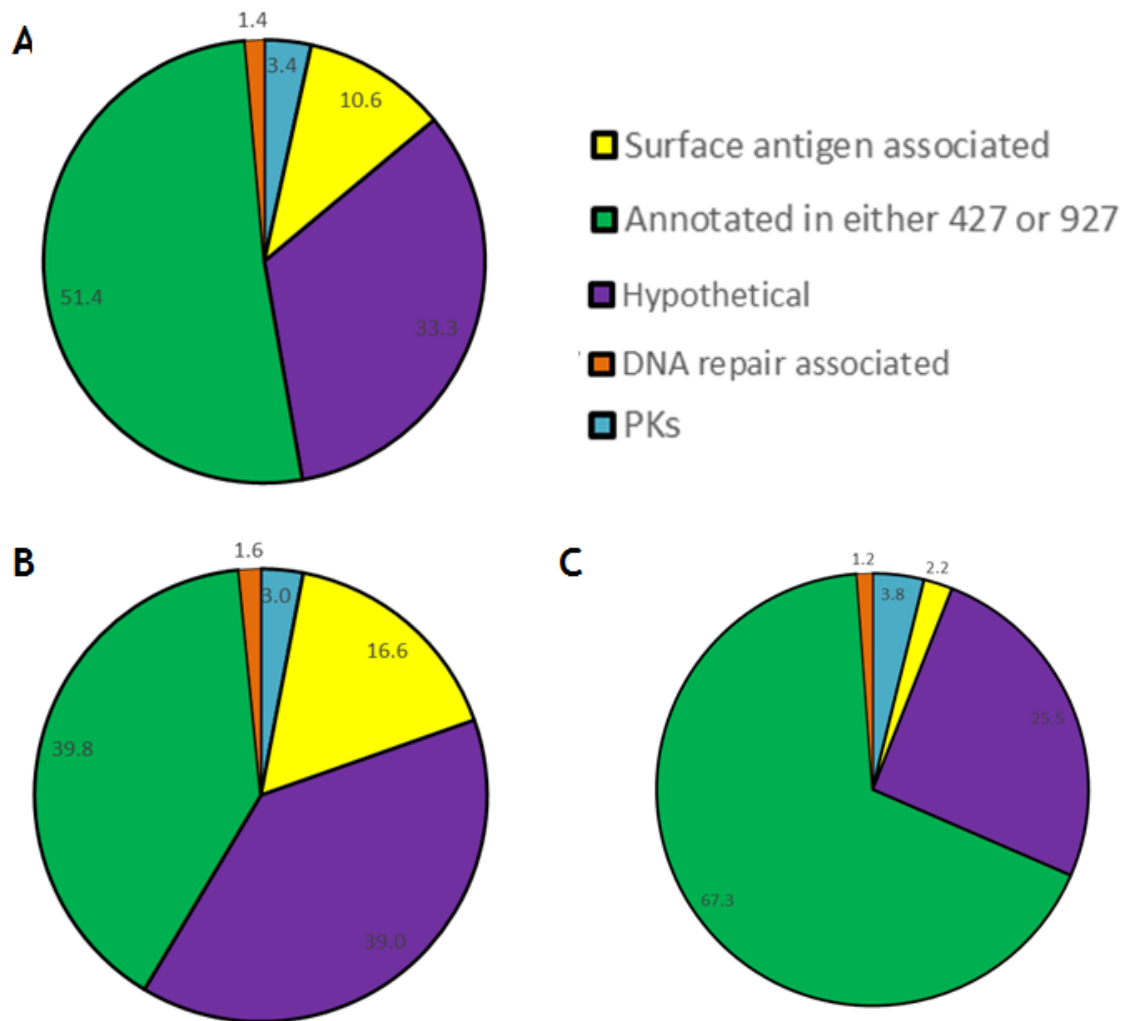


Figure 6-25: Pie charts summarising the data recovered at 36 hrs post TbATR downregulation

All differentially expressed genes were classified into four categories: DNA damage associated, surface antigen associated genes with annotations and hypothetical genes and expressed as a percentage of the total number of genes (1431 for A, 831 for B and 600 for C). Genes with annotations refers to genes which were annotated in either the Lister 427 or the TREU 927 reference genome. (A) details the overall distribution of the transcripts and their corresponding gene annotations across all differentially expressed transcripts (1431 in total). (B) details the genes corresponding to transcripts which were up-regulated and (C) details the genes corresponding to transcripts which were down-regulated.

At 36 hrs the majority of differentially expressed transcripts were functionally annotated in either the Lister 427 or TREU 927 genes (~ 50 %; Figure 6-25 A). Given this, GO term enrichment was analysed again (Figure 6-26) and, perhaps significantly given the effects of TbATR loss on nuclear structure and chromosome segregation, the most highly enriched terms were those associated with regulation of nuclear division, mitosis and the cell cycle. In addition,

several nuclear membrane associated and ribosome biogenesis genes showed altered expression, which may relate to the changes in nuclear structure described above and emerging roles for ATR in monitoring nuclear envelope and nucleolus structural integrity (Larsen & Stucki 2016; Kidiyoor et al. 2016).

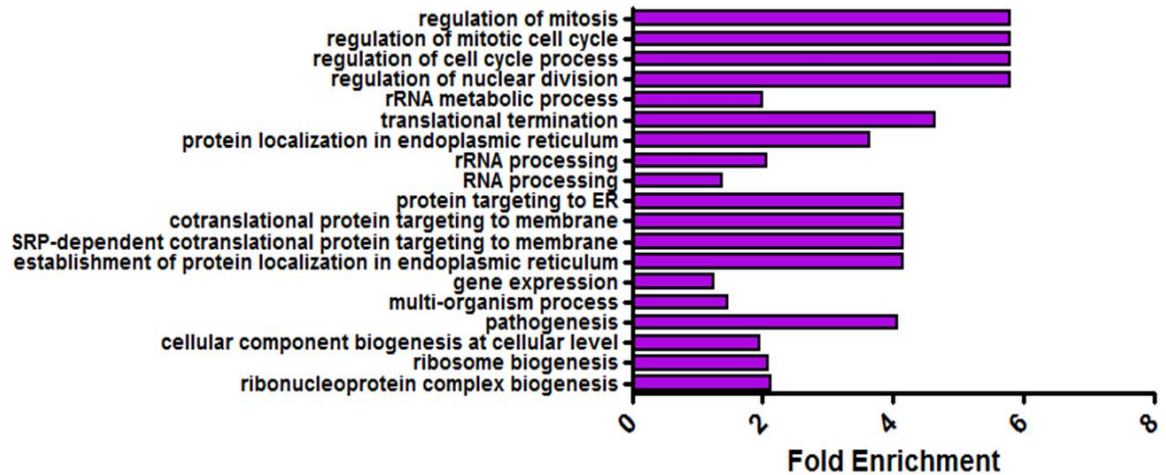


Figure 6-26: GO terms enriched at 36hrs post knockdown of TbATR in BSF cells
GO terms were retrieved from TriTrypDB based on the gene annotations associated with each gene.

We again asked if PKs and DNA repair genes displayed altered expression at 36 hrs. Unlike 24 hrs, differentially expressed transcripts corresponding to PKs could be detected, including PKs associated with control of the cell cycle; for instance, *cdc2*-related PKs TbCRK10 (Tb427.03.4670) and TbCRK4 (Tb427.08.5390) were up-regulated (FC ~1.5 and 1.6), while TbCRK6 (Tb427tmp.47.0031) was down-regulated (FC -1.4). In addition, several DNA damage associated proteins were seen to change expression, with the majority up-regulated (65 %; Figure 6-25 B&C; Table 6-8). Potentially, this data suggests that in the absence of TbATR, proteins associated with some DNA repair pathways are up-regulated.

Gene ID	Annotation	Up/Down	Pathway/Function	Fold Change
Tb427.03.4280	mismatch repair protein MSH5, putative		MMR	1.385
Tb427.03.5030	KU70 protein (KU70)		NHEJ	1.289
Tb427.08.6740	DNA repair protein, putative		?	1.291
Tb427tmp.01.6420	DNA repair and recombination helicase protein PIF1, putative (TbPIF4)		?	1.321
Tb427tmp.211.1210	RAD51/dmc1 protein, putative		HR	1.28
Tb427tmp.211.2870	DNA repair protein RAD2, putative		?	1.293
Tb427.01.1060	Cell cycle checkpoint protein RAD1-like, putative		?	1.327
Tb427.03.830	flap endonuclease-1 (FEN-1), putative		BER	1.249
Tb427.05.2020	Hypothetical		?	1.323
Tb427.03.1220	GIY-YIG catalytic domain containing protein, putative		?	1.457
Tb427.02.5750	tyrosyl-DNA Phosphodiesterase (Tdp1), putative		?	1.365
Tb427tmp.01.3910	endonuclease III, putative		?	1.302
Tb427.02.2260	phosphatidylinositol kinase domain protein, putative		Damage sensing	1.349
Tb427.08.700	DNA repair and recombination helicase protein PIF1, putative (TbPIF7)		?	-1.276
Tb427tmp.02.3250	DNA polymerase theta, putative		?	-1.25
Tb427tmp.02.3400	SNF2 DNA repair protein, putative		?	-1.389
Tb427tmp.02.4700	14-3-3 protein		?	-1.393
Tb427.07.610	DNA ligase, putative		?	-1.433
Tb427tmp.01.6300	phosphatidylinositol 3-related kinase, putative		Damage sensing	-3.079
Tb427tmp.02.3570	Inhibitor of apoptosis-promoting Bax1, putative		?	-1.6

Table 6-8: DNA damage associated proteins differentially regulated in BSF *T. brucei* 36 hrs TbATR RNAi induction
Genes up-regulated are marked as pale pink, and those down-regulated are marked as blue.

6.3.9.5 Does loss of TbATR induce VSG switching?

The qRT-PCR and the RNAseq data both suggest that loss of TbATR is associated with increased expression of transcripts from the silent ESs. To test whether these transcripts are translated and expressed, leading to VSG protein, a western blot analysis was performed. Antisera to detect the VSGs shown to be up-regulated by qRT-PCR and by RNAseq analysis were unavailable, and so antiserum against VSG121 (situated in BES3; referred to as BES15 in the spreadsheet in accompanying CD; [RNAseqDatasetATRBSF2016](#); kindly provided by L.Glover) was used. In addition, expression of VSG221 in the active BES was examined with anti-VSG221 antiserum. The TbATR CL1 cell line was RNAi induced and whole cell extracts prepared at 24 and 36 hrs, as well as from non-

induced cultures (Figure 6-27 A). As a control for VSG221 expression, 2T1 cell extracts were also collected at the same time point and, as a control for VSG121 expression, a cell line predominantly expressing VSG121 was used (strain 1.6; kindly provided by L.Glover). Even at 36 hrs post induction in the ATR RNAi cell line, expression of VSG121 could not be detected and there was no evidence of reduced VSG221 levels (Figure 6-27 B), despite RNAseq suggesting loss of transcription from BES1. A low level of VSG221 could be detected in the VSG121 cells, but this has been seen previously (personal communication D.Paape and L.Glover).

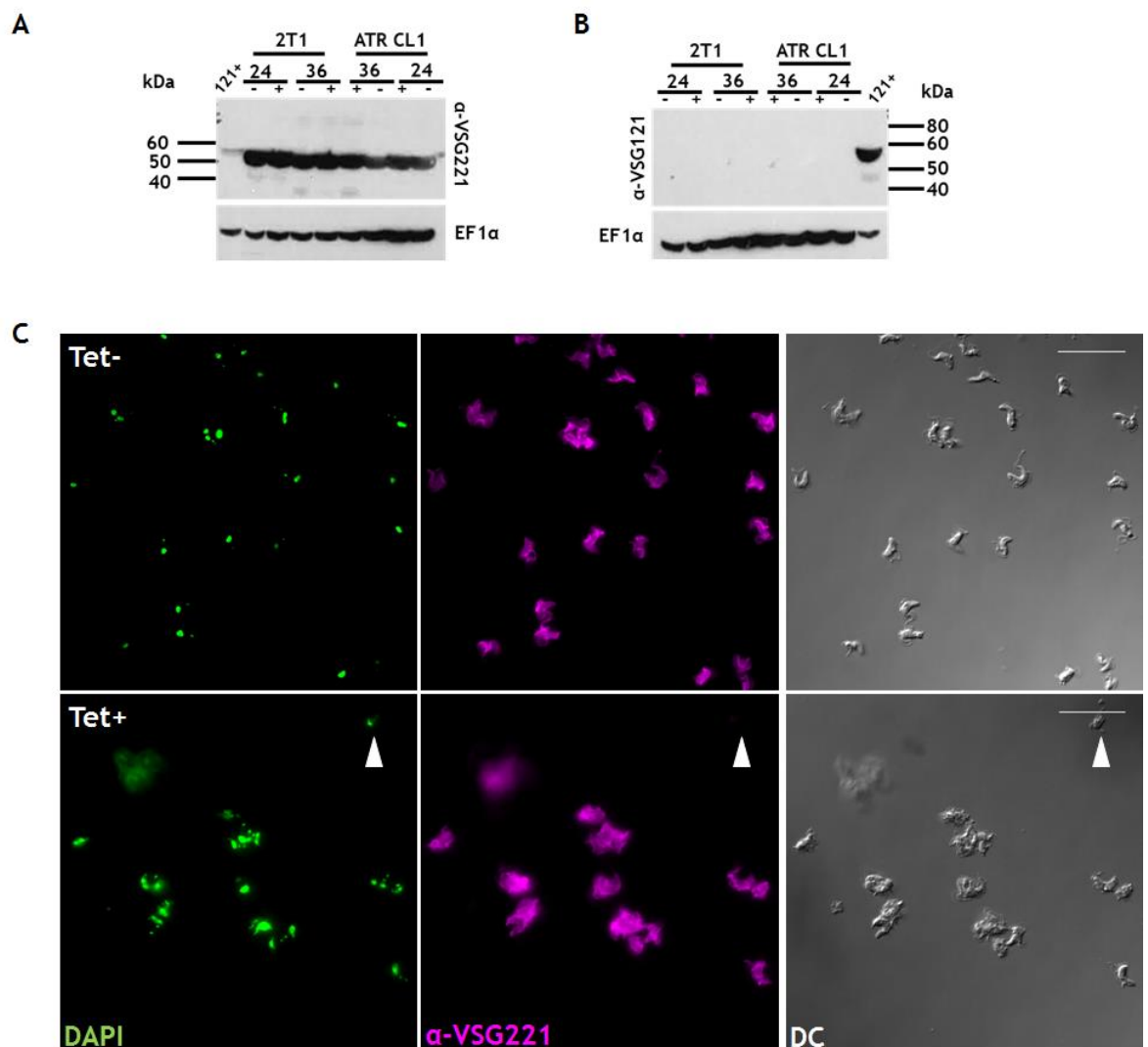


Figure 6-27: Some TbATR depleted cells do not express VSG221 on their surface
 Western blotting was performed at 24 and 36hrs post induction (+) in the ATR RNAi CL1 cell line as described in section 2.12.2, as well as in uninduced cells (-). 2T1 cells were used as a control for the presence of VSG221. The cell line known as 1.6 (kind gift, L.Glover) was used as a positive control for the presence of VSG121. Membranes were probed with α-VSG221 antiserum (A) or α-VSG121 antiserum (kind gift L.Glover; B). EF1α was used as a loading control. Sizes markers are shown. (C) Indirect IF analysis was performed as per section 2.11.4 on TbATR RNAi cells at 36 hrs post induction (Tet+), or in controls without induction

(-). Cells were stained with DAPI (green) and α -VSG221 (magenta). The cell body was visualised by differential interference contrast (DC) microscopy. Cells were imaged on a Zeiss Axioskop 2 and processed as per section 2.11.8. Images are representative images captured from TbATR RNAi CL2.; CL1 cells responded in the same way (data not shown). White arrow indicates a cell which has nDNA yet lacks α -VSG221 staining. Scale bar = 20 μ m.

Next, the presence of VSG221 on the surface of CL1 or CL2 cells induced for TbATR RNAi for 36 hrs was examined by indirect IF analysis (performed as per section 2.11.4) using the anti-VSG221 antiserum. In a culture that had not been induced for RNAi, <0.5 % (of over 200 counted per experiment; this experiment was performed as a duplicate) of cells did not have detectable anti-VSG221 staining. In cells in which TbATR RNAi had been induced, ~ 1 % of the population (in over 200 cells counted per experiment) appeared to have lost the VSG221 coat (Figure 6-27 C shows a representative image). These numbers are in keeping with a previous report (DuBois et al. 2012). Further work is needed to understand these preliminary data, including asking if increased numbers of cells express VSG121 on the surface after TbATR RNAi, which would indicate a VSG switch. However, it is also possible the lack of VSG221 on the surface of some cells is due to loss of viability, perhaps because protein trafficking is compromised.

6.4 Discussion

6.4.1 Both *T. brucei* ATR and ATM harbour a conserved PIKK KD

The crystal structures of PIKK family members from other eukaryotes have provided extensive insight into the organisation of these high molecular weight PKs (Baretić & Williams 2014). Generally, the C-terminal domain harbouring the KD is highly conserved between family members and the N-terminal domain is primarily organised as an α -solenoid arrangement of α -helices (Perry & Kleckner 2003; Baretić & Williams 2014). In addition, many smaller domains are conserved (notably HEAT repeats and FAT, FATC, PRD and LBE domains), each of which are important for facilitating kinase activity (Lempiainen & Halazonetis 2009; Baretić & Williams 2014; Mordes et al. 2008) either by invoking conformational changes or permitting interactions with other proteins. Based on the homology searches performed on both *T. brucei* ATR and ATM, the primary homology between the parasite kinases and ATR and ATM homologs in other eukaryotes is across the C-termini, in particular the KD. Indeed, remarkable sequence

conservation is found in the predicted catalytic and activation loops of both PKs, suggesting they are active kinases (section 6.3.1.2). Additionally, structural predictions suggest the presence of the α -solenoid regions, despite difficulty in identifying HEAT repeat domains, which are important for protein-protein interaction and contribute to the structural stability of these high molecular weight proteins. What proteins might interact with *T. brucei* ATM and ATR are currently unknown; for example, Tel2 in human cells binds HEAT repeats of ATR, ATM and mTOR (Takai et al. 2007), but its presence in *T. brucei* has not been examined.

Despite the overall structural conservation, several of the smaller domains appeared absent in both *T. brucei* ATR and ATM. For example, no clear LBE domain sequence could be identified. The LBE domain in mTOR is required for the binding of the protein ‘lethal with sec thirteen’ (LST8), which is a core component of the both the TORC1 and TORC2 complexes (Baretic et al. 2016). In *T. brucei* a potential LST8-like protein (accession number: Tb927.8.4210) could be identified, but its role or putative interaction with the *T. brucei* TOR, ATR or ATM PKs is unknown. The PRD domain of both *T. brucei* ATR and ATM was also not clearly detected. This absence may be significant for ATR, as the domain is required for the regulation of kinase activity via interaction with TopBP1 (Mordes et al. 2008; Burrows & Elledge 2008), ATM and the histone acetyltransferase Tip60 (Sun et al. 2007). Indeed, the specific residues required for TopBP1 activation appear to be lacking in TbATR, though in TbATM a lysine residue (K4237) predicted to be acetylated by Tip60 was present. A putative *T. brucei* homolog of TopBP1 has been identified, but a homolog of Tip60 has not, meaning it may be important to ask if TbATM and TbATR regulatory interactions are different. In this regard, it is notable that the histone acetyltransferase HAT3 is important for processing induced DSBs, substrates for ATM and ATR activity (Glover & Horn 2014).

Another striking absence was the lack of both a FAT and a TAN domain within the trypanosomatid ATM homolog. These domains are required for kinase activity and kinase localisation, respectively (Seidel et al. 2008; Baretic & Williams 2014). However, the *C. elegans* ATM-1 protein, which is greatly truncated (649 aa; Jones et al. 2014), also does not harbour either a FAT or a TAN domain. ATM-

1 is required to maintain the genomic stability in *C. elegans*, suggesting that the absence of these domains does not necessarily prevent ATM from exerting its function.

6.4.1.1 TbATR is essential for BSF cell survival *in vitro*

In other eukaryotes, the essential roles of ATR focus around monitoring the nuclear genome for signs of replicative stress (Nam & Cortez 2011; Paulsen & Cimprich 2007; Zeman & Cimprich 2014). DNA replication is a complex, multistep process that involves many multi-subunit protein complexes (see Masai et al. 2010 for a review of DNA replication). Though replication is tightly controlled, it can be impaired at many steps. For example, should the replisome encounter a bulky, alkylated base (perhaps as the result of exposure to a DNA alkylating agent such as MMS) progress may be halted, resulting in the generation of a stalled replication fork. ATR can function to stabilise the structures that form after stalling, preventing further DNA replication by slowing origin firing in the vicinity of the lesion, stalling the cell cycle and signalling the proteins required to restart the fork (Cimprich & Cortez 2008b; Zeman & Cimprich 2014). If the fork fails to resolve, ATR can recruit proteins, such as the MRN complex, to remodel the replication fork into a lesion resembling a DSB, thus triggering the activation of ATM, and initiating the DDR to resolve the lesion (Sowd et al. 2013; Schmidt et al. 2014; Zeman & Cimprich 2014; Ewald et al. 2008; Mazouzi et al. 2014). Despite extensive and ongoing characterisation of these functions in 'model' eukaryotic cells, TbATR function has not been examined in *T. brucei*, or any kinetoplastid.

In keeping with mutation of ATR in yeast and mammals, and with a previous report from Jones et al (2014), TbATR RNAi suggests the PK is essential, with loss resulting in reduced proliferation and cell cycle abnormalities. In contrast, ATR null mutants in *Arabidopsis* are viable (Culligan et al. 2004), with no observable growth defects in the absence of DNA damage. Indeed, a clear homolog of ATR is not seen in the protozoan parasite *Giardia lamblia*, though this organism is highly susceptible to genotoxic stress (Manning et al. 2011). Thus, the importance of ATR is not universal in eukaryotes. In *T. brucei*, as in yeast and mammals, TbATR loss reveals changes to the nuclear cell cycle. However, no changes in the kinetoplast cell cycle of *T. brucei* could be detected. These

effects manifest as increased numbers of 1N2K cells and the appearance of aberrant cells and cells with more than two kinetoplasts. In human and yeast cells, loss of ATR is associated with a stall during S-phase followed by the accumulation of cells with aberrant nuclear content (Brown & Baltimore 2000; Cha & Kleckner 2002). Further evidence of a nuclear function for *T. brucei* ATR is found in the observation that, 36 hrs after RNAi, ~ 50 % of the population harbour aberrant nuclear content: many of the nuclei were enlarged and misshapen, fragmented or had nuclear 'blebs'. Indeed, when the ultrastructure of the nucleus was examined by TEM, fragmentation of the nucleus was suggested by the presence of inappropriately positioned nuclear membranes throughout the cell. These phenotype severities after TbATR RNAi indicate widespread nuclear functions for ATR in *T. brucei*. However, the cell and DNA content analyses suggest that in the absence of TbATR, BSF cells do not completely halt at S-phase and instead progress through mitosis and the cell cycle; perhaps multiple times. Nonetheless, there is evidence of an S-phase stall, but why this occurs is known. Potentially, residual levels of TbATR after RNAi may be enough to permit the cells that have completed M phase with unrepaired damage to implement an S-phase stall. Alternatively, another factor may elicit this response. One candidate may be ATM, which in other eukaryotes can induce a stall during G1-S-phase in the presence of a DSB lesion (Shiloh & Ziv 2013).

The aberrant nuclei following TbATR loss may indicate the presence of chromosomal abnormalities. In this regard, examination of the positions of the telomeres (and thus locations of the chromosome ends in *T. brucei*) revealed abnormal telomere arrangements. In some cells telomeres could be detected, but overall nuclear content was clearly reduced, arguing for profound chromosome losses. In other cells, accumulations of telomeres were seen as large foci, perhaps due to the fusion of chromosomes. Both these observations are consistent with other eukaryotes, where loss of ATR is associated with sister chromatid fusions, loss of sister chromatids, chromosome deletions (Pennarun et al. 2010) and shortening of telomeres (Ritchie et al. 1999; Bi et al. 2005; Vespa et al. 2005; Denchi & de Lange 2007). The large 'clumps' of cells observed after TbATR RNAi may be explained by these profound chromosome abnormalities, suggesting that such cells may occasionally be unable to correctly initiate

cytokinesis. However, the presence of some *T. brucei* cells which lack any nuclear DNA (so called 'zoid' cells), may indicate that when cytokinesis can occur, the ability of the cell to monitor the division of the nucleus is impaired. In this regard, growing evidence in both human and yeast cells suggests loss of ATR is also associated with cytokinesis and abscission defects (Mackay & Ullman 2015; Eykelenboom et al. 2013), respectively.

6.4.1.2 TbATR deficient BSF cells are sensitive to genotoxic stress and show increased expression of γ H2A and RAD51

Loss of ATR hyper-sensitises human and yeast cells to a range of genotoxic agents such as UV, IR and, additionally in human cells, to HU, cisplatin and other chemotherapeutic compounds (Wilsker & Bunz 2007; Hurley et al. 2007; Pépin et al. 1995; Morrow et al. 1995). In keeping with observations, BSF *T. brucei* cells exposed to MMS, UV or HU, showed increased sensitivity after TbATR depletion. These data suggest that TbATR acts in the response to a similarly wide range of DNA lesions, spanning bulky base adducts, DNA strand crosslinks and replication stalling agents.

In addition to sensitising cells to genotoxic stress, cells deficient in ATR also increase expression of the modified histone γ H2A, and cause relocalisation and of the repair associated protein RAD51 (Chanoux et al. 2009; Podhorecka et al. 2011). γ H2A(X) can arise as the result of phosphorylation by ATR and ATM, though recently ~ 40 PKs have been implicated in its activation (Benzina et al. 2015). Nonetheless, H2A phosphorylation after damage in *T. brucei* and *Leishmania* is unconventional (Glover&Horn 2012; Damasceno et al. 2016), being on a threonine (T130) residue; as such, the kinase responsible is not simple to predict. γ H2A(X) is considered an early marker of a range of DNA damage (as reviewed by Kuo & Yang 2008; Mah et al. 2010; Dickey et al. 2009), whereas RAD51 catalyses homology-directed repair by associating with RPA-coated ssDNA (Chen et al. 2008; Baumann & West 1998; McCulloch & Barry 1999), much of which forms at DSBs. In *T. brucei*, RAD51 foci form readily in BSF cells treated with phleomycin (Devlin et al. 2016) or after IScel-mediated DSB (Glover et al., 2013) formation, whereas less foci are observed in cells treated with MMS or UV (data not shown). Thus, the pronounced accumulation of RAD51 foci after TbATR depletion suggests that at least some of the nucleus accumulates DSBs.

However, whether these or other potential lesions are genome-wide or localised after loss of TbATR is unknown.

6.4.1.3 Loss of TbATM is not associated with proliferation defects or increased sensitivity to genotoxic stress in BSF *T. brucei*

In human cells lacking ATM, chromosomal abnormalities occur, often predisposing cells to oncogenic transformations and resulting in genomic instabilities (Shiloh & Ziv 2013). Surprisingly, the loss of TbATM in BSF *T. brucei* did not disrupt normal cellular proliferation and nor could aberrant cells observed in the culture, suggesting this lifecycle stage does not require TbATM for *in vitro* survival. Even when TbATM was depleted in the presence of MMS or HU, no increased proliferation defects were observed, suggesting TbATM plays a limited role in the response to alkylation damage or replication stalling.

From this study, the roles of TbATM remain unclear. Though ATM is considered non-essential in other eukaryotes, recent studies have questioned this. Using ATM knockout mice and mice harbouring kinase dead ATM (expressed at physiologically relevant levels) Yamamoto et al (2012) showed that though mice lacking ATM in part phenocopied the human syndrome Ataxia-telangiectasia, those harbouring catalytically dead ATM failed to progress past early embryogenesis. The authors attribute this effect to the recruitment of the inactive kinase to DSB sites, but the inability of the kinase to elicit a damage response. Therefore, it is possible that simply depleting ATM may not result in a phenotype in *T. brucei*; expression of kinase-dead ATM variant may provide more insight. Additionally, as ATM is primarily activated in the presence of a DSB, exposing the TbATM RNAi cell line to this type of lesion may be required to elicit a phenotype. Nonetheless, the predicted downstream interaction partners of TbATM, such as the MRN complex and RAD51, do result in proliferative defects when deleted in *T. brucei* (McCulloch & Barry 1999; Tan et al. 2002). In addition, no predicted sites of phosphorylation could be detected in TbATM (Urbaniak et al. 2013), which is unusual since ATM activation in human cells relies on autophosphorylation. These data may therefore suggest TbATM functions in a highly divergent manner from that of other eukaryotes.

6.4.2 Loss of TbATR is associated with increased VSG expression from silent expression sites

Monoallelic expression of a single VSG variant on the surface of a BSF *T. brucei* cell is a complex process (recently reviewed by Günzl et al. 2015; Morrison et al. 2009; Horn & McCulloch 2010; Glover, et al. 2013). Only one BES is transcriptionally active and the remaining 14 (predicted in the Lister 427 strain; Hertz-Fowler et al. 2008) are considered transcriptionally silent (though in fact, some transcription in the vicinity of the promoters can be detected; Kassem et al. 2014). The detailed mechanisms that result in monoallelic expression have yet to be fully described, though a variety of factors, including chromatin modifiers, telomere associated proteins, the nuclear lamina (DuBois et al. 2012; Maishman et al. 2016), and a novel BES-associated factor (Glover et al. 2016), have been shown to be involved (Günzl et al. 2015).

The telomeres of eukaryotic organisms are comprised of repetitive sequences (reviewed by Churikov & Price 2001). These repeats allow telomere-mediated end-replication, preventing loss of sequence proximal to the chromosome ends, which can include genes. However, telomeres during replication often resemble DSB-like structures and thus, their presence should be sensed by either ATR or ATM, resulting in the activation of the DDR. To circumvent this, the telomeres and associated sequences are protected by the shelterin complex (refer to Palm & de Lange 2008 for a review on the Shelterin complex). A component of this complex, POT1, interacts with ATR to prevent activation, (Denchi & de Lange 2007) though in the absence of ATR, telomere ends become short (in keeping with advanced aging in adult ATR knockout mice; McNees et al. 2010; Murga et al. 2009). Shelterin binding to telomeres can result in silencing of genes in proximity with the telomeres; for instance, in yeast up 20 kb from the telomere can be silenced (Wyrick et al. 1999). The purpose of this telomere position effect (TPE) is not yet fully understood, but is a method by which eukaryotes can control gene expression. Evidence for an ATR-related role in TPE has emerged in both yeast and *Drosophila*; ATR (together with ATM) may load components of the shelterin complex, preventing activation of the DDR (Bi et al. 2005; Moser & Nakamura 2009; Moser et al. 2009) and mediating TPE.

Considering the above roles of ATR in telomere maintenance and TPE, is it possible that these functions may account for the profound changes in BES expression seen after TbATR RNAi? The fact that changes in BES expression preceded a more widespread impact on transcription (below) might indicate telomeres are particularly sensitive sites. As previously discussed, the immediate proximity of some telomeres and the BESs had led to tests of TPE as a means of silencing control and, indeed, loss of RAP1 (Pandya et al. 2013; Yang et al. 2009), TRF and TIF2 (Jehi et al. 2014; Jehi et al. 2016; each shelterin associated factors) have been shown to result in impaired BES silencing or increased VSG recombination. Thus, there is a parallel with the expression of previously silent VSG RNA transcripts in the absence of TbATR. However, several observations question whether the two outcomes are causally or functionally linked. Careful analysis of the extent of TPE in *T. brucei* has concluded that it stretches for only a few kb (Glover & Horn 2006), and does not encompass the whole BES. This limited spread appears compatible with the effect of RAP1 loss (Yang et al. 2009), which is more pronounced proximal to the telomeres of the silent BESs. Both these observations appear inconsistent with the RNAseq data, which suggest comparably increased transcript levels throughout the silent BES after TbATR loss. It is important to note that no proteins to date have been identified that interact with TbATR in *T. brucei*, including RAP1 or any shelterin component; indeed, whether POT1 (the best candidate ATR interactor) is present in *T. brucei* is unclear (Dreesen et al. 2007). Recent work has concluded that loss of RAP1 in BSF cells, unlike in PCF, causes limited changes in BES chromatin structure (Pandya et al. 2013) and it is questionable whether this is compatible with the marked accumulation of γ H2A after TbATR loss, though direct examination of the BES was not performed. If silent BES transcription does not result from altered TPE due to TbATR loss, it is possible the telomeres themselves have become impaired. No direct evaluation of telomeres after TbATR RNAi was conducted, but previous work has shown that the effects of telomere attrition after mutation of the telomerase are slow to accumulate (Dreesen et al. 2005; Dreesen et al. 2007). In addition, directly excising the telomere in either the active or a silent BES by ISceI (Glover et al., 2013) cleavage does not elicit a change in BES transcription or switching. In contrast, increased silent BES VSG expression after TbATR RNAi is detectable and rapid (as

was clearly seen 24 hrs and 36 hrs post induction by qRT-PCR and RNAseq analysis).

Another explanation for the increased expression of silent BES after TbATR RNAi loss may be alterations in the nuclear ultrastructure. Emerging data is revealing that ATR plays a crucial role in detecting and responding to structural stress, including to the nuclear membrane and to the nucleolus (Kidiyoor et al. 2016; Kumar et al. 2014). Strikingly, RNAi of TbNUP1 (DuBois et al. 2012) or TbNUP2 (Maishman et al. 2016), two distinct proteins that act in the *T. brucei* nuclear lamina, leads to increased expression of silent VSGs (and procyclin), as well as leading to malformed nuclei and inappropriately positioned telomeres. In addition, RNAi of TbNUP2 results in increased levels of γ H2A. Therefore, there is marked overlap between the effects of TbATR and TbNUP1 RNAi, though we have yet not been able to determine clearly if the loss of TbATR leads to VSG switching, as is seen in TbNUP-1 depleted cells (DuBois et al. 2012). However, it is unclear whether these overlapping phenotypes indicate a common causal effect that leads to alleviation of surface antigen gene silencing. In both NUP1 and TbNUP2 RNAi studies, a relatively limited number of genes showed increased or decreased RNA levels after RNAi: 62 and 142 genes, respectively, increased >2 fold 48 hrs after RNAi, while no genes and 200, respectively, decreased 2 fold. Though a number of factors complicate comparisons between experiments (e.g. different RNAi strategy, different analysis approach), the effects on transcription appear more severe and widespread after TbATR RNAi: >1400 genes were significantly affected after 36 hrs following RNAi induction, with a wider range of genes affected. In fact, DuBois et al (2012) reported nucleoporin RNAi analysis, which did not result in increased surface antigen gene expression, and concluded that TbNUP1 may play a specific role in gene silencing. As such, effects on nuclear integrity might not account entirely for the observed depression of surface antigen genes. Indeed, it is important to emphasise that the relatively specific changes in surface antigen expression after 24 hrs of TbATR RNAi appeared to precede the emergence of detectable alterations to the DNA content, the nucleus and the morphology of the BSF cells. Given this, a third hypothesis for the VSG ES changes seen after TbATR RNAi could be proposed (see below), though it is plausible that TbATR loss has both BES-specific and nucleus-wide effects. In this regard, the increased cohort of genes

that show altered expression after TbNUP2 RNAi relative to TbNUP1 might be explicable by more general nuclear defects after loss of the former lamina component, some of which may correlate with the putative roles ATR plays in monitoring nucleus (sub) structural integrity.

The third putative explanation for altered VSG BES expression is that loss of TbATR directly affects integrity of the BES. In this model, TbATR plays a role in signalling and co-ordinating the repair of lesions within the BES and, in its absence, these well-established DDR functions are lost, leading to inefficient repair and altered BES expression. Recent work has begun to examine the processes that initiate VSG switching, and have linked BES lesions to VSG recombination. Some work has modelled VSG switch initiation by the generation of DSBs within the active BES (Boothroyd et al. 2009; Glover, Alford, et al. 2013), leading to recombination, while another study has indicated the active BES is specifically targeted for early DNA replication (Devlin et al. 2016), which could generate replication stalls that initiate a VSG switch. Regardless of which model operates, TbATR is likely to play a role in recognising and signalling the initiating lesions. If such an activity is lost after RNAi, lesion repair would be impeded and continued cell cycle progression might lead to cells that no longer express the active VSG, which is predicted to be lethal (Aitcheson et al. 2005), leading to the selection of cells that have switched to another VSG for short term survival. The observation that potentially all of the silent BESs are expressed after TbATR RNAi might indicate the most common survival route is transcriptional activation of a silent BES. Indeed, such events, coupling BES deletion and transcriptional activation, have been detected previously in unperturbed cells (Rudenko et al. 1998; Cross et al. 1998) and in HR mutants (Devlin et al. 2016; Hartley & McCulloch 2008). Alternatively, elevated levels of BES lesions may lead to derepression of all silent BESs, a situation which could account for the BSF-specific increases in transcription from silent BESs after treatment with nuclear DNA damaging agents and after blocking nuclear DNA replication (Shedder et al. 2004); intriguingly, these treatments also result in depression of procyclin transcription, as we see after TbATR RNAi. Further work is required to test if integrity of the active and silent BESs are undermined after TbATR loss, but the inability to repair frequent lesions in the BES, leading to loss of the telomeric VSG, might link the repair data reported here with recent

proposals that the VSG can provide a homology signal, propagated by TbVEX1 (Glover et al. 2016) and DOT1B (Batram et al. 2014), to determine BES transcription status.

If the third model is correct, it may be the case that the later expression changes might not be the direct effect of TbATR signalling BES lesions, but reflect wider functions of TbATR. To ask if we could detect a signalling network, the remaining differentially expressed transcripts of annotated genes were examined. A number of kinases were identified as being differentially expressed, including several associated with control of the cell cycle. In addition, we observed changes in genes associated with mitosis, control of the cell cycle and RNA regulation, potentially in keeping with the S-phase cell cycle stall and the altered nuclear and cell morphology. However, further, protein-focused work will be needed to assess if these genes encode direct and indirect targets of TbATR's potentially wide functions in BSF *T. brucei*.

7 Future perspectives

Protein kinases (PKs) contribute extensively to the maintenance of genome integrity across the Eukarya. For example, loss of aurora B in human cells disrupts chromosome segregation during mitosis resulting in aneuploid cells (as reviewed by Carmena et al. 2012), whereas loss of either atypical PK ATR or ATM sensitises cells to genotoxic stress and increases genome fragility even in the absence of DNA damage (as reviewed by Weber & Ryan 2015; Marechal & Zou 2013). Considering the multitude of pathways required to protect genome integrity from a myriad of lesions types, many aspects of genome repair are conserved amongst the Eukarya. However, like all aspects of biology, though a common blueprint may describe the processes of DNA damage repair, alterations and divergence of this core process are apparent. Given the vast diversity of organisms and subsequent variety of cells encompassed within this domain of life, it is no surprise that tailoring repair responses to suit the requirements of individual organisms and cells has occurred. A further aspect of genome repair is the exploitation of such pathways to generate diversity within a cell and ultimately a population. The primary function of repair is normally genome maintenance and it is clear that cells with defective or altered repair responses, when faced with genotoxic lesions, contribute to formation of diseased states, such as the onset of cancer (in which de-regulation of kinase activity plays a significant role; (Shchemelinin et al. 2006; Lahiry et al. 2010; Gross et al. 2015)). However, if the generation of a lesion can be implemented within a specific region in the genome and the process controlled in a way to prevent loss of genome integrity, it is possible that the repair of this lesion may contribute to enhanced diversity. One such example is the use of the non-homologous end joining (NHEJ) pathway involved in the repair of double stranded breaks (DSBs) to generate the enormous variety of the antigen receptors displayed on the surface of lymphocyte cells (reviewed by Schatz & Ji 2011), giving rise to the complex and sophisticated humoral immune response of the human immune system. Another example is the exploitation of homologous recombination (HR) to facilitate the switching of the *T. brucei* VSG surface coat during antigenic variation (reviewed by McCulloch et al. 2015). Understanding the lesions which form in *T. brucei* that trigger VSG switching and how lesion repair is signalled and executed may yet reveal lineage-specific reactions, which may offer therapeutic targets for trypanosomiasis.

In 2005, the genomes of three kinetoplastid parasites (*T. cruzi*, *L. major* and *T. brucei*) were published and, in a follow up publication, the protein kinase complement (or ‘kinome’) of each was analysed (Parsons et al. 2005). In *T. brucei*, the kinome was subject to functional analysis, investigating PKs with roles in the progression of the cell cycle (Jones et al. 2014). Other work has probed the mechanisms and dynamics of DNA replication and DNA repair in all kinetoplastids, which is beginning to reveal divergence (as reviewed by Passos-Silva et al. 2010; Genois et al. 2014). Perhaps most prominently, NHEJ appears not to operate, with greater reliance on micro-homology-mediated end-joining (Glover et al. 2011; Zhang & Matlashewski 2015; Peng et al. 2015), while the kinetoplastid machinery that dictates nuclear genome replication initiation is non-canonical (Marques et al. 2016; reviewed by Tiengwe et al. 2014), as is the orchestration of *Leishmania* genome replication (Marques et al. 2015; Lombraña et al. 2016). This project represents the first steps in attempting to link PK function and genome maintenance by DNA repair.

T. brucei, like humans, dedicates ~2 % of the genome to PK genes. However, several PK families (e.g the NEK kinase family) have become expanded, and homologs of some DNA repair-centric kinases, such as DNA-PK, appear absent (Genois et al. 2014). To date, no PK in *T. brucei* has been shown to function in a genome repair pathway. To address this knowledge deficit, two RITseq screens, a whole genome and a kinome-focused, were performed in BSF parasites to ask which PKs are required for parasite survival in the presence of the alkylating agent MMS. In all, at least 11 PKs, based on initial identification in genome wide and kinome wide RITseq screens, and revealed to result in sensitisation of BSF cells to MMS. In fact, a total of 24 putative damage response PKs were suggested from the screens, amongst which only seven were considered ‘false-positives’. A total of five PK families were represented within just the 11 validated PKs which represent the first examination of PKs in the context of *T. brucei* DNA and cellular repair. Follow up characterisation was undertaken for four of the PKs, and some preliminary phenotypic and localisation analysis for several more, revealing considerable functional divergence. Additional analysis, perhaps to examine further the greater number of kinome-wide candidates, may also reveal novel and essential aspects of *T. brucei* biology in the context of genome repair.

Two PKs identified from the genome wide screen were examined in some depth, including the generation of BSF gene disruption null mutants for both. As previously published (Tu et al. 2006), RNAi knockdown of TbAUK2 did not result in obvious phenotypic abnormalities, but pronounced phenotypes were seen when the gene was disrupted in BSF cells, revealing a role for this kinase in maintaining nuclear genome integrity, potentially by preventing mis-segregation of the genome during mitosis. Further work is required to understand the intimate details of TbAUK2's role in *T. brucei*, but preliminary data suggest interaction with a helicase involved in DNA repair; though such interaction requires confirmation it is notable that AUKs in other eukaryotes, are part of wide networks of interacting proteins (chapter 4; Vader & Lens 2008; Carmena et al. 2009; Carmena et al. 2012). The second protein, a pseudokinase, when disrupted unexpectedly gave rise to an endocytic defect in BSF cells, suggesting that *T. brucei* may also require a functional endocytosis pathway in response to genotoxic stress. Again, further investigation is needed to determine which aspect of endocytosis is compromised; e.g. is the uptake of material in general inhibited, or is intracellular trafficking compromised, which prevents movement of material around the cell? Answering such questions will reveal if the putative repair defect of the mutants is a secondary phenotype, or if genome maintenance is part of the mode of action of the PK. A mitogen activated kinase (known as TbKFR1) was also preliminarily examined, and may warrant further investigation, as the PK appears to be essential for parasite survival (Hua & Wang 1997). However, the role this kinase plays in *T. brucei* remains mysterious, as does its potential conservation in *Leishmania*.

Surprisingly, the *T. brucei* homologs of ATR or ATM (two atypical kinases central to the DNA damage response in other eukaryotes; reviewed by Marechal & Zou 2013; Shiloh & Ziv 2013; Zeman & Cimprich 2014) were only predicted by the kinome screen as having a role in the *T. brucei* response to MMS. However, when TbATM function was examined by RNAi in BSF parasites, it was apparent that loss of PK did not compromise cell proliferation even in the presence of MMS damage. Thus, a role for TbATM in the *T. brucei* DDR remains unclear. Conversely, loss of TbATR severely impaired parasite survival, which may be attributed to the appearance of widespread nuclear defects, as suggested by the loss of nuclear structure, aberrant telomere arrangements and DNA damage

(seen in the formation of γ H2A and RAD51 foci following TbATR knockdown). Additionally, loss of TbATR resulted in de-repression of VSG genes in the silent BESs, providing the first link between any PK and antigenic variation. However, depression of life cycle specific genes, including surface antigen associated genes such as procyclin, expression site associated genes (ESAGs) and procyclin associated genes (PAGs), suggests loss of TbATR may have a wide impact on gene expression controls, some potentially related to RNA PolI function and consistent with a role for ATR in sensing (sub)nuclear structural stress, including in the nucleolus (Kumar et al. 2014). In the future, it would be interesting to ask whether TbATR is associated with particular regions of the *T. brucei* genome; for example, does the kinase play a particular role in monitoring lesions within the active VSG BES? For instance, investigating whether the previously silent VSG (and other surface antigen) transcripts are expressed as protein, using proteomics and IF analyses, will determine whether TbATR has a direct role the control of antigenic variation, or a genome-wide surveillance role. It was also be interesting to ask whether loss of TbATR has the same effects in PCF cells, the lifecycle stage lacking the VSG surface coat.

Overall, by asking what PKs contribute to BSF *T. brucei* parasite survival in the presence of MMS, it is clear that the process of genome and cellular repair in *T. brucei* may involve a complex network of interactions across a multitude of pathways, many of which may still require characterisation in this eukaryotic microbe. Given the reliance of many repair pathways on kinase activity to phosphorylate downstream interaction partners, this study has opened up opportunities for work in the future to investigate DNA damage associated kinases in *T. brucei*. Whether the putative DDR PKs examined in this study may be targets for the multitude of kinase inhibitory compounds that have been developed (as reviewed by Grant 2009; Gross et al. 2015) still remains an open question. Though at least two of the PKs are not essential in culture, it is possible that they assume important roles in the mammal. Equally, though TbATR (a current chemotherapeutic target; as reviewed by Karnitz & Zou 2015; Weber & Ryan 2015; Fokas et al. 2014) and TbKFR1 appear essential, whether these PKs harbour parasite specific functions which could be targeted without affecting the host PKs remains unknown.

References

- Abraham, R.T., 2001. Cell cycle checkpoint signaling through the ATM and ATR kinases. *Genes & Development*, 15, pp.2177-2196.
- Acosta-Serrano, a et al., 2001. The surface coat of procyclic *Trypanosoma brucei*: programmed expression and proteolytic cleavage of procyclin in the tsetse fly. *Proceedings of the National Academy of Sciences of the United States of America*, 98(4), pp.1513-8.
- Adl, S.M. et al., 2012. The revised classification of Eukaryotes. *Journal of Eukaryotic Microbiology*, 59(5), pp.429-514.
- Afonso, O., Figueiredo, A.C. & Maiato, H., 2016. Late mitotic functions of Aurora kinases. *Chromosoma*, pp.1-11.
- Ahn, S.-H., Acurio, A. & Kron, S.J., 1999. Regulation of G2/M progression by the STE Mitogen-activated protein kinase pathway in budding yeast filamentous growth. *Molecular Biology of the Cell*, 10(10), pp.3301-3316.
- Aitchison, N. et al., 2005. VSG switching in *Trypanosoma brucei*: antigenic variation analysed using RNAi in the absence of immune selection. *Molecular microbiology*, 57(6), pp.1608-1622.
- Allen, C. et al., 2011. More forks on the road to replication stress recovery. *Journal of Molecular Cell Biology*, 3(1), pp.4-12.
- Allen, C.L., Goulding, D. & Field, M.C., 2003. Clathrin-mediated endocytosis is essential in *Trypanosoma brucei*. *European Molecular Biology Organization Journal*, 22(19), pp.4991-5002.
- Alsford, N.S. et al., 2003. The identification of circular extrachromosomal DNA in the nuclear genome of *Trypanosoma brucei*. *Molecular Microbiology*, 47(2), pp.277-289.
- Alsford, S. et al., 2014. Cathepsin-L can resist lysis by human serum in *Trypanosoma brucei brucei*. *PLoS Pathogens*, 10(5): e1004130
- Alsford, S. et al., 2012. High-throughput decoding of antitrypanosomal drug efficacy and resistance. *Nature*, 482(7384), pp.232-236.
- Alsford, S. et al., 2011. High-throughput phenotyping using parallel sequencing of RNA interference targets in the African Trypanosome. *Genome Research*, 21(6), pp.915-924.
- Alsford, S. et al., 2005. Tagging a *T. brucei* RRNA locus improves stable transfection efficiency and circumvents inducible expression position effects. *Molecular and Biochemical Parasitology*, 144(2), pp.142-148.

- Alsford, S. & Horn, D., 2012. Cell-cycle-regulated control of VSG expression site silencing by histones and histone chaperones ASF1A and CAF-1b in *Trypanosoma brucei*. *Nucleic Acids Research*, 40(20), pp.10150-10160.
- Alsford, S. & Horn, D., 2008. Single-locus targeting constructs for reliable regulated RNAi and transgene expression in *Trypanosoma brucei*. *Molecular and Biochemical Parasitology*, 161(1), p.76-79.
- Alsford, S., Horn, D. & Glover, L., 2009. DNA breaks as triggers for antigenic variation in African Trypanosomes. *Genome Biology*, 10(6), p.223.
- Altschul, S.F. et al., 1990. Basic local alignment search tool. *Journal of Molecular Biology*, 215(3), pp.403-410.
- Ammazzalorso, F. et al., 2010. ATR and ATM differently regulate WRN to prevent DSBs at stalled replication forks and promote replication fork recovery. *The European Molecular Biology Organization Journal*, 29(18), pp.3156-3169.
- Andrews, N.W., Almeida, P.E. & Corrotte, M., 2014. Damage control: Cellular mechanisms of plasma membrane repair. *Trends in Cell Biology*, 24(12), pp.734-742.
- Vickerman, K. and Preston, T.M., 1976. Comparative cell biology of the Kinetoplastid flagellates. *Biology of the Kinetoplastida*, 1, pp. 35-130.
- Arora, S. et al., 2010. RNAi screening of the kinome identifies modulators of cisplatin response in ovarian cancer cells. *Gynecologic Oncology*, 118(3), pp.220-227.
- Aslett, M. et al., 2010. TriTrypDB: a functional genomic resource for the Trypanosomatidae. *Nucleic Acids Research*, 38(2), pp.D457-D462.
- Asteriti, I.A., De Mattia, F. & Guarguaglini, G., 2015. Cross-talk between AURKA and Plk1 in mitotic entry and spindle assembly. *Frontiers in Oncology*, 5, pp.1-9.
- Bacchi, C.J. et al., 1983. In vivo effects of alpha-DL-difluoromethylornithine on the metabolism and morphology of *Trypanosoma brucei brucei*. *Molecular and Biochemical Parasitology*, 7(3), pp.209-225.
- Badjatia, N. et al., 2016. Cyclin-Dependent Kinase CRK9, required for spliced leader trans splicing of Pre-mRNA in Trypanosomes, functions in a complex with a new L-Type cyclin and a Kinetoplastid-specific protein. *PLoS Pathogens*, 12(3): e1005498.
- Baharoglu, Z. et al., 2006. RuvAB is essential for replication forks reversal in certain replication mutants. *The European Molecular Biology Organization Journal*, 25(3), pp.596-604.

- Baker, N., Alsford, S. & Horn, D., 2011. Genome-wide RNAi screens in African Trypanosomes identify the nifurtimox activator NTR and the eflornithine transporter AAT6. *Molecular and Biochemical Parasitology*, 176(1), pp.55-57.
- Bakkenist, C.J. & Kastan, M.B., 2003. DNA damage activates ATM through intermolecular autophosphorylation and dimer dissociation. *Nature*, 421(6922), pp.499-506.
- Balboula, A.Z. & Schindler, K., 2014. Selective disruption of Aurora C kinase reveals distinct functions from Aurora B kinase during Meiosis in mouse oocytes. *PLoS Genetics*, 10(2): e1004194
- Baretic, D. et al., 2016. Tor forms a dimer through an N-terminal helical solenoid with a complex topology. *Nature Communications*, 7, p.11016.
- Baretić, D. & Williams, R.L., 2014. PIKKs - the solenoid nest where partners and kinases meet. *Current Opinion in Structural Biology*, 29, pp.134-142.
- Barry, J.D. et al., 1998. VSG gene control and infectivity strategy of metacyclic stage *Trypanosoma brucei*. *Molecular and Biochemical Parasitology*, 91(1), pp.93-105.
- Bartek, J., Lukas, C. & Lukas, J., 2004. Checking on DNA damage in S phase. *Nature reviews. Molecular Cell Biology*, 5(10), pp.792-804.
- Bassik, M.C. et al., 2009. Rapid creation and quantitative monitoring of high coverage shRNA libraries. *Nature Methods*, 6(6), pp.443-445.
- Batram, C. et al., 2014. Expression site attenuation mechanistically links antigenic variation and development in *Trypanosoma brucei*. *eLife*, 3, p.e02324.
- Baumann, P. & West, S.C., 1998. Role of the human RAD51 protein in homologous recombination and double-stranded-break repair. *Trends in biochemical sciences*, 23(7), pp.247-251.
- de Beer, T. et al., 2000. Molecular mechanism of NPF recognition by EH domains. *Nature Structural Biology*, 7(11), pp.1018-1022.
- Benedetti, A. De, 2012. The Tousled-like kinases as guardians of genome integrity. *International Scholarly Research Notes Molecular Biology*, 2012, p.627596.
- Benmerzouga, I. et al., 2013. *Trypanosoma brucei* Orc1 is essential for nuclear DNA replication and affects both VSG silencing and VSG switching. *Molecular Microbiology*, 87(1), pp.196-210.
- Bentley, N.J. et al., 1996. The *Schizosaccharomyces pombe* rad3 checkpoint

- gene. *The European Molecular Biology Organization Journal*, 15(23), pp.6641-6651.
- Benz, C. et al., 2012. Cytokinesis in bloodstream stage *Trypanosoma brucei* requires a family of Katanins and Spastin. *PLoS ONE*, 7(1): e30367.
- Benzina, S. et al., 2015. A kinome-targeted RNAi-based screen links FGF signaling to H2AX phosphorylation in response to radiation. *Cellular and Molecular Life Sciences*, 72(18), pp.3559-3573.
- Berman, Wilson, Haas, and L., 2003. A Novel MAP Kinase Regulates Flagellar Length in *Chlamydomonas*. *Current Biology*, 13, pp.1145-1149.
- Bernards, A. et al., 1981. Activation of trypanosome surface glycoprotein genes involves a duplication-transposition leading to an altered 3' end. *Cell*, 27(3 Pt 2), pp.497-505.
- Berriman, M. et al., 2005. The genome of the African Trypanosome *Trypanosoma brucei*. *Science*, 309(5733), pp.416-422.
- Bi, X. et al., 2005. Drosophila ATM and ATR checkpoint kinases control partially redundant pathways for telomere maintenance. *Proceedings of the National Academy of Sciences of the United States of America*, 102(42), pp.15167-15172.
- Blisnick, T. et al., 2014. The intraflagellar transport dynein complex of trypanosomes is made of a heterodimer of dynein heavy chains and of light and intermediate chains of distinct functions. *Molecular Biology of the Cell*, 25(17), pp.2620-2633.
- Boothroyd, C.E. et al., 2009. A yeast-endonuclease-generated DNA break induces antigenic switching in *Trypanosoma brucei*. *Nature*, 459(7244), pp.278-281.
- Borner, G.H.H. et al., 2012. Multivariate proteomic profiling identifies novel accessory proteins of coated vesicles. *Journal of Cell Biology*, 197(1), pp.141-160.
- Borst, P. et al., 1996. Antigenic variation in trypanosomes. *Archives of Medical Research*, 27(3), pp.379-388.
- Boudeau, J. et al., 2006. Emerging roles of pseudokinases. *Trends in Cell Biology*, 16(9), pp.443-452.
- Bray, S., 2006. Notch signalling: a simple pathway becomes complex. *Molecular Cell Biology*, 7, pp.678-689.
- Brown, E.J. & Baltimore, D., 2000. ATR disruption leads to chromosomal fragmentation and early embryonic lethality. *Genes and Development*, 14(4), pp.397-402.

- Burri, C. & Brun, R., 2003. Eflornithine for the treatment of human African Trypanosomiasis. *Parasitology Research*, 90 (Supp 1), pp.S49-52.
- Burrows, A.E. & Elledge, S.J., 2008. How ATR turns on: TopBP1 goes on ATRIP with ATR. *Genes and Development*, 22(11), pp.1416-1421.
- Burton, P. et al., 2007. Ku heterodimer-independent end joining in *Trypanosoma brucei* cell extracts relies upon sequence microhomology. *Eukaryotic Cell*, 6(10), pp.1773-1781.
- Cahoon, L.A. & Seifert, H.S., 2009. An alternative DNA structure is necessary for pilin antigenic variation in *Neisseria gonorrhoeae*. *Science*, 325(5941), pp.764-767.
- Cai, Y. et al., 2003. Identification of new subunits of the multiprotein mammalian TRRAP/TIP60-containing histone acetyltransferase complex. *Journal of Biological Chemistry*, 278(44), pp.42733-42736.
- Caljon, G. et al., 2016. The dermis as a delivery site of *Trypanosoma brucei* for Tsetse flies. *PLoS Pathogens*, 12(7): e1005744.
- Callejas, S. et al., 2006. Hemizygous subtelomeres of an African Trypanosome chromosome may account for over 75% of chromosome length. *Genome Research*, 16(9), pp.1109-1118.
- Calonge, T.M. et al., 2010. Transformation/transcription domain-associated protein (TRRAP)-mediated regulation of wee1. *Genetics*, 185(1), pp.81-93.
- Capasso, H. et al., 2002. Phosphorylation activates Chk1 and is required for checkpoint-mediated cell cycle arrest. *Journal of Cell Science*, 115(23), p.4555 LP-4564.
- Capewell, P. et al., 2011. Differences between *Trypanosoma brucei gambiense* groups 1 and 2 in their resistance to killing by trypanolytic factor 1. *PLoS Neglected Tropical Diseases*, 5(9): e1287
- Capewell, P. et al., 2016. The skin is a significant but overlooked anatomical reservoir for vector-borne African trypanosomes. *eLife*, 5: e17716.
- Carmena, M. et al., 2012. The chromosomal passenger complex (CPC): from easy rider to the godfather of mitosis. *Nature Reviews Molecular Cell Biology*, 13(12), pp.789-803.
- Carmena, M. & Earnshaw, W.C., 2003. The cellular geography of aurora kinases. *Nature Reviews Molecular Cell Biology*, 4(11), pp.842-854.
- Carmena, M., Ruchaud, S. & Earnshaw, W.C., 2009. Making the Auroras glow: regulation of Aurora A and B kinase function by interacting proteins. *Current Opinion in Cell Biology*, 21(6), pp.796-805.

- Carpenter, A.E. & Sabatini, D.M., 2004. Systematic genome-wide screens of gene function. *Nature Reviews. Genetics*, 5(1), pp.11-22.
- Casas-Sánchez, A. & Acosta-Serrano, Á., 2016. Skin deep. *eLife*, 5, p.e21506.
- Castro, A. et al., 2002. The D-Box-activating domain (DAD) is a new proteolysis signal that stimulates the silent D-Box sequence of Aurora-A. *European Molecular Biology Organization Reports*, 3(12), pp.1209-1214.
- Cerqua, C. et al., 2010. Trichoplein/mitostatin regulates endoplasmic reticulum-mitochondria juxtaposition. *European Molecular Biology Organization Reports*, 11(11), pp.854-60.
- Cestari, I. & Stuart, K., 2015. Inositol phosphate pathway controls transcription of telomeric expression sites in trypanosomes. *Proceedings of the National Academy of Sciences of the United States of America*, 112(21), pp.E2803-12.
- Cha, R.S. & Kleckner, N., 2002. ATR homolog Mec1 promotes fork progression, thus averting breaks in replication slow zones. *Science*, 297(5581), pp.602-606.
- Chai, L.Y.A. et al., 2009. Fungal strategies for overcoming host innate immune response. *Medical Mycology*, 47(3), pp.227-236.
- Chan, C.S.M. & Botstein, D., 1993. Isolation and characterization of chromosome-gain and increase-in-ploidy mutants in yeast. *Genetics*, 135(3), pp.677-691.
- Chang, D.J. & Cimprich, K.A., 2009. DNA damage tolerance: when it's OK to make mistakes. *Nature Chemical Biology*, 5(2), pp.82-90.
- Chang, M. et al., 2002. A genome-wide screen for methyl methanesulfonate-sensitive mutants reveals genes required for S phase progression in the presence of DNA damage. *Proceedings of the National Academy of Sciences of the United States of America*, 99(26), pp.16934-16939.
- Chanoux, R.A. et al., 2009. ATR and H2AX cooperate in maintaining genome stability under replication stress. *Journal of Biological Chemistry*, 284(9), pp.5994-6003.
- Chaturvedi, P. et al., 1999. Mammalian Chk2 is a downstream effector of the ATM-dependent DNA damage checkpoint pathway. *Oncogene*, 18(28), pp.4047-4054.
- Chauhan, S.S. et al., 2003. Reduced endocytosis and altered lysosome function in cisplatin-resistant cell lines. *British Journal of Cancer*, 88(8), pp.1327-1334.
- Chaves, I. et al., 1999. Control of variant surface glycoprotein gene-expression

sites in *Trypanosoma brucei*. *The European Molecular Biology Organization Journal*, 18(17), pp.4846-4855.

- Chen, Z., Yang, H. & Pavletich, N.P., 2008. Mechanism of homologous recombination from the RecA-ssDNA/dsDNA structures. *Nature*, 453(7194), pp.489-494.
- Chhajer, R. et al., 2016. *Leishmania donovani* Aurora kinase: A promising therapeutic target against visceral leishmaniasis. *Biochimica et Biophysica Acta (BBA)*, 1860(9), pp.1973-1988.
- Chien, C.T. et al., 1998. Numb-associated kinase interacts with the phosphotyrosine binding domain of Numb and antagonizes the function of Numb *in vivo*. *Molecular and Cellular Biology*, 18(1), pp.598-607.
- Churikov, D. & Price, C.M., 2001. Telomeric and Subtelomeric Repeat Sequences. In: *Encyclopedia of Life Sciences (eLS)*. John Wiley & Sons, Ltd: Chichester.
- Ciccia, A. & Elledge, S.J., 2010. The DNA damage response: Making it safe to play with knives. *Molecular Cell*, 40(2), pp.179-204.
- Cimprich, K.A. et al., 1996. cDNA cloning and gene mapping of a candidate human cell cycle checkpoint protein. *Proceedings of the National Academy of Sciences of the United States of America*, 93(7), pp.2850-2855.
- Cimprich, K.A. & Cortez, D., 2008a. ATR: an essential regulator of genome integrity. *Nature reviews. Molecular Cell Biology*, 9(8), pp.616-27.
- Cimprich, K.A. & Cortez, D., 2008b. ATR: an essential regulator of genome integrity. *Nature Reviews. Molecular Cell Biology*, 9(8), pp.616-627.
- St. Clair, S. & Manfredi, J.J., 2006. The dual specificity phosphatase Cdc25C is a direct target for transcriptional repression by the tumor suppressor p53. *Cell Cycle*, 5(7), pp.709-713.
- Cliby, W.A. et al., 1998. Overexpression of a kinase-inactive ATR protein causes sensitivity to DNA-damaging agents and defects in cell cycle checkpoints. *The European Molecular Biology Organization Journal*, 17(1), pp.159-169.
- Cocucci, E., Gaudin, R. & Kirchhausen, T., 2014. Dynamin recruitment and membrane scission at the neck of a clathrin-coated pit. *Molecular Biology if the Cell*, 25(22), pp.3595-3609.
- Cohen-Armon, M., 2007. PARP-1 activation in the ERK signaling pathway. *Trends in Pharmacological Sciences*, 28(11), pp.556-560.
- Coley, A.F. et al., 2011. Glycolysis in the african trypanosome: targeting enzymes and their subcellular compartments for therapeutic development.

Molecular Biology International, 2011, p.123702.

- Collins, B.M. et al., 2002. Molecular architecture and functional model of the endocytic AP2 complex. *Cell*, 109(4), pp.523-535.
- Conner, S.D. & Schmid, S.L., 2003. Differential requirements for AP-2 in clathrin-mediated endocytosis. *Journal of Cell Biology*, 162(5), pp.773-779.
- Conway, C. et al., 2002. Ku is important for telomere maintenance, but not for differential expression of telomeric VSG genes, in African Trypanosomes. *Journal of Biological Chemistry*, 277(24), pp.21269-21277.
- Cordon-Obras, C. et al., 2013. *Trypanosoma brucei* gambiense adaptation to different mammalian sera is associated with VSG expression site plasticity. *PLoS ONE*, 8(12): e85072.
- Crane, R., Kloepfer, A. & Ruderman, J. V, 2004. Requirements for the destruction of human Aurora-A. *Journal of Cell Science*, 117(Pt 25), pp.5975-83.
- Cross, M., Taylor, M.C. & Borst, P., 1998. Frequent loss of the active site during variant surface glycoprotein expression site switching *in vitro* in *Trypanosoma brucei*. *Molecular and Cellular Biology*, 18(1), pp.198-205.
- Croteau, D.L. et al., 2014. Human RecQ helicases in DNA repair, recombination, and replication. *Annual Review of Biochemistry*, 83, pp.519-552.
- Culligan, K., Tissier, A. & Britt, A., 2004. ATR regulates a G2-phase cell-cycle checkpoint in *Arabidopsis thaliana*. *The Plant Cell*, 16(5), pp.1091-1104.
- D'Assoro, A.B., Haddad, T. & Galanis, E., 2015. Aurora-A kinase as a promising therapeutic target in cancer. *Frontiers in Oncology*, 5(January), p.295.
- Damasceno, J.D. et al., 2016. Functional compartmentalization of Rad9 and Hus1 reveals diverse assembly of the 9-1-1 complex components during the DNA damage response in *Leishmania*. *Molecular Microbiology*, 101(6), pp.1054-1068.
- Damasceno, J.D., Nunes, V.S. & Tosi, L.R.O., 2013. LmHus1 is required for the DNA damage response in *Leishmania major* and forms a complex with an unusual Rad9 homologue. *Molecular Microbiology*, 90(5), pp.1074-1087.
- Daniel, J.A. et al., 2012. Loss of ATM kinase activity leads to embryonic lethality in mice. *Journal of Cell Biology*, 198(3), pp.295-304.
- Daniels, J.P., Gull, K. & Wickstead, B., 2010. Cell Biology of the Trypanosome Genome. *Microbiology and Molecular Biology Reviews*, 74(4), pp.552-569.

- DaRocha, W.D. et al., 2004. Tests of cytoplasmic RNA interference (RNAi) and construction of a tetracycline-inducible T7 promoter system in *Trypanosoma cruzi*. *Molecular and Biochemical Parasitology*, 133(2), pp.175-186.
- David Barry, J. & McCulloch, R., 2001. Antigenic variation in trypanosomes: Enhanced phenotypic variation in a eukaryotic parasite. *Advances in Parasitology*, 49, pp. 1-70.
- Deitsch, K.W., Lukehart, S.A. & Stringer, J.R., 2009. Common strategies for antigenic variation by bacterial, fungal and protozoan pathogens. *Nature Reviews. Microbiology*, 7(7), pp.493-503.
- Delaval, B. et al., 2004. Aurora B -TACC1 protein complex in cytokinesis. *Oncogene*, 23(26), pp.4516-4522.
- Denchi, E.L. & de Lange, T., 2007. Protection of telomeres through independent control of ATM and ATR by TRF2 and POT1. *Nature*, 448(7157), pp.1068-1071.
- Denninger, V. et al., 2010. The FACT subunit TbSpt16 is involved in cell cycle specific control of VSG expression sites in *Trypanosoma brucei*. *Molecular Microbiology*, 78(2), pp.459-474.
- Denninger, V. & Rudenko, G., 2014. FACT plays a major role in histone dynamics affecting VSG expression site control in *Trypanosoma brucei*. *Molecular Microbiology*, 94(4), pp.945-962.
- Deshmukh, A.S. et al., 2015. Regulation of *Plasmodium falciparum* Origin Recognition Complex subunit 1 (PfORC1) function through phosphorylation mediated by CDK-like kinase PK5. *Molecular Microbiology*, 98(1), pp.17-33.
- Devaiah, B.N. et al., 2012. BRD4 is an atypical kinase that phosphorylates Serine2 of the RNA Polymerase II carboxy-terminal domain. *Proceedings of the National Academy of Sciences*, 109(18), pp.6927-6932.
- Devlin, R., 2015. *An investigation into the initiation of VSG switching in Trypanosoma brucei*. University of Glasgow. Available at: http://encore.lib.gla.ac.uk/iii/encore/record/C__Rb3142010.
- Devlin, R. et al., 2016. Mapping replication dynamics in *Trypanosoma brucei* reveals a link with telomere transcription and antigenic variation. *eLife*, 5, p.e12765.
- Dickey, J.S. et al., 2009. H2AX: Functional roles and potential applications. *Chromosoma*, 118(6), pp.683-692.
- Diehl, P., Tedesco, D. & Chenchik, A., 2014. Use of RNAi screens to uncover resistance mechanisms in cancer cells and identify synthetic lethal interactions. *Drug Discovery Today: Technologies*, 11(1), pp.11-18.

- Dieterich, K. et al., 2007. Homozygous mutation of AURKC yields large-headed polyploid spermatozoa and causes male infertility. *Nature Genetics*, 39(5), pp.661-665.
- Dixit, A. et al., 2010. PfSRPK1, a novel splicing-related kinase from *Plasmodium falciparum*. *Journal of Biological Chemistry*, 285(49), pp.38315-38323.
- Dixit, A. & Verkhivker, G.M., 2009. Hierarchical modeling of activation mechanisms in the ABL and EGFR kinase domains: Thermodynamic and mechanistic catalysts of kinase activation by cancer mutations R. *PLoS Computational Biology*, 5(8): e1000487.
- Dlugonska, H., 2008. Toxoplasma rhoptries: Unique secretory organelles and source of promising vaccine proteins for immunoprevention of Toxoplasmosis. *Journal of Biomedicine and Biotechnology*, 2008, p.632424.
- Dobson, R. et al., 2011. Interactions among *Trypanosoma brucei* RAD51 paralogues in DNA repair and antigenic variation. *Molecular Microbiology*, 81(2), pp.434-456.
- Doe, C.L. & Whitby, M.C., 2004. The involvement of Srs2 in post-replication repair and homologous recombination in fission yeast. *Nucleic Acids Research*, 32(4), pp.1480-1491.
- Doua, F. et al., 1996. The efficacy of Pentamidine in the treatment of early-late stage *Trypanosoma brucei gambiense* Trypanosomiasis. *The American Journal of Tropical Medicine and Hygiene*, 55(6), pp.586-588.
- Downward, J., 2003. Targeting RAS signalling pathways in cancer therapy. *Nature Review Cancer*, 3(1), pp.11-22.
- Dreesen, O., Li, B. & Cross, G.A.M., 2007. Telomere structure and function in trypanosomes: a proposal. *Nature Review Microbiology*, 5(1), pp.70-75.
- Dreesen, O., Li, B. & Cross, G.A.M., 2005. Telomere structure and shortening in telomerase-deficient *Trypanosoma brucei*. *Nucleic Acids Research*, 33(14), pp.4536-4543.
- DuBois, K.N. et al., 2012. NUP-1 is a large coiled-coil nucleoskeletal protein in trypanosomes with lamin-like functions. *PLoS Biology*, 10(3): e1001287.
- Duong-Ly, K.C. & Peterson, J.R., 2013. The human kinome and kinase inhibition. *Current Protocols in Pharmacology*, Chapter 2, p.Unit2.9: doi: [10.1002/0471141755.ph0209s60](https://doi.org/10.1002/0471141755.ph0209s60)
- Duursma, A.M. et al., 2013. A Role for the MRN Complex in ATR activation via TOPBP1 recruitment. *Molecular Cell*, 50(1), pp.116-122.
- Duursma, A.M. & Cimprich, K.A., 2010. Checkpoint recovery after DNA damage:

a rolling stop for CDKs. *European Molecular Biology Organization Reports*, 11(6), p.411 LP-412.

- Echeverri, C.J. & Perrimon, N., 2006. High-throughput RNAi screening in cultured cells: a user's guide. *Nature Review Genetics*, 7(5), pp.373-84.
- Eisenberg, E. & Greene, L.E., 2007. Multiple roles of auxilin and Hsc70 in clathrin-mediated endocytosis. *Traffic*, 8(6), pp.640-646.
- Elkin, S.R., Lakoduk, A.M. & Schmid, S.L., 2016. Endocytic pathways and endosomal trafficking: a primer. *Wiener Medizinische Wochenschrift*, pp.1-9.
- El-Sayed, N.M. et al., 2005. Comparative genomics of trypanosomatid parasitic protozoa. *Science*, 309(5733), pp.404-409.
- El-Sayed, N.M. et al., 2000. The African trypanosome genome. *International Journal for Parasitology*, 30(4), pp.329-345.
- Engstler, M. et al., 2007. Hydrodynamic flow-mediated protein sorting on the cell surface of Trypanosomes. *Cell*, 131(3), pp.505-515.
- Eswaran, J. et al., 2008. Structure of the human protein kinase MPSK1 reveals an atypical activation loop architecture. *Structure*, 16(1), pp.115-124.
- Ewald, B., Sampath, D. & Plunkett, W., 2008. ATM and the Mre11-Rad50-Nbs1 complex respond to nucleoside analogue-induced stalled replication forks and contribute to drug resistance. *Cancer Research*, 68(19), pp.7947-7955.
- Eykelenboom, J. et al., 2013. ATR activates the S-M checkpoint during unperturbed growth to ensure sufficient replication prior to mitotic onset. *Cell Reports*, 5(4), pp.1095-1107.
- Faini, M. et al., 2013. Vesicle coats: Structure, function, and general principles of assembly. *Trends in Cell Biology*, 23(6), pp.279-288.
- Falchook, G.S., Bastida, C.C. & Kurzrock, R., 2015. Aurora kinase inhibitors in oncology clinical trials: Current state of the progress. *Seminars in Oncology*, 42(6), pp.832-848.
- Farr, H. & Gull, K., 2012. Cytokinesis in trypanosomes. *Cytoskeleton*, 69(11), pp.931-941.
- Field, M.C. & Carrington, M., 2009. The trypanosome flagellar pocket. *Nature Reviews. Microbiology*, 7(11), pp.775-86.
- Figueiredo, L.M., Janzen, C.J. & Cross, G.A.M., 2008. A histone methyltransferase modulates antigenic variation in African Trypanosomes

PLoS Biology, 6(7): e161.

Fleckenstein, M.C. et al., 2012. A *Toxoplasma gondii* pseudokinase inhibits host irg resistance proteins. *PLoS Biology*, 10(7), p.14.

Florimond, C. et al., 2015. BILBO1 is a scaffold protein of the flagellar pocket collar in the pathogen *Trypanosoma brucei*. *PLoS Pathogens*, 11(3): e1004654.

Flott, S. et al., 2011. Regulation of Rad51 function by phosphorylation. *European Molecular Biology Organization Reports*, 12(8), pp.833-839.

Fokas, E. et al., 2014. Targeting ATR in DNA damage response and cancer therapeutics. *Cancer Treatment Reviews*, 40(1), pp.109-117.

Formichi, P. et al., 2000. Apoptotic response and cell cycle transition in ataxia telangiectasia cells exposed to oxidative stress. *Life Sciences*, 66(20), pp.1893-1903.

Forsythe, G.R., 2012. DNA damage and the *Trypanosoma brucei* cell cycle. *PhD Thesis, University of Glasgow*. Available at: http://encore.lib.gla.ac.uk/iii/encore/record/C_Rb2926197

Franco, J.R. et al., 2014. Epidemiology of human African trypanosomiasis. *Clinical Epidemiology*, 6(1), pp.257-275.

Frise, E. et al., 1996. The Drosophila Numb protein inhibits signaling of the Notch receptor during cell-cell interaction in sensory organ lineage. *Proceedings of the National Academy of Sciences of the United States of America*, 93(21), pp.11925-11932.

Fritz, M. et al., 2015. Novel insights into RNP granules by employing the trypanosome's microtubule skeleton as a molecular sieve. *Nucleic Acids Research*, 43(16), pp.8013-8032.

Fry, A.M. et al., 2012. Cell cycle regulation by the NEK family of protein kinases. *Journal of Cell Science*, 125, pp.4423-33.

Fu, J. et al., 2007. Roles of Aurora kinases in mitosis and tumorigenesis. *Molecular Cancer Research : MCR*, 5(1), pp.1-10.

Gale, M., Carter, V. & Parsons, M., 1994. Translational control mediates the developmental regulation of the *Trypanosoma brucei* Nrk protein-kinase. *Journal of Biological Chemistry*, 269, pp.31659-31665.

Gale, M. & Parsons, M., 1993. A *Trypanosoma brucei* gene family encoding protein kinases with catalytic domains structurally related to Nek1 and NIMA. *Molecular and Biochemical Parasitology*, 59, pp.111-121.

- Gatti, R.A. et al., 1988. Localization of an ataxia-telangiectasia gene to chromosome 11q22-23. *Nature*, 336(6199), pp.577-580.
- Genois, M.-M. et al., 2014. DNA repair pathways in trypanosomatids: from DNA repair to drug resistance. *Microbiology and Molecular Biology Reviews*, 78(1), pp.40-73.
- Gentili, C. et al., 2015. Chromosome missegregation associated with RUVBL1 deficiency. *PLoS ONE*, 10(7), pp.1-19.
- Giet, R. et al., 2002. Drosophila Aurora A kinase is required to localize D-TACC to centrosomes and to regulate astral microtubules. *Journal of Cell Biology*, 156(3), pp.437-451.
- Giet, R., Petretti, C. & Prigent, C., 2005. Aurora kinases, aneuploidy and cancer, a coincidence or a real link? *Trends in Cell Biology*, 15(5), pp.241-250.
- Ginger, M.L. et al., 2002. *Ex vivo* and *in vitro* identification of a consensus promoter for VSG genes expressed by Metacyclic-stage Trypanosomes in the Tsetse fly. *Eukaryotic Cell*, 1(6), pp.1000-1009.
- Glover, Lucy Horn, D., 2012. Trypanosomal histone γ H2A and the DNA damage response. *Molecular & Biochemical Parasitology*, 183(1), pp.78-83.
- Glover, L., Hutchinson, S., et al., 2013. Antigenic variation in African trypanosomes: The importance of chromosomal and nuclear context in VSG expression control. *Cellular Microbiology*, 15(12), pp.1984-1993.
- Glover, L. et al., 2015. Genome-scale RNAi screens for high-throughput phenotyping in bloodstream-form African trypanosomes. *Nature Protocols*, 10 pp. 106-133.
- Glover, L. et al., 2016. VEX1 controls the allelic exclusion required for antigenic variation in trypanosomes. *Proceedings of the National Academy of Sciences*, 113(26), p.7225-7230.
- Glover, L., Alsford, S. & Horn, D., 2013. DNA break site at fragile subtelomeres determines probability and mechanism of antigenic variation in African Trypanosomes. *PLoS Pathogens*, 9(3): e1003260.
- Glover, L. & Horn, D., 2014. Locus-specific control of DNA resection and suppression of subtelomeric VSG recombination by HAT3 in the African trypanosome. *Nucleic Acids Research*, 42(20), pp.12600-12613.
- Glover, L. & Horn, D., 2006. Repression of polymerase I-mediated gene expression at *Trypanosoma brucei* telomeres. *European Molecular Biology Organization Reports*, 7(1), pp.93-99.
- Glover, L., Jun, J. & Horn, D., 2011. Microhomology-mediated deletion and gene

- conversion in African trypanosomes. *Nucleic Acids Research*, 39(4), pp.1372-1380.
- Glover, L., McCulloch, R. & Horn, D., 2008. Sequence homology and microhomology dominate chromosomal double-strand break repair in African Trypanosomes. *Nucleic Acids Research*, 36(8), pp.2608-2618.
- Goldenson, B. & Crispino, J.D., 2015. The aurora kinases in cell cycle and leukemia. *Oncogene*, 34(5), pp.537-45.
- Gould, M.K. et al., 2013. Cyclic AMP effectors in African Trypanosomes revealed by genome-scale RNA interference library screening for resistance to the phosphodiesterase inhibitor CpdA. *Antimicrobial Agents and Chemotherapy*, 57(10), pp.4882-4893.
- Gourguechon, S. & Wang, C.C., 2009. CRK9 contributes to regulation of mitosis and cytokinesis in the procyclic form of *Trypanosoma brucei*. *BioMedCentral Cell Biology*, 10, p.68.
- Grant, S.K., 2009. Therapeutic protein kinase inhibitors. *Cellular and Molecular Life Sciences* 66(7), pp.1163-1177.
- Grazielle-Silva, V. et al., 2015. Distinct phenotypes caused by mutation of MSH2 in *Trypanosome* insect and mammalian life cycle forms are associated with parasite adaptation to oxidative stress. *PLoS Neglected Tropical Diseases*, 9(6): e0003870
- Gross, S. et al., 2015. Targeting cancer with kinase inhibitors. *Journal of Clinical Investigation*, 125(5), pp.1780-1789.
- Gruenberg, J., 2001. The endocytic pathway: a mosaic of domains. *Nature Reviews Molecular Cell Biology*, 2(10), pp.721-30.
- Grynberg, P. et al., 2012. *Trypanosoma cruzi* gene expression in response to gamma radiation. *PLoS ONE*, 7(1), pp.1-14.
- Gu, M. et al., 2008. μ 2 adaptin facilitates but is not essential for synaptic vesicle recycling in *Caenorhabditis elegans*. *Journal of Cell Biology*, 183(5), pp.881-892.
- Guleria, A. & Chandna, S., 2015. ATM kinase: Much more than a DNA damage responsive protein. *DNA Repair*. 39, pp. 1-20.
- Gully, C.P. et al., 2012. Aurora B kinase phosphorylates and instigates degradation of p53. *Proceedings of the National Academy of Sciences of the United States of America*, 109(24), pp.E1513-22.
- Günzl, A. et al., 2015. Mono-allelic VSG expression by RNA polymerase I in *Trypanosoma brucei*: expression site control from both ends? *Gene*, 556(1),

pp.68-73.

- Günzl, A. et al., 2003. RNA Polymerase I transcribes procyclin genes and variant surface glycoprotein gene expression sites in *Trypanosoma brucei*. *Eukaryotic Cell*, 2(3), pp.542-551.
- Guruharsha, K.G., Kankel, M.W. & Artavanis-Tsakonas, S., 2012. The Notch signalling system: recent insights into the complexity of a conserved pathway. *Nature reviews. Genetics*, 13(9), pp.654-66.
- Hall, B. et al., 2004. Both of the Rab5 subfamily small GTPases of *Trypanosoma brucei* are essential and required for endocytosis. *Molecular and Biochemical Parasitology*, 138(1), pp.67-77.
- Hall, J.P.J., 2012. *Mosaic VSGs in Trypanosoma brucei antigenic variation*. University of Glasgow. Available at: http://encore.lib.gla.ac.uk/iii/encore/record/C__Rb2958122.
- Hall, J.P.J., Wang, H. & Barry, J.D., 2013. Mosaic VSGs and the scale of *Trypanosoma brucei* antigenic variation. *PLoS Pathogens*, 9(7): e1003502.
- Hammarton, T.C., 2007. Cell cycle regulation in *Trypanosoma brucei*. *Molecular and Biochemical Parasitology*, 153(1), pp.1-8.
- Hammarton, T.C. et al., 2003. Stage-specific differences in cell cycle control in *Trypanosoma brucei* revealed by RNA interference of a mitotic cyclin. *Journal of Biological Chemistry*, 278(25), pp.22877-22886.
- Hammarton, T.C., Engstler, M. & Mottram, J.C., 2004. The *Trypanosoma brucei* cyclin, CYC2, is required for cell cycle progression through G1 phase and for maintenance of procyclic form cell morphology. *Journal of biological chemistry*, 279(23), pp.24757-64.
- Hanks, S.K. & Hunter, T., 1995. Protein kinases 6. The eukaryotic protein kinase superfamily: kinase (catalytic) domain structure and classification. *Federation of American Societies for Experimental Biology Journal*, 9(8), pp.576-596.
- Hargreaves, I.P., 2014. Coenzyme Q10 as a therapy for mitochondrial disease. *International Journal of Biochemistry and Cell Biology*, 49(1), pp.105-111.
- Hartley, C.L. & McCulloch, R., 2008. *Trypanosoma brucei* BRCA2 acts in antigenic variation and has undergone a recent expansion in BRC repeat number that is important during homologous recombination. *Molecular Microbiology*, 68(5), pp.1237-1251.
- Henne, W.M., Buchkovich, N.J. & Emr, S.D., 2011. The ESCRT pathway. *Developmental Cell*, 21(1), pp.77-91.

- Herr, P. et al., 2015. A genome-wide IR-induced RAD51 foci RNAi screen identifies CDC73 involved in chromatin remodeling for DNA repair. *Cell Discovery*, 1, p.15034.
- Hertz-Fowler, C. et al., 2008. Telomeric expression sites are highly conserved in *Trypanosoma brucei*. *PLoS ONE*, 3(10): e3527.
- Higgins, M.K. et al., 2013. Structure of the trypanosome haptoglobin-hemoglobin receptor and implications for nutrient uptake and innate immunity. *Proceedings of the National Academy of Sciences of the United States of America*, 110(5), pp.1905-1910.
- Hirumi, H. & Hirumi, K., 1989. Continuous cultivation of *Trypanosoma brucei* blood stream forms in a medium containing a low concentration of serum protein without feeder cell layers. *The Journal of Parasitology*, 75(6), pp.985-989.
- Hoar, K. et al., 2007. MLN8054, a small-molecule inhibitor of Aurora A, causes spindle pole and chromosome congression defects leading to aneuploidy. *Molecular and Cellular Biology*, 27(12), pp.4513-4525.
- Horn, D. & McCulloch, R., 2010. Molecular mechanisms underlying the control of antigenic variation in African Trypanosomes. *Current Opinion in Microbiology*, 13(6), pp.700-705.
- Hornef, M.W. et al., 2002. Bacterial strategies for overcoming host innate and adaptive immune responses. *Nature Immunology*, 3(11), pp.1033-1040.
- Hovel-Miner, G. et al., 2016. A conserved DNA repeat promotes selection of a diverse repertoire of *Trypanosoma brucei* surface antigens from the genomic archive. *PLoS genetics*, 12(5): e1005994
- Hsu, P.P. et al., 2011. The mTOR-regulated phosphoproteome reveals a mechanism of mTORC1-mediated inhibition of growth factor signaling. *Science*, 332(6035), pp.1317-1322.
- Hua, S.B. & Wang, C.C., 1994. Differential accumulation of a protein kinase homolog in *Trypanosoma brucei*. *Journal of Cellular Biochemistry*, 54(1), pp.20-31.
- Hua, S.B. & Wang, C.C., 1997. Interferon-gamma activation of a mitogen-activated protein kinase, KFR1, in the bloodstream form of *Trypanosoma brucei*. *Journal of Biological Chemistry*, 272(16), pp.10797-10803.
- Huck, J.J. et al., 2010. MLN8054, an inhibitor of Aurora A kinase, induces senescence in human tumor cells both *in vitro* and *in vivo*. *Molecular Cancer Research*, 8(3), pp.373-384.
- Hurley, P.J., Wilsker, D. & Bunz, F., 2007. Human cancer cells require ATR for

- cell cycle progression following exposure to ionizing radiation. *Oncogene*, 26(18), pp.2535-2542.
- Imhof, S. et al., 2014. Social motility of African Trypanosomes is a property of a distinct life-cycle stage that occurs early in Tsetse fly transmission. *PLoS Pathogens*, 10(10), pp.1-10.
- In, J.G. et al., 2014. Serine/threonine kinase 16 and MAL2 regulate constitutive secretion of soluble cargo in hepatic cells. *Biochemical Journal*, 463(2), pp.201-213.
- Inoue, N. et al., 2002. Tetracycline-regulated RNA interference in *Trypanosoma congolense*. *Molecular and Biochemical Parasitology*, 120(2), pp.309-313.
- Ito, K. et al., 2007. Regulation of reactive oxygen species by Atm is essential for proper response to DNA double-strand breaks in lymphocytes. *Journal of Immunology*, 178(1), pp.103-110.
- Jackson, A.P. et al., 2003. Clathrin promotes incorporation of cargo into coated pits by activation of the AP2 adaptor μ 2 kinase. *Journal of Cell Biology*, 163(2), pp.231-236.
- Jackson, L.P. et al., 2010. A large-scale conformational change couples membrane recruitment to cargo binding in the AP2 clathrin adaptor complex. *Cell*, 141(7), pp.1220-1229.
- Jamonneau, V. et al. 2005, Mixed infections of trypanosomes in tsetse and pigs and their epidemiological significance in a sleeping sickness focus of Côte d'Ivoire. *Parasitology*, 129(6), pp.693-702.
- Janssens, P.G. & De Muynck, A., 1977. Clinical trials with "nifurtimox" in African trypanosomiasis. *Annales de la Societe Belge de Medecine Tropicale*, 57(4-5), pp.475-480.
- Janzen, C.J. et al., 2004. Telomere length regulation and transcriptional silencing in KU80-deficient *Trypanosoma brucei*. *Nucleic Acids Research*, 32(22), pp.6575-6584.
- Jehi, S.E. et al., 2014. Suppression of subtelomeric VSG switching by *Trypanosoma brucei* TRF requires its TTAGGG repeat-binding activity. *Nucleic Acids Research*, 42(20), pp.12899-12911.
- Jehi, S.E., Nanavaty, V. & Li, B., 2016. *Trypanosoma brucei* TIF2 and TRF suppress VSG switching using overlapping and independent mechanisms. *PLoS ONE*, 11(6): e0156746.
- Jehi, S.E., Wu, F. & Li, B., 2014. *Trypanosoma brucei* TIF2 suppresses VSG switching by maintaining subtelomere integrity. *Cell Research*, 24(7), pp.870-885.

- Jennings, F.W. et al., 1983. Treatment with suramin and 2-substituted 5-nitroimidazoles of chronic murine *Trypanosoma brucei* infections with central nervous system involvement. *Transactions of the Royal Society of Tropical Medicine and Hygiene*, 77(5), pp.693-698.
- Jensen, R.E. & Englund, P.T., 2012. Network news: The replication of Kinetoplast DNA. *Annual Review of Microbiology*, 66(1), pp.473-491.
- Jones, N.G. et al., 2014. Regulators of *Trypanosoma brucei* cell cycle progression and differentiation identified using a kinome-wide RNAi screen. *PLoS Pathogens*, 10(1): e1003886
- Kakarougkas, A. & Jeggo, P.A., 2014. DNA DSB repair pathway choice: an orchestrated handover mechanism. *The British Journal of Radiology*, 87(1035), p.20130685.
- Källberg, M. et al., 2012. Template-based protein structure modeling using the RaptorX web server. *Nature Protocols*, 7(8), pp.1511-22.
- Kannan, N. et al., 2007. Structural and functional diversity of the microbial kinome. *PLoS Biology*, 5(3), p.e17.
- Karnitz, L.M. & Zou, L., 2015. Molecular pathways: Targeting ATR in cancer therapy. *Clinical cancer research*, 21(21), pp.4780-4785.
- Kassem, A., Pays, E. & Vanhamme, L., 2014. Transcription is initiated on silent variant surface glycoprotein expression sites despite monoallelic expression in *Trypanosoma brucei*. *Proceedings of the National Academy of Sciences of the United States of America*, 111(24), pp.8943-8948.
- Katayama, H. et al., 2012. Aurora Kinase-A inactivates DNA damage-induced apoptosis and spindle assembly checkpoint response functions of p73. *Cancer Cell*, 21(2), pp.196-211.
- Katsha, A. et al., 2015. Aurora kinase A in gastrointestinal cancers: time to target. *Molecular Cancer*, 14, p.106.
- Kavanaugh, G. et al., 2015. A whole genome RNAi screen identifies replication stress response genes. *DNA Repair*, 35, pp.55-62.
- Kawasumi, M. et al., 2011. Protection from UV-induced skin carcinogenesis by genetic inhibition of the ataxia telangiectasia and Rad3-related (ATR) kinase. *Proceedings of the National Academy of Sciences of the United States of America*, 108(33), pp.13716-13721.
- Kaye, P. & Scott, P., 2011. Leishmaniasis: complexity at the host-pathogen interface. *Nature Review Microbiology*, 9(8), pp.604-615.
- Kelly, S. et al., 2007. Functional genomics in *Trypanosoma brucei*: A collection

of vectors for the expression of tagged proteins from endogenous and ectopic gene loci. *Molecular and Biochemical Parasitology*, 154(1-4), pp.103-109.

- Kennedy, P.G.E., 2013. Clinical features, diagnosis, and treatment of human African trypanosomiasis (sleeping sickness). *The Lancet Neurology*, 12(2), pp.186-194.
- Kidiyoor, G.R., Kumar, A. & Foiani, M., 2016. ATR-mediated regulation of nuclear and cellular plasticity. *DNA Repair*, 44, pp.143-150.
- Kim, H.-S. & Cross, G.A.M., 2011. Identification of *Trypanosoma brucei* RMI1/BLAP75 homologue and its roles in antigenic variation. *PLoS ONE*, 6(9): e25313.
- Kim, S., Mohapatra, G. & Haber, D.A., 2008. *In vitro* phosphorylation of BRCA2 by the checkpoint kinase CHEK2. *British Journal of Cancer*, 99(8), pp.1302-1306.
- Kimmins, S. et al., 2007. Differential functions of the Aurora-B and Aurora-C kinases in mammalian spermatogenesis. *Molecular Endocrinology*, 21(3), pp.726-739.
- King, R.W., 2008. When $2 + 2 = 5$: The origins and fates of aneuploid and tetraploid cells. *Biochimica et Biophysica Acta - Reviews on Cancer*, 1786(1), pp.4-14.
- Knighton, D.R. et al., 1991. Crystal structure of the catalytic subunit of cyclic adenosine monophosphate-dependent protein kinase. *Science*, 253(5018), pp.407-414.
- Kolev, N.G., Tschudi, C. & Ullu, E., 2011. RNA interference in protozoan parasites: Achievements and challenges. *Eukaryotic Cell*, 10(9), pp.1156-1163.
- Kondo, N. et al., 2010. DNA damage induced by alkylating agents and repair pathways. *Journal of Nucleic Acids*, 2010, pp.1-7.
- Korolchuk, V.I. & Banting, G., 2002. CK2 and GAK/auxilin2 are major protein kinases in clathrin-coated vesicles. *Traffic*, 3(6), pp.428-39.
- Kotov, I.N. et al., 2014. Whole genome RNAi screens reveal a critical role of REV3 in coping with replication stress. *Molecular Oncology*, 8(8), pp.1747-1759.
- Krejci, L. et al., 2012. Homologous recombination and its regulation. *Nucleic Acids Research*, 40(13), pp.5795-5818.
- Kremer, J.R., Mastronarde, D.N. & McIntosh, J.R., 1996. Computer visualization

- of three-dimensional image data using IMOD. *Journal of Structural Biology*, 116(1), pp.71-76.
- Krishna, S.S., Majumdar, I. & Grishin, N. V, 2003. Structural classification of zinc fingers: Survey and summary. *Nucleic Acids Research* , 31(2), pp.532-550.
- Krystyniak, A. et al., 2006. Inhibition of Aurora A in response to DNA damage. *Oncogene*, 25(3), pp.338-48.
- Kumar, A. et al., 2014. ATR mediates a checkpoint at the nuclear envelope in response to mechanical stress. *Cell*, 158(3), pp.633-646.
- Kuo, L.J. & Yang, L.-X., 2008. Gamma-H2AX - a novel biomarker for DNA double-strand breaks. *In vivo*, 22(3), pp.305-9.
- Kurose, A. et al., 2006. Effects of hydroxyurea and aphidicolin on phosphorylation of ataxia telangiectasia mutated on Ser 1981 and histone H2AX on Ser 139 in relation to cell cycle phase and induction of apoptosis. *The Journal of the International Society for Analytical Cytology*, 69(4), pp.212-221.
- Laffitte, M.-C.N. et al., 2016. Chromosomal translocations in the parasite *Leishmania* by a MRE11/RAD50-independent microhomology-mediated end joining mechanism. *PLoS Genetics*, 12(6): e1006117.
- Lahiry, P. et al., 2010. Kinase mutations in human disease: interpreting genotype-phenotype relationships. *Nature Review Genetics*, 11(1), pp.60-74.
- Lampson, M.A. & Cheeseman, I.M., 2011. Sensing centromere tension: Aurora B and the regulation of kinetochore function. *Trends in Cell Biology*, 21(3), pp.133-140.
- Landeira, D. et al., 2009. Cohesin regulates VSG monoallelic expression in trypanosomes. *The Journal of Cell Biology*, 186(2), pp.243-254.
- De Lange, T. et al., 1983. Telomere conversion in trypanosomes. *Nucleic Acids Research*, 11(23), pp.8149-8165.
- Langousis, G. & Hill, K.L., 2014. Motility and more: the flagellum of *Trypanosoma brucei*. *Nature Review Microbiology*, 12(7), pp.505-518.
- Larsen, D.H. & Stucki, M., 2015. Nucleolar responses to DNA double-strand breaks. *Nucleic Acids Research*, 44(2), pp.538-44.
- Larsen, D.H. & Stucki, M., 2016. Nucleolar responses to DNA double-strand breaks. *Nucleic Acids Research*, 44(2), pp.538-544.

- Lee, D. et al., 2005. Depletion of GAK/auxilin 2 inhibits receptor-mediated endocytosis and recruitment of both clathrin and clathrin adaptors. *Journal of Cell Science*, 118, pp.4311-4321.
- Lempiäinen, H. & Halazonetis, T.D., 2009. Emerging common themes in regulation of PIKKs and PI3Ks. *The European Molecular Biology Organization Journal*, 28(20), pp.3067-73.
- Leontovich, A.A. et al., 2013. Inhibition of Cdk2 activity decreases Aurora-A kinase centrosomal localization and prevents centrosome amplification in breast cancer cells. *Oncology Reports*, 29(5), pp.1785-1788.
- Levenson, J.D. et al., 2002. The Schizosaccharomyces pombe Aurora-related Kinase Ark1 Interacts with the Inner Centromere Protein Pic1 and Mediates Chromosome Segregation and Cytokinesis. *Molecular Biology of the Cell*, 13(4), pp.1132-1143.
- Li, H. et al., 2008. Dictyostelium Aurora kinase has properties of both Aurora A and Aurora B kinases. *Eukaryotic Cell*, 7(5), pp.894-905.
- Li, W. et al., 2013. The annotation-enriched non-redundant patent sequence databases. *Database*, 2013, pp.1-6.
- Li, Z., Lee, J.H., et al., 2008. Identification of a novel chromosomal passenger complex and its unique localization during cytokinesis in *Trypanosoma brucei*. *PLoS ONE*, 3(6): e2354
- Li, Z., Gourguechon, S. & Wang, C.C., 2007. Tousled-like kinase in a microbial eukaryote regulates spindle assembly and S-phase progression by interacting with Aurora kinase and chromatin assembly factors. *Journal of Cell Science*, 120(Pt 21), pp.3883-3894.
- Li, Z., Umeyama, T. & Wang, C.C., 2009. The Aurora kinase in *Trypanosoma brucei* plays distinctive roles in metaphase-anaphase transition and cytokinetic initiation. *PLoS Pathogens*, 5(9): e1000575
- Li, Z., Umeyama, T. & Wang, C.C., 2008. The chromosomal passenger complex and a mitotic kinesin interact with the tousled-like kinase in Trypanosomes to regulate mitosis and cytokines. *PLoS ONE*, 3(11): e3814
- Li, Z. & Wang, C.C., 2006. Changing roles of aurora-B kinase in two life cycle stages of *Trypanosoma brucei*. *Eukaryotic Cell*, 5(7), pp.1026-1035.
- Lila Koumandou, V. et al., 2013. Evidence for recycling of invariant surface transmembrane domain proteins in African Trypanosomes. *Eukaryotic Cell*, 12(2), pp.330-342.
- Lim, D.C. et al., 2012. *Toxoplasma* and *Plasmodium* protein kinases: Roles in invasion and host cell remodelling. *International Journal for Parasitology*,

42(1), pp.21-32.

- Lindon, C., Grant, R. & Min, M., 2016. Ubiquitin-mediated degradation of Aurora kinases. *Frontiers in Oncology*, 5, p.307.
- Lindqvist, A., Rodríguez-Bravo, V. & Medema, R.H., 2009. The decision to enter mitosis: feedback and redundancy in the mitotic entry network. *Journal of Cell Biology*, 185(2), pp.193-202.
- Liu, L. et al., 2012. Comparison of next-generation sequencing systems. *Journal of Biomedicine and Biotechnology*, 2012, p.251364.
- Liu, Q. et al., 2000. Chk1 is an essential kinase that is regulated by Atr and required for the G2/M DNA damage checkpoint. *Genes and Development*, 14(12), pp.1448-1459.
- Liu, S. et al., 2011. ATR Autophosphorylation as a molecular switch for checkpoint activation. *Molecular Cell*, 43(2), pp.192-202.
- Lobrich, M. & Jeggo, P.A., 2007. The impact of a negligent G2/M checkpoint on genomic instability and cancer induction. *Nature Reviews. Cancer*, 7(11), pp.861-869.
- Lombraña, R. et al., 2016. Transcriptionally driven DNA replication program of the human parasite *Leishmania major*. *Cell Reports*, 16(6), pp.1774-1786.
- Lopez-Farfan, D. et al., 2014. SUMOylation by the E3 ligase TbSIZ1/PIAS1 positively regulates VSG expression in *Trypanosoma brucei*. *PLoS Pathogens*, 10(12): e1004545.
- Lu, L.-Y. et al., 2008. Aurora A is essential for early embryonic development and tumor suppression. *Journal of Biological Chemistry*, 283(46), pp.31785-90.
- Luan, S., 2009. The CBL-CIPK network in plant calcium signaling. *Trends in Plant Science*, 14(1), pp.37-42.
- Lukeš, J. et al., 2014. Evolution of parasitism in kinetoplastid flagellates. *Molecular and Biochemical Parasitology*, 195(2), pp.115-122.
- Lustig, A.J. & Petes, T.D., 1986. Identification of yeast mutants with altered telomere structure. *Proceedings of the National Academy of Sciences of the United States of America*, 83(5), pp.1398-1402.
- Lye, L.-F. et al., 2010. Retention and loss of RNA interference pathways in trypanosomatid protozoans. *PLoS Pathogens*, 6(10): e1001161.
- MacGregor, P. et al., 2012. Trypanosomal immune evasion, chronicity and transmission: an elegant balancing act. *Nature Reviews. Microbiology*,

10(6), pp.431-438.

- Machado, C.R. et al., 2014. Nucleotide excision repair in *Trypanosoma brucei*: Specialization of transcription-coupled repair due to multigenic transcription. *Molecular Microbiology*, 92(4), pp.756-776.
- Mackay, D.R. & Ullman, K.S., 2015. ATR and a Chk1-Aurora B pathway coordinate postmitotic genome surveillance with cytokinetic abscission. *Molecular Biology of the Cell*, 26(12), pp.2217-2226.
- Mackey, Z.B. et al., 2011. High-throughput analysis of an RNAi library identifies novel kinase targets in *Trypanosoma brucei*. *Chemical Biology & Drug Design*, 78(3), pp.454-463.
- Magalska, A. et al., 2016. RuvB-like ATPases function in chromatin decondensation at the end of mitosis. *Developmental Cell*, 31(3), pp.305-318.
- Mah, L.-J., El-Osta, A., & Karagiannis, T.C., 2010. gammaH2AX: a sensitive molecular marker of DNA damage and repair. *Leukemia*, 24(4), pp.679-686.
- Maishman, L. et al., 2016. Co-dependence between trypanosome nuclear lamina components in nuclear stability and control of gene expression. *Nucleic Acids Research*, 44(22), pp. 10554-10570.
- Maity, A.K., Goswami, A. & Saha, P., 2011. Identification of substrates of an S-phase cell cycle kinase from *Leishmania donovani*. *The Federation of European Biochemical Societies Letters*, 585(17), pp.2635-2639.
- Manna, P.T., Kelly, S. & Field, M.C., 2013. Adaptin evolution in kinetoplastids and emergence of the variant surface glycoprotein coat in African Trypanosomatids. *Molecular Phylogenetics and Evolution*, 67(1), pp.123-128.
- Manning, G. et al., 2011. The minimal kinome of *Giardia lamblia* illuminates early kinase evolution and unique parasite biology. *Genome Biology*, 12(7), p.R66.
- Manning, G. et al., 2002. The protein kinase complement of the human genome. *Science*, 298(5600), p.1912 LP-1934.
- Marcello, L. & Barry, J.D., 2007. Analysis of the VSG gene silent archive in *Trypanosoma brucei* reveals that mosaic gene expression is prominent in antigenic variation and is favoured by archive substructure. *Genome Research*, 17(9), pp.1344-1352.
- Marechal, A. & Zou, L., 2013. DNA damage sensing by the ATM and ATR kinases. *Cold Spring Harbor Perspectives in Biology*, 5(9): 5:a012716

- Maresca, T.J. & Salmon, E.D., 2009. Intrakinetochore stretch is associated with changes in kinetochore phosphorylation and spindle assembly checkpoint activity. *Journal of Cell Biology*, 184(3), pp.373-381.
- Marques, C.A. et al., 2016. Diverged composition and regulation of the *Trypanosoma brucei* origin recognition complex that mediates DNA replication initiation. *Nucleic Acids Research*, 44(10), pp.4763-4784.
- Marques, C.A. et al., 2015. Genome-wide mapping reveals single-origin chromosome replication in *Leishmania*, a eukaryotic microbe. *Genome Biology*, 16(1), pp.1-12.
- Marumoto, T. et al., 2003. Aurora-A kinase maintains the fidelity of early and late mitotic events in HeLa cells. *Journal of Biological Chemistry*, 278(51), pp.51786-51795.
- Masai, H. et al., 2010. Eukaryotic chromosome DNA replication: where, when, and how? *Annual Review of Biochemistry*, 79, pp.89-130.
- Matheson, C.J., Backos, D.S. & Reigan, P., 2016. Targeting WEE1 kinase in cancer. *Trends in Pharmacological Sciences*, 37(10), pp.1-10.
- Matthews, K.R., 2005. The developmental cell biology of *Trypanosoma brucei*. *Journal of Cell Science*, 118(Pt 2), pp.283-290.
- Mazouzi, A., Velimezi, G. & Loizou, J.I., 2014. DNA replication stress: Causes, resolution and disease. *Experimental Cell Research*, 329(1), pp.85-93.
- McCulloch, R. & Barry, J.D., 1999. A role for RAD51 and homologous recombination in *Trypanosoma brucei* antigenic variation. *Genes and Development*, 13(21), pp.2875-2888.
- McCulloch, R. & Field, M.C., 2015. Quantitative sequencing confirms VSG diversity as central to immune evasion by *Trypanosoma brucei*. *Trends in Parasitology*, 31(8), pp.346-349.
- McCulloch, R., Morrison, L.J. & Hall, J.P.J., 2015. DNA recombination strategies during antigenic variation in the African Trypanosome. *Microbiology Spectrum*, 3(2): MDNA3-0016-2014.
- McCulloch, R., Rudenko, G. & Borst, P., 1997. Gene conversions mediating antigenic variation in *Trypanosoma brucei* can occur in variant surface glycoprotein expression sites lacking 70-base-pair repeat sequences. *Molecular and Cellular Biology*, 17(2), pp.833-843.
- McKean, P.G., 2003. Coordination of cell cycle and cytokinesis in *Trypanosoma brucei*. *Current Opinion in Microbiology*, 6(6), pp.600-607.
- McMahon, S.B. et al., 1998. The novel ATM-related protein TRRAP is an essential

- cofactor for the c-Myc and E2F oncoproteins. *Cell*, 94(3), pp.363-374.
- McNees, C.J. et al., 2010. ATR suppresses telomere fragility and recombination but is dispensable for elongation of short telomeres by telomerase. *Journal of Cell Biology*, 188(5), pp.639-652.
- Medeiros, L.C.S. et al., 2012. Visualizing the 3D architecture of multiple erythrocytes infected with *plasmodium* at nanoscale by focused ion beam-scanning electron microscopy. *PLoS ONE*, 7(3): e33445
- Melero, R. et al., 2014. Structures of SMG1-UPFs complexes: SMG1 contributes to regulate UPF2-dependent activation of UPF1 in NMD. *Structure*, 22(8), pp.1105-1119.
- Melo, M.B., Jensen, K.D.C. & Saeij, J.P.J., 2011. *Toxoplasma gondii* effectors are master regulators of the inflammatory response. *Trends in Parasitology*, 27(11), pp.487-495.
- Michaeli, S., 2011. Trans-splicing in trypanosomes: machinery and its impact on the parasite transcriptome. *Future Microbiology*, 6(4), pp.459-474.
- Miyashita, T. & Reed, J.C., 1995. Tumor suppressor p53 is a direct transcriptional activator of the human bax gene. *Cell*, 80(2), pp.293-299.
- Moniz, L. et al., 2011. Nek family of kinases in cell cycle, checkpoint control and cancer. *Cell Division*, 6(1), p.18.
- Mony, B.M. et al., 2014. Genome-wide dissection of the quorum sensing signalling pathway in *Trypanosoma brucei*. *Nature*, 505(7485), pp.681-5.
- Mora-Bermúdez, F., Gerlich, D. & Ellenberg, J., 2007. Maximal chromosome compaction occurs by axial shortening in anaphase and depends on Aurora kinase. *Nature Cell Biology*, 9(7), pp.822-831.
- Mordes, D.A. et al., 2008. TopBP1 activates ATR through ATRIP and a PIKK regulatory domain. *Genes and Development*, 22(11), pp.1478-1489.
- Moretti, L Niermann, K Schleicher, S Giacalone, NJ Varki, V Kim, KW Kopsombut, P Jung, DK Lu, B., 2011. MLN8054, a small molecule inhibitor of aurora kinase a, sensitizes androgen-resistant prostate cancer to radiation. *International Journal of Radiation Oncology Biology Physics*, 80(4), pp.1189-1197.
- Morgan, J.R. et al., 2000. A conserved clathrin assembly motif essential for synaptic vesicle endocytosis. *The Journal of Neuroscience*, 20(23), pp.8667-8676.
- Morgan-Lappe, S. et al., 2006. RNAi-based screening of the human kinome identifies Akt-cooperating kinases: a new approach to designing efficacious

- multitargeted kinase inhibitors. *Oncogene*, 25(9), pp.1340-1348.
- Morris, J.C. et al., 2002. Glycolysis modulates trypanosome glycoprotein expression as revealed by an RNAi library. *The European Molecular Biology Organization Journal*, 21(17), pp.4429-4438.
- Morris, J.C. et al., 2001. Replication of kinetoplast DNA: an update for the new millennium. *International Journal for Parasitology*, 31(5-6), pp.453-458.
- Morrison, L.J., Marcello, L. & McCulloch, R., 2009. Antigenic variation in the African Trypanosome: molecular mechanisms and phenotypic complexity. *Cellular Microbiology*, 11(12), pp.1724-1734.
- Morrow, D.M. et al., 1995. TEL1, an *S. cerevisiae* homolog of the human gene mutated in ataxia telangiectasia, is functionally related to the yeast checkpoint gene MEC1. *Cell*, 82(5), pp.831-840.
- Mortusewicz, O., Herr, P. & Helleday, T., 2013. Early replication fragile sites: where replication-;transcription collisions cause genetic instability. *The European Molecular Biology Organization Journal*, 32(4), pp.493-495.
- Moser, B.A. et al., 2009. Fission yeast Tel1ATM and Rad3ATR promote telomere protection and telomerase recruitment. *PLoS Genetics*, 5(8), pp.1-11.
- Moser, B.A. & Nakamura, T.M., 2009. Protection and replication of telomeres in fission yeast. *Biochemistry and Cell Biology* 87(5), pp.747-758.
- Mountzios, G., Terpos, E. & Dimopoulos, M.A., 2008. Aurora kinases as targets for cancer therapy. *Cancer Treatment Reviews*, 34(2), pp.175-182.
- Mugnier, M.R., Cross, G.A.M. & Papavasiliou, F.N., 2015. The *in vivo* dynamics of antigenic variation in *Trypanosoma brucei*. *Science*, 347(6229), p.1470 LP-1473.
- Mugnier, M.R., Stebbins, C.E. & Papavasiliou, F.N., 2016. Masters of disguise: antigenic variation and the VSG coat in *Trypanosoma brucei*. *PLoS Pathogens*, 12(9): e1005784.
- Muhich, M.L. & Boothroyd, J.C., 1988. Polycistronic transcripts in trypanosomes and their accumulation during heat shock: evidence for a precursor role in mRNA synthesis. *Molecular and Cellular Biology*, 8(9), pp.3837-46.
- Murga, M. et al., 2009. A mouse model of ATR-Seckel shows embryonic replicative stress and accelerated aging. *Nature Genetics*, 41(8), pp.891-898.
- Nagaoka-Yasuda, R. et al., 2007. An RNAi-based genetic screen for oxidative stress resistance reveals retinol saturase as a mediator of stress resistance. *Free Radical Biology and Medicine*, 43(5), pp.781-788.

- Nam, E.A. & Cortez, D., 2011. ATR signalling: more than meeting at the fork. *The Biochemical Journal*, 436(3), pp.527-36.
- Narayanan, M.S. & Rudenko, G., 2013. TDP1 is an HMG chromatin protein facilitating RNA polymerase I transcription in African trypanosomes. *Nucleic Acids Research*, 41(5), pp.2981-2992.
- Navarro, M. & Gull, K., 2001. A pol I transcriptional body associated with VSG mono-allelic expression in *Trypanosoma brucei*. *Nature*, 414(6865), pp.759-763.
- Neveu, G. et al., 2015. AP-2-associated protein kinase 1 and cyclin G-associated kinase regulate hepatitis C virus entry and are potential drug targets. *Journal of Virology*, 89(8), pp.4387-404.
- Ngô, H. et al., 1998. Double-stranded RNA induces mRNA degradation in *Trypanosoma brucei*. *Proceedings of the National Academy of Sciences of the United States of America*, 95(25), pp.14687-14692.
- Nguyen, T.N. et al., 2014. Promoter occupancy of the basal class I transcription factor A differs strongly between active and silent VSG expression sites in *Trypanosoma brucei*. *Nucleic Acids Research*, 42(5), pp.3164-3176.
- Niu, H. et al., 2009. Regulation of meiotic recombination via Mek1-mediated Rad54 phosphorylation. *Molecular Cell*, 36(3), pp.393-404.
- Nogueira, A., Catarino, R. & Medeiros, R., 2011. DNA damage repair and cancer : The role of RAD51 protein and its genetic variants. *DNA Repair and Human Health*, Chapter 3, pp. 73-92.
- Nolan, D.P., Geuskens, M. & Pays, E., 1999. N-linked glycans containing linear poly-N-acetyllactosamine as sorting signals in endocytosis in *Trypanosoma brucei*. *Current Biology*, 9(20), pp.1169-1172.
- O'Driscoll, M. et al., 2003. A splicing mutation affecting expression of ataxia-telangiectasia and Rad3-related protein (ATR) results in Seckel syndrome. *Nature Genetics*, 33(4), pp.497-501.
- O'Driscoll, M. et al., 2004. An overview of three new disorders associated with genetic instability: LIG4 syndrome, RS-SCID and ATR-Seckel syndrome. *DNA Repair*, 3(8-9), pp.1227-1235.
- O'Driscoll, M. & Jeggo, P.A., 2003. Clinical impact of ATR checkpoint signalling failure in humans. *Cell Cycle*, 2(3), pp.194-195.
- O'Hara, A.M. & Shanahan, F., 2006. The gut flora as a forgotten organ. *European Molecular Biology Organization Reports*, 7(7), pp.688-693.
- Ochiana, S.O. et al., 2013. The human Aurora kinase inhibitor danusertib is a

lead compound for anti-trypanosomal drug discovery via target repurposing. *European Journal of Medicinal Chemistry*, 62, pp.777-784.

- Ohshima, K. et al., 1996. TTA.TAA triplet repeats in plasmids form a non-H bonded structure. *Journal of Biological Chemistry*, 271(28), pp.16784-16791.
- Olowe, S.A., 1975. A case of congenital trypanosomiasis in Lagos. *Transactions of the Royal Society of Tropical Medicine and Hygiene*, 69(1), pp.57-59.
- Opperdoes, F.R. & Borst, P., 1977. Localization of nine glycolytic enzymes in a microbody-like organelle in *Trypanosoma brucei*: The glycosome. *The Federation of European Biochemical Societies Letters*, 80(2), pp.360-364.
- Owen, D.J. et al., 1999. A structural explanation for the binding of multiple ligands by the μ - adaptin appendage domain. *Cell*, 97(6), pp.805-815.
- Palm, W. & de Lange, T., 2008. How shelterin protects mammalian telomeres. *Annual Review of Genetics*, 42, pp.301-334.
- Palmer, G.H., Bankhead, T. & Lukehart, S.A., 2009. "Nothing is permanent but change" -- Antigenic variation in persistent bacterial pathogens. *Cellular Microbiology*, 11(12), pp.1697-1705.
- Pan, X. et al., 2012. Identification of novel genes involved in DNA damage response by screening a genome-wide *Schizosaccharomyces pombe* deletion library. *BioMedCentral Genomics*, 13, pp.1-15.
- Pandya, U.M., Sandhu, R. & Li, B., 2013. Silencing subtelomeric VSGs by *Trypanosoma brucei* RAP1 at the insect stage involves chromatin structure changes. *Nucleic Acids Research*, 41(16), pp.7673-7682.
- Park, B.-C. et al., 2015. The clathrin-binding and J-domains of GAK support the uncoating and chaperoning of clathrin by Hsc70 in the brain. *Journal of Cell Science*, pp.3811-3821.
- Parsons, M. et al., 2005. Comparative analysis of the kinomes of three pathogenic trypanosomatids: *Leishmania major*, *Trypanosoma brucei* and *Trypanosoma cruzi*. *BioMedCentral Genomics*, 6, p.127.
- Parsons, M. et al., 1991. Distinct patterns of tyrosine phosphorylation during the life cycle of *Trypanosoma brucei*. *Molecular and Biochemical Parasitology*, 45(2), pp.241-248.
- Passos-Silva, D.G. et al., 2010. Overview of DNA Repair in *Trypanosoma cruzi*, *Trypanosoma brucei*, and *Leishmania major*. *Journal of Nucleic Acids*, (2010), pp.840768.
- Paulsen, R.D. & Cimprich, K.A., 2007. The ATR pathway: Fine-tuning the fork.

DNA Repair, 6(7), pp.953-966.

- Pays, E. et al., 2001. The VSG expression sites of *Trypanosoma brucei*: multipurpose tools for the adaptation of the parasite to mammalian hosts. *Molecular and Biochemical Parasitology*, 114(1), pp.1-16.
- Peacock, L. et al., 2011. Identification of the meiotic life cycle stage of *Trypanosoma brucei* in the tsetse fly. *Proceedings of the National Academy of Sciences*, 108(9), pp.3671-3676.
- Peixoto, L. et al., 2010. Integrative genomic approaches highlight a family of parasite-specific kinases that regulate host responses. *Cell Host & Microbe*, 8(2), pp.208-218.
- Peng, D. et al., 2015. CRISPR-Cas9-mediated single-gene and gene family disruption in *Trypanosoma cruzi*. *mBio*, 6(1): e02097-14.
- Peng, Y.H. et al., 2009. Nak regulates Dlg basal localization in *Drosophila* salivary gland cells. *Biochemical and Biophysical Research Communications*, 382(1), pp.108-113.
- Pennarun, G. et al., 2010. ATR contributes to telomere maintenance in human cells. *Nucleic Acids Research*, 38(9), pp.2955-2963.
- Pépin, J. et al., 1995. Risk factors for encephalopathy and mortality during melarsoprol treatment of *Trypanosoma brucei gambiense* sleeping sickness. *Transactions of the Royal Society of Tropical Medicine and Hygiene*, 89(1), pp.92-97.
- Perry, J. & Kleckner, N., 2003. The ATRs, ATMs, and TORs are giant HEAT repeat proteins. *Cell*, 112(2), pp.151-155.
- Petsalaki, E. & Zachos, G., 2013. Chk1 and Mps1 jointly regulate correction of merotelic kinetochore attachments. *Journal of Cell Science*, 126(5), pp.1235-1246.
- Picozzi, K. et al., 2005. Sleeping sickness in Uganda: a thin line between two fatal diseases. *British Medical Journal*, 331(7527), pp.1238-1241.
- Podhorecka, M., Skladanowski, A. & Bozko, P., 2011. H2AX phosphorylation: Its role in DNA damage response and cancer therapy. *Journal of Nucleic Acids*, 2011, pp.1-9.
- Povelones, M.L. et al., 2012. Histone H1 plays a role in heterochromatin formation and VSG expression site silencing in *Trypanosoma brucei*. *PLoS Pathogens*, 8(11): e1003010.
- Praefcke, G.J.K. & McMahon, H.T., 2004. The dynamin superfamily: universal membrane tubulation and fission molecules? *Nature Reviews. Molecular cell*

biology, 5(2), pp.133-47.

- Preußner, C., Jaé, N. & Bindereif, A., 2012. mRNA splicing in trypanosomes. *International Journal of Medical Microbiology*, 302(4-5), pp.221-224.
- Priotto, G. et al., 2007. Nifurtimox-Eflornithine combination therapy for second-stage *Trypanosoma brucei gambiense* Sleeping Sickness: A randomized clinical trial in Congo. *Clinical Infectious Diseases*, 45(11), pp.1435-1442.
- Proudfoot, C. & McCulloch, R., 2006. *Trypanosoma brucei* DMC1 does not act in DNA recombination, repair or antigenic variation in bloodstream stage cells. *Molecular and Biochemical Parasitology*, 145(2), pp.245-253.
- Prudêncio, M. et al., 2008. Kinome-side RNAi screen implicates at least 5 host hepatocyte kinases in *Plasmodium* sporozoite infection. *PLoS Pathogens*, 4(11): e1000201
- Putters, J. et al., 2011. Jak2 is a negative regulator of ubiquitin-dependent endocytosis of the growth hormone receptor. *PLoS ONE*, 6(2): e14676
- Puttick, J., Baker, E.N. & Delbaere, L.T.J., 2008. Histidine phosphorylation in biological systems. *Biochimica et Biophysica Acta (BBA) - Proteins and Proteomics*, 1784(1), pp.100-105.
- Ravi, D. et al., 2009. A network of conserved damage survival pathways revealed by a genomic RNAi screen. *PLoS Genetics*, 5(6): e1000527
- Regis-da-Silva, C.G. et al., 2006. Characterization of the *Trypanosoma cruzi* Rad51 gene and its role in recombination events associated with the parasite resistance to ionizing radiation. *Molecular and Biochemical Parasitology*, 149(2), pp.191-200.
- Reiterer, V., Eyers, P. a. & Farhan, H., 2014. Day of the dead: pseudokinases and pseudophosphatases in physiology and disease. *Trends in Cell Biology*, 24(9), pp.489-505.
- Reynolds, D. et al., 2014. Regulation of transcription termination by glucosylated hydroxymethyluracil, base J, in *Leishmania major* and *Trypanosoma brucei*. *Nucleic Acids Research*, 42(15), pp.9717-9729.
- Ricotta, D. et al., 2002. Phosphorylation of the AP2 β subunit by AAK1 mediates high affinity binding to membrane protein sorting signals. *Journal of Cell Biology*, 156(5), pp.791-795.
- Riefler, G.M., Dent, S.Y.R. & Schumacher, J.M., 2008. Tousled-mediated activation of Aurora B kinase does not require tousled kinase activity in vivo. *Journal of Biological Chemistry*, 283(19), pp.12763-12768.
- Ritchey, L. & Chakrabarti, R., 2014. Aurora A kinase modulates actin

cytoskeleton through phosphorylation of Cofilin: Implication in the mitotic process. *Biochimica et Biophysica Acta - Molecular Cell Research*, 1843(11), pp.2719-2729.

- Ritchie, K.B., Mallory, J.C. & Petes, T.D., 1999. Interactions of TLC1 (which encodes the RNA subunit of telomerase), TEL1, and MEC1 in regulating telomere length in the yeast *Saccharomyces cerevisiae*. *Molecular and Cellular Biology*, 19(9), pp.6065-6075.
- Rocha, G. et al., 2004. Possible cases of sexual and congenital transmission of sleeping sickness. *Lancet*, 363(9404), p.247.
- Rohban, S. & Campaner, S., 2015. Myc induced replicative stress response: How to cope with it and exploit it. *Biochimica et Biophysica Acta (BBA) - Gene Regulatory Mechanisms*, 1849(5), pp.517-524.
- Rooney, J.P. et al., 2009. Systems based mapping demonstrates that recovery from alkylation damage requires DNA repair, RNA processing, and translation associated networks. *Genomics*, 93(1), pp.42-51.
- Rudenko, G. et al., 1998. Selection for activation of a new variant surface glycoprotein gene expression site in *Trypanosoma brucei* can result in deletion of the old one. *Molecular and Biochemical Parasitology*, 95(1), pp.97-109.
- Rudenko, G. et al., 1996. Telomere exchange can be an important mechanism of Variant Surface Glycoprotein gene switching in *Trypanosoma brucei*. *Molecular and Biochemical Parasitology*, 80(1), pp.65-75.
- Ruzankina, Y. et al., 2007. Deletion of ATR gene in adult mice leads to stem cell loss. , 1(1), pp.113-126.
- Samudio, I. & Vélez, J., 2015. Targeted Therapy of Acute Myeloid Leukemia. *Targeted Therapy of Acute Myeloid Leukemi*, pp.725-733.
- Santolini, E. et al., 2000. Numb is an endocytic protein. *Journal of Cell Biology*, 151(6), pp.1345-1351.
- Sasai, K. et al., 2004. Aurora-C kinase is a novel chromosomal passenger protein that can complement Aurora-B kinase function in mitotic cells. *Cell Motility and the Cytoskeleton*, 59(4), pp.249-263.
- Satoh, D. et al., 2008. Spatial control of branching within dendritic arbors by dynein-dependent transport of Rab5-endosomes. *Nature Cell Biology*, 10(10), pp.1164-1171.
- Savitsky, K. et al., 1995. A single ataxia telangiectasia gene with a product similar to PI-3 kinase. *Science*, 268(5218), p.1749 LP-1753.

- Schatz, D.G. & Ji, Y., 2011. Recombination centres and the orchestration of V(D)J recombination. *Nature Review Immunology*, 11(4), pp.251-263.
- Schindelin, J. et al., 2012. Fiji: an open-source platform for biological-image analysis. *Nature Methods*, 9(7), pp.676-682.
- Schmelzle, T. & Hall, M.N., 2000. TOR, a central controller of cell growth. *Cell*, 103(2), pp.253-262.
- Schmidt, L. et al., 2014. ATMIN is required for the ATM-mediated signaling and recruitment of 53BP1 to DNA damage sites upon replication stress. *DNA Repair*, 24, pp.122-130.
- Schwede, A. et al., 2011. The VSG C-terminal domain is inaccessible to antibodies on live trypanosomes. *Molecular and Biochemical Parasitology*, 175(2), pp.201-204.
- Seidel, J.J., Anderson, C.M. & Blackburn, E.H., 2008. A novel Tel1/ATM N-terminal motif, TAN, is essential for telomere length maintenance and a DNA damage response. *Molecular and Cellular Biology*, 28(18), pp.5736-46.
- Semerdjieva, S. et al., 2008. Coordinated regulation of AP2 uncoating from clathrin-coated vesicles by rab5 and hRME-6. *Journal of Cell Biology*, 183(3), pp.499-511.
- Shchemelinin, I., Sefc, L. & Necas, E., 2006. Protein kinases, their function and implication in cancer and other diseases. *Folia Biologica*, 52(3), pp.81-100.
- Sheder, K., te Vruchte, D. & Rudenko, G., 2004. Bloodstream form-specific up-regulation of silent vsg expression sites and procyclin in *Trypanosoma brucei* after inhibition of DNA synthesis or DNA damage. *Journal of Biological Chemistry*, 279(14), pp.13363-13374.
- Shechter, D., Costanzo, V. & Gautier, J., 2004. ATR and ATM regulate the timing of DNA replication origin firing. *Nature Cell Biology*, 6(7), pp.648-655.
- Shen, D.-W. et al., 2012. Cisplatin resistance: a cellular self-defense mechanism resulting from multiple epigenetic and genetic changes. *Pharmacological Reviews*, 64(3), pp.706-21.
- Shiloh, Y. & Ziv, Y., 2013. The ATM protein kinase: regulating the cellular response to genotoxic stress, and more. *Nature Reviews. Molecular Cell Biology*, 14(4), pp.197-210.
- Shin, H.W. et al., 2005. An enzymatic cascade of Rab5 effectors regulates phosphoinositide turnover in the endocytic pathway. *Journal of Cell Biology*, 170(4), pp.607-618.
- Shiotani, B. et al., 2013. Two distinct modes of ATR activation orchestrated by

- Rad17 and Nbs1. *Cell Reports*, 3(5), pp.1651-1662.
- Sibanda, B.L., Chirgadze, D.Y. & Blundell, T.L., 2010. Crystal structure of DNA-PKcs reveals a large open-ring cradle comprised of HEAT repeats. *Nature*, 463(7277), pp.118-21.
- Sibley, L.D. et al., 2009. Forward genetics in *Toxoplasma gondii* reveals a family of rhoptry kinases that mediates pathogenesis. *Eukaryotic Cell*, 8(8), pp.1085-1093.
- Siegel, T.N. et al., 2009. Four histone variants mark the boundaries of polycistronic transcription units in *Trypanosoma brucei*. *Genes & Development*, 23(9), pp.1063-1076.
- Silljé, H.H.W. et al., 1999. Mammalian homologues of the plant Tousled gene code for cell-cycle-regulated kinases with maximal activities linked to ongoing DNA replication. *European Molecular Biology Organization Journal*, 18(20), pp.5691-5702.
- Simo, G. et al., 2006. High prevalence of *Trypanosoma brucei gambiense* group 1 in pigs from the Fontem sleeping sickness focus in Cameroon. *Veterinary Parasitology*, 139(1-3), pp.57-66.
- Simpson, A.G.B., Stevens, J.R. & Lukeš, J., 2006. The evolution and diversity of kinetoplastid flagellates. *Trends in Parasitology*, 22(4), pp.168-174.
- Sims, D. et al., 2011. High-throughput RNA interference screening using pooled shRNA libraries and next generation sequencing. *Genome Biology*, 12(10), pp.1-13.
- Smith, A.J. et al., 2012. *Giardia lamblia* Nek1 and Nek2 kinases affect mitosis and excystation. *International Journal for Parasitology*, 42(4), pp.411-419.
- Smith, S.C. et al., 2014. A gemcitabine sensitivity screen identifies a role for NEK9 in the replication stress response. *Nucleic Acids Research*, 42(18), pp.11517-11527.
- Smith, S.L. et al., 2005. Overexpression of aurora B kinase (AURKB) in primary non-small cell lung carcinoma is frequent, generally driven from one allele, and correlates with the level of genetic instability. *British Journal of Cancer*, 93(6), pp.719-729.
- Smythe, E. & Ayscough, K., 2003. The Ark1/Prk1 family of protein kinases. *European Molecular Biology Organization Reports*, 4(3), pp.246-251.
- Sorensen, E.B. & Conner, S.D., 2008. AAK1 regulates Numb function at an early step in clathrin-mediated endocytosis. *Traffic*, 9(10), pp.1791-1800.
- Sorrell, F.J. et al., 2016. Family-wide structural analysis of human Numb-

Associated protein kinases. *Structure*, 24(3), pp.401-411.

- Sourisseau, T. et al., 2010. Aurora-A expressing tumour cells are deficient for homology-directed DNA double strand-break repair and sensitive to PARP inhibition. *European Microbiology Biology Organization Molecular Medicine*, 2(4), pp.130-142.
- Sowd, G.A., Li, N.Y. & Fanning, E., 2013. ATM and ATR Activities maintain replication fork integrity during SV40 chromatin replication. *PLoS Pathogens*, 9(4): e1003283
- Stephens, N. a. et al., 2012. Trypanosome resistance to human innate immunity: Targeting Achilles' heel. *Trends in Parasitology*, 28(12), pp.539-545.
- Steverding, D., 2008. The history of African trypanosomiasis. *Parasites & Vectors*, 1(1), p.3.
- Stewart, S. & Fang, G., 2005. Destruction box-dependent degradation of Aurora B is mediated by the anaphase-promoting complex/cyclosome and Cdh1. *Cancer Research*, 65(19), pp.8730-8735.
- Stijlemans, B. et al., 2016. Immune evasion strategies of *Trypanosoma brucei* within the mammalian host: Progression to pathogenicity. *Frontiers in Immunology*, 7, p.233.
- Stuart, K.D. et al., 2016. Complex management: RNA editing in trypanosomes. *Trends in Biochemical Sciences*, 30(2), pp.97-105.
- Sudarshi, D. et al., 2014. Human African Trypanosomiasis presenting at least 29 years after infection. What can this teach us about the pathogenesis and control of this neglected tropical disease? *PLoS Neglected Tropical Diseases*, 8(12), pp.8-12.
- Sun, H. et al., 2014. Aurora-A controls cancer cell radio- and chemoresistance via ATM/Chk2-mediated DNA repair networks. *Biochimica et Biophysica Acta - Molecular Cell Research*, 1843(5), pp.934-944.
- Sun, Y. et al., 2007. DNA damage-induced acetylation of lysine 3016 of ATM activates ATM kinase activity. *Molecular and Cellular Biology*, 27(24), pp.8502-8509.
- Suwaki, N., Klare, K. & Tarsounas, M., 2011. RAD51 paralogs: Roles in DNA damage signalling, recombinational repair and tumorigenesis. *Seminars in Cell & Developmental Biology*, 22(8), pp.898-905.
- Takai, H. et al., 2007. Tel2 regulates the stability of PI3K-Related protein kinases. *Cell*, 131(7), pp.1248-1259.
- Tan, K.S.W., Leal, S.T.G. & Cross, G.A.M., 2002. *Trypanosoma brucei* MRE11 is

- non-essential but influences growth, homologous recombination and DNA double-strand break repair. *Molecular and Biochemical Parasitology*, 125(1-2), pp.11-21.
- Tao, Y. et al., 2007. Enhancement of radiation response by inhibition of Aurora-A kinase using siRNA or a selective Aurora kinase inhibitor PHA680632 in p53-deficient cancer cells. *British Journal of Cancer*, 97(12), pp.1664-1672.
- Tao, Y. et al., 2008. Enhancement of radiation response in p53-deficient cancer cells by the Aurora-B kinase inhibitor AZD1152. *Oncogene*, 27(23), pp.3244-3255.
- Taylor, S.S. & Kornev, A.P., 2011. Protein kinases: evolution of dynamic regulatory proteins. *Trends in Biochemical Sciences*, 36(2), pp.65-77.
- Tiengwe, C. et al., 2012. Genome-wide analysis reveals extensive functional interaction between DNA replication initiation and transcription in the genome of *Trypanosoma brucei*. *Cell Reports*, 2(1), pp.185-197.
- Tiengwe, C., Marques, C.A. & McCulloch, R., 2014. Nuclear DNA replication initiation in kinetoplastid parasites: New insights into an ancient process. *Trends in Parasitology*, 30(1), pp.27-36.
- Towbin, B.D., Meister, P. & Gasser, S.M., 2009. The nuclear envelope – a scaffold for silencing? *Current Opinion in Genetics & Development*, 19(2), pp.180-186.
- Trenaman, A. et al., 2013. *Trypanosoma brucei* BRCA2 acts in a life cycle-specific genome stability process and dictates BRC repeat number-dependent RAD51 subnuclear dynamics. *Nucleic Acids Research*, 41(2), pp.943-960.
- Trenz, K. et al., 2006. ATM and ATR promote Mre11 dependent restart of collapsed replication forks and prevent accumulation of DNA breaks. *The European Molecular Biology Organization Journal*, 25(8), pp.1764-1774.
- Trindade, S. et al., 2016. *Trypanosoma brucei* parasites occupy and functionally adapt to the adipose tissue in mice. *Cell Host & Microbe*, 19(6), pp.837-848.
- Tu, X. et al., 2006. An aurora kinase homologue is involved in regulating both mitosis and cytokinesis in *Trypanosoma brucei*. *Journal of Biological Chemistry*, 281(14), pp.9677-9687.
- Tu, X. & Wang, C.C., 2004. The involvement of two cdc2-related kinases (CRKs) in *Trypanosoma brucei* cell cycle regulation and the distinctive stage-specific phenotypes caused by CRK3 depletion. *Journal of Biological Chemistry*, 279(19), pp.20519-20528.
- Turner, C.M. & Barry, J.D., 1989. High frequency of antigenic variation in

Trypanosoma brucei rhodesiense infections. *Parasitology*, 99 Pt 1, pp.67-75.

- Umeda, A., Meyerholz, A. & Ungewickell, E., 2000. Identification of the universal cofactor (auxilin 2) in clathrin coat dissociation. *European Journal of Cell Biology*, 79(5), pp.336-42.
- Urbaniak, M.D., Martin, D.M.A. & Ferguson, M.A.J., 2013. Global quantitative SILAC phosphoproteomics reveals differential phosphorylation is widespread between the procyclic and bloodstream form lifecycle stages of *Trypanosoma brucei*. *Journal of Proteome Research*, 12(5), pp.2233-2244.
- Urwyler, S. et al., 2007. A family of stage-specific alanine-rich proteins on the surface of epimastigote forms of *Trypanosoma brucei*. *Molecular Microbiology*, 63(1), pp.218-228.
- Vader, G. & Lens, S.M.A., 2008. The Aurora kinase family in cell division and cancer. *Biochimica et Biophysica Acta (BBA)*, 1786(1), pp.60-72.
- Vader, G., Medema, R.H. & Lens, S.M.A., 2006. The chromosomal passenger complex: Guiding Aurora-B through mitosis. *Journal of Cell Biology*, 173(6), pp.833-837.
- Vespa, L. et al., 2005. ATM and ATR make distinct contributions to chromosome end protection and the maintenance of telomeric DNA in *Arabidopsis*. *Genes and Development*, 19(18), pp.2111-2115.
- Vieira, H.G.S. et al., 2014. Proteomic analysis of *Trypanosoma cruzi* response to ionizing radiation stress. *PLoS ONE*, 9(5): e97526
- Walsh, P. et al., 2004. The J-protein family: modulating protein assembly, disassembly and translocation. *European Molecular Biology Organization Reports*, 5(6), pp.567-571.
- Wang, Q. et al., 2014. Structural basis for the extended CAP-Gly domains of p150glued binding to microtubules and the implication for tubulin dynamics. *Proceedings of the National Academy of Sciences*, pp.1-6.
- Wang, X. et al., 2016. Structure of the intact ATM/Tel1 kinase. *Nature Communications*, 7, p.11655.
- Wang, X.X. et al., 2006. Overexpression of Aurora-A kinase promotes tumor cell proliferation and inhibits apoptosis in esophageal squamous cell carcinoma cell line. *Cell Research*, 16(4), pp.356-366.
- Wang, Y. et al., 2014. Aurora-A: A potential DNA repair modulator. *Tumor Biology*, 35(4), pp.2831-2836.
- Weber, A.M. & Ryan, A.J., 2015. ATM and ATR as therapeutic targets in cancer. *Pharmacology and Therapeutics*, 149, pp.124-138.

- Wegner, D.H. & Rohwedder, R.W., 1972. Experience with nifurtimox in chronic Chagas' infection. Preliminary report. *Arzneimittel-Forschung*, 22(9), pp.1635-1641.
- Wei, Y. & Li, Z., 2014. Distinct roles of a mitogen-activated protein kinase in cytokinesis between different life cycle forms of *Trypanosoma brucei*. *Eukaryotic Cell*, 13(1), pp.110-118.
- Weimer, A.K. et al., 2016. Aurora Kinases Throughout Plant Development. *Trends in Plant Science*, 21(1), pp.69-79.
- Wheeler, R.J. et al., 2013. Cytokinesis in *Trypanosoma brucei* differs between bloodstream and tsetse trypomastigote forms: implications for microtubule-based morphogenesis and mutant analysis. *Molecular Microbiology*, 90(6), pp.1339-1355.
- Wickstead, B., Ersfeld, K. & Gull, K., 2004. The small chromosomes of *Trypanosoma brucei* involved in antigenic variation are constructed around repetitive palindromes. *Genome Research*, 14(6), pp.1014-1024.
- Wiese, M., 1998. A mitogen-activated protein (MAP) kinase homologue of *Leishmania mexicana* is essential for parasite survival in the infected host. *The European Molecular Biology Organization Journal*, 17(9), pp.2619-2628.
- Wilsker, D. & Bunz, F., 2007. Loss of ataxia telangiectasia mutated- and Rad3-related function potentiates the effects of chemotherapeutic drugs on cancer cell survival. *Molecular Cancer Therapeutics*, 6(4), pp.1406-1413.
- Wilson, R.C. & Doudna, J.A., 2013. Molecular Mechanisms of RNA Interference. *Annual Review of Biophysics*, 42(1), pp.217-239.
- Woodward, R. & Gull, K., 1990. Timing of nuclear and kinetoplast DNA replication and early morphological events in the cell cycle of *Trypanosoma brucei*. *Journal of Cell Science*, 95(1), p.49 LP-57.
- Wyatt, M.D. & Pittman, D.L., 2006. Methylating agents and DNA repair responses: Methylated bases and sources of strand breaks. *Chemical Research in Toxicology*, 19(12), pp.1580-1594.
- Wyrick, J.J. et al., 1999. Chromosomal landscape of nucleosome-dependent gene expression and silencing in yeast. *Nature*, 402(6760), pp.418-421.
- Xie, S. et al., 2001. Reactive oxygen species-induced phosphorylation of p53 on serine 20 is mediated in part by polo-like kinase-3. *Journal of Biological Chemistry*, 276(39), pp.36194-36199.
- Xing, Y. et al., 2010. Structure of clathrin coat with bound Hsc70 and auxilin: mechanism of Hsc70-facilitated disassembly. *The European Molecular Biology Organization Journal*, 29(3), pp.655-665.

- Xu, Y. et al., 1996. Targeted disruption of ATM leads to growth retardation, chromosomal fragmentation during meiosis, immune defects, and thymic lymphoma. *Genes & Development*, 10(19), pp.2411-2422.
- Yamamoto, K. et al., 2012. Kinase-dead ATM protein causes genomic instability and early embryonic lethality in mice. *Journal of Cell Biology*, 198(3), pp.305-313.
- Yang, G. et al., 2010. Aurora Kinase A promotes ovarian tumorigenesis through dysregulation of the cell cycle and suppression of BRCA2. *Clinical Cancer Research*, 16(12), p.3171 LP-3181.
- Yang, H. et al., 2013. mTOR kinase structure, mechanism and regulation. *Nature*, 497(7448), pp.217-23.
- Yang, W.K. et al., 2011. Nak regulates localization of clathrin sites in higher-order dendrites to promote local dendrite growth. *Neuron*, 72(2), pp.285-299.
- Yang, X. et al., 2009. RAP1 is essential for silencing telomeric variant surface glycoprotein genes in *Trypanosoma brucei*. *Cell*, 137(1), pp.99-109.
- Yu, H., 2007. Chk1: A double agent in cell cycle checkpoints. *Developmental Cell*, 12(2), pp.167-168.
- Zeman, M.K. & Cimprich, K.A., 2014. Causes and Consequences of Replication Stress. *Nature Cell Biology*, 16(1), pp.2-9.
- Zeqiraj, E. & van Aalten, D.M.F., 2010. Pseudokinases-remnants of evolution or key allosteric regulators? *Current Opinion in Structural Biology*, 20(6), pp.772-781.
- Zhang, C.X. et al., 2005. Multiple roles for cyclin G-associated kinase in clathrin-mediated sorting events. *Traffic*, 6(12), pp.1103-1113.
- Zhang, H. et al., 2012. The role of pseudokinases in cancer. *Cellular Signalling*, 24(6), pp.1173-1184.
- Zhang, W. & Matlashewski, G., 2015. CRISPR-Cas9-Mediated Genome Editing in *Leishmania donovani*. *American Society for Microbiology*, 6(4), p.e00861.
- Zhou, Q. et al., 2016. Two distinct cytokinesis pathways drive trypanosome cell division initiation from opposite cell ends. *Proceedings of the National Academy of Sciences of the United States of America*, 113(12), pp.3287-92.
- Ziegelbauer, K. & Overath, P., 1993. Organization of two invariant surface glycoproteins in the surface coat of *Trypanosoma brucei*. *Infection and Immunity*, 61(11), pp.4540-4545.

- Zíková, A. et al., 2009. The F0F1-ATP synthase complex contains novel subunits and is essential for procyclic *Trypanosoma brucei*. *PLoS Pathogens*, 5(5): e1000436
- Zilfou, J.T. & Lowe, S.W., 2009. Tumor suppressive functions of p53. *Cold Spring Harbor Perspectives in Biology*, 1(5), pp.1-12.
- Zuber, J. et al., 2011. Toolkit for evaluating genes required for proliferation and survival using tetracycline-regulated RNAi. *Nature Biotechnology*, 29(1), pp.79-83.